

Bone growth in a baby
titanosaur pp. 395 & 450

Making magnetic
graphene pp. 415 & 437

Why flu is worse in
the elderly p. 463

Science

\$15
22 APRIL 2016
sciencemag.org

AAAS



Malaria wars

Battling multiple
drug resistance in
Southeast Asia p. 398

CONTENTS



394

Horned beetles put evolution to the test

22 APRIL 2016 • VOLUME 352 • ISSUE 6284



FEATURES

398 MALARIA WARS

Can malaria be eliminated from the Mekong region before multiple-drug resistance makes it untreatable? *By L. Roberts*

403 Skirmishing over the scope of the threat

By L. Roberts

404 Rubber workers on the front lines

By L. Roberts

405 THE UNLIKELY DIPLOMAT

Myaing Myaing Nyunt fled Myanmar in 1988; now she is back, forging alliances against malaria *By L. Roberts*

407 THE VILLAGE RECRUITER

In tests of a controversial strategy, advance liaison to often-skeptical villagers is crucial *By L. Roberts*

ON THE COVER



Migrant workers such as this man, one of nearly 50 workers employed at a farm in Palin, Cambodia, near the border with

Thailand, are at especially high risk of contracting malaria. Reaching them is one of many challenges facing an ambitious new effort to wipe out all malaria from the Greater Mekong subregion by 2030. See page 398. *Photo: Jeffrey Lau*

NEWS

IN BRIEF

388 News at a glance

IN DEPTH

391 REFUGEE CRISIS BRINGS NEW HEALTH CHALLENGES

Imported pathogens are a much bigger threat to migrants than they are to Europeans *By K. Kupferschmidt*

392 HOW SIGN LANGUAGES EVOLVE

Young sign languages develop in predictable ways, offering clues to language evolution *By C. Maticic*

393 NO DEADLINE, FEWER REQUESTS

National Science Foundation trial spurs drop in proposals *By E. Hand*

394 TEMPLETON GRANT FUNDS EVOLUTION RETHINK

\$8.7 million to test controversial ideas about how organisms influence their evolution *By E. Pennisi*

395 THE TINIEST TITAN

Fossil shows that even the youngest titanosaurs were ready to take on the world *By P. Monahan*

► REPORT P. 450

396 DATA CHECK: WHEN THE PAYOFF FOR ACADEMICS DROPS, COMMERCIALIZATION SUFFERS

A change in Norway's laws leads to sharp drop in the number of patents and startups by academics *By J. Mervis*

397 CADAVER STUDY CHALLENGES BRAIN STIMULATION METHODS

Unusual test of transcranial stimulation shows that little electrical current penetrates the skull *By E. Underwood*

INSIGHTS

PERSPECTIVES

408 WASTE NOT, WANT NOT, EMIT LESS

Reducing food waste in the supply chain and at home can help to reduce carbon emissions *By J. Aschemann-Witzel*

410 ELECTRONS CATCH A TERAHERTZ WAVE

Far-infrared fields control ultrashort electron pulses *By C. Ropers*

► RESEARCH ARTICLE P. 429

411 MINERAL CLUES TO PAST VOLCANISM

A study of zircon minerals from around the world shows that volcanism is a key driver of long-term climate change *By L. Kump*

► REPORT P. 444

413 RISK LITERACY IN MEDICAL DECISION-MAKING

How can we better represent the statistical structure of risk?

By J. T. Operskalski and A. K. Barbey

415 PAINTING MAGNETISM ON A CANVAS OF GRAPHENE

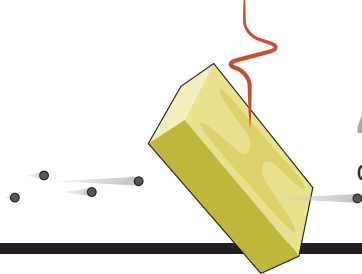
Hydrogen adatoms can give long-range magnetic order to graphene

By S. M. Hollen and J. A. Gupta

► REPORT P. 437



411 & 444



410 & 429

Controlling electron bursts



427

How immune cells remember

416 FILLING IN BIODIVERSITY THREAT GAPS

Only 5% of global threat data sets meet a "gold standard" *By L. N. Joppa et al.*

BOOKS ET AL.

420 CLEOPATRA'S NEEDLES

By B. Brier, reviewed by A. Robinson

421 LYSENKO'S GHOST

By L. Graham, reviewed by M. Meloni

LETTERS

422 INSTITUTING RECRUITING MERITOCRACY IN ITALY

By J. Assad

422 INVASIVE SPECIES SHAPE EVOLUTION

By P. E. Hulme and J. J. Le Roux

422 RESPONSE

By F. Sarrazin and J. Lecomte

423 TECHNICAL COMMENT ABSTRACTS

RESEARCH

IN BRIEF

424 From *Science* and other journals

REVIEW

427 INNATE IMMUNITY

Trained immunity: A program of innate immune memory in health and disease *M. G. Netea et al.*

REVIEW SUMMARY; FOR FULL TEXT:

dx.doi.org/10.1126/science.aaf1098

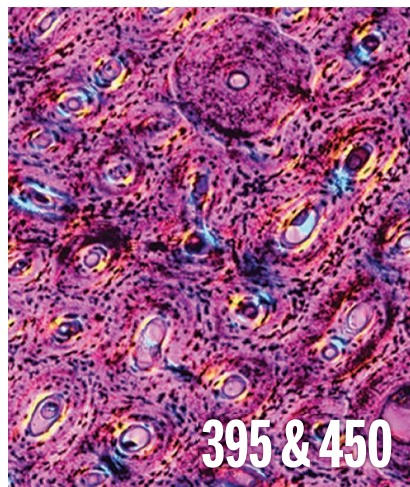
RESEARCH ARTICLES

428 MICROTUBULES

Detyrosinated microtubules buckle and bear load in contracting cardiomyocytes *P. Robison et al.*

RESEARCH ARTICLE SUMMARY; FOR FULL TEXT:

dx.doi.org/10.1126/science.aaf0659



429 ULTRAFAST OPTICS

All-optical control and metrology of electron pulses *C. Kealhofer et al.*

► PERSPECTIVE P. 410

REPORTS

433 ORGANIC CHEMISTRY

Catalytic asymmetric addition of Grignard reagents to alkenyl-substituted aromatic *N*-heterocycles *R. P. Jumde et al.*

437 MAGNETISM

Atomic-scale control of graphene magnetism by using hydrogen atoms *H. González-Herrero et al.*

► PERSPECTIVE P. 415

441 QUANTUM OPTICS

Bell correlations in a Bose-Einstein condensate *R. Schmied et al.*

444 GEOLOGY

Continental arc volcanism as the principal driver of icehouse-greenhouse variability *N. R. McKenzie et al.*

► PERSPECTIVE P. 411

448 BIOINORGANIC CHEMISTRY

Light-driven dinitrogen reduction catalyzed by a CdS:nitrogenase MoFe protein biohybrid *K. A. Brown et al.*

450 PALEONTOLOGY

Precocity in a tiny titanosaur from the Cretaceous of Madagascar *K. C. Rogers et al.*

► NEWS STORY P. 395; PODCAST

453 CELL QUIESCENCE

RNA-binding proteins ZFP36L1 and ZFP36L2 promote cell quiescence *A. Galloway et al.*

459 IMMUNOLOGY

Hobit and Blimp1 instruct a universal transcriptional program of tissue residency in lymphocytes *L. K. Mackay et al.*

463 INNATE IMMUNITY

Mx1 reveals innate pathways to antiviral resistance and lethal influenza disease *P. S. Pillai et al.*

467 STRUCTURAL BIOLOGY

The 3.8 Å resolution cryo-EM structure of Zika virus *D. Sirohi et al.*

470 EVOLUTIONARY GENETICS

A beak size locus in Darwin's finches facilitated character displacement during a drought *S. Lamichhaney et al.*

474 HUMAN GENOMICS

Health and population effects of rare gene knockouts in adult humans with related parents *V. M. Narasimhan et al.*

DEPARTMENTS

387 EDITORIAL

Due process in the Twitter age *By Marcia McNutt*

486 WORKING LIFE

Growth can come in phases *By He Fu*

Science Staff	386
New Products	478
Science Careers	480

SCIENCE (ISSN 0036-8075) is published weekly on Friday, except the last week in December, by the American Association for the Advancement of Science, 1200 New York Avenue, NW, Washington, DC 20005. Periodicals mail postage (publication No. 484460) paid at Washington, DC, and additional mailing offices. Copyright © 2016 by the American Association for the Advancement of Science. The title SCIENCE is a registered trademark of the AAAS. Domestic individual membership and subscription (51 issues): \$165 (\$74 allocated to subscription). Domestic institutional subscription (51 issues): \$1522; foreign postage extra: Mexico, Caribbean (surface mail) \$55; other countries (air assist delivery) \$89. First class, airmail, student, and emeritus rates on request. Canadian rates with GST available upon request. GST #R1254 88122. Publications Mail Agreement Number 1069624. Printed in the U.S.A. Change of address: Allow 4 weeks, giving old and new addresses and 8-digit account number. Postmaster: Send change of address to AAAS, P.O. Box 96178, Washington, DC 20090-6178. Single-copy sales: \$15.00 current issue, \$20.00 back issue prepaid includes surface postage; bulk rates on request. Authorization to photocopy material for internal or personal use under circumstances not falling within the fair use provisions of the Copyright Act is granted by AAAS to libraries and other users registered with the Copyright Clearance Center (CCC) Transactional Reporting Service, provided that \$35.00 per article is paid directly to CCC, 222 Rosewood Drive, Danvers, MA 01923. The identification code for Science is 0036-8075. Science is indexed in the Reader's Guide to Periodical Literature and in several specialized indexes.

Editor-in-Chief Marcia McNutt

Executive Editor Monica M. Bradford **News Editor** Tim Appenzeller

Managing Editor, Research Journals Katrina L. Kelner

Deputy Editors Lisa D. Chong, Andrew M. Sugden(UK), Valda J. Vinson, Jake S. Yeston

Research and Insights

DEPUTY EDITOR, EMERITUS Barbara R. Jasny **SR. EDITORS** Caroline Ash(UK), Gilbert J. Chin, Julia Fahrenkamp-Uppenbrink(UK), Pamela J. Hines, Stella M. Hurlley(UK), Paula A. Kiberstis, Marc S. Lavine(Canada), Kristen L. Mueller, Ian S. Osborne(UK), Beverly A. Purnell, L. Bryan Ray, Guy Riddihough, H. Jesse Smith, Jelena Stajic, Peter Stern(UK), Phillip D. Szurromi, Sacha Vignieri, Brad White, Nicholas S. Wigginton, Laura M. Zahn **ASSOCIATE EDITORS** Brent Grocholski, Keith T. Smith **ASSOCIATION BOOK REVIEW EDITOR** Valerie B. Thompson **LETTERS EDITOR** Jennifer Sills **CHIEF CONTENT PRODUCTION EDITOR** Cara Tate **SR. CONTENT PRODUCTION EDITORS** Harry Jach, Lauren Kmec **CONTENT PRODUCTION EDITORS** Jeffrey E. Cook, Chris Filiatreau, Cynthia Howe, Barbara P. Ordway, Catherine Wolner **SR. EDITORIAL COORDINATORS** Carolyn Kyle, Beverly Shields **EDITORIAL COORDINATORS** Aneera Dobbins, Joi S. Granger, Lisa Johnson, Anita Wynn **PUBLICATIONS ASSISTANTS** Jeffrey Hearn, Dona Mathieu, Le-Toya Mayne Flood, Shannon McMahon, Scott Miller, Caitlyn Phillips, Jerry Richardson, Alice Whaley(UK), Brian White **EXECUTIVE ASSISTANT** Anna Bashkirova **ADMINISTRATIVE SUPPORT** Janet Clements(UK), Lizzanne Newton(UK), Maryrose Madrid

News

NEWS MANAGING EDITOR John Travis **INTERNATIONAL EDITOR** Richard Stone **DEPUTY NEWS EDITORS** Robert Coontz, Elizabeth Culotta, David Grimm, David Malakoff, Leslie Roberts **CONTRIBUTING EDITOR** Martin Enserink(Europe) **SR. CORRESPONDENTS** Daniel Clery(UK), Jeffrey Mervis, Elizabeth Pennisi **NEWS WRITERS** Adrian Cho, Jon Cohen, Jennifer Couzin-Frankel, Carolyn Gramling, Eric Hand, Jocelyn Kaiser, Catherine Maticic, Kelly Servick, Robert F. Service, Erik Stokstad(Cambridge, UK), Emily Underwood **INTERNS** Patrick Monahan **CONTRIBUTING CORRESPONDENTS** John Bohannon, Warren Cornwall, Ann Gibbons, Mara Hvistendahl, Sam Kean, Eli Kintisch, Kai Kupferschmidt(Berlin), Andrew Lawler, Christina Larson(Beijing), Mitch Leslie, Charles C. Mann, Eliot Marshall, Virginia Morell, Dennis Normile(Shanghai), Heather Pringle, Tania Rabesandratana(London), Gretchen Vogel(Berlin), Lizzie Wade(Mexico City) **CAREERS** Donisha Adams, Rachel Bernstein(Editor) **COPY EDITORS** Julia Cole, Dorie Cheveln, Jennifer Levin (Chief) **ADMINISTRATIVE SUPPORT** Jessica Adams

Executive Publisher Rush D. Holt

Interim Publisher Bill Moran **Chief Digital Media Officer** Rob Covey

BUSINESS OPERATIONS AND PORTFOLIO MANAGEMENT DIRECTOR Sarah Whalen **PRODUCT DEVELOPMENT DIRECTOR** Will Schweitzer **PRODUCT DEVELOPMENT ASSOCIATE** Hal Moore **BUSINESS SYSTEMS AND FINANCIAL ANALYSIS DIRECTOR** Randy Yi **MANAGER OF FULFILLMENT SYSTEMS** Neal Hawkins **SYSTEMS ANALYST** Nicole Mehmedovich **ASSISTANT DIRECTOR, BUSINESS OPERATIONS** Eric Knott **MANAGER, BUSINESS OPERATIONS** Jessica Tierney **SENIOR BUSINESS ANALYST** Cory Lipman **BUSINESS ANALYSTS** Sandy Kim, Meron Kebede **FINANCIAL ANALYST** Robert Clark **DIRECTOR, COPYRIGHTS LICENSING SPECIAL PROJECTS** Emilie David **PERMISSIONS ASSOCIATE** Elizabeth Sandler **RIGHTS, CONTRACTS, AND LICENSING ASSOCIATE** Lili Kiser

MARKETING DIRECTOR Elise Swinehart **ASSOCIATE MARKETING DIRECTOR** Christina Schlecht **MARKETING MANAGER** Elizabeth Sattler **MARKETING ASSOCIATE** Steven Goodman **CREATIVE DIRECTOR** Scott Rodgerson **SENIOR ART ASSOCIATES** Seil Lee, Paula Fry **ART ASSOCIATE** Kim Huynh **PROGRAM DIRECTOR, AAAS MEMBER CENTRAL** Peggy Mihelich **FULFILLMENT SYSTEMS AND OPERATIONS** membership@aaas.org **MANAGER, MEMBER SERVICES** Pat Butler **SPECIALISTS** Terrance Morrison, Latasha Russell **MANAGER, DATA ENTRY** Mickie Napoleoni **DATA ENTRY SPECIALISTS** Brenden Aquilino, Fiona Giblin

PUBLISHER RELATIONS MANAGER Catherine Holland **PUBLISHER RELATIONS, EASTERN REGION** Keith Layson **PUBLISHER RELATIONS, WESTERN REGION** Ryan Rexroth **SALES RESEARCH COORDINATOR** Aiesha Marshall **MANAGER, SITE LICENSE OPERATIONS** Iquo Edim **SENIOR OPERATIONS ANALYST** Lana Guz **FULFILLMENT ANALYST** Judy Lillibridge **ASSOCIATE DIRECTOR, MARKETING** Christina Schlecht **MARKETING ASSOCIATE** Isa Sesay-Bah

WEB TECHNOLOGIES SR. DEVELOPER Chris Coleman **DEVELOPERS** Dan Berger, Jimmy Marks, Ryan Jensen **SR. PROJECT MANAGER** Trista Smith **PROJECT MANAGER** Nick Fletcher

DIGITAL MEDIA DIRECTOR OF ANALYTICS Enrique Gonzales **DIGITAL REPORTING ANALYST** Eric Hossinger **SR. WEB PRODUCER** Sarah Crespi **WEB PRODUCER** Alison Crawford **VIDEO PRODUCER** Nguyen Nguyen **SOCIAL MEDIA PRODUCER** Brice Russ

DIRECTOR OF OPERATIONS PRINT AND ONLINE Lizabeth Harman **DIGITAL/PRINT STRATEGY MANAGER** Jason Hillman **QUALITY TECHNICAL MANAGER** Marcus Spiegler **PROJECT ACCOUNT MANAGER** Tara Kelly **DIGITAL PRODUCTION MANAGER** Lisa Stanford **ASSISTANT MANAGER** **DIGITAL/PRINT** Rebecca Doshi **SENIOR CONTENT SPECIALISTS** Steve Forrester, Antoinette Hodal, Lori Murphy, Anthony Rosen **CONTENT SPECIALISTS** Jacob Hedrick, Kimberley Oster

DESIGN DIRECTOR Beth Rakouskas **DESIGN EDITOR** Marcy Atarod **SENIOR DESIGNER** Garvin Grullón **DESIGNER** Chrystal Smith **GRAPHICS MANAGING EDITOR** Alberto Cuadra **SENIOR SCIENTIFIC ILLUSTRATORS** Chris Bickel, Katharine Sutfiff **SCIENTIFIC ILLUSTRATOR** Valerie Altounian **SENIOR ART ASSOCIATES** Holly Bishop, Nathalie Cary, Preston Huey **PHOTOGRAPHY MANAGING EDITOR** William Douthitt **PHOTO EDITORS** Leslie Blizard, Christy Steele

DIRECTOR, GLOBAL COLLABORATION, CUSTOM PUBLICATIONS, ADVERTISING Bill Moran **EDITOR, CUSTOM PUBLISHING** Sean Sanders: 202-326-6430 **ADVERTISING MARKETING MANAGER** Justin Sawyers: 202-326-7061 **science_advertising@aaas.org** **ADVERTISING SUPPORT MANAGER** Karen Foote: 202-326-6740 **ADVERTISING PRODUCTION OPERATIONS MANAGER** Deborah Tompkins **SR. PRODUCTION SPECIALIST/GRAPHIC DESIGNER** Amy Hardcastle **SR. TRAFFIC ASSOCIATE** Christine Hall **SALES COORDINATOR** Shirley Young **ASSOCIATE DIRECTOR, COLLABORATION, CUSTOM PUBLICATIONS/CHINA/TAIWAN/KOREA/SINGAPORE** Ruolei Wu: +86-186 0082 9345, rwu@aaas.org **COLLABORATION/CUSTOM PUBLICATIONS/JAPAN** Adarsh Sandhu + 81532-81-5142 asandhu@aaas.org **EAST COAST/E. CANADA** Laurie Faraday: 508-747-9395, FAX 617-507-8189 **WEST COAST/W. CANADA** Lynne Stickrod: 415-931-9782, FAX 415-520-6940 **MIDWEST** Jeffery Dembski: 847-498-4520 x3005, Steven Loerch: 847-498-4520 x3006 **UK EUROPE/ASIA** Roger Gonçalves: TEL/FAX +41 43 243 1358 **JAPAN** Katsuyoshi Fukamizu(Tokyo): +81-3-3219-5777 fukamizu@aaas.org **CHINA/TAIWAN** Ruolei Wu: +86-186 0082 9345, rwu@aaas.org

WORLDWIDE ASSOCIATE DIRECTOR OF SCIENCE CAREERS Tracy Holmes: +44 (0) 1223 326525, FAX +44 (0) 1223 326532 tholmes@science-int.co.uk **CLASSIFIED** advertising@sciencecareers.org **U.S. SALES** Tina Burks: 202-326-6577, Nancy Toerna: 202-326-6578 **EUROPE/ROW SALES** Sarah Lelarge **SALES ASSISTANT** Kelly Grace **JAPAN** Hiroyuki Mashiki(Kyoto): +81-75-823-1109 hmarshiki@aaas.org **CHINA/TAIWAN** Ruolei Wu: +86-186 0082 9345 rwu@aaas.org **MARKETING MANAGER** Allison Pritchard **MARKETING ASSOCIATE** Aimee Aponte

AAAS BOARD OF DIRECTORS, CHAIR Geraldine L. Richmond **PRESIDENT** Barbara A. Schaaf **PRESIDENT-ELECT** Susan Hockfield **TREASURER** David Evans Shaw **CHIEF EXECUTIVE OFFICER** Rush D. Holt **BOARD** Cynthia M. Beall, May R. Berenbaum, Carlos J. Bustamante, Stephen P.A. Fodor, Claire M. Fraser, Michael S. Gazzaniga, Laura H. Greene, Elizabeth Loftus, Mercedes Pascual

SUBSCRIPTION SERVICES For change of address, missing issues, new orders and renewals, and payment questions: 866-434-AAAS (2227) or 202-326-6417, FAX 202-842-1065. Mailing addresses: AAAS, P.O. Box 96178, Washington, DC 20090-6178 or AAAS Member Services, 1200 New York Avenue, NW, Washington, DC 20005

INSTITUTIONAL SITE LICENSES 202-326-6730 **REPRINTS:** Author Inquiries 800-635-7181 **COMMERCIAL INQUIRIES** 803-359-4578 **PERMISSIONS** 202-326-6765, permissions@aaas.org **AAAS Member Services** 202-326-6417 or <http://membercentral.aaas.org/discounts>

Science serves as a forum for discussion of important issues related to the advancement of science by publishing material on which a consensus has been reached as well as including the presentation of minority of conflicting points of view. Accordingly, all articles published in Science—including editorials, news and comment, and book reviews—are signed and reflect the individual views of the authors and not official points of view adopted by AAAS or the institutions with which the authors are affiliated.

INFORMATION FOR AUTHORS See pages 624 and 625 of the 5 February 2016 issue or access www.sciencemag.org/authors/science-information-authors

SENIOR EDITORIAL BOARD

Gary King, Harvard University, Susan M. Rosenberg, Baylor College of Medicine, Ali Shilatifard, Northwestern University Feinberg School of Medicine

BOARD OF REVIEWING EDITORS (Statistics board members indicated with \$)

Adriano Aguzzi, U. Hospital Zürich
Takuzo Aida, U. of Tokyo
Leslie Aiello, Wenner-Gren Foundation
Judith Allen, U. of Edinburgh
Sonia Altizer, U. of Georgia
Sebastian Amigorena, Institut Curie
Kathryn Anderson, Memorial Sloan-Kettering Cancer Center
Meinrat O. Andreae, Max-Planck Inst. Mainz
Paola Ariotti, Harvard U.
Johan Auwerx, EPFL
David Awechselom, U. of Chicago
Clare Baker, University of Cambridge
Nene Ban, ETH Zurich
Jordi Bascompte, University of Zurich
Ray H. Baughman, U. of Texas, Dallas
David Baum, U. of Wisconsin
Carlo Beenakker, Leiden U.
Kamran Behnia, ESPCI-ParisTech
Yasmine Belkaid, NIAID, NIH
Philip Benfey, Duke U.
May Berenbaum, U. of Illinois
Gabriele Bergers, U. of California, San Francisco
Bradley Bernstein, Massachusetts General Hospital
Peer Bork, EMBL
Bernard Bourdon, Ecole Normale Supérieure de Lyon
Chris Bowler, Ecole Normale Supérieure
Ian Boyd, U. of St. Andrews
Emily Brodsky, U. of California, Santa Cruz
Ron Brookmeyer, U. of California, Los Angeles (\$)
Christian Büchel, U. Hamburg-Eppendorf
Joseph A. Burns, Cornell U.
Carter Tribley Butts, U. of California, Irvine
Gyorgy Buzsaki, New York U. School of Medicine
Blanche Capel, Duke U.
Mats Carlsson, U. of Oslo
Ib Chorkendorff, U. of Denmark
David Clapham, Children's Hospital Boston
Joel Cohen, Rockefeller U., Columbia U.
James J. Collins, MIT
Robert Cook-Deegan, Duke U.
Lisa Coussens, Oregon Health & Science U.
Alan Cowman, Walter & Eliza Hall Inst.
Robert H. Crabtree, Yale U.
Roberta Croce, Vrije Universiteit
Janet Currie, Princeton U.
Jeff L. Dangl, U. of North Carolina
Tom Daniel, U. of Washington
Frans de Waal, Emory U.
Stanislas Dehaene, Collège de France
Robert Desimone, MIT
Claude Desplais, New York U.
Dennis Discher, U. of Pennsylvania
Gerald W. Dorn II, Washington U. School of Medicine
Jennifer A. Doudna, U. of California, Berkeley
Bruce Dunn, U. of California, Los Angeles
William Dunphy, Caltech
Christopher Dye, WHO
Todd Ehlers, U. of Toebingen
David Ehrhardt, Carnegie Inst. of Washington
Tim Elston, U. of North Carolina at Chapel Hill
Gerhard Ertl, Fritz-Haber-Institut, Berlin
Barry Everitt, U. of Cambridge
Ernst Fehr, U. of Zurich
Anne C. Ferguson-Smith, U. of Cambridge
Michael Feuer, The George Washington U.
Toren Finkel, NHLBI, NIH
Kate Fitzgerald, U. of Massachusetts
Peter Fratzl, Max-Planck Inst.
Elaine Fuchs, Rockefeller U.
Daniel Geschwind, UCLA
Karl-Heinz Glassmeier, TU Braunschweig
Ramon Gonzalez, Rice U.
Julia R. Greer, Caltech
Elizabeth Grove, U. of Chicago
Nicolas Gruber, ETH Zurich
Kip Guy, St. Jude's Children's Research Hospital
Taekjip Ha, U. of Illinois at Urbana-Champaign
Wolf-Dietrich Hardt, ETH Zurich
Christian Haass, Ludwig Maximilians U.
Sharon Hammes-Schiffer, U. of Illinois at Urbana-Champaign
Michael Hasselmo, Boston U.
Martin Heimann, Max-Planck Inst. Jena
Yka Helariutta, U. of Cambridge
James A. Hendler, Rensselaer Polytechnic Inst.
Janet G. Hering, Swiss Fed. Inst. of Aquatic Science & Technology
Kai-Uwe Hinrichs, U. of Bremen
David Hodell, U. of Cambridge
Lora Hooper, UT Southwestern Medical Ctr. at Dallas
Tamas Horvath, Yale University
Raymond Huey, U. of Washington
Fred Hughson, Princeton U.
Auke Ijspeert, EPFL Lausanne
Stephen Jackson, USGS and U. of Arizona
Steven Jacobsen, U. of California, Los Angeles
Kai Johnsson, EPFL Lausanne
Peter Jonas, Inst. of Science & Technology (IST) Austria
Matt Kaeberlein, U. of Washington
William Kaelin Jr., Dana-Farber Cancer Inst.
Daniel Kahne, Harvard U.
Daniel Kammen, U. of California, Berkeley
Abby Kavner, U. of California, Los Angeles
Masashi Kawasaki, U. of Tokyo
V. Narry Kim, Seoul National U.

Joel Kingsolver, U. of North Carolina at Chapel Hill
Robert Kingston, Harvard Medical School
Etienne Koechlin, Ecole Normale Supérieure
Alexander Kolodkin, Johns Hopkins U.
Thomas Langer, U. of Cologne
Mitchell A. Lazar, U. of Pennsylvania
David Lazer, Harvard U.
Thomas Lecuit, IBDM
Virginia Lee, U. of Pennsylvania
Stanley Lemon, U. of North Carolina at Chapel Hill
Ottoline Leyser, Cambridge U.
Wendell Lim, U.C. San Francisco
Marcia C. Linn, U. of California, Berkeley
Jiangcuo Liu, Michigan State U.
Luis Liz-Marzan, CIC bioMaGUNE
Jonathan Losos, Harvard U.
Ke Lu, Chinese Acad. of Sciences
Christian Lüscher, U. of Geneva
Laura Machesky, CRUK Beaton Inst. for Cancer Research
Anne Magurran, U. of St. Andrews
Osacar Marin, CSIC & U. Miguel Hernández
Charles Marshall, U. of California, Berkeley
C. Robertson McClung, Dartmouth College
Graham Medley, U. of Warwick
Tom Misteli, NCI
Yasushi Miyashita, U. of Tokyo
Mary Ann Moran, U. of Georgia
Richard Morris, U. of Edinburgh
Alison Motsinger-Reif, NC State U. (\$)
Thomas Murray, The Hastings Center
Daniel Neumark, U. of California, Berkeley
Pär Nijlmeijer, U. of Twente
Kitty Nordlund, Karolinska Inst.
Helga Nowotny, European Research Advisory Board
Ben Olken, MIT
Joe Orenstein, U. of California
Berkeley & Lawrence Berkeley National Lab
Harry Orr, U. of Minnesota
Pilar Ossorio, U. of Wisconsin
Andrew Oswald, U. of Warwick
Steve Palumbi, Stanford U.
Jane Parker, Max-Planck Inst. of Plant Breeding Research
Giovanni Parmiani, Dana-Farber Cancer Inst. (\$)
John H. J. Petrini, Memorial Sloan-Kettering Cancer Center
Samuel Pfaff, Salk Institute for Biological Studies
Joshua Plotkin, U. of Pennsylvania
Albert Polman, FOM Institute AMOLF
Philippe Poulin, CNRS
Jonathan Pritchard, Stanford U.
David Randall, Colorado State U.
Felix Rey, Institut Pasteur
Trevor Robbins, U. of Cambridge
Jim Roberts, Fred Hutchinson Cancer Research Ctr.
Barbara A. Romanowicz, U. of California, Berkeley
Amy Rosenzweig, Northwestern University
Mike Ryan, U. of Texas, Austin
Mitsunori Saitou, Kyoto U.
Shimon Sakaguchi, Kyoto U.
Miquel Salmeron, Lawrence Berkeley National Lab
Jürgen Sandkühler, Medical U. of Vienna
Alexander Schier, Harvard U.
Vladimir Shaloev, Purdue U.
Robert Siliciano, Johns Hopkins School of Medicine
Deni Simon, Arizona State U.
Uri Simonsohn, U. of Pennsylvania
Alison Smith, John Innes Centre
Richard Smith, U. of North Carolina (\$)
John Speakman, U. of Aberdeen
Allan C. Spradling, Carnegie Institution of Washington
Jonathan Sprent, Garvan Inst. of Medical Research
Eric Steig, U. of Washington
Paula Stephan, George State U. and National Bureau of Economic Research
Molly Stevens, Imperial College London
V. S. Subrahmanian, U. of Maryland
Ira Tabas, Columbia U.
Sarah Teichmann, Cambridge U.
John Thomas, North Carolina State U.
Shubha Tole, Tata Institute of Fundamental Research
Christopher Tyler-Smith, The Wellcome Trust Sanger Inst.
Herbert Virgin, Washington U.
Bert Vogelstein, Johns Hopkins U.
Cynthia Volkert, U. of Göttingen
David Wallach, Weizmann Inst. of Science
Ian Walsmsley, U. of Oxford
Jane-Ling Wang, U. of California, Davis (\$)
David A. Wardle, Swedish U. of Agric. Sciences
David Waxman, Fudan U.
Jonathan Weissman, U. of California, San Francisco
Chris Wikle, U. of Missouri (\$)
Ian A. Wilson, The Scripps Res. Inst. (\$)
Timothy D. Wilson, U. of Virginia
Rosemary Wyse, Johns Hopkins U.
Jan Zaenen, Leiden U.
Kenneth Zaret, U. of Pennsylvania School of Medicine
Jonathan Zehr, U. of California, Santa Cruz
Len Zon, Children's Hospital Boston
Maria Zuber, MIT

BOOK REVIEW BOARD

David Bloom, Harvard U. Samuel Bowring, MIT, Angela Creager, Princeton U., Richard Sweder, U. of Chicago, Ed Wasserman, DuPont

Due process in the Twitter age

Until recently, the only insight that the research community had into published papers that might be suspect, and thus candidates for retraction, was through the formal investigations by institutions or funders and the official announcements made by journals. Today, online communities such as PubPeer and Retraction Watch could be the first to raise an alert that a paper may require additional scrutiny. The involvement of such online entities has made the standardization of processes to address allegations more complex and has led to less patience from the scientific community and the public with what are often long timelines in institutional misconduct investigations. Editors are caught in the middle: They want to correct the literature as quickly as possible to avoid misleading readers with flawed information, but they also want to ensure that authors have received due process, even as rumors of scientific misconduct may be amplified through social media. Last month, a Journals Summit convened by the U.S. National Academy of Sciences tackled this topic in the larger context of research integrity, and several solutions emerged.

Journals have their own requirements for author certification of the openness, transparency, and quality of a research paper and can take preemptive action to retract papers if the authors falsify those certifications, even before misconduct investigations have concluded. One example provided was a paper retracted based on lack of availability of the data, falsification of funding sources, and misrepresentation of approval by an institutional review board. In situations where a journal lacks authority to act, but preliminary evidence suggests that a paper will need to be retracted, an “editorial expression of con-

cern” can suitably alert the community that the results may be suspect, without the journal taking irreversible action. Although the summit attendees agreed that only institutions had the necessary access to conduct investigations, those institutions would benefit from the involvement and oversight of an experienced, independent party with no conflict of interest in the matter to speed up the process and ensure a quality outcome. Many participants felt that the stigma of having a retraction is so great that it might discourage authors from removing papers that are flawed because of honest

errors. Finding some other terminology for such situations would help clean up the literature and reward good behavior.

Should there be a statute of limitation on retractions? Two panelists had experiences as editors with requests to retract papers that were published more than 50 years ago. This clearly raises the question of due process. None of the authors were alive to respond to the charges of misconduct. Only incomplete records survived regarding how decisions about those papers were made. The requests were declined. Although panelists did not come up with a fixed amount of time beyond which a paper would be too old to retract, consideration of a paper's current influence and whether evidence exists to provide due process

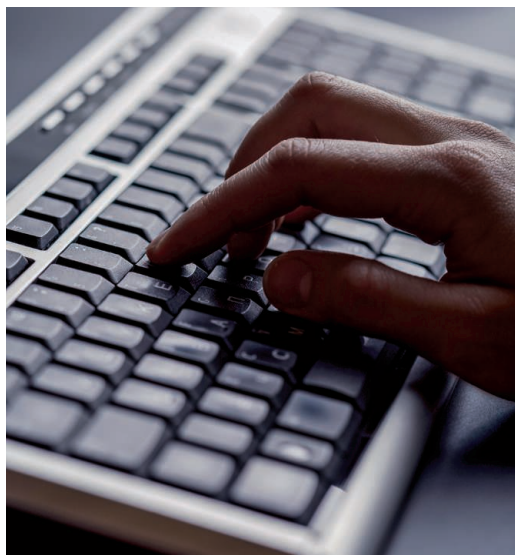
should weigh into the course of action in such cases.

Editors are often caught in the crossfire between impatient readers who may reach conclusions about the validity of misconduct allegations on the basis of incomplete information online, and authors who are concerned about damage to their reputation. In the final analysis, the editor's paramount concern should be for the integrity of the scientific record.

– Marcia McNutt



Marcia McNutt
Editor-in-Chief
Science Journals



“...rumors of scientific misconduct may be amplified through social media.”

“I don't think he was unhappy with us, or lonely, as octopus are solitary creatures. But he is such a curious boy.”

Rob Yarrell of New Zealand's National Aquarium to *The Guardian* about Inky the octopus, who escaped his tank and became a Twitter hero.

IN BRIEF

Quakes devastate Japan, Ecuador



A bridge in Japan's Kumamoto prefecture on Kyushu Island collapsed following a pair of strong quakes.

The collapse of numerous residences during two earthquakes in Japan last week could foreshadow what's in store if a similar temblor strikes California, says Peter Yanev, an earthquake engineer based in Orinda, California. The two quakes, with magnitudes of 6.2 and 7.0, struck Kyushu Island 28 hours apart, killing at least 44 people and totally or partially destroying more than 2000 buildings. More than 200,000 people are homeless. Yanev says the damage to residential structures is as bad as anything he has seen in the 100-plus earthquakes he has investigated. He suspects that the region's geology, combined with the shallow 10-kilometer- and 11-kilometer-deep focus of the quakes, produced “ground motions stronger than what the building code is based on”; the implications for those codes, he adds, “are worth extensive investigation.” Megumi Sugimoto, a hazard management specialist at Kyushu University in Fukuoka, Japan, believes the shallow focus of the quakes also led to numerous landslides that blocked or swept away roads. A far more powerful magnitude 7.8 quake caused extensive damage and killed more than 400 people.

AROUND THE WORLD

CRISPR foods dodge USDA

WASHINGTON, D.C. | The U.S. Department of Agriculture (USDA) has recently clarified its stance on foods modified by the CRISPR-Cas9 gene-editing system, which allows gene editing much more quickly and easily than in the past. Last week, USDA said it would not regulate a genetically modified white button mushroom, engineered by plant pathologist Yinong Yang of Pennsylvania State University, University Park, to reduce the enzyme activity that leads to browning. USDA told Yang that the mushroom doesn't fall under its jurisdiction because the CRISPR-Cas9 method does not incorporate foreign DNA from viruses or bacteria into the mushroom's genome. There are no plans yet to bring the mushroom to market. Meanwhile, Des Moines-based DuPont Pioneer, which produces hybrid seeds for agriculture, announced this week that USDA has affirmed that it will not regulate a waxy corn hybrid edited using CRISPR-Cas9. Waxy corn is high in amylopectin starch, an easily digestible form of starch that is also used in adhesives and high-gloss paper. DuPont Pioneer says it expects to make the corn available to U.S. growers within 5 years, making it the company's first CRISPR-edited commercial product.

Isle Royale's last two wolves

ISLE ROYALE, MICHIGAN | The two remaining wolves on the Lake Superior island of Isle Royale in Michigan have reached a genetic dead end. The wolves, a male and female, are more inbred than any known wild wolves; their relationship is so close that “we don't have a word



Isle Royale's two surviving wolves are highly inbred.

to describe [it]," says wildlife ecologist Rolf Peterson of Michigan Technological University in Houghton. Researchers have tracked the fate of wolves on Isle Royale since 1958, in the world's longest running predator-prey study. On 19 April, the National Park Service (NPS) released the annual report on the Isle Royale predator-prey study, documenting the genetic identities of the two wolves spotted the previous winter: They are father and daughter as well as half-siblings, born 2 years apart to the same mother. NPS decided against new wolf introductions in 2014, but in March announced plans to study that option, with a decision expected next year. <http://scim.ag/IsleRoywolves>

Organ imaging study begins

STOCKPORT, U.K. | UK Biobank, a nonprofit biological data repository, announced 13 April that it plans to scan the organs of 100,000 people in the United Kingdom over the next 6 to 8 years. The snapshots, taken with MRI and other standard techniques, will be linked to diverse data on health and lifestyle, allowing researchers to improve understanding and diagnoses of diseases such as cancer, dementia, arthritis and osteoporosis, and coronary heart disease. UK Biobank, set up in 2006 by the Medical Research Council and the Wellcome Trust, plans to gather health-relevant data—such as diet, physical activity, lifestyle, and cognitive function—as well as samples of blood and DNA from a half-million people in the United Kingdom by the end of the year. Data will be accessible to health scientists who register with UK Biobank. <http://scim.ag/UKBiobank>

Polio vaccine's big switch

GENEVA, SWITZERLAND | It's being heralded as the largest synchronized vaccine rollout in history—and as a harbinger of the imminent eradication of polio. Between 17 April and 1 May, 155 countries that currently use the live, trivalent oral polio vaccine (tOPV), which protects against all three strains of the wild polio virus, will switch to live, bivalent OPV (bOPV), which protects against the last two remaining wild strains, types 1 and 3. (Type 2 wild polio virus has been eradicated.) The change, which will be overseen by thousands of independent monitors, is intended to reduce the small risk of type 2 polio cases caused by the weakened type 2 strain used in the live polio vaccine. Michel Zaffran, the new head of the Global Polio Eradication Initiative here, says, "we have



The call of the hoary bat (*Lasiurus cinereus*) is now part of an international catalog.

Preserving the calls of Mexico's chatty bats

The human ear can't normally hear the ultrafast chirps, beeps, and whistles of bats—but a new catalog of bat calls may help a computer discern them. Ecologist Kate Jones of the University of Cambridge in the United Kingdom had previously compiled calls from bats across Europe and in New York City, creating a database called Echobank. Now, Jones has teamed up with Mexican graduate student Veronica Zamora at Cambridge, who needed to identify bats in her study area of northern Mexico to investigate impacts of land use and climate change. For 1.5 years, Zamora braved skeptical locals and drug cartel-controlled territory to record the calls of more than 900 bats. Those calls, along with thousands recorded by other researchers working in Mexico, were added to Echobank. Then, the team built a computer program that could help identify the bats by their calls. The program is able to distinguish 59 of Mexico's 130 bat species, the team reported 14 April in *Methods in Ecology and Evolution*. The team is also setting up a citizens' science group to regularly visit key bat habitats in Mexico to listen in and find out how they are doing.

never been this close" to eradicating polio. He says the initiative hopes to stop transmission of all wild polio virus in 2016.

Wheat fungus research needed

DHAKA | Alarmed at the first outbreak of a devastating wheat disease in Asia, scientists this week launched www.wheatblast.net to pin down the origin of the fungus behind the disease. In February, wheat fields in central Bangladesh began to suffer from bleached heads and shrivelled kernels; yields fell by up to 90% on more than 15,000 of Bangladesh's 420,000 hectares of wheat grown from 2015 to 2016. Last week, researchers at The Sainsbury Laboratory (TSL) in Norwich, U.K., sequenced wheat samples from Bangladesh and confirmed that the culprit is the fungus *Magnaporthe oryzae*, which also infects rice and many kinds of grasses. But additional genetic data are needed, says plant pathologist Sophien Kamoun of TSL, to determine how the wheat blast struck Bangladesh. Fungicides

are of limited use, so breeders will need to develop resistant varieties, says geneticist Nick Talbot of the University of Exeter in the United Kingdom, who studies the fungus. In a briefing paper released this month, the International Maize and Wheat Improvement Center issued a grim warning: "The consequences of a wider outbreak in South Asia could be devastating to a region of 300 million undernourished people."

Brazil legalizes cancer pill

BRASÍLIA | Responding to political pressure and popular demand for a largely untested cancer drug, on 14 April Brazilian President Dilma Rousseff signed into law a measure that allows synthetic phosphoethanolamine to be produced and sold legally as a cancer therapy in Brazil. Apart from a few studies in mouse models and in cell lines, there is no laboratory evidence that synthetic phosphoethanolamine works as a cancer drug. The compound was developed in the early 1990s by Gilberto Chierice, an

analytical chemist at the University of São Paulo in Brazil whose lab distributed it to patients free of charge, without regulatory approval or clinical oversight. The university tried to shut down Chierice's operation in June 2014, but more than 15,000 people sued the university. Scientists scorned the president's decision, contending it puts patients at risk. This was a "political decision inspired by a messianic surge of pseudoscience," says Gustavo Fernandes, president of the Brazilian Society of Clinical Oncology here. "It was the worst possible way of dealing with this problem." <http://scim.ag/Brazilcancerpill>

Yellow fever anxiety rises

LUANDA | The yellow fever epidemic in Angola has spread farther within the country and is spilling across its borders, according to the World Health Organization (WHO), which says the outbreak now "constitutes a potential threat for the entire world." The virus has sickened 1822

Angolans so far and killed 244; 16 of the country's 18 provinces have now reported cases. Travelers have also brought the virus to neighboring Democratic Republic of the Congo (DRC), as well as to Kenya and China. The DRC has reported more than 150 cases so far, including 21 deaths. "For now, there seems to be no local transmission" in the DRC, a WHO spokesperson says, but the risk remains high because the yellow fever mosquito is widespread there and many people are susceptible to the disease. Uganda has also reported 10 yellow fever deaths, but it's not yet clear whether they are linked to the Angolan outbreak. WHO says it aims to end the outbreak in Angola by 15 May by vaccinating more people and increasing efforts to control the mosquitoes.

Harsh grades for 'Europe's MIT'

LUXEMBOURG CITY | The European Institute of Innovation and Technology (EIT) received poor grades from the European Union's financial watchdog,

the European Court of Auditors, in a report released 14 April. Launched in 2008, EIT was the idea of former president of the European Commission José Manuel Barroso, who hoped that the European Union could create an institute that forges links between education, innovative science, and business to help overcome a perceived "innovation gap" in Europe. But expert commissions criticized the idea as "ill-conceived and doomed to failure." Although EIT has made progress—including the creation of five Knowledge and Innovation Communities (KICs) intended to bring together scientists from universities, research institutes, and businesses around themes such as climate and sustainable energy—the Court of Auditors found that the institute has a long way to go. The report found "little evidence of tangible results or impact to date" for the KICs, and stated that EIT needs "significant adjustments" to the rules that govern it to allow it to work more smoothly with its partners, especially businesses. <http://scim.ag/EITgrades>



Jacob Leggette with President Barack Obama at the White House Science Fair last week.

Young inventor pitches novel idea: child science advisers

Jacob Leggette thinks that providing science advice to the White House should be kid's play. Last week, the 9-year-old home-schooled youngster from Baltimore, Maryland, participated in the sixth White House Science Fair—and the last to be thrown by President Barack Obama and his science adviser, John Holdren. After using a 3D printer to make everything from a replica of the White House to a bubble wand, Leggette bent the president's ear with a pitch for the commander-in-chief to enlist children in figuring out how the government should foster innovation. "John, Jacob had a very good idea," Obama told the audience, adding that "we're going to follow up on that." A White House official said, "We're very excited about the idea" of asking children to, as Obama put it, "explain to us what's interesting to them ... and help us shape advances in STEM [science, technology, engineering, and mathematics] education."

BY THE NUMBERS

1%

Decrease, from 2014 to 2015, in global hectares of genetically modified crops—the first decrease in 2 decades, according to the nonprofit International Service for the Acquisition of Agri-biotech Applications.

\$4

Return for every \$1 invested in treatment for depression and anxiety, manifesting as better health and ability to work, according to a World Health Organization–led study (*The Lancet*).

15%

Fraction of 500 food production scenarios that could feed the global population in 2050 without expanding farmland—if people are consuming a meat-heavy diet. For vegan diets, it is 100% (*Nature Communications*).



A Syrian family arrives
on the Greek island of
Kos in August 2015.

INFECTIOUS DISEASES

Refugee crisis brings new health challenges

Imported pathogens are a much bigger threat to migrants than they are to Europeans

By Kai Kupferschmidt, in Amsterdam

Christoph Lange had never felt particularly proud to be German before, but when he saw pictures last year of volunteers in Munich greeting thousands of newly arriving refugees with food, clothes, and toys, he nearly cried. “I felt lucky to live in a country that can be so generous,” he says.

Yet Lange, a tuberculosis (TB) expert at the Leibniz Center for Biomedical Research in Borstel, Germany, also has firsthand experience of some of the public health challenges that Europe’s greatest migrant influx since World War II poses. Many of the migrants come from countries where public health systems are in disarray, and some are infected with pathogens that are rare, or even unheard of, in Europe. “The infectious disease character of Europe is changing,” says Manuel Carballo, the executive director of the International Centre for Migration, Health and Development in Geneva, Switzerland.

It’s a sensitive issue. Scientists who discussed the problem here last week at the annual conference of the European Society of Clinical Microbiology and Infectious Diseases worry that right wing politicians will use it to stoke unfounded fears. They

agreed that the influx of unusual infections is far less of a threat to native-born Europeans than to the health of the refugees themselves. At the same time, Carballo says, “we have to be careful not to deny [it].”

Many say too little is known about the health needs of migrants because science has neglected the issue. “I have worked on migrant health for about 15 years and there has been almost no funding,” says Sally Hargreaves, a researcher at the international health unit at Imperial College London. “Now, suddenly we have all these migrants. And suddenly there is money and interest.”

More than a million refugees and migrants entered Europe last year, according to the Office of the United Nations High Commissioner for Refugees, mostly from Syria, Afghanistan, and Iraq. There’s no question that they sometimes bring unwelcome companions. At the meeting, Dutch scientists presented evidence of scabies, a mite infestation, in up to a third of asylum seekers from the Horn of Africa; another study showed that about one in 300 refugees screened in the German state of Thuringia was a carrier of *Salmonella* or *Shigella*, an unusually high percentage.

European doctors need to be prepared for diseases they have never seen, such as *Echinococcus*, an intestinal tapeworm,

or liver abscess caused by amoebae, says Winfried Kern, an infectious disease specialist at the University of Freiburg in Germany. Antibiotic-resistant pathogens are also more prevalent in countries where Europe’s migrants originate; a study in four centers in Switzerland showed that refugees were 10 times more likely than the local population to be colonized by methicillin-resistant *Staphylococcus aureus*.

There is little evidence, however, that newly imported pathogens are spreading in Europe. Late last year, the European Centre for Disease Prevention and Control (ECDC) in Stockholm produced four reports estimating the risk that migrants could touch off outbreaks of louse-borne relapsing fever, shigellosis, malaria, and other diseases; they concluded that the risk to European residents is “extremely low.”

TB is a case in point. After a decline over the last 15 years, Germany suddenly saw the number of new cases go up by 30% in 2015, to 5865. That sounds dramatic, but it’s still a low burden for a country of more than 80 million, Lange says. And although a few people have contracted TB from refugees—Lange treated a guard at a refugee facility recently—such cases are rare. Still, the increase in cases and the likelihood that many refugees carry a latent TB infection

makes it unlikely that Germany can eliminate the disease anytime soon, he says.

A practical question is which diseases newly arriving refugees should be screened for in order to catch and treat infections early. Screenings vary by country, and many are probably not cost-effective because the diseases are rare even in the migrant population, Kern says. ECDC is developing guidelines, but Kern says countries should only screen for diseases they are prepared to treat; that would rule out testing for hepatitis C, for which treatment costs about €50,000.

The bigger challenge is how to ensure that refugees don't get sick after their arrival. Many have made perilous journeys, and they are often housed in overcrowded facilities with unsanitary conditions; sometimes clean water is in short supply. Those conditions favor the spread of diseases such as hepatitis A, cholera, and typhoid fever, says Hakan Leblebicioğlu, an infectious disease specialist at Ondokuz Mayıs University in Samsun, Turkey, who has studied the health of the more than 2.7 million Syrian refugees living in his country.

Many refugees also arrive unprotected from deadly diseases, because war and unrest have interrupted vaccination programs in their home countries. In Syria, polio broke out in unvaccinated children in 2013, triggering fears that the disease could return to Europe. Some countries responded by vaccinating newly arriving Syrian kids. Measles struck a refugee encampment in Calais, France, earlier this year; 13 cases were confirmed before a large scale vaccination campaign stopped the virus. Migrants probably didn't import the virus, however. In a paper published last month in *Eurosurveillance*, researchers reported that the index case had arrived in France more than a month before getting sick, and that the virus's genotype matched strains circulating in Spain and the United Kingdom, suggesting that a volunteer working in the camp touched off the outbreak.

The health disparity doesn't end after migrants become permanently settled in their new country. "We have collections of Somali communities around our hospital in Hammersmith that have higher rates of tuberculosis than in Somalia," Hargreaves says. "Technically they have access to a first-class health service"—they just don't always use it. Finding out why is as important as diagnosing and treating disease, Carballo says. "We need more behavioral epidemiology or social epidemiology," he says. "We need to know much more about the extent to which people from different backgrounds access health and how to lower the barriers for them." ■



LINGUISTICS

How sign languages evolve

Young sign languages develop in predictable ways, offering clues to the evolution of linguistic complexity

By Catherine Maticic, in New Orleans, Louisiana

Simi Etedgi leans forward as she tells her story for the camera: The year was 1963, and she was just 15 as she left Morocco for Israel, one person among hundreds of thousands leaving for the new state. But her forward lean isn't a casual gesture. Etedgi, now 68, is one of about 10,000 signers of Israeli Sign Language (ISL), a language that emerged only 80 years ago. Her lean has a precise meaning, signaling that she wants to get in an aside before finishing her tale. Her eyes sparkle as she explains that the signs used in the Morocco of her childhood are very different from those she uses now in Israel.

In fact, younger signers of ISL use a different gesture to signal an aside—and they have different ways to express many other meanings as well. A new study presented at the Evolution of Language meeting here last month shows that the new generation has come up with richer, more grammatically complex utterances that use ever more parts of the body for different purposes.

Most intriguing for linguists: These changes seem to happen in a predictable order from one generation to the next. That same order has been seen in young sign languages around the world, showing in visible fashion how linguistic complexity unfolds. This leads some linguists to think that they may have found a new model for the evolution of language.

"This is a big hypothesis," says cognitive

scientist Ann Senghas of Barnard College in New York City, who has spent her life studying Nicaraguan Sign Language (NSL). "It makes a lot of predictions and tries to pull a lot of facts together into a single framework." Although it's too early to know what the model will reveal, linguists say it already may have implications for understanding how quickly key elements of language, from complex words to grammar, have evolved.

Sign languages, like spoken ones, have established systems for combining stable words or signs into meaningful sentences. Because they evolved apart from spoken languages—often when previously isolated deaf individuals came together—they are more than just signed versions of their spoken counterparts. Most have been around for centuries. But a few, like ISL and NSL, have emerged only in recent decades, offering linguists a unique opportunity to watch how languages evolve in real time.

Linguist Wendy Sandler of the University of Haifa in Israel first explored this evolution while studying Al-Sayyid Bedouin Sign Language (ABSL) in the early 2000s. ABSL, used by roughly 150 villagers in Israel's Negev desert, was born in the 1930s, when several deaf descendants of the village's founder invented a system of signs to communicate with each other. Because their deafness was hereditary, soon almost everyone had at least one deaf relative and almost everyone was signing.

Once the community of signers reached a critical mass, the language started becoming more complex: People in the first generation could link words, but not in consistently

New sign languages emerge and change when deaf individuals come together in larger communities, as with this class of Nicaraguan Sign Language users.

meaningful ways, whereas people in the second and third generations had full systems for marking complex sentences, conversational asides, and clauses, as Sandler reported in *Gesture* in 2012.

Further, Sandler realized that as the speakers refined their language, they were slowly enlisting different parts of the body to express more and more complex thoughts. Whereas first generation signers relied primarily on their dominant hands, second generation signers added their heads and third generation signers added their faces, all for specific linguistic purposes. Those in the fourth generation recruited their non-dominant hands and their upper bodies, tilting them to the right or left to convey additional meanings.

Could the same thing be happening in other signed languages? To find out, Sandler and colleague Rose Stamp turned to ISL, a language born as deaf immigrants converged on what is now Israel before World War II. Sandler and Stamp divided 15 native ISL signers into three age groups: those 18–30 years old, those 31–50 years old, and those, like Etedgi, older than 50. Then the researchers video recorded their subjects narrating a short life story. The researchers analyzed 2-minute segments from each video, marking the movement of key body parts with

special coding software. They collected more than 7000 data points and compared movements among signers.

The linguistic structures showed a clear trend: They became more complex from one generation to the next. To Sandler's surprise, the signers recruited body parts in the exact same order as the ABSL signers. "As I saw the relationship [unfold] between different parts of the body and linguistic complexity, I was thinking, 'I can't believe it!'" she says. For example, when younger signers wanted to signal an aside, they no longer leaned their entire bodies forward like Etedgi. Instead, they tilted their bodies to one side and then tilted their heads to the opposite side. A similar head tilt is used in ABSL. Even more intriguing, some of these changes also appear in NSL, a 40-year-old language from halfway around the world.

The use of new body parts and the increasingly detailed division of bodily labor "allow us to see [the addition of linguistic functions] with stunning clarity," Sandler says. Spoken languages of course don't involve the body. But, Sandler says, "it is reasonable to assume that the same [linguistic] functions would have emerged at the dawn of spoken language as well, because they are basic to communication."

The use of new parts also makes language more efficient: The youngest ISL signers can express themselves much faster than the oldest—153.2 signs per minute compared with 103.5 signs per minute.

The findings also show that social interaction is essential for language evolution. When a new generation establishes a system for signing, Sandler says, it stays more or less the same as its members age. Her work has shown that when young signers enter a community, they add complexity through experimentation with their peers in what she calls "a social game." The more players, the more innovations.

This evolution takes time, notes evolutionary linguist Marieke Schouwstra of the University of Edinburgh, and so "contradicts certain views of the emergence of language." Some researchers have argued that a single mutation powered the "leap" from an animal-like communication system to something uniquely human (*Science*, 22 November 2002, p. 1596), and that some level of complexity was necessary from the outset. "This work shows that that's definitely not the case," Schouwstra says.

The evolutionary process may also be inevitable, reflecting the workings of our brains, Senghas says. "If there are systematic ways that we see it happening across all languages," she says, "that means there are similar ways of packaging information in all of our brains. That's what language is." ■

FUNDING

No deadline, fewer requests

National Science Foundation trial spurs drop in proposals

By Eric Hand

The National Science Foundation (NSF) in Arlington, Virginia, has found a potentially powerful tool for tamping down the workload created by some 48,000 grant proposals annually: It can simply eliminate deadlines.

Last week, NSF officials revealed that proposals to four geoscience grant programs dropped by 59% after they eliminated deadlines in favor of anytime submissions, evaluated on a rolling basis. "We've found something that many programs around the foundation can use," said Roger Wakimoto, NSF's assistant director for geosciences, at a 13 April advisory panel meeting.

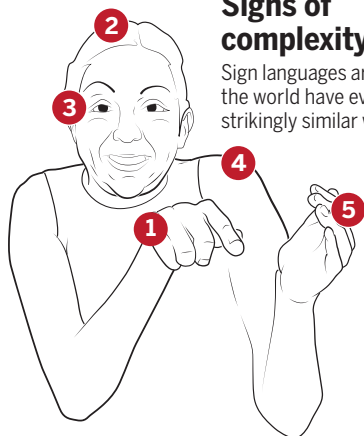
The no-deadline experiment is part of a multifaceted NSF effort to manage the agency's workload (*Science*, 4 December 2015, p. 1143). In 2011, NSF's geoscience division decided to try it first with a small grant program for earth science instruments and facilities; after the switch, the number of proposals dropped by more than 50%. Last year, Alex Isern, head of the surface earth processes section within geosciences, expanded the approach to four other programs. The number of proposals plummeted, from 804 in 2014 to just 327 in the 11 months from April 2015 to March.

Isern says scientists like the flexibility. Geologist Paul Bierman of the University of Vermont in Burlington believes the switch produces better proposals by creating a "filter for the most highly motivated people, and the ideas for which you feel the most passion." When on review panels, he found that half of proposals appeared to have been rushed to meet a deadline. "My hope is that this has taken off the bottom 50%," he says.

Other NSF program managers might try the idea, says Carol Frost, head of the earth sciences division. She has one concern, however: If proposals drop and success rates rise, programs might lose a talking point for bigger budgets. "One of the arguments ... has been, 'Look, we have such proposal pressure, give us more money,'" she says. The experiment, she notes, provides evidence that proposal pressure can easily be controlled. ■

Signs of complexity

Sign languages around the world have evolved in strikingly similar ways.



1 Hands Signers start by making signs with their dominant hands.

2 Head They add the head for indicating topics and questions.

3 Facial expression The face comes next. The squint here signals a relative clause.

4 Torso Signers then use their upper bodies to show whom or what they are talking about.

5 Nondominant hand Finally, signers use their other hand for topic continuity and classification.

DIAGRAM: VALTOUNIAN/SCIENCE



EVOLUTION

Templeton grant funds evolution rethink

\$8.7 million to test controversial ideas that go beyond genes and natural selection

By Elizabeth Pennisi

For many evolutionary biologists, nothing gets their dander up faster than proposing that evolution is anything other than the process of natural selection, acting on random mutations. Suggestions that something is missing from that picture—for example, that evolution is somehow directed or that genetic changes can't fully explain it—play into the hands of creationists, who leap on them as evidence against evolution itself.

No wonder some evolutionary biologists are uneasy with an \$8.7 million grant to U.K., Swedish, and U.S. researchers for experimental and theoretical work intended to put a revisionist view of evolution, the so-called extended evolutionary synthesis, on a sounder footing. Using a variety of plants, animals, and microbes, the researchers will study the possibility that organisms can influence their own evolution and that inheritance can take place through routes other than the genetic material.

Adding to the controversy is the source of the grant, announced 7 April: the John Templeton Foundation in West Conshohocken, Pennsylvania, which Templeton, a philanthropist, set up in 1987 to address big questions about “human purpose and ultimate reality.” Evolutionary biologists shouldn't accept its money, says Jerry Coyne, an evolutionary biologist at the University of Chicago in Illinois, who has been a persistent critic of the foundation for linking science and religion. “It really slants the way science is done,” he told *Science*.

Templeton's executive vice president for programs, Michael Murray, says the foundation just wants to bring “greater clarity” to the mechanisms of the extended evolutionary synthesis. Now, there's the opportunity “to show there is something there or to move on to other things,” he says.

Some scholars and scientists agree. “The amount of money is obviously significant, and that allows for a much larger scale project than would otherwise be possible,” says Alan Love, a philosopher at the University of Minnesota, Twin Cities, who has followed the debate over the extended synthesis. Greg Wray, an evolutionary biologist at Duke University in Durham, North Carolina, who doesn't see a need for such revisionist thinking, adds that for its advocates, “this is a chance to really show us they are right.”

The extended evolutionary synthesis is a term coined in 2007 to imply that the pre-eminent current evolutionary theory, the so-called modern synthesis, needed to broaden its focus because it concentrated too much on the role of genes in evolution and lacked adequate incorporation of new insights from development and other areas of biology. The

“We can't solve all the questions in 3 years, but we can ... encourage researchers to think about evolution in another way.”

Kevin Laland, University of St. Andrews

idea has gradually gathered momentum since its advocates first met in Germany in 2008 (*Science*, 11 July 2008, p. 196). Later, Kevin Laland, an evolutionary biologist at the University of St. Andrews in the United Kingdom, and several colleagues took up the cause, arranging for a point-counterpoint discussion in *Nature* in 2014 and a comprehensive review last year in the *Proceedings of the Royal Society B's* annual Darwin Review.

Advocates stress that animals, plants, and even microbes modify their environments, exhibit plasticity in their physical traits, and be-

have differently depending on the conditions they face. Chemical modifications of the DNA that affect gene activity—so-called epigenetic changes—seem to explain some of this flexibility. These and other factors suggest to some biologists that an organism's development is not simply programmed by the genetic sequences it inherits. For them, such plasticity implies that parents can influence offspring not just through their DNA but by passing on the microorganisms they host or by transmitting epigenetic marks to subsequent generations. “Innovation may be a developmental response that becomes stabilized through genetic changes,” explains Armin Moczek, an evolutionary developmental biologist at Indiana University, Bloomington.

Nor is evolution controlled only by natural selection, the winnowing process by which the fittest survive and reproduce, Laland and others argue. Organisms, by transforming their environments and responding to environmental factors, help control its course, they contend. As such, the extended synthesis “represents a nascent alternative conceptual framework for evolutionary biology,” Laland and dozens of colleagues wrote in a funding proposal to the Templeton Foundation last year.

Some prominent evolutionary biologists have pushed back against this seeming rebellion. “It's a mixture of old ideas that aren't novel and reasonable ideas that haven't been shown to be of any importance,” Coyne says. He and others insist that evolutionary biology has already incorporated some of these ideas or is in the process of doing so—meaning no “extension” is necessary. Furthermore, although they might disagree, extended synthesis advocates “are saying these things with very little empirical data,” adds Hopi Hoekstra, an evolutionary biologist at Harvard University.

The Templeton Foundation, however,

Studies of horned beetles will address several aspects of the extended evolutionary synthesis.

was intrigued by the debate in *Nature*, and it approached Laland about what would be needed to resolve it. He and Tobias Uller, an evolutionary biologist from Lund University in Sweden, then assembled 49 researchers from different fields and plotted out 22 interconnected projects across eight institutions to test the extended synthesis.

One thematic group, which includes philosophers, will pull together the history of the extended synthesis, crystallize how it differs from traditional evolutionary biology, and refine the underlying theory. Another will tackle evolutionary innovations, exploring how novelty can arise. Some of those grantees will study what influences a green algae called *Chlamydomonas* to sometimes become multicellular, for example, hoping for insights into the evolution of more complex organisms. Others, probing the origins of social behavior, will try to come up with “rules” that nest-building social insects follow in response to local conditions. And studies of horned beetles will compare invasive with native species to understand how environmental-induced variation in horn size—the result of developmental plasticity—can become genetically locked into bigger or smaller horns.

Still other researchers will investigate nongenetic forms of inheritance. Some experiments, for example, will look at how the evolution of dung beetles was shaped by microbes that the mothers put into their eggs and by the dung itself. And some will assess the importance of “niche construction,” in which individuals modify their environments—as termites do by building mounds—creating a different set of conditions for individuals and their offspring that can affect natural selection. Over the next 3 years, several groups will come up with a theory that incorporates these nongenetic inheritance factors into evolutionary thinking.

Finally, the grantees will try to understand how all these factors together could influence the diversification of species. “The point is not to figure out whether any of these areas could be important—we are done with that and there are enough case studies,” Moczek says. “Now, we need to look systematically to see how important they are.”

The Templeton project “has the potential to really make a big difference,” by providing the data demanded by critics of the extended synthesis, says Scott Gilbert, an evolutionary developmental biologist at Swarthmore College in Pennsylvania. Laland is also optimistic. “We can’t solve all the questions in 3 years, but we can ... encourage researchers to think about evolution in another way.” ■

PALEONTOLOGY

The tiniest titan

Fossil of a baby titanosaur shows that even the youngest of these giant dinosaurs were ready to take on the world

By Patrick Monahan

In 2012, paleontologist Kristina Curry Rogers was digging through drawers of miscellaneous crocodile fossils at the State University of New York at Stony Brook when she saw something both familiar and unfamiliar: the bones of a giant dinosaur, in miniature. Even out of context, she realized instantly that they had come from a class of long-necked plant-eaters called titanosaurs. “They looked exactly like the bones I’d spent 15 years of my life studying,” she says. That similarity, along with clues from bone structures inside the fossils, has now yielded the first clear evidence that hatchlings of at least some of

care,” says Thomas Holtz, a paleontologist at the University of Maryland, College Park. But until now, there was no way to tell for sure.

The bones were unearthed in Madagascar in 1998 and 2003 but were misclassified until Curry Rogers, who works at Macalester College in Saint Paul, noticed them. She and her colleagues started by measuring the proportions of the terrier-sized creature and found that they closely matched those of adults. Then the team examined cross-sections of the fossils to determine how it grew. One key finding was a hatching line: a shift in the internal structure of the bone that in modern lizards and crocodilians indicates when an animal emerged from its egg. That feature enabled the researchers to estimate both the juvenile’s size when it emerged from its egg and its age when it died. In the dinosaur’s short life—between 39 and 77 days long—it grew by an order of magnitude, from about 3.4 kilograms to 40 kilograms, the team reports on p. 450.

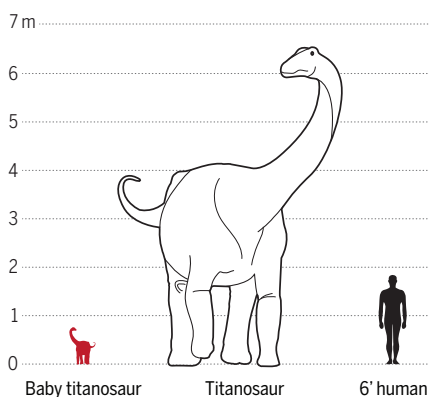
Having adultlike body proportions at such a young age indicates that this species left the egg able to walk and probably feed itself—unlike duck-billed dinosaurs, which were probably nest-bound and relied on their parents for food at that age. In another sign of an active life, the young titanosaur’s bones had been remodeled. That means the tiny dinosaur was constantly keeping its bones the right shape as it grew—evidence that they had undergone the biomechanical stress of walking around.

The bones also hint at an unpleasant death. Cartilage at the ends of bones stops growing in starving animals—and in the *Rapetosaurus* specimen, the preserved calcified cartilage regions are extremely thin. That fits with what researchers know about the site, a drought-ridden and stressful environment at the time the young dinosaur lived there. “It’s very exciting,” says Holly Woodward, a paleohistologist at Oklahoma State University, Tulsa. “There’s direct evidence of starvation for the mode of death.”

Holtz says other titanosaurs probably shared *Rapetosaurus*’s growth strategy. But he cautions against concluding that all long-necked giants were born self-sufficient. “To most people, all sauropods look alike: tiny at one end, tiny at the other, big in the middle,” he says. “But that doesn’t mean there wasn’t a lot of variation within them.” ■

Big self-starter

Rapetosaurus grew from terrier- to bus-sized without changing shape—a sign that its young could manage without much parental care.



the largest dinosaurs were essentially self-sufficient, scaled-down adults.

The bones, of a dinosaur called *Rapetosaurus krausei*, were a rare find. Researchers have found later-stage juveniles and fossilized eggs of sauropods—the group of long-necked dinosaurs to which *Rapetosaurus* and other titanosaurs belong—but none that had just hatched. Evidence from fossilized embryos in a nesting site in Argentina hinted that another titanosaur species was precocial: self-sufficient right after hatching. And thanks to their massive size as adults, “it’s always seemed a bit weird to think of titanosaurs having much in the way of parental

BEHIND THE NUMBERS

When the payoff for academics drops, commercialization suffers

By Jeffrey Mervis

For decades, innovation experts have urged other nations to adopt the U.S. approach to nurturing innovation on campus. One essential element of that model is the practice of giving universities a majority share, typically two-thirds, of the value of a patent or spinoff company that results from the discovery. But a new study from Norway suggests that such a formula may actually make it less likely that researchers try to commercialize their work.

In 2002, Norway passed a law that ended its long-running practice of giving academics 100% ownership of their intellectual property (IP). The policy, known as “professor’s privilege,” was replaced with a U.S.-style system that gives academics just a one-third share.

Economist Hans Hvide of the University of Bergen in Norway realized the law created a natural experiment to test how the allocation of IP rights affected university commercialization. He knew that Germany, Austria, Denmark, and Finland had passed similar laws around the same time. But only Norway maintains a comprehensive database of business activity that includes details on the formation and performance of all companies. To help with the analysis, and in hopes of attracting a U.S. audience for his research, Hvide teamed up with economist Benjamin Jones of Northwestern University, Evanston, in Illinois.

Their results, in a paper posted last month by the National Bureau of Economic Research, may shock those enamored with the standard U.S. approach to divvying up IP rights. Commercialization cratered in the 5 years after Norway’s change: The per-capita number of patents dropped by 53%, while the per-capita formation of university-backed startup companies plunged by 67%, the researchers report. They also found evidence that the quality of the commercial activity declined, as measured by how well the companies did and the number of citations garnered by patents relating to each discovery. (The

database is small, Hvide and Jones admit: Professors in Norway started 128 companies between 2000 and 2007, and received 750 patents between 1995 and 2010.)

“Our results go against conventional policies, but not necessarily against conventional wisdom,” Jones says. “It’s not obvious how best to split the IP rights among the parties. But clearly, giving one party more decreases the incentives for the other parties.”

Some experts in the field say they are surprised by the findings, and somewhat skeptical. “In most countries, switching to

The results don’t surprise one Norwegian researcher and serial entrepreneur. “Creative people like to be in control of what they do, and if you take that away, then maybe they will lose interest and creativity will drop,” says Bjørn Angelsen, a professor of biomedical engineering at the Norwegian University of Science and Technology in Trondheim. He has started companies involved in ultrasound imaging that were later purchased by the likes of General Electric.

The allocation of IP is only one of many factors that determine whether academic discoveries are commercialized. U.S. researchers, for instance, can tap into a rich innovation ecosystem, with angel investors, venture capitalists, incubators, mentors, and the like. Angelsen says those resources exist in Norway but are typically found off-campus. “The people I have worked with have a successful track record” in nurturing startups, Angelsen says. “Otherwise they wouldn’t be in business. Most tech transfer offices don’t have that level of expertise.”

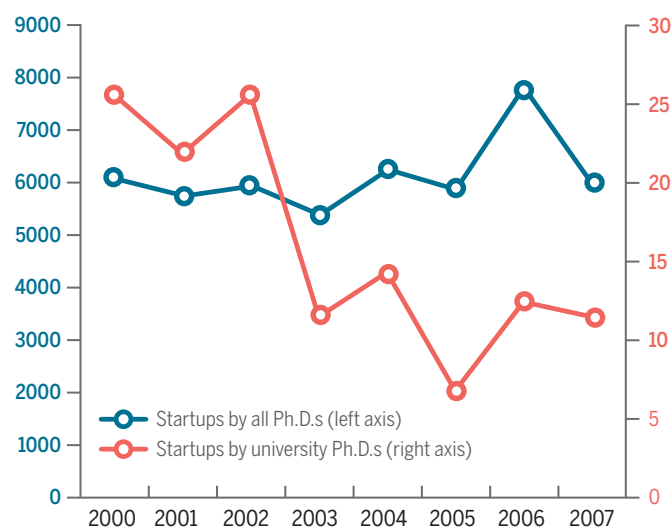
It will take time for Nordic universities to acquire that expertise, agrees Ursula Hass, who leads a Swedish association of tech transfer managers that is based in Stockholm. The authors, however, found no evidence for an uptick in activity even 5 years after the change went into effect in Norway.

Angelsen says Norway’s law hasn’t diminished his interest in finding commercial applications for his work and that it’s still possible for academics to negotiate their own IP terms. For instance, he persuaded his university to take just a 10% stake in his latest company. “There is the law, and then there’s what actually happens,” he says. “But I think my situation is quite special. I brought my own money to the table.”

To Hvide, the biggest takeaway message from the study is that countries trying to boost innovation need to pay attention to the fact that “rights matter.” Ignoring that reality, he adds, could result in “much of the world ... producing much less university-based innovation than it could, and than many policymakers desire.” ■

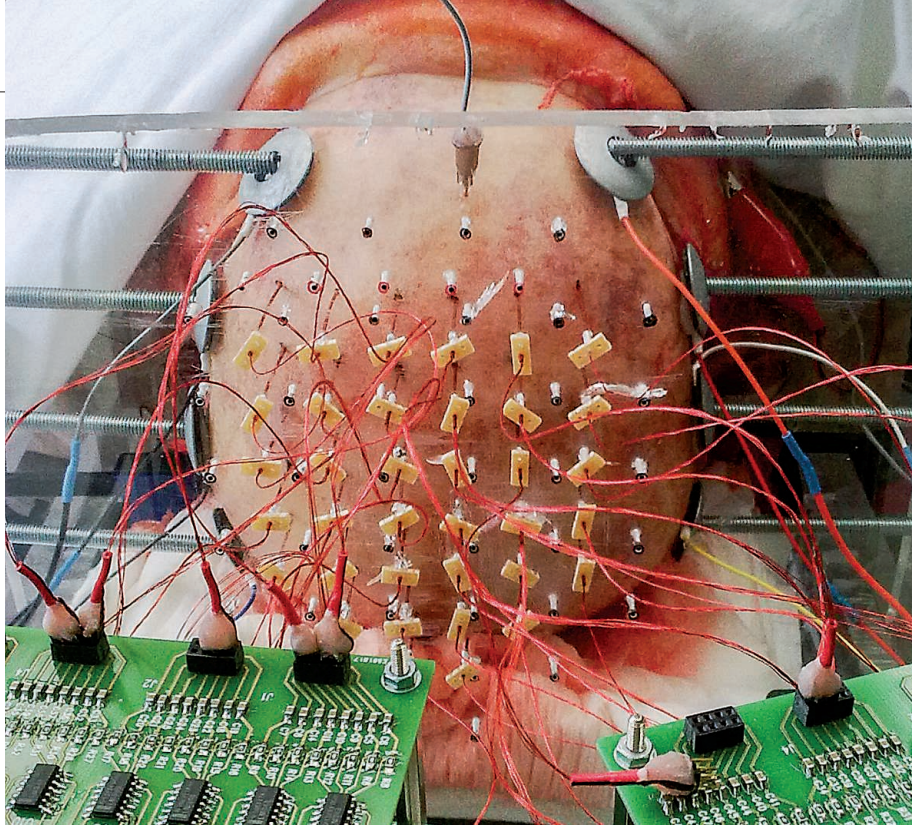
Law stifles innovation

Academic researchers in Norway (red line) formed far fewer startups after 2002, when universities were given a financial stake in the companies.



university ownership has generally led to significantly higher rates of patenting and startups,” says Lita Nelsen, the longtime head of the Technology Licensing Office at the Massachusetts Institute of Technology in Cambridge. “The university takes the risks on patent filings, and the technology licensing offices are able to develop professional approaches” to commercializing the invention, she adds. “I would guess that something else is in play besides the fraction of royalties that inventors receive.”

Hvide and Jones say they have looked in vain for alternative explanations for the decline, which was far larger than they had anticipated. “We were also surprised by the drop in quality,” Hvide adds. He expected universities to focus on the most promising opportunities. “But that didn’t happen,” he says.



NEUROSCIENCE

Cadaver study challenges brain stimulation methods

Unusual test of transcranial stimulation shows that little electrical current penetrates the skull

By Emily Underwood

Earlier this month, György Buzsáki of New York University (NYU) in New York City showed a slide that sent a murmur through an audience in the Grand Ballroom of New York's Midtown Hilton during the annual meeting of the Cognitive Neuroscience Society. It wasn't just the grisly image of a human cadaver with more than 200 electrodes inserted into its brain that set people whispering; it was what those electrodes detected—or rather, what they failed to detect.

When Buzsáki and his colleague, Antal Berényi, of the University of Szeged in Hungary, mimicked an increasingly popular form of brain stimulation by applying alternating electrical current to the outside of the cadaver's skull, the electrodes inside registered little. Hardly any current entered the brain. On closer study, the pair discovered that up to 90% of the current had been redirected by the skin covering the skull, which acted as a "shunt," Buzsáki said.

For many meeting attendees, the unusual

study heightened serious doubts about the mechanism and effectiveness of transcranial direct current stimulation (tDCS), an experimental, noninvasive treatment that uses electrodes to deliver weak current to a person's forehead, and the related tACS, which uses alternating current. Little is known about how these techniques might influence the brain. Yet many scientific papers have claimed that they can boost mood, alleviate chronic pain, and even make people better at math by directly affecting neuronal activity. This has spawned a cottage industry of do-it-yourself gadgets promising to make people smarter and happier.

The new, unpublished cadaver data make dramatic effects on neurons unlikely, Buzsáki says. Most tDCS and tACS devices deliver about 1 to 2 milliamps of current. Yet based on measurements from electrodes inside multiple cadavers, Buzsáki calculated that at least 4 milliamps—roughly equivalent to the discharge of a stun gun—would be necessary to stimulate the firing of living neurons inside the skull. Buzsáki notes he got dizzy when he tried 5 milliamps on his own scalp.

Popular brain stimulation methods can't trigger neuronal firing, a study in cadavers suggests.

"It was alarming," he says, warning people not to try such intense stimulation at home.

The cadaver research "should make the crowd nervous that favors tDCS and tACS," says David Poeppel, a neuroscientist and psychologist at NYU. Others who heard Buzsáki's talk or were informed of the results maintain that transcranial stimulation does work—and the only question is how. Neuroscientist Vince Clark of the University of New Mexico, Albuquerque, for example, has found that applying 2 milliamps of current to a person's scalp for just 30 minutes can double the speed at which they learn a game in which players must detect a concealed "threat," such as a bomb or sniper, in a video clip. Several labs have replicated those results, he says, adding that the idea that 10% or less of the current gets through to the brain is not new, and doesn't necessarily mean the methods are ineffective. "If it works, you know 10% is enough," Clark says.

Marom Bikson, a biomedical engineer at The City College of New York in New York City who uses computer models and slices of rat brain to study the mechanisms of tDCS and tACS, says that many in the field already accepted that the 1 or 2 milliamps the methods use don't directly trigger firing. It can make neurons more likely to fire or form new connections, he and others believe. Unlike techniques that rely on magnetic fields or higher current to actively trigger neurons, such as electroconvulsive therapy, tDCS and tACS likely subtly alter ongoing brain activity, Bikson says. Using cadavers to test these methods is a "complicated choice" because dead tissue conducts electricity differently from living tissue, he adds.

Buzsáki expects a living person's skin would shunt even more current away from the brain because it is better hydrated than a cadaver's scalp. He agrees, however, that low levels of stimulation may have subtle effects on the brain that fall short of triggering neurons to fire. Electrical stimulation might also affect glia, brain cells that provide neurons with nutrients, oxygen, and protection from pathogens, and also can influence the brain's electrical activity. "Further questions should be asked" about whether 1- to 2-millamp currents affect those cells, he says.

Buzsáki, who still hopes to use such techniques to enhance memory, is more restrained than some critics. The tDCS field is "a sea of bullshit and bad science—and I say that as someone who has contributed some of the papers that have put gas in the tDCS tank," says neuroscientist Vincent Walsh of University College London. "It really needs to be put under scrutiny like this." ■

FEATURES

MALARIA WARS

Can malaria be eliminated from the Mekong region before multiple-drug resistance makes it untreatable?

By **Leslie Roberts**, in Pailin, Cambodia



No one knows exactly why resistance to malaria drugs always emerges first in this remote western province of Cambodia, nestled in the Cardamom Mountains. “The reasons are as much social as biological,” says malariologist Tom Peto, who is here in this dusty, unremarkable-looking town battling the latest threat to global malaria control: multiple drug-resistant (MDR) malaria.

Rubies certainly play a role. For decades, the gems and the once-lush stands of teak have lured people here, along the Thai border, where the forests and jungle are thick with mosquitoes that transmit the malaria

parasite. Then there’s Pailin’s tragic history as the last stronghold of the Khmer Rouge, which left the population shattered, isolated, uneducated, suspicious, and devastatingly poor. Health care is abysmal; there is a surfeit of fake or lousy drugs—and a long-standing practice of not taking them all. Paradoxically, the low malaria transmission contributes, and there is something about the parasite circulating here, maybe its genetics, that helps it mutate fast and ensures that the hardiest, most resistant survive. Or maybe, says Peto, who is part of the Mahidol Oxford Tropical Medicine Research Unit, better known as MORU, in Bangkok, “it’s because we look here first.”

Whatever the reason, this is where it starts. Resistance to chloroquine surfaced here in the 1950s before sweeping through the wider Mekong region and then into India and Africa, causing millions of deaths. Sulfadoxine-pyrimethamine went next, in the 1960s. Mefloquine failed in the 1970s.

Then in late 2008 and 2009 came reports that rocked the malaria world: Artemisinin, the so-called wonder drug that has sent malaria deaths plummeting across the globe over the past decade, was losing its effectiveness here. That sparked global alarm and prompted an ultimately futile emergency plan to contain resistance in Cambodia before the last, best drug was lost.



Downloaded from <http://science.sciencemag.org/> on April 21, 2016

PHOTO: PAULA BRONSTEIN/GETTY IMAGES



The Mekong delta at Chau Doc, Vietnam, one of six countries in the region threatened by drug-resistant malaria. A Khmer family in Cambodia (left) being screened soon after artemisinin-resistant malaria was first discovered.

Now, Pailin is the epicenter of what some say is the greatest threat yet to malaria control: the deadliest malaria parasite, *Plasmodium falciparum*, has become resistant not only to artemisinin, but to a key partner drug, piperaquine, or PPQ, that is used in combination with artemisinin and is critical to its success. The emergence of this MDR parasite is raising the specter of untreatable malaria in the Mekong region and perhaps beyond.

PPQ resistance is a “disaster,” says Peto’s boss, Arjen Dondorp, who is the head of malaria research at MORU. It’s now confined to Cambodia, but “I’m afraid it is just a matter of time until it will reach the other countries in the region,” he says. That’s

the “nightmare scenario,” adds François Nosten, who runs the Mahidol group’s Shoklo Malaria Research Unit (SMRU) in Mae Sot, Thailand, along the border with Myanmar. “If that happens,” he says, “that’s it, we are done, and malaria will come back.”

The only way to avert that crisis, says a growing chorus of malaria researchers, international agencies, and donors, is to wipe out all malaria from the entire Greater Mekong subregion—five countries and a southwestern spit of China bound together by the world’s 12th longest river. The World Health Organization (WHO), the Global Fund, and other international agencies and donors are rallying around an ambitious

plan to do just that by 2030. The aim is to ensure that every last parasite is gone from the region, focusing first on *P. falciparum* because of the urgent threat of multiple-drug resistance. The Bill & Melinda Gates Foundation (BMGF) is lobbying hard, and the five countries, some better known for their corruption than their cooperation, are on board, on paper at least.

But it is not at all clear they can pull it off, or whether it is already too late. Malaria has been eliminated before, in the “easy” places such as the southern United States, Europe, and Turkey, and similar efforts are underway elsewhere. But no one has ever eliminated the disease in a place as socially and

epidemiologically complex as the Mekong.

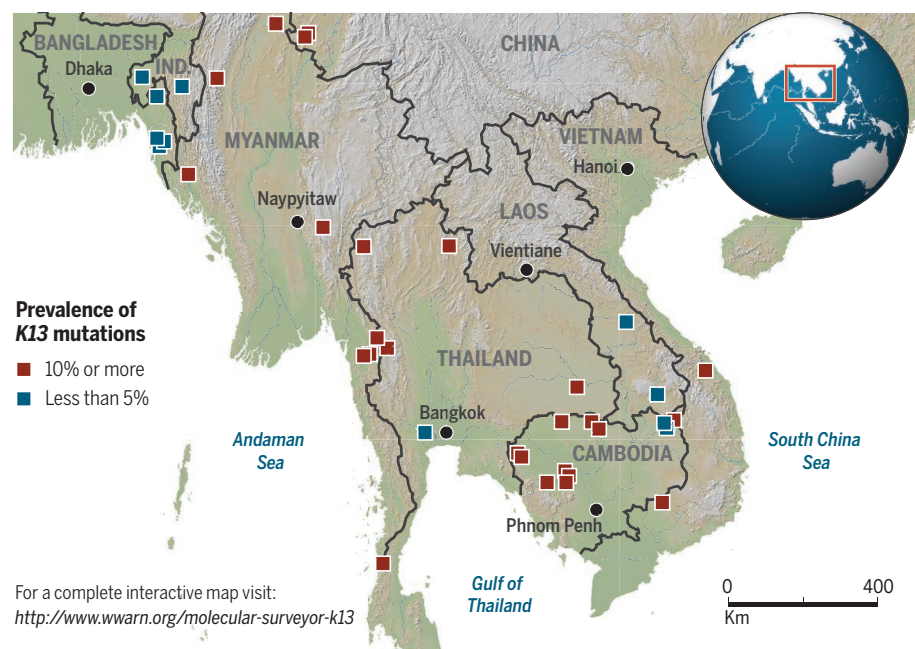
The science is uncertain, the data imperfect, the tools far too crude. Researchers here, many with outsize personalities and egos to match, argue over everything from the strength of the evidence to the ethics of clinical trials—even to the magnitude of the MDR malaria disaster: Is it a category 4 or category 5? Is there enough time for careful studies to see what really works, or is the situation so dire that you must throw largely untested strategies at it, whatever the risks, and hope something sticks?

All the while they face one disquieting conundrum: how to eliminate a disease when there's no vaccine, the very drugs you need are failing, and the parasite is evolving faster than people can keep up.

MALARIA IS A DIFFERENT BEAST in the Mekong than it is in Africa, where it kills roughly 500,000 children a year. The main vector across Africa, *Anopheles gambiae*, is so ubiquitous that people can be exposed to thousands of infectious bites a year, and transmission is the highest in the world.

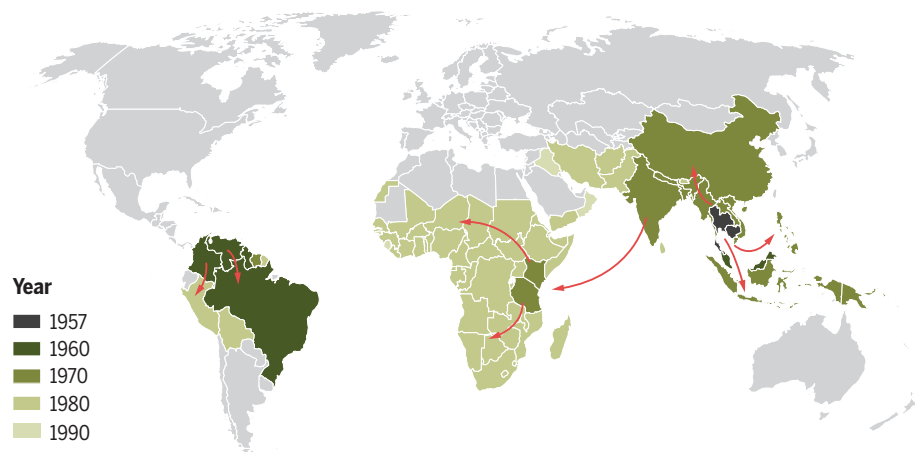
A growing threat

Artemisinin-resistant parasites are now widespread in the Mekong. Resistance has been linked to mutations in the parasites' *K13* gene; this map shows the percentage of samples with *K13* mutations reported since 2010.



The path of chloroquine resistance

Malaria parasites resistant to chloroquine swept out of the Mekong region and spread around the world. So far, artemisinin resistance hasn't followed that path, and researchers are debating the likelihood it will.



In the Mekong, by contrast, malaria is a disease of the edges, and there are fewer than 200 deaths a year. The expansive lowlands are largely malaria-free, but as the rice paddies give way to hills and then mountains, the risk rises, and malaria holds sway in the shrinking forest fringe where the mosquito vectors thrive. Its victims, too, are literally off the map: people who work in the forest—largely poor, itinerant loggers, miners, or migrant workers, and marginalized ethnic minorities who live along the messy international borders. The majority of cases occur in adult men, most in Myanmar, which bears the greatest malaria burden of any country in the Greater Mekong.

It's not the sheer toll of malaria here, but the uncanny ability of the parasite population to mutate and acquire resistance to any drug thrown at it, that has put the Mekong front and center in the global fight against malaria.

The roots of the problem go back decades and are mired in the misuse of malaria drugs. Many of those who streamed into the forests decades ago in search of riches, or were forced from the cities to the countryside by the Khmer Rouge, came from areas without malaria, so they had no natural immunity and were especially vulnerable. When they got sick, people often treated themselves with whatever drugs they could get by the bagful from the local shopkeeper, which, if they were lucky, might contain an anti-malarial at some unspecified dose. Or people would take a few tablets of chloroquine for protection before entering the forest and then pocket the rest. Either way, taking anti-malarials at low doses, for a short period, is a surefire way to generate resistance.

Artemisinin was especially easy to misuse. The drug was available here as a monotherapy, not a combination, long before the rest of the region, thanks to the Khmer Rouge's close ties to China, where the drug was developed. (The Chinese scientists who rediscovered the remarkable malaria-fighting properties of this ancient herbal remedy won the Nobel Prize in Medicine last year.) What sets artemisinin apart is its speed of action—it can clear almost all malaria parasites from the bloodstream in just 48 hours, so fast that people often don't finish the course, enabling the parasite to evolve under low drug pressure.

"Artemisinin is quite simply the best drug we've ever had," says Nicholas White, a U.K. malariologist who presides over MORU's far-flung enterprise from Bangkok and who seems to have mentored just about everyone who works in malaria in Southeast Asia.

Invariably called "brilliant" and usually "hard-headed," White helped bring artemis-



inin out of obscurity in the 1990s. His group did pivotal clinical trials of artemisinin and its derivatives, paired with a partner drug that mops up residual parasites. These so-called artemisinin combination therapies (ACTs)—there are six combinations—are designed to stave off resistance, in much the same way that combinations curb HIV’s ability to develop resistance to any single drug. Then White and his colleagues began a bruising, decadelong battle to get WHO to endorse ACTs as the first-line therapy for malaria worldwide.

THE FIRST SIGNS OF TROUBLE appeared around 2007. Dondorp’s MORU group was working here when it found artemisinin took twice as long to clear parasites from the bloodstream of malaria patients there as it did in Wang Pha, Thailand, where the drug had only recently been introduced. A group from the Armed Forces Research Institute of Medical Science (AFRIMS) in Bangkok, working nearby, found similar, disturbing indications. Dondorp, Nosten, White, and a who’s who of malaria researchers from across the region sounded the alarm in a 2009 paper in *The New England Journal of Medicine*. Without immediate action, they said, artemisinin resistance would fol-

low the arc of chloroquine resistance, race westward through Myanmar into Bangladesh and India, and ultimately into Africa, destroying all the gains of the past decade.

From the outset, a few scientists questioned whether what the group described was really drug resistance or should instead be called “slow clearance” of the parasite—and some even accused the Mahidol group of crying wolf (see box, p. 403). After all, unlike chloroquine, which fails to kill resistant parasites, artemisinin still worked, just more slowly.

Still, it was a significant threat, and in 2011 WHO and the Roll Back Malaria Partnership launched what became an “emergency response” to artemisinin resistance in the Mekong. The strategy was containment: Build a firewall around areas of drug resistance by ramping up control measures, such as bed-nets, rapid diagnostic tests, and ACTs.

Despite the plan, artemisinin resistance spread. It has yet to sweep into Africa, as feared, and there is some debate over whether it will. But it has now been found in five countries in the Mekong. Some blame a bumbling global response and corrupt and inefficient governments ill-equipped to handle the bolus of money that came their way; others point to new

Migrant workers, like these in Cambodia, are hard to reach in a major effort to wipe out malaria in the Greater Mekong subregion.

genetic evidence that shows that, in addition to spreading, artemisinin resistance is popping up independently in multiple spots across the region, dooming any attempt to build a firewall.

It was simply too late, adds Didier Ménard, who directs the malaria molecular epidemiology unit at the Pasteur Institute in Phnom Penh. Last year, his group found the hotly sought molecular marker of artemisinin resistance, the Kelch 13 or *K13* gene, enabling researchers to map its extent and spread in exquisite detail. Those retrospective analyses suggest that as early as 2001–2002, 50% of the parasites here were already resistant to artemisinin—there’s no way they could be stuffed back into the bottle.

Whatever the reason, the failure to rein in artemisinin resistance set the stage for the current crisis: MDR malaria.

NO ONE SHOULD HAVE been surprised when resistance to the partner drug exploded in Cambodia. “We predicted it,” says Dondorp, who is known as the calm, measured voice of the MORU group but

who is clearly exasperated. When the artemisinin component of an ACT doesn't clear the parasite quickly, Dondorp explains, the weaker and slower-acting companion drug must carry an extra load. It's essentially like monotherapy.

The first hints again came from around Pailin, where the ACT of choice is a combination of dihydroartemisinin, an artemisinin derivative, and PPQ, known as DHA-PPQ. Scattered reports started coming in that people on DHA-PPQ were not being cured. "You treat the sick, and 3 weeks later they are sick again, and they keep getting sick," Ménard says. This was not just the slow clearance seen so far with artemisinin resistance—it was actual treatment failure.

Two teams nailed the connection, one led by Ménard, the other by David Saunders of AFRIMS. Both groups confirmed in genetic, cell, and clinical studies that, for the first time, the parasite had developed resistance to both drugs used in an ACT. (Rick Fairhurst's group at the U.S. National Institutes of Health in Bethesda, Maryland, provided even more evidence in January of this year.)

The MDR parasites are spreading at a frightening rate. "Overall in Cambodia, the DHA-PPQ failure rate is 50%," Ménard says. "In Pailin, it is 70%, probably higher." And it bodes poorly for other ACTs, Nosten says. "If we lose one partner drug, any partner drug, they are all going to fall like dominoes very quickly."

There are a few stopgap measures—if countries can be nimble. After years on the shelf, mefloquine is effective again in Cambodia, and WHO has recommended that the country switch to a combination of artesunate and mefloquine. But it's a short-term fix: "Mefloquine will fail in 6 months," Ménard predicts. "It is like a race. The problem here is the parasite is working fast, so we have to also work fast." MORU is testing triple ACTs—a combination of three instead of two drugs—to see whether they can outwit resistance, but the results aren't in yet.

"I think it is one of our few choices to go for elimination," Dondorp says. "The longer we wait, the longer we are not successful, the more difficult it will get to treat malaria—and thus to eliminate it."

At its September 2014 meeting, the influential Malaria Policy Advisory Committee at WHO endorsed an aggressive plan for

malaria elimination in the Mekong, and the World Health Assembly signed off on it in May 2015. The goal is to rid the region of *P. falciparum* by 2025 and its milder relative *P. vivax* by 2030, for an estimated cost of \$3 billion. For Cambodia, the birthplace of drug-resistant malaria, the target date for *P. falciparum* is even sooner—less than 4 years away.

As Frank Smithuis, an irrepressible Dutch malariologist who works with MORU and runs his own nongovernmental organization out of one of Yangon, Myanmar's crumbling buildings, puts it: "Then we had better hurry."

ELIMINATION IS MALARIA CONTROL on steroids. "In malaria control, what we are trying to do is detect people with malaria and treat them, prevent people from dying

ers tend to spend several nights at a time in the forest, where transmission occurs, sleeping outside in hammocks. Many don't know that mosquitoes transmit malaria, and even if they do, it is too hot and muggy to don long-sleeved shirts and pants. The main vectors, *A. dirus* and *A. minimus*, bite outdoors, so in contrast to Africa, bed-nets are of limited use. "How do you deal with a vector that doesn't fit the paradigm of *Anopheles*?" asks Tom Kanyok, BMGF's point person for malaria elimination in the Mekong.

The biggest challenge to elimination in the Mekong, however, is the "asymptomatic reservoir"—people who carry the parasite without any symptoms but are, to some unknown extent, still involved in disease transmission. Confounding matters, they



Multiple drug-resistant malaria was first discovered in this poor, remote region of Pailin, Cambodia.

and being sick," Nosten explains. "In elimination we are doing that plus eliminating the parasite. We are going after the malaria parasite everywhere we can."

But in the Mekong, the parasite is very hard to find. "The people you most want to reach in malaria are the most difficult to reach," Peto says. They live in isolated villages days from any town on foot, or hours away by jeep or motorbike, down rutted dirt roads that become impassable in the monsoon rains. Some are in rebel-held areas off-limits to government health workers or too dangerous for aid groups to enter. No maps show the routes migrant workers take, and those who are working illegally don't want to be found.

Rubber plantation workers and oth-

harbor parasites at such low levels they can be detected only with the highly sensitive polymerase chain reaction (PCR); rapid diagnostic tests, and even microscopy, will miss them.

In Africa, where transmission is high, the phenomenon is well-known—many people have built up enough immunity that they can carry the parasite without getting sick. But the common wisdom in the Mekong and other low-transmission areas has been that "people here get bitten by an infected mosquito, they get sick, end of story," Nosten explains. "We saw the extent of it and said, 'Wow,'" Dondorp recalls.

Everyone agrees the asymptomatic reservoir must be drained to have any chance of

Skirmishing over the scope of the threat

Almost as soon as researchers discovered that artemisinin, the best drug against malaria, was losing its effectiveness in Cambodia, the fighting began. Just how bad would it be? Would resistance retrace the route of chloroquine, an earlier malaria drug, sweeping west out of the Mekong into India and then Africa, causing millions of deaths? Where is the line between science and advocacy? And what, exactly, is the definition of “resistance” anyway?

Now, science is yielding some answers—and it’s showing that artemisinin resistance is very different from chloroquine resistance and has a very different pattern of spread. But that hasn’t quelled the arguments.

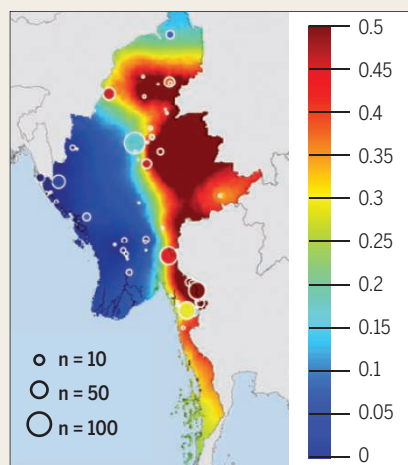
Nick White has been the loudest voice of alarm. When members of the group he heads, the Mahidol Oxford Tropical Medicine Research Unit in Bangkok, reported the emergence of artemisinin resistance in 2009, they warned that the drug could quickly follow chloroquine’s path. And he and his colleagues have continued to sound similar warnings.

“It was a reasonable assumption” at the time, says malariologist Chris Plowe of the University of Maryland School of Medicine in Baltimore. Pascal Ringwald of the Global Malaria Programme at the World Health Organization (WHO) in Geneva, Switzerland, agrees. “Ten years ago there was quite a panic. We thought our whole armamentarium would be lost.”

But several recent studies have revealed a much more complex pattern. “Artemisinin resistance is different than what White predicted,” says Ringwald, who has tracked antimalarial drug resistance for years. “He’s a great scientist and malariologist. But I do not agree with him. ... Artemisinin resistance still could become a big problem. [But] when people say it is a major disaster, we haven’t seen it so far.”

First there’s the definition of “resistance.” Several scientists questioned the Mahidol team’s word choice in their seminal 2009 paper. “It was a political, not a scientific decision,” says Didier Ménard of the Pasteur Institute in Phnom Penh. That’s because, when the parasite is resistant to artemisinin, the drug continues to work, although much more slowly. Chloroquine, in contrast, fails completely.

Nor is artemisinin resistance following the chloroquine model. Caused by several mutations in the *K13* gene of the *Plasmodium falciparum* parasite, it is both spreading throughout the Mekong and arising independently in many places. In a paper published last year in *The Journal of Infectious Diseases*, Plowe and his co-authors from several institutions reported that resistance had spread from western Cambodia into Vietnam, but in Myanmar, considered the “gateway” to Africa, resistant parasites had emerged de novo. The “tsunami” of



Artemisinin resistance in Myanmar

(surveyed via the *K13* marker)

Mutations associated with resistance have been found near the Indian border, but predicted prevalence is highest in the east (dark brown) and lowest in the west (dark blue). Circles are sized according to the number of samples.

westward spread hasn’t happened, Plowe says; instead, resistance is “popping” and “jumping” in the region.

Mutations have popped up independently in Africa, too. When Ménard and a big collaborative team analyzed 14,000 DNA samples of *P. falciparum* from 59 countries, they found that many different *K13* mutations were present at low levels—1% or 2%—in Africa and elsewhere. But those mutants emerged de novo, and, more surprising, they do not seem to blunt the effect of artemisinin. The reason, researchers suspect, is that for artemisinin resistance to evolve, the

mutations need to change the configuration of the so-called propeller domain of the *K13* protein, and not all of them do. Moreover, it seems that mutations in a few other genes are essential to survive and take off—a genetic background that is not yet present in Africa. In other words, *K13* mutations are necessary but not sufficient to cause artemisinin resistance.

So Ringwald and Plowe were taken aback in April 2015 when they read a paper in *The Lancet Infectious Diseases* by the Mahidol group and collaborators that suggested that artemisinin resistance had begun its westward march. The group reported that resistance was much more widespread in Myanmar than previously believed, and that they had detected it just 25 km from the border with India. In a letter in the September 2015 issue, Plowe and Ringwald pounced: “Although the story of a westward spread of artemisinin resistance from Cambodia through Myanmar to India and Africa is compelling to news organizations, this story is not supported by the available data.”

White doesn’t care much how you define it. “If you look at the map of where resistance was a few years ago and where it is today, then it’s spreading, hopping, jumping, emerging, popping, whatever the word is—it is expanding its domain rapidly,” he says. Most alarming, he says, is its arrival at the Indian border.

The factions agree, however, that artemisinin resistance has an alarming consequence: Once parasites are resistant to artemisinin they can evolve resistance to the partner drug used in artemisinin combination therapies, today’s best treatment for malaria. The result is actual treatment failure. Experts on both sides of the debate are backing a radical effort to wipe out the parasite in the Mekong (see main story, p. 398) before it becomes untreatable there—which WHO predicts could happen in Cambodia in just a few years—and to avert the small chance that multiple drug-resistant malaria could spread to and take off into Africa, which, all agree, would be a disaster.

White agrees that artemisinin resistance is much more nuanced than it originally appeared, but he brushes aside the criticism that he and his group have been crying wolf. “If I remember correctly,” he wrote a few years ago, “the wolf did eat the flock.” —Leslie Roberts

eliminating malaria. But consensus crumbles on how to do that, and things can get downright nasty.

"In malaria science, a lot of people are religiously for or against things, and I think religion and science don't mix very well," Smithuis says.

In the malaria world, religion is often code for mass drug administration, or MDA, which involves giving everyone in a region antimalarial drugs, whether or not they are sick. And its high priests, according to the critics, are Nosten, White, *et al.* They are accused of dogmatically pushing a risky strategy with little evidence it works. (MDA has long been used for lymphatic filariasis and other parasitic diseases but has a checkered history with malaria.)

For the past couple of years, Nosten has been conducting a pilot study of MDA in four remote villages along the Thai/Myanmar border, where he has worked with refugees from Myanmar's beleaguered Karen ethnic minority for the past 30 years. With support from the Wellcome Trust, the Global Fund, and BMGF, the team identifies villages that are "hot spots" of transmission and then gives everyone the standard 3-day course of DHA-PPQ and one dose of primaquine, a drug that targets another stage of the parasite's life cycle, each month for 3 months.

Nosten's team is still analyzing the data, but their first impression is that MDA is safe, well-tolerated, largely acceptable—and sometimes remarkably successful. "I can tell you after one-and-a-half years of trying very hard, we are eliminating malaria, and

it's going down very fast," Nosten says. But, he concedes, MDA is extremely time- and labor-intensive, especially because it entails convincing healthy people to take drugs and have their blood drawn repeatedly (see p. 407). The SMRU group is now scaling up and has "mapped" the parasite loads in 1200 villages in Karen state and conducted MDAs in 34.

WHO has just given MDA its blessing in some circumstances in the Mekong, but the strategy remains highly controversial.

***"You treat the sick,
and 3 weeks later they
are sick again, and they
keep getting sick."***

Didier Ménard, Pasteur Institute

Ménard says there is a very real risk MDA could backfire. "Are we sure we will kill all the parasites and not select resistant ones? If you want to select drug-resistant parasites, maybe this is the best strategy," he says. MDR malaria "is an emergency, and we need to act, but I am not sure we need MDA. I am not against it, but we need to conduct studies, and with the results we will make decisions." Malariologist Chris Plowe, who heads the Institute for Global Health at the University of Maryland School of Medicine in Baltimore, says his own work in Myanmar suggests that the size of the

asymptomatic reservoir varies enormously, even in close-by villages, and that means a very targeted approach is in order. "There is no 'cookie-cutter approach,'" he contends.

Often, it is not so much Nosten and White's message that riles people, but the stridency with which they push it. "François has a big mouth," his close colleague Dondorp says. "But he also has a big heart."

For now, Ménard thinks a better strategy is to develop tools that approach the sensitivity of PCR but can be deployed in the field. With those in hand, it would be possible to test everyone for asymptomatic infection and then treat just those who are infected. Such work is already well underway in his lab and others. Plowe's group, for instance, is experimenting with collecting blood spots on filter paper with a simple finger stick and then analyzing those with ultrasensitive PCR in the lab. BMGF is funding research to develop more sensitive rapid diagnostic tests. And the race is on to find a molecular marker for PPQ resistance, the equivalent of the *K13* gene. "This is the beginning of the story," says Ménard, who believes the science is moving so fast that there is time to get it right.

"We have wasted so much time we don't have more time to waste," Nosten moans in response. "We still have to learn about the submicroscopic infection, but we don't want to wait until we understand everything about it before eliminating it. It's a catch-22 thing. People are saying there is no evidence. But if you don't do this [MDA] on a large scale to see what it does, then you don't get the evidence."



Rubber workers on the front lines

To tap a rubber tree, you have to cut the bark just so, at an angle, running halfway around the tree, and not too deep or you will kill it. Immediately the viscous, white liquid begins to ooze, collecting slowly in a small wooden bowl tied to the tree that looks like a coconut shell.

Srey Kheng, the manager of Try Pheap plantation in Kampong Thom province, right in the middle of Cambodia, is demonstrating with his special,

Tha Sitheth was 13 years old when he got malaria while working on a rubber plantation.

ebony-handled chisel—the actual tapping is done late at night with far cruder implements.

The young men who perform this task have some of the highest rates of malaria in the country—and they and their counterparts throughout the Greater Mekong subregion are one of the greatest challenges to the new plan to eliminate malaria there (see main story, p. 398). Plantation workers are some of the hardest people to reach, moving frequently to follow jobs and living in remote areas in squalid conditions. They work and sleep outside with no protection

Besides, White asks, what else is on the table? “The only other option I’ve heard is to do nothing.” Except, of course, have more meetings “with heartfelt pleas for how hard this is and all that bureaucratic language to do with strengthening and capacity building and transformative and god knows what else—a lot of stupid buzzwords. The Belgians call it fried air.”

Even if the researchers could agree on the best way forward, the plan could still be hobbled by bureaucratic inertia and corruption. More than 2 years after WHO recommended Cambodia switch from DHA-PPQ to an artesunate-mefloquine combination, the drugs are just arriving.

Transparency International ranks Cambodia and Myanmar among the most corrupt countries in the world. Recently, the Global Fund froze millions of dollars intended to pay malaria workers while it investigated travel expenses and other irregularities in the Cambodian national malaria control program. (The dispute was finally resolved and money released in December 2015.)

“It is too crazy for words,” Smithuis says. “If you are a malaria parasite and you want to stay ahead of drugs and you are looking at all this you think, ‘Yo, this is exactly what I need. I need a bunch of people falling all over each other with so much envy and bickering and so little action.’ The parasite must be laughing.” ■

Reporting for this package of stories was supported by a grant from the Pulitzer Center on Crisis Reporting.

THE UNLIKELY DIPLOMAT

Myaing Myaing Nyunt fled Myanmar in 1988; now she is back, forging alliances against malaria

By Leslie Roberts

On a blistering hot October day last year, the air thick with impending rain, Myaing Myaing Nyunt and I lurch in a wooden oxcart toward Sa-ka-pin, a small village in the rich agricultural lowlands about 20 kilometers northeast of Mandalay, Myanmar. We grip the splintery sides of the cart as the animals plunge chest deep in the muck; when they swish their tails, mud splatters everywhere. It’s 1 month before Myanmar’s historic election, and with us in the back is a young doctor with “NLD,” the initials of Aung San Suu Kyi’s opposition party, the National League for Democracy, shaved into

his close-cropped hair. A second cart carrying township medical officers follows close behind. We stop at a wide, shallow river, where a man in a dugout canoe ferries us across. Two more carts are waiting for us.

Nyunt, a malariologist at the University of Maryland School of Medicine (UMD) in Baltimore, is visiting Sa-ka-pin to assess the

extent of one of the biggest problems facing an ambitious campaign to wipe out malaria from the Mekong region (see main story, p. 398): the number of people infected with malaria who have no symptoms. It’s part of a unique collaboration led by Nyunt and her husband, molecular epidemiologist and malariologist Chris Plowe, who heads the Institute for Global Health



Myaing Myaing Nyunt

from the abundant mosquitoes that transmit the disease. Repeatedly infected, they often forgo treatment or take substandard drugs or monotherapies, which fuel resistance to malaria drugs. Private plantation owners, sometimes engaged in illegal logging, are loath to let in outsiders, even to treat or prevent malaria.

But Try Pheap is taking part in a program run by Population Services Khmer (PSK), part of the non-governmental organization (NGO) Population Services International (PSI), to bring rapid malaria diagnosis and early treatment to the plantations. “NGOs just don’t waltz in,” explains Abigail Pratt,

a technical adviser to PSI’s malaria and child survival program in Phnom Penh. Persuading the owners “is a delicate dance,” she says, assuring them that PSI is interested only in improving health and will not report any violations such as illegal logging or underage workers.

The community on the plantation has elected a local malaria worker—in this case, the manager, Kheng, who is supplied with free drugs and trained to treat only those with confirmed cases of malaria. When a tapper or family member develops a fever, Kheng uses a rapid diagnostic test that shows whether someone is infected with one of the two

malaria parasites circulating here, *Plasmodium vivax* or *P. falciparum*, or both. Almost a third of the fevers tested on this plantation are malaria, Pratt says. There were five cases of *P. vivax*, the milder form of the disease, in the past 8 months.

One worker recently had malaria three times, showing up sick again 2 months after treatment. It could be drug-resistant malaria or new infections, but most likely, he felt better after a couple days and didn’t finish his medicine.

As we talk, the workers, who look considerably younger than the legal age of 20, are running and punching each other and peeking out at the

foreigners from behind the dizzyingly straight rows of trees. They finally come out to pose for a photograph.

At first PSK offered just malaria services, but few people came for a fever alone, says Mak Sarath, who directs the malaria program in Phnom Penh. Now, PSK is moving into integrated health care, offering diarrhea treatment kits, condoms, and deworming tablets. Supplies are an issue, however. Right now Kheng is out of diarrhea kits and has just three courses of malaria drugs left.

Since 2013, PSK has signed up 118 plantations in Cambodia. They have about 500 to go. —Leslie Roberts

at UMD. They are working with government scientists in Myanmar to forge the scientific and political links needed to drive malaria from her native country. The project has brought Nyunt back to Myanmar after more than a quarter-century of living abroad, much of it in exile.

She was 22 years old and in the sixth and final year of medical training at Rangoon University (now the University of Yangon) on 8 August 1988 when her country exploded. Tens of thousands of students and then doctors, monks, and ordinary Burmese took to the streets, demanding an end to the repressive military regime led by Ne Win. Hundreds, perhaps thousands of protesters were killed before the uprising ended 18 September 1988 with a military coup. The day is memorialized as 8-8-88.

Nyunt and many other students fled to

2008, both from Johns Hopkins University in Baltimore. “For 20 years I cut myself off from all things Burmese,” she says. “I was immersing myself in American culture. I was finishing medical school and raising a daughter.”

That changed during a second outbreak of turmoil in Myanmar, the Saffron Revolution of 2007, when she watched in horror on TV as soldiers gunned down protesting Buddhist monks in the streets. “I realized that whatever we [the West] had been doing for the past 20 years wasn’t working. The economic sanctions didn’t stop the regime but left the people in appalling isolation and poverty.” By then she was married to Plowe, and they began talking about what they could do, settling on science—particularly malaria—as a way to bridge some of the many divides.

Nyunt cobbled together funds, including

lage, a midwife-turned-malaria researcher greets us at the small rural health center. She is dressed in a bright red longyi and impossibly white, starched blouse, and her cheeks are smeared with bark paste known as thanaka to protect her skin from the sun.

Plowe is trying to develop surveillance methods that hit the “sweet spot,” by which he means sensitive enough to detect very low parasite loads in asymptomatic carriers—microscopy is too crude—but portable enough to use in the field. One is being tested here as the midwife uses a finger stick to collect 300 microliters of blood, just five or six drops, in a small tube, then she treats the samples with a DNA/RNA shield, essentially detergent to prevent degradation. “Her samples are impeccable,” Nyunt tells me.

“You can stick the tube in your pocket and carry it around at room temperature for a couple of weeks,” Plowe says, until someone is able to transport it to a government lab in Yangon. There, scientists trained by Plowe’s group run the samples through a high-throughput, ultrasensitive polymerase chain reaction machine, compliments of UMD and BMGF, to detect the parasite’s DNA.

Nyunt and Plowe are also forging political alliances. In August of last year, they organized an unusual meeting in Washington, D.C., where many of the splintered factions in Myanmar sat down at the same table to talk. Participants included high-level military scientists, representatives of Myanmar’s president and government ministries, then-opposition leader Aung San Suu Kyi, and three prominent ethnic minority groups. All must be involved if elimination is to succeed, Nyunt and Plowe contend.

Also in attendance were most of the big funders in malaria research in the United States. Tense at first, discussions yielded an unexpected consensus statement: The group would rise above politics and eliminate malaria. “It was very emotional,” Nyunt says.

Not everyone is persuaded by Nyunt and Plowe’s brand of diplomacy, arguing that they risk being co-opted by the government and that malaria experts should just get on with the job. Nyunt says her eyes are wide open as she waits to see whether all the “nice gestures” translate into action. But, she cautions, “malaria will not be eliminated by expat scientists or international NGOs [nongovernmental organizations]. It must be done by the Burmese.” ■



Myaing Myaing Nyunt fled Burma when soldiers brutally ended an uprising for democracy, pictured here on 26 August 1988.

the Thai border, where she “floated” for a year, eventually ending up in Bangkok selling luggage. There she met malariologist Nick White of the Mahidol Oxford Tropical Medicine Research Unit in Bangkok. White and some friends helped get Nyunt out of the country and to the United Kingdom in 1989—he still will not say how—to continue her medical education.

But with no papers and no passport, no school would take her. So Nyunt worked as a waitress and a companion to an elderly woman in Oxford. In 1990 she immigrated to the United States, where a small liberal arts college in the Northeast agreed to accept her as a junior. She finished her medical degree in 2000 and her Ph.D. and fellowship in clinical pharmacology in

from George Soros’s Open Society Foundation. In 2012, when the United States loosened some sanctions, she landed a small grant from the National Institutes of Health to conduct a study of malaria in pregnancy in 12 villages. Plowe was training local investigators in molecular epidemiology and tracking the spread of artemisinin resistance. Soon their work evolved into the current collaboration: a \$4.6 million project funded by the Bill & Melinda Gates Foundation (BMGF). The aim is to conduct molecular surveillance of the so-called asymptomatic reservoir and also to build the political will within Myanmar for malaria elimination.

Sa-ka-pin is one of 44 villages in nine states and regions where the partners are working. When we finally reach the vil-



Virtually all the inhabitants of a village are given antimalaria drugs in pilot tests like this one in western Cambodia.

THE VILLAGE RECRUITER

In tests of a controversial strategy, advance liaison to often-skeptical villagers is crucial

By Leslie Roberts

On the road out of Pailin, Cambodia, the signs reflect the perils of life here. On the left, one announces that the field has been cleared of mines, a serious danger in one of the most heavily land-mined countries in the world. On the right, a sign warns parents to keep their children away from cook stoves. Others posted along the road promote rapid diagnostic tests for malaria and quality-assured artemisinin combination therapies (ACTs), part of a huge push to stop the use of fake or substandard malaria medicines.

We're heading to the remote village of Veal Roulem, which means "rainy field" in Khmer, one of several sites where a team from the Mahidol Oxford Tropical Medicine Research Unit in Bangkok is wrapping up a pilot study of a radical approach to eliminating malaria. Known as mass drug administration (MDA), it essentially entails giving an entire village—a so-called malaria hot spot—of healthy people powerful malaria drugs in the hope of wiping out the malaria parasite *Plasmodium falciparum*.

It's a "somewhat unpopular, somewhat controversial" strategy, says Tom Peto, a co-leader with Rupam Tripura of the study, which is being done in collaboration with the Cambodian national malaria program. And it is the job of Chhoeun Heng, who is widely known as Mr. Heng, to sell it to an understandably suspicious community.

When we pull up to a house that does double duty as a field office and sometimes dormitory for the Mahidol team, a small girl runs out and jumps into Mr. Heng's arms. He laughs and carries her to the outdoor kitchen, where her adoptive parents, farmers in their 50s, are sitting in the shade. Like almost everyone in the village, they were conscripted into the Khmer Rouge, and the mother lost a leg when she stepped on a landmine bringing food to the battlefield in 1983. After 2 decades in the province, Mr. Heng still marvels at people's lack of bitterness. Laughter comes easily as the three catch up over a lunch of omelets and rice.

It's a far cry from how the team was received about a year earlier, when they arrived to launch their study. "Some thought we were here to test medicines on them,

and they would die in a year or two," says Mr. Heng, a Cambodian nurse who worked in a refugee camp before signing on with the Mahidol group to head community recruiting. HIV/AIDS was a fear: About 100 people in the same province had recently been infected when an unlicensed doctor, since convicted, reused dirty needles, according to press reports. The villagers also worried that they would be weakened by frequent blood draws.

The team had already set up shop in another village. But they decided to relocate when the rumors here threatened to scuttle the entire project. "We came here to build trust," Mr. Heng says. During the study, the team would stay in the village for 15 to 20 days at a stretch. Other times they would be stranded here when swollen rivers rose too high to ford and washed away bridges.

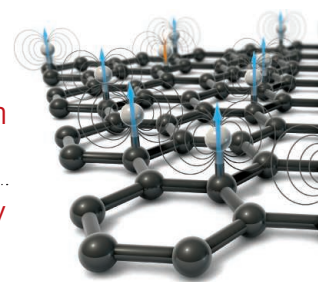
The study is similar to a clinical trial the Mahidol group recently completed along the Thai/Myanmar border (see main story, p. 398). Volunteers are given the standard 3-day course of an ACT 1 month apart for 3 months, whether or not they have malaria. At baseline and every 3 months after for a year, the researchers draw blood from a vein in the arm and then send the samples to Bangkok for analysis. The hypothesis is that if, after treatment, the parasites are gone from almost all the village's population, the cycle of transmission will be broken.

To get people on board, the team visited village leaders, accompanied by officials from the local health department and the governor's office. Then came a series of community meetings to explain the study; informed consent was obtained house by house. Several evenings Mr. Heng and the crew brought in bands and dancers or embarrassed themselves singing karaoke.

Enrollment in the first round was an impressive 90%. But trust proved fragile, Mr. Heng says. Many villagers caught colds. Others complained of weakness and nausea, and they, too, blamed the drug. Enrollment in the second round dropped to 72%.

The team redoubled its efforts, holding focus groups with women, who make the decisions about health in a family. At community meetings, they refined their message. And they brought in well-respected authorities—the police, the army, and border guards—to vouch for them. Buddhist monks blessed the project. In round three, enrollment hit 85%.

Final results aren't in yet, but one thing is already abundantly clear, Peto says: "MDA is not impossible, but it is not a trivial thing." ■



PERSPECTIVES



What a waste. In developed nations, an average of 10 to 30% of household food is thrown away.

FOOD WASTE

Waste not, want not, emit less

Reducing food waste in the supply chain and at home can help to reduce carbon emissions

By Jessica Aschemann-Witzel

Ensuring a sufficient supply of quality food for a growing human population is a major challenge, aggravated by climate change and already-strained natural resources. Food security requires production of some food surpluses to

safeguard against unpredictable fluctuations (1). However, when food is wasted, not only has carbon been emitted to no avail, but disposal and decomposition in landfills create additional environmental impacts. Decreasing the current high scale of food waste is thus crucial for achieving resource-efficient, sustainable food systems (2). But, although

avoiding food waste seems an obvious step toward sustainability, especially given that most people perceive wasting food as grossly unethical (3), food waste is a challenge that is not easily solved.

MAPP Centre, Department of Management, Aarhus University, 8000 Aarhus C, Denmark. Email: jeaw@mgmt.au.dk

About one-third (in weight) of the world's food overall (4) or one-fourth (in kilocalories) of the world's crops (5) are lost or wasted. Food loss encompasses loss of agricultural produce—for example, when crops are damaged during production, harvest, storage, transport, and processing. Food waste refers to the wastage of items fit for human consumption—for example, when foods are discarded in the retail trade, in food service, or in households because they are regarded as “suboptimal” when close to the “best-before” date or due to minor product flaws. Some authors expand the definition and argue that crops potentially for human consumption but grown for nonfood purposes, such as animal feed or energy, should be regarded as food losses and that overnutrition leading to obesity constitutes food waste (6).

Food loss and waste are caused by many factors across the supply chain and differ by the country and commodity in question, but can be roughly separated into two areas of concern. Developing countries suffer the greatest loss during the early, upstream part of the supply chain. For example, 75% of food losses occur during production and postharvest in Africa. In contrast, industrialized countries waste most downstream, especially in the consumption stage. For example, household-level waste accounts for 50% of overall loss and waste of crops in North America and Oceania (5). The share of food that is lost or wasted is particularly high for perishable products such as fresh fruits and vegetables (6, 7). However, the environmental impact of wastage is especially notable for meat because of its large carbon footprint. Food loss and waste in total are greatest in Asia (4, 5), but per capita they are highest in high-income countries; great within-country differences due to income disparities are suspected (1, 5, 6).

In developing countries, policy recommendations for tackling food loss and waste include building better infrastructure through transfer of knowledge and technology and improving collaboration and market opportunities in the food supply chain (4, 6). Achieving this might hinge on good political governance (5) and should include locally adapted small-scale farming (6) to bring about effective and sustainable production. However, urbanization and dietary transition, especially in countries such as BRIC (Brazil, Russia, India, and China), is expected to increase food-waste volumes and shift a greater share of it to the consumption stage in households and catering (6).

In developed countries, food waste in the consumption stage is influenced by societal factors such as the economic situation, technological innovation, and food legislation, but also by more immedi-

ate factors such as product and packaging characteristics and retailer marketing strategies. Furthermore, an individual's demographics and mindset can explain food-waste levels (8, 9). For example, families, younger consumers, and single households waste relatively more (6). However, levels of food waste also depend on an individual's values, attitudes, and motivation and his or her skills in food provisioning and handling (9). Moreover, culture, habits, and emotions (such as cultural norms that prescribe offering plenty of food to guests, food safety misperceptions, and exaggerated disgust) partly explain why, on average, 10 to 30% of a household's food basket is thrown away (8, 10). Often, causes of food waste boil down to a trade-off: Consumers want to avoid wasting food, but then prioritize taste, convenience, or health concerns in the day-to-day situation (9).

Given the complex drivers of food waste, involvement of numerous stakeholders is crucial. To reduce food waste, experts rec-

“...the problem of food waste is a symptom of the currently unsustainable food supply.”

ommend that governments develop legislation to make date labels (such as sell-by, best-before, and consume-by) more user-friendly for consumers (11) and that retailers loosen aesthetic standards (12).

Governments can provide a supportive context, for example, by regulating retailer food waste and changing overly strict food safety laws to allow use of suboptimal foods. Producers can help with innovative product and packaging solutions, for example, to allow easy withdrawal of small amounts while the rest remains fresh (7). Retailers should act responsibly, for example, by abolishing or changing “buy 1 get 2” offers and better aligning orders with demand. Campaigners and NGOs can trigger consumer interest and action, for example, with “Feeding the 5000” events (9).

Food-waste reduction campaigns encourage consumers to become more aware of the extent and consequences of food waste and how adopting small, daily behavioral changes (such as checking the fridge prior to shopping) can help to tackle the problem (8). Efforts seem fruitful, so far. Consumers appear receptive to discounts on food nearing its expiration date, or to retailers advertising imperfections in fruits and vegetables as natural and lovable. Redistribution of surplus food through food-banks has gained considerable foothold,

and there are indications that societal campaigns successfully contribute to shifting social norms and consumer motivation (8, 9). However, many actions are at an experimentation stage.

Greater food-waste reduction requires collaborative, multifaceted mitigation actions and policies. These should work hand in hand with other food policy goals. Sometimes the solutions may be counter-intuitive: When a food item has a high environmental impact, more packaging might help to reduce food waste (7). Price reductions of food close to the expiration date and alternative redistribution are not effective if they simply postpone wastage from retailers to households, but the exact relation between pricing, consumer behavior, and food waste is underexplored (9). There are also trade-offs to consider: Care must be taken that an increased societal focus on food-waste avoidance does not cause consumers to dismiss legitimate food safety concerns—such as eating fish beyond the consume-by date (11).

Food-waste reduction efforts should not distract public attention from the fact that buying less meat—particularly red meat—is even more effective for reducing both carbon emissions and pressure on our natural resources (13). After all, the problem of food waste is a symptom of the currently unsustainable food supply. A broad range of efforts are needed to move toward sustainable food security for all, and each individual consumer contributes both to the problem and the solution (2). The fact that consumers and stakeholders alike perceive food waste as obviously unethical makes it a good starting point for individual consumers to become engaged in sustainability. ■

REFERENCES AND NOTES

1. E. Papargyropoulou et al., *J. Cleaner Production* **76**, 106 (2014).
2. J. A. Foley et al., *Nature* **478**, 337 (2011).
3. D. Evans, *Food Waste: Home Consumption, Material Culture and Everyday Life* (Bloomsbury, London, 2014).
4. Food and Agriculture Organization, *Food waste footprint: Impacts on natural resources. Summary report* (FAO, Rome, 2013); www.fao.org/docrep/018/i3347e/i3347e.pdf.
5. M. Kummu et al., *Sci. Total Environ.* **438**, 477 (2012).
6. J. Parfitt, M. Barthel, S. Macnaughton, *Philos. Trans. R. Soc. B* **365**, 3065 (2010).
7. F. Wikström et al., *J. Cleaner Production* **73**, 100 (2014).
8. T. E. Quested et al., *SI: Resourceful Behaviours* **79**, 43–51 (2013).
9. J. Aschemann-Witzel et al., *Sustainability* **7**, 6457 (2015).
10. J. C. Buzby, J. Hyman, *Food Policy* **37**, 561 (2012).
11. S. Van Boxtael et al., *Food Control* **37**, 85 (2014).
12. T. Stuart, *Waste: Uncovering the Global Waste Scandal* (Penguin, London, 2009).
13. C. Hoolohan et al., *Energy Policy* **63**, 1065 (2013).

ACKNOWLEDGMENTS

I thank the COSUS (cosus.nmbu.no) research team for excellent collaboration and B. Steffensen, V. Kulikovskaja, L. Haahr, and T. Hesselund Nielsen for valuable feedback on the text.

10.1126/science.aaf2978

ULTRAFAST OPTICS

Electrons catch a terahertz wave

Far-infrared fields control ultrashort electron pulses

By Claus Ropers

Electron microscopy and diffraction are incredibly successful techniques for studying the structure of matter on the atomic scale. Making these techniques “ultrafast”—that is, using pulses of femtosecond duration—could provides us with unprecedented microscopic vistas into how materials evolve on time scales typical of atomic motions (1, 2). One of the key challenges in this research area is the controlled generation of short flashes of electrons. On page 429 of this issue, Kealhofer *et al.* demonstrate a powerful means to shape electron beams in time through their interaction with terahertz electromagnetic fields (3).

Producing short bursts of electrons is far from easy, although the first step is straightforward: Illuminate a metal surface with a laser pulse, and electrons will be emitted into vacuum by the photoelectric effect. Unfortunately, these electrons will have different velocities, and although they may be ejected all at once, they will spread apart as they fly away from the surface (see the figure). Moreover, if many electrons per pulse are

produced, they will repel each other by Coulomb forces. Both effects lead to a stretching of the pulse as it propagates. However, the time resolution of an ultrafast electron diffraction or microscopy experiment crucially depends on the electron pulse duration at the sample position, which should be as short as possible.

A number of strategies have been developed to alleviate this pulse spreading, in-

“If the strength of the fields and the timing are perfect, one can make sure that the electrons will all meet up at a point further downstream in the beam...”

volving the use of compact electron guns (4), nanoscopic electron-source designs (5–7), or active manipulation of the electron bunch (8, 9). A prominent example of this latter approach involves radio-frequency technology (8): An already stretched electron pulse is injected into a microwave cavity at exactly the right moment, such that the electrons at the front of the pulse

are slowed down a little by the microwave field, while the trailing ones are sped up by just the right amount. If the strength of the fields and the timing are perfect, one can make sure that the electrons will all meet up at a point further downstream in the beam; the pulse has successfully been compressed. A number of laboratories worldwide have mastered and continuously optimized this technique. It requires a synchronization of high-power microwave electronics with pulsed laser sources, but comes with the drawback of a small but unavoidable jitter in timing.

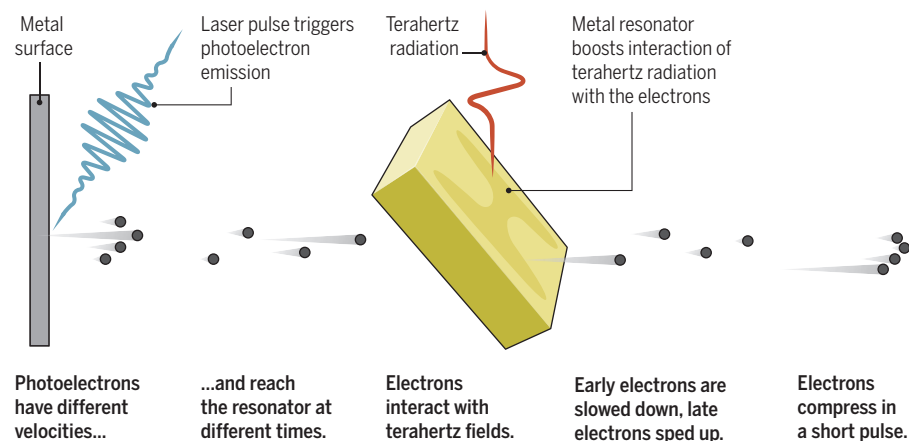
Kealhofer *et al.* take a different route that uses only the laser field itself, together with some nonlinear optics, to produce, compress, and measure the electron pulses. In this way, there are virtually no synchronization issues remaining. In particular, they use terahertz fields—far-infrared radiation at the intersection of optics and microwave electronics—to act on the electrons within bowtie-shaped microstructures enhancing the fields (see the figure). The compression that slows early electrons and accelerates late electrons is achieved by tilting one of these structures, thus allowing the terahertz fields to act in the forward direction.

The authors then characterize the electron pulses in what is essentially a miniaturized, extremely fast version of a cathode ray tube used in oscilloscopes or television tubes: The terahertz fields in a second microstructure deflect the electron beam on a screen, and the width of the resultant streak evidences the electron pulse duration.

Using their setup, Kealhofer *et al.* were able to measure electron pulse durations of 75 fs, a factor of greater than ten reduction from the value in the absence of the terahertz compression, and with negligible long-term jitter of only a few femtoseconds. With data of impressive quality, the study successfully joins various concepts involving intense terahertz radiation, such as near-field streaking (10), electron acceleration (11), and a proposed streak camera (12), to create a terahertz-driven electron-pulse beamline for time-resolved imaging and diffraction applications.

So far, the scheme has been applied to pulses containing only a single electron on average, thus avoiding the Coulomb repulsion problem. Yet there is an ongoing debate as to the effectiveness of single-electron

4th Physical Institute and International Center for Advanced Studies of Energy Conversion, University of Göttingen, D-30707 Göttingen, Germany. Email: c.ropers@gwdg.de



Terahertz pulse compression. Electrons with a distribution of velocities are ejected from a metal surface by a laser pulse shown in blue. As the electron ensemble propagates, it spreads out in time and space. A properly timed terahertz pulse (red) incident on an apertured microstructure decelerates the early-arriving electrons while accelerating those arriving later. This process causes a compression of the electron pulse, which facilitates experiments with enhanced temporal resolution.

pulses in ultrafast imaging. Many processes are irreversible and must be probed with one massive electron burst, whereas others can be sampled in a stroboscopic fashion with many single- or few-electron pulses. It will be interesting to see whether and how effective terahertz compression techniques can also be applied to electron pulses containing large numbers of electrons. Most likely, adaptations would have to be made to account for the stronger initial pulse stretching arising from Coulomb forces. Lower-frequency fields, and perhaps cascaded stages with multiple interaction regions operating at different frequencies, may be a solution.

The rapid ongoing development in high-power laser sources is clearly widening the scope of possibilities, and Kealhofer *et al.* provide a very elegant solution to all-optical temporal beam shaping and characterization that could serve as the blueprint for future developments. More generally, the work is an excellent example of a trend toward optical manipulation of beams of electrons (9). In electron microscopy, lithographically produced phase plates are gaining interest as a means of preparing well-defined orbital angular momentum states and achieving miniaturized aberration correction. However, these devices are static and yield control only over the transverse properties of the beam, perpendicular to its propagation direction. Time-dependent fields, on the other hand, are required to influence the beam along its direction. In the future, quantum coherent optical interactions with free electron states (2, 13, 14) will enable tailored and configurable control over both the longitudinal and transverse variables of the quantum mechanical electron wave function, possibly resulting in electron microscopy and spectroscopy with attosecond precision. Beyond microscopy, the growing means to exert optical control over free electrons may also have an impact on other research fields, including benefits to the spatial and temporal beam properties of synchrotrons and free-electron laser sources. ■

REFERENCES

1. R. J. D. Miller, *Science* **343**, 1108 (2014).
2. A. H. Zewail, *Science* **328**, 187 (2010).
3. C. Kealhofer *et al.*, *Science* **352**, 429 (2016).
4. B. Siwick *et al.*, *Science* **302**, 1382 (2003).
5. M. Gulde *et al.*, *Science* **345**, 200 (2014).
6. M. Müller *et al.*, *Nat. Commun.* **5**, 5292 (2014).
7. J. Hoffrogge *et al.*, *J. Appl. Phys.* **115**, 094506 (2014).
8. T. van Oudheusden *et al.*, *Phys. Rev. Lett.* **105**, 264801 (2010).
9. E. Hemsing *et al.*, *Rev. Mod. Phys.* **86**, 897 (2014).
10. L. Wimmer *et al.*, *Nat. Phys.* **10**, 432 (2014).
11. E. A. Nanni *et al.*, *Nat. Commun.* **6**, 8486 (2015).
12. J. Fabianska *et al.*, *Sci. Rep.* **4**, 5645 (2014).
13. F. J. García de Abajo, *Nano Lett.* **10**, 1859 (2010).
14. A. Feist *et al.*, *Nature* **521**, 200 (2015).

10.1126/science.aaf6393

CLIMATE CHANGE

Mineral clues to past volcanism

A study of zircon minerals from around the world shows that volcanism is a key driver of long-term climate change

By Lee Kump

Over tens to hundreds of millions of years, Earth's climate has repeatedly swung from icehouse, with large ice sheets like today, to greenhouse, when even near-polar climates were temperate (1). The modern paradigm attributes these swings to a dynamic interplay of volcanism, which spews carbon dioxide (CO₂) into the atmosphere, and the chemical weathering of rocks on land, which removes CO₂ from the atmosphere (2). Documenting how these driving forces have varied through time has been a challenge. On page 444 of this issue, McKenzie *et al.* (3) argue that volcanic CO₂ emissions have been the main driver of climate change over the past several hundred million years.

The authors base their conclusion on an analysis of the age distribution of zircon (zirconium silicate) grains from sedimentary rocks around the world. Zircons crystallize from magmas, especially when oceanic plates are subducted beneath continental plates and form continental volcanic arcs, like those in the Andes and the Cascade volcanoes in North America. Because zircon grains are highly resistant to weathering, they are eroded as sand-sized grains, deposited in sedimentary basins, and incorporated into sedimentary rocks. They survive several rounds of subsequent erosion, deposition, burial, lithification, metamorphism, and uplift. As a result, zircons in a given sedimentary rock include some that may have just formed (often associated with volcanic activity) and others of various older ages.

Because zircons contain uranium, thorium, and lead impurities, their ages can be determined precisely through isotope analysis. A high proportion of young zircons in rocks of a given age suggests high volcanic activity at the time of sediment deposition. If, instead, old zircons predominate, volcanic activity is presumed to have been low when the sediment formed.

When McKenzie *et al.* compiled published analyses of ~120,000 zircons, they found an intriguing pattern: Greenhouse intervals, like the Cambrian (~500 million years ago) and Jurassic/Cretaceous (from 200 to 65

million years ago) have sedimentary rocks with a relatively high proportion of young zircons. In contrast, young zircons were rare in the Neoproterozoic (the "Snowball Earth" interval ~700 million years ago), the Carboniferous and early Permian (a time of extensive glaciation ~300 million years ago), and the Cenozoic (the past 65 million years, during which extensive ice sheets have spread across Antarctica, Greenland, and cyclically across North America and Northern Europe).

The swings from icehouse to greenhouse roughly follow the drift of the continents (1). The large continents of the icehouse Neoproterozoic rifted apart, were widely dispersed by the greenhouse Cambrian, and then gradually amalgamated into the supercontinent Pangea by the icehouse Carboniferous-Permian. They then rifted

"The correspondence... between zircon age distributions and long-term climate change is compelling evidence that volcanism has been an important climate driver for the past 700 million years."

apart and dispersed again during the greenhouse Jurassic-Cretaceous. McKenzie *et al.* argue that rifting and dispersal are driven by the creation of new ocean crust, which also demands that old ocean crust be destroyed in subduction zones. Subduction fuels continental arc volcanism, releasing CO₂ to the atmosphere and creating zircons that become part of the sedimentary record. Continental amalgamation leads to the slowing of subduction and a reduction in continental-arc volcanism and associated zircon formation.

The correspondence documented by McKenzie *et al.* between zircon age distributions and long-term climate change is compelling evidence that volcanism has been an important climate driver for the past 700 million years. Of course, a full consideration of the

Department of Geosciences, Pennsylvania State University, University Park, PA 16802, USA. Email: lkump@psu.edu



A mineral window to the past. Based on an analysis of ~120,000 zircon minerals, McKenzie *et al.* argue that changes in volcanic activity along continent-ocean tectonic plate boundaries—as seen today in the Andes—are a key driver of climate change on time scales of millions of years. The photo shows the Tungurahua Volcano in Ecuador.

overall effect of volcanism on atmospheric CO₂ and climate must include the long-term effects of volcanic rocks. During eruption, CO₂ release and its warming effect can certainly dominate. But after eruptions cease, the easily weathered volcanic rocks remain. The CO₂ demand from the eventual weathering of a given volume of erupted lava vastly exceeds the CO₂ released during its emplacement (4). Therefore, volcanism can be a net sink for CO₂ on million-year time scales. Indeed, recent studies of long-term controls on atmospheric CO₂ have tended to focus on volcanic rock weathering (5), with suggestions that global cooling has been driven by intensified weathering of volcanic regions (6, 7).

Interpreting variations in the age distribution of zircons in terms of global volcanic

CO₂ emission requires careful assessment of the assumption that the preserved record accurately reflects the actual age distribution that existed tens to hundreds of millions of years ago. It also presumes that trends in the many forms of volcanism that do not produce abundant zircons, such as mid-ocean ridge and hot-spot volcanism, are unimportant. However, the commonly used approach to reconstructing volcanic emission rates through geologic history (8), using changes in long-term sea level as a proxy, is perhaps even more problematic, involving a string of highly simplified assumptions that have been challenged (9). Zircons are forever (or nearly so) but cannot hide their age, and those ages may be the key to climate change on geologic time scales. ■

REFERENCES

1. A. F. Fischer, in *Biotic Crises in Ecological and Evolutionary Time*, M. H. Nitecki, Ed. (Academic Press, 1981), pp. 103–131.
2. J. C. G. Walker, P. B. Hays, J. F. Kasting, *J. Geophys. Res.* **86**, 9776 (1981).
3. N. R. McKenzie *et al.*, *Science* **352**, 444 (2016).
4. H. D. Holland, *The Chemical Evolution of the Atmosphere and Oceans* (Princeton Univ. Press, 1984).
5. C. Dessert, B. Dupré, J. Gaillardet, L. M. François, C. J. Allègre, *Chem. Geol.* **202**, 257 (2003).
6. O. Jagoutz, F. Macdonald, L. Royden, *Proc. Natl. Acad. Sci. U.S.A.* **10.1073/pnas.1523667113** (2016).
7. D. V. Kent, G. Muttoni, *Proc. Natl. Acad. Sci. U.S.A.* **105**, 16065 (2008).
8. R. Berner, *Geochim. Cosmochim. Acta* **70**, 5653 (2006).
9. R. Moucha, A. M. Forte, J. X. Mitrovica, D. B. Rowley, S. Quere, *Earth Planet. Sci. Lett.* **271**, 101 (2008).

10.1126/science.aaf6612

MEDICINE

Risk literacy in medical decision-making

How can we better represent the statistical structure of risk?

By **Joachim T. Operskalski**
and **Aron K. Barbey**

Imagine that you have received a positive result on a routine cancer screening test. Follow-up biopsies were inconclusive, and the decision to treat aggressively or monitor conservatively is yours. Consider the following information: 0.1% of the population has a terminal version of this form of cancer, 99% of those people will appear positive on the test you have been administered, and 5% of those without terminal cancer will still have a benign condition that tests positive. Given your test result, what is the probability that you have terminal cancer and should treat it aggressively? When judging risks and trying to predict the future, how should you decide? We need to better understand the structure of risks and how the human mind creates representations of risk and probability.

In the scenario above, if your rapid impression of the information at hand supports the intuition that the probability of terminal cancer is close to 95%, then your line of thinking is not surprising, but you would be wrong. The true probability is 2%, with a complementary 98% risk of having undergone unnecessary (and even dangerous) treatment (1). This is hard to grasp intuitively without using Bayes' theorem of conditional probability (2); even physicians and medical students are prone to this error without having been explicitly instructed on the statistics of rare events (3). However, it might be understood more readily if you considered the situation in another way: The small number of false positives in the large population without cancer is a greater number than the majority of true positives in the smaller subpopulation that actually have the disease.

Far from being a statistical curiosity, this is the exact dilemma faced by patients and their physicians every day, and it will become more common as we learn more about the genetic factors that affect health. A "precision medicine" approach formalizes the insight that no two patients are alike (4, 5). Improving medical diagnostic technology will improve many people's lives, but to

prevent doing harm, the medical field and society at large need to understand that technological advances will not remove uncertainty. By understanding the way we think about risk, we can bring insight from the pages of statistical textbooks into legislative sessions, hospital exam rooms, and family discussions alike.

Contemporary research on medical decision-making originates from two traditions in the psychological sciences. The "heuristics and biases" view claims that errors in reasoning are an unavoidable consequence of our mental architecture as humans. Under this view, we each possess a fast and impression-based system of decision-making, in addition to a slower, reflective one capable of complex calculations that checks and verifies our quick impressions (6). Errors in reasoning may result when time pressure or situational complexity cause the reflective system to accept as fact the incorrect output of the impression-based system. Thus, the primary solution to such errors is education in statistics and awareness of our own biases. The "ecological rationality"

"The mind embodies a natural capacity to perform elementary set operations..."

view of decision-making offers another way out, however. By considering reasoning errors as the consequence of having evolved to mentally process information in specific formats, we can better understand risk and uncertainty by communicating with one another using the right types of information (3). For example, abstract concepts, such as single-event probabilities (e.g., 1% chance), would not have appeared naturally in environments inhabited by primitive humans, so we never evolved to think about single-event probability with ease (7). Instead, thinking about long-run frequencies relative to a reference class (e.g., 1 out of 100 times) is easier because it conveys the same information as percents or probabilities in a way that reflects how we experience the natural world. Indeed, even experts in statistics have difficulty making judgments of single-event probabilities without explicitly calculating them. However, when the same

problems are represented as event frequencies, even the statistical layperson can generate a response in accordance with Bayes' theorem. For example, when a sample of college undergraduates was asked to solve problems on the basis of single-event probabilities, only 12% generated a Bayesian response, whereas 56% of another sample did so when given numbers in a natural frequency format (8). Using probing questions and visual aids depicting frequency information raised the accuracy to 76% and 92%, respectively.

Few believe that numerical formats automatically endow us with the ability to mentally calculate the probability of some event by counting observations and comparing them to our prior beliefs. Which cognitive processes, then, account for this remarkable facilitation of Bayesian inference under "natural" or event frequencies? The mind embodies a natural capacity to perform elementary set operations, such as taking the intersection of sets (e.g., "A and B") and union of sets (e.g., "A or B") (9). Such set operations can be induced by frequency formats, which provide cues to the set structure of the problem and therefore facilitate Bayesian inference (9). Indeed, the key variable that predicts accurate inference is not the statistical format of the problem but the transparency of nested set relations (8, 9). As long as the nested set structure of events in a larger reference class is made accessible, one can accurately understand and reason from single-event probabilities (10). However, when the set structure of the problem is obscured by the use of unusual (small or large) reference class sizes, even frequency formats are difficult to understand (11).

Where does contemporary research on human judgment and decision-making leave us as patients, physicians, and policymakers? Even among professionals, there remains a lack of consensus on screening guidelines for diseases such as breast or prostate cancer when their prognostic values are ambiguous (12). In 2014, the U.S. Preventive Services Task Force recommended against using prostate-specific antigen (PSA) test results in diagnosing and treating prostate cancer because the false positive rate and ambiguity of prognosis meant that men with benign or slow-growing tumors were undergoing unnecessary

Decision Neuroscience Laboratory, Beckman Institute, Urbana, IL 61801, USA. Email: barbey@illinois.edu

Visual representations of risk structure

As medical science reveals more about genetic health risk factors, patients will need tools to understand the uncertainty inherent in those risk factors.

Question: 0.1% of the population has a disease, and a test detects it 99% of the time but falsely identifies 5% of healthy people as sick. What is the likelihood of a positive test result being accurate?

Each format below conveys the same fundamental information about risk structure.

A Single-event probability format

Bayes' theorem is necessary (and difficult) when using single-event probabilities to calculate the probability of a hypothesis (having the disease) given the evidence for it (a positive test result).

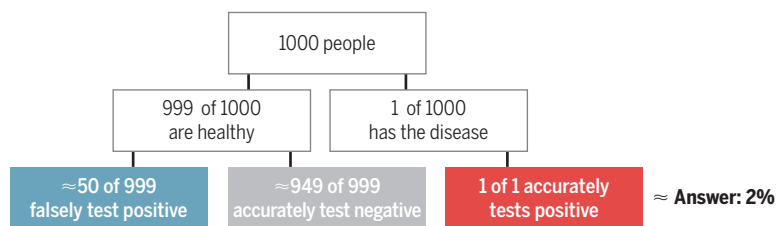
$$\begin{aligned} P(\text{disease}) &= 0.1\% \text{ prevalence of disease} \\ P(\text{positive test}|\text{disease}) &= 99\% \text{ true positive rate} \\ P(\text{positive test}|\text{no disease}) &= 5\% \text{ false positive rate} \end{aligned}$$

$$P(\text{disease}|\text{positive test}) = \frac{0.1\% \times 99\%}{(0.1\% \times 99\%) + (99.9\% \times 5\%)} = 1.94\% \approx \text{Answer: 2\%}$$

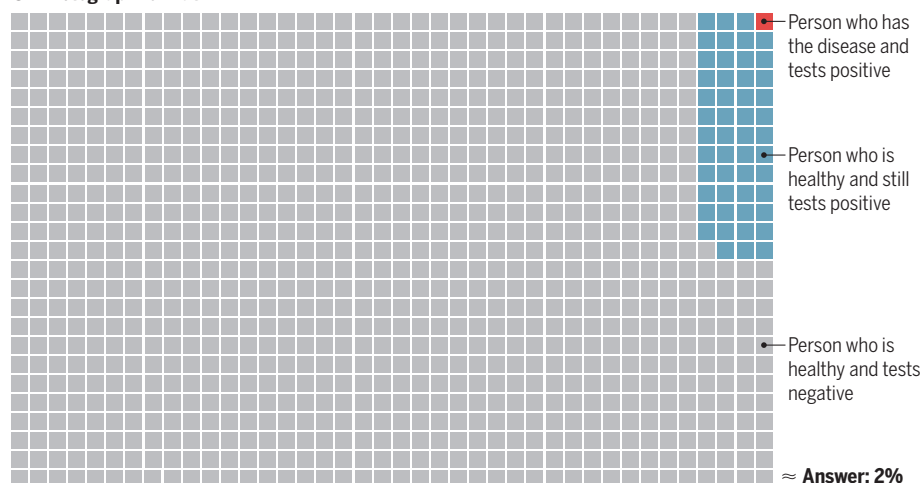
B Nested set format

This view facilitates accurate judgment because it represents base rates (prevalence) and reference class size (1 of 1000) without having to multiply a conditional probability by the base rate.

$$P(\text{disease}|\text{positive test}) = \frac{P(\text{disease AND positive test})}{P(\text{positive test})} = \frac{1}{50 + 1} = 1.96\% \approx \text{Answer: 2\%}$$



C Pictograph format



and risky treatment procedures (13). How did policy-makers arrive at this decision? They understood the statistical structure of risk in medical health problems. Health care systems that screened healthy men for PSA regularly had an approximately 98% 5-year survival rate for those diagnosed with cancer, whereas those that tested only men with symptoms had a 71% survival rate. Why, then, was there no significant difference in cancer mortality (26 versus

27 out of 100,000) between the systems across the entire population? Screening people aggressively when they are young ends up diagnosing extra cases who do not truly have cancer, or whose cancer is so slow-growing that they would not have been at risk for far beyond 5 years anyway. This may seem like an innocuous difference, but the extra diagnoses are associated with treatments that have their own risks. Using natural frequencies and draw-

ing attention to the appropriate reference class (the whole population, not just people who are diagnosed before dying) draws attention to the fact that a higher survival rate is associated with a higher overall rate of positive test results and no difference in base rates of cancer (as indicated by mortality in the whole population) (14). Our instincts may tell us that 5-year survival rates are important, but only if placed in the appropriate context—natural frequencies or nested sets.

What measures can be applied to improve the ability to draw accurate statistical inferences and to fully appreciate the risks posed by medical decisions? It is important to consider conditions that lead to errors, such as risks that could be framed equivalently as gains or losses. Considering all possible outcomes (instead of only survival or mortality) can prevent inappropriate use of heuristics. Representing the problem in natural frequency formats or highlighting its nested set structure is helpful, and depicting outcomes using visual diagrams can facilitate fully informed decision-making via the creation of mental simulations (see the figure).

In the era of precision medicine, we are using a data-driven approach to understand patients as individuals rather than group averages. We are moving away from doctors telling patients with certainty what is wrong and what to do, toward a model in which doctors empower patients to take charge of their own care. To facilitate safe self-stewardship, the biomedical field needs to equip patients with the tools to make well-informed decisions in the face of uncertainty. ■

REFERENCES

1. D. M. Eddy, in *Judgment Under Uncertainty: Heuristics and Biases*, D. Kahneman, P. Slovic, A. Tversky, Eds. (Cambridge Univ. Press, 1982), pp. 249–267.
2. G. Gigerenzer, U. Hoffrage, *Psychol. Rev.* **102**, 684 (1995).
3. G. Gigerenzer, *Med. Decis. Making* **16**, 273 (1996).
4. www.whitehouse.gov/the-press-office/2015/01/30/fact-sheet-president-obama-s-precision-medicine-initiative
5. F. S. Collins, H. Varmus, *N. Engl. J. Med.* **372**, 793 (2015).
6. K. Stanovich, R. West, *Behav. Brain Sci.* **23**, 645 (2000).
7. P. M. Todd, G. Gigerenzer, *Curr. Dir. Psychol. Sci.* **16**, 167 (2007).
8. L. Cosmides, J. Tooby, *Cognition* **58**, 1 (1996).
9. A. K. Barbey, S. A. Sloman, *Behav. Brain Sci.* **30**, 241 (2007).
10. W. P. Neace, S. Michaud, L. Bolling, K. Deer, L. Zecevic, *Judgment Decis. Making* **3**, 140 (2008).
11. S. A. Sloman, D. Over, L. Slovic, J. M. Stibel, *Organ. Behav. Hum. Decis. Process.* **91**, 296 (2003).
12. K. Jorgensen, P. Gotzsche, *JAMA* **315**, 1402 (2016).
13. U.S. Preventive Services Task Force, "Final Recommendation Statement: Prostate Cancer: Screening" (2012); www.uspreventiveservicestaskforce.org/Page/Document/RecommendationStatementFinal/prostate-cancer-screening.
14. G. Gigerenzer, *Psychol. Sci. Public Interest* **8**, 2 (2010).

10.1126/science.aaf7966

Painting magnetism on a canvas of graphene

Hydrogen adatoms can give long-range magnetic order to graphene

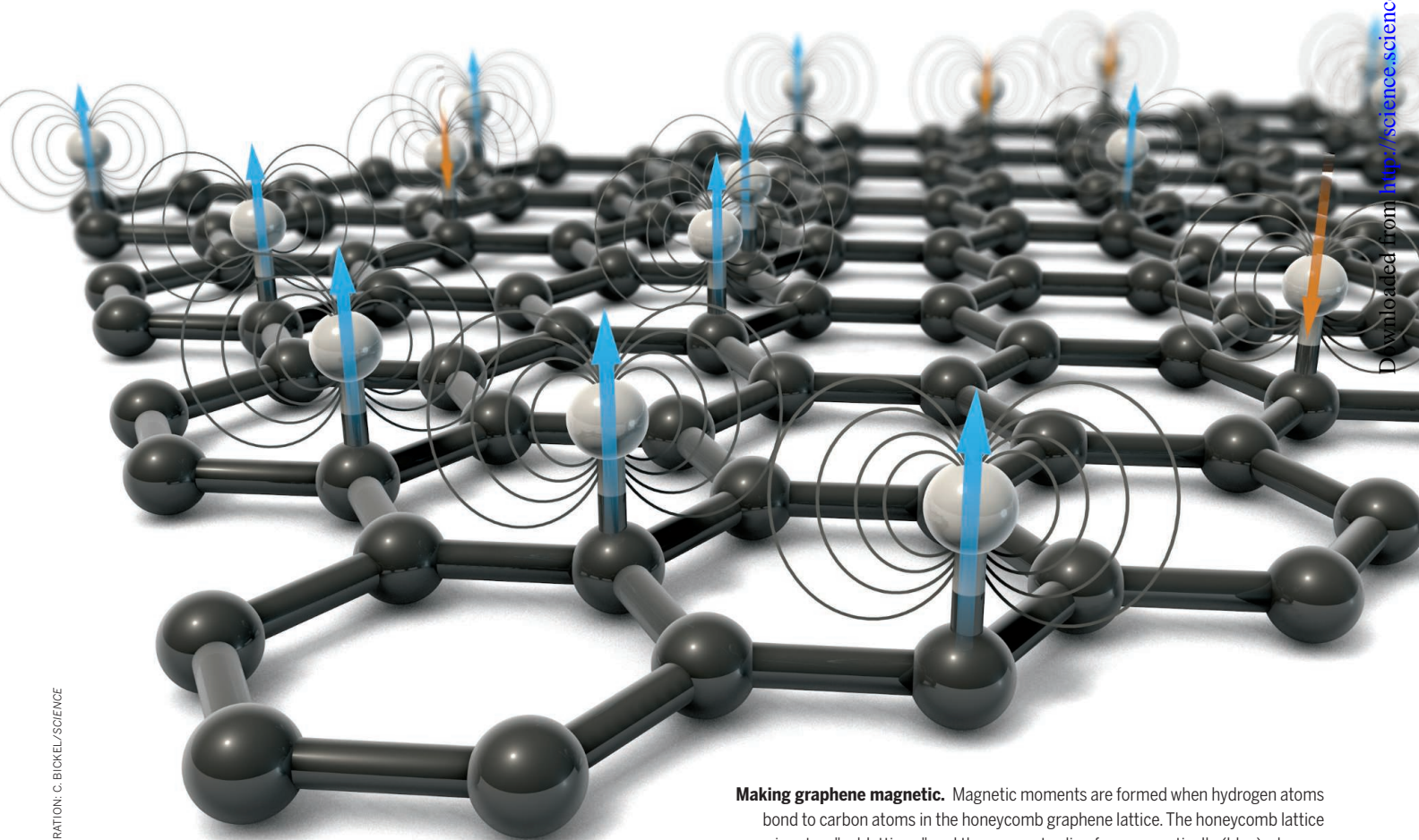
By S. M. Hollen¹ and J. A. Gupta²

An inherent aspect of any two-dimensional (2D) sheet is that all atoms in the material lie on the surface. This leads to a concept of 2D crystals as a “canvas,” where different chemical groups or “ink” on the surface can lead to a palette of distinct materials properties. The most well-studied 2D crystal is graphene, a one-atom-thick sheet of carbon atoms arranged in a honeycomb lattice. Although graphene’s superlative materials properties and novel physical phenomena have led to a variety of applications

(1), better tunability of these properties is still required. Toward this end, hydrogenated graphene (graphane) was predicted to have a wide band gap and exhibit magnetic order (2–4), in contrast to graphene, which is (semi)metallic and diamagnetic. The chemical stability of graphene makes hydrogenation difficult to control, and this has hampered efforts to tune its electronic or magnetic properties. On page 437 of this issue, González-Herrero *et al.* (5) report direct evidence that hydrogen atoms on graphene do indeed yield a magnetic moment and that these moments can order ferromagnetically over relatively large distances. If these methods can be extended to industrial scales, then one can imagine storing information at unprecedented densities by painting magnetic bits on graphene canvases (see the figure).

Magnetism in graphene arises when there is an imbalance in the two hexagonal sublattices that combine to form the overall honeycomb lattice. Although the sublattices are indistinguishable in the ideal, isolated single sheet, the number of atoms in each sublattice can be made unequal because of factors such as point defects or geometric shape. A hydrogen adatom, for example, bonds with the carbon’s p_z -orbital, thus removing it from the network responsible for graphene’s band structure. A counting rule emerges, predicting an integer number of spin-polarized states equal to this imbalance, which can lead to magnetism. The experimental search for magnetic carbon has a controversial history, starting first in organic materials, then later in graphite and graphene. For example, early reports of ferromagnetism in polymerized C_{60} (6) were

¹Department of Physics, University of New Hampshire, Durham, NH 03824, USA. ²Department of Physics, Ohio State University, Columbus, OH 43210, USA.
Email: jgupta@physics.osu.edu



Making graphene magnetic. Magnetic moments are formed when hydrogen atoms bond to carbon atoms in the honeycomb graphene lattice. The honeycomb lattice comprises two “sublattices,” and the moments align ferromagnetically (blue) when on the same sublattice and antiferromagnetically (orange) when on the opposing sublattice.

later attributed to trace amounts of iron in the samples (7). Ferromagnetic graphite, upon proton irradiation (8), was difficult to attribute to magnetic impurities, but was not well understood, owing to the variety of defects formed upon high-energy ion bombardment. Graphene was first isolated around this time as well, and was quickly incorporated into high-quality spin valve devices, analogous to those used in hard disk drives. Such devices provided additional evidence for magnetic carbon, as a signature of spin scattering was observed due to magnetic moments formed when the graphene was exposed to hydrogen or bombarded to create vacancies (9). These results were consistent with magnetometry measurements that showed evidence for paramagnetism (10). However, neither of these approaches were able to observe ferromagnetism, and the atomic origin of the moments could not be directly determined.

González-Herrero *et al.* study one fundamental building block of this magnetic state—namely, individual hydrogen

“...one can imagine storing information at unprecedented densities by painting magnetic bits on graphene canvases.”

adatoms and dimers with controlled sublattice site and spacing. Graphene growth, hydrogenation, and characterization were all performed in the same ultrahigh-vacuum chamber, which was critical in overcoming shortcomings of prior approaches. Few-layer graphene was grown by heating a SiC single crystal, thus minimizing the possibility of magnetic impurities or contamination from the environment. Relatively low-energy atomic hydrogen from thermal cracking of H₂ yielded a low surface coverage of a single class of defect, rather than the variety of defects and complexes produced by high-energy ion irradiation. Lastly, in situ scanning tunneling microscopy (STM) was used to characterize the quality of the sample before and after hydrogenation and to directly probe the electronic states associated with individual hydrogen atoms on the surface. This method avoids the ensemble averaging typical of more conventional magnetic characterization techniques.

To prove that the hydrogen adatoms were magnetic, the authors drew insight from the Anderson model of impurity magnetism, a model that predicts sensitivity to doping. This was observed by the collapse of

a spin-split doublet of states into a single state, upon n-type or p-type doping of the graphene. More quantitative density functional theory (DFT) calculations validated this interpretation and provided insight into magnetic ordering between adatoms. Experimentally, González-Herrero *et al.* were able to directly probe interactions by using STM atomic manipulation to form hydrogen dimers with varying spacing and sublattice site. As explained by the DFT calculations, and realized experimentally, dimers on the same sublattice create an imbalance and order ferromagnetically, whereas dimers on opposing sublattices maintain the balance and are nonmagnetic. These interactions persist at relatively large separations compared to conventional magnets based on more localized atomic orbitals.

There are several key challenges toward realizing robust magnetic graphene for applications. First, the sensitivity of the magnetic state to doping offers the opportunity for control with a gate electrode, but may be problematic in typical graphene devices, where charged impurities in a SiO₂ substrate create random puddles of n- and p-doping. Future work could probe whether wide band-gap graphene is as vulnerable to charge puddles, or reduce their influence through sandwich structures of other 2D materials, such as boron nitride. Second, although longer-range magnetic ordering is promising, it also places a premium on control over the hydrogen adsorption site. This atomic-scale precision is very difficult to realize on a large scale, though preferential adsorption may be possible by breaking the degeneracy of the sublattices through interactions with other graphene layers or other 2D materials in close registry. Ferromagnetic ordering above room temperature has been predicted for magnetic graphene, but it remains to be seen if this target can be realized experimentally. If these challenges can be met while preserving the intrinsic quality of graphene for electron and spin transport, then graphene may indeed become a leading candidate material in the roadmap for next-generation information technologies based on electron spin. ■

REFERENCES

1. A. C. Ferrari *et al.*, *Nanoscale* **7**, 4598 (2014).
2. J. Sofo, A. Chaudhari, G. Barber, *Phys. Rev. B* **75**, 153401 (2007).
3. O. V. Yazyev, *Rep. Prog. Phys.* **73**, 056501 (2010).
4. J. Zhou *et al.*, *Nano Letters* **9**, 3867 (2009).
5. H. González-Herrero, *Science* **352**, 437 (2016).
6. T. L. Makarova *et al.*, *Nature* **413**, 716 (2001).
7. T. L. Makarova *et al.*, *Nature* **440**, 707 (2006).
8. P. Esquinazi *et al.*, *Phys. Rev. Lett.* **91**, 227201 (2003).
9. K. M. McCreary *et al.*, *Phys. Rev. Lett.* **109**, 186604 (2012).
10. R. R. Nair *et al.*, *Nature Phys.* **8**, 199 (2012).

BIG DATA AND BIODIVERSITY

Filling in biodiversity threat gaps

Only 5% of global threat data sets meet a “gold standard”

By L. N. Joppa,*† B. O'Connor, P. Visconti, C. Smith, J. Geldmann, M. Hoffmann, J. E. M. Watson, S. H. M. Butchart, M. Virah-Sawmy, B. S. Halpern, S. E. Ahmed, A. Balmford, W. J. Sutherland, M. Harfoot, C. Hilton-Taylor, W. Foden, E. Di Minin, S. Pagad, P. Genovesi, J. Hutton, N. D. Burgess

The diversity of life on Earth—which provides vital services to humanity (1)—stems from the difference between rates of evolutionary diversification and extinction. Human activities have shifted the balance (2): Species extinction rates are an estimated 1000 times the “background” rate (3) and could increase to 10,000 times the background rate should species threatened with extinction succumb to pressures they face (4). Reversing these trends is a focus of the Convention on Biological Diversity’s 2020 Strategic Plan for Biodiversity and its 20 Aichi Targets and is explicitly incorporated into the United Nations’ 2030 Agenda for Sustainable Development and its 17 Sustainable Development Goals (SDGs). We identify major gaps in data available for assessing global biodiversity threats and suggest mechanisms for closing them.

Reducing rates of biodiversity loss and achieving environmental goals requires understanding what is threatening biodiversity, where risks occur, how fast threats are changing in type and intensity, and what are the most appropriate actions to avert them (5). A UN report proposed specific policy recommendations for mobilizing the “big data” revolution for sustainable development and environmental protection (7). The combination of crowd-sourced data, large-scale ground-based monitoring schemes, and satellite earth-observation missions is seemingly capable of unprecedented insight into global threats to biodiversity and how human interventions are altering those threats [e.g., (7)].

*See supplementary materials for complete list of author affiliations. †Email: ljoppa@microsoft.com

DELUGE OR DROUGHT? We used a threat classification scheme (8) (see the graph) that, although not without shortcomings (9, 10), has been widely deployed for tens of thousands of conservation assessments for species, sites, and projects. By “threat,” we mean “The proximate human activities or processes that have caused, are causing, or may cause the destruction, degradation, and/or impairment of biodiversity targets” (8). Determining the impact of a threat on a species or ecosystem is a separate process often included in a conservation assessment. We followed a structured data collection procedure and associated each data set with one or more classes of threat [see supplementary materials (SM) for details]. We omit three threat classes from our analysis: two (Geological Events; Other Options) are not exclusively anthropogenic; one (Climate Change and Severe Weather) received comprehensive treatment by the Fifth Assessment Report for the Intergovernmental Panel on Climate Change. We restricted our search to spatial data sets with a global extent. We assume that the data sets identified by this initial search will grow as additional data sets and metadata become known or are created. Over time, we recommend inclusion of the numerous available regional data sets (even if they do not meet data set attributes identified here) to create more globally representative information.

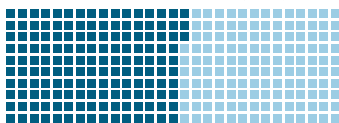
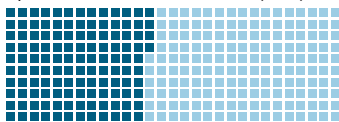
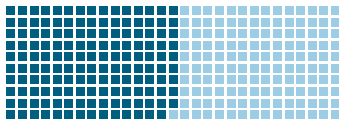
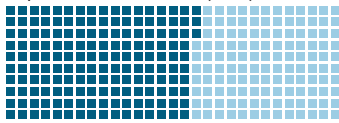
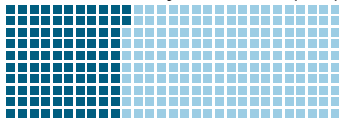
We identified 290 unique data sets (table S1) across nine threat classes from data sources ranging from remote sensing via satellites to citizen-science initiatives (fig. S1). Six data providers account for more than a fifth of the entire catalog of data sets. This apparent data deluge is misleading: Our analysis reveals how little is actually available, at the global level, about the spatial and temporal distribution of anthropogenic threats to biodiversity.

In order to assess whether data on different threats were available in proportion to their importance for biodiversity, we used threat information (for threatened taxa that have been comprehensively assessed) from the International Union for Conservation of Nature’s Red List of Threatened Species (IUCN Red List), the repository of information on the global extinction risk of species. We find that the frequency of threats to marine or terrestrial and inland water species on the Red List is disproportionate to the availability of data sets on those threats (see the graph and table S2). Biological Resource Use (including direct and indirect impacts of hunting, fishing, and logging) is one of the most common threats to species, yet accounts for just 5% of threat data sets.

To assess how much threat information is available and actionable, we examined

Qualifying attributes of biodiversity data sets

Five data-set attributes considered key for use in biodiversity threat assessments.

ATTRIBUTE	DEFINITION AND JUSTIFICATION
<p>Freely available - 153 data sets (53%)</p> 	<p>These data sets are freely available (at least for noncommercial use). Being freely available is necessary, but insufficient, as a free data set may be impossible to access, depending on the technical capacity of users.</p>
<p>Spatial resolution - 124 data sets (43%)</p> 	<p>These data sets are at a gridded spatial resolution of $\leq 10 \text{ km} \times 10 \text{ km}$ or are stored in vector format. Of species on the IUCN Red List, 23% have ranges smaller than 1000 km^2, which could be covered with no more than 10 grid cells, a minimum desirable resolution for most analyses.</p>
<p>Up to date - 149 data sets (51%)</p> 	<p>These data sets were produced within the last decade: a time frame sufficiently recent to inform current and future policy.</p>
<p>Repeated - 163 data sets (56%)</p> 	<p>These data sets are available for at least two time points. Changes over time are fundamental for many conservation assessment criteria and for understanding impacts of regulatory policies.</p>
<p>Assessed for accuracy - 112 data sets (39%)</p> 	<p>These data sets are likely either direct observations or modeled data sets that have been assessed for accuracy at a global scale. Conservation assessments are generally subject to independent review, and data sets used must be of sufficient scientific rigor.</p>

the data sets with respect to five desirable data attributes (see the table above and table S1). We note that determining accurate attribute values was often difficult because of a lack of formal metadata, which creates uncertainty in the absolute number of data sets that might satisfy all criteria. Regardless, only 14 data sets (5%) satisfy all five attributes and not all threat classes are represented (see fig. S2, SM, and table S1 for details). Data sets that do comply are often applicable to only a few taxa or habitats.

BUSINESS MODELS. The conservation community should aspire to at least one “gold-standard” data set—that meets at a minimum all five attributes in the table and is applicable to as many taxa as possible—for each class and subclass of threat. This will require working with data providers to develop business models that leverage new, longer-term funding mechanisms and partnerships with government and the private sector.

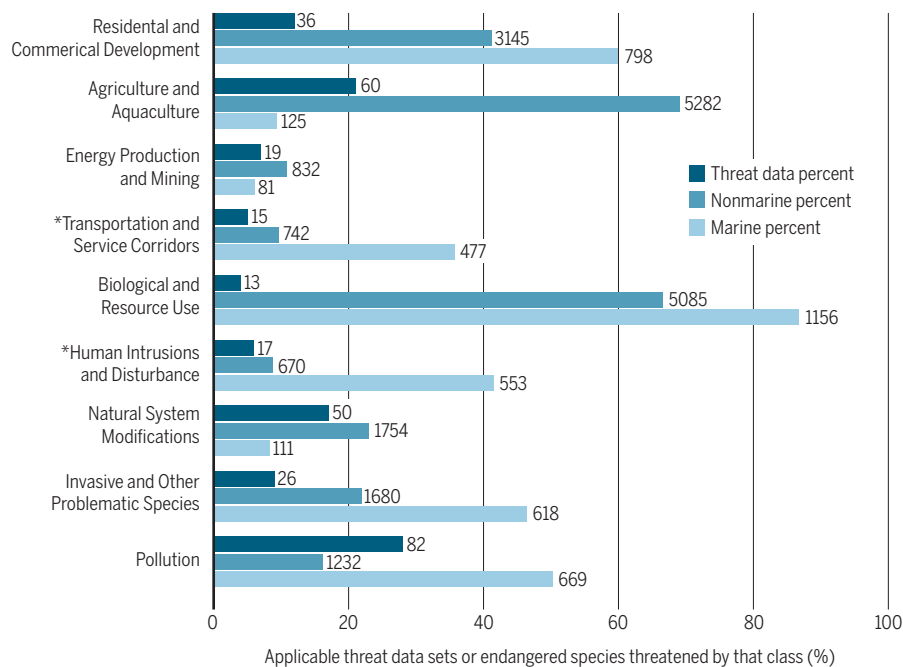
Partnerships with data owners and creators. In certain instances, data required for effective conservation policy already exist but are not accessible [e.g., owing to access cost, commercial considerations, or

intellectual property (IP) arrangements] to organizations or agencies mandated to conserve biodiversity. Sometimes these data result from taxpayer-funded initiatives that can result in major success stories (6). In 2008, NASA announced the free, public release of the Landsat image archive, dating back to 1978. This empowered the scientific community to begin studies of land cover change at an actionable resolution. Since then the European Space Agency opened the Sentinel Scientific Data hub, a free and open-access data portal for imagery from the Copernicus Sentinel missions, and the French Space Agency declared 5-year-old or older SPOT satellite data free of charge to noncommercial users.

Private-sector data also have potential to fill major gaps. Gaining access will require partnerships that respect the IP of companies and the right of conservation organizations to use data for conservation actions. One such agreement between the UN Environment Programme (UNEP) World Conservation Monitoring Center and the IHS Company enables detailed and comprehensive data on oil and gas activity worldwide to be used for biodiversity assessments. More broadly, the conservation community should

Data sets and types of threats

The percentage of all threat data sets (dark blue) that relate to each threat class and the percentage of threatened terrestrial and inland water (medium blue) and marine (light blue) species on the IUCN Red List affected by each threat class. Number of data sets or species in each class is indicated beside each bar. Threat classes not covered by a single data set are denoted by an * in the figure labels. See table S2 for details on species included.



emulate the UN's Data for Climate Action initiative, which is laying the groundwork for working with the private sector to access big data—with options ranging from companies making data freely available to arrangements for scientists to access data within the company's protected network.

Funding mechanisms. In July 2015, the UN's Third International Conference for Financing for Development produced a comprehensive framework—the Addis Ababa Action Agenda (AAAA). The AAAA specifies >100 measures for how to finance the sustainable development agenda and explicitly recognizes the need to fund “science, technology, innovation and capacity building,” as well as “data, monitoring and follow-up” (11). The AAAA “encourage[s] the mobilization of financial resources from all sources and at all levels to conserve and sustainably use biodiversity and ecosystems.” This is an important recognition of the need to finance the achievement of SDG 15 (the most relevant to halting the loss of biodiversity), although critically missing is any specific mention of the need to fund the data required to achieve that goal.

THE DATA PIPELINE. For many threat classes the creation of a gold-standard data set need not start from scratch. Existing

data sets and data pipelines, if provided with appropriate resources or mandates, can be scaled up. We highlight this potential with two issues where data scarcity on threats is a major obstacle.

Invasive and problematic species. Invasive alien species homogenize global biodiversity and are a significant threat to native species, particularly those endemic to islands and specific ecosystems. National and regional policy mechanisms are in place to prevent, control, and minimize the impact of alien species. Effective policy must be empowered with comprehensive data on which species are where and pathways by which they move (as the European Union's legal framework explicitly requires). These data allow implementation agencies to monitor transmission routes, prevent invasive species' entry or departure, and respond rapidly to early detections. The Threatened Island Biodiversity Database and the IUCN's Global Invasive Species Database are backed by international institutions and networks of experts and, if appropriately resourced, are capable of scaling up to meet the five key data attributes in the table.

Land use and cover change. Habitat loss is a leading cause of biodiversity decline, and most countries have local, regional,

and national legislation protecting natural landscapes. Yet globally, we do not have a standard land use and cover change assessment tool for biodiversity conservation end users. New and standardized land cover change detection approaches for the 2000–2010 interval are emerging, at both high (30-m) (12) and moderate (300-m) resolution (13). Although these products have promise, it is impossible to obtain a global and standardized overview of how natural landscapes are changing on a time scale that allows appropriate conservation action. Changing this requires breaking the practice of repeatedly modifying remote-sensing algorithms—interesting for the field itself but exasperating for end users—and, instead, agreeing to a series of global maps comparable through time and space.

To be useful, threat data sets must be integrated with conservation assessment processes. The IUCN Red List compiles input from >10,000 species experts into easily and freely available conservation assessments for nearly 80,000 species that influence international and national policy mechanisms. Connecting such efforts to gold-standard data sets for each major class of threat will help bring actionable insights into what conservation actions are needed, and where, for the most imperiled species and populations. In so doing, we can better leverage the technology of the Information Age to counter biodiversity loss, a defining feature of the Anthropocene. ■

REFERENCES AND NOTES

1. R. S. De Groot, M. A. Wilson, R. M. J. Boumans, *Ecol. Econ.* **41**, 393 (2002).
2. W. Steffen, J. Crutzen, J. R. McNeill, *Ambio* **36**, 614 (2007).
3. J. M. De Vos, L. N. Joppa, J. L. Gittleman, P. R. Stephens, S. L. Pimm, *Conserv. Biol.* **29**, 452 (2015).
4. S. L. Pimm et al., *Science* **344**, 1246752 (2014).
5. J. Geldmann, L. N. Joppa, N. D. Burgess, *Conserv. Biol.* **28**, 1604 (2014).
6. Independent Expert Advisory Group, *A World That Counts: Mobilising the Data Revolution for Sustainable Development* (2015); <http://bit.ly/Data4SustDev>.
7. W. Turner, *Science* **346**, 301 (2014).
8. N. Salafsky et al., *Conserv. Biol.* **22**, 897 (2008).
9. A. Balmford et al., *Conserv. Biol.* **23**, 482 (2009).
10. N. Salafsky et al., *Conserv. Biol.* **23**, 488 (2009).
11. Addis Ababa Action Agenda, Third International Conference on Financing for Development, 13 to 16 July 2015, Addis Ababa (2015); <http://bit.ly/AAAAFundDev>.
12. P. Gong et al., *Int. J. Remote Sens.* **34**, 2607 (2013).
13. European Space Agency, *Climate Change Initiative* (CCI, ESA, Paris, 2016); www.esa-landcover-cci.org/?q=node/1.

ACKNOWLEDGMENTS

See supplementary materials for complete listing of acknowledgments.

SUPPLEMENTARY MATERIALS

www.sciencemag.org/content/352/6284/416/suppl/DC1

BOOKS *et al.*

ENGINEERING

A monumental challenge

Erecting an Egyptian obelisk is no small feat

By Andrew Robinson

“If you had to pick the most remarkable object ever produced in ancient Egypt, what would you choose?” asks Egyptologist Bob Brier at the beginning of *Cleopatra's Needles*. Tutankhamun's gold mask? The bust of Queen Nefertiti? The Great Pyramid? The Rosetta Stone? Brier's choice is a massive, unfinished granite obelisk lying on its side in a quarry in Aswan, still encircled by grooves scraped by ancient Egyptian laborers. Almost 42 meters in length, and weighing more than 1000 tons—more than two jumbo jets—it would have been the largest obelisk ever, had it not cracked before it could be freed from its surrounding rock some 3500 years ago. “I have been to the quarry more than 100 times and every time I am amazed,” writes Brier. “How were they going to move it? Stand it up?” Despite almost a century of research, the answers remain unclear.

So prized by the ancient Romans were Egyptian obelisks that, at one time, more of them stood in Rome than in Egypt. In the Middle Ages, most fell and lay buried until their reerection during the Italian Renaissance. That is, except for one, which is perhaps the most famous.

Weighing 320 tons, the structure that many now know as the Vatican Obelisk was transported in a specially constructed ship powered by three tiers of hundreds of oarsmen from Alexandria to Rome by the emperor Caligula in about CE 37. It was erected in the Vatican Circus, where it stood until 1586, when it was laboriously shifted to the square in front of St. Peter's Basilica and reerected with a Christian cross on its tip. This celebrated engineering operation was directed by the architect of St. Peter's, Domenico Fontana, on the orders of Pope Sixtus V.

In the 19th century, France, Britain, and

the United States—inspired by Napoleon Bonaparte's expedition to Egypt in 1798—acquired their own major obelisks from Alexandria and Luxor. The monuments were erected in Paris's Place de la Concorde, on London's Thames embankment, and in New York's Central Park. Other ancient Egyptian obelisks can be found in Florence, Istanbul, Munich, and a country estate in southern England. The last is a small one from Philae inscribed with the names Ptolemy and Cleopatra, which happened to prove vital in



Work on the Aswan obelisk was suspended when cracks appeared in the granite.

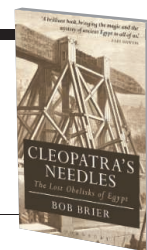
the 1820s decipherment of the Egyptian hieroglyphs by Jean-François Champollion (a keen advocate for the Paris obelisk).

Brier's relatively brief book, illustrated with period drawings and photographs of the innovative contraptions and procedures required to move the obelisks, is chronological. It begins with a chapter on the engineering challenges faced by the ancient Egyptians and their putative solutions, moves on to the obelisks of Rome, with a separate chapter on the Vatican obelisk, and then recounts the stories behind the acquisition, transport, and erection of the Paris, London, and New York obelisks. Although some of this history was covered in a recent study by art historians (*1*), Brier brings an Egyptologist's perspective, a fascination with engineering, considerable storytelling skills, and a conversational tone honed by

Cleopatra's Needles The Lost Obelisks of Egypt

Bob Brier

Bloomsbury Academic,
2016. 238 pp.



professional broadcasting. Together, this makes for a generally enjoyable read.

As he intriguingly observes, “it seems that as technology advanced, moving obelisks became more difficult.” The ancient Egyptians kept largely silent on the subject, apart from a single depiction of an obelisk lying on a Nile barge. Likewise, it seems that the ancient Romans felt that the transportation and erection of these cumbersome structures were hardly worth recording.

Yet when Fontana moved the Vatican obelisk in the 16th century, it was treated as “one of the engineering triumphs of the Renaissance” and celebrated with a lavishly illustrated publication (including depictions of the first “hard hats”). In the 19th century, the drama increased still further, with extensive coverage in the *Illustrated London News* of the London obelisk's disaster-prone journey from Egypt, during which six seamen lost their lives. A parade of 8500 Freemasons (who were convinced that the pedestal carried Masonic emblems) heralded the New York obelisk's arrival in 1880. “This only increases my admiration for the ancient Egyptian engineers who erected dozens and dozens of obelisks with just rope, wood, and sand,” observes Brier.

The book's only serious weakness—apart from the indifferent reproduction of some illustrations—is to underplay the obelisks' hieroglyphic inscriptions. There is no reference to the importance of the Coptic language, no discussion of the Philae obelisk, and only a passing mention of the Rosetta Stone. In Brier's view, “It is the obelisk people remember, not the inscriptions.” No doubt the ancient Romans agreed, given their own neglect of hieroglyphics. (The same goes for America's best-known obelisk, the Washington Monument.) Yet if, like the Romans, we were still unable to read the hieroglyphic script, how much could we really understand about the obelisks?

REFERENCES

1. B. A. Curran, A. Grafton, P. O. Long, B. Weiss, *Obelisk: A History* (MIT Press, 2009).

10.1126/science.aaf5477

The reviewer is the author of *Cracking the Egyptian Code: The Revolutionary Life of Jean-François Champollion* (Oxford University Press, 2012). Email: andrew@andrew-robinson.org

Rethinking Lysenko's legacy

Advances in epigenetics spur modern support for a long-discredited theory of inheritance

By **Maurizio Meloni**

Few topics are more polarizing in the history of biology than the historical significance of the inheritance of acquired characteristics. Many believe that acquired inheritance—frequently referred to as Lamarckism—is a relic of the past, irremediably superseded by the modern understanding of heredity inaugurated by genetics. For others, the variegated history of 20th-century investigations of heredity merits further consideration.

In *Lysenko's Ghost*, Loren Graham explores the latest attempts to restore the legacy of the Ukrainian agronomist Trofim Lysenko (1898–1976), who spearheaded a campaign to reject Mendelian genetics in favor of a pseudoscientific theory of environmentally induced heredity in the USSR from the late 1920s to the mid-1960s. Today, in the midst of a period of high nationalist and anti-Western sentiments, it seems that a quirky coalition of Russian right wingers, Stalinists, a few qualified scientists, and even the Orthodox Church is now claiming that Lysenko has been vindicated by the latest findings in molecular epigenetics.

Graham, professor emeritus of the history of science at MIT, is well positioned to critically assess this phenomenon. A leading figure in the history of Soviet science, Graham is also one of the few people still alive in the West who met Lysenko. The riveting details of this encounter in 1971, including Lysenko's subtle attempts to dissociate himself from the Soviet system, are beautifully told in chapter 5.

In the 1920s, the Soviet Union was at the center of an intense debate on heredity and its social and political implications. Figures as diverse as the American geneticist H. J. Muller and the Austrian biologist Paul Kammerer (vividly remembered in the book) weighed in. Eugenics featured prominently in the debate, given its relationship to social planning.

The reviewer is the author of Political Biology: Science and Social Values in Human Heredity from Eugenics to Epigenetics (Palgrave, Basingstoke, 2016). Email: m.meloni@sheffield.ac.uk

On the heels of the radical change in social and economic policies that accompanied Stalin's "Great Break" in 1929, an ambitious "barefoot scientist" from a remote Ukrainian village took advantage of the struggle against "bourgeois experts" to affirm his view of biology. Lysenko gained early support from the Soviet government by claiming that he had developed a new agricultural technique that would dramatically increase Soviet crop yields. He would go on to develop a broader theory of heredity, radically opposed to the "formalism" of Western genetics, in which he denied "the existence



Soviet agronomist Trofim Lysenko, ca. 1949

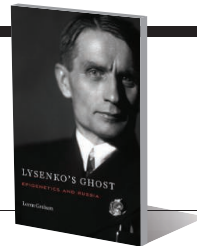
... of a separate hereditary substance which is independent of the body" (1).

Today, some Russian ideologues are attempting to use epigenetics to revive Lysenko's legacy. At the same time, the "ghost" of Lysenko is being used in the West as a polemical weapon against epigenetics (2). Graham's book is a timely and important antidote to the idea that everything that is not mainstream heredity is Lysenkoism.

Graham succeeds in dissociating Lysenko both from the inheritance of acquired characteristics and from epigenetics, arguing that Lysenko's experiments were "careless and usually unverifiable" and that the inheritance theory was not even an important

Lysenko's Ghost Epigenetics and Russia

Loren Graham
Harvard University Press,
2016. 219 pp.



feature of his scientific doctrine. As Graham shows, a number of high-profile proponents of acquired characteristics in the USSR were also fiercely opposed to Lysenko's theories. "If Lysenko had lived in a normal democratic country," Graham writes, "he would be remembered, if at all, as a talented farmer ... employing idiosyncratic methods but never garnering much support." Graham further maintains that someone like Lysenko, who stubbornly denied the value of molecular biology, can't really be seen as an anticipator of epigenetics.

With *Lysenko's Ghost*, Graham opens as many lines of potential research as he addresses. It is evident, for example, that Russia is and has been a particularly fertile land for ideas of inheritance of acquired characteristics. This relationship between scientific ideas and places is of keen interest in the history of science—and biology in particular. One likewise wonders how culture and specific sociohistorical factors have influenced the making of Western views of heredity.

Two key differences exist between the Soviet-era rise of Lysenkoism and its contemporary resurgence. During its initial rise, Lysenkoism represented an inward closure of Soviet biology, as epitomized by the cancellation of the International Genetics Congress in Moscow in 1937. On the other hand, contemporary attempts to reestablish Lysenko's credibility purposely cite global flows of knowledge as a means of legitimizing the Soviet hero.

In addition, Lysenkoist theories were initially only applied to plants and animals, never to human beings (for broader Marxist reasons). Contemporary epigenetic research, however, is not shy about looking at the effect of events like famine, smoking, or traumas on human heredity. It will be interesting to see how this affects the circulation of epigenetics in Russia. As Graham points out, there are not yet studies of the multigenerational effects of the Leningrad siege.

REFERENCES

1. T. Lysenko, *The Science of Biology Today* (International Publishers, New York, 1948).
2. F. Maderspacher, *Curr. Biol.* **20**, 835 (2010).

10.1126/science.aaf5314

LETTERS

Edited by Jennifer Sills

Instituting recruiting meritocracy in Italy

AS A HARVARD University professor who worked at the Italian Institute of Technology (IIT), it is dismaying to read L. Margottini's In Depth news article criticizing the proposed IIT-managed Human Technopole (HT) project in Milan ("Plans for new research hub get critical reception," 11 March, p. 1127). The claims that IIT is not accountable and does not follow international standards are inaccurate. I helped to design IIT's new tenure-track system, which follows open, meritocratic, international recruitment standards that are otherwise exceedingly rare in Italy. (I still have a small consulting contract with IIT.) IIT's tenure-track system offers top young scientists full intellectual and financial independence, and it holds those scientists individually accountable. Modeled according to IIT's blueprint, the HT project foresees international recruitment of about 100 new principal investigators at steady state.

This is more than rhetoric: In 2015, I helped coordinate IIT's first tenure-track recruitment for independent junior principal investigators (1). As with any proper search, we placed advertisements in top journals and sent targeted email solicitations to hundreds of scientists worldwide, encouraging their best young colleagues to apply. We received close to 400 applications—unprecedented by Italian standards—the vast majority from outside Italy, including many non-Italians. We assembled international search committees to review applications and interview short-listed candidates. The winning candidates are superb young scientists qualified for faculty positions at top research universities and institutes worldwide. This experience and success in recruiting bodes well for the HT project.

IIT's international recruiting standards must be contrasted with the recruiting practices of Italian universities and public research institutes, where calls are frequently honed to fit the profile of favored local candidates, and most new researchers are not independent by any meaningful standard. Italy has thus been less competitive in recruiting and retaining top young scientific talent. Italian science would indeed benefit from increased funding, but international,

meritocratic recruitment is paramount. Young scientists deserve open competition and independence in Italy; IIT and the HT project are critical steps in that direction.

John Assad

Department of Neurobiology,
Harvard Medical School, Boston, MA 02115, USA.
Email: jassad@hms.harvard.edu

REFERENCE

1. IIT, Tenure Track Results (www.iit.it/careers/tenure-track-results).

Invasive species shape evolution

IN THEIR PERSPECTIVE "Evolution in the Anthropocene" (26 February, p. 922), F. Sarrazin and J. Lecomte suggest a greater investment in securing the long-term evolutionary potential of species to safeguard biodiversity. However, evidence from



Invasive weedy rice has evolved from cultivated rice in fields worldwide.

biological invasions, a major feature of the Anthropocene, challenges the assumptions that evolutionary processes necessarily occur over long time scales, are constrained by human activities, or can in any way be predicted.

Invasive alien species pose a substantial threat to biodiversity (1), but they may also increase evolutionary diversification (2). Contemporary adaptation as a result of biological invasions highlights that evolutionary time scales can be surprisingly short. Not only can alien species evolve rapidly to changing environments despite small founder populations (3), but native species are known to adapt within a few generations in response to invasion (4).

Far from constraining the evolutionary trajectories of species, the Anthropocene may accelerate rates of evolution, given the often strong selection pressures in anthropic environments. Weedy rice has arisen multiple times in rice fields

worldwide, often through parallel evolution from different cultivated rice varieties, despite the limited genetic variability in cultivated rice varieties (5). Even in a highly domesticated species, there might be ample genetic variation to allow subsequent evolution.

Forecasting the risk and consequences from alien species is notoriously difficult (6) and, similar to all life forms, their evolutionary trajectories will depend on context. For example, hybridization between native and alien species can result in new species with greater invasion potential (7), lead to the replacement of native species with fitter hybrids possessing novel traits (8), or facilitate the transfer of genes across distinct evolutionary lineages (9). Whether such genetic diversification brings biodiversity benefits, as some have argued (10), is debatable, but demonstrates that proposals to conserve the evolutionary trajectories of nonhuman species will still

be guided by human perceptions of what is desired. The evolutionary implications of biological invasions are likely illustrative of other biotic pressures on biodiversity in the Anthropocene and suggest that defining operational metrics of evolutionary potential to guide conservation in a rapidly changing world will be difficult and possibly impractical.

**Philip E. Hulme^{1*} and
Johannes J. Le Roux^{1,2}**

¹The Bio-Protection Research Centre, Lincoln University, Lincoln 7647, Canterbury, New Zealand.

²Centre for Invasion Biology, Department of Botany and Zoology, Stellenbosch University, Matieland 7602, South Africa.

*Corresponding author.
Email: philip.hulme@lincoln.ac.nz

REFERENCES

1. D. P. Tittensor *et al.*, *Science* **346**, 241 (2014).
2. R. T. Vellend, *Trends Ecol. Evol.* **22**, 481 (2007).
3. R. I. Colautti, S. C. H. Barrett, *Science* **342**, 364 (2013).
4. Y. E. Stuart *et al.*, *Science* **346**, 463 (2014).
5. X. Qi *et al.*, *Mol. Ecol.* **24**, 3329 (2015).
6. B. Leung *et al.*, *Ecol. Lett.* **15**, 1475 (2012).
7. P. S. Soltis, D. E. Soltis, *Annu. Rev. Plant Biol.* **60**, 561 (2009).
8. R. G. Harrison, E. L. Larson, *J. Hered.* **105**, 795 (2014).
9. D. B. McDonald *et al.*, *Proc. Natl. Acad. Sci. U.S.A.* **105**, 10837 (2008).
10. C. D. Thomas, *Nature* **502**, 7 (2013).

Response

WE AGREE WITH Hulme and Le Roux that invasive species speed up evolution. Although we did not explicitly list invasion in the spectrum of current evolutionary drivers in our Perspective, we classify it as an "alteration of interaction networks and

coevolutionary networks” likely to generate evolutionary responses. We also agree that evolution can occur on short time scales. As we advocated, evolution-focused (evo-centric) conservation targets nonhuman fitness and thus considers both micro- and macroevolution.

We disagree with Hulme and Le Roux that our call for maintaining evolutionary potential equates to a call for maximizing evolutionary diversification. Evolution-focused conservation neither asks for more evolution nor states that rapid evolution will solve conservation issues. Rather, it strives for maximum evolutionary freedom: Nonhuman species should be allowed to evolve independent of humans. In that context, Hulme and Le Roux’s focus on the evolutionary impact of invasive species in agrosystems, particularly weedy rice, perfectly exemplifies our argument. Weedy rice is an unexpected evolutionary consequence of domestication, at the scale of not only individual traits but plant community. The emergence of weeds, pathogens, and pests in agrosystems is largely due to directional selective pressures of agricultural practices [e.g., (1)], standardization of monocultures (2), and creation of vacant niches through homogenized and simplified environments.

In the same way, the examples cited by Hulme and Le Roux (3, 4) are unexpected outputs from purely short-term anthropocentric efforts to increase human well-being. Alien and invasive species are only one element of the process by which human activities drive nonhuman evolution. Evolution-focused conservation considers not only the proximate causes of evolutionary processes, but also the ultimate ones. This is central to discriminate “anthropogenic” from “nonanthropogenic” evolution. We cannot act against aliens without acknowledging our responsibility in their emergence.

Finally, we agree that defining operational metrics of evolutionary potential is highly challenging for theory and biometry. We believe that it is better to address this challenge than to ignore it.

François Sarrazin^{1*} and Jane Lecomte²

¹Sorbonne Universités, UPMC Univ. Paris 06, Muséum National d’Histoire Naturelle, CNRS, CESCO, UMR 7204, 75005 Paris, France. ²Ecologie Systématique Evolution, Univ. Paris-Sud, CNRS, AgroParisTech, Université Paris-Saclay, 91400 Orsay, France.

*Corresponding author. Email: sarrazin@mnhn.fr

REFERENCES

1. E. Snell-Rood *et al.*, *Evol. Appl.* **8**, 635 (2015).
2. E. H. Stukenbrock, B. A. McDonald, *Annu. Rev. Phytopathol.* **46**, 75 (2008).
3. R. I. Colautti, S. C. H. Barrett, *Science* **342**, 364 (2013).
4. D. B. McDonald *et al.*, *Proc. Natl. Acad. Sci. U.S.A.* **105**, 10837 (2008).

TECHNICAL COMMENT ABSTRACTS

Comment on “Slow adaptation in the face of rapid warming leads to collapse of the Gulf of Maine cod fishery”

Michael C. Palmer, Jonathan J. Deroba, Christopher M. Legault, Elizabeth N. Brooks

Pershing *et al.* (Reports, 13 November 2015, p. 809) concluded that failure to account for temperature in the assessment and management of Gulf of Maine Atlantic cod caused overfishing. We argue that the “extra mortality” calculation driving this conclusion is an artifact. Environmental factors affect all stocks, but attribution of additional mortality to temperature alone by Pershing *et al.* is unsupported by the data.

Full text at <http://dx.doi.org/10.1126/science.aad9674>

Comment on “Slow adaptation in the face of rapid warming leads to collapse of the Gulf of Maine cod fishery”

Douglas P. Swain, Hugues P. Benoît, Sean P. Cox, Noel G. Cadigan

Pershing *et al.* (Reports, 13 November 2015, p. 809) concluded that recent warming in the Gulf of Maine contributed to the collapse of Gulf of Maine cod. We argue that this conclusion is based on a flawed analysis of the population dynamics of this cod stock. We believe that understanding the potential role of climate change in the collapse of this stock requires more defensible analyses.

Full text at <http://dx.doi.org/10.1126/science.aad9346>

Response to Comment on “Slow adaptation in the face of rapid warming leads to collapse of the Gulf of Maine cod fishery”

Andrew J. Pershing, Michael A. Alexander, Christina M. Hernandez, Lisa A. Kerr, Arnault Le Bris, Katherine E. Mills, Janet A. Nye, Nicholas R. Record, Hillary A. Scannell, James D. Scott, Graham D. Sherwood, Andrew C. Thomas

Palmer *et al.* and Swain *et al.* suggest that our “extra mortality” time series is spurious. In response, we show that including temperature-dependent mortality improves abundance estimates and that warming waters reduce growth rates in Gulf of Maine cod. Far from being spurious, temperature effects on this stock are clear, and continuing to ignore them puts the stock in jeopardy.

Full text at <http://dx.doi.org/10.1126/science.aae0463>

TECHNICAL COMMENT

CLIMATE CHANGE

Comment on “Slow adaptation in the face of rapid warming leads to collapse of the Gulf of Maine cod fishery”

Michael C. Palmer,* Jonathan J. Deroba, Christopher M. Legault, Elizabeth N. Brooks

Pershing *et al.* (Reports, 13 November, p. 809) concluded that failure to account for temperature in the assessment and management of Gulf of Maine Atlantic cod caused overfishing. We argue that the “extra mortality” calculation driving this conclusion is an artifact. Environmental factors affect all stocks, but attribution of additional mortality to temperature alone by Pershing *et al.* is unsupported by the data.

Pershing *et al.* (1) use estimates from the 2014 Gulf of Maine Atlantic cod stock assessment (2) as error-free data (3). The stock assessment model (4) estimates population abundance and fishing mortality at age and year, given (i) input data on observed total catch, fishery age compositions, abundance indices, and index age compositions; and (ii) fixed values of natural mortality. Observations of fishery catches at each age are incorrectly combined with model estimates of population abundance and natural mortality rates to derive “extra mortality.” Combining the observed catch data directly with the estimated population at a particular age ignores both the fitting process and the structural equations used to derive the population estimates and results in an artifact related to the assessment residuals (i.e., the difference between observations and model predictions).

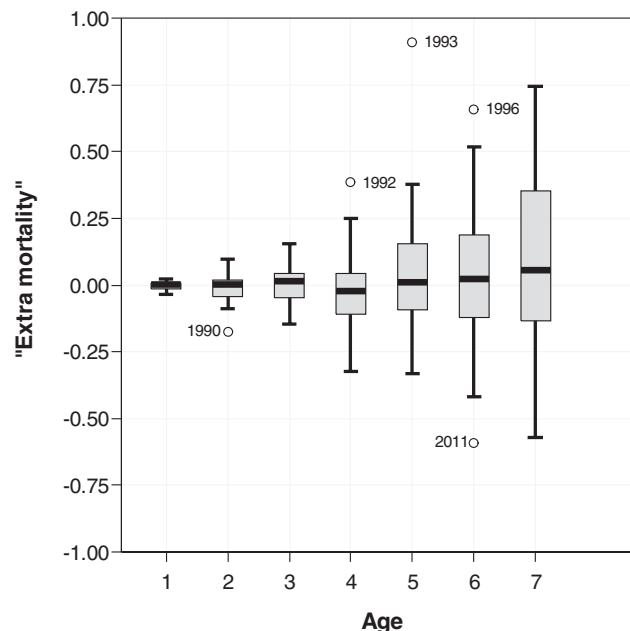
The “extra mortality” in Pershing *et al.* was calculated by subtracting fishing and natural mortality from total mortality (Fig. 1). Total mortality was calculated as the difference in the log of abundances of adjacent age groups in sequential years, where abundance was estimated by the stock assessment and premised on the model predicted catches and estimated fishing mortality rates. Pershing *et al.*, however, ignored these dependencies in calculating fishing mortalities outside the assessment model using observed catches. This method makes “extra mortality” simultaneously conditioned on catch and fishing mortality being known perfectly and with error, which cannot both be true. Analyzing stock assessment estimates (or parameters) as actual data using assumptions that differ from the assessment model can lead to spurious correlations (3).

That the “extra mortality” calculation bears no relationship to mortality is demonstrated by the strong negative correlation of “extra mortality” with the age composition residuals from the assessment model (Table 1). The lack of a relationship between the “extra mortality” calculations and true natural mortality can be further demonstrated by repeating the analysis with the *M*-ramp cod assessment model, where natural mortality (*M*) increases through time (5). Changing the assumed mortality in the assessment should lead to changes in the relationships between a reasonable representation of “extra mortality” and

temperature. However, when the analysis is repeated with the *M*-ramp model, the results (as noted by Pershing *et al.* in their supplementary materials) are nearly identical because the *M*-ramp model provides nearly identical fits with similar residuals for the catch and age composition data as the *M* = 0.2 model. Thus, the spurious correlations reported in Pershing *et al.* are related to assessment residuals rather than changes in temperature.

Other factors contributed to the spurious relationships in Pershing *et al.* They restricted their analysis to the years 1993 to 2012 (6) due to “several obvious outliers” [supplementary materials for (1)] reported in the mortality estimates before 1993, but without providing any clear rationale. We repeated the analysis of “extra mortality” using all years and examined the results for the presence of outliers. Although there are several outliers in the time series, only two of the five outliers occur before 1993 (Fig. 1). We used a jackknife procedure (7) on the entire 1982 to 2012 time series (8) to evaluate the influence of these outliers on the subsequent “extra mortality” and sea surface temperature (SST) correlations. Ages 1 and 4 were the only two ages where a positive correlation between “extra mortality” and SST was consistently obtained across time blocks, although 98% of the age-1 and 80% of the age-4 relationships were not statistically significant (9). The only way to obtain significant positive relationships for age 4 across all time blocks was to exclude 1992 from the analysis, which was effectively done by Pershing *et al.* by starting the time series in 1993. Curiously, age 6 exhibited the most consistent significant correlations (except for the second quarter), but these were negative (“extra mortality” decreased with

Fig. 1. Distribution of estimated Gulf of Maine Atlantic cod “extra mortality” by age. These box plots show the distribution of the 1982 to 2012 “extra mortality” estimates calculated by Pershing *et al.* The horizontal black bars represent the median values; gray boxes represent the interquartile range (IQR) (25th and 75th percentiles); and the whiskers represent $1.5 \times \text{IQR}$. The “extra mortality” at age *j* in year *t* was calculated as $Z_{j(t)} - F_{j(t)} - M_{j(t)}$, where *M* is assumed equal to 0.2 as in the 2014 assessment model. The $Z_{j(t)}$ in the “extra mortality” is calculated from the estimated numbers at age (*N*) from the stock assessment model $Z_{j(t)} = \log N_{j(t)} - \log N_{j+1(t+1)}$, premised on catch *C* and fishing mortality *F* containing error, and the $F_{j(t)}$ is derived from the observed catch (assumed error free): $F_{j(t)} = C_{j(t)} Z_{j(t)} / [N_{j(t)} - N_{j+1(t+1)}]$.



Northeast Fisheries Science Center, Population Dynamics Branch, 166 Water Street, Woods Hole, MA 02543, USA.

*Corresponding author. Email: michael.palmer@noaa.gov

Table 1. Age-specific correlation coefficients (*r*) between the Pershing *et al.* “extra mortality” and the catch-at-age residuals from the 2014 Gulf of Maine Atlantic cod *M* = 0.2 stock assessment model. Residuals have been calculated as Pearson residuals ($O_{j(t)} - P_{j(t)})/\sqrt{[P_{j(t)}(1-P_{j(t)})]}$, where $O_{j(t)}$ and $P_{j(t)}$ are the observed and predicted catch at age *j* in year *t*, respectively. The significance level *P* and sample size *n* are provided.

Age	<i>r</i>	<i>P</i>	<i>n</i>
1	−0.94	<0.001	31
2	−0.90	<0.001	31
3	−0.83	<0.001	31
4	−0.91	<0.001	31
5	−0.84	<0.001	31
6	−0.90	<0.001	31
7	−0.84	<0.001	31

increasing temperature). We conclude that there was no objective rationale for excluding the years before 1993. In fact, restricting the time series to only 1993 to 2012 reduced the most consistent relationship that existed within the time series (age 6 and SST), although this negative correlation runs counter to the central hypothesis of the paper.

Pershing *et al.* posit that the proposed biological mechanism for the age-4 relationship with temperature is an energetic bottleneck that occurs with the onset of reproduction and the transition from pelagic to benthic prey. The empirical evidence that Pershing *et al.* provide to support this hypothesis is recent below-average body mass at age (i.e., smaller fish) and poor condition of Gulf of Maine cod, all of which can be evaluated from information contained in the 2014 stock assessment (2). The age of 50% maturity is approximately 2.6 years, with nearly 90% of cod mature by age 4. If the energetic bottleneck associated with the onset of reproduction were causing higher mortality, then significant positive relationships with temperature should have been apparent at ages 2 or 3. Furthermore, the average body mass in Gulf of Maine cod

younger than age 6 has not declined, nor are fish currently in poor condition as claimed (2). The biological mechanism proposed by Pershing *et al.* is not supported by the data.

Although it is tangential to the “extra mortality” hypothesis, Pershing *et al.* imply that errors in projected recruitment resulting from a failure to incorporate temperature effects in the stock-recruit relationship also contributed to the overfishing of this stock. The age at 50% selectivity to the fishery is 3.7 years for Gulf of Maine cod (2). Over the past decade, the catch projections have been updated before the projected recruits enter the fishery (10). Consequently, the quotas resulting from the stock projections were largely insensitive to errors in the projected recruitment estimates.

Environmental factors do affect fish stocks, although these are often difficult to disentangle from harvest decisions (11). We argue that the analyses of Pershing *et al.* provide no evidence to support the hypothesis that failure to account for increases in temperature led to overfishing of the Gulf of Maine Atlantic cod stock. Future explorations of environmental effects should be investigated by directly incorporating these within the stock assessment model, where assumptions are

explicit and consistent and their merit can be appropriately evaluated.

REFERENCES AND NOTES

1. A. J. Pershing *et al.*, *Science* **350**, 809–812 (2015).

2. M. C. Palmer, “2014 Assessment Update Report of the Gulf of Maine Atlantic Cod Stock” (U.S. Department of Commerce, 2014).

3. E. N. Brooks, J. J. Deroba, *Can. J. Fish. Aquat. Sci.* **72**, 634–641 (2015).

4. NOAA Fisheries Toolbox, 2008. Age Structured Assessment Program, Version 3.0.17, <http://nft.nfsc.noaa.gov>.

5. There are two accepted Gulf of Maine Atlantic cod assessment models used to manage the stock that vary only in their assumptions of natural mortality (*M*). The *M* = 0.2 model assumes an age- and time-invariant value of *M* = 0.2 throughout the assessment time series, and the *M*-ramp model assumes an age-invariant *M* that increases from 0.2 early in the time series (1982 to 1988) to 0.4 at the end of the time series (2003 to 2013). In the intervening years (1989 to 2002) *M* increases linearly.

6. Pershing *et al.* reported that their “extra mortality” analysis extended through 2013; however, an examination of the codM02.csv file provided in their supplementary materials revealed that the time series extended only to 2012. This is presumably due to the lack of population estimates in 2014 that would be needed to calculate total mortality in 2013, although the “extra mortality” could have been estimated from the fully selected fishing mortality, fishery selectivity, and assumed natural mortality available in the 2014 cod assessment using the equation $F_{j(t)} = C_{j(t)}Z_{j(t)} / [N_{j(t)}(1 - e^{-Z_{j(t)}})]$, where $F_{j(t)}$ is the fishing mortality, $C_{j(t)}$ is the observed catch, $Z_{j(t)}$ is the “extra mortality,” and $N_{j(t)}$ is the numbers at age *j* in year *t*. In our analyses, we have used only the 1982 to 2012 time series to ensure comparability with the Pershing *et al.* results.

7. R. G. Miller, *Biometrika* **61**, 1–15 (1974).

8. In each iteration of the jackknife procedure, a single year was dropped from the time series and the correlation analysis was repeated until all years had been dropped from the analysis once.

9. Statistical significance is based on $\alpha = 0.05$, as in Pershing *et al.*

10. Since 2004, the maximum age of projected recruits has exceeded age 2 only three times (age 3 in 2005, 2008, and 2011). Gulf of Maine cod age 2 and younger are less than 5% selected to the fishery.

11. C. J. Walters, J. S. Collie, *Can. J. Fish. Aquat. Sci.* **45**, 1848–1854 (1988).

ACKNOWLEDGMENTS

We thank F. Serchuk and P. Rago for comments that improved this manuscript.

30 November 2015; accepted 25 March 2016
10.1126/science.aad9674

TECHNICAL COMMENT

CLIMATE CHANGE

Comment on “Slow adaptation in the face of rapid warming leads to collapse of the Gulf of Maine cod fishery”

Douglas P. Swain,¹ Hugues P. Benoît,^{1*} Sean P. Cox,² Noel G. Cadigan³

Pershing *et al.* (*Science*, 13 November 2015, p. 809) concluded that recent warming in the Gulf of Maine contributed to the collapse of Gulf of Maine cod. We argue that this conclusion is based on a flawed analysis of the population dynamics of this cod stock. We believe that understanding the potential role of climate change in the collapse of this stock requires more defensible analyses.

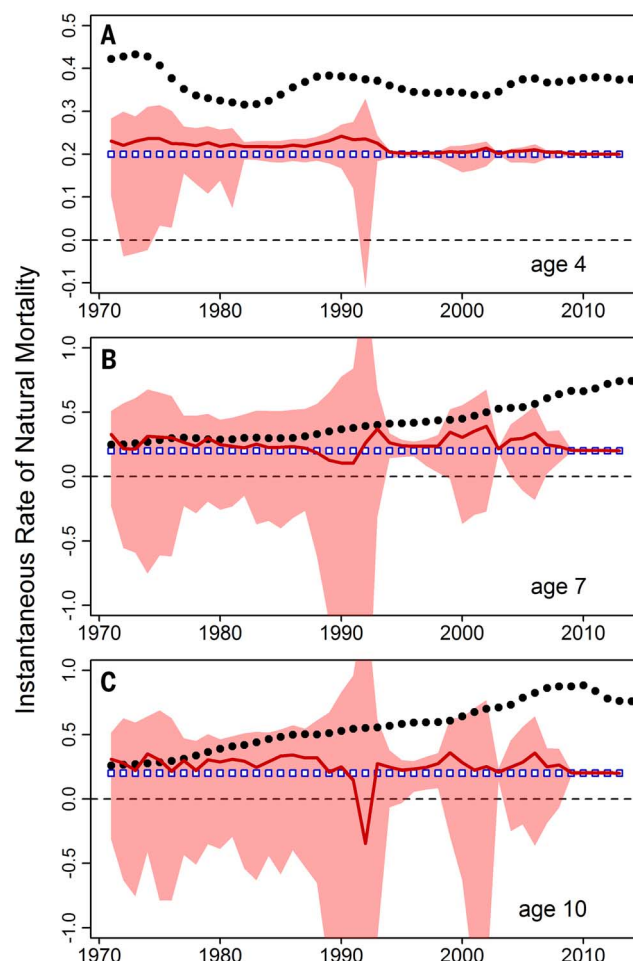
Pershing *et al.* (1) claim to demonstrate that recent ocean warming has resulted in reduced recruitment and increased rates of natural mortality (M) (e.g., predation and starvation) of Gulf of Maine cod, contributing to the collapse of this stock. They calculated M using abundance estimates from the assessment model for Gulf of Maine cod (2) and fishery catch at age (CAA) (the number of cod caught in the fishery at each age and in each year) inputs to that model [equations 5 and 6 in their supplementary materials (SM)]. They assumed that deviations between their calculated annual values of M and the value of M used in the assessment model reflected “extra mortality.” We assert that the values for M calculated by Pershing *et al.* do not accurately represent the true values of M .

Pershing *et al.* based their calculations on abundance estimates from a model that assumed constant $M = 0.2 \text{ year}^{-1}$ for all ages and years. If they had used the CAA predicted by this model in their calculations, their estimates of M would have been the same as this constant M value. However, unlike the model, they assumed that CAA was known without error, which is unreasonable given the numerous uncertainties and assumptions that go into determining CAA. The first implication is that their estimates of M will differ from the original model M used in the assessment, because the assessment model takes uncertainty in CAA into account. Therefore, the abundances used by the authors to calculate M , as well as the recruit and spawner abundances used in their stock-recruitment analyses (equations 1 to 4 in their SM), will not be consistent

with the authors' M values. Furthermore, if the values of M used in the assessment model are biased, as the authors imply, then these abundances will also be biased. Ignoring observation

Fig. 1. A simulation illustrating that the methods of Pershing *et al.* do not recover actual changes in natural mortality.

Instantaneous rates of natural mortality M estimated using the method in Pershing *et al.* (red lines and shading) compared with the true values used in the simulation (black circles) and the value used in the assessment model fit to the simulated data (open squares). The red line is the median Pershing estimate, and the shading denotes the 95% confidence band based on 200 simulations. Results are shown for three ages of cod: (A) 4 years, (B) 7 years, and (C) 10 years.



¹Fisheries and Oceans Canada, Gulf Fisheries Centre, Moncton, NB E1C 9B6, Canada. ²School of Resource and Environmental Management, Simon Fraser University, Burnaby, BC V5A 1S6, Canada. ³Centre for Fisheries Ecosystems Research, Marine Institute of Memorial University of Newfoundland, St. John's, NL A1C 5R3, Canada. *Corresponding author. E-mail: hugues.benoit@dfo-mpo.gc.ca

error in the catch and using biased abundance estimates will not produce unbiased estimates of M (or deviations in M as used by the authors, which were termed “extra mortality” or “mortality correction”). The correlations that the authors obtained between deviations in M and temperature thus are likely to be spurious. Likewise, abundance estimates that are thought to be biased should not be used for the authors' stock-recruitment modeling.

For readers not familiar with stock assessment models, we use a simple simulation to illustrate that values for M calculated using the procedures of Pershing *et al.* (equations 5 and 6 in their SM) will not resemble the true values. We based this simulation on the stock assessment of cod in the southern Gulf of St. Lawrence (3). This assessment uses a statistical CAA model (SCA) that estimates time-varying M . The southern Gulf of St. Lawrence cod stock provides a pertinent basis for the simulation because an increasing trend in M is identified for this stock, similar to the increase in M of Gulf of Maine cod hypothesized by Pershing *et al.* For the purpose of this simulation, we constructed a synthetic population based on the assessment model estimates. We constructed time series of fishery CAA and survey abundance indices at age using the model estimates of population abundance by age

and year, fishing and natural mortality rates by age and year, and selectivity and catchability to the fishery and surveys. Error was added to these time series based on the assessment estimates of observation error in the survey biomass indices and the fishery and survey CAA data [see (4) for an example]. Variability was added to the total fishery catch based on a coefficient of variation of 5%. We then fit an SCA model to these simulated time series, assuming a constant value of 0.2 for M of all ages in all years (as in the Gulf of Maine cod model that produced the abundance estimates used in the authors' calculations). Using the fishery CAA input to the $M = 0.2$ model and its abundance estimate outputs, we calculated values for M using the method in Pershing *et al.* (equations 5 and 6 in their SM). We repeated this procedure 200 times. The calculated values for M bore no resemblance to the "true" values (Fig. 1). Furthermore, the calculated values were negative in some simulations, which is not possible for true values of M .

In any type of modeling, it is inappropriate to take outputs from a model that is based on specific assumptions (e.g., constant M of 0.2 and error in the CAA) and use them in analyses that implicitly or explicitly make fundamentally different assumptions. The results of those analyses will be consistent with neither the original nor the new assumptions. A more defensible way to estimate potential climate effects on natural mortality and recruitment would estimate variation in M and recruitment within the assessment model [e.g., (5–7)], which would take various observation and process uncertainties into account. The reliability of model results should also be assessed by simulation [e.g., (4)] before making such strong claims about factors leading to the collapse of commercially and socially important fish stocks. Furthermore, consistent with best practice in fisheries science and science in general (8), multiple other working hypotheses about causes of changes to M and recruitment should also be considered and their relative support

assessed [e.g., (7)]. We believe that it is necessary to reserve judgment on the role of climate change in the collapse of Gulf of Maine cod until more defensible analyses are conducted to address this issue.

REFERENCES

1. A. J. Pershing *et al.*, *Science* **350**, 809–812 (2015).
2. Northeast Fisheries Science Center, "55th Northeast Regional Stock Assessment Workshop (55th SAW) Assessment Report" (U.S. Department of Commerce, 2013).
3. D. P. Swain, L. Savoie, S. P. Cox, E. Aubry, Assessment of the southern Gulf of St. Lawrence Atlantic cod (*Gadus morhua*) stock of NAFO Div. 4T and 4Vn (November to April), March 2015 (DFO Can. Sci. Advis. Sec. Res. Doc. 2015/080, 2015).
4. J. J. Deroba *et al.*, *ICES J. Mar. Sci.* **72**, 19–30 (2015).
5. Y. Jiao, E. P. Smith, R. O'Reilly, D. J. Orth, *ICES J. Mar. Sci.* **69**, 105–118 (2012).
6. N. G. Cadigan, *Can. J. Fish. Aquat. Sci.* 1–13 (2015).
7. D. P. Swain, H. P. Benoit, *Mar. Ecol. Prog. Ser.* **519**, 165–182 (2015).
8. T. C. Chamberlin, *Science* **15**, 92–96 (1890).

24 November 2015; accepted 25 March 2016
10.1126/science.aad9346

TECHNICAL RESPONSE

CLIMATE CHANGE

Response to Comments on “Slow adaptation in the face of rapid warming leads to collapse of the Gulf of Maine cod fishery”

Andrew J. Pershing,^{1*} Michael A. Alexander,² Christina M. Hernandez,³ Lisa A. Kerr,¹ Arnault Le Bris,¹ Katherine E. Mills,¹ Janet A. Nye,⁴ Nicholas R. Record,⁵ Hillary A. Scannell,⁶ James D. Scott,^{2,7} Graham D. Sherwood,¹ Andrew C. Thomas⁸

Palmer *et al.* and Swain *et al.* suggest that our “extra mortality” time series is spurious. In response, we show that including temperature-dependent mortality improves abundance estimates and that warming waters reduce growth rates in Gulf of Maine cod. Far from being spurious, temperature effects on this stock are clear, and continuing to ignore them puts the stock in jeopardy.

In their Comments on our Report (1), Palmer *et al.* (2) and Swain *et al.* (3) both expressed concerns about our “extra mortality” calculation. Although they raise important issues about the role of simultaneous estimation of parameters within stock assessment models, their critiques miss the key point of our analysis.

The goal of our “extra mortality” calculation was not to consider how changing natural mortality assumptions would alter the model output. Rather, it was meant to evaluate how well the assessment model could predict the future state of the cod population, assuming a constant natural mortality of 0.2 and observed landings. Our analysis clearly shows that including a temperature effect would have improved the catch advice for Gulf of Maine cod. Although, as suggested in both Comments, post hoc analysis of stock assessments may push analytical limits, neither Comment addresses the critical question of why there is a strong correlation between model residuals and temperature. It is worth noting that Palmer *et al.*’s suggestion to remove outliers via a jack-knife procedure finds the same temperature correlations, including one for older fish reported in our supplementary materials, as our procedure

using a continuous, consistent section of the time series.

Our interpretation of the projection skill presumes an accurate estimate of abundance; however, a major challenge for the management of this stock has been the presence of a large retrospective pattern in the stock assessment. A retrospective pattern means that the abundance estimated for a given year changes as additional years of data are added. For Gulf of Maine cod, adding another year of data has consistently led to a downward adjustment of biomass in previous years (Fig. 1A). Thus, the projections for this stock started from an erroneous assumption that there were more fish and then were projected assuming that more would survive.

To further evaluate the assertions in our original Report, we investigated whether including

temperature-dependent natural mortality would improve the performance of the Gulf of Maine cod assessment. We built a scenario for natural mortality (M) that depends on temperature (T)

$$M_j(T_j, T_{j-3}) = \max(a T_j + b T_{j-3} + c, 0.05)$$

where the subscript j indicates the year, $a = 0.0828$, $b = 0.0695$, and $c = 0.1204$ [see (1)]. We then used this scenario to reconstruct the stock status using the same model, catch, survey indices, and model parameters used in the most recent assessment (4).

Using temperature-dependent mortality reduces the retrospective pattern (Fig. 1B). The value of Mohn’s ρ , a statistic developed to quantify the magnitude of a retrospective pattern (5), declines from 0.54 to 0.19. Therefore, incorporating temperature would have reduced the positive bias in the stock assessment, allowed for better projections of future survival, and, thus, would have supported improved management of Gulf of Maine cod. We agree with both Palmer *et al.* and Swain *et al.* that it would be preferable to fit environmental relationships within the assessment. The success of our scenario using natural mortality linked to temperature strongly suggests that further exploration of temperature effects in this stock is warranted.

The remaining question is whether there are mechanisms that can explain increased natural mortality during warm years. Although we did not attempt to identify a specific cause, we articulated several hypotheses. We considered how temperature effects on metabolism and predation could lead to higher mortality, and it is likely that a combination of these mechanisms act together to increase natural mortality.

Elevated temperature leads to higher metabolic rate (6, 7) and, when coupled with the fact that oxygen levels decrease in warmer waters, helps determine the equatorward limit of fish distributions, including cod (8, 9). The effect of increased metabolic rate is complex and depends on size, age, and reproductive status. If caloric intake does

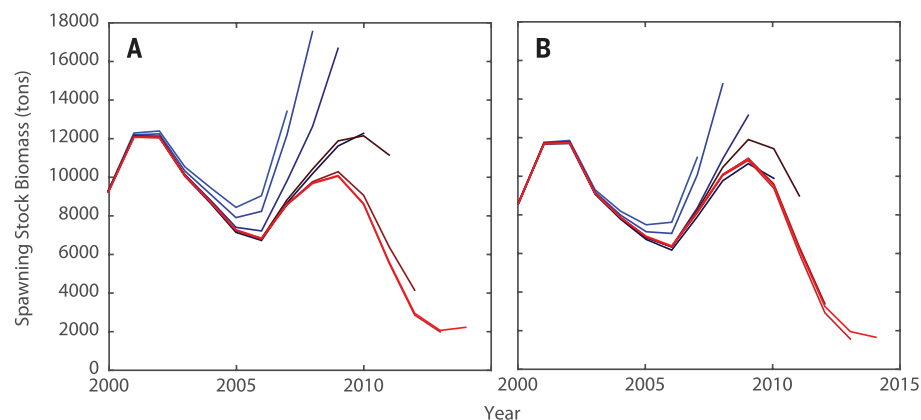


Fig. 1. Spawning stock biomass estimates for Gulf of Maine cod. (A) Spawning stock biomass estimated using a constant natural mortality of $M = 0.2$. The model was run seven times, each time adding another year of data. (B) Same as (A) but using a natural mortality scenario that incorporates summer temperatures.

¹Gulf of Maine Research Institute, 350 Commercial Street, Portland, ME 04101, USA. ²National Oceanic and Atmospheric Administration (NOAA) Earth System Research Laboratory, Boulder, CO 80305, USA. ³Woods Hole Oceanographic Institution, 86 Water Street, Woods Hole, MA 02543, USA. ⁴School of Marine and Atmospheric Sciences, Stony Brook University, Stony Brook, NY 11794, USA. ⁵Bigelow Laboratory for Ocean Sciences, 60 Bigelow Drive, East Boothbay, ME 04544, USA. ⁶University of Washington School of Oceanography, 1503 Northeast Boat Street, Seattle, WA 98105, USA. ⁷Cooperative Institute for Research in Environmental Sciences, University of Colorado Boulder, Boulder, CO 80309, USA. ⁸School of Marine Sciences, University of Maine, 5706 Aubert Hall, Orono, ME 04469, USA. *Corresponding author. Email: apershing@gmri.org

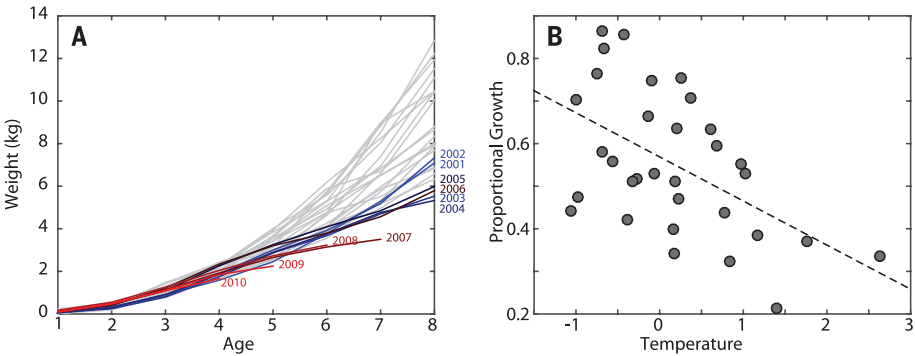


Fig. 2. Relationships between Gulf of Maine cod weight and temperature. (A) Growth of different cohorts. Year classes before 2001 are plotted in gray. The final 10-year classes are plotted starting with 2001 in blue and grading to 2010 in red. (B) Relationship between the change in weight between ages 5 and 6, expressed as a proportion of the age-5 weight and the summer temperature ($R^2 = 0.283$, $P < 0.1$).

Table 1. Linear models relating quarterly and annual temperatures to annual proportional growth increments. If $w_{j,k}$ is the weight of age j fish in year k , then the proportional growth increment $g_{j,k}$ is defined as $(w_{j+1,k+1} - w_{j,k})/w_{j,k}$. For each relationship, we report the coefficient m of the linear model $g_{j,k}(T_k) = m T_k + b$, the coefficient of determination (R^2), the P value of the relationship, and the P value after accounting for autocorrelation (P_{acf}). Relationships significant at the 95% level are in bold. Those that are also significant at the 90% level when accounting for autocorrelation are in bold and italic.

Age (years)	Statistic	Winter	Spring	Summer	Fall	Year
1 to 2	m	4.8×10^{-6}	8.3×10^{-6}	1.0×10^{-5}	1.1×10^{-5}	1.2×10^{-5}
	R^2	0.028	0.099	0.184	0.134	0.144
	P	0.36	0.08	0.01	0.04	0.03
	P_{acf}	0.31	0.19	0.12	0.15	0.14
2 to 3	m	$1.9 \times 10^{+00}$	$1.1 \times 10^{+00}$	4.1×10^{-2}	-3.8×10^{-1}	8.7×10^{-1}
	R^2	0.046	0.021	0.000	0.002	0.009
	P	0.24	0.43	0.97	0.82	0.62
	P_{acf}	0.25	0.33	0.49	0.45	0.39
3 to 4	m	-6×10^{-1}	-3.5×10^{-1}	-1.7×10^{-1}	-5.5×10^{-1}	-5.3×10^{-1}
	R^2	0.222	0.093	0.027	0.181	0.149
	P	0.01	0.09	0.37	0.02	0.03
	P_{acf}	0.08	0.22	0.35	0.13	0.17
4 to 5	m	-2.0×10^{-2}	-5.4×10^{-2}	-3.1×10^{-2}	-2.2×10^{-2}	-4.5×10^{-2}
	R^2	0.003	0.028	0.012	0.004	0.014
	P	0.76	0.36	0.55	0.74	0.52
	P_{acf}	0.44	0.32	0.38	0.43	0.37
5 to 6	m	-4.8×10^{-2}	-1.1×10^{-1}	-1×10^{-1}	-1×10^{-1}	-1.3×10^{-1}
	R^2	0.038	0.233	0.283	0.174	0.236
	P	0.28	0.01	0.00	0.02	0.00
	P_{acf}	0.29	0.10	0.08	0.14	0.10
6 to 7	m	-7.0×10^{-2}	-8.4×10^{-2}	-7.8×10^{-2}	-1.1×10^{-1}	-1.2×10^{-1}
	R^2	0.079	0.136	0.151	0.196	0.188
	P	0.12	0.04	0.03	0.01	0.01
	P_{acf}	0.21	0.16	0.16	0.12	0.13

not increase in proportion with metabolism, then we would expect to see fish that are either poorly conditioned or undersized (low weight for a given age). In our Report, we highlighted the former, based on the report that condition factor had been at or below the long-term mean since 2002 (10). However, condition factor has recovered in

recent years (2, 11), but this recovery has come at the expense of growth. Young cod are now larger than in the past, whereas fish age 5 and older are smaller (Fig. 2A). Growth from age 1 to 2 is positively related to temperature, whereas warmer waters produce smaller growth increments in older fish (Table 1). The

strongest negative relationships are for age 5 fish (Fig. 2B and Table 1). Because of the strong trend in the temperature data, several of the relationships are not significant when corrected for autocorrelation. However, the overall relationship of increased growth in young fish and decreased growth in older fish is a classic response to warming (12). Given the general relationship between body size and mortality in the ocean (13), we would expect higher mortality in the current population of smaller fish.

Our Report did not claim to have a definite answer to what is causing cod mortality to increase. Rather, we claimed that this increase is real, that it is likely related to temperature, and that failing to account for it led to catch advice that allowed for overfishing. There have been more than 900 studies describing temperature effects on cod and more than 8000 on fish (14). Given the importance of temperature on fish behavior, growth, and ecology, any model that does not consider temperature effects should be viewed with suspicion, especially for stocks near the edge of their range. In particular, any model used to make projections for a commercially important species should reflect current and likely future conditions in the ocean. In contrast to the assertion that stock assessment outputs should not be subjected to post hoc analyses (15), we feel that it is vital to evaluate the implications of these models and to strive to improve their ability to accurately represent the state of nature.

REFERENCES AND NOTES

1. A. J. Pershing *et al.*, *Science* **350**, 809–812 (2015).
2. M. C. Palmer, J. J. Deroba, C. M. Legault, E. N. Brooks, *Science* **352**, 423 (2016).
3. D. P. Swain, H. P. Benoît, S. P. Cox, N. G. Cadigan, *Science* **352**, 423 (2016).
4. Model inputs are available at the NOAA Northeast Fisheries Science Center Stock Assessment Support Information website, www.nefsc.noaa.gov/saw/sasi/sasi_report_options.php. We used ASAP v.3.0.17 and the inputs for the most recent (2015) Gulf of Maine cod assessment.
5. R. Mohn, *ICES J. Mar. Sci.* **56**, 473–488 (1999).
6. A. Clarke, N. M. Johnston, *J. Anim. Ecol.* **68**, 893–905 (1999).
7. J. F. Gillooly, J. H. Brown, G. B. West, V. M. Savage, E. L. Charnov, *Science* **293**, 2248–2251 (2001).
8. C. Deutsch, A. Ferrel, B. Seibel, H.-O. Pörtner, R. B. Huey, *Science* **348**, 1132–1135 (2015).
9. H. O. Pörtner *et al.*, *Clim. Res.* **37**, 253–270 (2008).
10. Northeast Fisheries Science Center, “55th Northeast Regional Stock Assessment Workshop (55th SAW) Assessment Report” (U.S. Department of Commerce, 2013).
11. M. C. Palmer, “2014 Assessment Update Report of the Gulf of Maine Atlantic Cod Stock” (U.S. Department of Commerce, 2014).
12. C. C. Taylor, *J. Conseil* **23**, 366–370 (1958).
13. I. Peterson, J. Wroblewski, *Can. J. Fish. Aquat. Sci.* **41**, 1117–1120 (1984).
14. Citation statistics from Web of Science on 1/3/16. We searched for articles using *Gadus morhua* and temperature in the title, abstract, or keywords. We found 2121 total articles, with 916 listed in the category “fisheries.” We repeated the search using fish and temperature and found 27,087 total, with 8294 categorized in “fisheries.” Only articles in the Science Citation and Social Science Citation databases were included.
15. E. N. Brooks, J. J. Deroba, M. Wilberg, *Can. J. Fish. Aquat. Sci.* **72**, 634–641 (2015).

REVIEW SUMMARY

INNATE IMMUNITY

Trained immunity: A program of innate immune memory in health and disease

Mihai G. Netea,* Leo A. B. Joosten, Eicke Latz, Kingston H. G. Mills, Gioacchino Natoli, Hendrik G. Stunnenberg, Luke A. J. O'Neill, Ramnik J. Xavier

BACKGROUND: Host immune responses are classically divided into innate immune responses, which react rapidly and nonspecifically upon encountering a pathogen, and adaptive immune responses, which are slower to develop but are specific and build up immunological memory. The dogma that only adaptive immunity can build immunological memory has recently been challenged by studies showing that innate immune responses in plants and invertebrates (organisms lacking adaptive immune responses) can mount resistance to reinfection. Furthermore, in certain mammalian models of vaccination, protection from reinfection has been shown to occur in-

dependently of T and B lymphocytes. These observations led to the hypothesis that innate immunity can display adaptive characteristics after challenge with pathogens or their products. This de facto immunological memory has been termed “trained immunity” or “innate immune memory.”

ADVANCES: In recent years, emerging evidence has shown that after infection or vaccination, prototypical innate immune cells (such as monocytes, macrophages, or natural killer cells) display long-term changes in their functional programs. These changes lead to increased responsiveness upon secondary stim-

ulation by microbial pathogens, increased production of inflammatory mediators, and enhanced capacity to eliminate infection. Mechanistic studies have demonstrated that trained immunity is based on epigenetic reprogramming, which is broadly defined as sustained changes in transcription programs and cell physiology that do not involve permanent genetic changes, such as mutations

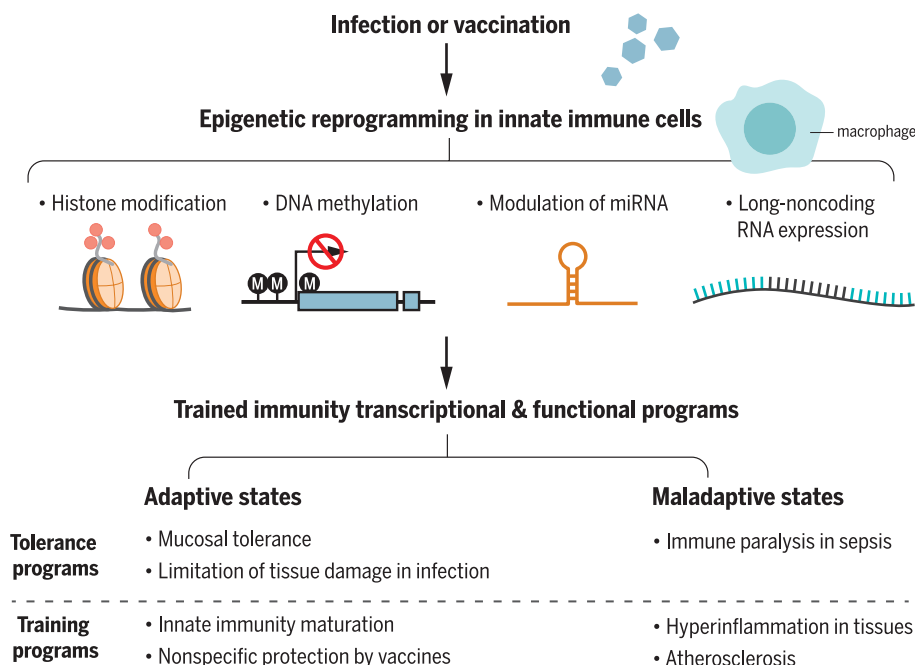
ON OUR WEBSITE

Read the full article at <http://dx.doi.org/10.1126/science.aaf1098>

and recombination. Histone modifications with chromatin reconfiguration have proven to be a central process for trained immunity, but other mechanisms—such as DNA methylation

or modulation of microRNA and/or long non-coding RNA expression—are also expected to be involved. This leads to transcriptional programs that rewire the intracellular immune signaling of innate immune cells but also induce a shift of cellular metabolism from oxidative phosphorylation toward aerobic glycolysis, thus increasing the innate immune cells' capacity to respond to stimulation. Trained immunity programs have evolved as adaptive states that enhance fitness of the host (e.g., protective effects after infection or vaccination, or induction of mucosal tolerance toward colonizing microorganisms). Proof-of-principle experimental studies support the hypothesis that trained immunity is one of the main immunological processes that mediate the nonspecific protective effects against infections induced by vaccines, such as bacillus Calmette-Guérin or measles vaccination. However, when inappropriately activated, trained immunity programs can become maladaptive, as in postsepsis immune paralysis or autoimmune-inflammatory diseases.

OUTLOOK: The discovery of trained immunity has revealed an important and previously unrecognized property of human immune responses. This advance opens the door for future research to explore trained immunity's effect on disease, for both diseases with impaired host defense, such as postsepsis immune paralysis or cancers, and autoimmune-inflammatory diseases, in which there is inappropriate activation of inflammation. These findings have considerable potential for aiding in the design of new therapeutic strategies, such as new generations of vaccines that combine classical immunological memory and trained immunity, the activation of trained immunity for the treatment of postsepsis immune paralysis or other immune deficiency states, and modulation of exaggerated inflammation in autoimmune-inflammatory diseases. ■



Innate immune activation by infections or vaccinations leads to histone modifications and functional reprogramming of cells (such as monocytes, macrophages, or NK cells) termed “trained immunity” or “innate immune memory.” Trained immunity evolved to lead to adaptive states that protect the host during microbial colonization or after infections. However, in certain situations, trained immunity may result in maladaptive states such as postsepsis immune paralysis or hyperinflammation. miRNA, microRNA.

The list of author affiliations is available in the full article online.
*Corresponding author. Email: mihai.netea@radboudumc.nl
Cite this article as M. G. Netea *et al.*, *Science* 352, aaf1098 (2016). DOI: 10.1126/science.aaf1098

REVIEW

INNATE IMMUNITY

Trained immunity: A program of innate immune memory in health and disease

Mihai G. Netea,^{1*} Leo A. B. Joosten,¹ Eicke Latz,^{2,3,4} Kingston H. G. Mills,⁵ Gioacchino Natoli,⁶ Hendrik G. Stunnenberg,⁷ Luke A. J. O'Neill,⁵ Rannik J. Xavier^{8,9}

The general view that only adaptive immunity can build immunological memory has recently been challenged. In organisms lacking adaptive immunity, as well as in mammals, the innate immune system can mount resistance to reinfection, a phenomenon termed “trained immunity” or “innate immune memory.” Trained immunity is orchestrated by epigenetic reprogramming, broadly defined as sustained changes in gene expression and cell physiology that do not involve permanent genetic changes such as mutations and recombination, which are essential for adaptive immunity. The discovery of trained immunity may open the door for novel vaccine approaches, new therapeutic strategies for the treatment of immune deficiency states, and modulation of exaggerated inflammation in autoinflammatory diseases.

Most immune responses are classically divided into innate immune responses, which react rapidly and nonspecifically upon encountering a pathogen, and adaptive immune responses, which are slower to develop but are specific (due to antigen receptor gene rearrangements) and result in classical immunological memory. This schematic distinction has been challenged by the discovery of pattern recognition receptors (PRRs) that confer some specificity to the recognition of microorganisms by innate immune cells (1), as well as by a growing body of literature showing that the innate immune system can adapt its function after previous insults (2, 3). Protection against reinfection has been reported, not only in plants and invertebrates that do not have adaptive immunity (4), but also in mammals, with old and new studies demonstrating cross-protection between infections with different pathogens (5). These studies have led to the hypothesis that innate immunity can be influenced by previous encounters with

pathogens or their products, and this property has been termed “trained immunity” or “innate immune memory.”

Compared with classical immunological memory, trained immunity has a number of defining characteristics. First, it involves a set of cells [myeloid cells, natural killer (NK) cells, and innate lymphoid cells (ILCs)] and germline-encoded recognition and effector molecules (e.g., PRRs, cytokines) that are different from those involved in classical immunological memory. Second, and in contrast to classical immunological memory that depends on gene rearrangement and proliferation of antigen-specific lymphocyte clones, the increased responsiveness to secondary stimuli during trained immunity is not specific for a particular pathogen and is mediated through signals impinging on transcription factors and epigenetic reprogramming. These are broadly defined as sustained changes in transcription programs through epigenetic rewiring, leading to changes in cell physiology that do not involve permanent genetic changes such as mutations and recombination. Finally, trained immunity relies on an altered functional state of innate immune cells that persists for weeks to months, rather than years, after the elimination of the initial stimulus.

In this context, it important to note that some innate immune cells, such as NK cells, display both trained immunity characteristics, as defined above, and antigen-dependent (or even antigen-specific) immunity related to the classical immunological memory mediated by T and B lymphocytes (see below for a detailed description). In addition, it is important to clearly discriminate between trained immunity and other immunological processes, such as immune cell activation and differentiation. During immune cell activa-

tion, transcription of genes takes place at the time of stimulation in response to a ligand directly acting on the cell. In contrast, during trained immunity, innate immune cells display gene- or locus-specific changes in their chromatin profiles, induced by a previous stimulation. However, these changes allow increasing response to restimulation of the cells through both the same and different PRRs. The discrimination between trained immunity and immune cell differentiation is more difficult and, to a certain degree, is even semantic: One could argue that macrophage differentiation could also be considered an example of trained immunity. However, immune cell differentiation can (and does) also occur during homeostatic conditions, whereas trained immunity is defined as a reaction to a foreign insult. In addition, although the term “circulating differentiated monocyte” could also be used instead of “trained monocyte,” we believe that this may be confusing, as monocyte differentiation is generally considered equivalent to the process through which blood monocytes differentiate into macrophages in the tissues. Moreover, differentiated cells such as macrophages can be trained as well (e.g., after infection or vaccination), and thus their capacity to display increased function should be defined differently than cell differentiation.

Defining the properties of trained immunity will critically integrate our understanding of host defense. In this Review, we will describe this concept and discuss recent data that support its important role in health and disease. We will not delve into classical immunological memory, as this topic has already been the subject of many thorough reviews.

Immunological memory in plants and invertebrate animals

A first line of evidence that the innate immune system has the capacity to build memory to previous insults comes from a plethora of immunological studies in plants. Collectively, these studies provide compelling evidence of the capacity to respond more efficiently to reinfection, a phenomenon termed “systemic acquired resistance” (SAR) (6). The molecular mechanisms and biochemical mediators of SAR are largely known (6), with epigenetic-based rewiring of host defense playing a central role (7). In addition, there is increasing evidence to suggest that innate immunity displays memory traits, not only in plants but also in invertebrate animals (4). For example, the microbiota has been shown to induce innate immune memory to protect mosquitoes against *Plasmodium* (8), the social insect *Bombus terrestris* displays innate immune memory against three different pathogens (9), and the tapeworm *Schistocephalus solidus* induces memory in the copepod crustacean (10). In these models, the organism is protected against reencounter with the pathogen by an improved clearance of the infection. It is therefore reasonable to conclude that immunological memory is found in plants and lower animals (3, 4), as well as in vertebrates.

¹Department of Internal Medicine and Radboud Center for Infectious Diseases, Radboud University Medical Center, Nijmegen, Netherlands. ²Institute of Innate Immunity, Bonn University, Bonn, Germany. ³Division of Infectious Diseases and Immunology, Department of Medicine, University of Massachusetts Medical School, Worcester, MA 01655, USA.

⁴German Center for Neurodegenerative Diseases (DZNE), Bonn, Germany. ⁵School of Biochemistry and Immunology, Trinity College, Dublin, Ireland. ⁶Department of Experimental Oncology, European Institute of Oncology, Milan, Italy.

⁷Department of Molecular Biology, Faculties of Science and Medicine, Radboud Institute of Molecular Life Sciences, Radboud University, Nijmegen, Netherlands. ⁸The Broad Institute of MIT and Harvard, Cambridge, MA 02142, USA.

⁹Center for Computational and Integrative Biology and Gastrointestinal Unit, Massachusetts General Hospital, Harvard Medical School, Boston, MA 02114, USA.

*Corresponding author. Email: mihai.netea@radboudumc.nl

Table 1. Overview of innate immune memory mechanisms described for various types of innate immune cells.					
Innate immune cell type	Primary challenge	Type of memory	Pathway involved	Mechanism	References
Monocytes and macrophages	LPS	Tolerance/trained immunity	TLR4/MAPK-dependent ATF7-dependent	Epigenetic changes: latent enhancers (H3K4me1), other modifications (H3K4me3, H2K27me, H3K9me2)	Foster et al. (50), Ostuni et al. (75), Yoshida et al. (80)
Monocytes and macrophages	β-glucan, <i>Candida</i> infection, BCG vaccination	Trained immunity	Dectin-1/Raf1/Akt-dependent STAT1-dependent NOD2-dependent	Epigenetic changes (H3K4me1, H3K4me3, H2K27Ac, H3K9me2), metabolic rewiring	Quintin et al. (26), Saeed et al. (51), Cheng et al. (79), Yoshida et al. (80)
NK cells	Hapten-induced influenza A, vaccinia virus, HIV-1 infection	Antigen-specific	Not described	CXCR6-dependent, NKG2D-dependent	O'Leary et al. (30), Paust et al. (57), Gillard et al. (58), Reeves et al. (64)
NK cells	CMV infection	Antigen-dependent	Atg3-mediated mitophagy	BNIP3/BNIP3L-dependent	Sun et al. (31), O'Sullivan et al. (61)
NK cells	CMV infection	Trained immunity	Stable down-regulation of adaptors and transcription factors (e.g., Syk, PLZF)	Epigenetic modification of gene promoters DNA methylation	Lee et al. (65), Schlums et al. (34)

Several mechanisms have been proposed to account for innate immune memory in invertebrates, including the sustained up-regulation of immune regulatory pathways [such as the Toll and Imd receptors on the haematocytes (11)] or of the bacterial peptidoglycan recognition molecules and lectins (12), and quantitative and phenotypic changes in immune cell populations (8). Alternatively, memory may be due to the presence of diversity-generating mechanisms in insects, such as generation of variation in fibrinogen-related proteins (probably acting as pathogen sensors) with high rates of diversification at the genomic level through point mutations and recombinatorial processes (13). The Toll-like receptors (TLRs)—the animal counterpart of Toll in *Drosophila*—also show great diversity in the sea urchin, which has an estimated 222 receptors (14).

Innate immune memory in vertebrates

The presence of memory characteristics in innate host defense of different plant and animal lineages suggests that innate immune memory may be present in vertebrates as well (Table 1). Important clues indicating that vertebrate innate immunity also has adaptive characteristics came from experimental studies in mice showing that priming (or training) of mice with microbial ligands of PRRs can protect against a subsequent lethal infection. For example, trained immunity induced by β-glucan (a polysaccharide component of mainly fungal cell walls) induces protection against infection with *Staphylococcus aureus* (15, 16). Similarly, the peptidoglycan component muramyl dipeptide induces protection against *Toxoplasma* (17), and prophylactic treatment with TLR9 agonists (such as oligodeoxynucleotides containing unmethylated CpG dinucleotides) 3 days before the infection protects against

sepsis and meningitis caused by *Escherichia coli* (18). Furthermore, flagellin can induce protection against *S. pneumonia* (19) and rotavirus (20), the latter being independent of adaptive immunity and induced by dendritic cell-derived interleukin (IL)-18, which in turn drives production of IL-22 by epithelial cells. In addition to microbial ligands, there is evidence that certain proinflammatory cytokines may induce trained immunity: Injection of mice with one dose of recombinant IL-1 3 days before infection with *Pseudomonas aeruginosa* protected the mice against mortality (21). The nonspecific character of the trained immunity provides evidence against a classical immunological memory effect and instead suggests the activation of nonspecific innate immune mechanisms.

Compelling evidence that trained immunity is induced in vertebrates and mediates at least some of the protective effects of vaccination came from studies showing that immunization of mice with bacillus Calmette-Guérin [(BCG), the tuberculosis vaccine that is also the most commonly used vaccine worldwide] induces T cell-independent protection against secondary infections with *Candida albicans* or *Schistosoma mansoni* (22, 23). The hypothesis that trained immunity can be elicited in vertebrates is further supported by studies investigating the mechanism of protection against disseminated candidiasis conferred by attenuated strains of *C. albicans*. For example, when an attenuated PCA-2 strain of *C. albicans* that is incapable of germination is injected in mice, protection is induced against the virulent strain CA-6 (24). This protection was also induced in athymic mice and *Rag1*-deficient animals (i.e., those that cannot rearrange their antigen receptors), demonstrating a lymphocyte-independent mechanism (25, 26). The protection against reinfection was instead

dependent on macrophages (24) and proinflammatory cytokine production (27), both prototypical innate immune components.

In addition to BCG and *C. albicans*, some viral and parasitic organisms can exert protective effects through mechanisms independent of adaptive immunity. Herpesvirus latency increases resistance to the bacterial pathogens *Listeria monocytogenes* and *Yersinia pestis* (28), with protection achieved through enhanced production of the cytokine interferon-γ (IFN-γ) and systemic activation of macrophages. Similarly, infection with the helminth parasite *Nippostrongylus brasiliensis* induces a long-term macrophage phenotype that, on one hand, damages the parasite and, on the other, induces T and B lymphocyte-independent protection from reinfection (29).

Other studies have shown that NK cells also display immune memory. This was first demonstrated in mice that showed hapten-induced contact hypersensitivity dependent on NK cells that persisted for at least 4 weeks (30). Consistent with this notion, several subsequent studies reported that infection with murine cytomegalovirus (mCMV) induces immunological memory independent of T and B cells (31–34). The protection in these models is mediated by NK cells, which proliferate and persist in lymphoid and nonlymphoid organs. Upon reinfection, these memory NK cells undergo a secondary expansion, rapidly degranulating and releasing cytokines, thus inducing a protective immune response (31). Additionally, NK cells have been shown to prime monocytes in the bone marrow during infection, and this may also induce long-term effects on innate immune responses (35).

In addition to experimental studies showing induction of innate immune memory in mice, emerging data suggest that similar trained immunity effects can be generated in humans.

First, a large number of epidemiological studies have shown nonspecific beneficial effects of live vaccines—such as BCG, measles vaccines, and oral polio vaccine—against infections other than the target diseases (36). The identification of these nonspecific (or heterologous) effects suggests that these vaccines induce trained immunity that protects against unrelated pathogens. This hypothesis was proposed in proof-of-principle trials with BCG vaccine in healthy adult volunteers (37) and was subsequently validated in clinical trials in newborn children vaccinated with BCG (38) or exposed in utero to hepatitis B vaccine (39). Second, certain infections such as malaria can also induce a state of hyperresponsiveness that is functionally equivalent to the induction of trained immunity (40, 41). Finally, nonspecific protective effects through innate immunity-dependent mechanisms are provided by the use of BCG for treatment of malignancies such as bladder cancer (42), melanoma (43), leukemia (44), and lymphoma (45): Although direct inflammatory effects are probably important, long-term innate immune memory persisting between the BCG treatments is also likely to be involved. In this respect, Buffen *et al.* have recently suggested that these anticancer effects of BCG are directly dependent on the capacity to mount trained immunity, as individuals unable to mount trained immunity due to autophagy defects show a diminished recurrence-free survival after BCG treatment in bladder carcinoma (46).

Taken together, these complementary murine and human studies suggest that innate immune responses have the capacity to be primed or trained and thereby exert a new type of immunological memory upon reinfection, for which the term “trained immunity” has been proposed (Fig. 1).

Mechanisms responsible for mediating trained immunity

Innate immune cells that build innate immune memory

Innate immune memory properties have been described in several cell populations, including monocytes, macrophages, and NK cells. Preliminary observations suggest that similar characteristics may also be present in other cell types, such as ILCs or polymorphonuclear leukocytes. Unlike lymphocytes, innate immune cells do not express rearranging antigen receptor genes, but they do express PRRs and other receptors that allow them to recognize and respond to pathogen-derived structures [pathogen-associated molecular patterns (PAMPs)] and endogenous danger signals (damage-associated molecular patterns) (47, 48). Although these responses are not specific to the degree conferred by antigen receptors, there is evidence to suggest that expression of distinct members of PRR families (e.g., TLRs, NOD-like receptors, C-type lectin receptors, RIG-I-like receptors, or combinations thereof) on macrophages and dendritic cells triggers different signaling pathways that lead to innate immune responses that are tailored to the particular type of pathogen encountered (49).

Among the various cell types implicated in innate immune memory, the major focus has been on monocytes, macrophages, and NK cells. We note that this attention does not necessarily mean that these cells are more amenable to training than other innate immune cells. Instead, this focus may merely reflect historical connection of these cells with lipopolysaccharide (LPS)-induced tolerance (LPS is a component of Gram-negative bacterial cell walls). Some of the earliest evidence that macrophages may exhibit memory-like features came from investigations of LPS-induced tolerance at the molecular level (50). In one such study, gene-specific chromatin modifications were associated with silencing of genes coding for inflammatory molecules while priming other genes coding for antimicrobial molecules (50). These findings suggested that macrophages could be primed by LPS to become more or less responsive to subsequent activation signals. This observation was expanded by studies demonstrating that exposure of monocytes and macrophages to *C. albicans* or β -glucan enhanced their subsequent response to stimulation with unrelated pathogens or PAMPs, a process termed “trained immunity” (26). Training was demonstrated to be accompanied by significant reprogramming of chromatin marks (26, 50, 51), as detailed further below. Besides bacterial and fungal pathogens, monocytes and macrophages can also mount trained immunity responses after infection with parasitic (29) and viral (28) pathogens.

Regarding trained immunity in monocytes, it is important to consider the life span of these cells. Monocytes are cells with a short half-life in circulation, with recent studies suggesting it to be up to 1 day (52). The observation that trained monocytes have been identified in the circulation of BCG-vaccinated individuals for at least 3 months after vaccination (37) suggests that reprogramming must take place at the level of progenitor cells in the bone marrow as well. Indeed, recent evidence has emerged to indicate that innate immune memory can be transferred via hematopoietic stem and progenitor cells. Macrophages derived from hematopoietic stem and progenitor cells rendered tolerant by TLR2 ligand exposure and transferred to irradiated mice retain a tolerant phenotype and produce lower amounts of inflammatory cytokines and reactive oxygen species in response to inflammatory stimulation (53). Furthermore, exposure of mouse skin to ultraviolet radiation induces immunosuppression that was originally attributed to defective T cell priming by dendritic cells (54) but was subsequently shown to involve epigenetic reprogramming and a long-lasting effect on dendritic cell progenitors in the bone marrow that altered the function of their differentiated progeny (55). In addition, recent studies have suggested that microbiota can induce long-term functional reprogramming of bone marrow progenitors—and, subsequently, dendritic cells—to protect against *Entamoeba histolytica* (56). Whether vaccines such as BCG automatically stimulate trained immunity and also confer or

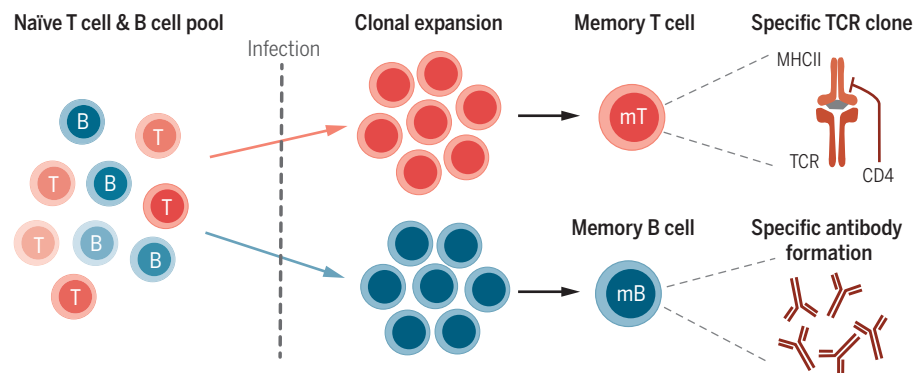
induce similar effects at the level of progenitor cells remains to be established.

Emerging evidence suggests that NK cells also respond more vigorously after a previous challenge. NK cell memory has been documented after exposure to cytokine combinations (e.g., IL-12, IL-15, and IL-18) (32) or hapten sensitization, which induced long-lived NK cells that mediate contact hypersensitivity and long-lived antigen-specific recall responses, independently of B and T cells (30). In addition, NK cells undergo expansion during virus infections, such as those with mCMV (31), influenza A (57), or vaccinia virus (58). Studies of CMV infection have shown that NK cell activation may provide T cell-independent protection against reinfection by rapidly degranulating and producing cytokines (31). Furthermore, adoptive transfer experiments have demonstrated that activated NK cells can proliferate in vivo and protect naïve recipient mice against virus infection, which suggests that they could confer protective immunological memory. The nonspecific protective effects of BCG infection have also been linked with activation of NK cells. NK cells from BCG-vaccinated individuals have enhanced proinflammatory cytokine production in response to mycobacteria and other unrelated pathogens, and studies in mice have shown that BCG confers nonspecific protection against *C. albicans*, at least partially through NK cells (59).

A number of mechanisms have been put forward that may mediate the memory properties of NK cells: some of them are responsible for induction of innate immune memory and others for the survival of the NK memory cells. The former include enhanced responsiveness of the IL-12/IFN- γ axis (32) or the activation of the costimulatory molecule DNAM-1 (DNAX accessory molecule-1, also known as CD226) on the membrane of the cells (60). However, survival of the memory NK cells during the contraction phase after mCMV infection necessitates mitophagy through an *Atg3*-dependent mechanism (61).

The issue of specificity of the NK memory immune responses is complex. Evidence that NK memory is specific was provided by the demonstration that, in the mouse, mCMV-induced NK cells protected against mCMV but not Epstein-Barr virus, another herpesvirus (62). Notably, mCMV impaired heterologous immunity against influenza and *L. monocytogenes* (57, 63). Memory responses of NK cells toward other stimuli such as haptens and viruses also induced antigen-specific immune memory (41). Another important aspect concerns the mechanisms responsible for the persistence of NK memory cells. NK cell memory of haptens and viruses depends on CXCR6, a chemokine receptor on hepatic NK cells that is required for the persistence of memory NK cells but not for antigen recognition (41). In addition, recent studies revealed evidence of NK memory in primates: Splenic and hepatic NK cells from adenovirus 26-vaccinated macaques efficiently lysed antigen-matched but not antigen-mismatched targets 5 years after vaccination. These data demonstrate that robust, durable,

A Classical immunological memory



B Trained immunity: adaptive characteristics of innate immune cells

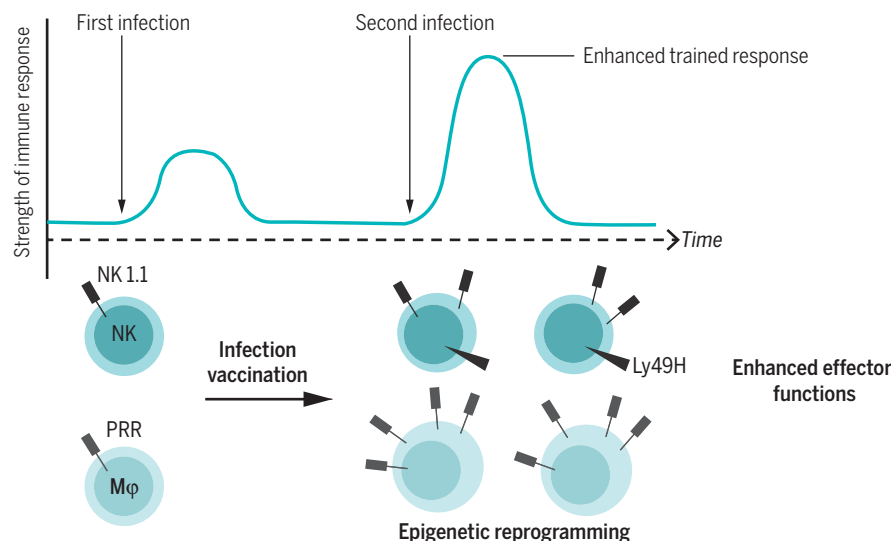


Fig. 1. Classical immunological memory versus trained immunity. (A) Classical adaptive immunological memory involves gene recombination in B and T lymphocytes, which confers high specificity and, very often, long-term, pathogen-specific protection (up to decades). (B) Trained immunity defines a de facto innate immune memory that induces enhanced inflammatory and antimicrobial properties in innate immune cells, resulting in an increased nonspecific response to subsequent infections and improved survival of the host. Mφ, macrophage.

antigen-specific NK cell memory can be induced in primates after both infection and vaccination. This finding has important implications for the development of vaccines against HIV-1 and other pathogens (64).

In addition to studies showing antigen-specific mechanisms of NK cell immune memory, other recent investigations have suggested that memory in NK cells is also mediated by epigenetic changes. In a study in patients recovering from CMV virus infection, the DNA methylation patterns of NK cells and cytotoxic T cells were similar, and very different from those of canonical NK cells. Subsequently, the capacity of these adaptive NK cells to secrete cytokines was modulated, and this was dependent on the transcription factor promyelocytic leukemia zinc finger (PLZF) (34, 65). Similarly, another study showed that these memory-like NK cells are defective in the Syk-dependent stimulation pathway, which

is correlated with epigenetic changes at the level of the gene promoter (60).

Taken together, the published data suggest that NK immune memory is complex and may display aspects of both antigen-dependent (and, in certain circumstances, antigen-specific) memory and epigenetic reprogramming as seen in trained immunity.

The molecular basis of trained immunity: Transcriptional and epigenetic reprogramming

A distinguishing feature of the trained innate immune cell is its ability to mount a qualitatively different—and to some extent quantitatively stronger—transcriptional response compared with untrained cells when challenged with pathogen or danger signals. The molecular bases of such enhanced activation of a subset of inflammatory genes are only partially defined, but ev-

idence supports the convergence of multiple regulatory layers, including changes in chromatin organization and the persistence of microRNAs (miRNAs) induced by the primary stimulus.

In myeloid cells, many loci encoding inflammatory genes are in a repressed configuration (66–68), as inferred by their limited accessibility to nucleases (used as tools to probe chromatin structure), the low acetylation of the nucleosomal histones, and the very low amount of RNA polymerase II loaded onto both the coding body of the genes and the genomic regulatory elements (enhancers and promoters) that control their expression (69). Upon primary stimulation, the changes observed at these loci, in terms of gain in chromatin accessibility, increased histone acetylation and RNA polymerase II recruitment, are massive, and are of magnitudes not commonly observed in other responses to micro-environmental changes. These considerable alterations—which, in some cases, result in the activation of gene expression that is hundreds of times higher than baseline levels in a short window of time—are driven by the recruitment of stimulation-responsive transcription factors (e.g., NF-κB, AP-1, and STAT family members) to enhancers and gene promoters, which are usually premarked by lineage-determining transcription factors such as PU.1 (70–73). In turn, transcription factors control the recruitment of coactivators (including histone acetyltransferases and chromatin remodelers) (67, 68) that locally modify chromatin to make it more accessible to transcriptional machinery.

Maintenance of such enhanced accessibility may underlie the more efficient induction of genes primed by the initial stimulation (50). Moreover, because histone modifications are specifically bound by recognition domains contained in various proteins implicated in transcriptional control (as in the case of the bromodomain–acetyl lysine interaction) (74), the persistence of histone modifications deposited at promoters or enhancers after the initial stimulus may itself affect the secondary response (26). The possible contribution of chromatin modifications to trained immunity must be examined while accounting for the different stability of individual covalent chromatin modifications, with more stable modifications (e.g., histone methylation) being potentially more suitable to perpetuate a functional change than those with a typically short half-life (e.g., histone acetylation). Therefore, the observed long-term persistence of some histone modifications in myeloid cells after removal of the initial activation stimulus may reflect either their stability or, alternatively, the sustained activation of the upstream signaling pathways and transcription factors that control their deposition.

One interesting paradigm is provided by latent or de novo enhancers (75, 76), which are genomic regulatory elements that are epigenetically unmarked or marked at low levels in unstimulated cells but gain histone modifications characteristic of enhancers [such as monomethylation of histone H3 at K4 (H3K4me1)] only in response to specific stimuli. In vitro, upon removal of the

stimulus that triggered their functionalization, a fraction of latent enhancers retain their modified histones and can undergo a stronger activation in response to restimulation (Fig. 2). This observation is reminiscent of the fact that in vivo macrophages acquire repertoires of active enhancers that are largely instructed by the microenvironmental signals specific to a given tissue and are thus substantially different, depending on the organ in which a macrophage is located (77, 78). In turn, such signals act by specifically inducing regulation by distinct combinations of transcription factors that are eventually responsible for the activation of different sets of genes mediated by epigenetic modifying enzymes. Transferring macrophages from one tissue to another results in an extensive reprogramming of the enhancer repertoire (78). Therefore, a complex equilibrium exists between mechanisms that promote the persistence of the modified epigenome instructed by the previously encountered stimuli and mechanisms that reprogram it in response to a changing environment. The very same dynamic equilibrium probably underlies the persistence of chromatin states that are relevant to enhanced transcriptional responses in trained immunity.

Recent studies have investigated the changes in epigenomic programs in innate immune cells during the induction of trained immunity. One early study proposed that changes in epigenetic status underlie the repression of inflammatory genes during LPS tolerance. However, genes mainly involved in antimicrobial responses were either normally produced or even displayed an increased production capacity (50). The repression of inflammatory mediator production and the potentiation of antimicrobial proteins synthesis were accompanied by histone-repressive or -activating marks, respectively. Similarly, exposure of monocytes and macrophages to *C. albicans* or β -glucan modulated their subsequent response to stimulation with unrelated pathogens or PAMPs, and the changed functional landscape of the trained monocytes was accompanied by epigenetic reprogramming (26, 51). Pathway analysis identified important immunological (cAMP-PKA activation) and metabolic (aerobic glycolysis) pathways that play crucial roles in the induction of trained immunity (51, 79). Additionally, a recent study showed that both LPS and β -glucan induce trained immunity through a mitogen-activated protein kinase (MAPK)-dependent pathway that phosphorylates the transcription factor ATF7, subsequently reducing the repressive histone mark H3K9me2 (80). Moreover, the immunological networks activated in trained monocytes depend on STAT1 activation (80), and the importance of STAT1 for the induction of trained immunity is supported by the defects in trained immunity reported in patients with chronic mucocutaneous candidiasis due to *STAT1* mutations (81).

BCG vaccination has also been shown to result in an increase in inflammatory mediators produced by monocytes from healthy volunteers, which correlated with parallel changes in a histone modification associated with gene activa-

tion (37). Similar to observations for monocytes and macrophages, the induction of CMV-induced NK cell memory at least partially relies on epigenetic reprogramming, which is linked to reduced expression of PLZF (34) and the tyrosine kinase SYK (65). Human CMV also drives epigenetic priming of the *IFNG* locus in NK cells, which “tags” the gene and leads to consistent IFN- γ production in a subset of NK cells, providing a molecular basis for the adaptive feature of these cells (82). The epigenetic machinery of the immune system may also be hijacked by certain bacterial pathogens, such as *L. monocytogenes* (83), and this may represent a more general mechanism of escape from host defense (84, 85).

microRNAs may also contribute to trained immunity (86), mainly because of the reportedly long half-life of these molecules (87) that, combined with the limited proliferative ability of myeloid cells, would result in their persistence after removal of the primary stimulus. Among miRNAs, miR-155 may have particular relevance because its up-regulation in response to inflammatory signals (such as microbial components) is associated with the hyperactivation of myeloid cells, possibly due to the derepression of phosphatases that negatively regulate transducers of several signaling pathways (88). It is reasonable to predict that myeloid cells expressing miR-155 in a sustained manner would remain in a primed, hypersensitive state: Upon exposure to a secondary stimulus of identical strength, these cells could respond in an enhanced manner compared with their response to the primary stimulation.

Although the discussion above addresses the role of epigenetic programming as a mechanism for mediating innate immune memory, one crucial aspect remains unknown: What cellular processes induce and maintain these epigenetic changes? There is increasing evidence to suggest that rewiring of cellular metabolism is involved, with a role for metabolites as cofactors for enzymes involved in epigenetic modulation of gene transcription.

Immunometabolic circuits: The role of cellular metabolites for shaping the epigenetic program of trained innate immune cells

Recent work revealed extensive rewiring of metabolic pathways in different immune cells upon activation (89). The best example concerns macrophages, where the M1 phenotype (i.e., macrophages activated with LPS and IFN- γ , producing mainly inflammatory cytokines) and M2 phenotype (macrophages activated by IL-4-related cytokines and expressing genes involved in tissue repair) use distinct metabolic pathways (90, 91). M1 macrophages are largely glycolytic, with impairment of oxidative phosphorylation and disruption of the Krebs cycle at two steps: after citrate and after succinate. Citrate is withdrawn for fatty acid biosynthesis (which enables the increased production of inflammatory prostanoids), whereas succinate activates the transcription factor HIF1 α , which regulates a wide

range of genes, including the one encoding the inflammatory mediator IL-1 β (90, 91). In M2 macrophages, the Krebs cycle is intact. A key feature is the synthesis of uridine diphosphate

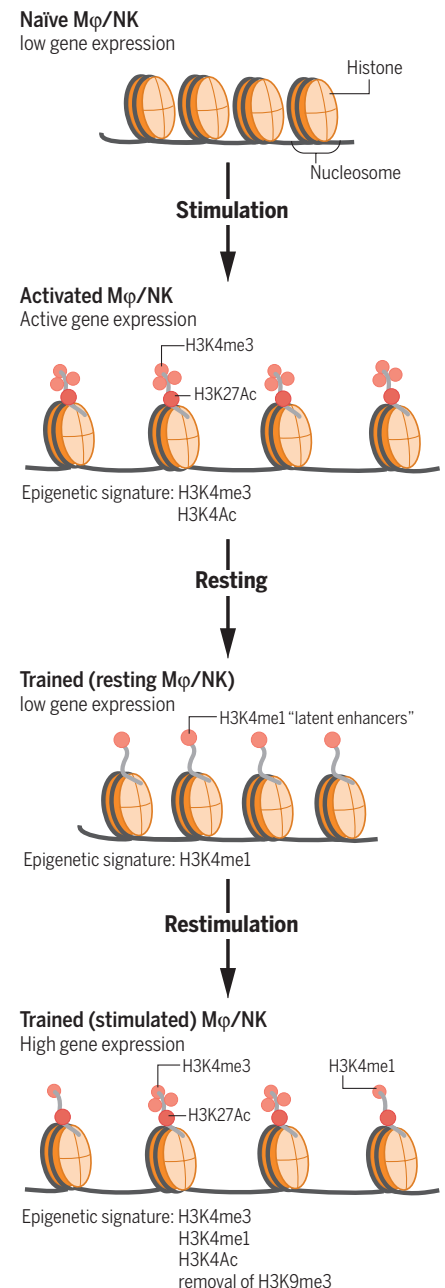


Fig. 2. Epigenetic rewiring underlies the adaptive characteristics of innate immune cells during trained immunity. Initial activation of gene transcription is accompanied by the acquisition of specific chromatin marks, which are only partially lost after elimination of the stimulus. The enhanced epigenetic status of the innate immune cells, illustrated by the persistence of histone marks such as H3K4me1 characterizing “latent enhancers,” results in a stronger response to secondary stimuli upon rechallenge.

N-acetylglucosamine from glucose and glutamine, which is needed for the extensive glycosylation occurring in receptors such as mannose-binding lectin, which are hallmarks of the M2 phenotype (97).

The importance of cellular metabolism for macrophage programming suggests that similar mechanisms may play a role for the long-term functional changes in monocytes and macrophages during trained immunity. In line with this, an important role for a shift from oxidative phosphorylation toward glycolysis through an Akt/mTOR/HIF-1 α -dependent pathway has recently been reported to be essential for trained immunity induced by β -glucan (51, 79). Whether and how this shift influences epigenetic processes in trained immunity is still under investigation, but important clues have been provided by studies linking chromatin regulation to intermediary metabolism (92, 93). In this respect, a critical metabolic intermediate that is increased in trained monocytes (acetyl-coenzyme A) is required for histone acetylation. Additionally, the ratio of the Krebs cycle metabolites α -ketoglutarate and succinate is a critical determinant for the activity of two families of enzymes controlling epigenetic modifications: the JMJD family of lysine demethylases and the TET family of methyl-cytosine hydroxylases (51, 94). These enzymes require α -ketoglutarate as a cofactor, whereas succinate limits their activity (Fig. 3). An additional possibility for innate immune memory may be that stimulation of macrophages causes an elevation in the level of succinate; this would then inhibit JMJD3, leading to enhanced H3K27 trimethylation of particular genes (e.g., those associated with the M2 phenotype), thus suppressing their expression (95). This process would maintain a proinflammatory phenotype of trained macrophages upon restimulation. Important links between altered metabolites and epigenetic changes have also been demonstrated in LPS-induced tolerance, in which nicotinamide adenine dinucleotide-dependent activation of class III histone deacetylases (sirtuins) functions with sirtuin-1 and sirtuin-6 in coordinating a switch from glucose to fatty acid oxidation (96). The remaining challenges are to explain how these potentially nonspecific functions of metabolites could have locus- and/or gene-specific effects and to provide direct evidence for metabolites altering the activity of enzymes that modify DNA and histones during trained immunity.

Adaptive and maladaptive programs

As described above, trained immunity most likely evolved as a primitive form of immune memory, aimed to provide improved protection of the host against reinfection, with beneficial effects for survival. It is also likely that trained immunity plays an important role in ontogeny, enabling the maturation of the innate immune system of the newborn (97), a process in which microbiota plays an important role (98). In line with the notion that microbiota might influence the functional program of immune cells, a recent

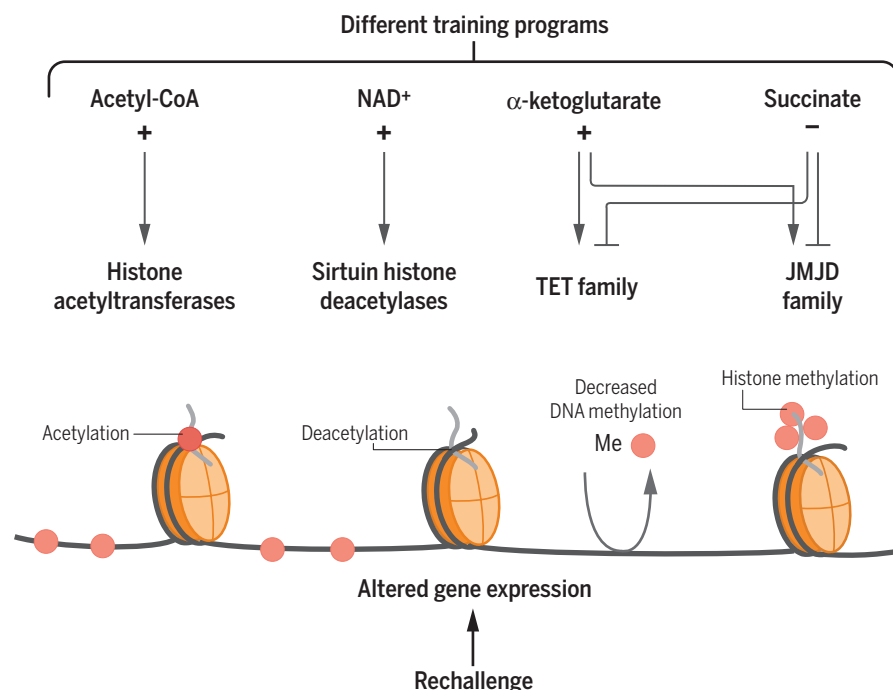


Fig. 3. Stimulation of innate immune cells with training stimuli induces changes in cellular metabolism. Various metabolites function as cofactors for epigenetic enzymes, which in turn induce chromatin and DNA modifications, modulate gene transcription, and result in different trained immunity programs. CoA, coenzyme A; NAD⁺, nicotinamide adenine dinucleotide; Me, methyl.

study showed increased H3K4me3 in NK cells from conventionally housed mice compared with germ-free animals (99). However, there may also be situations in which reprogramming of innate immunity and increased inflammatory responses to exogenous or endogenous stimuli could have deleterious effects.

Several pathological conditions have been described in which innate immune reprogramming may have adverse effects. During LPS-induced tolerance, reprogramming of innate immune cells probably plays a beneficial role in maintaining a relatively high threshold of cellular activation in organs where LPS naturally occurs at physiological levels, such as in the gastrointestinal tract (50). In contrast, in the case of systemic activation of innate immune cells during sepsis, LPS-induced tolerance can contribute to immune paralysis, placing the individual at greater risk for opportunistic infections (100). Persistent silencing of important host defense genes, possibly due to epigenetic mechanisms, has been proposed to mediate these effects (101, 102). Hence, maladaptive responses that inappropriately affect cell populations, such as systemic monocytes (as opposed to local tissue-resident macrophages), can have detrimental effects for the host.

Deleterious systemic consequences of trained immunity have also been documented. In general, trained immunity is an adaptation that results in the long-lasting capacity to respond more strongly to stimuli (36). Although this type of high-alert immune state has beneficial effects

during host defense, it could also trigger enhanced tissue damage during chronic inflammatory conditions in which trained immunity is induced by endogenous ligands of innate receptors. For example, there is strong epidemiological evidence for an increased susceptibility of atherosclerosis in patients with autoimmunity or chronic inflammatory conditions such as rheumatoid arthritis (103). It is tempting to speculate that the maladaptive state of innate immune cells triggered by the underlying chronic inflammatory condition would change the local immune responsiveness of immune cells in atherosclerotic lesions and that this could contribute to increased disease risk (104). It is also possible that Western-type diets, which are known to trigger systemic inflammatory responses, can precipitate maladaptive trained immune responses. A strong argument for this hypothesis is the recent demonstration of trained immunity induced by oxidized low-density lipoprotein in human monocytes via epigenetic reprogramming (105). Furthermore, this type of maladaptation of innate immune cells could be a culprit for other common inflammatory diseases prevalent in Western societies, such as type 2 diabetes or Alzheimer's disease. In diabetes, a bout of hyperglycemia can result in long-term deleterious effects, a process termed "hyperglycemic memory." This condition is accompanied by sustained NF- κ B activation by increased H3K4me1 and decreased H3K9me3 at selected genes (106).

The data presented above indicate that the adaptive ability of innate immune cells to tune

their responses to changing environments appears to be an important feature that evolved to prepare innate immune cells for unpredictable events, such as invading pathogens. However, the epigenetic mechanisms that control the memory of the environmental trigger may also lead to persistence of disease-associated phenotypes. Hence, altering the changed epigenetic landscape by pharmacologic means or behavioral changes could be a promising strategy to restore homeostatic healthy gene expression patterns.

Trained immunity: A modified steady-state of innate immunity after infection

In this Review, we reappraised the various arguments pointing to the presence of innate immune memory in plants, lower animals, and vertebrates. We defined trained immunity as a nonspecific immunological memory resulting from rewiring the epigenetic program and the functional state of the innate immune system, eventually resulting in protection against secondary infections. We also compared data assessing the mechanisms of tolerance and trained immunity. However, one important question remains: Are tolerance and training two fundamentally divergent functional programs, or do they represent different facets of the same phenomenon?

Considering the traditional appraisal of the effects of tolerance as a hypoinflammatory state and trained immunity resulting in an increased production of proinflammatory cytokines, these two programs may seem to be functional opposites. However, one must consider the evidence carefully: Whole-genome transcriptional and epigenetic analyses have clearly demonstrated that while in the process of LPS-induced tolerance, many proinflammatory genes are down-regulated, and others are not modified or even up-regulated (50). Similarly, the assessment of the trained immunity program induced by β -glucans also shows that it contains both up- and down-regulated genes (51). Thus, both tolerance and training evidently represent manifestations of long-term epigenetic reprogramming of the innate immune system after encountering an infection or a microbial ligand.

A crucial aspect of trained immunity that needs further investigation is its duration. In vitro studies of monocytes and macrophages have demonstrated long-term memory effects lasting days (26, 75), whereas experimental studies have reported effects that extended for weeks (26, 107). Epidemiological studies on the non-specific effects of vaccines such as BCG or measles have suggested positive effects on susceptibility to infections, lasting for months and even years (36), although it is highly unlikely for this protection to be as long-lived as classical immunological memory. These data are supported by proof-of-principle studies demonstrating the presence of trained immunity effects on circulating monocytes of volunteers for 3 months and even 1 year after vaccination with BCG (108). This would imply effects of vaccination on bone marrow progenitors as well, as pointed out earlier. More studies are warranted to better describe

the duration of trained immunity effects after infection and vaccination.

Conclusions and future directions for research

The arguments presented above suggest that trained immunity is a fundamental property of host defense in the mammalian immune response. Whereas classical immunological memory mediated by T and B lymphocytes is specific and antigen-dependent, with antigen specificity being mediated by gene rearrangement in specific lymphocyte clones that undergo expansion and contraction, trained immunity (innate immune memory) is nonspecific and mediated through epigenetic reprogramming in myeloid cells or NK cells. An important difference between classical immunological memory and trained immunity also concerns the persistence of the effects: Memory within trained immunity has a shorter duration than classical adaptive immune memory.

Much remains to be learned in this exciting new field over the coming years. First, the molecular mechanisms that mediate trained immunity should be elucidated at the level of the cell types involved, and the immunological, metabolic, and epigenetic processes mediating it need to be unraveled further. It will be also important to delineate the duration of innate immune memory and its effect on the innate immune cell precursors in the bone marrow and tissue macrophage populations. Second, the fast progress of cutting-edge technologies such as single-cell transcriptomics and epigenomics—in particular, DNA methylation—will permit the identification of the potential novel subpopulations of cells that are prone to displaying innate immune memory characteristics. This will enhance our understanding of immunological processes and open up possibilities for new therapeutics that target specific cell subpopulations. Third, future research should explore the effect of trained immunity on disease: its role in diseases with impaired host defense, such as postsepsis immune paralysis or cancers, as well as its role in autoinflammatory and autoimmune diseases in which maladaptive programs may be in place.

Finally, the concept of innate immune memory has considerable potential for aiding in the design of novel therapeutic approaches, with at least three potential lines of investigation: (i) the design of new-generation vaccines that combine adaptive and innate immune memory, as recently proposed with a novel *Bordetella pertussis* vaccine (109); (ii) the use of inducers of trained immunity for the treatment of immune paralysis, such as the muramyl dipeptide preparation mufamurtide for osteosarcoma (110) or β -glucan in various cancer types (111); and (iii) the modulation of the potentially deleterious consequences of trained immunity in autoinflammatory diseases (e.g., the potential use of the recently described iBET inhibitors). Only when these investigations are accomplished will the discovery of trained immunity reach its full therapeutic potential.

REFERENCES AND NOTES

1. R. Medzhitov, C. Janeway Jr., Innate immune recognition: Mechanisms and pathways. *Immunol. Rev.* **173**, 89–97 (2000). doi: [10.1034/j.1600-065X.2000.917309.x](https://doi.org/10.1034/j.1600-065X.2000.917309.x); pmid: [10719670](https://pubmed.ncbi.nlm.nih.gov/10719670/)
2. D. M. Bowdish, M. S. Loffredo, S. Mukhopadhyay, A. Mantovani, S. Gordon, Macrophage receptors implicated in the “adaptive” form of innate immunity. *Microbes Infect.* **9**, 1680–1687 (2007). doi: [10.1016/j.micinf.2007.09.002](https://doi.org/10.1016/j.micinf.2007.09.002); pmid: [18023392](https://pubmed.ncbi.nlm.nih.gov/18023392/)
3. M. G. Netea, J. Quintin, J. W. van der Meer, Trained immunity: A memory for innate host defense. *Cell Host Microbe* **9**, 355–361 (2011). doi: [10.1016/j.chom.2011.04.006](https://doi.org/10.1016/j.chom.2011.04.006); pmid: [21575907](https://pubmed.ncbi.nlm.nih.gov/21575907/)
4. J. Kurtz, Specific memory within innate immune systems. *Trends Immunol.* **26**, 186–192 (2005). doi: [10.1016/j.jit.2005.02.001](https://doi.org/10.1016/j.jit.2005.02.001); pmid: [15797508](https://pubmed.ncbi.nlm.nih.gov/15797508/)
5. J. Quintin, S. C. Cheng, J. W. van der Meer, M. G. Netea, Innate immune memory: Towards a better understanding of host defense mechanisms. *Curr. Opin. Immunol.* **29**, 1–7 (2014). doi: [10.1016/j.coi.2014.02.006](https://doi.org/10.1016/j.coi.2014.02.006); pmid: [24637148](https://pubmed.ncbi.nlm.nih.gov/24637148/)
6. A. Kachroo, G. P. Robin, Systemic signaling during plant defense. *Curr. Opin. Plant Biol.* **16**, 527–533 (2013). doi: [10.1016/j.pbi.2013.06.019](https://doi.org/10.1016/j.pbi.2013.06.019); pmid: [23870750](https://pubmed.ncbi.nlm.nih.gov/23870750/)
7. E. Luna, J. Ton, The epigenetic machinery controlling transgenerational systemic acquired resistance. *Plant Signal. Behav.* **7**, 615–618 (2012). doi: [10.4161/psb.20155](https://doi.org/10.4161/psb.20155); pmid: [22580690](https://pubmed.ncbi.nlm.nih.gov/22580690/)
8. J. Rodrigues, F. A. Brayner, L. C. Alves, R. Dixit, C. Barillas-Mury, Hemocyte differentiation mediates innate immune memory in *Anopheles gambiae* mosquitoes. *Science* **329**, 1353–1355 (2010). doi: [10.1126/science.1190689](https://doi.org/10.1126/science.1190689); pmid: [20829487](https://pubmed.ncbi.nlm.nih.gov/20829487/)
9. B. M. Sadd, P. Schmid-Hempel, Insect immunity shows specificity in protection upon secondary pathogen exposure. *Curr. Biol.* **16**, 1206–1210 (2006). doi: [10.1016/j.cub.2006.04.047](https://doi.org/10.1016/j.cub.2006.04.047); pmid: [16782011](https://pubmed.ncbi.nlm.nih.gov/16782011/)
10. J. Kurtz, K. Franz, Innate defence: Evidence for memory in invertebrate immunity. *Nature* **425**, 37–38 (2003). doi: [10.1038/425037a](https://doi.org/10.1038/425037a); pmid: [12955131](https://pubmed.ncbi.nlm.nih.gov/12955131/)
11. M. Boutros, H. Agaisse, N. Perrimon, Sequential activation of signaling pathways during innate immune responses in *Drosophila*. *Dev. Cell* **3**, 711–722 (2002). doi: [10.1016/S1534-5807\(02\)00325-8](https://doi.org/10.1016/S1534-5807(02)00325-8); pmid: [12431377](https://pubmed.ncbi.nlm.nih.gov/12431377/)
12. H. Steiner, Peptidoglycan recognition proteins: On and off switches for innate immunity. *Immunol. Rev.* **198**, 83–96 (2004). doi: [10.1111/j.0105-2896.2004.0120.x](https://doi.org/10.1111/j.0105-2896.2004.0120.x); pmid: [15199956](https://pubmed.ncbi.nlm.nih.gov/15199956/)
13. S. M. Zhang, C. M. Adema, T. B. Kepler, E. S. Loker, Diversification of Ig superfamily genes in an invertebrate. *Science* **305**, 251–254 (2004). doi: [10.1126/science.1088069](https://doi.org/10.1126/science.1088069); pmid: [15247481](https://pubmed.ncbi.nlm.nih.gov/15247481/)
14. T. Hibino et al., The immune gene repertoire encoded in the purple sea urchin genome. *Dev. Biol.* **300**, 349–365 (2006). doi: [10.1016/j.ydbio.2006.08.065](https://doi.org/10.1016/j.ydbio.2006.08.065); pmid: [17027739](https://pubmed.ncbi.nlm.nih.gov/17027739/)
15. N. R. Di Luzio, D. L. Williams, Protective effect of glucan against systemic *Staphylococcus aureus* septicemia in normal and leukemic mice. *Infect. Immun.* **20**, 804–810 (1978). pmid: [352959](https://pubmed.ncbi.nlm.nih.gov/352959/)
16. M. J. Marakalala et al., Dectin-1 plays a redundant role in the immunomodulatory activities of β -glucan-rich ligands in vivo. *Microbes Infect.* **15**, 511–515 (2013). doi: [10.1016/j.micinf.2013.03.002](https://doi.org/10.1016/j.micinf.2013.03.002); pmid: [23518266](https://pubmed.ncbi.nlm.nih.gov/23518266/)
17. J. L. Krahenbuhl, S. D. Sharma, R. W. Ferraresi, J. S. Remington, Effects of muramyl dipeptide treatment on resistance to infection with *Toxoplasma gondii* in mice. *Infect. Immun.* **31**, 716–722 (1981). pmid: [7216470](https://pubmed.ncbi.nlm.nih.gov/7216470/)
18. S. Ribes et al., Intraperitoneal prophylaxis with CpG oligodeoxynucleotides protects neutropenic mice against intracerebral *Escherichia coli* K1 infection. *J. Neuroinflammation* **11**, 14 (2014). doi: [10.1186/1742-2094-11-14](https://doi.org/10.1186/1742-2094-11-14); pmid: [24456653](https://pubmed.ncbi.nlm.nih.gov/24456653/)
19. N. Muñoz et al., Mucosal administration of flagellin protects mice from *Streptococcus pneumoniae* lung infection. *Infect. Immun.* **78**, 4226–4233 (2010). doi: [10.1128/IAI.00224-10](https://doi.org/10.1128/IAI.00224-10); pmid: [20643849](https://pubmed.ncbi.nlm.nih.gov/20643849/)
20. B. Zhang et al., Prevention and cure of rotavirus infection via TLR5/NLRCA4-mediated production of IL-22 and IL-18. *Science* **346**, 861–865 (2014). doi: [10.1126/science.1256999](https://doi.org/10.1126/science.1256999); pmid: [25395539](https://pubmed.ncbi.nlm.nih.gov/25395539/)
21. J. W. van der Meer, M. Barza, S. M. Wolff, C. A. Dinarello, A low dose of recombinant interleukin 1 protects granulocytopenic mice from lethal Gram-negative infection.

- Proc. Natl. Acad. Sci. U.S.A. **85**, 1620–1623 (1988). doi: [10.1073/pnas.85.5.1620](#); pmid: [3125553](#)
22. J. W. van't Wout, R. Poell, R. van Furth, The role of BCG/PPD-activated macrophages in resistance against systemic candidiasis in mice. *Scand. J. Immunol.* **36**, 713–719 (1992). doi: [10.1111/j.1365-3083.1992.tb03132.x](#); pmid: [1439583](#)
 23. J. Tribouley, J. Tribouley-Duret, M. Apfriou, Effect of Bacillus Calmette Guérin (BCG) on the receptivity of nude mice to *Schistosoma mansoni*. *C. R. Seances Soc. Biol. Fil.* **172**, 902–904 (1978). pmid: [157204](#)
 24. F. Bistoni *et al.*, Evidence for macrophage-mediated protection against lethal *Candida albicans* infection. *Infect. Immun.* **51**, 668–674 (1986). pmid: [3943907](#)
 25. F. Bistoni *et al.*, Immunomodulation by a low-virulence, agerminative variant of *Candida albicans*. Further evidence for macrophage activation as one of the effector mechanisms of nonspecific anti-infectious protection. *J. Med. Vet. Mycol.* **26**, 285–299 (1988). doi: [10.1080/02681218880000401](#); pmid: [2853217](#)
 26. J. Quintin *et al.*, *Candida albicans* infection affords protection against reinfection via functional reprogramming of monocytes. *Cell Host Microbe* **12**, 223–232 (2012). doi: [10.1016/j.chom.2012.06.006](#); pmid: [22901542](#)
 27. A. Vecchiarelli *et al.*, Protective immunity induced by low-virulence *Candida albicans*: Cytokine production in the development of the anti-infectious state. *Cell. Immunol.* **124**, 334–344 (1989). doi: [10.1016/0008-8749\(89\)90135-4](#); pmid: [2510940](#)
 28. E. S. Barton *et al.*, Herpesvirus latency confers symbiotic protection from bacterial infection. *Nature* **447**, 326–329 (2007). doi: [10.1038/nature05762](#); pmid: [17507983](#)
 29. F. Chen *et al.*, Neutrophils prime a long-lived effector macrophage phenotype that mediates accelerated helminth expulsion. *Nat. Immunol.* **15**, 938–946 (2014). doi: [10.1038/ni.2984](#); pmid: [25173346](#)
 30. J. G. O'Leary, M. Goodarzi, D. L. Drayton, U. H. von Andrian, T cell- and B cell-independent adaptive immunity mediated by natural killer cells. *Nat. Immunol.* **7**, 507–516 (2006). doi: [10.1038/ni1332](#); pmid: [16617337](#)
 31. J. C. Sun, J. N. Beilke, L. L. Lanier, Adaptive immune features of natural killer cells. *Nature* **457**, 557–561 (2009). doi: [10.1038/nature07665](#); pmid: [19136945](#)
 32. J. C. Sun *et al.*, Proinflammatory cytokine signaling required for the generation of natural killer cell memory. *J. Exp. Med.* **209**, 947–954 (2012). doi: [10.1084/jem.20111760](#); pmid: [22493516](#)
 33. T. Nabekura, J. P. Girard, L. L. Lanier, IL-33 receptor ST2 amplifies the expansion of NK cells and enhances host defense during mouse cytomegalovirus infection. *J. Immunol.* **194**, 5948–5952 (2015). doi: [10.4049/jimmunol.1500424](#); pmid: [25926677](#)
 34. H. Schlums *et al.*, Cytomegalovirus infection drives adaptive epigenetic diversification of NK cells with altered signaling and effector function. *Immunity* **42**, 443–456 (2015). doi: [10.1016/j.immuni.2015.02.008](#); pmid: [25786176](#)
 35. M. H. Askenase *et al.*, Bone-marrow-resident NK cells prime monocytes for regulatory function during infection. *Immunity* **42**, 1130–1142 (2015). doi: [10.1016/j.immuni.2015.05.011](#); pmid: [26070484](#)
 36. C. S. Benn, M. G. Netea, L. K. Selin, P. Aaby, A small jab—a big effect: Nonspecific immunomodulation by vaccines. *Trends Immunol.* **34**, 431–439 (2013). doi: [10.1016/j.it.2013.04.004](#); pmid: [23680130](#)
 37. J. Kleinnijenhuis *et al.*, Bacille Calmette-Guérin induces NOD2-dependent nonspecific protection from reinfection via epigenetic reprogramming of monocytes. *Proc. Natl. Acad. Sci. U.S.A.* **109**, 17537–17542 (2012). doi: [10.1073/pnas.1202870109](#); pmid: [22988082](#)
 38. K. J. Jensen *et al.*, Heterologous immunological effects of early BCG vaccination in low-birth-weight infants in Guinea-Bissau: A randomized-controlled trial. *J. Infect. Dis.* **211**, 956–967 (2015). doi: [10.1093/infdis/jiu508](#); pmid: [25210141](#)
 39. M. Hong *et al.*, Trained immunity in newborn infants of HBV-infected mothers. *Nat. Commun.* **6**, 6588 (2015). doi: [10.1038/ncomms7588](#); pmid: [25807344](#)
 40. M. B. McCall *et al.*, *Plasmodium falciparum* infection causes proinflammatory priming of human TLR responses. *J. Immunol.* **179**, 162–171 (2007). doi: [10.4049/jimmunol.179.1.162](#); pmid: [17579034](#)
 41. M. A. Ataide *et al.*, Malaria-induced NLRP12/NLRP3-dependent caspase-1 activation mediates inflammation and hypersensitivity to bacterial superinfection. *PLOS Pathog.* **10**, e1003885 (2014). pmid: [24453977](#)
 42. G. Redelman-Sidi, M. S. Glickman, B. H. Bochner, The mechanism of action of BCG therapy for bladder cancer—A current perspective. *Nat. Rev. Urol.* **11**, 153–162 (2014). doi: [10.1038/nrurol.2014.15](#); pmid: [24492433](#)
 43. J. H. Stewart, E. A. Levine, Role of bacillus Calmette-Guérin in the treatment of advanced melanoma. *Expert Rev. Anticancer Ther.* **11**, 1671–1676 (2011). doi: [10.1586/era.11.163](#); pmid: [22050015](#)
 44. J. M. Grange, J. L. Stanford, C. A. Stanford, K. F. Kölmel, Vaccination strategies to reduce the risk of leukaemia and melanoma. *J. R. Soc. Med.* **96**, 389–392 (2003). doi: [10.1258/jrsm.96.8.389](#); pmid: [12893854](#)
 45. M. Villumsen *et al.*, Risk of lymphoma and leukaemia after Bacille Calmette-Guérin and smallpox vaccination: A Danish case-cohort study. *Vaccine* **27**, 6950–6958 (2009). doi: [10.1016/j.vaccine.2009.08.103](#); pmid: [19747577](#)
 46. K. Buffen *et al.*, Autophagy controls BCG-induced trained immunity and the response to intravesical BCG therapy for bladder cancer. *PLOS Pathog.* **10**, e1004485 (2014). doi: [10.1371/journal.ppat.1004485](#); pmid: [25356988](#)
 47. M. E. Bianchi, DAMPs, PAMPs and alarmins: All we need to know about danger. *J. Leukoc. Biol.* **81**, 1–5 (2007). doi: [10.1189/jlb.0306164](#); pmid: [17032697](#)
 48. T. Kawai, S. Akira, The role of pattern-recognition receptors in innate immunity: Update on Toll-like receptors. *Nat. Immunol.* **11**, 373–384 (2010). doi: [10.1038/ni.1863](#); pmid: [20404851](#)
 49. K. H. Mills, TLR-dependent T cell activation in autoimmunity. *Nat. Rev. Immunol.* **11**, 807–822 (2011). pmid: [22094985](#)
 50. S. L. Foster, D. C. Hargreaves, R. Medzhitov, Gene-specific control of inflammation by TLR-induced chromatin modifications. *Nature* **447**, 972–978 (2007). pmid: [17538624](#)
 51. S. Saeed *et al.*, Epigenetic programming of monocyte-to-macrophage differentiation and trained innate immunity. *Science* **345**, 1251086 (2014). pmid: [25258085](#)
 52. S. Yona *et al.*, Fate mapping reveals origins and dynamics of monocytes and tissue macrophages under homeostasis. *Immunity* **38**, 79–91 (2013). doi: [10.1016/j.immuni.2012.12.001](#); pmid: [23273845](#)
 53. A. Yáñez *et al.*, Detection of a TLR2 agonist by hematopoietic stem and progenitor cells impacts the function of the macrophages they produce. *Eur. J. Immunol.* **43**, 2114–2125 (2013). doi: [10.1002/eji.201343403](#); pmid: [23661549](#)
 54. R. L. Ng, J. L. Bissley, S. Gorman, M. Norval, P. H. Hart, Ultraviolet irradiation of mice reduces the competency of bone marrow-derived CD11c⁺ cells via an indomethacin-inhibitable pathway. *J. Immunol.* **185**, 7207–7215 (2010). doi: [10.4049/jimmunol.1001693](#); pmid: [21078903](#)
 55. R. L. Ng *et al.*, Altered immunity and dendritic cell activity in the periphery of mice after long-term engraftment with bone marrow from ultraviolet-irradiated mice. *J. Immunol.* **190**, 5471–5484 (2013). doi: [10.4049/jimmunol.1202786](#); pmid: [23636055](#)
 56. S. L. Burgess *et al.*, Bone marrow dendritic cells from mice with an altered microbiota provide interleukin 17A-dependent protection against *Entamoeba histolytica* colitis. *mBio* **5**, e01817-14 (2014). doi: [10.1128/mBio.01817-14](#); pmid: [25370489](#)
 57. S. Paust *et al.*, Critical role for the chemokine receptor CXCR6 in NK cell-mediated antigen-specific memory of haptens and viruses. *Nat. Immunol.* **11**, 1127–1135 (2010). doi: [10.1038/ni.1953](#); pmid: [20972432](#)
 58. G. O. Gillard *et al.*, Thyl1⁺ NK cells from vaccinia virus-primed mice confer protection against vaccinia virus challenge in the absence of adaptive lymphocytes. *PLOS Pathog.* **7**, e1002141 (2011). doi: [10.1371/journal.ppat.1002141](#); pmid: [21829360](#)
 59. J. Kleinnijenhuis *et al.*, BCG-induced trained immunity in NK cells: Role for non-specific protection to infection. *Clin. Immunol.* **155**, 213–219 (2014). doi: [10.1016/j.clim.2014.10.005](#); pmid: [25451159](#)
 60. T. Nabekura *et al.*, Costimulatory molecule DNAM-1 is essential for optimal differentiation of memory natural killer cells during mouse cytomegalovirus infection. *Immunity* **40**, 225–234 (2014). doi: [10.1016/j.immuni.2013.12.011](#); pmid: [24440149](#)
 61. T. E. O'Sullivan, L. R. Johnson, H. H. Kang, J. C. Sun, BNIP3- and BNIP3L-mediated mitophagy promotes the generation of natural killer cell memory. *Immunity* **43**, 331–342 (2015). doi: [10.1016/j.immuni.2015.07.012](#); pmid: [26253785](#)
 62. D. W. Hendricks *et al.*, Cutting edge: NKG2C^{hi}CD57⁺ NK cells respond specifically to acute infection with cytomegalovirus and not Epstein-Barr virus. *J. Immunol.* **192**, 4492–4496 (2014). doi: [10.4049/jimmunol.1303211](#); pmid: [24740502](#)
 63. G. Min-Oo, L. L. Lanier, Cytomegalovirus generates long-lived antigen-specific NK cells with diminished bystander activation to heterologous infection. *J. Exp. Med.* **211**, 2669–2680 (2014). pmid: [25422494](#)
 64. R. K. Reeves *et al.*, Antigen-specific NK cell memory in rhesus macaques. *Nat. Immunol.* **16**, 927–932 (2015). doi: [10.1038/ni.3227](#); pmid: [26193080](#)
 65. J. Lee *et al.*, Epigenetic modification and antibody-dependent expansion of memory-like NK cells in human cytomegalovirus-infected individuals. *Immunity* **42**, 431–442 (2015). doi: [10.1016/j.immuni.2015.02.013](#); pmid: [25786175](#)
 66. S. Sacconi, S. Pantano, G. Natoli, Two waves of nuclear factor κ B recruitment to target promoters. *J. Exp. Med.* **193**, 1351–1359 (2001). doi: [10.1084/jem.193.12.1351](#); pmid: [11413190](#)
 67. V. R. Ramirez-Carrozzi *et al.*, A unifying model for the selective regulation of inducible transcription by CpG islands and nucleosome remodeling. *Cell* **138**, 114–128 (2009). doi: [10.1016/j.cell.2009.04.020](#); pmid: [19596239](#)
 68. V. R. Ramirez-Carrozzi *et al.*, Selective and antagonistic functions of SWI/SNF and Mi-2 β nucleosome remodeling complexes during an inflammatory response. *Genes Dev.* **20**, 282–296 (2006). doi: [10.1101/gad.1383206](#); pmid: [16452502](#)
 69. S. T. Smale, A. Tarakhovskiy, G. Natoli, Chromatin contributions to the regulation of innate immunity. *Annu. Rev. Immunol.* **32**, 489–511 (2014). doi: [10.1146/annurev-immunol-031210-101303](#); pmid: [24555473](#)
 70. S. Ghisletti *et al.*, Identification and characterization of enhancers controlling the inflammatory gene expression program in macrophages. *Immunity* **32**, 317–328 (2010). doi: [10.1016/j.immuni.2010.02.008](#); pmid: [20206554](#)
 71. S. Heinz *et al.*, Simple combinations of lineage-determining transcription factors prime cis-regulatory elements required for macrophage and B cell identities. *Mol. Cell* **38**, 576–589 (2010). doi: [10.1016/j.molcel.2010.05.004](#); pmid: [20513432](#)
 72. I. Barozzi *et al.*, Coregulation of transcription factor binding and nucleosome occupancy through DNA features of mammalian enhancers. *Mol. Cell* **54**, 844–857 (2014). doi: [10.1016/j.molcel.2014.04.006](#); pmid: [24813947](#)
 73. S. T. Smale, G. Natoli, Transcriptional control of inflammatory responses. *Cold Spring Harb. Perspect. Biol.* **6**, a016261 (2014). doi: [10.1101/cshperspect.a016261](#); pmid: [25213094](#)
 74. E. Nicodem *et al.*, Suppression of inflammation by a synthetic histone mimic. *Nature* **468**, 1119–1123 (2010). doi: [10.1038/nature09589](#); pmid: [21068722](#)
 75. R. Ostuni *et al.*, Latent enhancers activated by stimulation in differentiated cells. *Cell* **152**, 157–171 (2013). doi: [10.1016/j.cell.2012.12.018](#); pmid: [23332752](#)
 76. M. U. Kaikkonen *et al.*, Remodeling of the enhancer landscape during macrophage activation is coupled to enhancer transcription. *Mol. Cell* **51**, 310–325 (2013). doi: [10.1016/j.molcel.2013.07.010](#); pmid: [23932714](#)
 77. D. Gosselin *et al.*, Environment drives selection and function of enhancers controlling tissue-specific macrophage identities. *Cell* **159**, 1327–1340 (2014). doi: [10.1016/j.cell.2014.11.023](#); pmid: [25480297](#)
 78. Y. Lavin *et al.*, Tissue-resident macrophage enhancer landscapes are shaped by the local microenvironment. *Cell* **159**, 1312–1326 (2014). doi: [10.1016/j.cell.2014.11.018](#); pmid: [25480296](#)
 79. S. C. Cheng *et al.*, mTOR- and HIF1 α -mediated aerobic glycolysis as metabolic basis for trained immunity. *Science* **345**, 1250684 (2014). doi: [10.1126/science.1250684](#); pmid: [25258083](#)
 80. K. Yoshida *et al.*, The transcription factor ATF7 mediates lipopolysaccharide-induced epigenetic changes in macrophages involved in innate immunological memory. *Nat. Immunol.* **16**, 1034–1043 (2015). doi: [10.1038/ni.3257](#); pmid: [26322480](#)
 81. D. C. Iffrim *et al.*, Defective trained immunity in patients with STAT-1-dependent chronic mucocutaneous candidiasis. *Clin. Exp. Immunol.* **181**, 434–440 (2015). doi: [10.1111/cei.12642](#); pmid: [25880788](#)
 82. M. Luetke-Eversloh *et al.*, Human cytomegalovirus drives epigenetic imprinting of the *IFNG* locus in NKG2C^{hi} natural killer cells. *PLOS Pathog.* **10**, e1004441 (2014). doi: [10.1371/journal.ppat.1004441](#); pmid: [25329659](#)
 83. H. A. Eskandarian *et al.*, A role for SIRT2-dependent histone H3K18 deacetylation in bacterial infection. *Science* **341**, 1238858 (2013). doi: [10.1126/science.1238858](#); pmid: [23908241](#)

84. M. A. Hamon, P. Cossart, Histone modifications and chromatin remodeling during bacterial infections. *Cell Host Microbe* **4**, 100–109 (2008). doi: [10.1016/j.chom.2008.07.009](https://doi.org/10.1016/j.chom.2008.07.009); pmid: [18692770](https://pubmed.ncbi.nlm.nih.gov/18692770/)
85. H. Bierre, M. Hamon, P. Cossart, Epigenetics and bacterial infections. *Cold Spring Harb. Perspect. Med.* **2**, a010272 (2012). doi: [10.1101/cshperspect.a010272](https://doi.org/10.1101/cshperspect.a010272); pmid: [23209181](https://pubmed.ncbi.nlm.nih.gov/23209181/)
86. S. Monticelli, G. Natoli, Short-term memory of danger signals and environmental stimuli in immune cells. *Nat. Immunol.* **14**, 777–784 (2013). doi: [10.1038/ni.2636](https://doi.org/10.1038/ni.2636); pmid: [23867934](https://pubmed.ncbi.nlm.nih.gov/23867934/)
87. J. Krol, I. Loedige, W. Filipowicz, The widespread regulation of microRNA biogenesis, function and decay. *Nat. Rev. Genet.* **11**, 597–610 (2010). pmid: [20661255](https://pubmed.ncbi.nlm.nih.gov/20661255/)
88. R. M. O'Connell, A. A. Chaudhuri, D. S. Rao, D. Baltimore, Inositol phosphatase SHIP1 is a primary target of miR-155. *Proc. Natl. Acad. Sci. U.S.A.* **106**, 7113–7118 (2009). doi: [10.1073/pnas.0902636106](https://doi.org/10.1073/pnas.0902636106); pmid: [19359473](https://pubmed.ncbi.nlm.nih.gov/19359473/)
89. K. Ganesan, A. Chawla, Metabolic regulation of immune responses. *Annu. Rev. Immunol.* **32**, 609–634 (2014). doi: [10.1146/annurev-immunol-032713-120236](https://doi.org/10.1146/annurev-immunol-032713-120236); pmid: [24655299](https://pubmed.ncbi.nlm.nih.gov/24655299/)
90. G. M. Tannahill et al., Succinate is an inflammatory signal that induces IL-1 β through HIF-1 α . *Nature* **496**, 238–242 (2013). doi: [10.1038/nature11986](https://doi.org/10.1038/nature11986); pmid: [23535595](https://pubmed.ncbi.nlm.nih.gov/23535595/)
91. A. K. Jha et al., Network integration of parallel metabolic and transcriptional data reveals metabolic modules that regulate macrophage polarization. *Immunity* **42**, 419–430 (2015). doi: [10.1016/j.immuni.2015.02.005](https://doi.org/10.1016/j.immuni.2015.02.005); pmid: [25786174](https://pubmed.ncbi.nlm.nih.gov/25786174/)
92. D. R. Donohoe, S. J. Bultman, Metaboloepigenetics: Interrelationships between energy metabolism and epigenetic control of gene expression. *J. Cell. Physiol.* **227**, 3169–3177 (2012). doi: [10.1002/jcp.24054](https://doi.org/10.1002/jcp.24054); pmid: [22261928](https://pubmed.ncbi.nlm.nih.gov/22261928/)
93. P. Gut, E. Verdin, The nexus of chromatin regulation and intermediary metabolism. *Nature* **502**, 489–498 (2013). doi: [10.1038/nature12752](https://doi.org/10.1038/nature12752); pmid: [24153302](https://pubmed.ncbi.nlm.nih.gov/24153302/)
94. P. B  nit et al., Unsuspected task for an old team: Succinate, fumarate and other Krebs cycle acids in metabolic remodeling. *Biochim. Biophys. Acta* **1837**, 1330–1337 (2014). doi: [10.1016/j.bbabi.2014.03.013](https://doi.org/10.1016/j.bbabi.2014.03.013); pmid: [24699309](https://pubmed.ncbi.nlm.nih.gov/24699309/)
95. B. W. Carey, L. W. Finley, J. R. Cross, C. D. Allis, C. B. Thompson, Intracellular α -ketoglutarate maintains the pluripotency of embryonic stem cells. *Nature* **518**, 413–416 (2015). doi: [10.1038/nature13981](https://doi.org/10.1038/nature13981); pmid: [25487152](https://pubmed.ncbi.nlm.nih.gov/25487152/)
96. T. F. Liu, V. T. Vachharajani, B. K. Yoza, C. E. McCall, NAD⁺-dependent sirtuin 1 and 6 proteins coordinate a switch from glucose to fatty acid oxidation during the acute inflammatory response. *J. Biol. Chem.* **287**, 25758–25769 (2012). doi: [10.1074/jbc.M112.362343](https://doi.org/10.1074/jbc.M112.362343); pmid: [22700961](https://pubmed.ncbi.nlm.nih.gov/22700961/)
97. O. Levy, Innate immunity of the newborn: Basic mechanisms and clinical correlates. *Nat. Rev. Immunol.* **7**, 379–390 (2007). doi: [10.1038/nri2075](https://doi.org/10.1038/nri2075); pmid: [17457344](https://pubmed.ncbi.nlm.nih.gov/17457344/)
98. T. B. Clarke, Microbial programming of systemic innate immunity and resistance to infection. *PLoS Pathog.* **10**, e1004506 (2014). doi: [10.1371/journal.ppat.1004506](https://doi.org/10.1371/journal.ppat.1004506); pmid: [25474680](https://pubmed.ncbi.nlm.nih.gov/25474680/)
99. S. C. Ganai et al., Priming of natural killer cells by nonmucosal mononuclear phagocytes requires instructive signals from commensal microbiota. *Immunity* **37**, 171–186 (2012). doi: [10.1016/j.immuni.2012.05.020](https://doi.org/10.1016/j.immuni.2012.05.020); pmid: [22749822](https://pubmed.ncbi.nlm.nih.gov/22749822/)
100. T. van der Poll, S. M. Opal, Host-pathogen interactions in sepsis. *Lancet Infect. Dis.* **8**, 32–43 (2008). doi: [10.1016/S1473-3099\(07\)70265-7](https://doi.org/10.1016/S1473-3099(07)70265-7); pmid: [18063412](https://pubmed.ncbi.nlm.nih.gov/18063412/)
101. W. F. Carson IV, K. A. Cavassani, Y. Dou, S. L. Kunkel, Epigenetic regulation of immune cell functions during post-septic immunosuppression. *Epigenetics* **6**, 273–283 (2011). doi: [10.4161/epi.6.3.14017](https://doi.org/10.4161/epi.6.3.14017); pmid: [21048427](https://pubmed.ncbi.nlm.nih.gov/21048427/)
102. M. Ishii et al., Epigenetic regulation of the alternatively activated macrophage phenotype. *Blood* **114**, 3244–3254 (2009). doi: [10.1182/blood-2009-04-217620](https://doi.org/10.1182/blood-2009-04-217620); pmid: [19567879](https://pubmed.ncbi.nlm.nih.gov/19567879/)
103. R. Mankad, Atherosclerotic vascular disease in the autoimmune rheumatologic patient. *Curr. Atheroscler. Rep.* **17**, 21 (2015). doi: [10.1007/s11883-015-0497-6](https://doi.org/10.1007/s11883-015-0497-6); pmid: [25721102](https://pubmed.ncbi.nlm.nih.gov/25721102/)
104. S. Bekkering, L. A. Joosten, J. W. van der Meer, M. G. Netea, N. P. Riksen, The epigenetic memory of monocytes and macrophages as a novel drug target in atherosclerosis. *Clin. Ther.* **37**, 914–923 (2015). doi: [10.1016/j.clinthera.2015.01.008](https://doi.org/10.1016/j.clinthera.2015.01.008); pmid: [25704108](https://pubmed.ncbi.nlm.nih.gov/25704108/)
105. S. Bekkering et al., Oxidized low-density lipoprotein induces long-term proinflammatory cytokine production and foam cell formation via epigenetic reprogramming of monocytes. *Arterioscler. Thromb. Vasc. Biol.* **34**, 1731–1738 (2014). doi: [10.1161/ATVBAHA.114.303887](https://doi.org/10.1161/ATVBAHA.114.303887); pmid: [24903093](https://pubmed.ncbi.nlm.nih.gov/24903093/)
106. D. Brasacchio et al., Hyperglycemia induces a dynamic cooperativity of histone methylase and demethylase enzymes associated with gene-activating epigenetic marks that coexist on the lysine tail. *Diabetes* **58**, 1229–1236 (2009). doi: [10.2337/db08-1666](https://doi.org/10.2337/db08-1666); pmid: [19208907](https://pubmed.ncbi.nlm.nih.gov/19208907/)
107. K. Yoshida, S. Ishii, Innate immune memory via ATF7-dependent epigenetic changes. *Cell Cycle* **15**, 3–4 (2016). pmid: [26556024](https://pubmed.ncbi.nlm.nih.gov/26556024/)
108. J. Kleinnijenhuis et al., Long-lasting effects of BCG vaccination on both heterologous Th1/Th17 responses and innate trained immunity. *J. Innate Immun.* **6**, 152–158 (2014). pmid: [24192057](https://pubmed.ncbi.nlm.nih.gov/24192057/)
109. C. Loch, N. Mielcarek, Live attenuated vaccines against pertussis. *Expert Rev. Vaccines* **13**, 1147–1158 (2014). doi: [10.1586/14760584.2014.942222](https://doi.org/10.1586/14760584.2014.942222); pmid: [25085735](https://pubmed.ncbi.nlm.nih.gov/25085735/)
110. P. A. Meyers et al., Children's Oncology Group, Osteosarcoma: The addition of muramyl tripeptide to chemotherapy improves overall survival—A report from the Children's Oncology Group. *J. Clin. Oncol.* **26**, 633–638 (2008). doi: [10.1200/JCO.2008.14.0095](https://doi.org/10.1200/JCO.2008.14.0095); pmid: [18235123](https://pubmed.ncbi.nlm.nih.gov/18235123/)
111. D. Muramatsu et al., β -Glucan derived from *Aureobasidium pullulans* is effective for the prevention of influenza in mice. *PLoS One* **7**, e41399 (2012). doi: [10.1371/journal.pone.0041399](https://doi.org/10.1371/journal.pone.0041399); pmid: [22844473](https://pubmed.ncbi.nlm.nih.gov/22844473/)

ACKNOWLEDGMENTS

M.G.N. is supported by a Vici grant from the Netherlands Organization for Scientific Research and a European Research Council (ERC) Consolidator Grant (310372). E.L. is supported by grants from the Deutsche Forschungsgemeinschaft and the Excellence Cluster ImmunoSensation and via an ERC Consolidator Grant. G.N.'s work on this topic was supported by an ERC grant (NORM). K.H.G.M. is supported by a PI grant from Science Foundation Ireland (11/P1/1036). We thank M. Gresnigt for the help with the figures. We apologize to the authors of studies that could not be cited due to space constraints.

10.1126/science.aaf1098

RESEARCH ARTICLE SUMMARY

MICROTUBULES

Detyrosinated microtubules buckle and bear load in contracting cardiomyocytes

Patrick Robison, Matthew A. Caporizzo, Hossein Ahmadzadeh, Alexey I. Bogush, Christina Yingxian Chen, Kenneth B. Margulies, Vivek B. Shenoy, Benjamin L. Prosser*

INTRODUCTION: Along with its well-documented role as a track for cargo transport, the microtubule (MT) cytoskeleton is linked to diverse structural and signaling roles in the cardiac myocyte. MTs can facilitate the rapid transmission of mechanical signals to intracellular effectors, a process termed mechanotransduction. A proliferated MT network may also provide a mechanical resistance to cardiac contraction in certain disease states. Yet our understanding of how MTs

resist compression and transmit mechanical signals has been impaired by a lack of direct observation and by the unpredictable effects of blunt pharmacological tools.

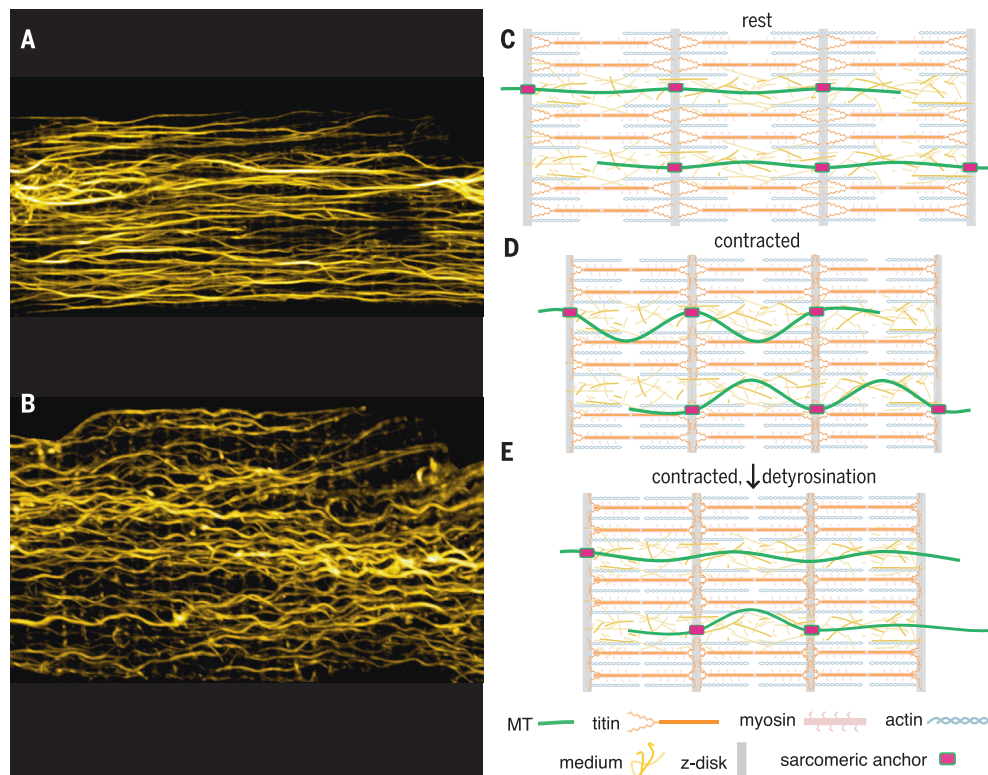
RATIONALE: Direct observation of MT mechanical behavior during contraction is the most straightforward way to elucidate the mechanisms underlying MT contributions to heart function. Advances in imaging have made this possible at temporal and spatial resolutions that permit quantification of MT geometry during the contraction cycle. Furthermore, recent

evidence suggests that posttranslational modification of the microtubule network, specifically “detyrosination,” regulates cardiac mechanotransduction. This raises the question of whether detyrosination alters how microtubules respond to the changing mechanical loads inherent to each cardiac cycle. To answer these questions, we used advanced imaging techniques to explore MT behavior in beating murine cardiomyocytes.

RESULTS: During contraction, MTs must somehow accommodate the changing geometry of the myocyte. In a typical myocyte, this was accomplished by deforming into a sinusoidal buckled configuration that returned to an identical resting configuration after each beat. The periodic nature of these buckles coincided with the repeating contractile units of the cardiomyocyte known as sarcomeres, which suggested a direct interaction. Desmin intermediate filaments were identified as a key component of an anchoring complex that links MTs to the sarcomere and imparts structural organization to the MT network.

The physical link between microtubules and the sarcomere was highly dependent on detyrosination. In myocytes where detyrosination was suppressed, MTs often accommodated the contraction by sliding past each other rather than buckling as the sarcomere shortened. Disrupting the MT-sarcomere interaction allowed the sarcomere to shorten farther and faster, as well as decreased overall stiffness. Conversely, promoting detyrosination was sufficient to increase myocyte stiffness and impede the contraction of the myocyte. Consistently, clinical data showed a direct correlation between excess detyrosination and functional decline in patients with hypertrophic cardiomyopathy.

CONCLUSION: Thus, microtubules can provide mechanical resistance to the myocyte through interactions with the sarcomere, forming load-bearing spring elements in parallel with the contractile apparatus. These interactions are mediated by a detyrosination-dependent association with desmin that regulates myocyte stiffness and contractility. Excess detyrosination promotes the interaction between MTs and the sarcomere, which increases resistance to contraction and may contribute to reductions in cardiac function in certain disease states. ■



MTs in the beating heart. When a cardiomyocyte (A) is compressed (B), as occurs during systolic contraction, MTs buckle under load. In a typical myocyte (C), detyrosinated MTs are mechanically coupled to the sarcomere and buckle during contraction (D). When detyrosination is reduced (E), this interaction is disrupted and MTs buckle less, which allows sarcomeres to shorten and stretch with less resistance.

The list of author affiliations is available in the full article online.

*Corresponding author. Email: bpross@mail.med.upenn.edu

Cite this article as P. Robison *et al.*, *Science* **352**, aaf0659 (2016). DOI: 10.1126/science.aaf0659

RESEARCH ARTICLE

MICROTUBULES

Detyrosinated microtubules buckle and bear load in contracting cardiomyocytes

Patrick Robison,¹ Matthew A. Caporizzo,² Hossein Ahmadzadeh,² Alexey I. Bogush,¹ Christina Yingxian Chen,¹ Kenneth B. Margulies,³ Vivek B. Shenoy,² Benjamin L. Prosser^{1*}

The microtubule (MT) cytoskeleton can transmit mechanical signals and resist compression in contracting cardiomyocytes. How MTs perform these roles remains unclear because of difficulties in observing MTs during the rapid contractile cycle. Here, we used high spatial and temporal resolution imaging to characterize MT behavior in beating mouse myocytes. MTs deformed under contractile load into sinusoidal buckles, a behavior dependent on posttranslational “detyrosination” of α -tubulin. Detyrosinated MTs associated with desmin at force-generating sarcomeres. When detyrosination was reduced, MTs uncoupled from sarcomeres and buckled less during contraction, which allowed sarcomeres to shorten and stretch with less resistance. Conversely, increased detyrosination promoted MT buckling, stiffened the myocyte, and correlated with impaired function in cardiomyopathy. Thus, detyrosinated MTs represent tunable, compression-resistant elements that may impair cardiac function in disease.

Along with its well-defined transport functions, the microtubule (MT) network serves multiple mechanical roles in the beating cardiomyocyte. MTs function as mechanotransducers, converting changing contractile forces into intracellular signals (1, 2). MTs may also act as compression-resistant elements, which could provide a mechanical impediment to cardiomyocyte contraction (3–5). If so, they must bear some of the compressive and tensile load of a working myocyte. Unfortunately, little is known about MT behavior during the contractile cycle. During this cycle, Ca^{2+} -mediated actin-myosin interaction first shortens repeating contractile units called sarcomeres, which are then stretched as the heart fills with blood during diastole.

Although an isolated MT would present minimal resistance to myocyte compression, the stiffness of the network within a living cell, with MT-associated proteins and other cytoskeletal elements, can change by orders of magnitude (6, 7). It is in this context that MTs are proposed to act as compression-resistant elements (6, 8) that may impair sarcomere shortening and thus cardiac function, particularly in disease states associated with MT proliferation (8–10). Posttranslational modification (PTM) of MTs (11, 12) could also

modify their mechanical properties and binding interactions. Detyrosination, a PTM of α -tubulin, has recently been shown to augment MT-dependent mechanotransduction in dystrophic cardiac and skeletal muscle (12). This specific PTM is also increased in animal models of heart disease (1, 13, 14), which raises a mechanistic question: If mechanotransduction is altered, have the mechanical properties of the myocyte changed?

Although the idea that a proliferated (and perhaps modified) MT network may mechanically interfere with contraction is attractive, the “MT hypothesis” has remained controversial [for reviews, see (15, 16)]. Two important limitations have hindered our understanding: (i) a reliance on blunt pharmacological tools (colchicine/Taxol) that have off-target consequences; (ii) a lack of direct observation of MTs under the stress and strain of the contractile cycle. Here, we characterized MTs under contractile loads using a high-resolution imaging technique and directly tested how MT detyrosination may regulate load-bearing and the mechanical properties of the myocyte.

MTs buckle under contractile load

MT networks in cardiomyocytes have two major features (Fig. 1A): an orthogonal grid just beneath the membrane that wraps the myofibrils and a deeper network composed primarily of longitudinal elements that interdigitate the myofibrils. Longitudinal MTs often run many sarcomeres in length but do not span the full cell. Given that cardiomyocytes change shape during contraction, the MT cytoskeleton must accommodate this change. There are three apparent possibilities:

MTs not anchored to other cytoskeletal or sarcomeric proteins could rearrange or slide passively with the surrounding medium; anchored MTs could directly experience contractile force and themselves deform under load; or the MTs could break and/or disassemble and reform. These possibilities offer divergent mechanisms for the regulation of mechano-signaling and the overall mechanics of the myocyte. Without direct observation, however, this behavior has been difficult to quantify.

Standard confocal imaging, although capable of resolving MTs in living cells (17), suffers from limitations in the signal-to-noise ratio when pushed to speeds that can resolve events on the time scale of cardiomyocyte contraction (Fig. 1B and movie S1). Consequently, we turned to a high-speed, subdiffraction limit technique called Airy-scan (see fig. S1). This technology maintains high signal-to-noise ratios at the required temporal resolution, while offering a 1.7-fold improvement in spatial resolution beyond the standard diffraction limit.

Using the MT-binding fluorogenic dye SiR-tubulin, based on the fluorophore silicon rhodamine (18) (Fig. 1C and movie S2), we imaged internal MTs during contractions triggered by a 1 Hz electrical field stimulation in isolated mouse cardiomyocytes. We were able to capture MT behavior during contraction and found that longitudinally oriented MTs frequently deformed and developed sinusoidal buckles. Because SiR-tubulin may polymerize MTs (18), we also generated adenovirus encoding a small fragment of the MT-binding protein α -tubulin fused to three copies of GFP (EMTB-3xGFP) to decorate MTs. We achieved similar results (table S1) but with improved signal-to-noise ratios (Fig. 1D and movie S3).

We measured blindly selected MTs for deformation with two parameters—amplitude and wavelength (Fig. 1G). Where possible, the same MT was followed through contraction. Amplitude rose quickly from resting to contracted levels (Fig. 1H), with clearly visible buckles. Using a threshold of two standard deviations above resting amplitude, we found that two-thirds of MTs buckle under control conditions (Fig. 1H).

MT buckles quickly reversed during relaxation, and the configuration of the MT network between contractions tightly colocalized with the network configuration from previous cycles (Fig. 1, E and F), with a minimal mean reduction in Pearson's colocalization of 0.01 per contractile cycle ($n = 18$ runs). The rapid and precise reversibility of the network deformations suggested tight coupling to the contractile apparatus, and it argues against MT breakage and regrowth contributing to mechanical properties and signaling over the time scale of myocyte contraction.

A notable feature of the MT buckles was the emergence of subpopulations of buckle wavelength centered at $\sim 1.65\ \mu\text{m}$, $3.3\ \mu\text{m}$, and perhaps even $4.7\ \mu\text{m}$ (Fig. 1I). These corresponded closely to the length of one, two, or three contracted sarcomeres, respectively. Although MTs buckling outside of these populations could be found in our data without difficulty, these subpopulations were strongly

¹Department of Physiology, Pennsylvania Muscle Institute, University of Pennsylvania Perelman School of Medicine, Philadelphia, PA 19104, USA. ²Department of Materials Science and Engineering, University of Pennsylvania School of Engineering and Applied Science, Philadelphia, PA 19104, USA. ³Department of Medicine, University of Pennsylvania Perelman School of Medicine, Philadelphia, PA 19104, USA. *Corresponding author. Email: bprosser@mail.med.upenn.edu

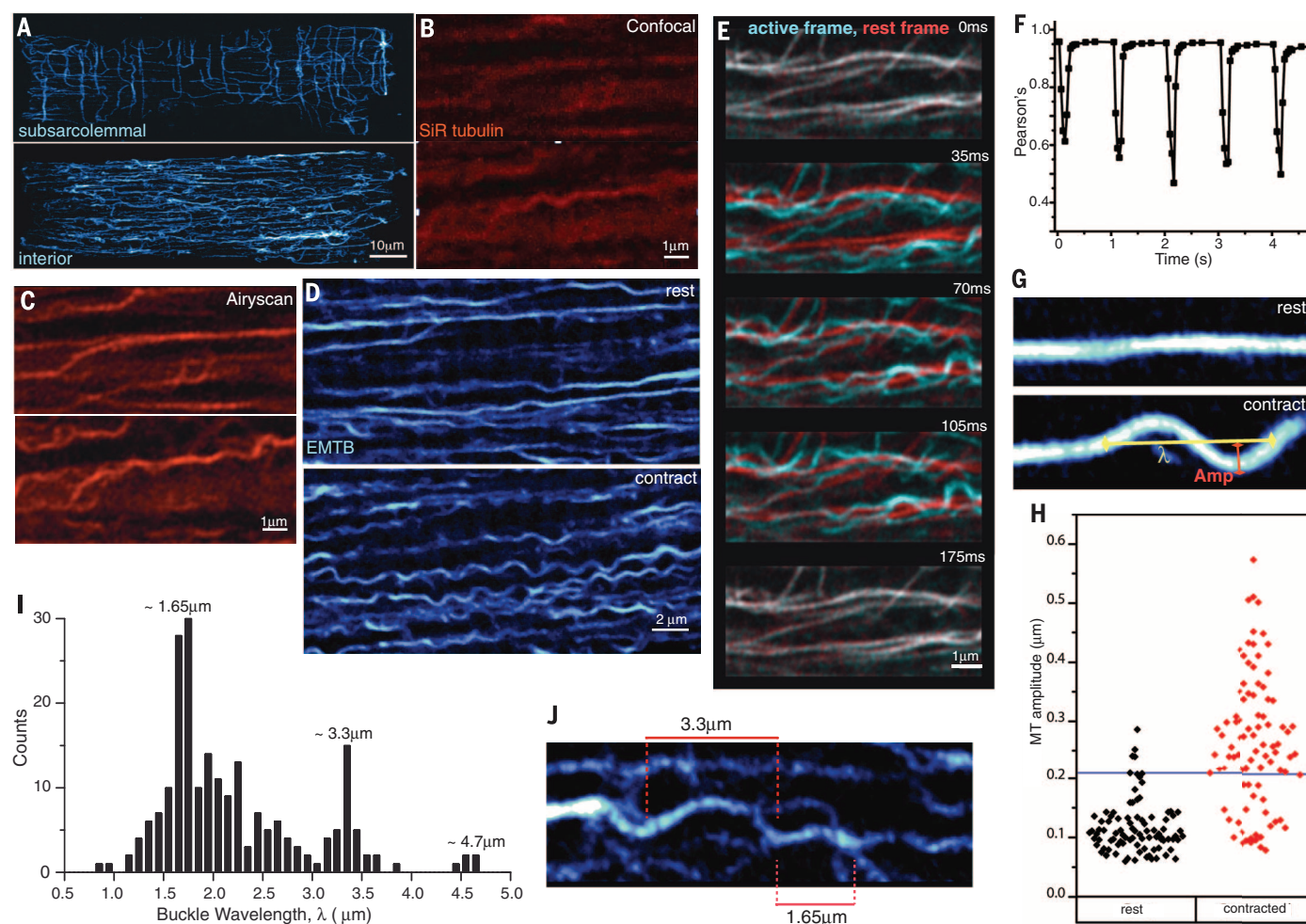


Fig. 1. MTs reversibly buckle in contracting cardiomyocytes. (A) The sub-surface (top) and interior (bottom) cardiomyocyte MT network. (B) High-speed confocal imaging of MTs at rest (top) and during contraction (bottom) labeled with SiR tubulin with brightness increased for comparison with (C). (C) Airyscan imaging of the same MTs as in (B) at rest and during contraction. (D) Wider view of MTs labeled with EMTB-3xGFP at rest (top) and during contraction (bottom). (E) MTs imaged throughout a contractile cycle (cyan) were overlaid onto the network configuration from the initial frame at rest (red). (F) Colocalization analysis of (E) shows that MTs repeatedly return to the same position. Pearson's coefficient is used to estimate goodness of fit to original MT configuration over several contractile

cycles. Initial drop to ~ 0.96 is due to imaging noise. (G) Quantification of buckling amplitude (measured from centerline to edge) and λ (wavelength measured as twice the distance between consecutive inflection points). (H) Amplitude of MTs labeled with EMTB-3xGFP in resting (black) and contracted (red) cardiomyocytes. The threshold to determine buckling occurrence (blue line) was two standard deviations above the mean resting value. (I) Distribution of buckling wavelengths in cardiomyocytes shows a dominant population between 1.6 and 1.7 μm , and a second population at 3.3 μm . (J) A representative MT demonstrating buckles with wavelengths that correspond to the distance between one (1.65 μm) or two (3.3 μm) adjacent sarcomeres.

indicative of ordered geometric constraints on the buckling MT. This was observed in certain cells where faint transverse staining at the Z-disc shows MTs buckling between sarcomeric constraints (movie S4).

Detyrosination regulates MT buckling in the heart

This robust buckling behavior of the MT network may be a result of a particularly high abundance of “detyrosinated” MTs in adult cardiomyocytes (19). Detyrosination is a PTM of α -tubulin where the C-terminal tyrosine residue has been cleaved by a tubulin carboxypeptidase (TCP); this process can be readily reversed by tubulin tyrosine ligase (TTL) (17). This tyrosination cycle is evolutionar-

ily conserved across eukaryotes (20) and appears required for life (21), yet its functional roles are still poorly understood. Because detyrosination can protect MTs from disassembly (22, 23) and can facilitate their cross-linking with intermediate filaments (IFs) (24, 25), we hypothesized that the high proportion of detyrosination may confer the resilient load-bearing capabilities of the cardiac cytoskeletal network.

Using antibodies specific to detyrosinated α -tubulin, we found a high abundance of detyrosination in the α -tubulin network of adult myocytes (Fig. 2, A and B), as expected (12, 19). To test the role of detyrosinated MTs, we generated adenovirus encoding TTL (AdV-TTL) with a *Discosoma* red fluorescent protein (DsRed) reporter. Express-

ing this construct in isolated cardiomyocytes could effectively reduce the level of detyrosination as shown by both immunofluorescence (Fig. 2, A and B) and immunoblot (Fig. 2, C and D), which resulted in a 71% reduction in the amount of polymerized, detyrosinated MTs, with a concomitant up-regulation of tyrosinated tubulin (Fig. 2, C and D, and fig. S2). Overexpression of TTL also resulted in a modest (10%) reduction in the density of the polymerized MT network (Fig. 2B), consistent with an increased disassembly of tyrosinated MTs (22, 23). We complemented this genetic strategy with a pharmacological approach to inhibit TCP using parthenolide (PTL) (26). PTL treatment also reduced the fraction of detyrosinated MTs, albeit to a lesser extent (42%) than

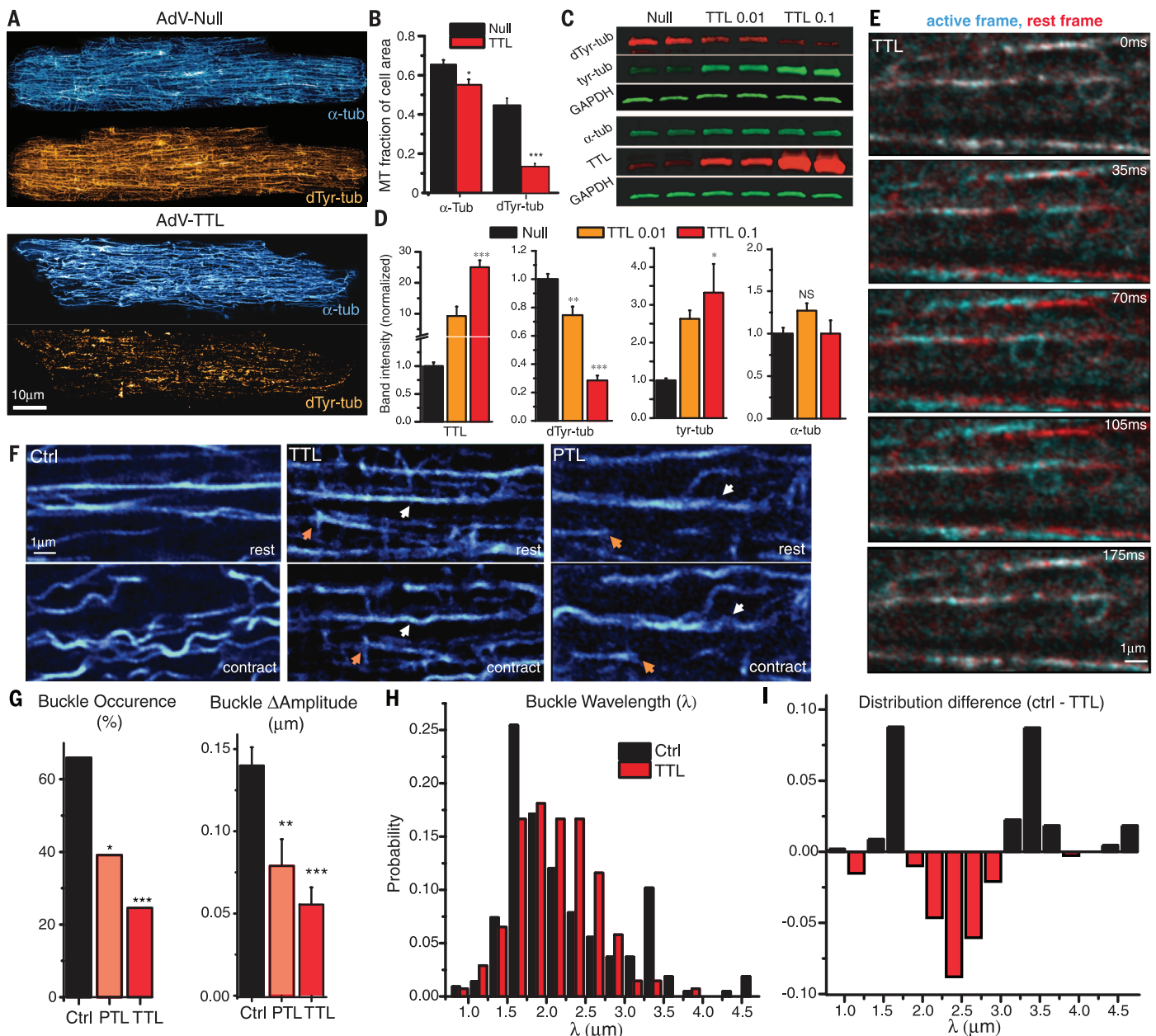


Fig. 2. Detyrosination underlies MT buckling. (A) The MT cytoskeleton (blue and aqua) in rat adult cardiomyocytes (top) is heavily detyrosinated (orange). TTL overexpression (bottom) reduces detyrosination dramatically but makes comparatively small changes in the overall MT network. (B) Quantification of the fraction of cell area covered by α -tubulin and detyrosinated tubulin (dTyr-tubulin) in null ($n = 14$) and TTL-overexpressing ($n = 13$) cells, as determined from thresholded images as shown in fig. S2E. (C and D) Western blots from cardiomyocyte lysates show the effects of viral overexpression of TTL. GAPDH, glyceraldehyde-3-phosphate dehydrogenase. (E) Time course of MTs in a contracting cardiomyocyte (cyan) transduced with AdV-TTL overlaid on the resting MT configuration (red). MTs appear to translocate along the con-

tractile axis rather than deforming. (F) Comparison of MTs in resting (top) and contracted (bottom) cardiomyocytes in control, TTL, and PTL groups. In TTL and PTL groups, some MTs slide (orange arrows) relative to others that deform (white arrows). Additional examples are provided in fig. S3. (G) Buckling occurrence and amplitude are reduced by overexpression of TTL or treatment with PTL. (H) Buckling wavelength distribution in control and TTL-overexpressing myocytes and (I) the difference between these distributions. Overexpression of TTL causes MTs to buckle more often at wavelengths between 2 and 3 μ m, and MTs are far less likely to buckle at distinct sarcomeric wavelengths (1.7 and 3.3 μ m) when detyrosination is reduced. Data are presented as means \pm SEM; * $P < 0.05$, ** $P < 0.01$, *** $P < 0.001$. Further statistical details are available in table S1.

AdV-TTL and with no effect on MT network density (fig. S2).

The load-bearing behavior of the MT network in cardiomyocytes overexpressing TTL or treated with PTL was dramatically different from control myocytes. Tyrosinated MTs frequently seemed to

simply slide in the moving cell (Fig. 2, E and F, orange arrows; movies S5 and S6; and fig. S3), rather than buckling under load. This behavior was again reversible, with a minimum reduction in Pearson's colocalization over successive contractions that was not different from controls

($P = 0.87$, $n = 19$ runs). The occurrence of buckling in TTL-overexpressing and PTL-treated cells fell significantly (Fig. 2G, left), whereas amplitude changes observed on the same MT between rest and contraction also dropped significantly (Fig. 2G, right, and table S1).

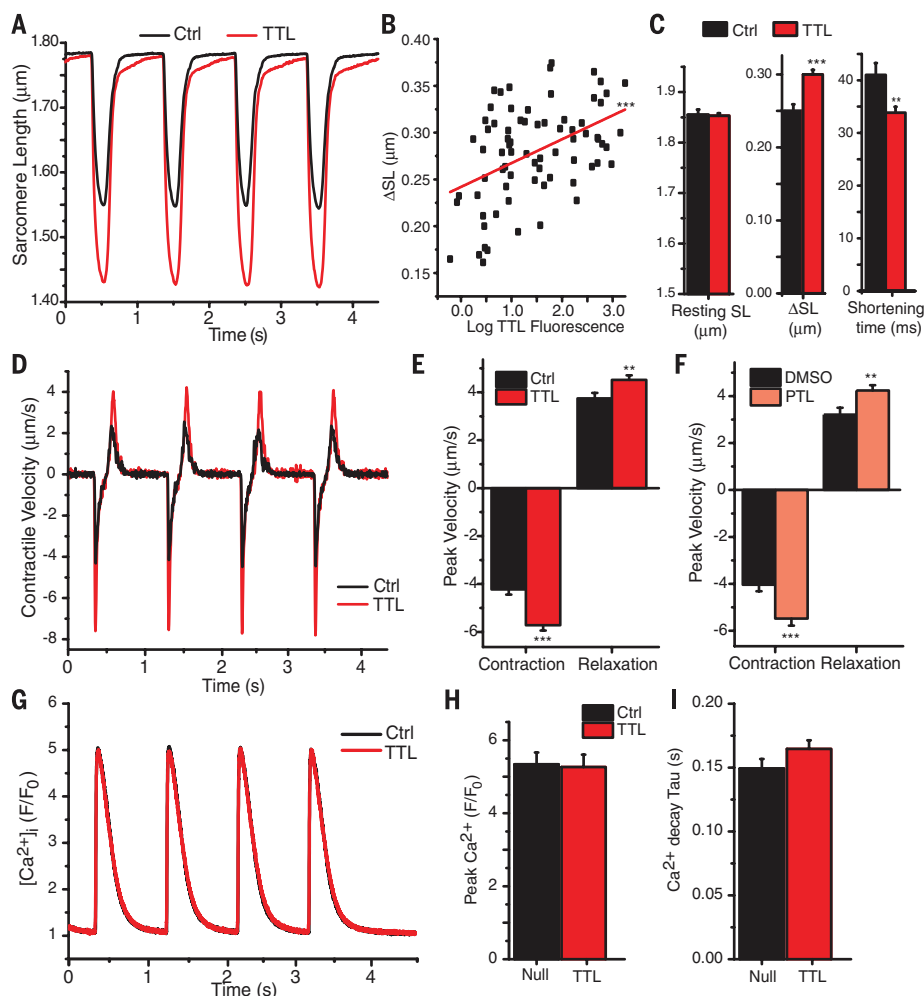


Fig. 3. Detyrosinated MTs impede contractility. (A) Sarcomere shortening (ΔSL) during contraction is increased in TTL-overexpressing myocytes. This change is (B) dose-dependent [$P = 1.2 \times 10^{-5}$, correlation coefficient (r^2) = 0.23] and (C) associated with a faster shortening time without affecting resting sarcomere length. (D) First derivative of traces in (A) demonstrate contractile velocities in control and TTL-overexpressing myocytes. (E) TTL-overexpressing myocytes demonstrate an increase in the peak velocity of both contraction and relaxation. (F) PTL-treated cells display similar behavior. (G to I) Despite the significant changes in contractility, no changes in the peak or kinetics of the global calcium transient were observable. F/F_0 , the change in fluorescence from the original fluorescence before stimulation. Data are presented as means \pm SEM; * $P < 0.05$, ** $P < 0.01$, *** $P < 0.001$. Further statistical details are available in table S2.

When MT buckling was observed, the mean wavelength was not significantly different between control and TTL-overexpressing cells (table S1). However, the majority of MTs in TTL-overexpressing myocytes no longer buckled at the wavelength of a single sarcomere, and no subpopulations at multiples of the sarcomeric period were observed (Fig. 2H). Instead, the majority of these MTs buckled in a single population at wavelengths between 2 and 3 μm , which suggested that MT buckling was less constrained by a sarcomeric interaction after detyrosination was reduced (Fig. 2I).

Detyrosinated MTs resist contractile compression

The energy required to deform detyrosinated MTs under compressive load could confer some mean-

ingful resistance to myocyte contraction. We thus tested directly if MT detyrosination affects contractility in beating cardiomyocytes. After overexpression of TTL, we found significant enhancements in both the magnitude (Fig. 3, A to C) and peak rate (Fig. 3, D and E) of sarcomere shortening (table S2). PTL had a similar effect on contractility (Fig. 3F and table S2). Peak relaxation rates were also increased, which could be because of a decrease in cellular viscosity (see below) or may reflect the increased magnitude of shortening and, therefore, compression of internal elastic elements (e.g., titin) that develop restoring force (27). These contractile changes were not associated with any significant difference in global calcium transients (Fig. 3, G to I) or resting sarcomere length (Fig. 3C), which suggested a change in intrinsic mechanical resistance associated with the

ability of detyrosinated MTs to bear compressive load.

Detyrosination regulates myocyte mechanical properties

We next measured mechanical resistance directly using atomic force microscopy (AFM). AFM measurements of transverse stiffness were performed across a range of indentation rates. Myocyte stiffness changed substantially with indentation rate and was well fit by a standard linear solid model (SLSM) [methods in supplementary materials (SM)] (fig. S4 and Fig. 4A). At low rates (100 nm/s), the stiffness of the cardiomyocyte was essentially elastic, reported as E_1 , and was reduced by PTL treatment and TTL overexpression (Fig. 4B). At higher rates, the modulus increased by E_2 , which reflects cross-linked material inside the cell that slips on the time scale of slower measurements but “turns on” (stiffens) at faster time scales ($> 2 \mu\text{m/s}$) (28). The viscosity derived by the SLSM defines the rate above which these cross-links are engaged. TTL overexpression significantly decreased E_2 and viscosity (Fig. 4B), which suggested that reducing detyrosination decreases the number of cross-links engaged at physiological strain rates in the cardiomyocyte.

The fact that MTs deform under load and resist sarcomere shortening implies a transfer of force between MTs and the sarcomere. If MTs resist longitudinal compression, they could also confer a tensile resistance when the sarcomeres are stretched, as occurs during diastolic filling. To test this idea, we measured passive stiffness directly along the longitudinal axis of TTL-overexpressing myocytes. We attached cardiomyocytes to laser-etched cell holders (Fig. 4C, fig. S5, and movie S7) via a biological adhesive (7) and subjected them to step-like changes in length, while simultaneously measuring sarcomere length and passive force with a high-sensitivity transducer (Fig. 4D). A typical force response (Fig. 4D, blue) showed a rapid rise to peak force during the high-velocity stretch (F_{peak}), containing both elastic and viscous elements, followed by a relaxation to a steady-state force (F_{ss}) that largely reflects the elastic stiffness of the myocyte. For a given step size, TTL-overexpressing myocytes exerted significantly reduced peak forces during physiological length changes, with modest reductions in steady-state force (fig. S5F). The TTL-overexpressing cells also underwent significantly larger changes in sarcomere length with any given step (fig. S5G), which indicated increased sarcomere compliance and which suggested that stiffer sarcomeres in control cells distribute the length change to other compliant components in series. As can be surmised from fig. S5, F and G, TTL overexpression decreased tension across the physiological range of sarcomere lengths achieved during diastolic filling (Fig. 4E), which indicated a role for detyrosinated MTs as tensile-resistant elements. Visual evidence supporting such a relation was seen in MT networks in a control cell at resting and stretched length (fig. S5 and Fig. 4C, cyan). At resting length, there was some inherent slack in the MT network, whereas the same MTs became

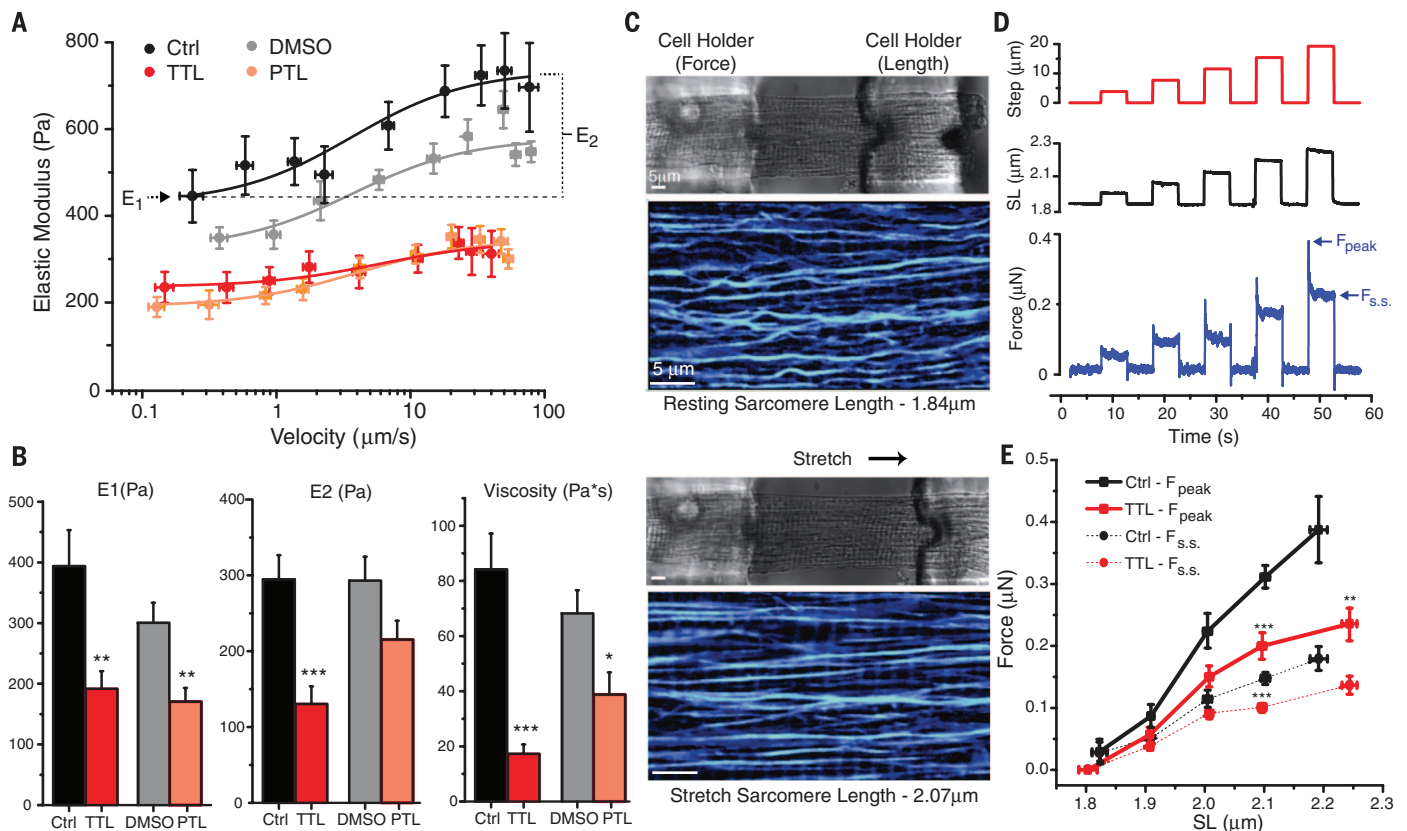


Fig. 4. Detyrosinated MTs regulate the viscoelasticity of cardiomyocytes.

(A) Elastic modulus of cardiomyocytes measured by AFM at various indentation velocities and fit to SLSM (see methods in SM). (B) Quantification of velocity-independent (E1) and velocity-dependent (E2) components of the elastic modulus, and SLSM fit-derived viscosity. Both TTL overexpression and PTL treatment significantly reduced elasticity and viscosity. There were no significant differences in these parameters between dimethyl sulfoxide (DMSO) (gray) and AdV-null (black) transduced cells ($P = 0.28, 0.34$, and 0.33 , respectively). Reductions in stiffness due to TTL overexpression are also apparent in cells under stretch along the longitudinal axis. (C) Myocytes were attached via glass cell holders (C, top, and fig. S5) to a force transducer and length

controller and were subjected to stretch. MTs visualized by EMTB-3xGFP (C, blue and aqua) at rest (top) and at a stretched length (bottom). (D) Representative force versus length protocol. A series of stepwise stretches (red) in 4-μm increments are applied to an isolated myocyte, which increases sarcomere length (SL, black). Passive tension (blue) generated by the step relaxes quickly from a peak value to a new steady state. (E) Force measurements binned according to measured change in sarcomere length with a given step size. TTL-overexpressing cells exert reduced peak passive tension during step changes in length, with a more modest reduction in steady-state tension. Data are presented as means \pm SEM; * $P < 0.05$, ** $P < 0.01$, *** $P < 0.001$. Further statistical details are available in tables S3 and S4.

taut when the cell was stretched and held at long sarcomere lengths (movie S8).

Model of MT contribution to cardiac contractility

We next sought to develop a mathematical model to recapitulate the experimentally measured changes in MT buckling and contractility when detyrosination is reduced. Previous work modeling MT buckles (6) suggests that three critical variables determine buckling behavior; MT stiffness, stiffness of the surrounding medium, and force incident on the long axis of the MT. How these three variables are predicted to alter MT behavior and myocyte mechanics is described in fig. S6. Of the three, only a decrease in incident force can explain our experimental observations after suppressing detyrosination. If MT anchoring to the sarcomere is disrupted, the reduced incident force on the MT may drop below the critical force required for buckling, which results in simultaneous decreases in buckling amplitude (Fig. 2) and viscoelasticity (Figs. 3 and 4). The

sarcomeric periodicity of buckles (Fig. 1I) also suggests an underlying structural constraint that changes in MT or medium stiffness alone cannot explain. We thus chose to model MT buckling within a contractile model that includes a MT compression-resistive element that's interaction with the sarcomere can be varied (see model in SM for details).

Using the mechanical scheme detailed in Fig. 5A, we fitted the contraction resulting from a log-normal force input to derive both contractile and buckling parameters. By modifying the incident force applied to a MT for a given amount of sarcomere shortening (Fig. 5A and model in SM), we simulated the effect of a sarcomeric anchor sliding and then catching at detyrosinated regions of the MT. Inclusion of a 100-nm slide (50 nm at each anchor, see model) before MTs engage with the rest of the sarcomere is reasonable, given the ~80% reduction in detyrosinated area observed by immunofluorescence with TTL overexpression (Fig. 2C), and reflects the fact that reductions in detyrosination would

increase the average distance between detyrosinated tubulins that could interact strongly with MT anchoring points. This disruption of MT-sarcomere coupling produced model outputs (Fig. 5, C and D) that closely recapitulated our experimental contractility and buckling results.

An alternate possibility to the sliding anchor is that the anchor is completely uncoupled by suppressing detyrosination and reverts to buckling behavior governed by local viscoelasticity rather than underlying structure, as proposed for less rigidly organized cell types, including developing myocytes (6). In either case, the coupling of MTs to the sarcomere is reduced, which impairs their ability to resist contraction.

Potential role for desmin as a sarcomeric MT anchor

The putative characteristics of the anchor—a mechanically stiff protein capable of forming complexes with MTs and restricted to a spatially defined region of the sarcomere—suggested the intermediate filament desmin as an immediate candidate.

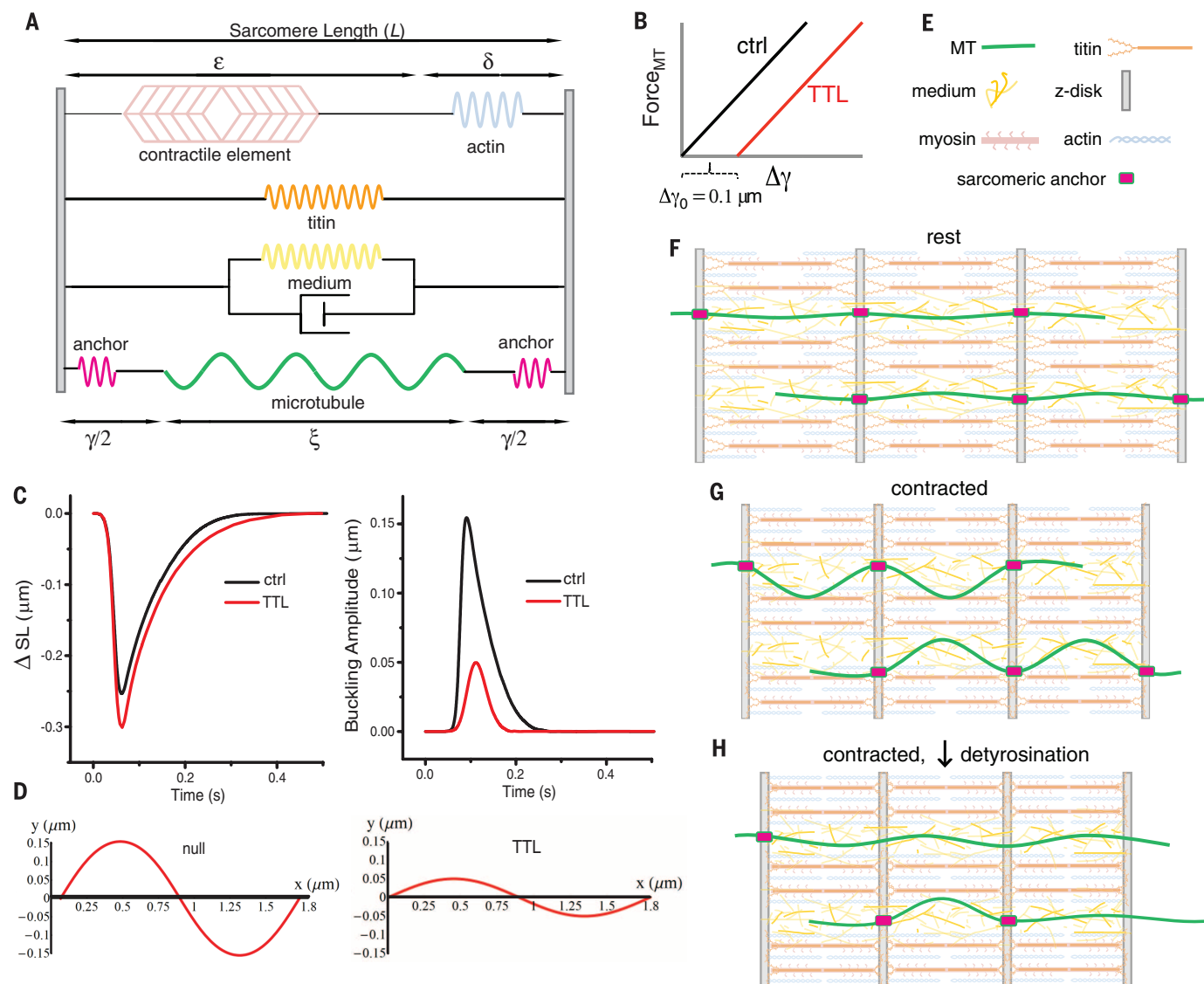


Fig. 5. Modeling MTs in the contracting sarcomere. (A) Mechanical schematic of the modeled sarcomere. A force-generating contractile arm (top) is coupled in parallel at the Z-disc to a spring element representing titin (orange), a viscoelastic medium (yellow spring and dashpot), and a MT (green) with anchors (fuschia pink) to the Z-disc (gray). The anchor to the Z-disc is only engaged at regions of MT detyrosination. (B) TTL overexpression is modeled by allowing the anchors to slide for 50 nm at each end before engaging and transmitting force to the MT at a detyrosinated subunit. (C) The change in

sarcomere length at peak contraction and buckling amplitude. (C) and (D) recapitulate experimental observations for TTL-overexpressing myocytes after this change. (E and F) The cardiac sarcomere, shown with MTs with putative stiff anchors to the sarcomere, here, at the Z-disc. Contraction reduces the distance between anchor points, which requires the MTs either to buckle (G) if the anchors are engaged or to slide (H), if the anchors are not engaged and force incident on the MT remains low. Mathematical model parameters are available in table S5.

Desmin forms structural bundles that form a complex with the Z-disc (29), and intermediate filaments can form detyrosination-dependent cross-links with MTs (30, 31).

We first sought to determine whether desmin preferentially associates with detyrosinated MTs. Cosedimentation of cardiomyocyte lysates showed that desmin forms pellets with polymerized MTs (Fig. 6A) in direct proportion to their level of detyrosination (Fig. 6, B and C), which indicated a specific and sensitive interaction. We also co-stained cardiomyocytes from desmin-depleted [knockout (KO)] and wild-type (WT) mice for desmin and both tyrosinated and detyrosinated tubulin to observe any preferential interaction.

The two populations of MTs show similar overall patterning in WT myocytes, except for a specific accumulation of detyrosinated (and not tyrosinated) tubulin in transverse bands at the Z-disc that colocalized with desmin (Fig. 6, D and E, and fig. S7). Note that KO animals lacked this transverse pattern completely (Fig. 6D and fig. S7H), although the Z-disc itself remained intact (fig. S7C). In addition, KO myocytes had a denser (fig. S7F) and more disorganized MT network (Fig. 6D and fig. S7, B and E), which suggested that desmin is required for proper MT network organization.

If desmin cross-links with detyrosinated MTs to structurally reinforce the network, then the

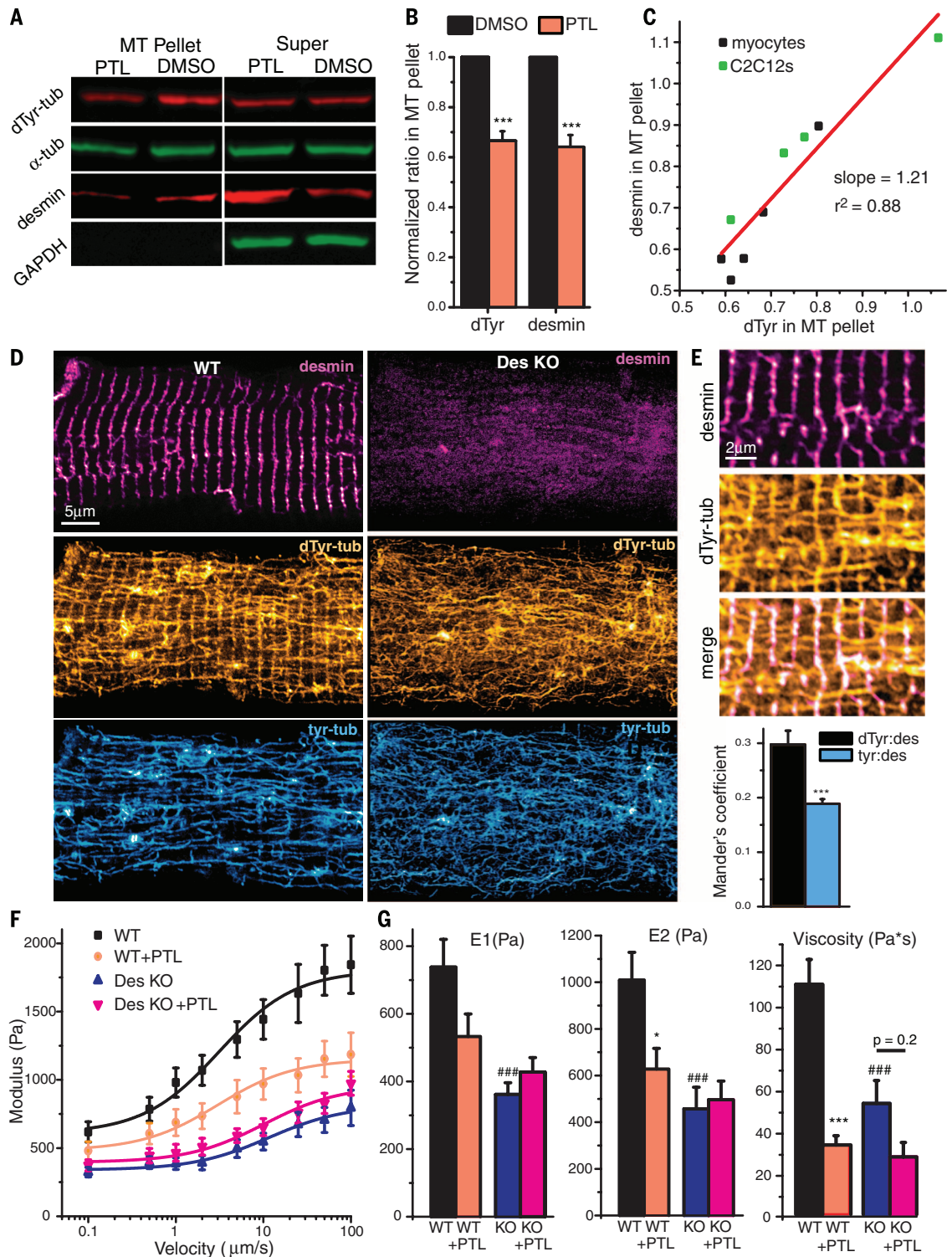
removal of desmin should both decrease cytoskeletal stiffness and prevent tyrosination-dependent changes in viscoelasticity. Blind studies in WT and KO myocytes revealed that desmin KO myocytes were significantly less stiff than WT counterparts (Fig. 6, F and G), and that treatment with PTL no longer reduced viscoelasticity (Fig. 6, F and G).

MT detyrosination is sufficient to impair cardiomyocyte contractility

Increasing detyrosination correlates with impaired function in animal models of heart disease (13, 14). Thus, we next tested whether increasing detyrosination could directly impair cardiac contractility.

Fig. 6. Desmin associates with detyrosinated MTs to increase cardio-myocyte stiffness. (A) MT cosedimentation

shows the interaction between polymerized MTs (pellet) and desmin. (B) Quantification of the amount of detyrosination and desmin (relative to the total amount of tubulin) in the MT pellet from cardiomyocyte lysates with and without PTL treatment. Data were normalized to DMSO level. (C) The amount of desmin associated with the MTs after PTL treatment is directly proportional to the amount of MT detyrosination across several experiments in rat cardiomyocytes and C2C12 cells. (D) Immunofluorescence of desmin, dTyr, and Tyr-tubulin shows dTyr-specific transverse pattern in WT, but not desmin KO, myocytes. (E) Overlay of dTyr-tubulin and desmin. (See fig. S7 for more examples.) (F and G) AFM measurements show a PTL-dependent reduction in myocyte stiffness and viscosity in WT, but not desmin KO myocytes. Viscoelasticity in desmin KO myocytes is not statistically different from WT with PTL treatment. Data are presented as means \pm SEM; * P < 0.05, ** P < 0.01, *** P < 0.001 with respect to DMSO treatment; ### P < 0.001 with respect to untreated WT myocytes. Further statistical details are available in table S6.



Using an adenoviral construct expressing short hairpin RNAs (shRNAs) against TTL (shTTL), we suppressed TTL expression, which enhanced detyrosination (Fig. 7A and fig. S8). shTTL-transduced myocytes were then tested for their viscoelastic and contractile properties. The excess detyrosination alone was sufficient to increase viscosity and stiffness (Fig. 7, B and C)

and suppressed contractile velocity and magnitude (Fig. 7, D and E).

We next examined whether this modification correlated with functional deficits in human heart disease. To this end, we analyzed left ventricular tissue samples from healthy patient donors and from patients exhibiting varying degrees of heart disease due to several underlying causes (table

S7). Detyrosinated tubulin was significantly increased in patients with clinically diagnosed hypertrophic and dilated cardiomyopathies (HCM and DCM, respectively), along with a modest increase in total tubulin content (Fig. 7, F and G). Blind analysis of HCM patient data showed that detyrosination inversely correlated with left ventricular ejection fraction (LVEF), a primary

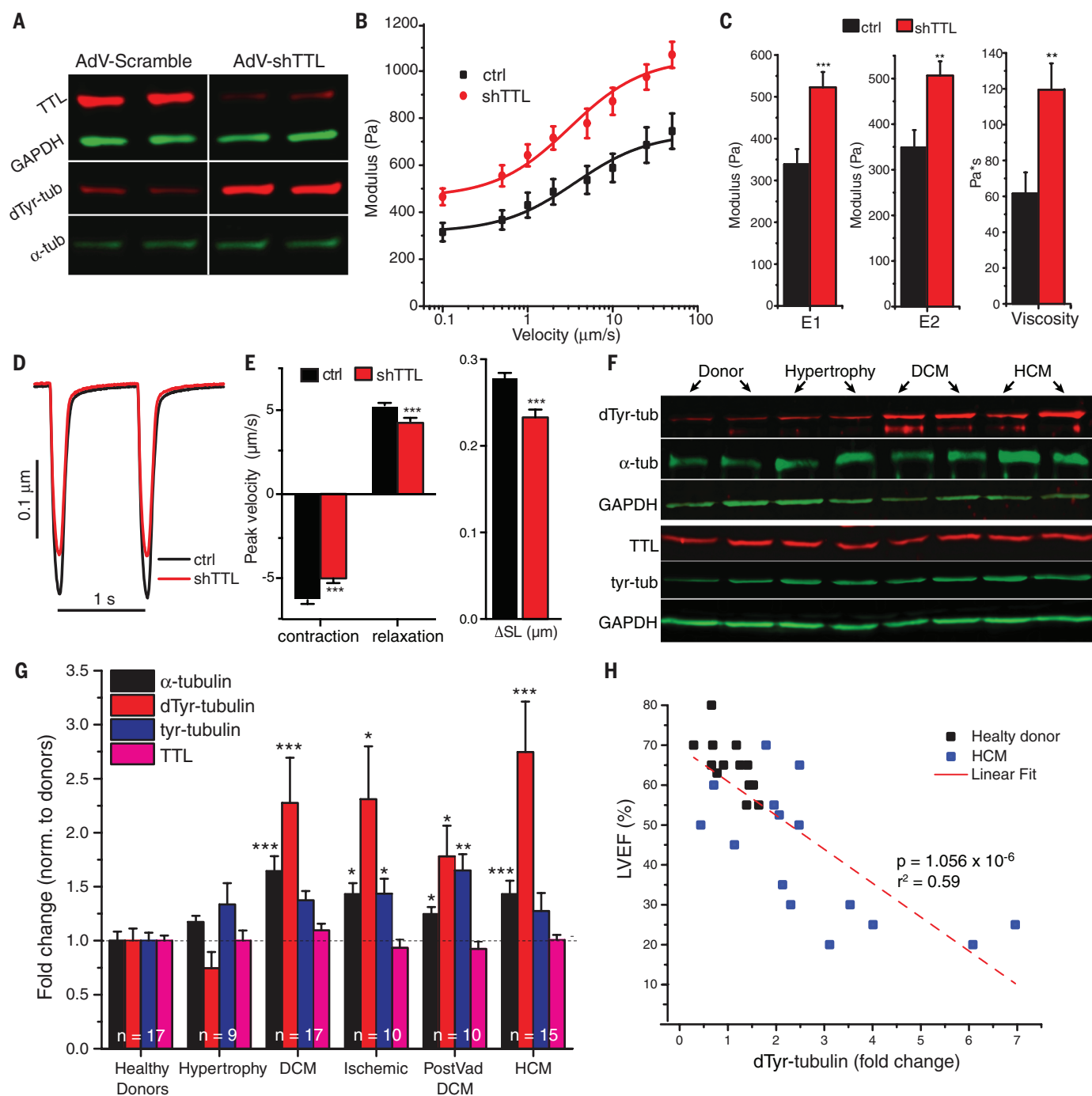


Fig. 7. Increasing detyrosination impairs contraction and is associated with human heart failure. (A) Western blot shows that shRNA against TTL selectively increases dTyr-tubulin without changing overall levels of α-tubulin. (B) Elastic modulus of control and shTTL-expressing myocytes at various indentation rates. (C) shTTL myocytes demonstrate increases in E1, E2, and viscosity. (D and E) TTL suppression significantly reduces contractile magnitude and velocity. (F) Representative Western blots from

human heart lysates. (G) Data from pooled analysis; $n = 17$ healthy donors, 9 hypertrophy, 17 DCM, 11 ischemic, 10 with DCM following ventricular assist device support (VAD DCM), and 15 HCM hearts. (H) There was a negative correlation between LVEF and dTyr-tubulin expression in control and hypertrophic cardiomyopathy patients. Data are presented as means \pm SEM; * $P < 0.05$, ** $P < 0.01$, *** $P < 0.001$. Further statistical details are available in tables S7 to S9.

indicator of cardiac contractility (Fig. 7H). There was no such correlation detected between LVEF and total or tyrosinated tubulin levels, nor any correlation between heart weight and detyrosination (fig. S9), which sug-

gested a specific link between detyrosination and LVEF. Myocardium from patients with DCM all demonstrated considerably depressed LVEF and variable, but increased, detyrosinated tubulin.

TTL was unchanged in all patient populations, which showed that a decreased expression of the tyrosinating enzyme does not explain the increase in detyrosinated tubulin in patients with heart disease (Fig. 7G). Because the molecular

identity of TCP is unknown, it is unclear if up-regulation of the detyrosinating enzyme may underlie this effect.

Discussion

Our findings demonstrate a regulatory pathway for MT load-bearing and myocyte mechanics through posttranslational detyrosination of tubulin. Detyrosinated MTs buckle under load in contracting cardiomyocytes, which confers mechanical resistance to contraction and regulating the viscoelastic properties of the myocyte.

The observation that MTs normally buckle, rather than break or slide, strongly indicates that they bear load and store elastic bending energy during the cardiac contractile cycle. This has implications for MT-dependent mechano-signaling in muscle and other tissues (1, 32, 33) but also has direct implications for contractility. Our model of myocyte contractility demonstrates how changing MT load-bearing and force transfer with the sarcomeres can substantially alter contractile properties. Our experimental data show that such changes in MT load-bearing can be achieved by posttranslational modifications of the MTs themselves, particularly detyrosination. The measured reductions in buckling and viscoelasticity and the increase in contractile speed of PTL-treated, TTL-overexpressing myocytes can all be attributed to changing the way MTs interact with the sarcomere and impairing their ability to act as compression resistors. It is also possible that detyrosinated MTs anchored to one sarcomere form bundles with MTs anchored to adjacent sarcomeres. If so, disrupting bundling would also effectively uncouple MTs from force-generating structures. Regardless of the mechanism, disrupting coupling to sarcomeres would reduce the incident force on the MT, and buckling occurrence would drop.

The striking periodicity of buckles in untreated myocytes lends further support to the idea of a sarcomeric anchor. The preferential association of desmin with detyrosinated tubulin and the insensitivity of desmin KO animals to changes in detyrosination strongly implicates desmin as at least one component of a sarcomeric anchoring complex of detyrosinated MTs. Note that myocytes lacking desmin have decreased viscoelasticity, despite a denser MT network, which supports the idea that MT network organization and cross-linking is a stronger determinant of myocyte mechanical properties than network density per se. Both the desmin and MT networks have elements perpendicular to their typical orientation, particularly near the sarcolemma, which may alter how those elements interact with the cytoskeleton and plasma membrane. However, we believe that the preponderance of the contractile resistance that results from detyrosination is due to longitudinal MTs in an orthogonal grid with transverse desmin IFs because of the simple numerical majority of cytoskeletal elements in this configuration.

Despite the fact that detyrosinated MTs store energy during sarcomere contraction, which provides compression resistance, little of this energy

appears to return in the form of a restoring force that would quicken sarcomere extension. This implies that energy used to deform MTs undergoes substantial loss. Buckling of the MT exerts compressive force on the surrounding matrix and deforms the cytoplasm, which, due to its intrinsic viscosity, can act as an energy sink during each cycle. This is reflected in the large viscous component of the MT contributions to myocyte mechanical properties observed at deformation rates consistent with contractile velocities both in this and previous work (34). However, we do note a slight prolongation of the late phase of relaxation in TTL-overexpressing myocytes, which may represent the loss of a MT contribution to restoring force. We consider it probable that the restoring force of other internal elastic elements, such as titin, are likely to play a more dominant role, at least in the initial return toward resting sarcomere length (27). Thus, an increase in detyrosination may increase myocyte stiffness and impair contraction by acting as an energy sink, without providing significant energetic return during relaxation.

Consistent with this, an increase in detyrosination was associated with clinical contractile dysfunction in human hearts. Our cellular studies demonstrate that acute reduction of detyrosination with genetic or pharmacologic approaches can boost contractility and reduce mechanical stiffness. Additionally, these approaches are able to induce large changes in detyrosination, while only slightly altering the overall MT cytoskeleton, which minimizes off-target consequences. Thus, interfering with detyrosination may represent an attractive and novel therapeutic strategy for increasing contractility.

In conclusion, our data show that MTs exhibit divergent mechanical behavior because of the differences in how they couple to the rest of the cardiac cytoskeleton. The tyrosinated portions of the network, moving readily with the myocyte during contraction, provide little contractile resistance. Conversely, the detyrosinated portions of the MT network, forming complexes with desmin IFs, produce a cross-linked MT-IF network that confers robust resistance to contraction. This orthogonal MT-IF grid requires tightly periodic MT deformations to accommodate myocyte morphology changes during contraction. These deformations require a considerable amount of energy to form and dissipate a large fraction of that energy due to viscous interactions. This has important implications for MT load-bearing across cell biology, as well as for the altered mechanical stiffness and mechano-signaling in cardiac disease.

REFERENCES AND NOTES

- B. L. Prosser, C. W. Ward, W. J. Lederer, X-ROS signaling: Rapid mechano-chemo transduction in heart. *Science* **333**, 1440–1445 (2011). doi: [10.1126/science.1202768](https://doi.org/10.1126/science.1202768); pmid: [21903813](https://pubmed.ncbi.nlm.nih.gov/21903813/)
- B. L. Prosser, C. W. Ward, W. J. Lederer, X-ROS signaling is enhanced and graded by cyclic cardiomyocyte stretch. *Cardiovasc. Res.* **98**, 307–314 (2013). doi: [10.1093/cvr/cvt066](https://doi.org/10.1093/cvr/cvt066)
- M. R. Zile et al., Constitutive properties of adult mammalian cardiac muscle cells. *Circulation* **98**, 567–579 (1998). doi: [10.1161/01.CIR.98.6.567](https://doi.org/10.1161/01.CIR.98.6.567); pmid: [9714115](https://pubmed.ncbi.nlm.nih.gov/9714115/)
- S. Nishimura et al., Microtubules modulate the stiffness of cardiomyocytes against shear stress. *Circ. Res.* **98**, 81–87 (2006). doi: [10.1161/01.RES.0000197785.51819.e8](https://doi.org/10.1161/01.RES.0000197785.51819.e8); pmid: [16306445](https://pubmed.ncbi.nlm.nih.gov/16306445/)
- H. L. Granzier, T. C. Irving, Passive tension in cardiac muscle: Contribution of collagen, titin, microtubules, and intermediate filaments. *Biophys. J.* **68**, 1027–1044 (1995). doi: [10.1016/S0006-3495\(95\)80278-X](https://doi.org/10.1016/S0006-3495(95)80278-X); pmid: [7756523](https://pubmed.ncbi.nlm.nih.gov/7756523/)
- C. P. Brangwynne et al., Microtubules can bear enhanced compressive loads in living cells because of lateral reinforcement. *J. Cell Biol.* **173**, 733–741 (2006). doi: [10.1083/jcb.200601060](https://doi.org/10.1083/jcb.200601060); pmid: [16754957](https://pubmed.ncbi.nlm.nih.gov/16754957/)
- M. Mehrbod, M. R. K. Mofrad, On the significance of microtubule flexural behavior in cytoskeletal mechanics. *PLOS ONE* **6**, e25627 (2011). doi: [10.1371/journal.pone.0025627](https://doi.org/10.1371/journal.pone.0025627); pmid: [21998675](https://pubmed.ncbi.nlm.nih.gov/21998675/)
- H. Tsutsui, K. Ishihara, G. Cooper 4th, Cytoskeletal role in the contractile dysfunction of hypertrophied myocardium. *Science* **260**, 682–687 (1993). doi: [10.1126/science.8097594](https://doi.org/10.1126/science.8097594); pmid: [8097594](https://pubmed.ncbi.nlm.nih.gov/8097594/)
- M. R. Zile et al., Role of microtubules in the contractile dysfunction of hypertrophied myocardium. *J. Am. Coll. Cardiol.* **33**, 250–260 (1999). doi: [10.1016/S0735-1097\(98\)00550-6](https://doi.org/10.1016/S0735-1097(98)00550-6); pmid: [9935038](https://pubmed.ncbi.nlm.nih.gov/9935038/)
- G. Cooper 4th, Cytoskeletal networks and the regulation of cardiac contractility: Microtubules, hypertrophy, and cardiac dysfunction. *Am. J. Physiol. Heart Circ. Physiol.* **291**, H1003–H1014 (2006). doi: [10.1152/ajpheart.00132.2006](https://doi.org/10.1152/ajpheart.00132.2006); pmid: [16679401](https://pubmed.ncbi.nlm.nih.gov/16679401/)
- C. Janke, J. C. Bulinski, Post-translational regulation of the microtubule cytoskeleton: Mechanisms and functions. *Nat. Rev. Mol. Cell Biol.* **12**, 773–786 (2011). doi: [10.1038/nrm3227](https://doi.org/10.1038/nrm3227); pmid: [22086369](https://pubmed.ncbi.nlm.nih.gov/22086369/)
- J. P. Kerr et al., Detyrosinated microtubules modulate mechanotransduction in heart and skeletal muscle. *Nat. Commun.* **6**, 8526 (2015). doi: [10.1038/ncomms9526](https://doi.org/10.1038/ncomms9526); pmid: [26446751](https://pubmed.ncbi.nlm.nih.gov/26446751/)
- H. Sato et al., Microtubule stabilization in pressure overload cardiac hypertrophy. *J. Cell Biol.* **139**, 963–973 (1997). doi: [10.1083/jcb.139.4.963](https://doi.org/10.1083/jcb.139.4.963); pmid: [9362514](https://pubmed.ncbi.nlm.nih.gov/9362514/)
- S. Belmadani, C. Poüs, R. Ventura-Clapier, R. Fischmeister, P.-F. Méry, Post-translational modifications of cardiac tubulin during chronic heart failure in the rat. *Mol. Cell. Biochem.* **237**, 39–46 (2002). doi: [10.1023/A:1016554104209](https://doi.org/10.1023/A:1016554104209); pmid: [12236585](https://pubmed.ncbi.nlm.nih.gov/12236585/)
- E. White, Mechanical modulation of cardiac microtubules. *Pflügers Arch.* **462**, 177–184 (2011). doi: [10.1007/s00424-011-0963-0](https://doi.org/10.1007/s00424-011-0963-0); pmid: [21487691](https://pubmed.ncbi.nlm.nih.gov/21487691/)
- G. Cooper 4th, Cardiocyte cytoskeleton in hypertrophied myocardium. *Heart Fail. Rev.* **5**, 187–201 (2000). doi: [10.1023/A:1009836918377](https://doi.org/10.1023/A:1009836918377); pmid: [16228904](https://pubmed.ncbi.nlm.nih.gov/16228904/)
- L. Cassimeris, P. Tran, *Methods Cell Biol.* **97**, xvii–xviii (2010). doi: [10.1016/S0091-679X\(10\)97031-3](https://doi.org/10.1016/S0091-679X(10)97031-3)
- G. Lukinavičius et al., Fluorogenic probes for live-cell imaging of the cytoskeleton. *Nat. Methods* **11**, 731–733 (2014). doi: [10.1038/nmeth.2972](https://doi.org/10.1038/nmeth.2972); pmid: [24859753](https://pubmed.ncbi.nlm.nih.gov/24859753/)
- S. Belmadani, C. Poüs, R. Fischmeister, P.-F. Méry, Post-translational modifications of tubulin and microtubule stability in adult rat ventricular myocytes and immortalized HL-1 cardiomyocytes. *Mol. Cell. Biochem.* **258**, 35–48 (2004). doi: [10.1023/B:MCBI.0000012834.43990.b6](https://doi.org/10.1023/B:MCBI.0000012834.43990.b6); pmid: [15030168](https://pubmed.ncbi.nlm.nih.gov/15030168/)
- C. Janke et al., Tubulin polyglutamylation enzymes are members of the TTL domain protein family. *Science* **308**, 1758–1762 (2005). doi: [10.1126/science.1113010](https://doi.org/10.1126/science.1113010); pmid: [15890843](https://pubmed.ncbi.nlm.nih.gov/15890843/)
- C. Erck et al., A vital role of tubulin-tyrosine-ligase for neuronal organization. *Proc. Natl. Acad. Sci. U.S.A.* **102**, 7853–7858 (2005). doi: [10.1073/pnas.0409626102](https://doi.org/10.1073/pnas.0409626102); pmid: [15899979](https://pubmed.ncbi.nlm.nih.gov/15899979/)
- L. Peris et al., Motor-dependent microtubule disassembly driven by tubulin tyrosination. *J. Cell Biol.* **185**, 1159–1166 (2009). doi: [10.1083/jcb.200902142](https://doi.org/10.1083/jcb.200902142); pmid: [19564401](https://pubmed.ncbi.nlm.nih.gov/19564401/)
- M. Sirajuddin, L. M. Rice, R. D. Vale, Regulation of microtubule motors by tubulin isoforms and post-translational modifications. *Nat. Cell Biol.* **16**, 335–344 (2014). doi: [10.1038/ncb2920](https://doi.org/10.1038/ncb2920); pmid: [24633327](https://pubmed.ncbi.nlm.nih.gov/24633327/)
- G. Kreitzer, G. Liao, G. G. Gundersen, Detyrosination of tubulin regulates the interaction of intermediate filaments with microtubules in vivo via a kinesin-dependent mechanism. *Mol. Biol. Cell* **10**, 1105–1118 (1999). doi: [10.1091/mbc.10.4.1105](https://doi.org/10.1091/mbc.10.4.1105); pmid: [10198060](https://pubmed.ncbi.nlm.nih.gov/10198060/)
- R. A. Whipple et al., Vimentin filaments support extension of tubulin-based microtentacles in detached breast tumor cells. *Cancer Res.* **68**, 5678–5688 (2008). doi: [10.1158/0008-5472.CAN-07-6589](https://doi.org/10.1158/0008-5472.CAN-07-6589); pmid: [18632620](https://pubmed.ncbi.nlm.nih.gov/18632620/)

26. X. Fonrose *et al.*, Parthenolide inhibits tubulin carboxypeptidase activity. *Cancer Res.* **67**, 3371–3378 (2007). doi: [10.1158/0008-5472.CAN-06-3732](https://doi.org/10.1158/0008-5472.CAN-06-3732); pmid: [17409447](https://pubmed.ncbi.nlm.nih.gov/17409447/)
27. M. Helmes, K. Trombitás, H. Granzier, Titin develops restoring force in rat cardiac myocytes. *Circ. Res.* **79**, 619–626 (1996). doi: [10.1161/01.RES.79.3.619](https://doi.org/10.1161/01.RES.79.3.619); pmid: [8781495](https://pubmed.ncbi.nlm.nih.gov/8781495/)
28. R. E. Mahaffy, C. K. Shih, F. C. MacKintosh, J. Käs, Scanning probe-based frequency-dependent microrheology of polymer gels and biological cells. *Phys. Rev. Lett.* **85**, 880–883 (2000). doi: [10.1103/PhysRevLett.85.880](https://doi.org/10.1103/PhysRevLett.85.880); pmid: [10991422](https://pubmed.ncbi.nlm.nih.gov/10991422/)
29. P. Konieczny *et al.*, Myofiber integrity depends on desmin network targeting to Z-disks and costameres via distinct plectin isoforms. *J. Cell Biol.* **181**, 667–681 (2008). doi: [10.1083/jcb.200711058](https://doi.org/10.1083/jcb.200711058); pmid: [18490514](https://pubmed.ncbi.nlm.nih.gov/18490514/)
30. G. Liao, G. G. Gundersen, Kinesin is a candidate for cross-bridging microtubules and intermediate filaments. Selective binding of kinesin to deetyrosinated tubulin and vimentin. *J. Biol. Chem.* **273**, 9797–9803 (1998). doi: [10.1074/jbc.273.16.9797](https://doi.org/10.1074/jbc.273.16.9797); pmid: [9545318](https://pubmed.ncbi.nlm.nih.gov/9545318/)
31. G. Guriland, G. G. Gundersen, Stable, deetyrosinated microtubules function to localize vimentin intermediate filaments in fibroblasts. *J. Cell Biol.* **131**, 1275–1290 (1995). doi: [10.1083/jcb.131.5.1275](https://doi.org/10.1083/jcb.131.5.1275); pmid: [8522589](https://pubmed.ncbi.nlm.nih.gov/8522589/)
32. R. J. Khairallah *et al.*, Microtubules underlie dysfunction in duchenne muscular dystrophy. *Sci. Signal.* **5**, ra56 (2012). doi: [10.1126/scisignal.2002829](https://doi.org/10.1126/scisignal.2002829); pmid: [22871609](https://pubmed.ncbi.nlm.nih.gov/22871609/)
33. M. Prager-Khoutorsky, A. Khoutorsky, C. W. Bourque, Unique interweaved microtubule scaffold mediates osmosensory transduction via physical interaction with TRPV1. *Neuron* **83**, 866–878 (2014). doi: [10.1016/j.neuron.2014.07.023](https://doi.org/10.1016/j.neuron.2014.07.023); pmid: [25123313](https://pubmed.ncbi.nlm.nih.gov/25123313/)
34. H. Tagawa *et al.*, Cytoskeletal mechanics in pressure-overload cardiac hypertrophy. *Circ. Res.* **80**, 281–289 (1997). doi: [10.1161/01.RES.80.2.281](https://doi.org/10.1161/01.RES.80.2.281); pmid: [9012750](https://pubmed.ncbi.nlm.nih.gov/9012750/)

ACKNOWLEDGMENTS

The authors thank C. W. Ward and E. L. Holzbaur for kindly providing TTL and EMTB-3xGFP plasmids, respectively, as well as for discussion; R. Bloch for providing desmin KO mice and littermate controls; Carl Zeiss Microscopy for Airyscan instrumentation use; IonOptix for technical support and cell holder materials; and Y. E. Goldman, E. L. Grishchuk, and R. J. Composto for discussion and guidance. B.L.P., P.R., M.A.C., A.I.B., and K.B.M. were responsible for experimental design; B.L.P., P.R., M.A.C., C.Y.C., and A.I.B. carried out experiments and analyzed data; H.A. and V.B.S. designed and executed the mathematical model. B.L.P. and P.R. cowrote the manuscript. All authors participated in the critical review and revision of the manuscript. This work was supported by funding from National Institute for Arthritis and Musculoskeletal and Skin Diseases (NIH) (T32AR053461-09 to P.R. and T32HL007954 to M.A.C.) and from National Heart, Lung, and Blood Institute (NIH)

(R00-HL114879 to B.L.P.). The VIVA experiments used shared experimental facilities from the Nano Science and Engineering Center on Molecular Function at the Nano-Bio Interface at the University of Pennsylvania supported by NSF under grant DMR08-32802. We thank R. Composto, who acknowledges the NSF Polymers Program under grant DMR09-07493. Procurement of human heart tissue was enabled by grants from NIH (HL089847 and HL105993) to K.B.M. H.A. and V.B.S. are supported by the National Institute of Biomedical Imaging and Bioengineering (NIH) under award number R01EB017753 and NSF grant CMMI-1312392. The data are included in the main manuscript and in the supplementary materials online.

SUPPLEMENTARY MATERIALS

www.sciencemag.org/content/352/6284/aaf0659/suppl/DC1
Materials and Methods
Supplementary Text
Figs. S1 to S11
Tables S1 to S9
References (35–42)
Movies S1 to S8

12 December 2015; accepted 29 January 2016
[10.1126/science.aaf0659](https://doi.org/10.1126/science.aaf0659)

RESEARCH ARTICLE

ULTRAFAST OPTICS

All-optical control and metrology of electron pulses

C. Kealhofer,^{1,2} W. Schneider,^{1,2} D. Ehberger,^{1,2} A. Ryabov,^{1,2} F. Krausz,^{1,2,*} P. Baum^{1,2,*}

Short electron pulses are central to time-resolved atomic-scale diffraction and electron microscopy, streak cameras, and free-electron lasers. We demonstrate phase-space control and characterization of 5-picometer electron pulses using few-cycle terahertz radiation, extending concepts of microwave electron pulse compression and streaking to terahertz frequencies. Optical-field control of electron pulses provides synchronism to laser pulses and offers a temporal resolution that is ultimately limited by the rise-time of the optical fields applied. We used few-cycle waveforms carried at 0.3 terahertz to compress electron pulses by a factor of 12 with a timing stability of <4 femtoseconds (root mean square) and measure them by means of field-induced beam deflection (streaking). Scaling the concept toward multiterahertz control fields holds promise for approaching the electronic time scale in time-resolved electron diffraction and microscopy.

Electron beams controlled with temporally varying electric fields enabled the first oscilloscopes and electronic computers; today, they are essential to free-electron lasers (1, 2), ultrafast streak cameras (3–5), and femtosecond imaging and diffraction techniques (6–8). Microwave technology at gigahertz frequencies has been the workhorse for ultrafast electron pulse control thus far, with applications ranging from particle acceleration to ultrafast pulse compression and high-resolution streak cameras. Unfortunately, microwave components suffer from appreciable phase drifts, and laser-microwave synchronization below 10 fs becomes technologically challenging (9–11). Laser field-driven dielectric accelerator structures operating near petahertz frequencies are being developed for next-generation particle accelerators (12, 13), but the short wavelength (~1 μm) and oscillation period (~1 fs) place extreme requirements on the input beam emittance and pulse duration (12, 13). In between, there is the regime of terahertz frequencies. Femtosecond laser-generated plasma waves exhibit terahertz longitudinal fields, which can accelerate electrons efficiently to the relativistic and ultrarelativistic energy domain (14). However, the excessive energy, divergence, and insufficient timing control of the resultant several- to multi-megaelectron volt electron pulses impair their utility for most of the above applications and particularly for ultrafast electron diffraction and microscopy.

Pulsed terahertz fields can be generated in a much more controlled way from the coherent nonlinear polarization of matter, such as by optical rectification (15). The pulses can reach field strengths on the order of 10¹⁰ V/m (16), and their

half-cycle durations ideally match practical electron bunch dimensions (femtosecond-picosecond in time and micrometer-millimeter in diameter). In addition, terahertz control fields derived from a single ultrafast laser via nonlinear optics result in near-perfect (potentially subfemtosecond) temporal synchronization, offering the potential to substantially surpass the performance of microwave-laser synchronization and obviating the need for locking electronics. Therefore, terahertz and infrared radiation generated from laser-driven coherent nonlinear polarization is ideally suited for controlling electron pulses, as indicated by simulations (17–21) and recent experiments on controlling nanoscale photoemission (22) and electron acceleration in a dielectric waveguide (23).

Concept and implementation

The experimental implementation of our terahertz-field-controlled electron beamline is depicted in Fig. 1 and consists of two functional units, one for pulse compression and one for temporal characterization by streaking (24). Near-1-ps pulses from a ytterbium:yttrium aluminum garnet (Yb:YAG)-based regenerative amplifier (25) drive two optical rectification stages for generating few-cycle terahertz pulses. With the same laser, electron pulses with on average approximately one electron per pulse are generated by two-photon photoemission from a gold thin-film photocathode and electrostatically accelerated to 70 keV. The optical rectification stages produce near-single-cycle pulses at a carrier frequency of 0.3 THz with pulse energies up to 40 nJ, implying field strengths of up to ~10⁶ V/m under gentle focusing conditions. These are used to control the electron pulse's momentum, energy, duration, or timing.

We used butterfly-shaped metal resonators (Fig. 1, inset) to mediate the interaction between the electrons and the terahertz fields. The terahertz electric field is enhanced in the plane of

the resonators and confined to subwavelength dimensions so that energy and momentum conservation in the electron-photon interaction can be satisfied (26).

Electrons passing through the resonator structures experience a net change in momentum that corresponds to the integral of the Lorentz force along their trajectories. This change varies sinusoidally as a function of arrival time of the electron in the terahertz field. The first terahertz control stage uses a tilted resonator to provide force components longitudinal to the electron beam for temporal compression. The second terahertz control stage, oriented normal to the beam, provides a delay-dependent deflection for temporal characterization.

The root-mean-square (RMS) electron beam radius is 3 μm at the compression resonator and 11 μm at the streaking resonator, at least 8 times smaller than the resonator mode dimensions. Because the electron pulse from the source is shorter than 1 ps and hence shorter than the half cycle of the terahertz field, the latter exerts a uniform but time-dependent force on the electron wavepacket in all dimensions. This force imparts acceleration and/or compression at the first stage and time-dependent deflection (streaking) at the second stage. As a result, the pulsed electron beam is entirely under the control of a single intense-pulse laser system and its optical fields.

Electron pulse compression

Even without any space charge, electron pulses unavoidably have a finite duration after acceleration because of dispersion (27). Electron pulse compression is therefore indispensable for reaching subphonon or electronic time scales in diffraction (28). Electron pulse compression requires deceleration and acceleration of the electron when arriving before or after the mean electron arrival time, respectively. For pulse compression with terahertz fields, the first butterfly microstructure is oriented at an angle of 45° with respect to the electron beam. Terahertz pulses are incident at an angle of 45° at the metal surface and hence normal to the electron beam (Fig. 1), so that the terahertz-excited resonance provides time-dependent force components parallel to the electron beam. In analogy to microwave compression, the time-dependent fields permit compression of the electron pulse substantially below its initial duration (28) and hence down to attosecond duration in the absence of space charge (27). In the limit of one- or few-electron pulses, the pulse duration is understood as the ensemble distribution of electron arrival times with respect to the laser reference.

The effective strength of the compression stage is quantified by g_E , the energy imparted to the electrons in the forward direction with changing delay time. In the experiment, g_E is proportional to the incoming terahertz peak field strength divided by the cycle period. After the interaction, the electron pulse becomes shorter as it propagates, reaching a minimum duration at a distance

$$f_c = m_e(\gamma\beta c)^3 / g_E \quad (1)$$

¹Ludwig-Maximilians-Universität München, Am Coulombwall 1, 85748 Garching, Germany. ²Max-Planck-Institute of Quantum Optics, Hans-Kopfermann-Strasse 1, 85748 Garching, Germany. *Corresponding author. Email: ferenc.krausz@lmu.de (F.K.); peter.baum@lmu.de (P.B.)

where c is the speed of light, m_e is the mass of the electron, β is the ratio of the electron speed to the speed of light, and $\gamma = 1/\sqrt{1-\beta^2}$. Localized terahertz fields enhanced to merely 10^6 V/m are sufficient to yield a g_E of 50 eV/ps and hence produce a convenient temporal focus at a distance of tens of centimeters from the compression stage, depending on central energy (24).

Temporal characterization

To measure the temporal profile of the electron pulse, the second stage is configured to provide a terahertz-driven delay-dependent deflection, which

we dub “streaking,” in analogy to microwave-driven and laser field-driven devices. We first tested the temporal characterization with the uncompressed pulse. The time-dependent deflection of the beam yields a deflectogram (Fig. 2B), the beam profile (in the plane of deflection) plotted versus delay of the electron pulse with respect to the terahertz field. At the zero crossings of the field, the deflection is a steep function of time, and the beam width increases because of the finite-duration electron pulse. Raw images of the electron beam were recorded on the phosphor-covered camera with the terahertz deflecting field switched on

and off and timed so as to yield maximum streaking of the beam (Fig. 2A). At the maxima and minima, minimal spreading occurs. The electron pulse duration and the time-dependent optical forces are determined by fitting the data of Fig. 2B assuming an instantaneous momentum transfer transverse to the electron beam induced by the terahertz field as a function of the electron arrival time.

The deflection is proportional to the integral of the Lorentz force along the electron's trajectory and closely follows the electric field's temporal profile inside the slit because of near-field confinement, as a consequence of the electron traversing the field-enhanced region within a tiny fraction of the field oscillation period (22, 29). This is in sharp contrast with attosecond streaking, which operates in the opposite limit (transit time much longer than the streaking field duration) so that the streaking spectrogram mimics the vector potential of the streaking field (30). A spline interpolation through four support points per picosecond is used for modeling time-dependent deflection, and a Gaussian temporal profile is assumed for the electron pulse. The calculated deflectogram with the fitted time-dependent deflection is shown in Fig. 2C. The electron pulse duration is 930 fs at full width at half maximum (FWHM), which is consistent with a propagation-induced temporal spread resulting from a 0.6-eV initial energy spread of the electron pulse.

The deflectogram displays sustained deflection oscillations far beyond the duration of the near-single-cycle incident terahertz driving pulse. The best fit yields a resonance frequency of 0.29 ± 0.01 terahertz of the resonator with a decay rate of 4.5 ± 0.4 ps resulting from radiative and resistive damping.

The resultant maximum streaking speed as a function of incident peak terahertz field strength in this range is shown in Fig. 2D. The highest value measured exceeds $8 \mu\text{rad/fs}$, corresponding to a streaking speed of $4.4 \mu\text{m/fs}$ at the camera in our experimental geometry. The distance over which all momentum change accumulates is determined by the terahertz near-field decay length ($\sim 100 \mu\text{m}$) and the foil thickness ($\sim 30 \mu\text{m}$). The resulting interaction length is some 100 times smaller than in conventional streak cameras (3, 4), removing a substantial limitation of their temporal resolution.

In the terahertz field-driven streak camera, temporal resolution is dictated by the beam quality and signal-to-noise ratio. At an incident terahertz field strength of 1.3×10^6 V/m, the RMS beam width on the camera of 1.6 pixels ($25 \mu\text{m}$) corresponds to 6-fs resolution (RMS). With ~ 1000 detected electrons, the beam quality and signal-to-noise ratio allow detection of displacements or spot width changes of 0.1 pixels ($1.56 \mu\text{m}$). A displacement of 0.1 pixels corresponds to 0.4 fs accuracy of arrival time measurements, whereas a 0.1-pixel increase of the spot size from the unstreaked value corresponds to a 2-fs (RMS) or ~ 4.5 -fs (FWHM) pulse duration. These resolutions are achieved with a signal accumulation

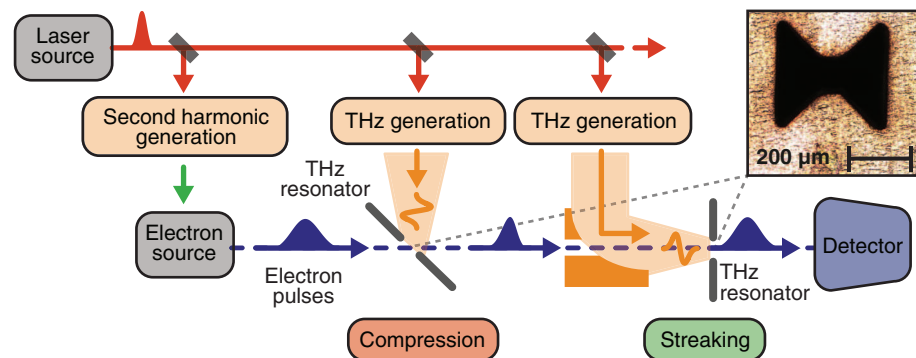


Fig. 1. Experimental setup. A 1-ps laser pulse from a Yb:YAG regenerative amplifier is frequency-doubled and generates an electron pulse from a thin-film gold photocathode. The laser also drives two optical-rectification stages, each generating single-cycle terahertz pulses with energy of up to 40 nJ. (Inset) Terahertz resonator structures are laser-machined in a 30- μm -thick aluminum foil. A first element, used for compression, is oriented at 45° to the electron beam, providing time-dependent longitudinal forces on the electrons. The second terahertz resonator, used for streaking, is oriented normal to the beam, resulting in time-dependent transverse deflection.

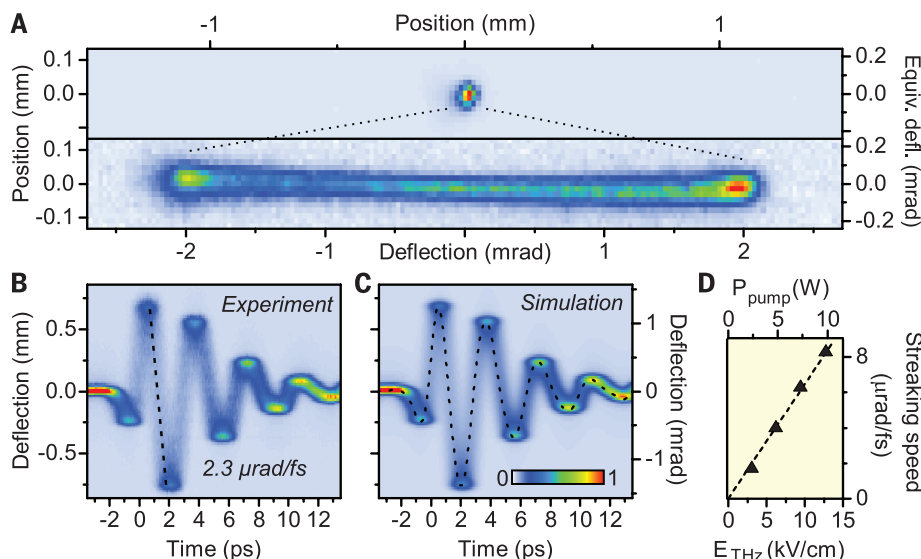


Fig. 2. All-optical terahertz streak camera. (A) Images of the electron beam on the camera with and without the terahertz field. The FWHM of the streaked beam is ~ 50 times larger than that of the unstreaked spot. (B) Time-dependent deflection (deflectogram) measured by varying the delay between the electron pulse and the streaking terahertz. Images of the beam are integrated along the unstreaked direction so as to determine a one-dimensional profile at each time delay. (C) Simulated deflectogram, result of a fit simultaneously characterizing the electron pulse duration and the streaking field (dotted line). The fitted electron pulse duration is 930 fs. (D) Streaking speed versus input terahertz field strength. The linear relationship supports a direct, field-driven interaction.

time of 6 s and improve with longer integration. These values represent a near-two-order-of-magnitude improvement over the state of the art of microwave streak cameras (3, 4), obtained already at terahertz fields of $\sim 10^6$ V/m as opposed to 10^{10} V/m available (16). As a consequence, our terahertz streaking concept may allow the direct measurement of subfemtosecond electron pulses (31, 32) and their timing drifts.

Compression and measurement

Streaking deflectograms are shown in Fig. 3, A and B, with and without terahertz field compression, respectively. In the latter, the terahertz field strength of the compression stage has been adjusted to produce a temporal focus at the streaking stage. A pronounced sharpening of the trace can be seen in the vertical (streaking) direction, indicating a substantial reduction in electron pulse duration.

The systematic evolution of measured electron temporal profile for a varying compression strength g_E is shown in Fig. 3C (33). The deflection as a function of time is reconstructed and used to perform the nonlinear transformation between the spatial profile of the streaked pulse and the underlying temporal profile of the terahertz field-manipulated incident pulse (24). The dotted lines depict the results of three-dimensional electron trajectory simulations (33).

The electron pulse (Fig. 3C, blue) first shortens to a minimum duration (Fig. 3C, fifth trace from bottom) and afterward lengthens again, with a double-peaked shape that is characteristic of overcompression by a sinusoidal field (31). The experimental and theoretical pulse durations versus terahertz-field strength and average power of the driving laser are shown in Fig. 3D. The shortest pulse (Fig. 3D, inset) has a FWHM duration of 75 fs, which is in excellent agreement with the simulation and a factor of 12 shorter than the original, 930-fs pulses and shorter than the half period of many fundamental phonon modes and molecular vibrations. Comparison of the shortest measured pulse shape with a Gaussian profile (dotted line) reveals a deviation; this is a consequence of the terahertz field's residual curvature over the time scale of the incoming, uncompressed electron pulse. Optimized electron sources with sub-100-fs duration (34) will reduce this effect; the particle-tracing simulations (24) show that 3-fs (FWHM) compressed pulses can be generated with a smaller source size and the 100-fs incoming pulses achievable if the photoemission energy is matched to the work function (7, 27). This would be an order of magnitude shorter than the 28-fs (FWHM) pulses generated in the single-electron regime so far (28) and allow the study of light-driven electronic motion via subcycle diffraction (35, 36).

Electron-laser timing metrology

Femtosecond pump-probe crystallography with electrons (7) or with x-ray free-electron lasers (1, 2) suffers from laser-electron timing jitter at the sample location, which is typically caused by imperfect laser-microwave synchronization (10, 11). In contrast to the statistical electronic

processes in the photodiodes used for microwave synchronization (9), laser-generated terahertz fields are, within the attosecond response time of the underlying nonlinear polarization, perfectly locked in time to the intensity profile of the pump pulses. Timing jitter/drift between the laser pump pulse and the electron probe pulse can only originate from extrinsic effects, such as fluctuations in path lengths or laser pulse energy.

Experimentally, we studied drifts of the electron pulse with respect to the terahertz field by setting the near-field-enhanced streak camera to a constant delay and recording the beam deflection over time (Fig. 4A). First, we scrutinized a possible role of amplitude-to-timing conversion in the nonlinear optical rectification process. The change in electron-terahertz field timing when varying the laser pump pulse intensity before the terahertz generation crystal is shown in Fig. 4B. We observed a systematic change in timing, but the slope at the operation conditions (7 W) is only 1.0 fs per 1% change in laser power, which is negligible for our laser system, whose intensity drifts and shot-to-shot energy fluctuations are below 2% (25).

In a second experiment, we measured drifts of the photoemission electrons with respect to the streaking terahertz field by turning the

terahertz control field off. For integration times longer than 1 s, we obtained 4.6 fs (RMS) over 15 min (Fig. 4C). Last, we repeated this measurement with the terahertz-driven pulse compression activated; with integration times of 6 s, and after ~ 2 hours of laboratory thermalization, we measured 3.7 fs RMS over 3 hours (Fig. 4E). This vastly outperforms the long-term stability of state-of-the-art laser-microwave synchronization with feedback loops (7) and also compares favorably with the record value (5 fs RMS) achieved with direct microwave extraction from a laser pulse train and data post-processing (9). We expect that the measured, residual 3.7-fs drift could be further decreased by minimizing the (currently meter-scale) optical path lengths and/or stabilizing them interferometrically. Synchronization in the all-optical scheme is entirely single-pulse-based, and therefore, few-femtosecond stability can be maintained at any—and especially at very low—laser repetition rate. A clock or master oscillator is not required.

Direct terahertz-electron interaction at a foil

Enhancement of the terahertz field by a microstructure resonator has proven highly beneficial for electron pulse control and metrology, but some experiments might require more direct control,

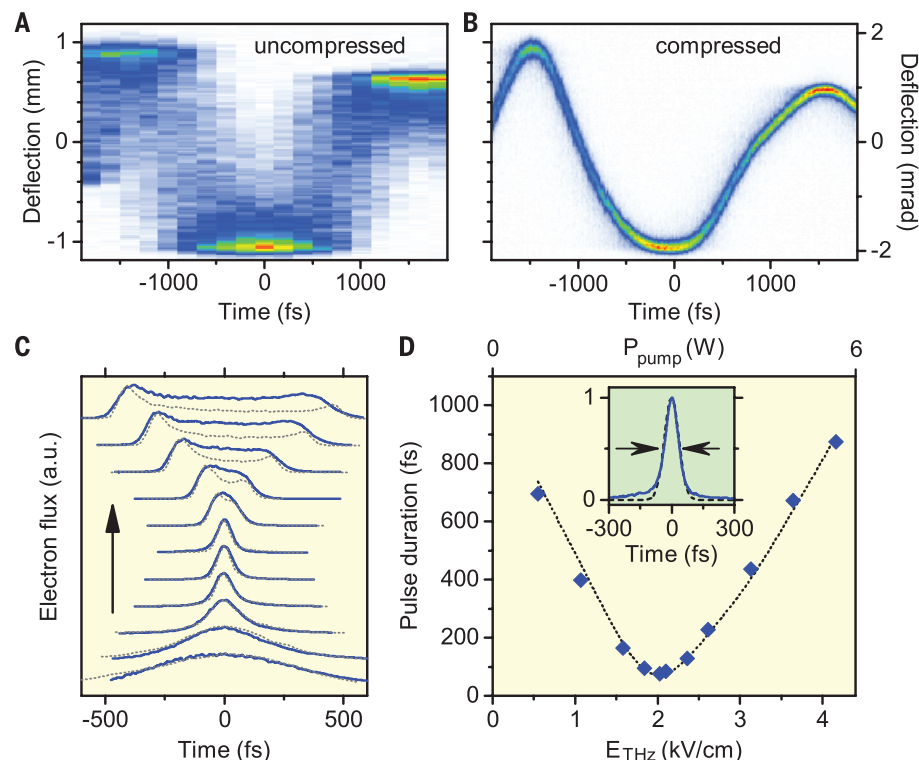


Fig. 3. Terahertz-driven electron pulse compression. (A and B) Comparison of deflectograms for (A) uncompressed (930 fs) and (B) compressed (75 fs) pulses at time steps of 200 and 10 fs, respectively. The deflectograms were measured sequentially and have a temporal resolution of ~ 9 fs (RMS). (C) Measured temporal profiles of the electron pulses (blue traces) as the compression strength is increased (black arrow), taking into account for long pulses the curvature of the time-dependent deflection. Simulated temporal profiles (10^4 particle trajectories) (24) are superimposed (dotted black lines). Differences between the measured and simulated pulses are due in part to the curvature of the streaking field, which reduces the streaking time-resolution at times far from zero. (D) Electron pulse duration (FWHM) versus incident terahertz field strength and optical pump power. The measured values are plotted as blue diamonds, and the simulation is shown as a dotted black line. (Inset) The shortest measured pulse profile [fifth trace from the bottom of (C)].

avoiding the localization and limited spectral response inextricably linked to resonators. For a direct electron-terahertz interaction, we realized a resonator-free interaction geometry based on a symmetry-breaking surface (29, 37). In the depicted concept (Fig. 5A), a thin metal foil (70-nm aluminum) acts as a mirror for terahertz radiation, and electrons transmitted through it experience an abrupt extinction of the electromagnetic field, leading to net deflection. The combination of angles is chosen so that extended beam profiles experience a homogeneous time dependence owing to lateral phase matching (29).

Measured and calculated streaking deflectograms of an uncompressed electron pulse are depicted in Fig. 5, C and D, at an energy of 90 keV, exhibiting excellent agreement. Although the peak deflection is smaller than for the resonator-based setting, the deflectogram clearly exhibits single-cycle behavior, preserving the incident terahertz pulse's ultrabroadband spectrum without alteration (25). The peak-to-peak deflection as a function of the incoming terahertz field strength is shown in Fig. 5B, revealing the expected linear dependence. Electrons delivered in a nearly collimated beam are directly (and spatially uni-

formly) deflected directly with the field cycles, advancing the century-old cathode-ray-tube oscilloscope to the terahertz domain. Owing to the 1-fs-scale timing accuracy of the sampling electron pulse, the cut-off frequency of this terahertz cathode-ray oscilloscope is dictated by the inverse electron pulse duration, which is >10 THz with the demonstrated compressed pulses, >100 THz with the few-femtosecond electron pulses predicted by the simulations, and >1 PHz with the isolated attosecond electron pulses feasible with multistage compression.

Conclusions and outlook

Our demonstrated generic and scalable all-optical methodology for the control and characterization of ultrafast electron pulses used laser-generated subcycle terahertz transients for 12-fold electron pulse compression, followed by temporal profile characterization with 10-fs resolution. Electron-transparent foils mediating the electron-field interaction permit time-energy phase-space manipulation of collimated electron beams of any size and, conversely, the temporal characterization of optical field transients up to frequencies only limited by the electron pulse duration, which—as opposed to the photon pulse in electro-optical sampling—may be shortened to <1 fs (27). Alternatively, resonant structures dramatically lower the terahertz power by a factor >1000 for effective compression and characterization of ultra-short electron pulses. Whereas the former opens the prospect of a petahertz-bandwidth cathode-ray oscilloscope as an alternative to attosecond photon-pulse metrology (30), the latter may lead to unprecedented spatiotemporal resolutions in pump-probe electron diffraction and imaging.

The moderate field strengths applied in our experiment offer the potential for increasing the interaction strengths by more than two orders of magnitude, limited by the high values of electrical breakdown at terahertz frequencies. This will result in correspondingly reduced propagation distances between subsequent terahertz control stages, which in turn should improve the passive few-femtosecond timing stability into the subfemtosecond regime. Simultaneous compression of 100-fs-scale input electron pulses to near-1-fs duration will permit spatiotemporal imaging of the fastest structural and infrared field-driven electron dynamics in molecular systems (36) as well as condensed matter (35) through single-electron diffraction (38) or microscopy (6) and allow measuring microscopic/atomic-scale electric field waveforms up to frequencies of visible light.

The demonstrated all-optical control may also be helpful for manipulating ultrabright multi-electron bunches. Compact electron guns have demonstrated sub-200-fs electron pulses with sufficient charge for single-shot structural dynamics studies (7). Our concept is directly applicable to them as well. Alternatively, single-shot ultrafast electron diffraction may be advanced into the few-femtosecond regime and possibly beyond by terahertz-streaking 100-fs-scale probe pulses after passage through the sample (4). The unprecedented

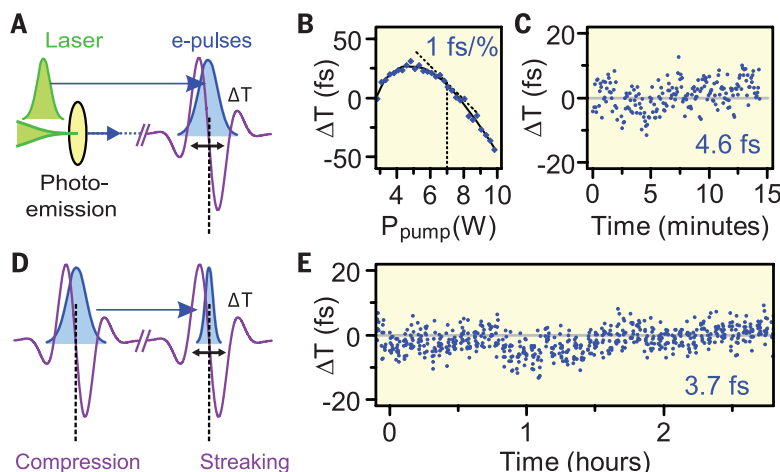


Fig. 4. Passive few-femtosecond synchronization. (A) Concept for measuring arrival-time drifts between the uncompressed electron pulses and the optical streaking field. (B) Systematic coupling of laser fluctuations to timing drifts. Measuring shifts in the terahertz zero-crossing time with increasing laser pump power reveals a slope of less than 1 fs per 1% change in laser power in a wide range of operation conditions. (C) Measured timing drift between photoemitted electron pulses and the terahertz field cycles at 10-s intervals. The integration time for each data point is 1 s. (D) Concept for measuring the arrival-time drift between terahertz-compressed electron pulses and the streaking field cycles. (E) Result with 6-s integration times reveals passive longer-term synchronization. The jitter values in (C) and (E) are RMS deviations; statistical errors are 3.5 and 2.7 fs, respectively.

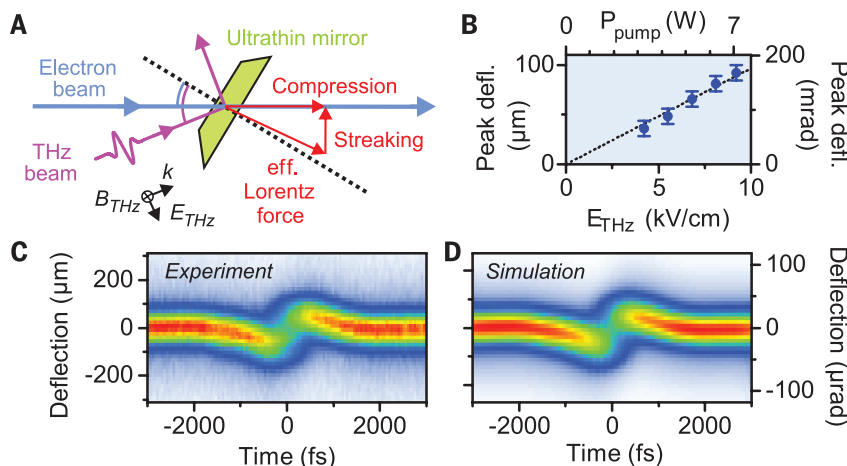


Fig. 5. Resonance-free single-cycle streaking. (A) Resonator-free concept for mediating the electron-terahertz interaction by using an ultrathin terahertz mirror. The angles of the terahertz and the electron beams with respect to the foil's surface normal (dotted line) are chosen for lateral phase matching across arbitrarily large electron and terahertz beam profiles. (B) Measurement of peak deflection versus incident terahertz field strength. (C) Experimental deflectogram revealing single-cycle behavior. (D) Simulated deflectogram with an electron pulse duration of 800 fs.

temporal resolution of the terahertz-driven streak camera could also be used to characterize electron microbunching in free-electron lasers, supplementing terahertz-based diagnostics for the x-ray output (39, 40). The demonstrated concept is scalable to higher terahertz frequencies and multiple stages, offering the potential for cascaded compression into the subfemtosecond regime or direct injection into a single optical cycle of a laser-field accelerator (12). This may, in the long run, lead to isolated attosecond electron pulses for recording dynamic changes of electron distribution in complex systems, including biological molecules and solid-state nanostructures.

REFERENCES AND NOTES

- W. Ackermann et al., *Nat. Photonics* **1**, 336–342 (2007).
- P. Emma et al., *Nat. Photonics* **4**, 641–647 (2010).
- G. H. Kassier et al., *Rev. Sci. Instrum.* **81**, 105103 (2010).
- C. M. Scoby, R. K. Li, E. Threlkeld, H. To, P. Musumeci, *Appl. Phys. Lett.* **102**, 023506 (2013).
- C. Kealhofer et al., *Opt. Lett.* **40**, 260–263 (2015).
- D. J. Flannigan, A. H. Zewail, *Acc. Chem. Res.* **45**, 1828–1839 (2012).
- G. Sciajini, R. J. D. Miller, *Rep. Prog. Phys.* **74**, 096101 (2011).
- J. Tenboer et al., *Science* **346**, 1242–1246 (2014).
- M. Walbran, A. Gliserin, K. Jung, J. Kim, P. Baum, *Phys. Rev. Appl.* **4**, 044013 (2015).
- S. Schulz et al., *Nat. Commun.* **6**, 5938 (2015).
- G. J. H. Brussaard et al., *Appl. Phys. Lett.* **103**, 141105 (2013).
- R. J. England et al., *Rev. Mod. Phys.* **86**, 1337–1389 (2014).
- E. Hemsing, G. Stupakov, D. Xiang, A. Zholents, *Rev. Mod. Phys.* **86**, 897–941 (2014).
- E. Esarey, C. B. Schroeder, W. P. Leemans, *Rev. Mod. Phys.* **81**, 1229–1285 (2009).
- M. C. Hoffmann, J. A. Fülöp, *J. Phys. D Appl. Phys.* **44**, 083001 (2011).
- M. Shalaby, C. P. Hauri, *Nat. Commun.* **6**, 5976 (2015).
- S. D. Vartak, N. M. Lawandy, *Opt. Commun.* **120**, 184–188 (1995).
- R. B. Yoder, J. B. Rosenzweig, *Phys. Rev. ST Accel. Beams* **8**, 113301 (2005).
- L. J. Wong, A. Fallahi, F. X. Kärtner, *Opt. Express* **21**, 9792–9806 (2013).
- J. Fabiańska, G. Kassier, T. Feurer, *Sci. Rep.* **4**, 5645 (2014).
- S. R. Greig, A. Y. Elezzabi, *Appl. Phys. Lett.* **105**, 241115 (2014).
- L. Wimmer et al., *Nat. Phys.* **10**, 432–436 (2014).
- E. A. Nanni et al., *Nat. Commun.* **6**, 8486 (2015).
- Materials and methods are available as supplementary materials on Science Online.
- W. Schneider et al., *Opt. Lett.* **39**, 6604–6607 (2014).
- F. J. García de Abajo, M. Kociak, *New J. Phys.* **10**, 073035 (2008).
- E. Fill, L. Veisz, A. Apolonski, F. Krausz, *New J. Phys.* **8**, 272 (2006).
- A. Gliserin, M. Walbran, F. Krausz, P. Baum, *Nat. Commun.* **6**, 8723 (2015).
- F. O. Kirchner, A. Gliserin, F. Krausz, P. Baum, *Nat. Photonics* **8**, 52–57 (2014).
- R. Kienberger et al., *Nature* **427**, 817–821 (2004).
- P. Baum, A. H. Zewail, *Proc. Natl. Acad. Sci. U.S.A.* **104**, 18409–18414 (2007).
- A. Feist et al., *Nature* **521**, 200–203 (2015).
- General Particle Tracer code (www.pulsar.nl/gpt).
- J. Hoffrogge et al., *J. Appl. Phys.* **115**, 094506 (2014).
- V. S. Yakovlev, M. I. Stockman, F. Krausz, P. Baum, *Sci. Rep.* **5**, 14581 (2015).
- H. C. Shao, A. F. Starace, *Phys. Rev. Lett.* **105**, 263201 (2010).
- T. Plettner et al., *Phys. Rev. Lett.* **95**, 134801 (2005).
- S. Lahme, C. Kealhofer, F. Krausz, P. Baum, *Struct. Dyn.* **1**, 034303 (2014).
- U. Fröhling et al., *Nat. Photonics* **3**, 523 (2009).
- I. Rgras et al., *Nat. Photonics* **6**, 852 (2012).

ACKNOWLEDGMENTS

This work was supported by the European Research Council and the Munich-Centre for Advanced Photonics. We thank D. Frischke for preparing ultrathin aluminum foils. The authors declare no competing financial interests.

SUPPLEMENTARY MATERIALS

www.sciencemag.org/content/352/6284/429/suppl/DC1
Materials and Methods
Fig. S1
References (41–43)

4 December 2015; accepted 2 March 2016
10.1126/science.aae0003

REPORTS

ORGANIC CHEMISTRY

Catalytic asymmetric addition of Grignard reagents to alkenyl-substituted aromatic *N*-heterocycles

Ravindra P. Jumde, Francesco Lanza, Marieke J. Veenstra, Syuzanna R. Harutyunyan*

Catalytic asymmetric conjugate addition reactions represent a powerful strategy to access chiral molecules in contemporary organic synthesis. However, their applicability to conjugated alkenyl-*N*-heteroaromatic compounds, of particular interest in medicinal chemistry, has lagged behind applications to other substrates. We report a highly enantioselective and chemoselective catalytic transformation of a wide range of β -substituted conjugated alkenyl-*N*-heteroaromatics to their corresponding chiral alkylated products. This operationally simple methodology can introduce linear, branched, and cyclic alkyl chains, as well as a phenyl group, at the β -carbon position. The key to this success was enhancement of the reactivity of alkenyl-heteroaromatic substrates via Lewis acid activation, in combination with the use of readily available and highly reactive Grignard reagents and a copper catalyst coordinated by a chiral chelating diphosphine ligand.

The majority (88%) of all known active pharmaceutical ingredients (APIs) contain functionalized heterocyclic aromatic rings with a preponderance of *N*-containing aromatic heterocycles (1). Furthermore, approximately half of all APIs are chiral (1). Because the two enantiomers of a chiral drug can exhibit markedly different bioactivity, any new chiral API must be produced as a single enantiomer. Catalytic asymmetric carbon-carbon (C-C) bond formation represents the most straightforward and atom-efficient strategy for the construction of organic chiral molecules (2–4). Organometallic reagents are used in a substantial fraction of the C-C bond-forming reactions used to construct API molecules (5–7). The conjugate addition of organometallic reagents to electron-deficient substrates (Michael acceptors) has proven to be a powerful method for creating new C-C bonds in a catalytic asymmetric manner for more than 20 years (7–12). In this context, the catalytic asymmetric addition of organometallics to conjugated alkenyl-heteroaromatic compounds represents an attractive strategy to access valuable chiral heterocyclic aromatic compounds in enantiopure form. Addition of carbon nucleophiles to conjugated vinyl-substituted heteroaromatic compounds, leading mainly to achiral molecules, is well known (13, 14). In contrast, there are only a handful of reports of nucleophilic additions to β -substituted analogs, in particular when organometallics are considered.

An early attempt at such a catalytic asymmetric reaction, reported in 1998, was the nickel-catalyzed addition of Grignard reagents to substituted 4-(1-alkenyl)pyridines (15). Although the reaction did

not appear to be ligand-accelerated and provided only 0 to 15% enantiomeric excess (ee), these results suggested that catalytic asymmetric versions of such transformations were feasible. It was not until 2010 that a highly enantioselective, Rh-catalyzed addition of an organometallic reagent to alkenyl-substituted heteroaromatic compounds—namely arylation with an arylboronic acid—was realized, furnishing a wide range of chiral products with high yields and enantioselectivities (16–19).

The limited number of reports on transition metal-catalyzed asymmetric conjugate addition of nucleophiles to β -substituted alkenyl-heteroaromatic compounds, restricted to precious metal-catalyzed arylations, is in striking contrast to the plethora of methodologies available for the catalytic asymmetric alkylations, arylations, alkylations, and allylations of common Michael acceptors, activated by carbonyl, nitrile, sulfonyl, and nitro groups (8–12). The paucity of methodologies for the nucleophilic addition to β -substituted alkenyl-heteroaromatic compounds is rooted in the intrinsically lower reactivity of these compounds, due to the relatively weak activation from the heteroaromatic moiety (13, 14). Furthermore, the numerous examples of nonasymmetric additions to vinyl-substituted heteroaromatic compounds indicate that the presence of a β -substituent decreases the reactivity further, presumably because of the steric hindrance it introduces.

We decided to explore the addition of Grignard reagents to β -substituted conjugated alkenyl-heteroaromatic compounds. Inexpensive and readily available Grignard reagents are some of the most commonly used organometallics in synthetic chemistry (20), especially in copper-catalyzed asymmetric conjugate addition to a variety of Michael acceptors (9–12). We reasoned

Stratingh Institute for Chemistry, 9747 AG Groningen, Netherlands.

*Corresponding author. Email: s.harutyunyan@rug.nl

that the high reactivity of Grignard reagents might be able to overcome the low reactivity of the β -substituted alkenyl heteroaromatics, and thus provide a solution to this long-standing challenge.

Here, we report an operationally simple, chemoselective, and highly enantioselective transformation of a wide range of β -substituted conjugated alkenyl-heteroaromatics to their corresponding chiral products via a copper-catalyzed addition of Grignard reagents, promoted by Lewis acid. Initially, we examined the reactivity of 2-styrylbenzoxazole (**1a**) toward EtMgBr (Et, ethyl) to produce racemic product **2a** (Fig. 1 and table S1). In the presence of CuBr·SMe₂ (Me, methyl), full conversion was not achieved and a complex mixture resulted after 24 hours at -25°C , which confirms the markedly lower reactivity of β -substituted alkenyl-heteroaromatic substrates

relative to typical Michael acceptors. Chiral ferrocenyl diphosphine ligand **L1** (Fig. 1A) did not improve the results.

The activation of electrophilic substrates toward nucleophilic addition is commonly achieved using Lewis acids (LAs) (21–23). We anticipated that LA activation of alkenyl-heteroaromatic substrates could be a viable strategy to overcome the reactivity issues. During our previous studies, focused on the synthesis of silyl-substituted chiral tertiary alcohols via addition of Grignard reagents to acyl silanes, we used LA mixtures to promote the addition over the reduction pathway (24). We also learned that LAs are compatible with both chiral copper catalysts and Grignard reagents, as long as reactions are carried out at temperatures below -50°C . Inspired by these findings, we set out to evaluate the effect of LA in the aforementioned reaction (table S1). To our surprise, no

conversion of **1a** was observed when EtMgBr was used as nucleophile in toluene at -78°C , in the presence of CuBr·SMe₂ and BF₃·OEt₂ as LA. However, the addition of chiral ligand **L1** led to the desired product **2a** with 59% isolated yield and 87% enantioselectivity. The effect of different LAs on the activation of **1a** was studied next; TiCl₄, trimethylsilyl chloride (TMSCl), MgBr₂, and trimethylsilyl trifluoromethanesulfonate (TMSOTf) were examined, but none performed better than BF₃·OEt₂ (table S1).

Having established the optimal LA for the activation of **1a** toward EtMgBr, we assessed the effect of the chiral ligand and different solvents (Fig. 1A and table S1). Chiral ligand screening revealed the sterically hindered ferrocenyl ligand **L2**, as well as phosphoramidite-type ligands **L6** and **L7**, to be ineffective, while ferrocenyl ligand **L3** furnished product **2a** in a modest yield and

A

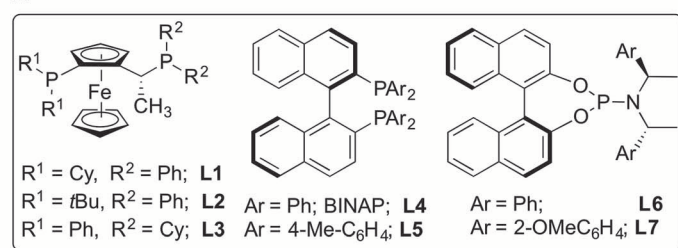
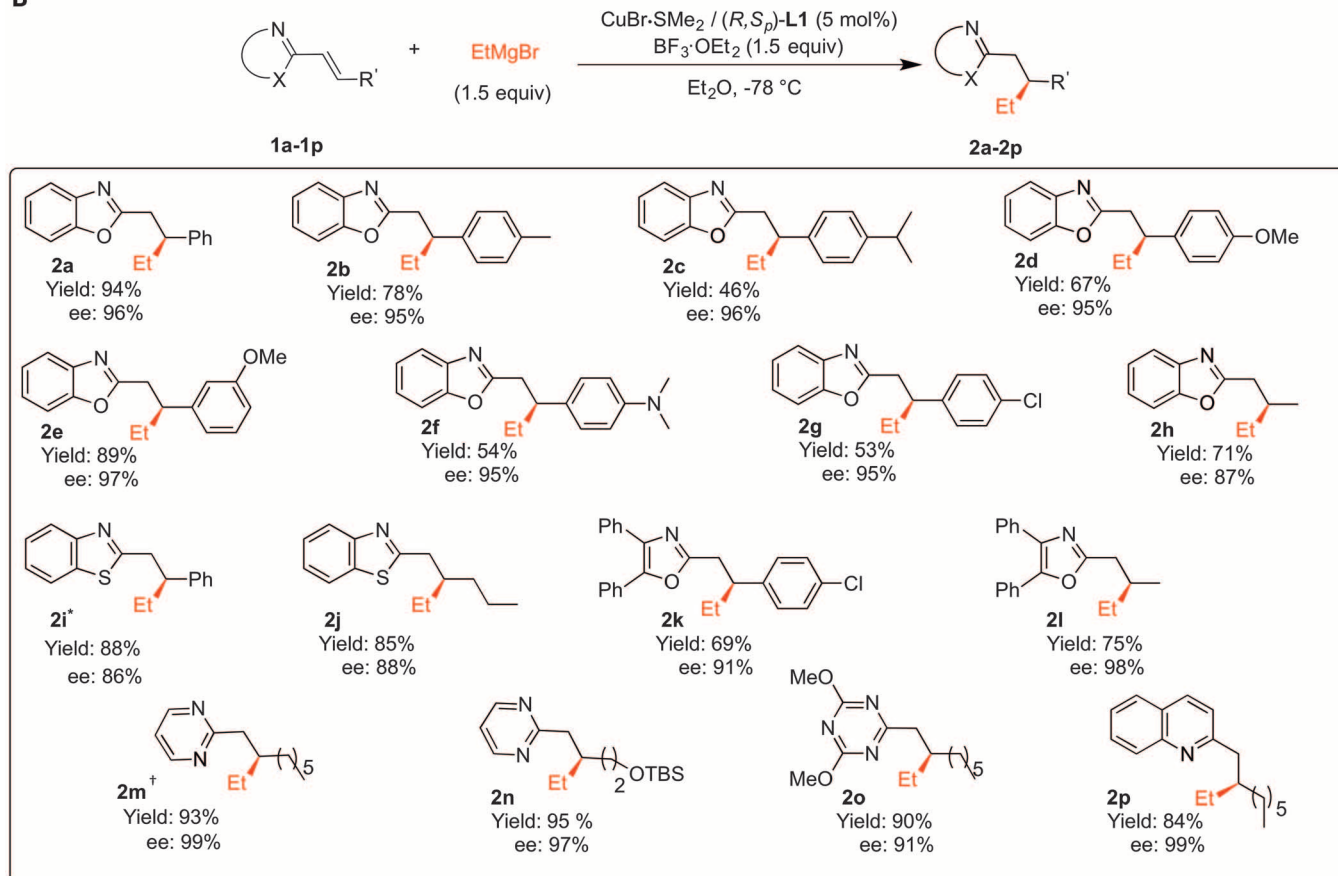


Fig. 1. Chiral ligands and heterocycle scope. (A) Structure of chiral ligands tested during the optimization studies. **(B)** Heterocycle scope. Reactions were conducted on a 0.2 mmol scale. Reported yields are for isolated products. Full conversion was obtained in all cases after 18 hours (isolated yields below 65% are due to the by-product derived from formal trapping of the product enolate by the substrate). Absolute configurations were assigned by analogy with the literature. *3 equiv of EtMgBr and 2.2 equiv of BF₃·OEt₂ were used in this case. †Using tBuOMe or toluene instead of diethyl ether provides the addition product **2m** with 92% and 80% isolated yields, respectively, and 99% ee.

B



enantioselectivity. Both binaphthyl diphosphine-type ligand **L4** (BINAP) and ligand **L5** performed better, furnishing the addition product with >90% ee.

We concluded that several chiral diphosphine ligands, in combination with a Cu(I) salt, are capable of effectively addressing the reactivity of the substrate and the enantioselectivity of the reaction. However, the superior yield obtained with ferrocenyl ligand **L1** prompted us to select it as the optimal ligand. Therefore, we studied the effect of different solvents (table S1) using the catalytic system derived from CuBr·SMe₂ and **L1**. With the exception of tetrahydrofuran, all solvents tested [Et₂O, *t*BuOMe (Bu, butyl), toluene, CH₂Cl₂] were effectively tolerated by the alkylation protocol, providing **2a** with excellent ee. The best results—excellent yield (94%) and enantioselectivity (96%)—were obtained in Et₂O. Thus, we

adopted the following optimized reaction conditions for the remainder of our experiments: CuBr·SMe₂/(*R,S*_p)-**L1** (5 mol %), Grignard reagent (1.5 equiv), BF₃·OEt₂ (1.5 equiv), 18 hours of reaction time at -78°C in Et₂O solvent.

For the evaluation of the substrate scope, we chose the reaction between alkenyl-heteroaromatic substrates **1a** to **1p** and EtMgBr (Fig. 1B). To assess the stereoelectronic effects of the β-substituent on the reaction, we synthesized a range of substrates **1a** to **1h**, derived from benzoxazole, and subjected them to our alkylation protocol.

The enantioselectivity of the reaction was found to be consistently high for substrates bearing both electron-rich and electron-poor substituents. However, the reactivity of the substrate proved to be strongly dependent on the nature of these substituents, providing products **2a** to **2g** with a

broad range of isolated yields and no clear trend. The addition of EtMgBr to benzoxazole **1h**, bearing an adjacent propenyl moiety, proceeded smoothly, furnishing the corresponding product **2h** in good yield and enantioselectivity. We also explored other heteroaromatic substrates, such as thiazoles (**1i** and **1j**), oxazoles (**1k** and **1l**), pyrimidines (**1m** and **1n**), triazines (**1o**), and quinoline (**1p**), and were pleased that our protocol was successful for all tested examples, furnishing the corresponding alkylated products with high yields and enantiopurities. This insensitivity to the presence of heteroatoms in the substrate, which might be expected to interfere with the stability of the chiral copper catalyst, makes the reaction remarkably general.

Next, we used two structurally different conjugated alkenyl-heteroaromatic compounds as

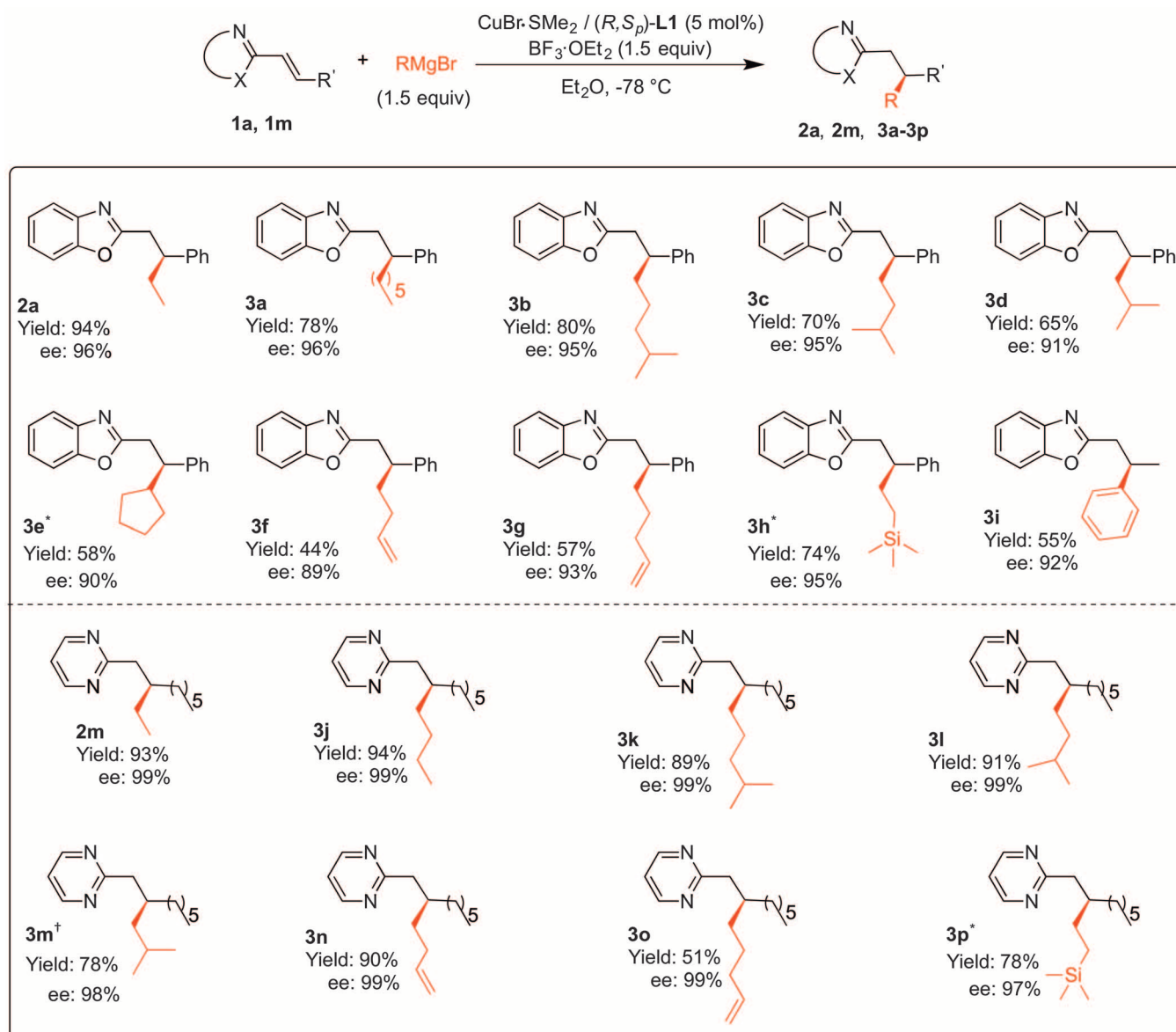


Fig. 2. Grignard scope. Reaction conditions were the same as specified in Fig. 1. *3 equiv of EtMgBr and 2 equiv of BF₃·OEt₂ were used in this case. †Solvent mixture Et₂O/CH₂Cl₂ (2:1) was used in this case.

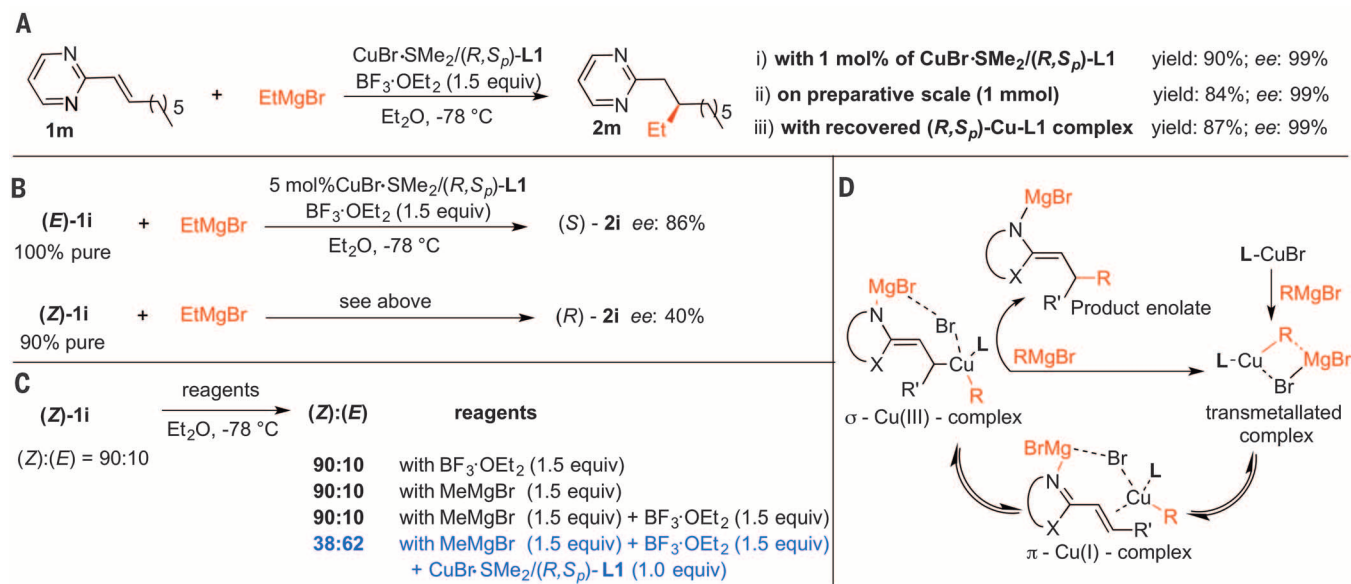


Fig. 3. Scale-up and mechanistic considerations. (A) Experiments (i) with 1 mol % of CuBr·SMe₂/(R,S_p)-L1, (ii) on a preparative scale, and (iii) with the recovered catalyst. (B) Catalytic asymmetric addition of EtMgBr to (E)-1i and (Z)-1i. (C) Studies on (E)/(Z) isomerization of 1i. (D) Hypothetical catalytic cycle.

substrates—1a and 1m, derived from benzoxazole and pyrimidine, respectively—to evaluate the scope of the nucleophile (Fig. 2). Nearly all Grignard reagents assessed provided excellent enantioselectivities. It was particularly gratifying that, where previous reports on additions to conjugated alkenyl-heteroaromatics were restricted to arylations, our catalytic system enabled the addition of a wide variety of alkyl Grignard reagents. Different chain lengths (Et, *n*-Bu, and *n*-hexyl) furnished the corresponding products (2a, 3a, 2m, and 3j) with excellent enantioselectivities (96 to 99%). Sterically more demanding α -, β -, γ -, and δ -branched Grignard reagents were also well tolerated, providing the corresponding products (3b to 3e; 3k to 3m) with enantioselectivities ranging from 90 to 99%.

The presence of an olefinic or trimethylsilyl moiety in the Grignard reagent was also tolerated, demonstrating that functionalized products (3f to 3h; 3n to 3p) can be obtained in high enantiopurity as well, albeit with moderate yields in a few cases. Only for the least reactive Grignard reagent, MeMgBr, was no conversion of either substrate obtained. Although the enantioselective arylation by organoboron reagents is a well-established methodology for this type of substrate (16), we were curious as to whether our protocol could tolerate aryl nucleophiles as well. To our satisfaction, we observed that the same protocol supported the addition of a phenyl group, and product 3i could be obtained with 92% enantioselectivity when PhMgBr was used as nucleophile. The addition of various Grignard reagents to the pyrimidine-derived substrate 1m provided the corresponding products 2m and 3j to 3p consistently with enantioselectivities above 97%. However, 1m is more sensitive than other heteroaromatic substrates to steric hindrance. For instance, no conversion of 1m was observed for the addition of *c*-pentyl-MgBr.

To examine the potential for the scaling up of these reactions, we performed a series of experiments for the addition of EtMgBr to substrate 1m: (i) with 1 instead of 5 mol % of CuBr·SMe₂/(R,S_p)-L1, (ii) on a preparative scale (1 mmol), and (iii) with recovered catalyst in the form of the Cu complex of (R,S_p)-L1 (Fig. 3A). In all three experiments, we were able to obtain the product 2m with excellent yield and enantioselectivity, without any erosion from the original values.

All heteroaromatic substrates prepared in this work were obtained with more than 99% (*E*)-configurational purity. Because the geometry of the double bond is expected to have substantial influence on the stereoselectivity in asymmetric reactions involving alkene transformations, we studied the effect of the alkene geometry in the addition of EtMgBr to (*E*)- and (*Z*)-stereoisomers of 2-styrylbenzothiazole (1i). Upon ultraviolet light irradiation of (*E*)-1i, its stereoisomer, (*Z*)-1i, was obtained with 90% purity. The enantioselective addition of EtMgBr to both (*E*)-1i and (*Z*)-1i, catalyzed by the CuBr·SMe₂/(R,S_p)-L1 catalyst, led to the addition product 2i with opposite configuration and distinctly different enantioselectivities [40% ee for (*Z*)-1i and 86% ee for (*E*)-1i] (Fig. 3B). The lower enantioselectivity obtained when (*Z*)-1i was used as substrate can be explained by partial isomerization of the substrate during the reaction, caused by the active catalyst. Unfortunately, the high reaction rate of the catalytic addition of EtMgBr to (*Z*)-1i prevented the analysis of the reaction mixture at different times. Using MeMgBr, with which no conversion occurs, we found that isomerization indeed took place, but only when CuBr·SMe₂, (R,S_p)-L1, BF₃·OEt₂, and MeMgBr were all present in solution (Fig. 3C). This isomerization is similar to that observed in the Cu(I)-catalyzed conjugate addition of Grignard reagents to α,β -unsaturated esters (25). By analogy, this isomerization supports the catalytic cycle (Fig. 3D)

involving transmetalation of the copper complex formed from CuBr·SMe₂ and L1, followed by reversible formation of the π -Cu(I) complex, the σ -Cu(III) complex, and finally, irreversible reductive elimination to form aza-enolate of 2i (25, 26).

The precise mechanism of this reaction remains under investigation, as the role of the LA additive is not clear. It seemed plausible for the LA to activate the heteroaromatic substrate toward the addition reaction. However, preliminary nuclear magnetic resonance (NMR) spectroscopic studies have revealed that new species are formed upon addition of BF₃·OEt₂ to each of the components of the reaction individually, indicating that the LA can modulate the reactivity of Grignard reagents and can also be involved in the structure of the catalytically active species.

REFERENCES AND NOTES

- J. A. Blacker, M. T. Williams, Eds., *Pharmaceutical Process Development: Current Chemical and Engineering Challenges* (Royal Society of Chemistry, 2011).
- E. N. Jacobsen, A. Pfaltz, H. Yamamoto, Eds., *Comprehensive Asymmetric Catalysis I–III* (Springer, 1999).
- I. Ojima, Ed., *Catalytic Asymmetric Synthesis* (Wiley, ed. 3, 2010).
- M. Gruttadauria, F. Giacalone, Eds., *Catalytic Methods in Asymmetric Synthesis: Advanced Materials, Techniques, and Applications* (Wiley, 2011).
- V. Farina, J. T. Reeves, C. H. Senanayake, J. J. Song, *Chem. Rev.* **106**, 2734–2793 (2006).
- G. G. Wu, F. X. Chen, K. Yong, in *Comprehensive Chirality*, E. M. Carreira, H. Yamamoto, Eds. (Elsevier, 2012), pp. 147–208.
- G. P. Howell, *Org. Process Res. Dev.* **16**, 1258–1272 (2012).
- T. Hayashi, K. Yamasaki, *Chem. Rev.* **103**, 2829–2844 (2003).
- A. Alexakis, N. Krause, S. Woodward, Eds., *Copper-Catalyzed Asymmetric Synthesis* (Wiley-VCH, 2014).
- S. R. Harutyunyan, T. den Hartog, K. Geurts, A. J. Minnaard, B. L. Feringa, *Chem. Rev.* **108**, 2824–2852 (2008).
- A. Alexakis, J. E. Backvall, N. Krause, O. Pàmies, M. Diéguez, *Chem. Rev.* **108**, 2796–2823 (2008).
- T. Jerphagnon, M. G. Pizzuti, A. J. Minnaard, B. L. Feringa, *Chem. Soc. Rev.* **38**, 1039–1075 (2009).
- D. A. Klumpp, *Synlett* **23**, 1590–1604 (2012).

14. D. Best, H. W. Lam, *J. Org. Chem.* **79**, 831–845 (2014).
15. I. N. Houpis et al., *Tetrahedron* **54**, 1185–1195 (1998).
16. G. Pattison, G. Piraux, H. W. Lam, *J. Am. Chem. Soc.* **132**, 14373–14375 (2010).
17. A. Saxena, H. W. Lam, *Chem. Sci.* **2**, 2326–2331 (2011).
18. L. Rupnicki, A. Saxena, H. W. Lam, *J. Am. Chem. Soc.* **131**, 10386–10387 (2009).
19. A. A. Friedman, J. Panteleev, J. Tsoung, V. Huynh, M. Lautens, *Angew. Chem. Int. Ed.* **52**, 9755–9758 (2013).
20. H. G. Richey, *Grignard Reagents: New Developments* (Wiley, 1999).
21. H. Yamamoto, Ed., *Lewis Acids in Organic Synthesis, Volume 1–2* (Wiley-VCH, 2000).
22. E. Marcantoni, M. Petrini, In *Lewis Acid Promoted Addition Reactions of Organometallic Compounds* (Elsevier, 2014), pp. 344–364.
23. Y. Yamamoto, S. Yamamoto, H. Yatagai, Y. Ishihara, K. Maruyama, *J. Org. Chem.* **47**, 119–126 (1982).
24. J. Rong, R. Oost, A. Desmarchelier, A. J. Minnaard, S. R. Harutyunyan, *Angew. Chem. Int. Ed.* **54**, 3038–3042 (2015).
25. S. R. Harutyunyan et al., *J. Am. Chem. Soc.* **128**, 9103–9118 (2006).
26. N. Yoshikai, E. Nakamura, *Chem. Rev.* **112**, 2339–2372 (2012).

ACKNOWLEDGMENTS

Supported by Netherlands Organization for Scientific Research NWO-Vidi and ECHO grants (S.R.H.) and

Ministry of Education, Culture and Science Gravity program grant 024.001.035 (S.R.H.). We thank J. T. A. de Jong, B. Maciá, and J. F. Collados for helpful comments on the manuscript.

SUPPLEMENTARY MATERIALS

www.sciencemag.org/content/352/6284/433/suppl/DC1
Materials and Methods

Table S1

NMR spectra

References (27–35)

6 January 2016; accepted 22 March 2016
10.1126/science.aaf1983

MAGNETISM

Atomic-scale control of graphene magnetism by using hydrogen atoms

Héctor González-Herrero,^{1,2} José M. Gómez-Rodríguez,^{1,2,3} Pierre Mallet,^{4,5} Mohamed Moaied,^{1,6} Juan José Palacios,^{1,2,3} Carlos Salgado,¹ Miguel M. Ugeda,^{7,8} Jean-Yves Veuillen,^{4,5} Félix Yndurain,^{1,2,3} Iván Brihuega^{1,2,3*}

Isolated hydrogen atoms absorbed on graphene are predicted to induce magnetic moments. Here we demonstrate that the adsorption of a single hydrogen atom on graphene induces a magnetic moment characterized by a ~20-millielectron volt spin-split state at the Fermi energy. Our scanning tunneling microscopy (STM) experiments, complemented by first-principles calculations, show that such a spin-polarized state is essentially localized on the carbon sublattice opposite to the one where the hydrogen atom is chemisorbed. This atomically modulated spin texture, which extends several nanometers away from the hydrogen atom, drives the direct coupling between the magnetic moments at unusually long distances. By using the STM tip to manipulate hydrogen atoms with atomic precision, it is possible to tailor the magnetism of selected graphene regions.

Adding magnetism to the long list of graphene's capabilities has been pursued since this material was first isolated (1). From a theoretical point of view, magnetic moments in graphene can be induced by removing a single p_z orbital from the π -graphene system; this removal creates a single π -state at the Fermi energy (E_F) around the missing orbital. The double occupation of this state by two electrons with different spins is forbidden by the electrostatic Coulomb repulsion; namely, once an electron occupies the state, a second one with opposite spin needs to "pay" an extra energy U . This leaves a single electron occupying the state and therefore a net magnetic moment (2–6). The strength of U , which determines the spin splitting, depends

on the spatial localization of the state, because this defines the proximity of the electrons (Fig. 1A). In contrast to magnetic moments of a strongly localized atomic character that are commonly found in magnetic materials, these induced moments are predicted to extend over several nanometers, suggesting a strong direct coupling between them at unusually long distances. The coupling rules between the induced magnetic moments are also expected to be simple. Because of the bipartite atomic structure of graphene—which consists of two equivalent triangular sublattices, labeled A and B—and according to Lieb's theorem (7), the ground state of the system possesses a total spin given by $S = 1/2 \times |N_A - N_B|$, where N_A and N_B are the number of p_z orbitals removed from each sublattice (4, 8, 9). Thus, to generate a net magnetic moment in a particular graphene region, a different number of p_z orbitals from each sublattice needs to be locally removed.

Many theoretical proposals have been put forward on this subject, involving zigzag edges, graphene clusters, grain boundaries, and atomic defects (2, 4, 5, 8–11). Experimentally, the removal of p_z orbitals from the π system has been achieved by randomly creating atomic vacancies or adsorbing adatoms (12–16). However, removing those p_z orbitals in a directed man-

ner has turned out to be challenging. In this work, we relied on the simplest (albeit demanding) experimental approach to remove a single p_z orbital from the graphene network by means of the adsorption of a single H atom. Atomic H chemisorbs on graphene on top of carbon atoms, changing the initial sp^2 hybridization of carbon to essentially sp^3 (17, 18) and effectively removing the corresponding p_z orbital (4, 19, 20). In this sense, chemisorbed H atoms are equivalent to carbon vacancies (4, 12, 14) but with the advantage that, unlike vacancies, they leave the graphene atomic lattice with no unsaturated dangling bonds, preserving the threefold symmetry. Our experiments, supported by ab initio calculations, provide a comprehensive picture of the origin, coupling, and manipulation of the magnetism induced by H atoms on graphene layers.

We deposited atomic H on graphene grown on a SiC(000-1) substrate (21). In this system, the rotational disorder of the graphene layers electronically decouples the π bands, leading to a stacking of essentially isolated graphene sheets (22–24). Scanning tunneling microscopy (STM) visualizes single H atoms as a bright protrusion (apparent height, ~2.5 Å) surrounded by a complex threefold $\sqrt{3} \times \sqrt{3}$ pattern that is rotated 30° degrees with respect to the graphene lattice. (25, 26) [Fig. 1B and section 1 in (27)]. The resolution that we achieved allowed us to identify the adsorbate as a single H atom and to determine the atomic site (and thus the corresponding atomic sublattice) where each H atom was chemisorbed by means of comparison with density functional theory (DFT)-simulated STM images [Fig. 1D and section 1 in (27)]. As depicted in Fig. 1A, graphene magnetic moments induced by H adsorption should be reflected in the appearance of a spin-polarized state at E_F , which, according to DFT calculations, should be characterized by two narrow peaks in the density of states (DOS) (Fig. 1E) (4).

Differential conductance spectra (dI/dV ; I , current; V , sample voltage) probe the energy-resolved local DOS under the STM tip position and thus are ideal for investigating this question. Figure 1C shows two dI/dV spectra, measured at 5 K, that are representative of our findings. The dI/dV spectra measured on clean graphene, located far enough away from defects, have the characteristic featureless V shape of graphene, with a minimum at E_F indicating the position of

¹Departamento de Física de la Materia Condensada, Universidad Autónoma de Madrid, E-28049 Madrid, Spain.

²Condensed Matter Physics Center (IFIMAC), Universidad Autónoma de Madrid, E-28049 Madrid, Spain. ³Instituto Nicolás Cabrera, Universidad Autónoma de Madrid, E-28049 Madrid, Spain.

⁴Université Grenoble Alpes, Institut NEEL, F-38042 Grenoble, France. ⁵Centre National de la Recherche Scientifique (CNRS), Institut NEEL, F-38042 Grenoble, France.

⁶Department of Physics, Faculty of Science, Zagazig University, 44519 Zagazig, Egypt. ⁷CIC nanoGUNE, 20018 Donostia-San Sebastian, Spain. ⁸Ikerbasque, Basque Foundation for Science, 48013 Bilbao, Spain.

*Corresponding author. Email: ivan.brihuega@uam.es

the Dirac point E_D . The dI/dV spectra measured on top of single H atoms have two narrow peaks, one below and one above E_F , separated in energy by a splitting of ~ 20 meV. We attribute these two features to the spin-polarized state, in which the Coulomb repulsion is large enough to fully separate the two spin components. The observed charge neutrality (the splitting is essentially symmetric around E_F) and the well-defined peak splitting indicate the complete spin polarization of the state. DFT calculations show that the magnetic moment associated with the unpaired electron that is left over in the graphene system after H adsorption would be 1 bohr magneton (fig. S7). Our interpretation of the experiment is fully supported by DFT calculations, as can be seen in Fig. 1E, which shows the expected DOS for a single H atom in a graphene super cell containing 218 carbon atoms. The theoretical energy splitting depends on the size of the graphene super cell (5). Our calculations show that the splitting decays with the size of the graphene super cell, suggesting a small but finite splitting for the isolated H [section 9 in (27)],

which is in agreement with the experimental observations.

An independent proof that the split dI/dV peaks are induced by magnetism can be obtained by changing the occupation of the split states (n_\uparrow , n_\downarrow) by means of graphene doping. This is based on the idea originally proposed in (28), according to which the transition from a magnetic state to a nonmagnetic one can be realized by tuning the energy position of the impurity level with respect to the Fermi level [section 3A in (27) gives a detailed description of this system in terms of the Anderson impurity model]. In graphene, the impurity level (zero-energy mode) should be dictated by the position of E_D [$E_\uparrow = E_D + U(n_\downarrow - 1/2)$; $E_\downarrow = E_D + U(n_\uparrow - 1/2)$] (29), which can be tuned by doping the graphene layers. For a large enough electron (hole) doping, the occupation of both the n_\uparrow and n_\downarrow levels can be tuned to 1 (0), in which case the energy levels will be degenerate, leading to a single nonmagnetic state close to E_D ($E_\uparrow = E_\downarrow \approx E_D$). In Fig. 1F, we show how graphene doping affects the splitting of the H-induced magnetic state. Our dI/dV spectra demonstrate that both

n- and p-type graphene doping cause the splitting of the H-induced graphene state to vanish; only one sharp peak appears at E_D , which we ascribe to a transition to the nonmagnetic state. This interpretation is fully supported by our DFT calculations for doped graphene layers [Fig. 1F and section 3B in (27)]. If the split peaks appearing in neutral graphene after H adsorption had an origin that was not associated with a magnetic moment (i.e., a single-electron origin), we would observe a rigid shift of the peak position with doping, and the doublet structure would remain unmodified [section 3 in (27)]. Our results are consistent with the case of sp^3 defects in graphene, for which the possibility to control graphene magnetic moments by molecular doping has been reported (15).

We explored, with atomic precision, the spatial extension of the spin-polarized electronic state induced by H atoms in undoped graphene. The relatively modest 20-meV energy splitting observed in our experiments suggests a large spatial extension of the magnetic state (Fig. 1A). Figure 2A shows a conductance map plotted with

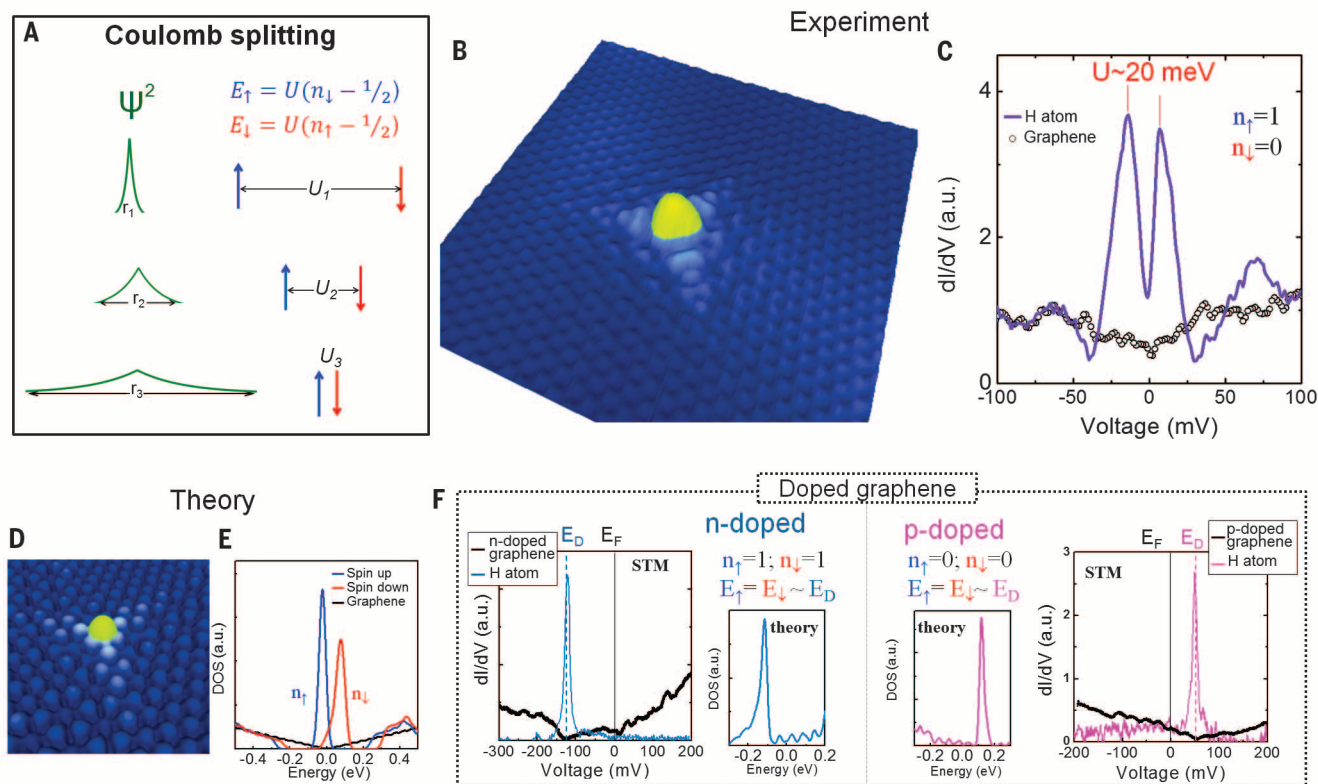


Fig. 1. Spin-split state induced by atomic H on graphene. (A) Illustration of the origin of the spin-split state in terms of its spatial extension (r) given by the square of its wave function ψ^2 , and the corresponding electrostatic Coulomb repulsion U . Arrows indicate the energy position of spin-up (n_\uparrow) and spin-down (n_\downarrow) levels. For a fully polarized one-electron state, the majority level spin is filled and the minority one is empty; therefore, $n_\uparrow = 1$ and $n_\downarrow = 0$, and the energy splitting ($E_\downarrow - E_\uparrow$) is given by U [section 3 in (27)]. (B) STM topography of a single H atom chemisorbed on neutral graphene (0.2 V, 0.1 nA, 7×7 nm 2). (C) dI/dV spectrum measured on the H atom, showing a fully polarized peak at E_F and measured on bare graphene far from the H atom (a.u., arbitrary units). The spectra

were acquired at a nominal junction impedance of 2 gigaohms (~ 100 mV, 50 pA). (D and E) DFT-simulated STM image (D) and DOS (E) of an H atom chemisorbed on neutral graphene. (F) dI/dV spectra and DFT calculation of the DOS induced by a single H atom on n- (left) and p-type (right) doped graphene. The minimum of the dI/dV spectra, acquired on bare graphene (black curves), determines the position of E_D . The spectra were acquired at a nominal junction impedance of 8 gigaohms (~ 400 mV, 50 pA). STM data were acquired and processed using the WSxM software (36). Calculations for all simulated images were performed at the same energy as in the corresponding experimental conditions. All experimental data were acquired at 5 K.

respect to distance and energy [$dI/dV(x, E)$], with the distance x measured along the 6-nm line that crosses the H atom in Fig. 2B. The state extends several nanometers away from the H atom, confirming that it is a quasi-localized graphene state (3). It presents strong atomic-scale modulations of the peak intensities, with maxima (bright yellow features in the conductance map) corresponding to carbon atoms in the sublattice opposite to the one on which H is chemisorbed. On carbon sites

in the same sublattice as H chemisorption, the peaks vanish almost completely (fig. S11). Because our results show a complete spin polarization of the state, the spatial evolution of the height of the dI/dV occupied peak provides the spatial distribution of the local magnetic moment induced by H chemisorption [DFT calculations in Fig. 2, C and D, and section 4 in (27)]. This is further illustrated in Fig. 2E, which shows that the magnetic moment is essentially induced on the carbon

atoms in the graphene sublattice opposite to the locus of H chemisorption.

The large extension of the local magnetic moments associated with H chemisorption suggests that long-range magnetic interactions mediated by direct exchange should take place. This is different from substrate-mediated interactions such as the Ruderman-Kittel-Kasuya-Yosida interaction, because in this case the coupling results from the direct overlap of magnetized graphene

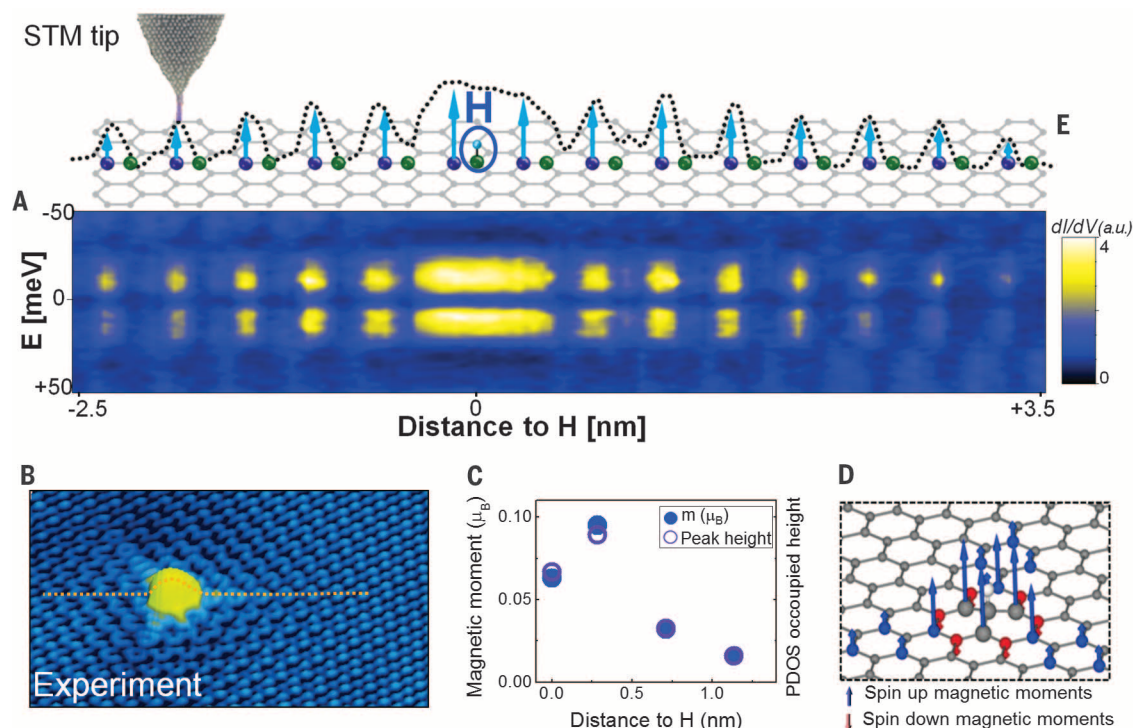


Fig. 2. Spatial extension of the spin-polarized electronic state induced by H atoms in undoped graphene. (A) Conductance map [$dI/dV(x, E)$] along the dashed line in (B). The spectra were acquired at a nominal junction impedance of 3 gigaohms (100 mV, 33 pA). (B) STM topography of a single H atom on graphene (0.2 V, 0.1 nA, $7 \times 5 \text{ nm}^2$). (C) Comparison between DFT calculations for the local magnetic moment and the height of the occupied projected DOS (PDOS) peak, calculated on different carbon atoms [section 4 in (27)]. (D) Calculated magnetic

moments induced by H chemisorption (the lengths of the arrows signify the relative magnitudes of the magnetic moments). (E) Schematic of the graphene structure along the dashed line in (B). Green (purple) balls indicate the positions of carbon atoms belonging to the same (opposite) sublattice with respect to the locus of H chemisorption. The dotted line shows the evolution of the height of the measured occupied peak, and the arrows show the relative magnetic moment contribution of each carbon atom. All experimental data were acquired at temperature $T = 5 \text{ K}$.

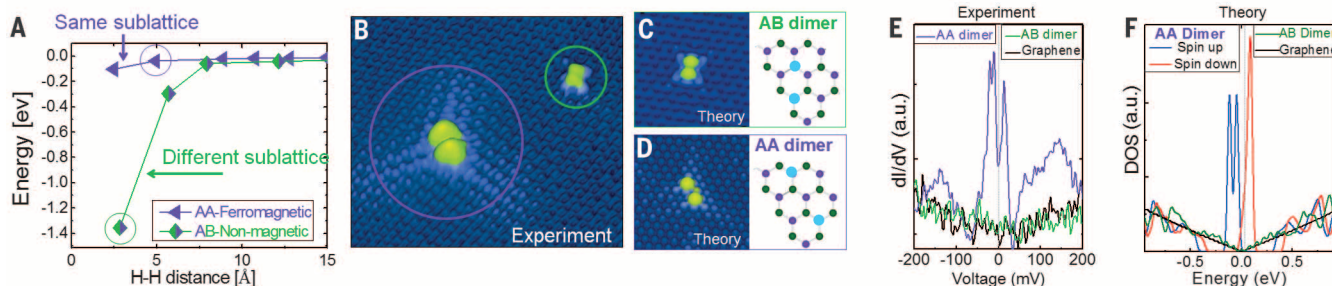


Fig. 3. Sublattice dependence of the magnetic coupling between neighboring H atoms. (A) Calculated total energy, relative to twice the adsorption energy of a single H atom, and magnetic state of a pair of H atoms adsorbed on the same (AA dimer) and different (AB dimer) sublattices, plotted as a function of the H-H distance. (B) STM image showing two different pairs of H atoms, with one pair in an AA (purple circle) and the other pair in an AB (green circle)

configuration (0.2 V, 0.1 nA, $7.8 \times 6.6 \text{ nm}^2$). (C) Calculated STM image of the AB dimer and (D) the AA dimer, with the corresponding diagrams for H atoms (blue balls) on graphene (purple and green balls). (E) Experimental dI/dV spectra and (F) calculated DOS for the AA dimer, AB dimer, and clean graphene. The spectra were acquired at a nominal junction impedance of 8 gigaohms (-400 mV , 50 pA). All experimental data were acquired at 5 K.

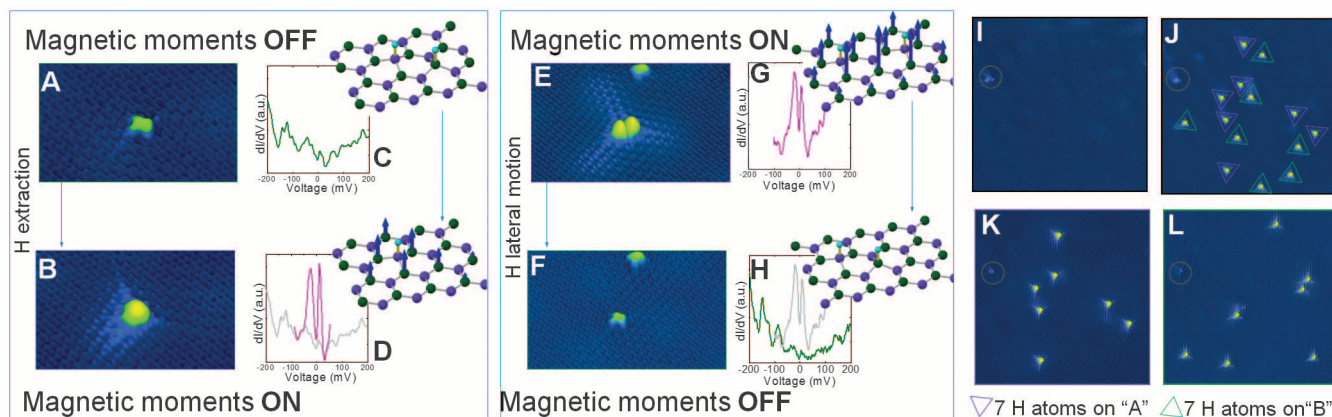


Fig. 4. Manipulation of graphene local magnetic moments by STM. (A) STM image of an H dimer in an AB configuration. (B) STM image after the removal of one H atom. (C) dI/dV spectra measured on the AB dimer in (A) and (D) the single H atom in (B). The spectra were acquired at a nominal junction impedance of 4 gigohms (200 mV, 50 pA). The insets show the corresponding DFT calculations for H atoms (blue balls) on graphene (purple and green balls), with blue arrows being the magnetic moments induced on graphene. (E) STM image of an H dimer in an AA configuration. (F) STM image after laterally moving one H atom. (G) dI/dV spectra measured on the AA dimer in (E) and (H) the AB

dimer in (F). The spectra were acquired at a nominal junction impedance of 4 gigohms (200 mV, 50 pA). An additional dI/dV spectrum that is better resolved in the vicinity of E_F measured on the AA dimer in (E) is shown in fig. S20. Insets show the corresponding DFT calculations. (I to L) STM images showing the same graphene region during different steps of a manipulation experiment involving a large number of H atoms. The point defect outlined with a gray circle is used as a reference. Tunneling parameters were 0.2 V, 0.1 nA, and $6.5 \times 4.0 \text{ nm}^2$ for (A) and (B); 0.2 V, 0.1 nA, and $9.5 \times 5.5 \text{ nm}^2$ for (E) and (F); and 0.4 V, 0.03 nA, and $28 \times 28 \text{ nm}^2$ for (I) to (L). All experimental data were acquired at $T = 5 \text{ K}$.

states. In addition, the critical sublattice dependence that we observed for the spin-polarized peak implies that the magnetic coupling should be radically different depending on whether H atoms are adsorbed on the same or different sublattices. Consistent with this expectation, our DFT calculations reveal that two H atoms chemisorbed on the same sublattice (AA dimer) show ferromagnetic coupling with a total spin $S = 1$, whereas for H atoms on different sublattices (AB dimer), the solution is nonmagnetic. This result is reproduced for all possible H-H arrangements up to the largest distances ($\sim 1.5 \text{ nm}$) achievable with our super cell sizes (Fig. 3A). For a separation of 1.5 nm, the computed exchange energy for AA dimers is $\sim 35 \text{ meV}$ [section 5 in (27)]. Furthermore, the total energy of all H dimers that we studied is lower than that of two isolated H atoms (Fig. 3A), confirming the observed tendency of H to form dimers on graphene surfaces at high enough H concentrations (30–32).

To test this scenario experimentally, we explored the local electronic structure of many different H dimers with high-resolution scanning tunneling spectroscopy (STS). The STM image in Fig. 3B shows two H dimers in AA (purple circle) and AB (green circle) configurations; the corresponding calculated STM images are shown in Fig. 3, C and D. The dI/dV spectra acquired on the AB dimer (green line in Fig. 3E) show a featureless local DOS that is indistinguishable from that measured on bare graphene (black), as would be expected for a nonmagnetic configuration. In contrast, dI/dV spectra measured on the AA dimer (purple) show the split state in the vicinity of E_F , as expected for a ferromagnetic coupling between the H atoms. As shown in Fig. 3F, our calculated DOS reproduce these observations, confirming the ferromagnetic (nonmagnetic) nature of the AA (AB) dimer. For all H dimers mea-

sured in this study, AA dimers presented a fully split state close to E_F , which was absent in AB dimers (fig. S12). Our STS data show that this sublattice-dependent magnetic coupling persists for very long distances, even for H dimers separated by more than 1 nm [section 5 in (27)].

We further demonstrated the capability of inducing magnetic moments on selected graphene regions by using STM to perform atomic manipulations (33–35). We proved that individual H atoms can be removed, laterally moved, and even deposited on graphene surfaces with atomic precision to ultimately tailor their local magnetic state [section 6 in (27)]. Figure 4 shows two representative examples of these manipulation experiments, in which the local graphene magnetism was selectively switched on and off. The graphene region in Fig. 4A shows two H atoms in an AB dimer configuration. Our STS data measured on those H atoms (Fig. 4C) show that this AB dimer configuration does not induce any magnetism on the graphene layer, in good agreement with the coupling rules previously discussed. Figure 4B shows the same graphene region as in Fig. 4A, after the controlled extraction of one H atom by carefully approaching it with the STM tip. As shown in Fig. 4D, a spin-split state immediately emerges on the graphene layer after the H removal, confirming the creation of a local magnetic moment in graphene. The insets show the corresponding DFT calculations of the resulting magnetic moment for each situation. We next performed a lateral manipulation on the H dimer, shown in the central region of Fig. 4E. Initially, the dimer was in an AA configuration, with both H atoms chemisorbed on the same carbon sublattice. The STS spectrum for that configuration (Fig. 4G) shows the presence of a spin-split state, as expected for ferromagnetic coupling. To switch off the graphene magnetic

moments induced by this H dimer, we turned it into a nonmagnetic AB dimer configuration by laterally moving one of its H atoms to the opposite sublattice. Figure 4F shows the same graphene region after the H manipulation (the AB dimer in the upper part of the image serves as reference). The STS spectrum measured on the constructed AB dimer shows the disappearance of the polarized peaks, indicating that local graphene magnetism was effectively switched off.

Last, we explored the possibility of selectively tuning the collective magnetic moment in a graphene region by inducing an imbalance between H atoms on opposing sublattices A and B. For this purpose, we systematically manipulated a large number of H atoms [section 6 in (27)]. In Fig. 4, I to L, we present an example in which we first removed all H atoms from a graphene region by using the STM tip (Fig. 4I). Then, we selectively deposited 14 H atoms on this same region to reach a configuration with seven H atoms chemisorbed on each graphene sublattice (Fig. 4J). Our experimental findings and existing calculations (4, 7) indicate that a very low (if any) net magnetic moment should be expected on this region, because of these equal sublattice populations. Next, by selectively removing all the H atoms chemisorbed on sublattice B, we created a ferromagnetic configuration with the seven remaining H atoms on sublattice A (Fig. 4K). As the final step, we combined several manipulation processes to reverse the situation and construct an H arrangement with all seven H atoms chemisorbed on sublattice B (Fig. 4L). The degree of complexity shown in our manipulation experiments demonstrates the high reproducibility of the procedure, which paves the way to the realization of atomically controlled experiments in graphene magnetism, an area

that has thus far been restricted to a purely theoretical framework.

REFERENCES AND NOTES

1. K. S. Novoselov *et al.*, *Science* **306**, 666–669 (2004).
2. P. O. Lehtinen, A. S. Foster, Y. Ma, A. V. Krasheninnikov, R. M. Nieminen, *Phys. Rev. Lett.* **93**, 187202 (2004).
3. V. M. Pereira, F. Guinea, J. M. Lopes dos Santos, N. M. R. Peres, A. H. Castro Neto, *Phys. Rev. Lett.* **96**, 036801 (2006).
4. O. V. Yazyev, L. Helm, *Phys. Rev. B* **75**, 125408 (2007).
5. O. V. Yazyev, *Rep. Prog. Phys.* **73**, 056501 (2010).
6. E. J. G. Santos, A. Ayuela, D. Sanchez-Portal, *New J. Phys.* **14**, 043022 (2012).
7. E. H. Lieb, *Phys. Rev. Lett.* **62**, 1201–1204 (1989).
8. J. Fernández-Rossier, J. J. Palacios, *Phys. Rev. Lett.* **99**, 177204 (2007).
9. J. J. Palacios, J. Fernández-Rossier, L. Brey, *Phys. Rev. B* **77**, 195428 (2008).
10. M. Fujita, K. Wakabayashi, K. Nakada, K. Kusakabe, *J. Phys. Soc. Jpn.* **65**, 1920–1923 (1996).
11. C. G. Tao *et al.*, *Nat. Phys.* **7**, 616–620 (2011).
12. M. M. Ugeda, I. Brihuega, F. Guinea, J. M. Gómez-Rodríguez, *Phys. Rev. Lett.* **104**, 096804 (2010).
13. R. R. Nair *et al.*, *Nat. Phys.* **8**, 199–202 (2012).
14. K. M. McCreary, A. G. Swartz, W. Han, J. Fabian, R. K. Kawakami, *Phys. Rev. Lett.* **109**, 186604 (2012).
15. R. R. Nair *et al.*, *Nat. Commun.* **4**, 2010 (2013).
16. J. Balakrishnan, G. Kok Wai Koon, M. Jaiswal, A. H. Castro Neto, B. Özyilmaz, *Nat. Phys.* **9**, 284–287 (2013).
17. L. Jelaouica, V. Sidis, *Chem. Phys. Lett.* **300**, 157–162 (1999).
18. X. W. Sha, B. Jackson, *Surf. Sci.* **496**, 318–330 (2002).
19. D. W. Boukhvalov, M. I. Katsnelson, A. I. Lichtenstein, *Phys. Rev. B* **77**, 035427 (2008).
20. D. Soriano *et al.*, *Phys. Rev. Lett.* **107**, 016602 (2011).
21. F. Varchon, P. Mallet, L. Magaud, J. Y. Veuillen, *Phys. Rev. B* **77**, 165415 (2008).
22. M. Sprinkle *et al.*, *Phys. Rev. Lett.* **103**, 226803 (2009).
23. G. H. Li *et al.*, *Nat. Phys.* **6**, 109–113 (2010).
24. G. Trambly de Laissardiére, D. Mayou, L. Magaud, *Nano Lett.* **10**, 804–808 (2010).
25. H. A. Mizes, J. S. Foster, *Science* **244**, 559–562 (1989).
26. P. Ruffieux, O. Groning, P. Schwallier, L. Schlapbach, P. Groning, *Phys. Rev. Lett.* **84**, 4910–4913 (2000).
27. Materials and methods are available as supplementary materials on Science Online.
28. P. W. Anderson, *Phys. Rev.* **124**, 41–53 (1961).
29. B. Uchoa, V. N. Kotov, N. M. R. Peres, A. H. Castro Neto, *Phys. Rev. Lett.* **101**, 026805 (2008).
30. L. Hornekar *et al.*, *Phys. Rev. Lett.* **97**, 186102 (2006).
31. Z. Slijvančanin *et al.*, *J. Chem. Phys.* **131**, 084706 (2009).
32. R. Balog *et al.*, *J. Am. Chem. Soc.* **131**, 8744–8745 (2009).
33. D. M. Eigler, E. K. Schweizer, *Nature* **344**, 524–526 (1990).
34. T. C. Shen *et al.*, *Science* **268**, 1590–1592 (1995).
35. A. A. Khajetoorians *et al.*, *Science* **339**, 55–59 (2013).
36. I. Horcas *et al.*, *Rev. Sci. Instrum.* **78**, 013705 (2007).

ACKNOWLEDGMENTS

We thank V. Cherkov (Institut NEEL, CNRS, and Université Grenoble Alpes) for his help with the fabrication of samples of graphene grown on SiC, and we thank D. Wong (University of California–Berkeley) for his careful reading of the manuscript. This work was supported by Spain's Ministerio de Economía y Competitividad under grant nos. MAT2013-41636-P, CSD2010-00024, PCIN-2015-030, FIS2013-47328, and FIS2012-37549-C05-03; the European Union structural funds and the Comunidad de Madrid MAD2D-CM program under grant nos. S2013/MIT-3007 and P2013/MIT-2850; the Generalitat Valenciana under grant no. PROMETEO/2012/011; the CNRS PICS (Projets Internationaux de Coopération Scientifique) program under grant no. 6182; and the European Union FP7 (7th Framework Programme for Research and Technological Development) Graphene Flagship (grant 604391) and FLAG-ERA programs. The authors acknowledge the computer resources and assistance provided by the Centro de Computación Científica de la Universidad Autónoma de Madrid.

SUPPLEMENTARY MATERIALS

www.sciencemag.org/content/352/6284/437/suppl/DC1
Materials and Methods
Figs. S1 to S20
Movie S1
References (37–59)

3 November 2015; accepted 21 March 2016
10.1126/science.aad8038

QUANTUM OPTICS

Bell correlations in a Bose-Einstein condensate

Roman Schmied,^{1*} Jean-Daniel Bancal,^{2,4*} Baptiste Allard,^{1*} Matteo Fadel,¹ Valerio Scarani,^{2,3} Philipp Treutlein,^{1†} Nicolas Sangouard^{4†}

Characterizing many-body systems through the quantum correlations between their constituent particles is a major goal of quantum physics. Although entanglement is routinely observed in many systems, we report here the detection of stronger correlations—Bell correlations—between the spins of about 480 atoms in a Bose-Einstein condensate. We derive a Bell correlation witness from a many-particle Bell inequality involving only one- and two-body correlation functions. Our measurement on a spin-squeezed state exceeds the threshold for Bell correlations by 3.8 standard deviations. Our work shows that the strongest possible nonclassical correlations are experimentally accessible in many-body systems and that they can be revealed by collective measurements.

Parts of a composite quantum system can share correlations that are stronger than any classical theory allows (*1*). These so-called Bell correlations represent the most profound departure of quantum from classical physics and can be confirmed experimentally by showing that a Bell inequality is violated by the system. The existence of Bell correlations at spacelike separations refutes local causality (*2*); thus, Bell correlations are also called non-local correlations. Moreover, they are a key resource for quantum technologies such as quantum key distribution and certified randomness generation (*3*). Bell correlations have so far been detected between up to 14 ions (*4*), four photons (*5, 6*), two neutral atoms (*7*), two solid-state spin qubits (*8*), and two Josephson phase qubits (*9*). Even though multipartite Bell inequalities are known (*1, 10–12*), the detection of Bell correlations in larger systems is challenging.

A central challenge in quantum many-body physics is to connect the global properties of a system to the underlying quantum correlations between the constituent particles (*13, 14*). For example, recent experiments in quantum metrology have shown that spin-squeezed states of atomic ensembles can enhance the precision of interferometric measurements beyond classical limits (*15–18*). This enhancement requires entanglement between atoms in the ensemble, which can be revealed by measuring an entanglement witness that involves only collective measurements on the entire system (*15, 19–22*). The role of Bell correlations in many-body systems, on the other hand, is largely unknown.

Whereas all Bell-correlated states are entangled, the converse is not true (*1*). In recent theoretical work, a family of Bell inequalities was derived that are symmetric under particle exchange and involve only first- and second-order correlation functions (*23*). It was suggested that this could enable the detection of Bell correlations by collective measurements on spin ensembles. Acting on this proposal, we derive a collective witness observable that is tailored to detect Bell correlations in spin-squeezed states of atomic ensembles. We report a measurement of this witness on 480 ultracold rubidium atoms, revealing Bell correlations in a many-body system.

We derive our Bell correlation witness in the context of a Bell test where N observers (indexed by $i = 1 \dots N$) each repeatedly perform one of two possible local measurements $\mathcal{M}_0^{(i)}$ or $\mathcal{M}_1^{(i)}$ on their part of a composite system and observe one of two possible outcomes $a_i = \pm 1$. For example, the system could be an ensemble of atomic spins where each observer is associated with one atom and the measurements correspond to spin projections along different axes. When all observers choose to measure \mathcal{M}_0 , one determines experimentally the sum of their average outcomes $S_0 = \sum_{i=1}^N \langle \mathcal{M}_0^{(i)} \rangle$ and correlations $S_{00} = \sum_{i,j=1(i \neq j)}^N \langle \mathcal{M}_0^{(i)} \mathcal{M}_0^{(j)} \rangle$ [see section 1 of the supplementary materials (*24*) for a definition in terms of measured frequencies]. Similarly, $S_{11} = \sum_{i,j=1(i \neq j)}^N \langle \mathcal{M}_1^{(i)} \mathcal{M}_1^{(j)} \rangle$ is determined when all observers choose \mathcal{M}_1 . A more complex correlation $S_{01} = \sum_{i,j=1(i \neq j)}^N \langle \mathcal{M}_0^{(i)} \mathcal{M}_1^{(j)} \rangle$ is quantified by letting all pairs of observers choose opposite measurements, which requires repeated observations of identically prepared states of the system because some of these measurements are mutually exclusive. In (*23*), a Bell inequality was derived that contains only these symmetric one- and two-body correlators.

$$2S_0 + \frac{1}{2}S_{00} + S_{01} + \frac{1}{2}S_{11} + 2N \geq 0 \quad (1)$$

If an experiment violates this inequality, the conditional probabilities $P(a_1, \dots, a_N | x_1, \dots, x_N)$

¹Quantum Atom Optics Laboratory, Department of Physics, University of Basel, Klingelbergstrasse 82, 4056 Basel, Switzerland. ²Centre for Quantum Technologies, National University of Singapore, 3 Science Drive 2, Singapore 117543. ³Department of Physics, National University of Singapore, 2 Science Drive 3, Singapore 117542. ⁴Quantum Optics Theory Group, Department of Physics, University of Basel, Klingelbergstrasse 82, 4056 Basel, Switzerland.

*These authors contributed equally to this work. †Corresponding author. Email: philipp.treutlein@unibas.ch (P.T.), nicolas.sangouard@unibas.ch (N.S.)

to obtain measurement results a_1, \dots, a_N for given measurement settings x_1, \dots, x_N (with $x_i \in \{0, 1\}$) cannot be explained by preestablished agreements; i.e., $P(a_1, \dots, a_N | x_1, \dots, x_N) \neq \int d\lambda P(\lambda) P(a_1 | x_1, \lambda) \cdots P(a_N | x_N, \lambda)$, where $P(\lambda)$ is the probability of using agreement λ . In this case, we say that the system is Bell-correlated. For illustration, consider again the situation where each observer performs measurements on the spin of an atom in a large ensemble. If the system is Bell-correlated, appropriate measurements on the atomic spins show statistics that cannot be explained by a recipe that determines the measurement results for each atom independently of the measurement results and settings of the other atoms.

The form of S_{01} demands that we can set the measurement type of each observer individually. Testing the Bell inequality in Eq. 1 thus requires more than collective measurements,

which are sometimes the only available option in many-body systems. A way around this requirement is to replace the Bell inequality, which guarantees both that the state is Bell correlated and that appropriate measurements were actually performed, by a witness inequality that assumes a quantum-mechanical description and correct experimental calibration of the measurements. A similar approach has been successfully employed to detect entanglement with collective measurements only (15, 19–22, 25). We associate each observer i with a spin 1/2 (in our experiment, a pseudospin representing two energy levels of an atom). The measurements are spin projections $\mathcal{M}_d^{(i)} = 2\hat{s}^{(i)} \cdot \mathbf{d}$ along an axis \mathbf{d} , where $2\hat{s}^{(i)} = \{\hat{\sigma}_x^{(i)}, \hat{\sigma}_y^{(i)}, \hat{\sigma}_z^{(i)}\}$ is the Pauli vector. All other energy levels of the atoms, as well as further degrees of freedom (e.g., atomic motion), are irrelevant for the measurements. We define the total spin observable $\hat{S}_d = \mathbf{d} \cdot \sum_{i=1}^N \hat{s}^{(i)}$ in the

direction \mathbf{d} , which can be probed by collective measurements on the entire system. For two unit vectors \mathbf{a} and \mathbf{n} , we now consider the observable

$$\hat{W} = -\left|\frac{\hat{S}_n}{N/2}\right| + (\mathbf{a} \cdot \mathbf{n})^2 \frac{\hat{S}_a^2}{N/4} + 1 - (\mathbf{a} \cdot \mathbf{n})^2 \quad (2)$$

defined in terms of total-spin observables only. Setting $\mathcal{M}_n^{(i)} = \mathcal{M}_0^{(i)}$ and $\mathcal{M}_m^{(i)} = \mathcal{M}_1^{(i)}$ with $\mathbf{m} = 2(\mathbf{a} \cdot \mathbf{n})\mathbf{a} - \mathbf{n}$, the expectation value of \hat{W} can be reexpressed in terms of one- and two-body correlations functions using $\langle \hat{S}_n \rangle = S_0/2$ and $16(\mathbf{a} \cdot \mathbf{n})^2 \langle \hat{S}_a^2 \rangle = S_{00} + 2S_{01} + S_{11} + 4N(\mathbf{a} \cdot \mathbf{n})^2$; see section 1 of (24). The Bell inequality in Eq. 1 then guarantees that $\langle \hat{W} \rangle \geq 0$ whenever the state of the system is not Bell-correlated. By construction, this Bell correlation witness \hat{W} only involves first and second moments of collective spin measurements along two directions \mathbf{a} and \mathbf{n} , making it well suited for experiments on many-body

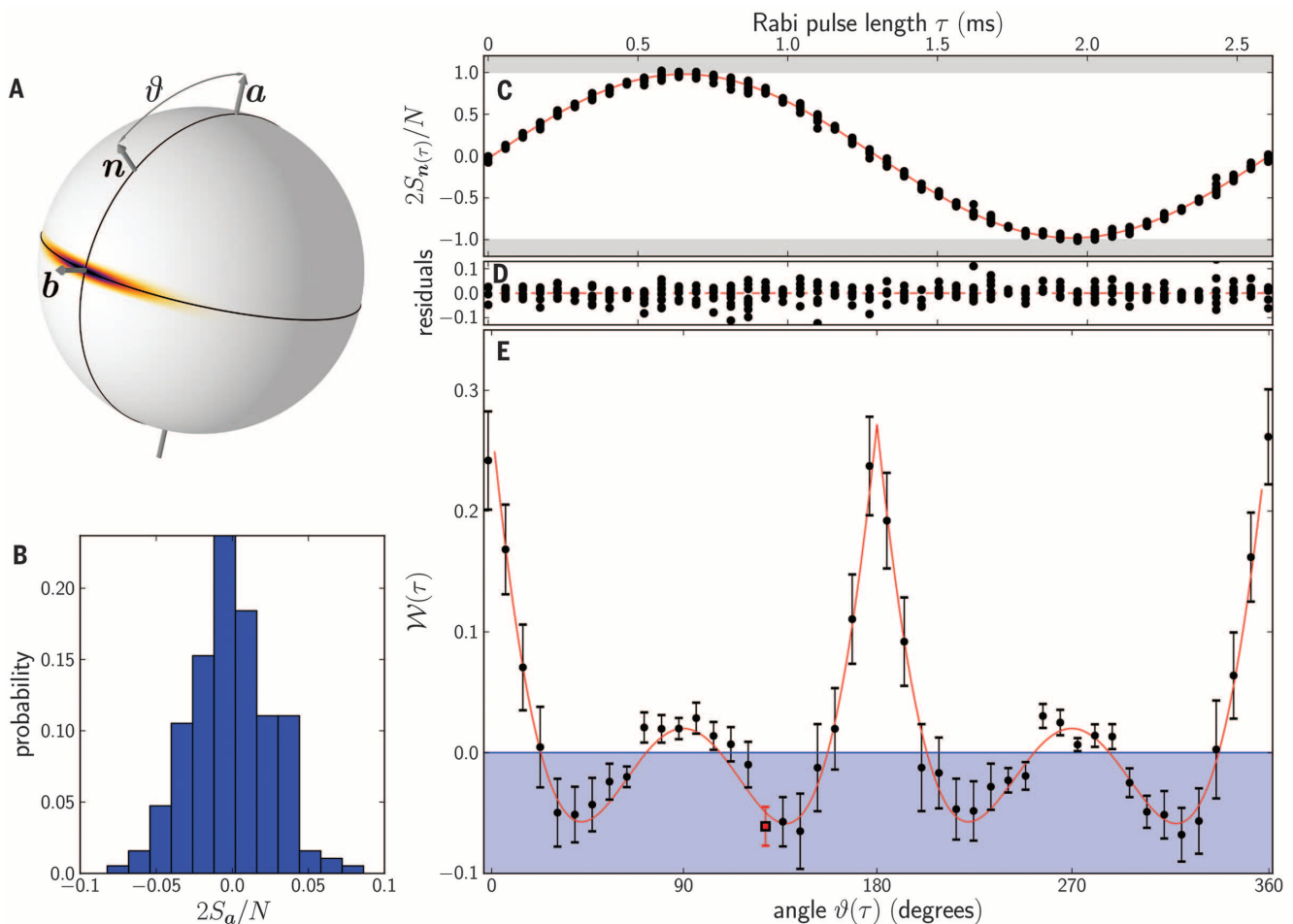


Fig. 1. Observation of Bell correlations in a BEC with the inequality in Eq. 3. (A) Illustration of the spin-squeezed state [Wigner function (32)] and the axes used in the measurement of the Bell correlation witness \mathcal{W} . The vector \mathbf{n} lies in the plane spanned by the squeezing axis \mathbf{a} and the state's center \mathbf{b} . The squeezing and antisqueezing planes are indicated with thin black lines. (B) Histogram of measurements of $2S_a/N$, from which we determine ζ_a^2 . (C) Individual measurements of $2S_{n(\tau)}/N$ as a function of Rabi pulse length τ . The

red line is a sinusoidal fit, from which we determine the Rabi contrast and $\mathbf{a} \cdot \mathbf{n}(\tau) = \cos[\vartheta(\tau)]$; see section 2 of (24). (D) Residuals of the fit in (C). (E) Measurement of $\mathcal{W}(\tau)$ as a function of $\vartheta(\tau)$. The red continuous line is the value of $\mathcal{W}(\tau)$ computed from the measurement of ζ_a^2 and the fitted Rabi oscillation [red line in (C)]. Bell correlations are present in the blue-shaded region. The observed four-fold symmetry of $\mathcal{W}(\tau)$ indicates that $\mathbf{a} \cdot \mathbf{n}(\tau)$ is well calibrated. The red square data point at $\vartheta = 128^\circ$ violates the inequality in Eq. 3 by 3.8 standard deviations.

systems, especially of indistinguishable particles. Although this inequality was derived with assumptions about the measurement settings, it does not make any assumptions about the measured state. In particular, we do not need to assume that the state is symmetric under particle exchange. Moreover, this inequality applies whether the particles are spatially separated or not, similar to entanglement witnesses (22), under the common assumption that particles do not communicate (interact) through unknown channels. Although such an assumption would be questioned in a Bell test aimed at disproving the locally causal nature of the world, it is a well-satisfied and common assumption in the present context, where the goal is to explore correlations in a many-body system, assuming quantum mechanics to be valid.

For collective measurements, N is taken to be the number of detected particles, which may fluctuate slightly between experimental runs. If this is the case, we can replace N in Eq. 2 by the observable \hat{N} and introduce the scaled collective spin $C_n = \langle \hat{S}_n / \hat{N} \rangle$ and the scaled second moment $\zeta_n^2 = \langle 4\hat{S}_n^2 / \hat{N} \rangle$; see section 1 of (24). The inequality then becomes

$$\mathcal{W} = -|C_n| + (\mathbf{a} \cdot \mathbf{n})^2 \zeta_n^2 + 1 - (\mathbf{a} \cdot \mathbf{n})^2 \geq 0 \quad (3)$$

which is valid for any two axes \mathbf{a} and \mathbf{n} and for all non-Bell-correlated states. From this inequality, a criterion follows that will facilitate comparison with well-known spin-squeezing criteria: For any two axes \mathbf{a} and \mathbf{b} perpendicular to each other,

$$\zeta_a^2 \geq \frac{1}{2} (1 - \sqrt{1 - C_b^2}) \quad (4)$$

holds for all non-Bell-correlated states [derivation in section 1.1 of (24)]. The experiment reported below shows a violation of the inequalities in Eqs. 3 and 4 in an atomic ensemble, hence demonstrating Bell correlations between the atomic spins.

We perform experiments with two-component Bose-Einstein condensates (BECs) of rubidium-87 atoms trapped magnetically on an atom chip (26) and prepared in a spin-squeezed state as in (18, 21) [see section 2 of (24)]. We start with a BEC without discernible thermal component in the ground-state hyperfine level $|F = 1, m_F = -1\rangle \equiv |1\rangle$. We are only concerned with the spin state of the atoms, whereas their uniform motional BEC state is irrelevant for the system's description. We perform only collective manipulations and measurements that are symmetric under particle exchange. A two-photon resonant Rabi field addresses the hyperfine transition from $|1\rangle$ to $|F = 2, m_F = 1\rangle \equiv |2\rangle$, with these two states representing a pseudospin 1/2 for each atom. The internal state of the entire BEC is described by a collective spin, with the component $\hat{S}_z = (\hat{N}_1 - \hat{N}_2)/2$ corresponding to half the atom number difference between the two states. With a $\pi/2$ Rabi pulse, we prepare a coherent spin state $[(|1\rangle + |2\rangle)/\sqrt{2}]^{\otimes N}$, in which the atomic spins are uncorrelated. To establish correlations between the spins, we make use of elastic

collisions, which give rise to a Hamiltonian $\hat{H} = \chi \hat{S}_z^2$. Controlling the rate χ with a state-dependent potential (21), we evolve the system in time with \hat{H} to produce a spin-squeezed state (19, 27), which has reduced quantum noise in one collective spin component (Fig. 1A). To characterize this state, we count the numbers of atoms N_1 and N_2 in the two hyperfine states by resonant absorption imaging (21). We correct the data for imaging noise and collisional phase shifts. From averages over many measurements, we determine C_z and ζ_z^2 . Projections along other spin directions are obtained by appropriate Rabi rotations before the measurement.

For the measurement of the Bell correlation witness \mathcal{W} , we use BECs with a total atom number of $N = 476 \pm 21$ (preparation noise after postselection) and $-5.5(6)$ dB of spin squeezing, according to the Wineland criterion (28). We first measure ζ_a^2 , choosing \mathbf{a} to be the squeezing axis where $C_a \approx 0$ and ζ_a^2 is minimized (Fig. 1B). We find $\zeta_a^2 = 0.272(37)$; all quoted uncertainties are statistical standard deviations (SD). For the measurement of C_n , we sweep the vector \mathbf{n} in the plane defined by the state's center \mathbf{b} and the vector \mathbf{a} (Fig. 1A) by applying a Rabi pulse of duration τ . The measurement of $C_{n(\tau)}$ as a function of τ is shown in Fig. 1C. From a sinusoidal fit to the observed Rabi oscillation, we obtain the Rabi contrast $C_b = 0.980(2)$ as well as a precise calibration of $\mathbf{a} \cdot \mathbf{n}(\tau) = \cos[\vartheta(\tau)]$ needed to evaluate \mathcal{W} . From the resulting measurement of $\mathcal{W}(\tau)$ (Fig. 1E), we observe a violation of the inequality in Eq. 3 over a large range of angles. For $\vartheta = 128^\circ$, we see the strongest violation with a statistical significance of 3.8 standard deviations (red square in Fig. 1E).

The inequality in Eq. 3 relies on a fine balance between competing terms, and a satisfactory demonstration of its violation depends on accurate knowledge of the angle ϑ between \mathbf{a} and \mathbf{n} . The inequality in Eq. 4, on the other hand, is more robust to uncertainties in this angle and shows that our entire data set is inconsistent with the hypothesis of our state not being Bell-correlated. The black data point in Fig. 2 represents

our data set by its Rabi contrast (the amplitude of the red fit in Fig. 1C) and squeezed second moment (Fig. 1B), giving an overall likelihood of 99.9% for Bell correlations [see section 2 of (24)]. This likelihood can be interpreted as a P value of 0.1% for excluding the hypothesis: Our data were generated by a state that has no Bell correlations, in the presence of Gaussian noise. An experiment closing the statistics loophole would exclude all possible non-Bell-correlated states, including those producing statistics with rare events. However, because of the way the bounds on \mathcal{W} vary with N , such an experiment would require a number of measurements that increases with the number of spins [see section 3 of (24)].

We now discuss how our Bell correlation witness is connected to entanglement measures that were used previously to characterize spin-squeezed BECs (15, 19–22). These entanglement measures depend on the squeezed variance, for which the squeezed second moment ζ_a^2 is an upper bound (with equality if $C_a = 0$, which is close to what we have measured). In terms of the latter, the Wineland spin-squeezing parameter (28) $\xi^2 \leq \zeta_a^2 / C_b^2$ witnesses entanglement (19) if $\xi^2 < 1$, shown as a red-shaded region in Fig. 2. Similarly, $(k+1)$ -particle entanglement is witnessed by measuring squeezed variances (and hence ζ_a^2) below the gray k -producibility curves (20) in Fig. 2. These entanglement witnesses refer to the Ramsey contrast, whereas our data point in Fig. 2 refers to the measured Rabi contrast; in our experiment, these two quantities have nearly identical values. We can thus draw conclusions about both entanglement and Bell correlations from Fig. 2. In particular, we conclude that our witness requires at least 3 dB of spin squeezing for detecting Bell correlations.

We have shown that Bell correlations can be created and detected in many-body systems. This result has been obtained from a witness that requires collective measurements only. Although we have tested this witness with a spin-squeezed BEC, it could also be tested on other systems, such as thermal atoms in a spin-squeezed state.

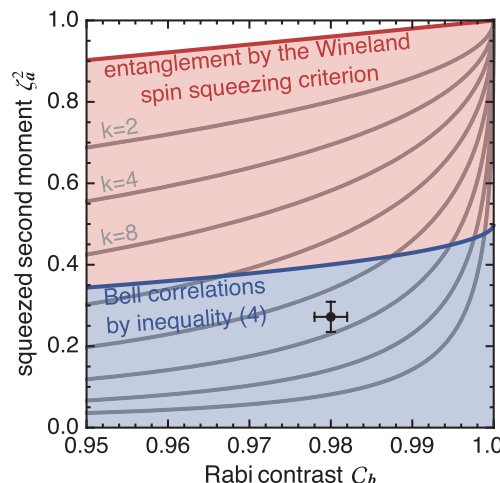


Fig. 2. Observation of Bell correlations in a BEC with the inequality in Eq. 4.

The black circle shows the data set of Fig. 1 expressed in terms of the Rabi contrast C_b and the squeezed second moment ζ_a^2 , with 1 SD error bars. The blue-shaded region shows Bell correlations detected by violation of the inequality in Eq. 4. A pair of random variables with the same parameters as our data set has a 99.9% overlap with this region [see section 2 of (24)]. The red-shaded region shows entanglement witnessed by spin squeezing (19, 28). The gray lines show limits on ζ_a^2 below which there is at least $(k+1)$ -particle entanglement (20), increasing in powers of two up to $k = 256$. Our data set has a 99% overlap with the area below the limit for $k = 24$ -particle entanglement.

Our results imply that the correlations between the atoms in a spin-squeezed Bose-Einstein condensate are strong enough to violate a Bell inequality. This Bell inequality could be violated directly by first localizing the atoms—e.g., through a nondestructive, spin-independent measurement of their position—and then measuring their internal states individually [see section 4 of (24)]. Further study of these states may enable insights into many-body correlations outside of the quantum formalism. Our results naturally raise the question of how our witness can be extended to detect genuine multipartite nonlocality (11) or to quantify the degree of nonlocality (29, 30), in a similar way as the degree of entanglement can be quantified in terms of k -producibility (Fig. 2) (20). Finally, Bell correlations are a resource in quantum information theory—e.g., for certifiable randomness generation. Although Bell-correlation-based randomness has been extracted from two-qubit systems (31), an implementation in a many-body system would considerably increase the amount of randomness per experimental run.

REFERENCES AND NOTES

- N. Brunner, D. Cavalcanti, S. Pironio, V. Scarani, S. Wehner, *Rev. Mod. Phys.* **86**, 419–478 (2014).
- J. S. Bell, *Between Science and Technology*, A. Sarlemijn, P. Kroes, Eds. (Elsevier, 1990), chap. 6.
- V. Scarani, *Acta Physica Slovaca* **62**, 347–409 (2012).
- B. P. Lanyon *et al.*, *Phys. Rev. Lett.* **112**, 100403 (2014).
- M. Eibl *et al.*, *Phys. Rev. Lett.* **90**, 200403 (2003).
- Z. Zhao *et al.*, *Phys. Rev. Lett.* **91**, 180401 (2003).
- J. Hofmann *et al.*, *Science* **337**, 72–75 (2012).
- W. Pfaff *et al.*, *Nat. Phys.* **9**, 29–33 (2013).
- M. Ansmann *et al.*, *Nature* **461**, 504–506 (2009).
- P. D. Drummond, *Phys. Rev. Lett.* **50**, 1407–1410 (1983).
- G. Svetlichny, *Phys. Rev. D Part. Fields* **35**, 3066–3069 (1987).
- M. Żukowski, Č. Brukner, *Phys. Rev. Lett.* **88**, 210401 (2002).
- L. Amico, R. Fazio, A. Osterloh, V. Vedral, *Rev. Mod. Phys.* **80**, 517–576 (2008).
- I. Bloch, J. Dalibard, W. Zwerger, *Rev. Mod. Phys.* **80**, 885–964 (2008).
- C. Gross, T. Zibold, E. Nicklas, J. Estève, M. K. Oberthaler, *Nature* **464**, 1165–1169 (2010).
- I. D. Leroux, M. H. Schleier-Smith, V. Vuletić, *Phys. Rev. Lett.* **104**, 250801 (2010).
- A. Louchet-Chauvet *et al.*, *New J. Phys.* **12**, 065032 (2010).
- C. F. Ockeloen, R. Schmied, M. F. Riedel, P. Treutlein, *Phys. Rev. Lett.* **111**, 143001 (2013).
- A. Sørensen, L.-M. Duan, J. I. Cirac, P. Zoller, *Nature* **409**, 63–66 (2001).
- A. S. Sørensen, K. Mølmer, *Phys. Rev. Lett.* **86**, 4431–4434 (2001).
- M. F. Riedel *et al.*, *Nature* **464**, 1170–1173 (2010).
- P. Hyllus, L. Pezzé, A. Smerzi, G. Tóth, *Phys. Rev. A* **86**, 012337 (2012).
- J. Tura *et al.*, *Science* **344**, 1256–1258 (2014).
- Materials and methods are available as supplementary materials on Science Online.
- J.-D. Bancal, N. Gisin, Y.-C. Liang, S. Pironio, *Phys. Rev. Lett.* **106**, 250404 (2011).
- P. Böhni *et al.*, *Nat. Phys.* **5**, 592–597 (2009).
- M. Kitagawa, M. Ueda, *Phys. Rev. A* **47**, 5138–5143 (1993).
- D. J. Wineland, J. J. Bollinger, W. M. Itano, D. J. Heinzen, *Phys. Rev. A* **50**, 67–88 (1994).
- J.-D. Bancal, C. Branciard, N. Gisin, S. Pironio, *Phys. Rev. Lett.* **103**, 090503 (2009).
- F. J. Curchod, N. Gisin, Y.-C. Liang, *Phys. Rev. A* **91**, 012121 (2015).
- S. Pironio *et al.*, *Nature* **464**, 1021–1024 (2010).
- R. Schmied, P. Treutlein, *New J. Phys.* **13**, 065019 (2011).

ACKNOWLEDGMENTS

We thank R. Augusiak, P. Drummond, and M. Lewenstein for fruitful discussions. R.S., J.-D.B., B.A., M.F., P.T., and N.S. acknowledge support from the Swiss National Science Foundation (SNSF) through grants PP00P2-150579, 20020-149901, and the National Centre of Competence in Research “Quantum Science and Technology” (NCCR QSIT). P.T. acknowledges support from the European Union through the project Simulators and Interfaces with Quantum Systems (SIQS). N.S. acknowledges the Army Research Laboratory Center for Distributed Quantum Information through the project SciNet. J.-D.B. and V.S. acknowledge funding from

the Singapore Ministry of Education (partly through Academic Research Fund Tier 3 MOE2012-T3-1-009) and the National Research Foundation of Singapore. Author contributions: N.S. and J.-D.B. initiated the study, with input from R.S. J.-D.B. derived optimal Bell inequalities and performed statistics tests, discussing with R.S., N.S., and V.S. R.S. and P.T. derived the witnesses from the Bell inequality, with support from J.-D.B. and N.S. B.A., M.F., and R.S. performed experiments and analyzed data, supervised by P.T. All authors discussed the results and contributed to the manuscript.

SUPPLEMENTARY MATERIALS

www.sciencemag.org/content/352/6284/441/suppl/DC1
Materials and Methods
Figs. S1 to S4
Reference (33)

13 November 2015; accepted 11 March 2016
10.1126/science.aad8665

GEOLOGY

Continental arc volcanism as the principal driver of icehouse-greenhouse variability

N. Ryan McKenzie,^{1,2,3,*} Brian K. Horton,^{2,4} Shannon E. Loomis,² Daniel F. Stockli,² Noah J. Planavsky,¹ Cin-Ty A. Lee⁵

Variations in continental volcanic arc emissions have the potential to control atmospheric carbon dioxide (CO₂) levels and climate change on multimillion-year time scales. Here we present a compilation of ~120,000 detrital zircon uranium-lead (U-Pb) ages from global sedimentary deposits as a proxy to track the spatial distribution of continental magmatic arc systems from the Cryogenian period to the present. These data demonstrate a direct relationship between global arc activity and major climate shifts: Widespread continental arcs correspond with prominent early Paleozoic and Mesozoic greenhouse climates, whereas reduced continental arc activity corresponds with icehouse climates of the Cryogenian, Late Ordovician, late Paleozoic, and Cenozoic. This persistent coupled behavior provides evidence that continental volcanic outgassing drove long-term shifts in atmospheric CO₂ levels over the past ~720 million years.

Earth experienced multiple shifts in climate state over the past ~720 million years (My), with extensive icehouse intervals during the Cryogenian (1, 2), latest Ordovician (3), late Paleozoic (4), and mid-late Cenozoic alternating with greenhouse intervals during the early Paleozoic and Mesozoic-early Cenozoic eras (5, 6). These shifts are attributed to changes in the partial pressure of atmospheric carbon dioxide (P_{CO₂}) (5–8). Long-term (≥10⁶ years) changes

in P_{CO₂} are controlled by the magnitude of carbon input to the ocean-atmosphere system from volcanic and metamorphic outgassing, as well as the removal of this carbon primarily through silicate weathering and subsequent precipitation and burial of carbonate minerals, along with organic carbon burial (8, 9). Although sporadic processes such as enhanced plume activity (10) and mountain building (11) have been invoked as drivers of specific greenhouse or icehouse intervals, no unifying model explains all of the observed fluctuations.

Arc magmatism along continental-margin subduction zones is thought to contribute more CO₂ to the atmosphere than other volcanic systems, owing to decarbonation of carbonates stored in the continental crust of the upper plate (12–16). Although direct measurements of CO₂ outgassing rates are limited, current continental volcanic arc (CVA) emissions are estimated to be as

¹Department of Geology and Geophysics, Yale University, New Haven, CT 06511, USA. ²Department of Geological Sciences, Jackson School of Geosciences, University of Texas at Austin, Austin, TX 78712, USA. ³Department of Earth Sciences, University of Hong Kong, Pokfulam, Hong Kong, China. ⁴Institute for Geophysics, Jackson School of Geosciences, University of Texas at Austin, Austin, TX 78712, USA. ⁵Department of Earth Sciences, Rice University, Houston, TX 77005, USA.

*Corresponding author Email: ryan.mckenzie@yale.edu

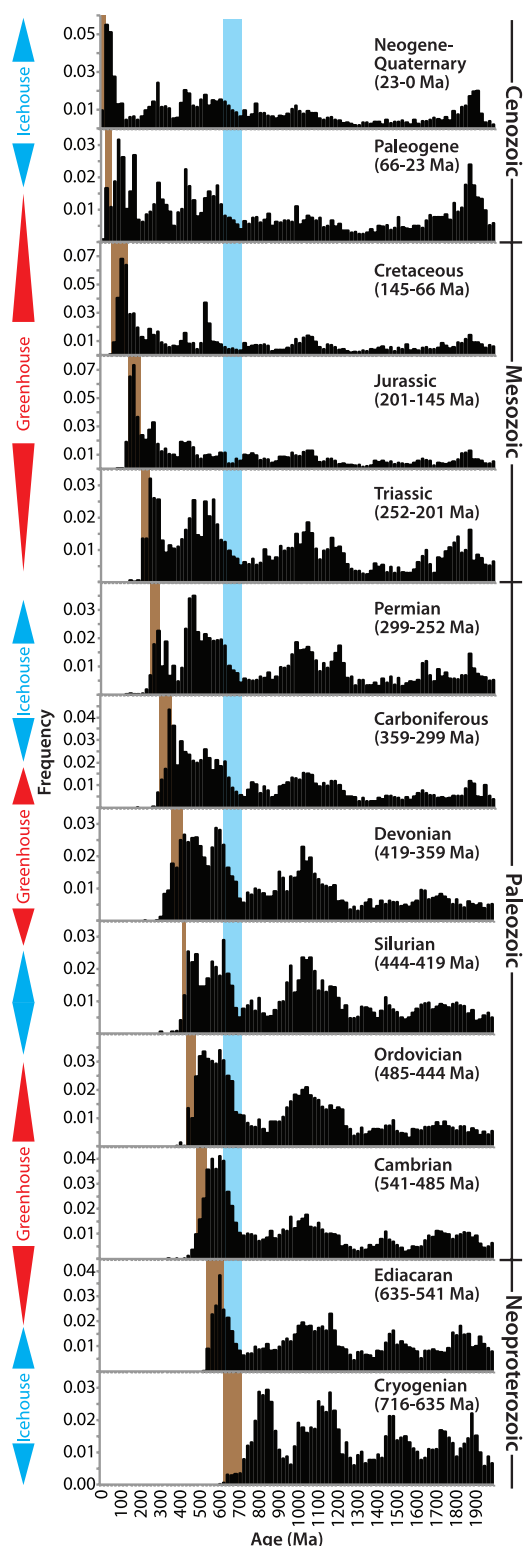


Fig. 1. Normalized composite zircon U-Pb age distributions for global Cryogenian to modern sedimentary deposits. Data are arranged by geologic period and plotted in age histograms using 20-My bins. Vertical brown bars demarcate the depositional age range of each geologic period. Vertical blue bars highlight the Cryogenian glacial interval to note the persistent low abundance of zircons transitioning into this interval.

high as ~150 teragrams C per year (Tg/year), in contrast to 12 to 60 Tg/year from ocean ridges and 1 to 30 Tg/year from oceanic intraplate volcanoes (14). Therefore, the spatial distribution of CVAs through geologic time, which varies due to changes in plate tectonic regimes (17), may play a prominent role in regulating Earth's climate state.

Because variations in CVA activity have few constraints through Earth history, it is difficult to model their role as drivers of climate change (16). Burial, erosion, or destruction of the arc can hinder our ability to track CVA systems in deep geologic time. The sedimentary record, however, provides an effective means to track the past presence of CVA systems. Although original arc rocks may be gone, their eroded components are distributed and archived in many adjacent sedimentary basins. Zircon, a key mineral for U-Pb geochronology, is chemically and physically resistant to degradation. Zircon grains are capable of enduring the rigors of erosion, transport, reworking, burial, moderate to high degrees of metamorphism, subduction, and return to the surface through magmatic processes, thus yielding particularly long residence times in the continental crust (18). Whereas mantle-derived mafic rocks (from high-temperature, low-silica dry magmas) associated with continental rifts, spreading ridges, and flood basalts have low-zircon yields, zircon-fertile rocks are mostly produced by low-temperature, high-silica hydrous melts along continental subduction zones (19). Siliciclastic strata deposited near active CVAs contain abundant young zircon grains (i.e., zircons with U-Pb crystallization ages close to the stratal depositional age) defining distinct age populations that track regional magmatic arc flare-ups (20), whereas large igneous provinces (LIPs), rift systems, and passive margins generally lack substantial young zircon populations (21, 22). Oceanic island arcs do not affect the continental sedimentary record until accretion, which introduces older grains. Therefore, we can employ the relative abundance of young detrital zircon grains in the stratigraphic record to assess the regional presence and importance of CVA systems.

We compiled ~120,000 new and published single-grain detrital zircon U-Pb ages from globally distributed clastic sedimentary rocks to track the spatial distribution of CVAs from the Cryogenian to the present. Using U-Pb data from strata with depositional ages constrained to at least the geologic period, we generated global age distributions to evaluate relative shifts in the abundance of young zircon grains, which are linked to regional silicic magmatism. Because global sampling is in-

complete and the quantity of age data available from different regions is variable, we applied a normalization process for our composite distributions (23). First, U-Pb ages were arranged regionally by geographic location (26 zones) (fig. S1) and temporally by geologic period (13 intervals) (table S1). Age frequency distributions were established for all data, and then the individual regional distributions were equally weighted to create global composite distributions for each geologic period. For periods lacking data in prominent regions with reasonably known geologic histories, we used regional age data from the next youngest period to backfill the empty bin (23). An outlier test was performed to identify anomalous data sets that significantly skewed the composite distributions and to ensure that the signal was indeed global (23).

We found that composite age distributions from rocks deposited during icehouse intervals contain relatively low proportions of young zircon, whereas distributions from greenhouse intervals are skewed toward younger populations (Fig. 1). This is best illustrated by the cumulative age distributions in which the Cryogenian, Silurian, Permian, and Cenozoic icehouse intervals yield low proportions of young zircon grains but the Cambrian, Jurassic, and Cretaceous greenhouse periods yield the greatest proportions of young grains (Figs. 2 and 3). The mean ages of the young populations in each interval vary with respect to modeled Phanerozoic CO₂ value, as the young mean ages converge on the depositional age transitioning into greenhouse climates and deviate from the depositional age during icehouse climates (Fig. 3). Overall, these data demonstrate a direct link between shifts in global detrital zircon production, CVA distribution, and major climate transitions over the past ~720 My.

The relationships between icehouse-greenhouse transitions and CVA spatiotemporal variations fit within the paleogeographic framework of continents. Continental breakup requires the opening of new ocean basins and the generation of new oceanic lithosphere. This, in turn, requires the consumption of old oceanic lithosphere elsewhere along subduction zones and produces CVAs, whereas continental collisions shut down subduction and lessen the global length of CVAs (15, 17, 22, 24). Therefore, intervals following continental breakup will consist of high continent dispersal with spatially extensive CVAs, and intervals during and after continental collision will consist of reduced CVAs.

The extent of the low-latitude Cryogenian Sturtian [716 million years ago (Ma)] and Marinoan (635 Ma) glaciations requires anomalously low levels of atmospheric CO₂ (25, 26). Increased silicate weathering due to continental rifting and emplacement of the low-latitude Franklin LIP, which produced highly weatherable mafic rocks, are cited as primary mechanisms for CO₂ consumption to trigger these "snowball Earth" events (2, 27). However, Mesoproterozoic (~1400 Ma) emplacement of prominent low-latitude LIPs did

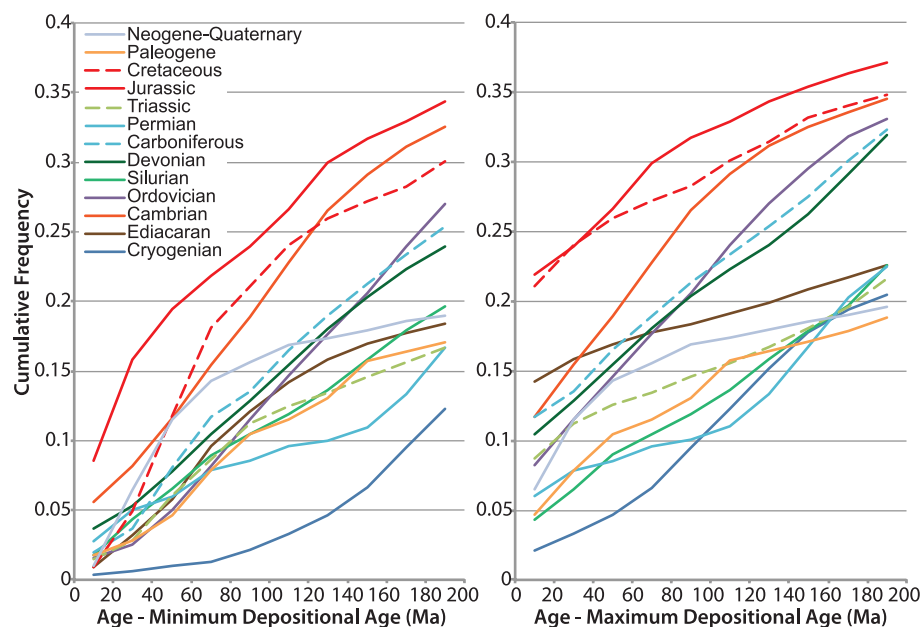
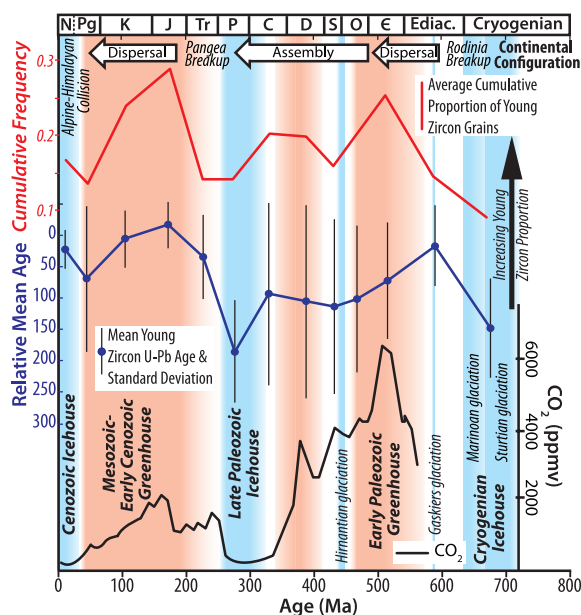


Fig. 2. Cumulative distribution functions (CDFs) of young zircon U-Pb ages. CDFs for each geologic period (greenhouse, warm colors; icehouse, cool colors) relative to the approximate minimum (left) and maximum (right) depositional ages. CDFs were normalized to zero by subtracting the ages from periods younger than the minimum and maximum depositional ages, respectively (23). Consideration of the young grain abundance relative to maximum depositional age removes inherent biases related to the differential duration of geologic periods relative to sample depositional ages. A 200-My window represents a reasonable approximation of the typical duration of CVA activity.

Fig. 3. Cumulative proportion of young grains compared to the mean age of young grains, configuration of continents, icehouse-greenhouse intervals, and modeled Phanerozoic CO₂ levels. Average cumulative proportion of young ages within 200 My of minimum depositional ages (from Fig. 2) (red line), and mean young ages calculated from the 300-My window relative to the minimum depositional age used in our statistical analysis (23) (blue line), are plotted against the average depositional age of each period. A value of 0 is assigned where the mean young age equals the average depositional age. Comparison of the cumulative proportion to the mean young ages provides insight into the relative abundance of young to older arc-derived grains (e.g., both the Ediacaran and Triassic periods contain low abundances of young to old grains coupled with relatively young mean ages, indicating that most young grains are from young CVAs). The low proportions of young grains and relatively older mean ages in the Cryogenian and Permian indicate that older grains dominate the distributions. The CO₂ curve was taken from (7). ppmv, parts per million by volume. N, Neogene; Pg, Paleogene; K, Cretaceous; J, Jurassic; Tr, Triassic; P, Permian; C, Carboniferous; D, Devonian; S, Silurian; O, Ordovician; e, Cambrian; Ediac., Ediacaran.



not yield known glaciations (28). The Phanerozoic record is also replete with LIPs (29) that did not induce glaciations. The Siberian traps erupted at the end of the late Paleozoic icehouse interval without subsequent glaciation, albeit in a high-latitude paleogeographic position. The Khalakindji, Central Atlantic, and Deccan provinces formed at lower latitudes (30), and contrastingly, these events all correspond with greenhouse intervals. Although the Franklin LIP was broadly contemporaneous with the Sturtian, there is no LIP matching the Marinoan glaciation. We find the assumption of a primary relationship between LIP emplacement and Cryogenian glaciations difficult to justify. Rather, we postulate that Cryogenian glaciations resulted from a major drop in volcanic CO₂ fluxes associated with the assembly of Rodinia.

The Rodinia supercontinent formed by ~900 Ma and underwent protracted Neoproterozoic rifting starting as early as 750 Ma, with diachronous final breakup around 600 Ma (31, 32). Rodinia's long existence included an interval of reduced CVAs with a progressive increase throughout the period of Neoproterozoic breakup, as evidenced by a young zircon lull ~720 Ma at the transition to the Cryogenian glacial interval and an increase toward the end of the interval (Fig. 1). The influence of diminished volcanic CO₂ fluxes on Cryogenian glaciations has been suggested (22), but our expanded data set illustrates the pronounced scale of this reduction, with the Cryogenian yielding the lowest proportion of young grains of all subsequent geologic periods (Figs. 1, 2, and 3). Nearly all regions contain data from Marinoan glacial deposits (~635 Ma) roughly equal to the minimum depositional age of the Cryogenian period, which makes for a pronounced gap between the minimum depositional age and the youngest abundant zircon population. The low-latitude Paleoproterozoic Huronian glaciations (2400 to 2300 Ma), the last known glaciations before the Cryogenian, also coincide with a prominent magmatic gap (33). Therefore, we assert that the severity of Cryogenian glaciations and the prominence of the zircon age lull are not coincidences and that the major reduction in the volcanic CO₂ flux was critical to allow extensive low-latitude glaciations.

A broad dispersal of continents persisted during the Ediacaran and Cambrian periods, until the assembly of Gondwana was complete by the Middle Ordovician (22). The Cambrian, which had the highest P_{CO2} of the Phanerozoic (5–7) (Fig. 3), was followed by Ordovician cooling that culminated with the Hirnantian glaciations (~445 Ma) (3). Ediacaran deposits show a notable increase in both the abundance and mean age of young grains, and Cambrian deposits contain high proportions of young zircon (Figs. 1, 2, and 3). Ordovician deposits show a reduction in young grains, and Silurian deposits, which account for the ~20-My interval following the Hirnantian glaciation, contain low proportions of young zircon (Figs. 2 and 3). Continental coalescence continued through the Paleozoic by newly formed subduction zones until the final amalgamation of Pangea by

the Carboniferous-Permian transition (24). Mid-Paleozoic warm conditions were followed by the late Paleozoic icehouse, which spanned at least from the Late Carboniferous to the Early Permian (4). The proportions of young zircon grains are modest in Devonian-Carboniferous strata and low in Permian strata. Pangea rifting initiated by the Triassic, with complete breakup by Jurassic-Cretaceous time marking another interval of relatively high continent dispersal, until Paleogene Alpine-Himalayan collision along southern Eurasia closed the Tethys Ocean, substantially reducing global CVA length (15, 34). Triassic deposits show an increase in young zircon grains, with very high proportions in the Jurassic-Cretaceous greenhouse world (6). A reduction in young zircon populations for Paleogene and Neogene-Quaternary deposits matches the Cenozoic record of global cooling (35). In sum, the abundance of young zircon grains in Cambrian and Jurassic-Cretaceous strata reflects high CVA distributions during those intervals of high continent dispersal and greenhouse climates, whereas the low abundance during the Cryogenian, Silurian, Permian, and Cenozoic demonstrates diminished CVA distributions during those intervals of continent amalgamation and icehouse climates.

Phanerozoic GEOCARB CO₂ models (7) (Fig. 3) broadly correspond with the CVA record because these models use approximated seafloor-spreading rates, largely inferred from Phanerozoic sea-level records, to estimate volcanic CO₂ fluxes. Spreading rates are driven by slab pull and suction associated with subduction, which increases with slab length (36). Geodynamic models demonstrate that spreading rates and sea level increase during intervals of continent dispersal (37). The composite U-Pb age distributions are normalized regionally, and the relative shifts in young zircon abundance are dependent on global shifts rather than accelerated production in a particular region. Therefore, the age distributions represent global zircon production and track the spatial distributions of CVAs through time. Increased fluxes from spreading centers due to rapid subduction during intervals of continent dispersal would certainly contribute to overall CO₂ outgassing, but the flux potential from CVAs is far greater (12, 14, 15).

A lack of constraints on deep-time volcanic CO₂ emissions has prompted many studies to propose changes in silicate weathering as the primary control on Pco₂ variations (9, 38). This notion appears to be at odds with the geologic record. No consistent relationship exists between LIP emplacement, which could change the weatherability of the crust, and long-term climate. Temporal variations in global uplift also cannot explain intervals of climate change. Non-collisional convergent margins with CVAs can produce large mountain belts through arc magmatism and retroarc shortening that thicken the crust of the upper plate. The extensive North and South American Cordilleras along the eastern Pacific subduction zones are prime examples. The two highest mountain belts on Earth, the Andes and the Himalaya, formed under similar

contractual tectonic regimes, despite their contrasting settings along subduction and collisional margins. Although increased weathering and erosion may be expected during intervals of extensive CVA dispersion due to a combination of uplift, production of weatherable volcanics, and moisture availability from adjacent oceans, intervals of continent dispersal correspond with greenhouse climates. Similarly, continental assembly should generally insulate continent collision belts from oceans and reduce weathering rates, yet these intervals correspond with icehouse climates. The paleogeographic position of continents can influence local weathering rates, but Cryogenian glaciations occurred with continents concentrated at low latitudes (32), whereas large landmasses were at high latitudes during late Paleozoic icehouse conditions (30). Likewise, the transition from the early Paleozoic greenhouse to the Hirnantian icehouse occurred without drastic changes in paleogeography. Therefore, we find no causative links between continental paleogeography or topographic variation and global climate change.

Silicate weathering increases with increased temperature, providing a feedback that prevents runaway greenhouse conditions and is critical to maintaining a habitable environment for life (9, 38). The temperature control on silicate weathering means that it operates as a function of, and is largely dependent on, the CO₂ flux into the atmosphere (39). Therefore, the input flux should exert the first-order control on atmospheric CO₂ fluctuations that dictate baseline climate. Spatiotemporal variation in the distribution of CVAs—contributors of the largest and most variable CO₂ input flux—exhibits a consistent correlation with all major icehouse-greenhouse transitions over the past ~720 My. Further, the correspondence of a prominent magmatic hull with the extensive Paleoproterozoic Huronian glaciations suggests that CVA CO₂ outgassing was a principal driver of Earth's long-term climate variability for the past ~2.4 billion years.

REFERENCES AND NOTES

- P. F. Hoffman, A. J. Kaufman, G. P. Halverson, D. P. Schrag, *Science* **281**, 1342–1346 (1998).
- F. A. Macdonald et al., *Science* **327**, 1241–1243 (2010).
- S. Finnegan et al., *Science* **331**, 903–906 (2011).
- I. P. Montañez, C. J. Poulsen, *Annu. Rev. Earth Planet. Sci.* **41**, 629–656 (2013).
- N. M. Bergman, T. M. Lenton, A. J. Watson, *Am. J. Sci.* **304**, 397–437 (2004).
- D. L. Royer, R. A. Berner, I. P. Montañez, N. J. Tabor, D. J. Beerling, *GSA Today* **14**, 4–10 (2004).
- R. A. Berner, Z. Kothavala, *Am. J. Sci.* **301**, 182–204 (2001).
- R. A. Berner, A. C. Lasaga, R. M. Garrels, *Am. J. Sci.* **283**, 641–683 (1983).
- L. R. Kump, S. L. Brantley, M. A. Arthur, *Annu. Rev. Earth Planet. Sci.* **28**, 611–667 (2000).
- R. L. Larson, *Geology* **19**, 547–550 (1991).
- M. E. Raymo, W. F. Ruddiman, *Nature* **359**, 117–122 (1992).
- M. R. Burton, G. M. Sawyer, D. Granieri, *Rev. Mineral. Geochem.* **75**, 323–354 (2013).
- R. Dasgupta, *Rev. Mineral. Geochem.* **75**, 183–229 (2013).

- C.-T. A. Lee, J. S. Lackey, *Elements* **11**, 125–130 (2015).
- C.-T. A. Lee et al., *Geosphere* **9**, 21–36 (2013).
- D. M. Kerrick, K. Caldeira, *Chem. Geol.* **145**, 213–232 (1998).
- P. G. Silver, M. D. Behn, *Science* **319**, 85–88 (2008).
- G. Gehrels, *Annu. Rev. Earth Planet. Sci.* **42**, 127–149 (2014).
- C.-T. A. Lee, O. Bachmann, *Earth Planet. Sci. Lett.* **393**, 266–274 (2014).
- S. R. Paterson, M. N. Ducea, *Elements* **11**, 91–98 (2015).
- P. A. Cawood, C. J. Hawkesworth, B. Dhuime, *Geology* **40**, 875–878 (2012).
- N. R. McKenzie, N. C. Hughes, B. C. Gill, P. M. Myrow, *Geology* **42**, 127–130 (2014).
- Materials and methods are available as supplementary materials on Science Online.
- D. C. Bradley, *Earth Sci. Rev.* **108**, 16–33 (2011).
- R. T. Pierrehumbert, D. S. Abbot, A. Voigt, D. Koll, *Annu. Rev. Earth Planet. Sci.* **39**, 417–460 (2011).
- D. P. Schrag, R. A. Berner, P. F. Hoffman, G. P. Halverson, *Geochim. Geophys. Geosyst.* **3**, 1–21 (2002).
- Y. Donnadieu, Y. Goddard, G. Ramstein, A. Nédélec, J. Meert, *Nature* **428**, 303–306 (2004).
- N. J. Planavsky et al., in *Earth-Life Transitions: Paleobiology in the Context of Earth System Evolution*, P. D. Polly, J. J. Head, D. L. Fox, Eds. (The Paleontological Society, 2015), vol. 21, pp. 47–82.
- R. E. Ernst, K. L. Buchan, I. H. Campbell, *Lithos* **79**, 271–297 (2005).
- C. R. Scotese, Plate tectonic maps and continental drift animations: PALEOMAP Project (2001); www.scotese.com.
- D. A. D. Evans, *Geol. Soc. Am. Bull.* **125**, 1735–1751 (2013).
- Z. X. Li et al., *Precambrian Res.* **160**, 179–210 (2008).
- K. C. Condie, C. O'Neill, R. C. Aster, *Earth Planet. Sci. Lett.* **282**, 294–298 (2009).
- D. G. Van Der Meer et al., *Proc. Natl. Acad. Sci. U.S.A.* **111**, 4380–4385 (2014).
- J. Zachos, M. Pagani, L. Sloan, E. Thomas, K. Billups, *Science* **292**, 686–693 (2001).
- C. P. Conrad, C. Lithgow-Bertelloni, *J. Geophys. Res.* **109**, B10407 (2004).
- A. Lenardic et al., *Geochim. Geophys. Geosyst.* **12**, Q10016 (2011).
- Y. Goddard, Y. Donnadieu, G. Le Hir, V. Lefebvre, E. Nardin, *Earth Sci. Rev.* **128**, 122–138 (2014).
- R. A. Berner, K. Caldeira, *Geology* **25**, 955–956 (1997).

ACKNOWLEDGMENTS

N.R.M. and B.K.H. acknowledge funding from NSF-Tectonics grant EAR-1348031. N.R.M. and S.E.L. acknowledge the Jackson School of Geosciences Distinguished Postdoctoral Program, University of Texas at Austin. N.R.M. acknowledges the Flint Postdoctoral Program, Yale University. C.-T.A.L. acknowledges funding from NSF award OCE-1338842. We thank C. Reinhard, M. Brandon, D. Evans, A. Smye, and O. Anfinson for helpful discussions. This is University of Texas Institute for Geophysics contribution no. 2955. Literature sources and data tables for new U-Pb ages used in the compilation are provided in the supplementary materials.

SUPPLEMENTARY MATERIALS

www.sciencemag.org/content/352/6284/444/suppl/DC1
Materials and Methods
Figs. S1 to S4
Tables S1 and S2
References (40–239)
Data S1

4 October 2015; accepted 11 March 2016
10.1126/science.aad5787

BIOINORGANIC CHEMISTRY

Light-driven dinitrogen reduction catalyzed by a CdS:nitrogenase MoFe protein biohybrid

Katherine A. Brown,¹ Derek F. Harris,² Molly B. Wilker,^{3*} Andrew Rasmussen,² Nimesh Khadka,² Hayden Hamby,³ Stephen Keable,⁴ Gordana Dukovic,³ John W. Peters,⁴ Lance C. Seefeldt,² Paul W. King^{1†}

The splitting of dinitrogen (N_2) and reduction to ammonia (NH_3) is a kinetically complex and energetically challenging multistep reaction. In the Haber-Bosch process, N_2 reduction is accomplished at high temperature and pressure, whereas N_2 fixation by the enzyme nitrogenase occurs under ambient conditions using chemical energy from adenosine 5'-triphosphate (ATP) hydrolysis. We show that cadmium sulfide (CdS) nanocrystals can be used to photosensitize the nitrogenase molybdenum-iron (MoFe) protein, where light harvesting replaces ATP hydrolysis to drive the enzymatic reduction of N_2 into NH_3 . The turnover rate was 75 per minute, 63% of the ATP-coupled reaction rate for the nitrogenase complex under optimal conditions. Inhibitors of nitrogenase (i.e., acetylene, carbon monoxide, and dihydrogen) suppressed N_2 reduction. The CdS:MoFe protein biohybrids provide a photochemical model for achieving light-driven N_2 reduction to NH_3 .

The reduction of dinitrogen (N_2) to ammonia (NH_3) is the single largest input of fixed nitrogen (N) into the global biogeochemical cycle. Although the overall reaction releases energy, the cleavage of the nitrogen-nitrogen triple bond has a very large activation barrier. In the industrial Haber-Bosch process, NH_3 is produced via a dissociative reaction involving coactivation of dihydrogen (H_2) and N_2 over an Fe-based catalyst (1). The H_2 used for the reaction is produced by steam reforming of natural gas and results in coproduction of appreciable amounts of CO_2 . The energy required ($>600 \text{ kJ mol}^{-1} NH_3$) to achieve the high temperatures (500°C) and pressures (200 atm) necessary to drive the reaction is also largely derived from fossil fuels (2, 3).

In nitrogen-fixing bacteria, the enzymatic reduction of N_2 to NH_3 is catalyzed by nitrogenase enzymes and proceeds via the hydrogenation of N_2 through metal-hydride intermediates rather than from reaction with H_2 (4). The Mo-dependent nitrogenase is a multiprotein complex composed of MoFe and Fe proteins, named after the metals in their active sites. Although nitrogenase functions at room temperature (25°C) and pressure (1 atm), it requires a large input of chemical energy provided by the hydrolysis of adenosine 5'-triphosphate (ATP) (Fig. 1A) (4). A minimum of 16 moles of ATP ($\Delta G^\circ = -488 \text{ kJ mol}^{-1}$ or 5 eV mol^{-1} of N_2 reduced) is required to re-

duce N_2 to NH_3 . During catalysis, the Fe protein associates with and dissociates from the MoFe protein, resulting in the eight sequential electron transfer/ATP hydrolysis events required to generate 1 mole of NH_3 (5). Reducing equivalents accumulate at the catalytic site FeMo co-factor (FeMo-co) as Fe-hydrides (6), which directly participate in conversion of N_2 to 2 moles of NH_3 with an obligatory stoichiometric reduction of two protons to make H_2 (Fig. 1A) (4, 7).

Low-potential chemical donors or photoexcited chromophores can directly deliver electrons to the MoFe protein. Complexes between MoFe protein and the low-potential donor Eu(II)-L (8, 9) or Ru-photosensitizers (10, 11) support the catalytic reduction of protons or nonphysiological C or N substrates (e.g., C_2H_2 , HCN, N_2H_4 , N_3^-). However, these complexes are unable to catalyze N_2 reduction, and rates for nonphysiological substrates are low (up to 8.5 min^{-1}) compared to physiological reaction rates (e.g., 500 min^{-1} for C_2H_2 reduction). In the case of Ru-photosensitizers, it was shown that the Ru conjugate was unstable, resulting in the loss of photocatalytic rates and low quantum yields ($QY \leq 1\%$) (10, 11).

Here, we examined N_2 reduction by the MoFe protein when it is adsorbed onto CdS nanocrystals to form biohybrid complexes (12). Semiconductor nanocrystals are quantum-confined materials with size-tunable photoexcited electron and hole energy levels (13). Different nanocrystalline materials were tested (table S1), and CdS nanorods ($d \approx 38 \pm 5 \text{ \AA}$, $l \approx 168 \pm 16 \text{ \AA}$; fig. S1) were observed to deliver photogenerated electrons to the MoFe protein with the highest enzymatic turnover. The size, shape, and surface electrostatics of the CdS nanorods complement the MoFe protein dimensions ($d \approx 69 \text{ \AA}$, $l \approx 110 \text{ \AA}$) and surface electrostatics to support self-assembly into complexes

(14, 15). The lowest-energy transition of the CdS nanorods is in the visible region of the solar spectrum ($E_g = 2.72 \text{ eV}$, $\lambda_{\text{absorption}} = 456 \text{ nm}$, fig. S1), and the reduction potential of the first photoexcited state transition, -0.8 V versus NHE (15–17), is sufficiently negative to reduce the MoFe protein (-0.31 V) (18) to drive electron transfer for catalytic reduction of N_2 to NH_3 (Fig. 1B).

Photoexcitation of the CdS:MoFe protein biohybrids under a 100% N_2 atmosphere resulted in the direct light-driven reduction of N_2 to NH_3 (Fig. 2, fig. S2 and tables S2 to S4). Transfer of low-potential electrons to the MoFe protein from the photoexcited CdS nanorod replaced ATP-coupled electron transfer by the Fe protein. The reaction required a sacrificial electron donor, HEPES, which produced a high turnover frequency (TOF) with a low background compared to other donors (table S2). Control reactions that lacked a key component (e.g., HEPES, CdS, light, or a functional MoFe protein) or utilized apo-MoFe protein that lacks FeMo-co did not produce NH_3 (tables S3 and S5). Illumination under $\sim 3.5 \text{ mW cm}^{-2}$ of 405-nm light led to peak NH_3 production rates of $315 \pm 55 \text{ nmol } NH_3 (\text{mg MoFe protein})^{-1} \text{ min}^{-1}$ at a TOF of 75 min^{-1} (Fig. 2 and table S6). The values correspond to 63% of the NH_3 production [$500 \text{ nmol } NH_3 (\text{mg MoFe protein})^{-1} \text{ min}^{-1}$], and TOF (119 min^{-1}) catalyzed by the Fe protein and ATP-dependent reaction under optimal conditions (table S6). The estimated QY of 3.3% for conversion of absorbed photons to NH_3 ($QY = 23.5\%$ for the coproduction of NH_3 and H_2 ; tables S7 and S8) is higher than reported for other nonphysiological reactions (10, 11). N_2 reduction persisted for up to 5 hours under constant illumination (Fig. 2, inset; tables S9 and S10) with a turnover number (TON) of $1.1 \times 10^4 \text{ mol } NH_3 (\text{mol MoFe protein})^{-1}$. This indicates that the MoFe protein in CdS:MoFe protein biohybrids can function at rates comparable to physiological TOF by nitrogenase.

The mechanism of N_2 reduction by the MoFe protein coproduces H_2 (Fig. 1), which was also observed as a coproduct during CdS:MoFe protein photocatalytic N_2 reduction (fig. S3 and tables S4 and S5). This supports a mechanism of N_2 reduction by the CdS:MoFe protein biohybrids that is analogous to the mechanism of MoFe protein:Fe protein catalysis. CdS inhibition of Fe protein-dependent catalysis (table S11) indicates that CdS binds at or near the Fe protein binding site on MoFe protein (Fig. 1B); however, it is not known whether the P cluster serves as an intermediate in electron transfer during photocatalysis.

Additional evidence that the N_2 reduction reaction occurs at FeMo-co of the MoFe protein was observed with known inhibitors of Mo-dependent nitrogenase activity. Acetylene (C_2H_2), carbon monoxide (CO), and H_2 are all known to specifically inhibit the N_2 reduction reaction at FeMo-co. Acetylene acts as a substrate to inhibit N_2 and proton reduction at FeMo-co (19, 20). In contrast, CO inhibits N_2 reduction by blocking the N_2 binding site at FeMo-co, but proton reduction to H_2 is unaffected (21). The addition of

¹Biosciences Center, National Renewable Energy Laboratory, Golden, CO 80401, USA. ²Department of Chemistry and Biochemistry, Utah State University, Logan, UT 84322, USA. ³Department of Chemistry and Biochemistry, University of Colorado Boulder, Boulder, CO 80309, USA. ⁴Department of Chemistry and Biochemistry, Montana State University, Bozeman, MT 59717, USA.

*Present address: Department of Chemistry, Luther College, Decorah, IA 52101, USA. †Corresponding author. Email: paul.king@nrel.gov

either H₂, CO, or C₂H₂ at 10% to a 90% N₂ gas phase decreased the N₂ reduction rates by CdS: MoFe protein biohybrids to the background levels observed with apo-MoFe protein (Fig. 2 and tables S12 and S13). The results are consistent with the effect of these inhibitors on preventing MoFe protein catalysis in the Fe protein, ATP-driven physiological reaction. Photochemical H₂ production by CdS:MoFe protein biohybrids was also inhibited by 10% C₂H₂, but only slightly decreased under 10% CO compared to rates under 100% N₂ (fig. S3). Consistent with N₂ being a substrate of CdS:MoFe protein biohybrids, the rates of H₂ production were 25% higher when N₂ was replaced with 100% argon (fig. S3). Together, the inhibition results are consistent with photocatalysis by CdS:MoFe protein biohybrids occurring at the FeMo-co site of the MoFe protein

by a mechanism that is similar to that for the Fe protein, ATP-coupled reaction.

Although the CdS nanorods have a low photoexcited state potential (−0.8 V versus NHE), other reductants, such as Eu(II)-L₃, have lower potentials (as low as −1.2 V versus NHE), yet only the CdS nanorods support N₂ reduction by MoFe protein. This indicates that some aspect of the nanorods, other than photochemical driving force alone, contributes to the achievement of N₂ reduction. One possible explanation is the rapid delivery of successive electrons due to strong light absorption by the CdS nanorods, which could allow achievement of the four-electron reduced FeMo-co state (E₄) that is required for N₂ binding and reduction (4, 6). Slow accumulation of electrons (low e-flux) on FeMo-co in the presence of other (photo)chemical donors

(8–11) could allow less reduced FeMo-co states (e.g., E₂) to oxidize by evolving H₂ before N₂ binds. It is also possible that the binding of the CdS nanorod to the MoFe protein could induce protein conformational changes necessary to achieve N₂ reduction that normally occur upon Fe protein binding (9).

The ability to create complexes between nanomaterials and MoFe protein and other enzymes establishes that photoexcited electrons can be used to drive difficult catalytic transformations while providing new tools for mechanistic investigations. Likewise, the light-harvesting properties of nanomaterials are highly tunable, and their unique optical properties can be used to probe in fine detail how changes in structure and energetics control electron transfer and macroscopic reaction rates. Biohybrid complexes can be used to examine how the flux and thermodynamics of photoexcited electron transfer influence the turnover and fidelity of catalytic product formation. Pairing biohybrid photochemical complexes with time-resolved methods is likely to enable profound new insights into the stepwise processes that underpin these challenging chemical reactions.

REFERENCES AND NOTES

- G. Ertl, *Angew. Chem. Int. Ed.* **47**, 3524–3535 (2008).
- D. Kim, K. K. Sakimoto, D. Hong, P. Yang, *Angew. Chem. Int. Ed.* **54**, 3259–3266 (2015).
- R. Lan, J. T. S. Irvine, S. Tao, *Sci. Rep.* **3**, 1145 (2013).
- B. M. Hoffman, D. Lukoyanov, Z.-Y. Yang, D. R. Dean, L. C. Seefeldt, *Chem. Rev.* **114**, 4041–4062 (2014).
- R. V. Hageman, R. H. Burris, *Proc. Natl. Acad. Sci. U.S.A.* **75**, 2699–2702 (1978).
- D. Lukoyanov, Z.-Y. Yang, D. R. Dean, L. C. Seefeldt, B. M. Hoffman, *J. Am. Chem. Soc.* **132**, 2526–2527 (2010).
- D. Lukoyanov et al., *J. Am. Chem. Soc.* **137**, 3610–3615 (2015).
- K. Danyal et al., *J. Am. Chem. Soc.* **132**, 13197–13199 (2010).
- K. Danyal et al., *Biochemistry* **54**, 2456–2462 (2015).
- L. E. Roth, J. C. Nguyen, F. A. Tezcan, *J. Am. Chem. Soc.* **132**, 13672–13674 (2010).
- L. E. Roth, F. A. Tezcan, *J. Am. Chem. Soc.* **134**, 8416–8419 (2012).
- Materials and methods are available on Science Online.
- A. P. Alivisatos, *Science* **271**, 933–937 (1996).
- K. A. Brown, S. Dayal, X. Ai, G. Rumbles, P. W. King, *J. Am. Chem. Soc.* **132**, 9672–9680 (2010).
- K. A. Brown, M. B. Wilker, M. Boehm, G. Dukovic, P. W. King, *J. Am. Chem. Soc.* **134**, 5627–5636 (2012).
- L. Brus, *J. Phys. Chem.* **90**, 2555–2560 (1986).
- H.-W. Tseng, M. B. Wilker, N. H. Damrauer, G. Dukovic, *J. Am. Chem. Soc.* **135**, 3383–3386 (2013).
- W. N. Lanzilotta, L. C. Seefeldt, *Biochemistry* **36**, 12976–12983 (1997).
- M. J. Dilworth, *Biochim. Biophys. Acta* **127**, 285–294 (1966).
- R. Schöllhorn, R. H. Burris, *Proc. Natl. Acad. Sci. U.S.A.* **58**, 213–216 (1967).
- H. C. Winter, R. H. Burris, *Annu. Rev. Biochem.* **45**, 409–426 (1976).
- G. Zhao, N. D. Chasteen, *Anal. Biochem.* **349**, 262–267 (2006).

ACKNOWLEDGMENTS

K.A.B. and P.W.K. were supported by a Laboratory Directed Research and Development Program seed project at the National Renewable Energy Laboratory for CdS:MoFe protein photochemical H₂ production experiments, and by the U.S. Department of Energy, Office of Basic Energy Sciences, Division of Chemical Sciences, Geosciences, and Biosciences; and the U.S. Department of Energy under Contract no. DE-AC36-08-GO28308 with the National Renewable Energy Laboratory for CdS:MoFe protein biohybrid N₂ reduction experiments. M.B.W., H.H., and G.D. conducted

Fig. 1. Reaction scheme for N₂ reduction to NH₃ by nitrogenase and the CdS:MoFe protein biohybrids. (A) The reaction catalyzed by nitrogenase Fe protein (homodimer represented in green; MgATP binding site, orange sphere; [4Fe–4S] cluster, brown square) and MoFe protein (α₂β₂ tetramer represented in gray and purple; FeMo-co, red hexagon; [8Fe–7S] P cluster, blue sphere). Hydrolysis of 16 ATP by Fe protein (E_m = −0.42 V) is required for the sequential transfer (signified by the equilibrium arrow) of eight electrons (e[−]) to MoFe protein (E_m = −0.31 V) for catalytic

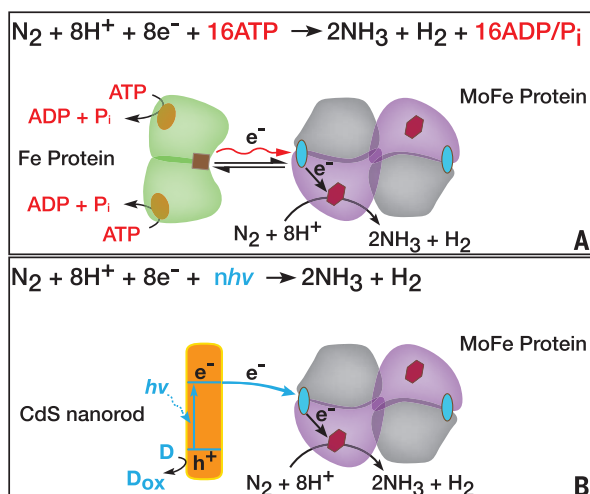
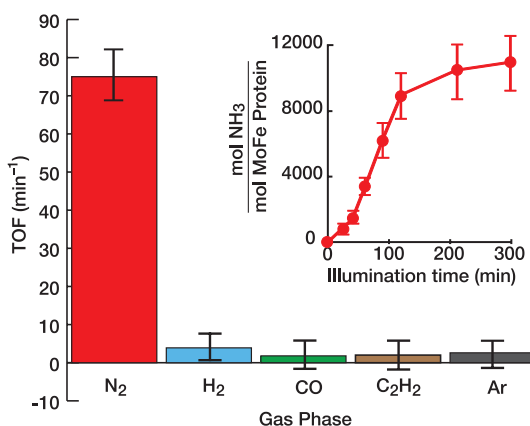


Fig. 2. Photochemical N₂ reduction to NH₃ by CdS:MoFe protein biohybrids. The TOF of catalytic reduction of N₂ to NH₃ was measured under 100% N₂ (red). The effects of MoFe protein inhibitors on the TOF are shown for 10% of either H₂ (cyan), carbon monoxide (CO, green), or acetylene (C₂H₂, brown) in a bulk phase of 90% N₂. TOF for the CdS:MoFe protein biohybrids under 100% Ar (gray) is shown as a negative control for comparison. Measured values were taken after 2 hours of illumination at 25°C for reactions comprising 1:1 molar ratios of CdS nanorods and MoFe protein tetramer.

Data are means of *N* = 4 independent measurements ± SD calculated by standard error propagation. (Inset) Time course of NH₃ production by CdS:MoFe protein biohybrids under 100% N₂ (12). TON = 1.1 × 10⁴ mol NH₃ (mol MoFe protein)^{−1} (table S10).



nanocrystal synthesis and ligand exchange under support by U.S. Department of Energy, Office of Basic Energy Sciences, Division of Materials Sciences and Engineering under Award DE-SC0010334. D.F.H., A.R., N.K., S.K., L.C.S., and J.W.P. were supported for nitrogenase purification and product quantification as part of the Biological and Electron Transfer and Catalysis (BETCy) EFRC, an Energy Frontier Research Center funded by the U.S. Department of Energy, Office of Science (DE-SC0012518). The authors thank W. Tumas and R. Greene for thoughtful advice and many helpful discussions, and B. Hoffman for helpful discussions and

constructive reading of the manuscript. Data are available in the supplementary materials. K.A.B. performed photochemical experiments, including colorimetric NH_3 measurements; N.K., A.R., D.F.H., and S.K. performed nitrogenase and MoFe protein purifications, physiological nitrogenase assays, and fluorometric NH_3 measurements; M.B.W. and H.H. performed CdS nanocrystal synthesis, ligand exchange, and transmission electron microscopy imaging; K.A.B., L.C.S., G.D., J.W.P., and P.W.K. conceived and designed the study. All authors contributed to the writing of the manuscript.

SUPPLEMENTARY MATERIALS

www.sciencemag.org/content/352/6284/448/suppl/DC1
Materials and Methods
Figs. S1 to S3
Tables S1 to S13
References (23–28)

15 January 2016; accepted 23 March 2016
10.1126/science.aaf2091

PALEONTOLOGY

Precocity in a tiny titanosaur from the Cretaceous of Madagascar

Kristina Curry Rogers,^{1*} Megan Whitney,² Michael D'Emic,³ Brian Bagley⁴

Sauropod dinosaurs exhibit the largest ontogenetic size range among terrestrial vertebrates, but a dearth of very young individuals has hindered understanding of the beginning of their growth trajectory. A new specimen of *Rapetosaurus krausei* sheds light on early life in the smallest stage of one of the largest dinosaurs. Bones record rapid growth rates and hatching lines, indicating that this individual weighed ~3.4 kilograms at hatching. Just several weeks later, when it likely succumbed to starvation in a drought-stressed ecosystem, it had reached a mass of ~40 kilograms and was ~35 centimeters tall at the hip. Unexpectedly, *Rapetosaurus* limb bones grew isometrically throughout their development. Cortical remodeling, limb isometry, and thin calcified hypertrophic metaphyseal cartilages indicate an active, precocial growth strategy.

Sauropod dinosaurs began life as hatchlings less than a meter long and 10 kg in body mass (1). From there, they grew to immense adult body sizes, achieving the greatest absolute ontogenetic size difference known for any terrestrial tetrapod group. Sauropod eggs containing embryos dispelled the misconception that sauropods were viviparous (1), but lack of data at critical perinatal ontogenetic intervals has hindered our understanding of the beginning of sauropod life history. Here we describe a diminutive *Rapetosaurus krausei* (Université d'Antananarivo UA 9998) collected from a single bone-bearing horizon at locality MAD 93-18 in the Upper Cretaceous Anembalemba Member of the Maevarano Formation (2, 3) (fig. S1). UA 9998 includes limb, girdle, and vertebral elements indistinguishable from those of other, larger *Rapetosaurus* specimens (3–5) (Fig. 1, figs. S2 and S3, and tables S1 and S2). The lengths of preserved hind limb elements suggest a hip height of ~35 cm, and autopodial scaling and developmental mass extrapolation (6) yield an estimated body mass of ~40 kg (3) (Fig. 1 and tables S2 and S3). We use bone histology and x-ray computed tomography (XRCT) (3) (table S4) to understand growth dynamics in perinatal *Rapetosaurus*.

Long bone cortices are almost exclusively composed of densely vascularized fibrolamellar primary bone tissue. Osteocyte lacunae are densely distributed within the woven bone component of the fibrolamellar complex (Fig. 2), and centripetal bone deposition within primary vascular canals diminishes porosity in deeper cortex regions. External, subperiosteal vascular canals retain an enlarged diameter because osteonal infilling had only just begun. Most primary vascular canals are longitudinal, but XRCT data highlight abundant anastomosing circular and radial canals (Fig. 3, MorphoBank, Project 2326). Lines of arrested growth (LAG) and annuli are absent in all elements, but a nearly ubiquitous perimedullary modulation of vascularity is represented by a ~435- μm -wide circumferential zone (Figs. 2, A to C, and 3) that is the consequence of one or two consecutive layers of primary vascular canals with diameters ~20 μm narrower than canals positioned in the deeper or more superficial cortex (Fig. 2, B and C). Zone morphology is consistent with hatching lines observed in squamates (7) and crocodylians (8), neonatal lines observed in mammals (9), and neonatal vascular transitions recorded in some mammals (10) and birds (11) (fig. S4). Hatching lines archive perinatal limb bone circumferences for UA 9998, and an isometric model of limb growth predicts a hind limb length of ~20 cm and a body mass of 2.5 to 4.3 kg at hatching (3) (tables S3 and S5). These data align with hypothesized sauropod hatchling sizes based on known egg dimensions and embryonic remains [e.g., (1)]. Daily appositional rates for fibrolamellar bone tissue in three

nonavian dinosaurs that bracket *Rapetosaurus* phylogenetically (12) suggest that 39 to 77 days transpired between hatching and the death of UA 9998.

A single generation of scattered secondary osteons exists in the midcortex of all elements (Figs. 2, A, B, and D, and 3). Proximal and distal ends of long bones preserve the calcified hypertrophic cartilage (CHC) component of the metaphyses and epiphyses (Figs. 1D and 4). The CHC regions are ~500 μm thick, with thicknesses varying slightly among elements and between proximal and distal ends of a single bone: In the tibia, the CHC is thicker at the proximal end (Fig. 4, A to C). The chondrocytes that form the CHC are spherical and exhibit a columnar orientation, particularly at the metaphyses (Fig. 4, D and E). The deep surface of the metaphysis is sharply demarcated and linear where endosteal bone has replaced calcified cartilage (Fig. 4D). Some metaphyseal vessels invade the zone of hypertrophy, and bone infiltrates the epiphyseal region at the margins of canals to result in small islands of hypertrophied chondrocytes within bony trabeculae more than a millimeter deep to the proximal and distal surfaces of the tibia (Fig. 4E).

Despite massive changes in body size throughout ontogeny, general morphology and proportions among appendicular elements of UA 9998 indicate that *Rapetosaurus* limb bones are similar in shape throughout life (3) (fig. S3 and table S2). Selection may act strongly on juvenile morphologies in precocial species and can lead to “ontogenetic canalization,” resulting in close resemblance of adults and juveniles [e.g., (13, 14)]. Lack of noticeable allometry in the long bones of neosauropods highlights the efficiency of long-limbed locomotion in adults (15) and might also indicate that early in ontogeny, locomotor scope was more varied than in adults, with a wider gait repertoire possible in young “overbuilt” juveniles [e.g., (15, 16)]. Similar patterns are documented for some mammals, in which the shape and relative proportions of skeletal elements scale isometrically to maintain mechanical integrity during rapid growth (16, 17). Maintenance of isometric relationships through ontogeny has recently been ascribed to a complex mechanism of bone scaling based on element-specific balance between proximal and distal epiphyseal growth rates combined with synchronous and directed bone remodeling (17). The single generation of secondary osteons extending into the midcortex of all sampled perinatal *Rapetosaurus* elements (Figs. 2D and 3)

¹Biology and Geology Departments, Macalester College, St. Paul, MN 55105, USA. ²Department of Biology, University of Washington, Seattle, WA 98185-1800, USA. ³Biology Department, Adelphi University, Garden City, NY 11530-0701, USA. ⁴Department of Earth Sciences, University of Minnesota, Minneapolis, MN 55455-1333, USA.

*Corresponding author. Email: rogersk@macalester.edu

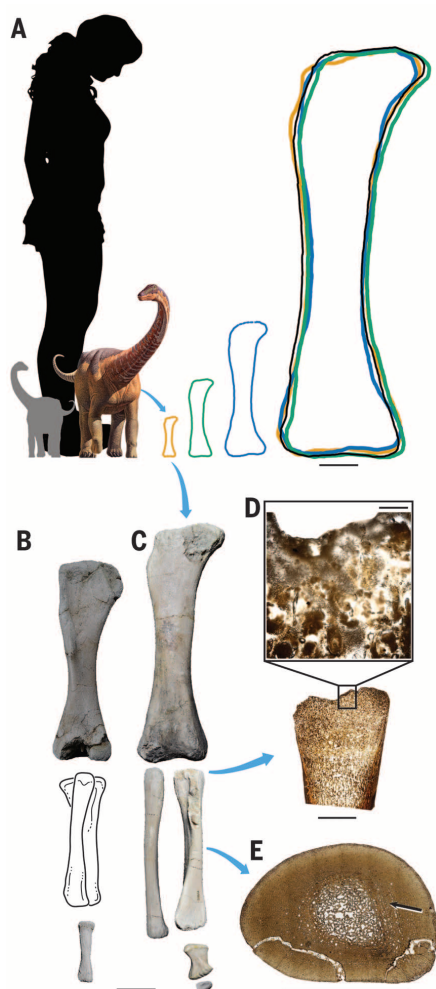


Fig. 1. Perinate *Rapetosaurus krausei* (UA 9998). (A) Isometric growth of limb elements illustrated by four femora throughout ontogeny. Gray silhouette represents hatchling, color represents UA 9998. Orange outline is UA 9998, black is largest known *Rapetosaurus* (length = 143 cm), green and blue are intermediate *Rapetosaurus* femora (3–5) (figs. S2 and S3 and tables S1 to S3). (B) Right humerus, metacarpal III. (C) Right femur, fibula, metatarsal I, phalanx I.1, left tibia (reversed) in anterior view. High-resolution images archived at MorphoBank (Project 2326). (D) Proximal tibia epiphyseal microstructure. (E) Mid-diaphyseal tibia microstructure; arrow indicates hatching line. Scale bars: 20 cm (A), 3 cm (B and C), 500 μ m [(D), inset], and 1 mm (D and E).

contrasts with other known dinosaurs that exhibit midcortex remodeling in “late juvenile” stages at the earliest (18, 19). Additional explanations for the triggering of bone remodeling relate to a combination of factors, including (i) a high basal metabolic rate (20); (ii) biomechanical loading (21); (iii) aging and microfracture repair (22); and (iv) mineral storage and remobilization (21). Our data corroborate the idea that the postcranial skeletons of very young *Rapetosaurus* were built to accommodate the

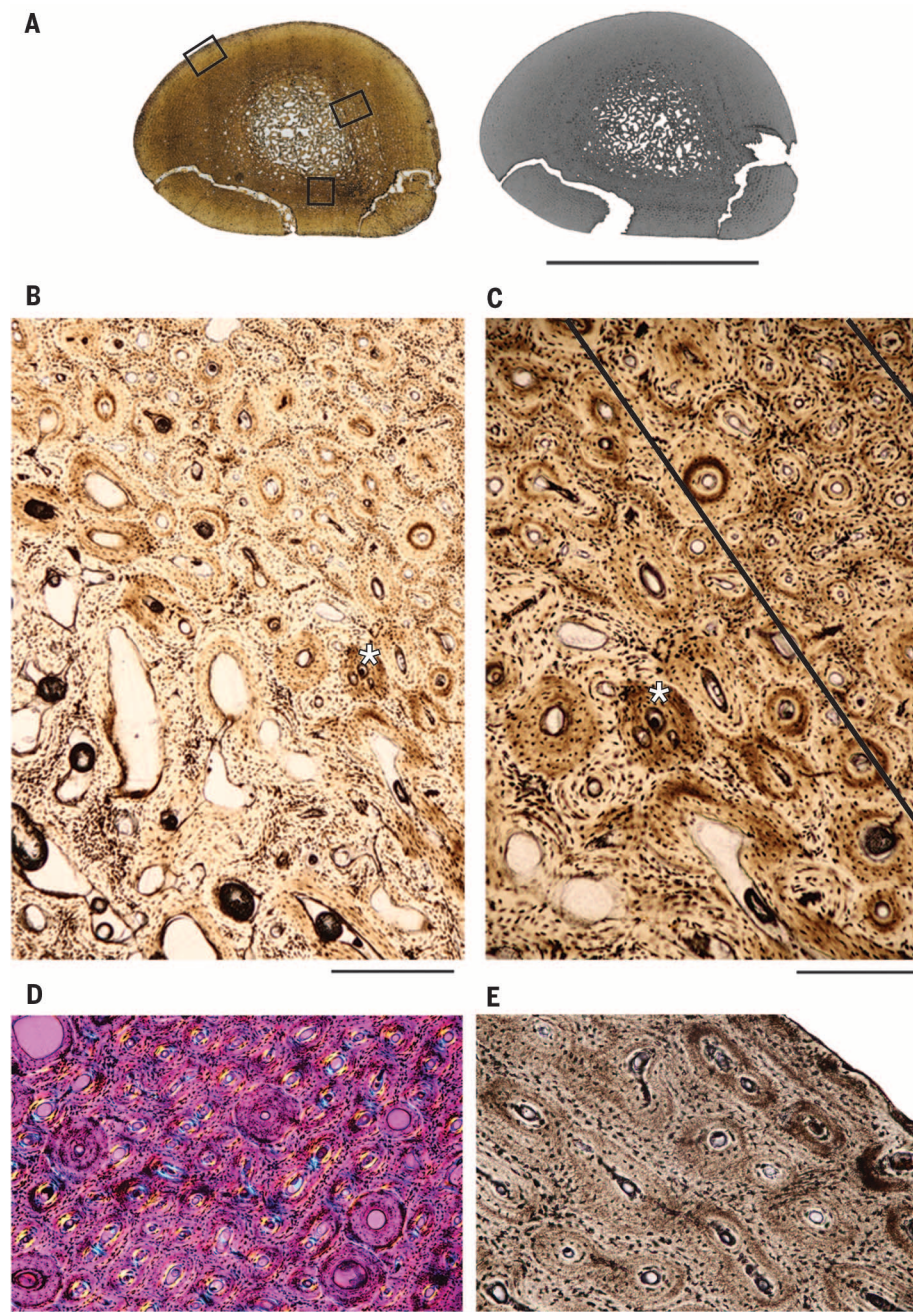


Fig. 2. Tibia mid-diaphyseal histology. (A) Histologic (left) and XRCT sections (right). Boxed areas are enlarged in (B) to (E). (B) Transition between embryonic (bottom left) and postnatal bone tissue (upper right); asterisk indicates the same location in (B) and (C). (C) Black bars bound hatching line zone, with decreased vascular canal dimensions. (D) Midcortex secondary remodeling in cross-polarized light. (E) Periosteal primary fibrolamellar bone. Scale bars: 1 cm (A), 500 μ m (B), 300 μ m (C and D), and 100 μ m (E).

massive adult sizes that they would eventually achieve. Moreover, the early onset of bone remodeling in weight-bearing elements, combined with the isometry of the *Rapetosaurus* limb skeleton throughout ontogeny, bolsters an interpretation of precocity in this taxon.

The calcified cartilage components of the epiphyseal-metaphyseal region can help to differentiate fossil vertebrates along the altricial-precocial

growth strategy spectrum [e.g., (19, 23–25)]. In birds, longitudinal bone growth rates are higher and calcified cartilage metaphyseal structures are thicker in altricial hatchlings (24, 25). In precocial birds, the reduced cartilage and increased bone content relate to balancing bone elongation and functional constraints, particularly in fast-growing organisms (24, 25), and calcified cartilage thickness declines posteclosion in accordance

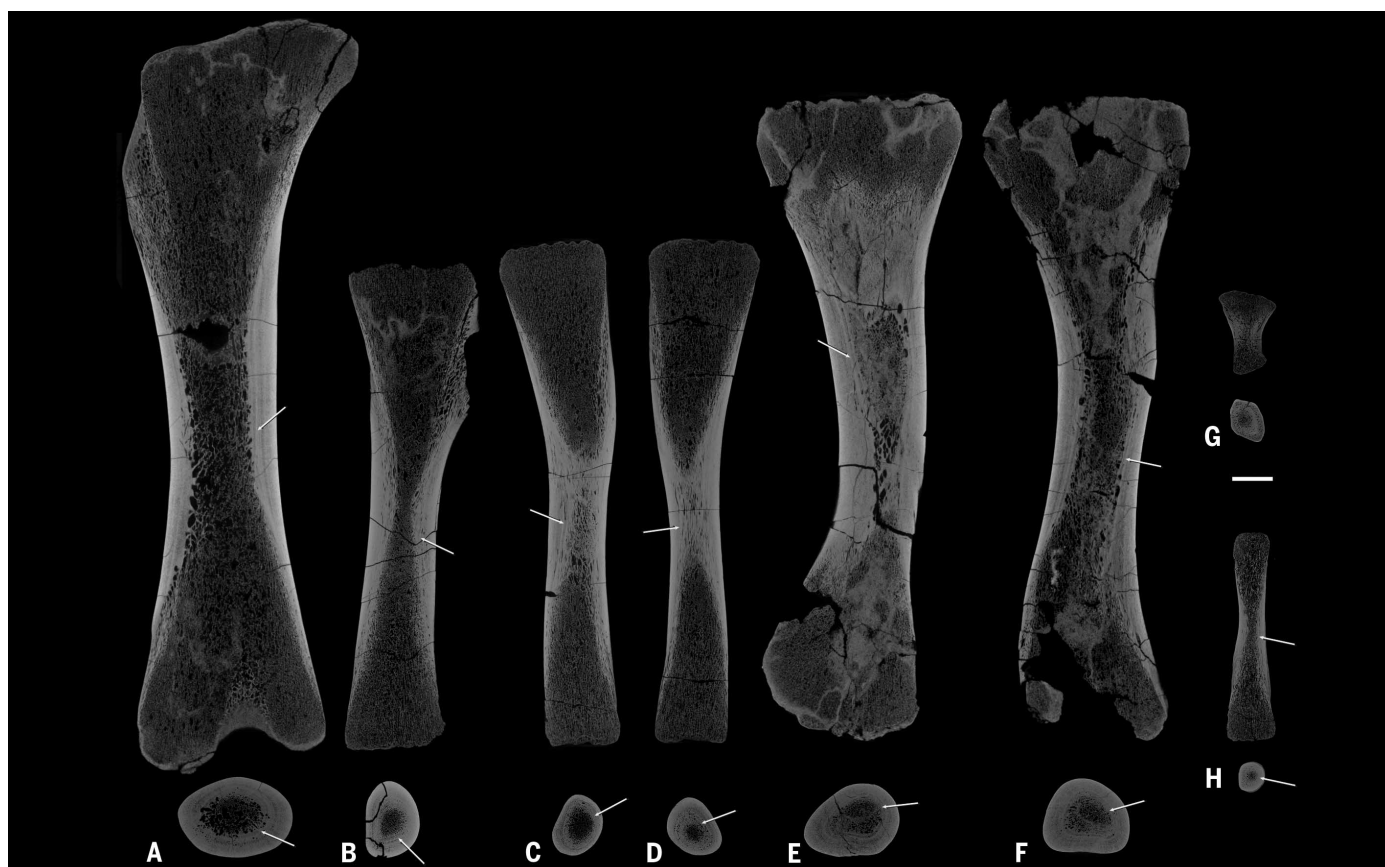
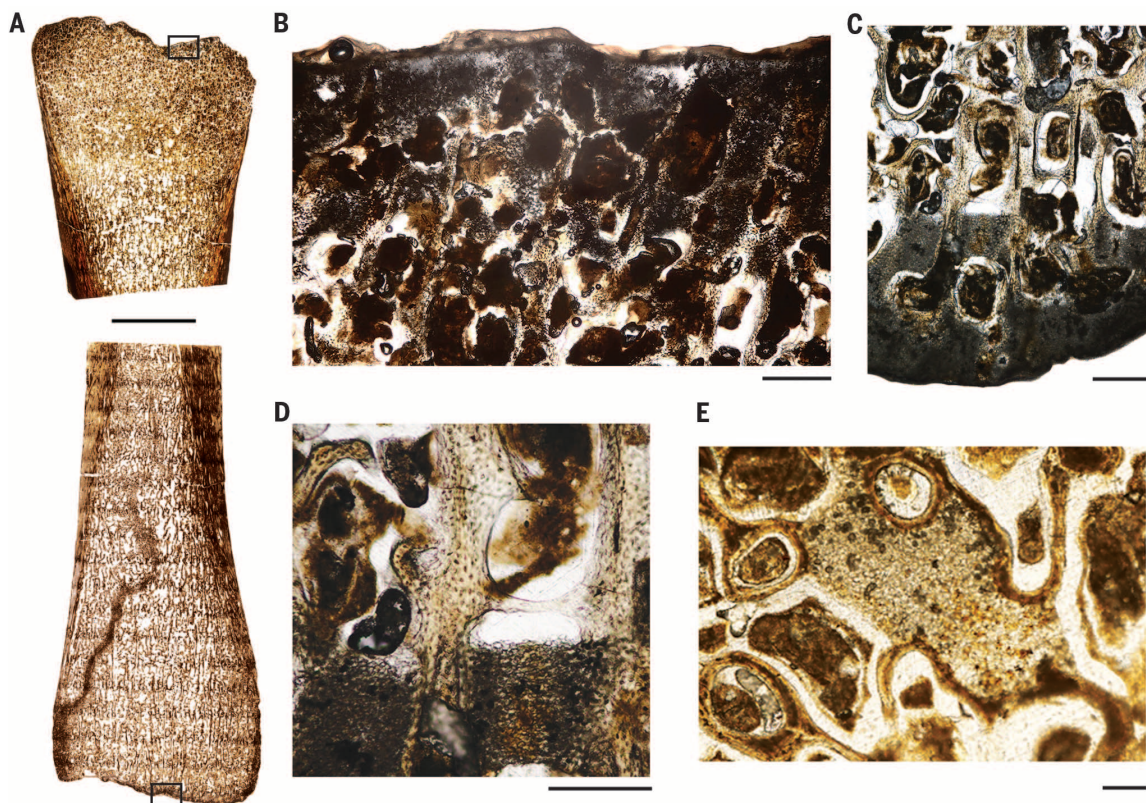


Fig. 3. Longitudinal and transverse XRCT sections. (A) Right femur; (B) left tibia; (C) right fibula; (D) left fibula; (E) right humerus; (F) left humerus; (G) right metatarsal I; (H) right metacarpal III. Arrows indicate hatching line. Scale bar: 1 cm.

Fig. 4. Tibia epiphyseal histology.

(A) Proximal (top) and distal sections (bottom). Boxed areas are enlarged in (B) and (C). (B) Proximal calcified hypertrophic cartilage (CHC). (C) Distal CHC. (D) Metaphyseal region of the distal tibia illustrating stout, sharp metaphyseal CHC. (E) Proximal metaphysis preserves CHC "islands" within bony trabeculae. Scale bars: 1 cm (A), 500 μ m (B and C), 300 μ m (D), and 100 μ m (E).



with growth slowdown prior to fledging (25). Among other embryonic and perinatal dinosaurs, the thickness of the CHC has been used as a proxy for altriciality or precocity. Hadrosaurs *Maiaasaura* and *Hypacrosaurus* preserve “massive amounts” of calcified cartilage and numerous diaphyseal cartilage islands hypothesized to indicate altricial behaviors (18, 19). Epiphyseal histology of the theropod *Troodon* records thinner CHC with only a few small, deeply located cartilage islands within the diaphysis, consistent with a more precocial growth strategy (19), but, unlike titanosaurs, paravians (including *Troodon*) are thought to have some degree of parental care (3, 26). UA 9998 CHC regions are thin (~500 μm), with sparse, deep cartilage islands that compare favorably with the CHC of precocial birds nearing fledging (23–25) and some perinatal dinosaurs (19). That said, UA 9998 is only ~11% the size of the largest known *Rapetosaurus* individual (3) (table S2), and it is unreasonable to assume that the thin CHC zones indicate growth slowdown at skeletal maturity. In extant vertebrates, bone elongation also slows during intervals of acute starvation via a decrease in chondroplasia and osteoblastic activity (27, 28). These shifts in cellular activity are signaled by modified metaphyseal morphology as osteogenesis outpaces the rate of cartilage proliferation, eventually restricting the CHC to result in a “stouter” metaphysis with a “sharper” chondro-osseous junction than that in healthy individuals (27). UA 9998 exhibits the stout, sharp CHC expected with acute starvation (27, 28). Drought and its attendant hardships have been well documented for the Maevarano Formation vertebrate assemblage [e.g., (2, 3, 29, 30)]. During the short interval between hatching and drought-related mortality, UA 9998 lived an active, precocial life evidenced by isometric scaling, rapid neonatal growth rates, midcortical remodeling, and calcified cartilaginous metaphyseal morphology.

REFERENCES AND NOTES

1. L. M. Chiappe *et al.*, *Nature* **396**, 258–261 (1998).
2. R. R. Rogers, *Geology* **33**, 297–300 (2005).
3. Materials and methods are available as supplementary materials on Science Online.
4. K. Curry Rogers, C. A. Forster, *Nature* **412**, 530–534 (2001).
5. K. Curry Rogers, *J. Vertebr. Paleontol.* **29**, 1046–1086 (2009).
6. G. M. Erickson, T. A. Tumanova, *Zool. J. Linn. Soc.* **130**, 551–566 (2000).
7. J. Hugli, M. R. Sánchez-Villagra, *J. Herpetol.* **46**, 312–324 (2012).
8. J. Castanet, H. Francillon-Viellet, F. J. Meunier, A. de Ricqlès, in *Bone*, vol. 7, *Bone Growth—B*, B. K. Hall, Ed. (CRC Press, 1993), chap. 9.
9. J. Castanet *et al.*, *J. Zool.* **263**, 31–39 (2004).
10. A. J. Curtin, A. A. Macdonald, E. G. Schaible, V. Louise Roth, *J. Vertebr. Paleontol.* **32**, 939–955 (2012).
11. J. M. Starck, A. Chinsamy, *J. Morphol.* **254**, 232–246 (2002).
12. J. M. Starck, N. Le Roy, C. Martinez-Maza, L. Montes, *Paleobiology* **38**, 335–349 (2012).
13. D. R. Carrier, *Physiol. Zool.* **69**, 467–488 (1996).
14. D. R. Carrier, R. Leon, *J. Zool. (Lond.)* **222**, 375–389 (1990).
15. M. F. Bonnan, *Anat. Rec.* **290**, 1089–1111 (2007).
16. A. A. Biewener, *J. Exp. Biol.* **208**, 1665–1676 (2005).
17. T. Stern *et al.*, *PLoS Biol.* **13**, e1002212 (2015).
18. J. R. Horner, A. de Ricqlès, K. Padian, *J. Vertebr. Paleontol.* **20**, 115–129 (2000).
19. J. R. Horner, K. Padian, A. de Ricqlès, *Paleobiology* **27**, 39–58 (2001).
20. A. Teti, A. Zallone, *Bone* **44**, 11–16 (2009).
21. A. G. Robling, A. B. Castillo, C. H. Turner, *Annu. Rev. Biomed. Eng.* **8**, 455–498 (2006).

22. R. B. Martin, *Calcif. Tissue Int.* **73**, 101–107 (2003).
23. C. Barreto, R. M. Albrecht, D. E. Bjorling, J. R. Horner, N. J. Wilsman, *Science* **262**, 2020–2023 (1993).
24. J. M. Starck, R. E. Ricklefs, *Avian Growth and Development: Evolution Within the Altricial-Precocial Spectrum* (Oxford Univ. Press, 1998).
25. L. Montes, E. de Margerie, J. Castanet, A. de Ricqlès, J. Cubo, *J. Anat.* **206**, 445–452 (2005).
26. D. J. Varricchio *et al.*, *Science* **322**, 1826–1828 (2008).
27. R. M. Acheson, M. N. Macintyre, *Br. J. Exp. Pathol.* **39**, 37–45 (1958).
28. R. M. Acheson, *J. Anat.* **93**, 123–130 (1959).
29. R. R. Rogers, D. W. Krause, K. Curry Rogers, *Nature* **422**, 515–518 (2003).
30. R. R. Rogers, D. W. Krause, K. Curry Rogers, A. Rasoaamiramanana, L. Rahantarisoa, *J. Vertebr. Paleontol.* **27** (suppl. 2), 21–31 (2007).

ACKNOWLEDGMENTS

Research was supported by the National Science Foundation (EAR-0955716). Higher-resolution images and XRCT .mpg files are

archived at MorphoBank (<http://morphobank.org/permalink/?P2326>). Original fossil material will be permanently deposited in the paleontology collection at the Université d'Antananarivo, with exact replicas (casts) housed at the Denver Museum of Nature and Science and at Macalester College. We thank the people of Berivotra and the Mahajanga Basin Project. R. Rogers, P. O'Connor, and three reviewers provided insightful comments. We thank J. Groenke and V. Heisey for preparation, J. Thole for photos, and T. Keillor, R. Martin, and D. Vital for artwork.

SUPPLEMENTARY MATERIALS

www.sciencemag.org/content/352/6284/450/suppl/DC1
Materials and Methods
Supplementary Text
Figs. S1 to S4
Tables S1 to S5
References (31–75)

24 December 2015; accepted 25 March 2016
10.1126/science.aaf1509

CELL QUIESCENCE

RNA-binding proteins ZFP36L1 and ZFP36L2 promote cell quiescence

Alison Galloway,¹ Alexander Saveliev,¹ Sebastian Łukasiak,^{1*} Daniel J. Hodson,^{1,2} Daniel Bolland,³ Kathryn Balmanno,⁴ Helena Ahlfors,¹ Elisa Monzón-Casanova,^{1,5} Sara Ciullini Mannurita,^{1†} Lewis S. Bell,¹ Simon Andrews,⁶ Manuel D. Díaz-Muñoz,¹ Simon J. Cook,⁴ Anne Corcoran,³ Martin Turner^{1‡}

Progression through the stages of lymphocyte development requires coordination of the cell cycle. Such coordination ensures genomic integrity while cells somatically rearrange their antigen receptor genes [in a process called variable-diversity-joining (VDJ) recombination] and, upon successful rearrangement, expands the pools of progenitor lymphocytes. Here we show that in developing B lymphocytes, the RNA-binding proteins (RBPs) ZFP36L1 and ZFP36L2 are critical for maintaining quiescence before precursor B cell receptor (pre-BCR) expression and for reestablishing quiescence after pre-BCR-induced expansion. These RBPs suppress an evolutionarily conserved posttranscriptional regulon consisting of messenger RNAs whose protein products cooperatively promote transition into the S phase of the cell cycle. This mechanism promotes VDJ recombination and effective selection of cells expressing immunoglobulin- μ at the pre-BCR checkpoint.

Lymphocyte development is characterized by dynamic shifts between quiescence and proliferation. Quiescence promotes variable-diversity-joining (VDJ) recombination, the process that generates immunoglobulin and T cell receptor genes, because RAG2 protein expression is restricted to the G₀-G₁ phase of the cell cycle (1–3). In B cells, VDJ recombination

leads to expression of an immunoglobulin- μ (I μ) heavy chain that, together with the surrogate light chains, forms a precursor B cell receptor (pre-BCR). Signals from the pre-BCR terminate the recombination process and trigger rapid proliferation associated with passage through the pre-BCR checkpoint (4). Later signals from the pre-BCR reestablish quiescence, allowing immunoglobulin light-chain recombination (fig. S1A) (5, 6).

The ZFP36 family of RNA-binding proteins (RBPs) regulate gene expression posttranscriptionally by promoting mRNA decay (7). This requires their direct binding to AU-rich elements (AREs) located in the 3' untranslated regions (3'UTRs) of mRNAs. ZFP36 destabilizes cytokine mRNAs and exerts an anti-inflammatory function (8, 9). In addition, ZFP36 antagonizes *Myc*-induced lymphomagenesis (10), and its paralogs ZFP36L1 and ZFP36L2 have redundant roles in preventing T cell leukemia in mice (11). The pathways controlled by these RBPs, however, have remained poorly understood.

¹Laboratory of Lymphocyte Signalling and Development, The Babraham Institute, Cambridge CB22 3AT, UK. ²Department of Haematology, University of Cambridge, The Clifford Allbutt Building, Cambridge Biomedical Campus, Hills Road, Cambridge CB2 0AH, UK. ³Laboratory of Nuclear Dynamics, The Babraham Institute, Cambridge CB22 3AT, UK.

⁴Laboratory of Signalling, The Babraham Institute, Cambridge CB22 3AT, UK. ⁵Department of Biochemistry, University of Cambridge, Tennis Court Road, Cambridge CB2 1QW, UK. ⁶Bioinformatics Group, The Babraham Institute, Cambridge CB22 3AT, UK.

*Present address: Wellcome Trust Sanger Institute, Hinxton, Cambridge CB10 1SA, UK. †Present address: Department of Neuroscience, Psychology, Pharmacology and Child Health (NEUROFARBA), Child Health Section, University of Florence, Meyer Children's Hospital, Florence, Italy. ‡Corresponding author. Email: martin.turner@babraham.ac.uk

In our study, all three ZFP36-family mRNAs were expressed throughout B cell development (fig. S1B). Conditional genetic deletion demon-

strated redundant roles for ZFP36L1 and ZFP36L2 in early B cell development that could not be compensated for by endogenous ZFP36 and that

were independent of NOTCH1, a known target of these RBPs (fig. S2) (11). We therefore generated mice in which *Zfp36l1* and *Zfp36l2* were

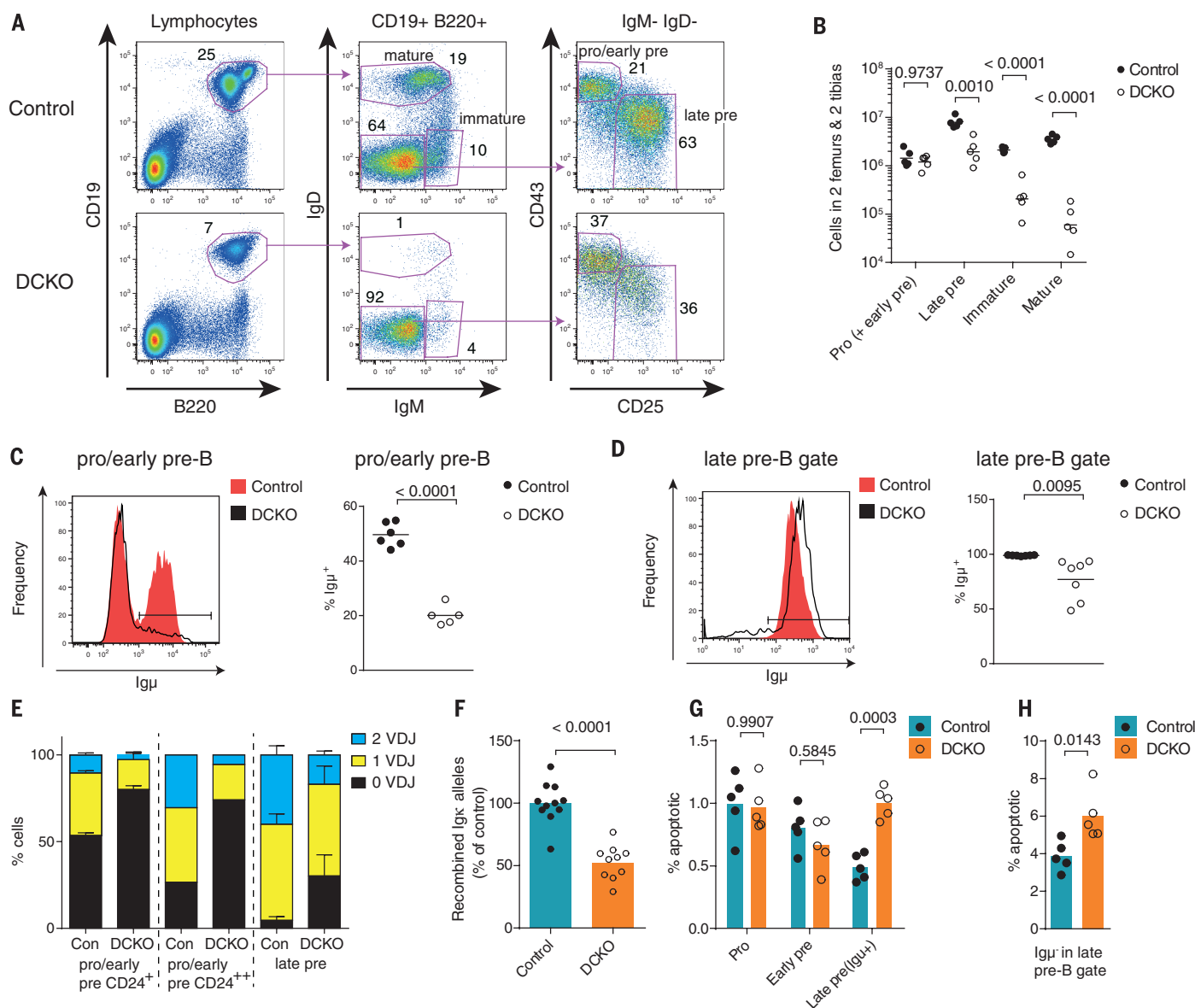


Fig. 1. Conditional knockout of *Zfp36l1* and *Zfp36l2* in pro-B cells abrogates pre-B cell development. (A) Representative scatter plots from flow cytometric analysis of B cell development in control and DCKO bone marrow. Numbers on plots indicate percentages of plotted cells in the gate (axes are in arbitrary units of fluorescence intensity). Purple arrows show the cell gating strategy. (B) Quantification of B cell developmental subsets in control ($n = 5$) and DCKO ($n = 5$) bone marrow from flow cytometry data shown in (A). Control and DCKO populations were compared by an analysis of variance (ANOVA) with Sidak's post-test. Data are representative of two independent experiments. (C and D) Flow cytometry measuring intracellular Igμ in control ($n = 6$) and DCKO ($n = 5$) pro- and early pre-B cells (C) and control ($n = 7$) and DCKO ($n = 7$) late pre-B cells (D). Representative histograms of flow cytometry data and summary data are shown. Control and DCKO populations were compared using a Student's t test. Data are representative of four (C) or two (D) independent experiments. (E) Quantification by DNA FISH (fluorescence in situ hybridization) of cells with zero, one, or two V-to-DJ-recombined IgH alleles within the CD24^{low} pro-B and early pre-B (enriched for pro-B cells; $n = 3$

biological replicates), CD24^{high} pro-B and early pre-B (enriched for early pre-B cells; $n = 1$ biological replicate), and late pre-B ($n = 3$ biological replicates) populations of control and DCKO mice. Data are from a single experiment; mean values and standard deviations (error bars) are shown. (F) Abundance of recombined Igx alleles in the late pre-B cells of control ($n = 11$) and DCKO ($n = 11$) mice, measured by qPCR (quantitative polymerase chain reaction). Control and DCKO samples were compared using a Student's t test. Data are included from three independent experiments. (G and H) Proportion of control ($n = 5$) and DCKO ($n = 5$) pro- and pre-B cells (G) or Igμ⁺ cells appearing in the late pre-B cell gate (H) that were in early apoptosis, measured by staining for activated caspases with FITC-VAD-FMK (fluorescein isothiocyanate-valyl-alanyl-aspartyl-[O-methyl]-fluoromethylketone). Control and DCKO samples were compared by an ANOVA with Sidak's post-test. Data are representative of two independent experiments. In (B) to (D) and (F) to (H), circles indicate biological replicates, bars represent means [geometric means in (B)], and P values are shown at the top of each panel.

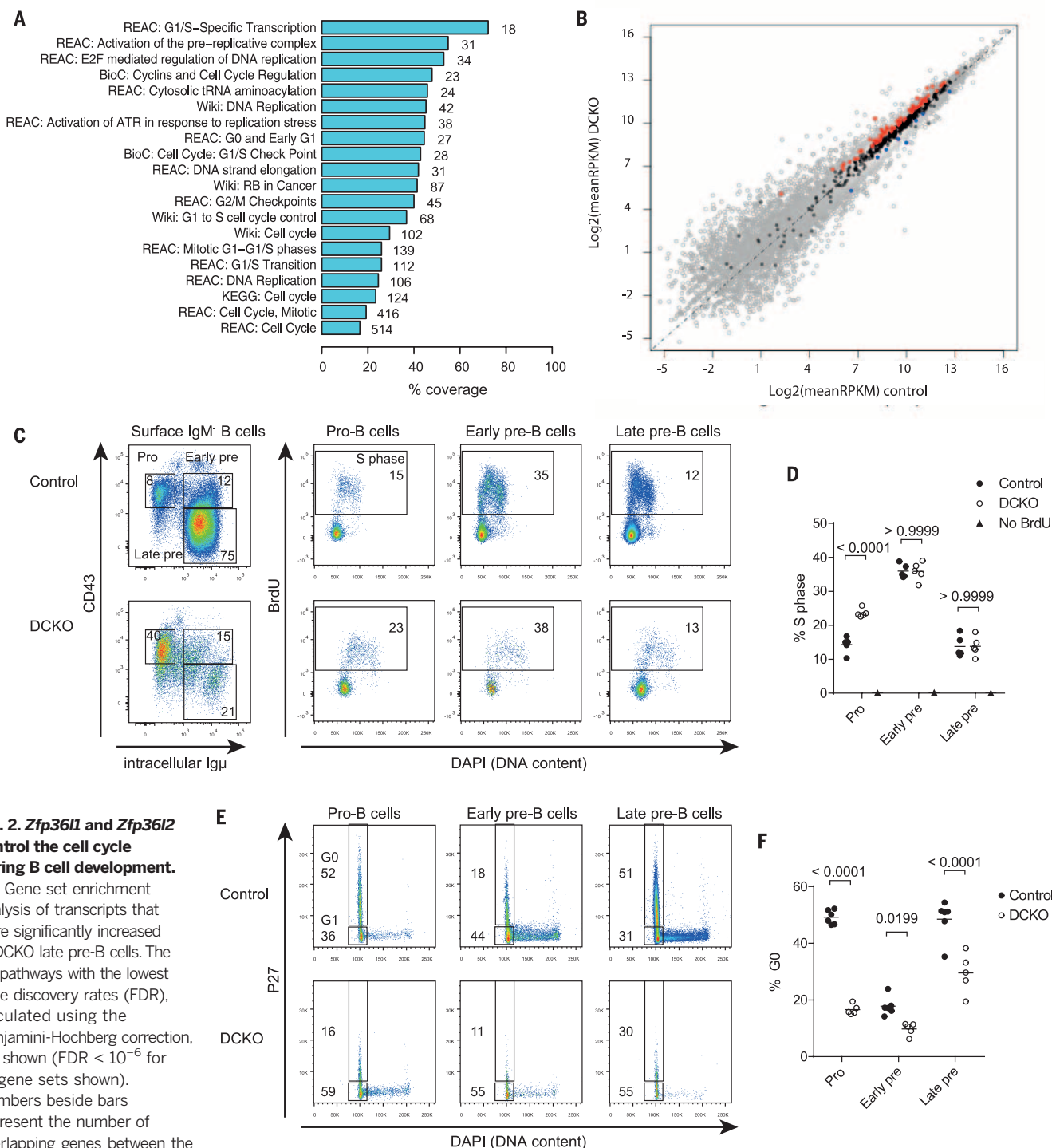


Fig. 2. *Zfp361l* and *Zfp3612* control the cell cycle during B cell development.

(A) Gene set enrichment analysis of transcripts that were significantly increased in DCKO late pre-B cells. The 20 pathways with the lowest false discovery rates (FDR), calculated using the Benjamini-Hochberg correction, are shown (FDR < 10^{-6} for all gene sets shown). Numbers beside bars represent the number of overlapping genes between the gene set and the transcripts that were increased in DCKO late pre-B cells. Data set abbreviations are as follows: REAC, Reactome; BIOC, Biocarta; Wiki, Wikipathways; and KEGG, Kegg pathways. (B) Scatter plot showing the average reads per kilobase per million (RPKM) in DCKO and control late pre-B cells for all genes (gray) and genes in the Reactome Cell Cycle pathway gene set that were significantly increased (red), unchanged (black), or significantly decreased in DCKO mice (blue). (C) Representative scatter plots from intracellular flow cytometry measuring BrdU (bromodeoxyuridine) incorporation after 2.5 hours of labeling in vivo in control and DCKO pro- and pre-B cells (DAPI, 4',6-diamidino-2-phenylindole). (D) Proportion of control ($n = 5$) and DCKO ($n = 5$) pro- and pre-B cells in the S phase

(incorporating BrdU), measured by flow cytometry as shown in (C). Data are representative of two independent experiments. (E) Representative scatter plots from intracellular flow cytometry measuring p27 in control and DCKO pro- and pre-B cells. (F) Proportion of control ($n = 6$) and DCKO ($n = 5$) pro- and pre-B cells in G₀ (expressing p27), measured by flow cytometry as shown in (E). Data are representative of two independent experiments. Numbers on flow cytometry plots indicate the percentages of plotted cells in the gate. Flow cytometry data for control and DCKO samples were compared by an ANOVA with Sidak's post-test. In (D) and (F), symbols indicate biological replicates, bars represent means, and P values are shown at the top of each panel.

deleted in pro-B cells (fig. S3). For simplicity, *Zfp361^{L1/L1} Zfp3612^{L1/L1} Mbl^{cre/+}* mice will be referred to as DCKO (double conditional knockout) mice, and their *Zfp361^{L1/L1} Zfp3612^{L1/L1} Mbl^{+/+}* littermates will be referred to as control mice. DCKO mice displayed reduced cellularity from the

pre-B stage onward, culminating in a 98% reduction in the number of mature B cells (Fig. 1, A and B). The proportion of CD43⁺ cells expressing Igu was greatly diminished (Fig. 1C), and a variable proportion of DCKO cells transited the pre-BCR checkpoint without Igu expression (Fig. 1D).

Within the compartment enriched for pro-B cells, DCKO mice had reduced proportions of cells containing one or two V-to-DJ-recombined IgH alleles (Fig. 1E and fig. S4). At later developmental stages, the DCKO mice failed to increase the proportion of recombined IgH alleles to control levels. The

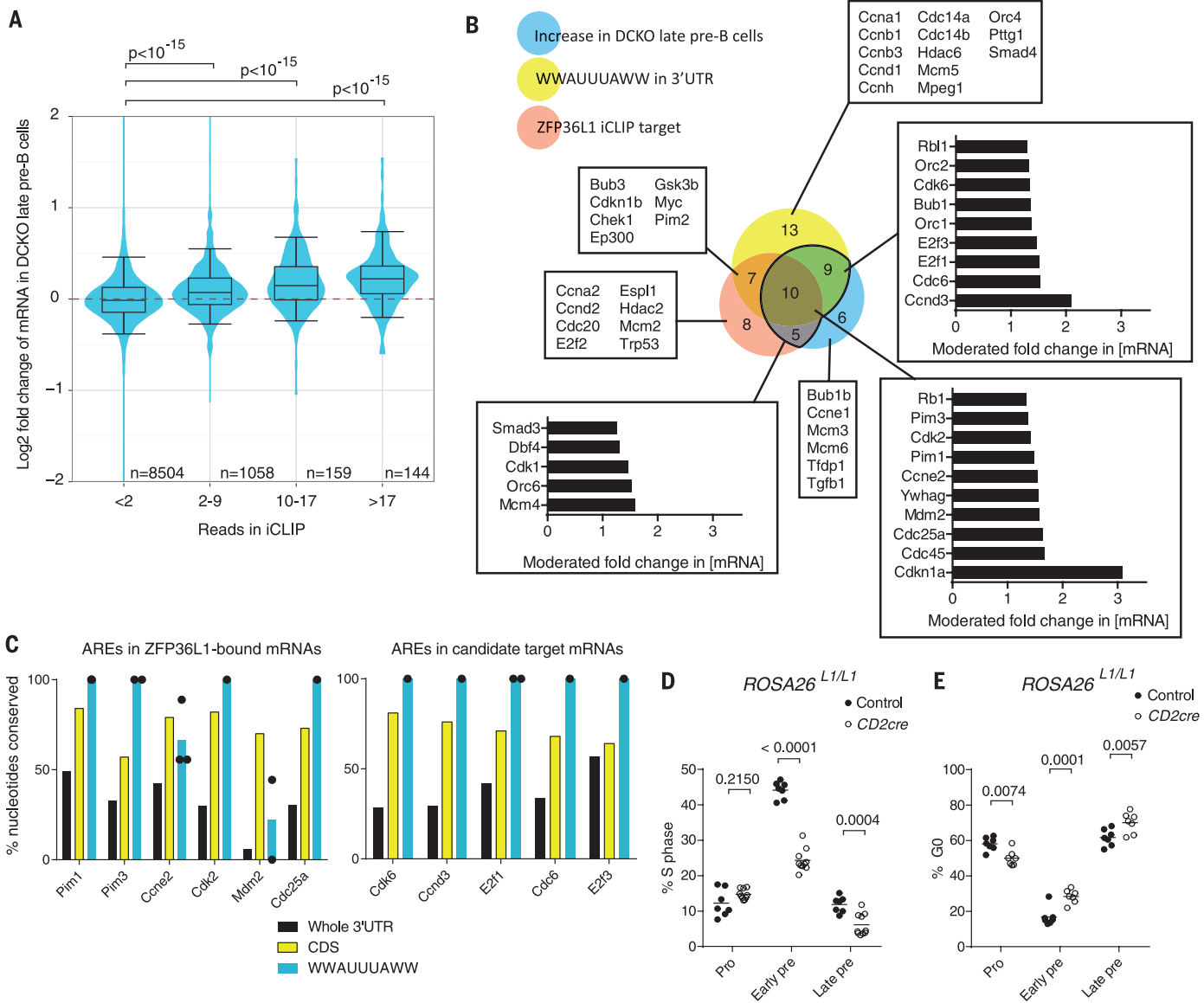


Fig. 3. Cell cycle mRNAs are direct targets of ZFP361 and ZFP362. The abundance of mRNAs in DCKO and control late pre-B cells was measured by RNA sequencing and was analyzed in DESeq. ZFP361 target mRNAs were identified by iCLIP in mitogen-stimulated lymph node B cells. **(A)** The moderated log₂ fold change in the abundance of RNA in DCKO relative to control late pre-B cells, grouped according to the number of ZFP361 iCLIP reads within significant peaks (FDR < 5%) in the 3'UTR of each gene. The number *n* of genes in each group is indicated. Boxes show medians and interquartile ranges; whiskers indicate the 5th and 95th percentiles. Groups of mRNAs were compared by an ANOVA with Tukey's post-test. **(B)** Venn diagram of cell cycle mRNAs, showing the overlap between mRNAs identified as ZFP361 targets by iCLIP, mRNAs with WWAUUUUAWW motifs in their 3'UTRs, and mRNAs that were significantly increased in DCKO relative to control late pre-B cells, as determined by a negative binomial test with a Benjamini-Hochberg correction for multiple testing in DESeq. The moderated log₂ fold changes in

mRNA abundance in DCKO late pre-B cells for selected groups of mRNAs are shown. **(C)** Sequence conservation among *Homo sapiens*, *Mus musculus*, *Loxodonta africana*, *Pteropus vampyrus*, *Canis lupus familiaris*, and *Bos taurus* CDS (coding sequences), 3'UTRs, and WWAUUUUAWW motifs for selected mRNAs that encode cell cycle regulators. **(D)** Proportion of pro- and pre-B cells from ROSA26^{L1/L1} (*n* = 7) and ROSA26^{L1/L1} CD2^{cre} (*n* = 10) mice in the S phase (incorporating BrdU), determined by flow cytometry after 2.5 hours of labeling in vivo. Flow cytometry scatter plots are shown in fig. S11A. Data are combined from two independent experiments. **(E)** Proportion of ROSA26^{L1/L1} control (*n* = 7) and ROSA26^{L1/L1} CD2^{cre} (*n* = 6) pro- and pre-B cells in G₀ (expressing p27). Flow cytometry scatter plots are shown in fig. S11B. Data are from a single experiment. Flow cytometry data for control and DCKO samples were compared by an ANOVA with Sidak's post-test. In (D) and (E), circles indicate biological replicates, bars represent means, and *P* values are shown at the top of each panel.

decrease in the proportions of V-to-DJ-recombined IgH alleles and $Ig\mu^+$ cells within the pro-B and early pre-B cell compartment of DCKO mice was similar, suggesting that the failure to express $Ig\mu$ is not due to an increase in nonproductive joints. Similarly, V-to-J recombination of the $Ig\kappa$ light-chain locus was reduced in DCKO late pre-B cells

(Fig. 1F). Thus, DCKO mice display reduced B cell numbers, delayed VDJ recombination, and failure of the pre-BCR checkpoint.

Expression of a productively rearranged $Ig\mu$ transgene failed to restore late pre-B, immature B, or mature B cell numbers in DCKO mice, indicating that reduced VDJ recombination of IgH is

not the sole defect (fig. S5). Consistent with this, we observed an increase in apoptosis of DCKO $Ig\mu^+$ late pre-B cells (Fig. 1G). The increased apoptosis was not susceptible to inhibition by BCL2, and we did not detect a DNA damage response (fig. S6). In both DCKO and control mice, a substantial number of $Ig\mu^-$ cells in the

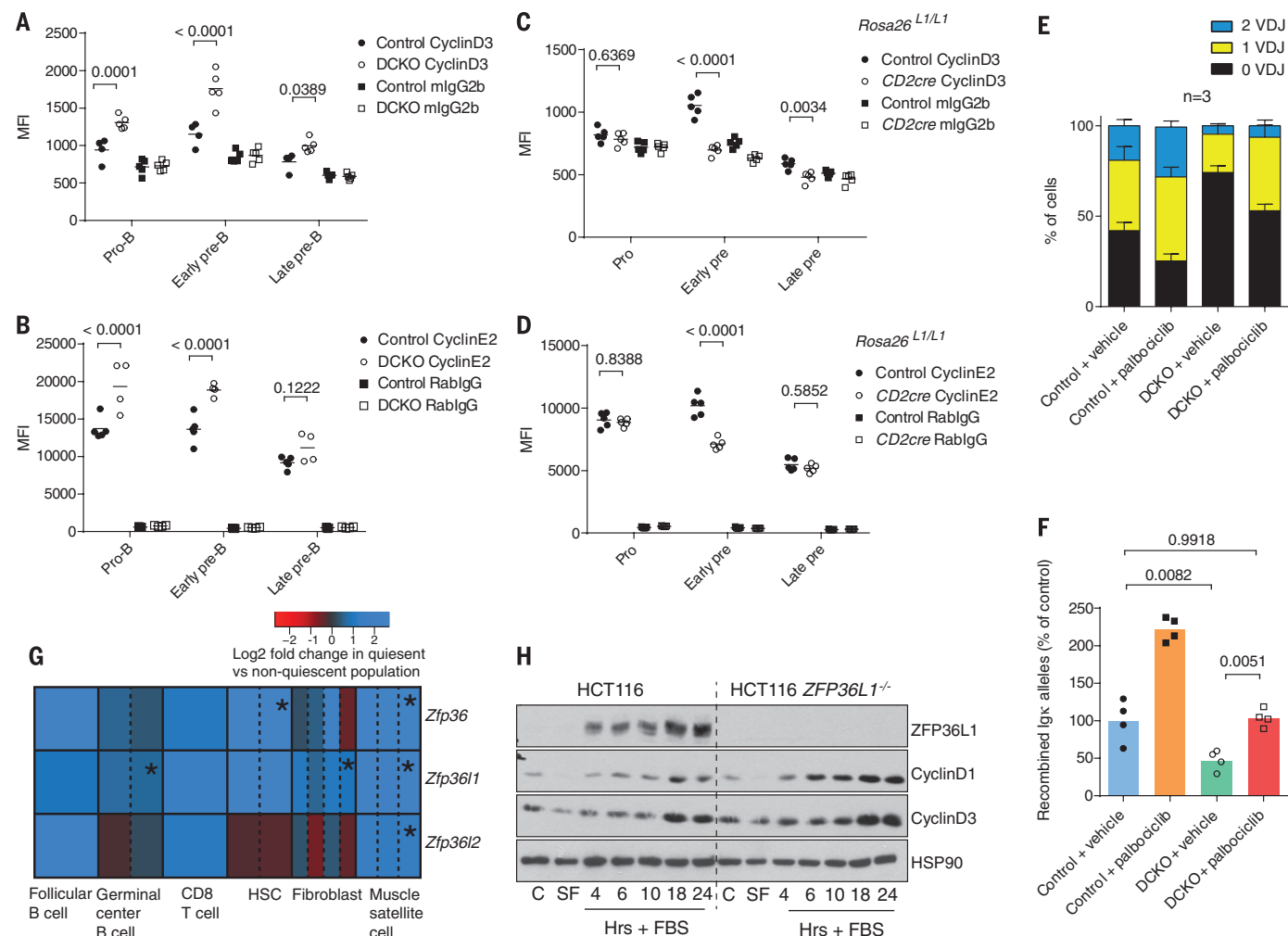


Fig. 4. Cyclin expression is repressed by ZFP36L1 and ZFP36L2 in B cell development, and this mechanism is required for efficient light-chain recombination. (A) MFI (median fluorescence intensity) of flow cytometry stains for cyclin D3 in control ($n = 4$) and DCKO ($n = 5$) pro- and pre-B cells. Scatter plots of flow cytometry are shown in fig. S12A. Data are representative of two independent experiments. (B) MFI of flow cytometry stains for cyclin E2 in control ($n = 5$) and DCKO ($n = 4$) pro- and pre-B cells. Scatter plots of flow cytometry are shown in fig. S12B. Data are representative of two independent experiments. (C) MFI of flow cytometry stains for cyclin D3 in *ROSA26*^{L1/L1} control ($n = 5$) and *CD2cre* ($n = 5$) pro- and pre-B cells. Scatter plots of flow cytometry are shown in fig. S12C. Data are from a single experiment. (D) MFI of flow cytometry stains for cyclin E2 in *ROSA26*^{L1/L1} control ($n = 5$) and *CD2cre* ($n = 5$) pro- and pre-B cells. Scatter plots of flow cytometry are shown in fig. S12D. Data are from a single experiment. Flow cytometry data for (A) to (D) were compared using an ANOVA with Tukey's post-test. (E) Quantification by DNA FISH of pro- and early pre-B cells with zero, one, or two V-to-DJ-recombined IgH alleles in control and DCKO mice after treatment with vehicle control or 150 mg/kg of palbociclib daily for 2 days. Data are from a single experiment ($n = 3$ for each group); mean values and standard deviations (error bars) are shown. (F) Abundance of recombined

$Ig\kappa$ alleles, measured by qPCR, in the late pre-B cells of control and DCKO mice treated with vehicle control or 150 mg/kg palbociclib daily for 2 days. Control and DCKO samples were compared using an ANOVA with Tukey's post-test. Data are from a single experiment. (G) The fold change (from published data sets) in expression of *Zfp36* family members, comparing resting (quiescent) and stimulated dividing (nonquiescent) follicular B cells ($n = 1$), light-zone (quiescent) and dark-zone (nonquiescent) germinal center B cells ($n = 2$), naive (quiescent) and effector (nonquiescent) CD8⁺ T cells ($n = 1$), adult (quiescent) and fetal (nonquiescent) hematopoietic stem cells (HSCs) ($n = 2$), p27^{high} (quiescent) and p27^{low} (nonquiescent) fibroblasts ($n = 4$), and resting (quiescent) and activated (nonquiescent) muscle satellite cells ($n = 3$). An asterisk indicates a P value less than 0.05. Solid lines separate independent data sets; dashed lines separate biological replicates. (H) Expression of ZFP36L1, cyclin D3, cyclin D1, and HSP90 proteins in parental and *ZFP36L1*^{-/-} HCT116 colon carcinoma cells after serum starvation and restimulation (C, continuous culture; SF, serum free for 24 hours; Hrs, hours; FBS, fetal bovine serum). Data are representative of three experiments. In (A) to (D) and (F), symbols represent biological replicates, bars indicate means, and P values are shown at the top of each panel.

late pre-B cell gate were apoptotic, indicating that although Igu⁺ DCKO cells were aberrantly selected, they did not bypass the requirement of pre-BCR expression for continued survival (Fig. 1H).

Within mRNAs that were overrepresented in DCKO late pre-B cell transcriptomes, there was a strong enrichment for pathways promoting cell cycle progression (Fig. 2, A and B, and tables S1 to S4). Because VDJ recombination is inhibited by cell cycle progression, and the pre-BCR checkpoint is mediated by the selective proliferation of Igu⁺ cells, we hypothesized that these aspects of the phenotype might be explained by uncontrolled cell cycle progression in DCKO mice. The apoptosis of DCKO late pre-B cells could be due to delayed light-chain recombination or overexpression of cell cycle regulators; these cells are destined to be quiescent and therefore may not tolerate activation of the E2F pathway, which regulates transition through the cell cycle and DNA synthesis. Loss of *E2f1* has been demonstrated to increase late pre-B cell numbers (12).

Cell cycle analysis showed an increase in the proportion of DCKO pro-B cells in the S phase (Fig. 2, C and D). The cyclin-dependent kinase inhibitor p27 (also known as CDKN1B) is known to regulate the cell cycle during pre-B cell development (5), and high expression of p27 (p27^{high}) is a marker of cellular quiescence (13). The proportion of p27^{high} G₀ cells was markedly reduced in DCKO pro-B cells and was moderately reduced in DCKO early and late pre-B cells (Fig. 2, E and F). Thus, ZFP36L1 and ZFP36L2 impose quiescence on developing B cells and inhibit entry into the S phase before expression of the pre-BCR.

We demonstrated that the transcription factors induced by the pre-BCR that promote quiescence in late pre-B cells were expressed in DCKO mice and that p27 mRNA was induced; additionally, factors mediating VDJ recombination were expressed, and the Igk locus was transcriptionally active (fig. S7). Therefore, DCKO late pre-B cells are transcriptionally poised to enter quiescence and undergo VDJ recombination, but posttranscriptional regulation mediated by ZFP36L1 and ZFP36L2 is required for the full activation of these processes.

Consistent with their role in promoting mRNA decay, ZFP36L1-bound transcripts identified by cross-linking immunoprecipitation (iCLIP) (14) were more abundant in DCKO late pre-B cells (Fig. 3A). Increased mRNA abundance in DCKO late pre-B cells was also associated with AREs in the 3'UTRs of mRNAs (fig. S8A) and with ZFP36 binding sites in the human homologs of mouse transcripts (fig. S8, B and C) (15). Thus, the specificity of ZFP36-family proteins is generally conserved across family members, species, and cell types.

ZFP36L1 binding sites were typically associated with AREs (table S5). In the mRNAs identified by iCLIP, cell cycle pathways were strongly enriched (tables S6 and S7), evidence that further connects ZFP36L1 to cell cycle regulation. From among mRNAs implicated in cell cycle control, we identified several candidate targets that have ZFP36L1 binding sites or AREs and that exhibited significant increases in mRNA abundance in DCKO late

pre-B cells (Fig. 3B and table S8). We validated the activity of the ZFP36L1 binding site in *Ccne2* (fig. S9). Among the putative targets are the mRNAs encoding PIM-family kinases and components of the CDK2-cyclin E complex that phosphorylates p27, promoting its destruction (16, 17); this mechanism is consistent with the reduced p27 protein but equivalent p27 mRNA in DCKO late pre-B cells, relative to those of control mice. Furthermore, the AREs in putative target mRNAs that have roles in cell cycle progression are very highly conserved in mammals (Fig. 3C). These data strongly suggest that ZFP36L1 and ZFP36L2 directly regulate an evolutionarily conserved posttranscriptional regulon that controls cell cycle progression (18).

A posttranscriptional mechanism for enforcing quiescence is well suited to the events surrounding the pre-BCR checkpoint, because it can be reversed more rapidly than changes that are mediated at the level of transcription. ZFP36L1 and ZFP36L2 are phosphorylated by MAPKAP2 downstream of p38 MAPK (mitogen-activated protein kinase), and this inhibits their mRNA-destabilizing effects (19). The activity of p38 is induced downstream of the pre-BCR, providing a mechanism to relieve the repression by ZFP36L1 and ZFP36L2 of mRNAs encoding cell cycle regulators (20). To examine the effects of ZFP36L1 overexpression at the pre-BCR checkpoint, we generated mice that conditionally expressed ZFP36L1 fused at its N terminus to green fluorescent protein (GFP); we refer to the allele as *ROSA26^{L1}* (fig. S10). There was a significantly reduced proportion of S-phase cells and a significantly increased proportion of G₀ cells in *ROSA26^{L1/L1} CD2cre* pre-B cells, compared with controls (Fig. 3, D and E, and fig. S11, A and B). Thus, enforced expression of ZFP36L1 suppresses proliferation at the pre-BCR checkpoint.

Cyclin D3, cyclin E2, and their partner kinases were identified among candidate ZFP36L1 and -2 targets in DCKO late pre-B cells. Cyclin D3 has an essential role in pre-BCR-mediated proliferation (21). Elevated protein expression of cyclin D3 and cyclin E2 was confirmed in DCKO pro-B and early pre-B cells (Fig. 4, A and B, and fig. S12, A and B), indicating that ZFP36L1 and ZFP36L2 limit the induction of cyclin D3 and cyclin E2 to cells that are transitioning pre-BCR selection. In contrast, *ROSA26^{L1} CD2cre* mice failed to properly induce cyclin D3 or cyclin E2 at the proliferative early pre-B cell stage, a result that further reinforces the role of ZFP36L1 in controlling the cell cycle at the point of pre-BCR selection (Fig. 4, C and D, and fig. S12, C to E).

Overexpression of cyclin D3 can inhibit VDJ recombination in pre-B cells through a mechanism involving loss of quiescence (22). Therefore, we treated DCKO and control mice with the CDK4 and -6 inhibitor palbociclib, which inhibits activation of the E2F pathway. Palbociclib treatment increased V-to-DJ recombination at the IgH locus of cells in the pro-B and early pre-B compartment (Fig. 4E and fig. S13, A and B). Consistent with increased recombination and reduced cell division, the proportion of pro- and pre-B cells

containing excised signal circles was increased after palbociclib treatment (fig. S13, C and D). Conversely, the frequency of recombination at the IgH locus of late pre-B cells was not restored by palbociclib treatment, reflecting the inhibition of the cell cycle, which prevents the proliferative selection of cells into the late pre-B cell pool (fig. S13E). Igk recombination was also restored in DCKO late pre-B cells after palbociclib treatment (Fig. 4F and fig. S13F). This indicates that the delays in VDJ recombination are caused by loss of quiescence in DCKO pro- and pre-B cells.

We found that increased *Zfp36*-family member mRNA expression was typically associated with quiescent cell phenotypes (Fig. 4G). Therefore, we generated a *ZFP36L1^{-/-}* HCT116 human colorectal carcinoma cell line and measured the expression of cyclin D3 and of cyclin D1, a putative ZFP36L1 target that is not expressed in B cells (15, 23). Expression of both D-type cyclins was increased in *ZFP36L1^{-/-}* HCT116 cells compared with the parental line (Fig. 4H). Additionally, genetic experiments have shown that the loss of *Zfp36l2* leads to depletion of hematopoietic stem cells (24), and the loss of *Zfp36* is associated with increased muscle satellite activation (25). Thus, these RBPs probably form part of a general mechanism for the posttranscriptional regulation of quiescence.

As many as 10% of human mRNAs contain AREs (26); this may enable interdependent cellular processes to be coordinated by the ZFP36 family. The dynamics of the transition between the G₀-G₁ and S phases are characterized by switching behavior that is mediated by positive feed-forward regulation in the E2F pathway (27); thus, this pathway may be particularly sensitive to moderate changes in the abundance of its components, as measured in DCKO pre-B cells (Fig. 3A). We propose that ZFP36L1 and ZFP36L2 suppress the expression of limiting factors for E2F pathway activation (16, 28–31) and DNA replication licensing, thus providing a robust mechanism for reversibly stabilizing the G₀-G₁ state. This mechanism would contribute to the ability of the progenitor cell populations to respond appropriately and dynamically to both mitogenic and antiproliferative signals.

REFERENCES AND NOTES

1. K. Johnson et al., *J. Immunol.* **188**, 6084–6092 (2012).
2. S. C. Bendall et al., *Cell* **157**, 714–725 (2014).
3. L. Zhang, T. L. Reynolds, X. Shan, S. Desiderio, *Immunity* **34**, 163–174 (2011).
4. I. L. Mårtensson, N. Almqvist, O. Grimsholm, A. I. Bernardi, *FEBS Lett.* **584**, 2572–2579 (2010).
5. S. Ma et al., *Mol. Cell. Biol.* **30**, 4149–4158 (2010).
6. M. R. Clark, M. Mandal, K. Ochiai, H. Singh, *Nat. Rev. Immunol.* **14**, 69–80 (2014).
7. S. A. Brooks, P. J. Blackshear, *Biochim. Biophys. Acta* **1829**, 666–679 (2013).
8. C. Molle et al., *J. Exp. Med.* **210**, 1675–1684 (2013).
9. E. Carballo, W. S. Lai, P. J. Blackshear, *Science* **281**, 1001–1005 (1998).
10. R. J. Rounbehler et al., *Cell* **150**, 563–574 (2012).
11. D. J. Hodson et al., *Nat. Immunol.* **11**, 717–724 (2010).
12. J. W. Zhu et al., *Mol. Cell. Biol.* **21**, 8547–8564 (2001).
13. T. Oki et al., *Sci. Rep.* **4**, 4012 (2014).
14. I. Huppertz et al., *Methods* **65**, 274–287 (2014).
15. N. Mukherjee et al., *Genome Biol.* **15**, R12 (2014).

16. D. Morishita, R. Katayama, K. Sekimizu, T. Tsuruo, N. Fujita, *Cancer Res.* **68**, 5076–5085 (2008).
17. R. J. Sheaff, M. Groudine, M. Gordon, J. M. Roberts, B. E. Clurman, *Genes Dev.* **11**, 1464–1478 (1997).
18. J. D. Keene, *Nat. Rev. Genet.* **8**, 533–543 (2007).
19. N. Herranz et al., *Nat. Cell Biol.* **17**, 1205–1217 (2015).
20. K. Ochiai et al., *Nat. Immunol.* **13**, 300–307 (2012).
21. A. B. Cooper et al., *Nat. Immunol.* **7**, 489–497 (2006).
22. B. J. Thompson et al., *J. Exp. Med.* **212**, 953–970 (2015).
23. M. Marderosian et al., *Oncogene* **25**, 6277–6290 (2006).
24. D. J. Stumpo et al., *Blood* **114**, 2401–2410 (2009).
25. M. A. Hausburg et al., *eLife* **4**, e03390 (2015).
26. A. S. Halees, R. El-Badrawi, K. S. Khabar, *Nucleic Acids Res.* **36**, D137–D140 (2008).
27. G. Yao, T. J. Lee, S. Mori, J. R. Nevins, L. You, *Nat. Cell Biol.* **10**, 476–482 (2008).
28. D. Resnitzky, S. I. Reed, *Mol. Cell. Biol.* **15**, 3463–3469 (1995).
29. E. Vigo et al., *Mol. Cell. Biol.* **19**, 6379–6395 (1999).
30. G. Leone, J. DeGregori, L. Jakoi, J. G. Cook, J. R. Nevins, *Proc. Natl. Acad. Sci. U.S.A.* **96**, 6626–6631 (1999).
31. A. C. Minella et al., *Genes Dev.* **22**, 1677–1689 (2008).

ACKNOWLEDGMENTS

We thank K. Vogel, R. Newman, C. Tiedje, and S. Bell for advice and comments on the manuscript; L. Matheson, A. Stark, and R. Venigalla for technical advice; S. Bell, K. Bates, D. Sanger, N. Evans, and The Babraham Institute's Biological Support Unit, Flow Cytometry Core Facility, and Next Generation Sequencing Facility for expert technical assistance; J. Ule and T. Curk for help with iCLIP; L. Dolken for the gateway-compatible psi-check vector; and R. Brink, D. Kioussis, and M. Reth for mice. This work was funded by the Biotechnology and Biological Sciences Research Council, a Medical Research Council (MRC) Collaborative Award in Science and Engineering (CASE) studentship with GlaxoSmithKline, a MRC centenary award (A.G.), and project grants from Bloodwise. D.J.H. was supported by a MRC Clinician Scientist Fellowship. The data

from this study are tabulated in the main paper and in the supplementary materials. Sequencing data from the RNA sequencing and iCLIP experiments have been deposited in the National Center for Biotechnology Information's Gene Expression Omnibus (GEO) and are accessible under GEO Series accession number GSE78249 (www.ncbi.nlm.nih.gov/geo/query/acc.cgi?acc=GSE78249). *Zfp361l^{fl}*, *Zfp3612^{fl}*, and *ROSA26^{fl}* mice are available from The Babraham Institute under a material transfer agreement.

SUPPLEMENTARY MATERIALS

www.sciencemag.org/content/352/6284/453/suppl/DC1
Materials and Methods
Figs. S1 to S13
Tables S1 to S16
References (32–50)

7 October 2015; accepted 26 February 2016
10.1126/science.aad5978

IMMUNOLOGY

Hobit and Blimp1 instruct a universal transcriptional program of tissue residency in lymphocytes

Laura K. Mackay,^{1,2†} Martina Minnich,³ Natasja A. M. Kragten,⁴ Yang Liao,^{5,6} Benjamin Nota,⁷ Cyril Seillet,^{5,6} Ali Zaid,¹ Kevin Man,^{5,6} Simon Preston,^{5,6} David Freestone,¹ Asolina Braun,¹ Erica Wynne-Jones,¹ Felix M. Behr,^{4,5,6,8} Regina Stark,⁴ Daniel G. Pellicci,^{1,2} Dale I. Godfrey,^{1,2} Gabrielle T. Belz,^{5,6} Marc Pellegrini,^{5,6} Thomas Gebhardt,¹ Meinrad Busslinger,³ Wei Shi,^{5,9} Francis R. Carbone,¹ René A. W. van Lier,⁴ Axel Kallies,^{5,6*†} Klaas P. J. M. van Gisbergen^{4,5,6,8*†}

Tissue-resident memory T (Trm) cells permanently localize to portals of pathogen entry, where they provide immediate protection against reinfection. To enforce tissue retention, Trm cells up-regulate CD69 and down-regulate molecules associated with tissue egress; however, a Trm-specific transcriptional regulator has not been identified. Here, we show that the transcription factor Hobit is specifically up-regulated in Trm cells and, together with related Blimp1, mediates the development of Trm cells in skin, gut, liver, and kidney in mice. The Hobit-Blimp1 transcriptional module is also required for other populations of tissue-resident lymphocytes, including natural killer T (NKT) cells and liver-resident NK cells, all of which share a common transcriptional program. Our results identify Hobit and Blimp1 as central regulators of this universal program that instructs tissue retention in diverse tissue-resident lymphocyte populations.

We recently identified a core set of genes specifically associated with tissue residency of CD8 T cells (1). Genes up-regulated in Trm cells included *Zfp683* (*LOC100503878*), also termed “homolog of Blimp1 in T cells” (Hobit), a transcription factor that we previously identified in NKT cells (2). Virus-specific CD8 T cells in skin, but not spleen, after herpes simplex virus (HSV) infection expressed large amounts of *Hobit* transcripts (Fig. 1A). *Hobit* expression in skin T cells was low at day 8 and high by day 30 postinfection (p.i.) (Fig. 1A). This was in contrast to *Prdm1* (hereafter, *Blimp1*), which peaked at day 8 p.i. and persisted at lower levels in splenic and skin memory CD8 T cells (Fig. 1B). Similarly, after acute infection with lymphocytic choriomeningitis virus (LCMV), *Hobit* was specifically induced in gut Trm cells, whereas *Blimp1* was expressed

ubiquitously in memory CD8 T cells (fig. S1, A and B). Thus, within the CD8 T cell lineage, Hobit is expressed in a Trm-specific manner.

To examine the function of Hobit and Blimp1 in Trm cell differentiation, we used a mouse model to generate skin Trm cells, by the intradermal injection of activated CD8 T cells, as previously described (1). After transfer, wild-type (WT) CD8 T cells persisted in skin and acquired a Trm phenotype (Fig. 1, C and D, and fig. S2A). Cotransferred Hobit-deficient CD8 T cells were reduced in skin, despite similar maintenance in spleen, as compared with WT cells (Fig. 1C), which suggested that Hobit was specifically required for Trm cell development. Blimp1 was not essential for skin Trm cell formation by itself, but collaborated with Hobit in a synergistic manner (Fig. 1C and fig. S2, A and B). Residual *Hobit* and *Blimp1* doubly deficient [double-knockout (DKO)]

CD8 T cells in the skin displayed reduced surface expression of Trm cell-associated molecules compared with WT CD8 T cells (Fig. 1D and fig. S2C). To study Trm cell development during viral infection, we infected mice with HSV and analyzed endogenous CD8 T cell responses. We used mixed-bone marrow (BM) chimeric mice, containing WT and mutant compartments at a 1:1 ratio, to minimize indirect effects through differences in viral clearance. This ratio was largely maintained in the antigen-specific CD8 T cells, regardless of location at the peak of the T cell response (Fig. 1E). In line with previous findings (3, 4), Blimp1, but not Hobit, was required for the formation of short-lived effectors and granzyme B expression, which resulted in increased proportions of Blimp1-deficient memory precursors (fig. S3, A and B, and fig. S4, A to G) and memory CD8 T cells (Fig. 1, E and F). The combined loss of Hobit and Blimp1 strongly compromised development of skin Trm cells but not of circulating memory cells (Fig. 1, E and F). After infection with LCMV, double deficiency in Hobit and Blimp1 abrogated the development of gut-resident CD8 T cells but not of splenic CD8 T cells (fig. S5, A and B). Thus, Hobit and Blimp1 cooperate to specifically promote Trm development.

Tissue residency has also been described for innate lymphocytes, including subpopulations of NK and NKT cells (5–8). Tissue-resident NK

¹Department of Microbiology and Immunology, The University of Melbourne, The Peter Doherty Institute for Infection and Immunity, Melbourne, Australia. ²Australian Research Council (ARC) Centre of Excellence in Advanced Molecular Imaging, University of Melbourne, Melbourne, Australia.

³Research Institute of Molecular Pathology (IMP), Vienna Biocenter (VBC), Vienna, Austria. ⁴Department of Hematopoiesis, Sanquin Research and Landsteiner Laboratory, Academic Medical Center (AMC), University of Amsterdam, Amsterdam, Netherlands. ⁵The Walter and Eliza Hall Institute of Medical Research, Melbourne, Australia.

⁶Department of Medical Biology, The University of Melbourne, Melbourne, Australia. ⁷Department of Blood Cell Research, Sanquin Research and Landsteiner Laboratory, AMC, University of Amsterdam, Amsterdam, Netherlands. ⁸Department of Experimental Immunology, AMC, Amsterdam, Netherlands. ⁹Department of Computing and Information Systems, The University of Melbourne, Melbourne, Australia.

*These authors contributed equally to this work. †Corresponding author. Email: lkmackay@unimelb.edu.au (L.K.M.); kallies@wehi.edu.au (A.K.); k.vangisbergen@sanquin.nl (K.P.J.M.v.G.)

(trNK) cells in the liver, also known as type 1 innate lymphoid cells (IL1), can be distinguished from conventional NK (cNK) cells through expression of the Trm cell-associated molecules CD49a and CD69 (7, 9–11). Liver trNK cells expressed *Hobit* to a similar extent as NKT cells, whereas cNK cells did not (Fig. 2A). In contrast, *Blimp1* was highly expressed in circulating cNK cells compared with trNK and NKT cells (Fig. 2B and fig. S6A). In line with this expression pattern, trNK cells in liver, but not cNK cells in liver or spleen, were *Hobit* dependent (Fig. 2, C to E, and fig. S6B). In contrast, cNK cells in liver were dependent on *Blimp1*, as previously shown (12). NKT cells are maintained as resident cells in thymus, spleen, and liver (5, 8). As were Trm cells, NKT cells were largely positive for CD49a and CD69 (fig. S7, A and B) and expressed *Hobit* and *Blimp1* (Fig. 2A and fig. S7C). Numbers of splenic and liver NKT cells were not substantially different in mice lacking either *Hobit* or *Blimp1*. In contrast, NKT cells lacking both *Hobit* and *Blimp1* were reduced in liver, but not spleen, a phenotype that was exacerbated in a competitive setting (Fig. 2, F and G, and fig. S8, A and B). *Hobit* and *Blimp1* were not required for migration but for

maintenance of liver NKT cells (fig. S9, A to E). Furthermore, the combined deficiency in *Hobit* and *Blimp1* reduced the proportions of Trm-type NKT cells in spleen (fig. S7, A and B). Thus, *Hobit* and *Blimp1* jointly regulate the development and maintenance of innate tissue-resident lymphocytes.

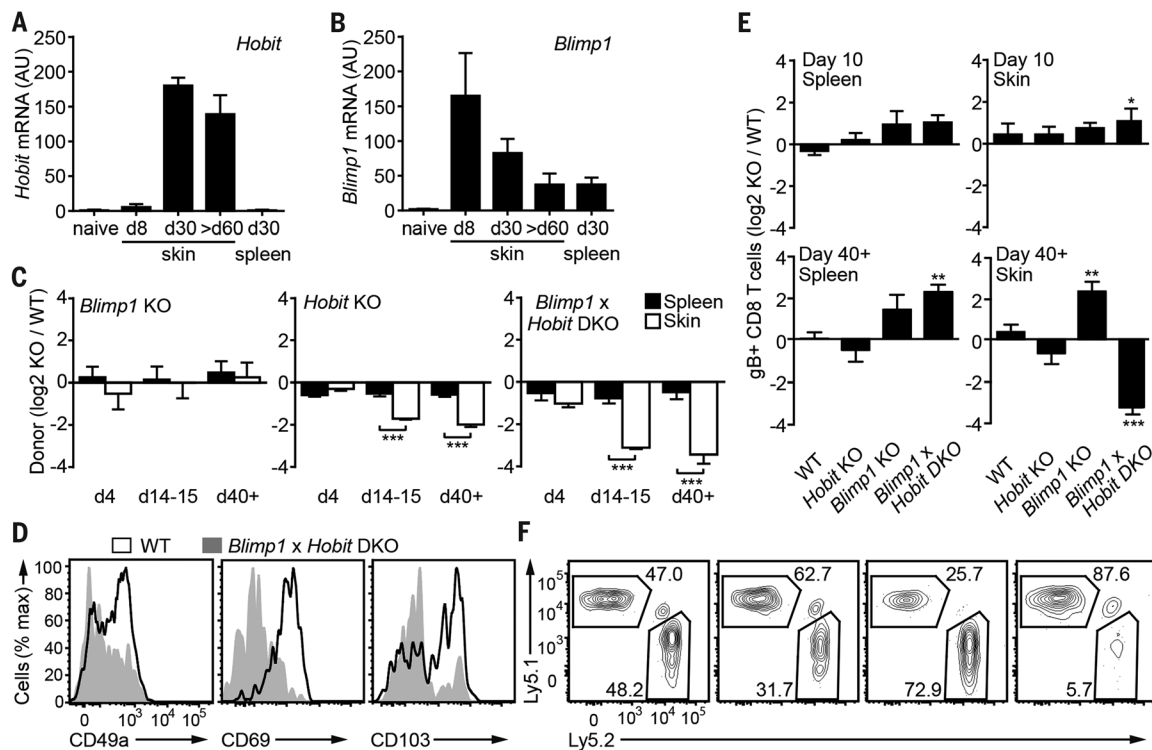
In line with a recent report (13), LCMV induced the differentiation of Trm-phenotype CD8 T cells in the liver that lacked CD103 expression (Fig. 3, A and B, and fig. S10, A to D). CD103⁺ Trm cells have also been described in other nonbarrier tissues (13–16), but it is unclear how the differentiation of these cells relates to that of CD103⁺ Trm cells at epithelial sites. As were CD103⁺ Trm cells, liver-derived Trm cells expressed and required both *Hobit* and *Blimp1* for differentiation (Fig. 3, C and D, and fig. S10, E and F), as did the CD103⁺ Trm population in kidney (fig. S10, G and H). Thus, resident lymphocytes at nonepithelial sites also require *Hobit* and *Blimp1* for development. Previously, we have shown that interleukin-15 (IL-15) and the transcription factor T-bet mediate Trm cell development and/or maintenance (17). Trm cells had reduced *Hobit* expression in an IL-15-deficient environment, and activated CD8 T cells up-regulated *Hobit* in

response to IL-15 in a T-bet-dependent manner (fig. S11, A and B). Overexpression of T-bet induced *Hobit* expression (fig. S11, B and C), which suggested that T-bet was both essential and sufficient. In contrast, *Blimp1* expression is not induced by IL-15 or T-bet (18). Transforming growth factor- β , which is also associated with Trm cell differentiation, did not induce *Hobit* expression (fig. S11B). In support of these notions, NKT1 cells, which depend on T-bet and IL-15 (19), but not NKT2 cells, expressed *Hobit* and *Blimp1* and displayed a phenotype consistent with tissue residency (fig. S12, A to C). These findings suggest that the molecular circuits that drive tissue residency are conserved between lymphocyte populations.

To identify a lineage-independent gene signature of tissue residency, we performed genome-wide transcriptional profiling. Antigen-specific Trm cells from the skin and gut of mice that were infected with HSV or LCMV, respectively, were compared with circulating CD8⁺ central memory T cells (Tcm) and effector memory T cells (Tem) of the same specificity. We obtained a set of 192 genes whose specific up- or down-regulation was associated with CD103⁺ Trm cells (fig. S13A). The gene expression profile of CD103⁺ LCMV-specific

Fig. 1. *Hobit* and *Blimp1* regulate the maintenance of Trm cells within the skin.

(A) *Hobit* and (B) *Blimp1* expression in naive and HSV glycoprotein B (gB)-specific CD8 T cell receptor transgenic T cells from skin and spleen at effector (day 8 p.i.) and memory (after day 30 p.i.) time points after HSV infection. AU, arbitrary units. (C and D) Activated congenically marked CD8 T cells from WT mice were cotransferred at a 1:1 ratio with *Blimp1*-deficient [knockout (KO)] (right), *Hobit* KO (center), or *Blimp1* × *Hobit* DKO CD8 T cells (left) into Ly5.1-recipient mice by intradermal injection. (C) Ratio (log₂) of transferred WT and mutant CD8 T cells in spleen and skin at the indicated time points after transfer (d, day). (D) CD49a (left), CD69 (center), and CD103 (right) expression in donor WT (black line) and *Blimp1* × *Hobit* DKO CD8 T cells (filled gray) 14 to 15 days posttransfer. (E and F) Mixed-BM chimeric mice containing congenically marked WT (Ly5.1⁺) and control WT, *Hobit* KO, *Blimp1* KO, or *Blimp1* × *Hobit* DKO cells (Ly5.2⁺) were infected with HSV, and antigen-specific CD8 T cells were enumerated in spleen and skin using gB tetramer. (E) The ratio (log₂) of gB⁺ WT and mutant CD8 T cells at effector (day 10 p.i.) and memory (day 40+ p.i.) times in spleen and skin. Ratio of CD103⁺ gB⁺ CD8 T cells is shown in skin at day 40+ p.i. (bottom right). (F) WT and



the indicated WT or mutant HSV-specific CD8 T cells were detected in the skin of mixed-BM chimeric mice at day 40+ p.i. by Ly5.1 and Ly5.2 expression, respectively. Plots were gated on CD103⁺ gB⁺ Trm cells. Data in (A) and (B) represent pooled results from three to six mice per group; data in (C) and (D) are pooled from two independent experiments with six to eight mice per time point; data in (E) and (F) are representative of two independent experiments with four or five mice per group. **P* < 0.05, ***P* < 0.01, ****P* < 0.001, as determined by two-tailed Student's *t* test (C) or by one-sample Student's *t* test (E). Error bars denote means ± SEM.

liver Trm cells showed that they did not equilibrate with circulating Tem in spleen or liver (fig. S13B). Genes associated with CD103⁺ Trm were

significantly enriched in liver Trm cells (fig. S13, C and D), which demonstrated overlap in the transcriptional profile of Trm cells at epithelial

and nonepithelial sites. A significant fraction of the gene signature of epithelial Trm was also retained in trNK and NKT cells compared with

Fig. 2. Hobit and Blimp1 regulate the maintenance of liver-resident NK and NKT cells.

(A) Hobit and (B) Blimp1 expression in cNK, trNK, and NKT cells from the liver. (C) Expression of CD49a and CD49b on spleen and liver NK cells (gated as TCRβ⁺NK1.1⁺) of WT (left) and *Hobit* KO mice (right). (D) Numbers of splenic cNK (left), liver cNK (center), and liver trNK (right) in WT and *Hobit* KO mice. (E) Ratio (log₂) of WT and *Hobit* KO cNK and trNK cells in spleen and liver in mixed-BM chimeric mice.

(F) Numbers of splenic (left) or liver NKT cells (right) from WT, *Hobit* KO, *Blimp1* KO, and *Blimp1* × *Hobit* DKO mice. (G) Ratio (log₂) of the indicated WT and mutant NKT cells from spleen and liver in mixed-BM chimeric mice. (A) and (B), pooled results with three mice per group; (C) to (E), pooled results from two independent experiments of 6 to 7 mice per group; (F), pooled from three independent experiments with 6 to 11 mice per group; and (G), pooled from four independent experiments with 6 mice per group. **P* < 0.05, ***P* < 0.01, ****P* < 0.001, as determined by two-tailed Student's *t* test (D) and (E), by one-way ANOVA (F), or by one-sample Student's *t* test (G). Error bars denote means ± SEM.

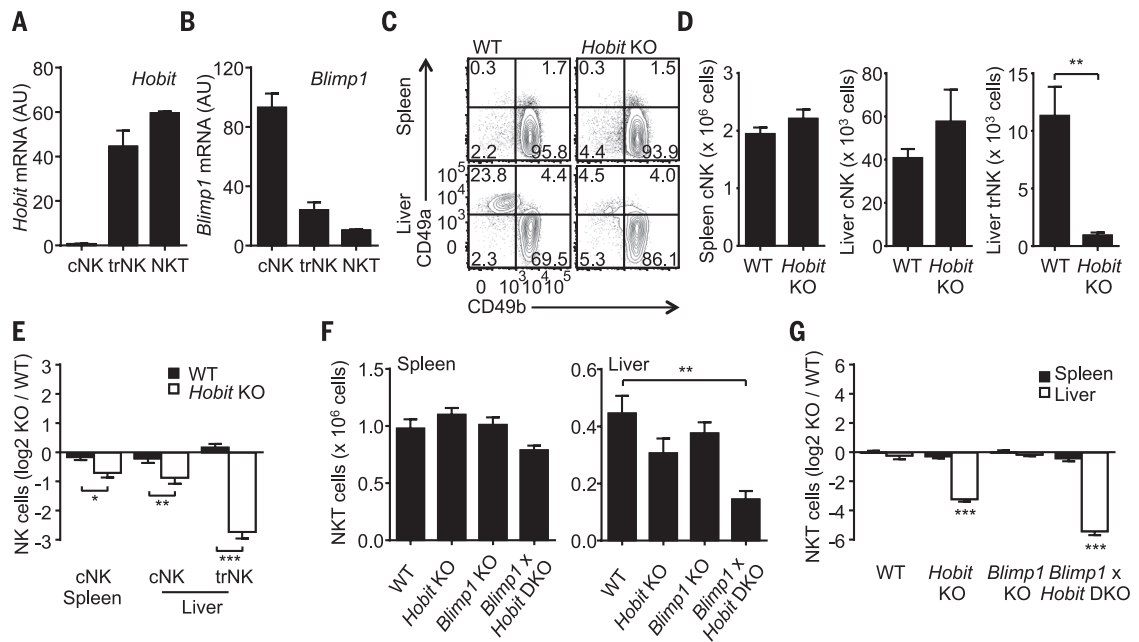
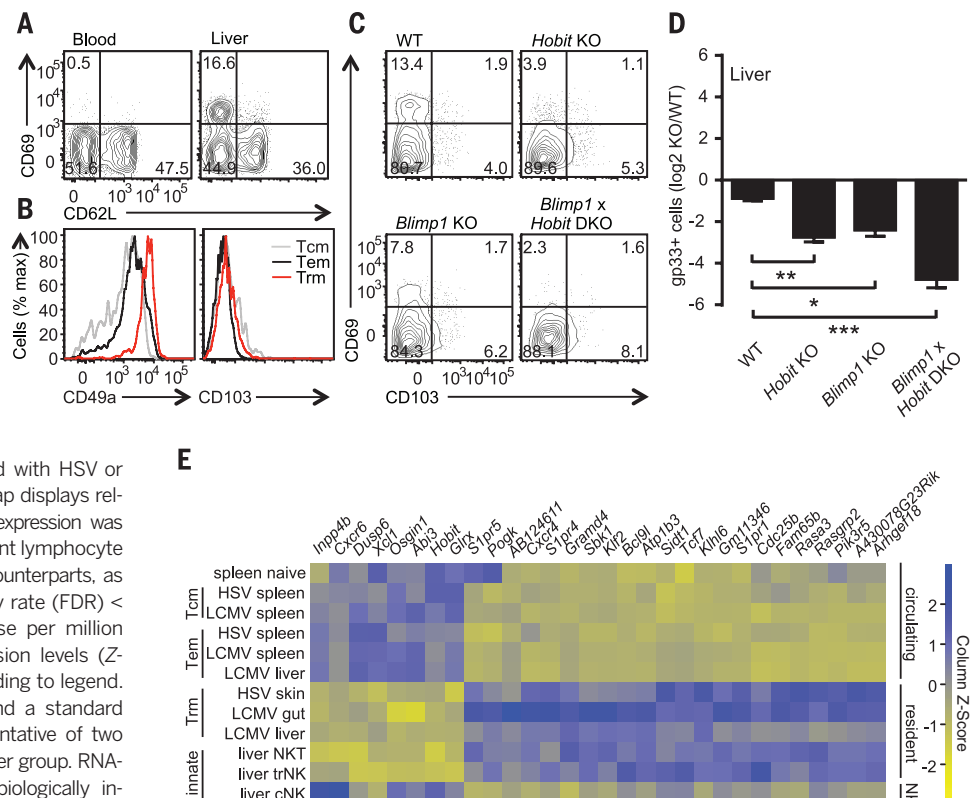


Fig. 3. Identification of a universal transcriptional program of lymphocyte tissue residency including CD103⁺ Trm, CD103⁺ liver Trm, and innate lymphocytes.

(A) Expression of CD62L and CD69 on LCMV-specific [glycoprotein 33-positive (gp33⁺)] CD8 T cells in blood and liver at day 40+ p.i. after LCMV. (B) CD49a and CD103 expression on CD62L⁺CD69⁺ Tcm (gray line), CD62L⁺CD69⁺ Tem (black line), and CD62L⁺CD69⁺ Trm cells (red line) from the liver. (C) Phenotype of LCMV-specific CD8 T cells and (D) ratio (log₂) of CD69⁺ LCMV-specific CD8 T cells of the indicated genotypes from the liver of mixed-BM chimeric mice at day 50+ after infection with LCMV. (E) Naïve CD8 T cells, cNK, trNK, and NKT cells were sorted from naïve mice, and Tcm, Tem, and Trm populations were sorted from indicated tissues of mice infected with HSV or LCMV at day 40+ p.i. (memory phase). Heat map displays relative amounts of transcripts of genes, whose expression was specifically up- or down-regulated in tissue-resident lymphocyte populations in comparison to their circulating counterparts, as determined by RNA sequencing [false discovery rate (FDR) < 0.05; fold change > 2; and reads per kilobase per million mapped reads (RPKM) > 8]. Relative expression levels (Z-scores) of genes are shown, color-coded according to legend. Columns are scaled to have a mean of 0 and a standard deviation of 1. Data in (A) to (D) are representative of two independent experiments with four to six mice per group. RNA-sequencing data in (E) is pooled from two biologically independent experiments. **P* < 0.05, ***P* < 0.01, ****P* < 0.001, as determined by one-way analysis of variance (ANOVA) (D). Error bars denote means ± SEM.

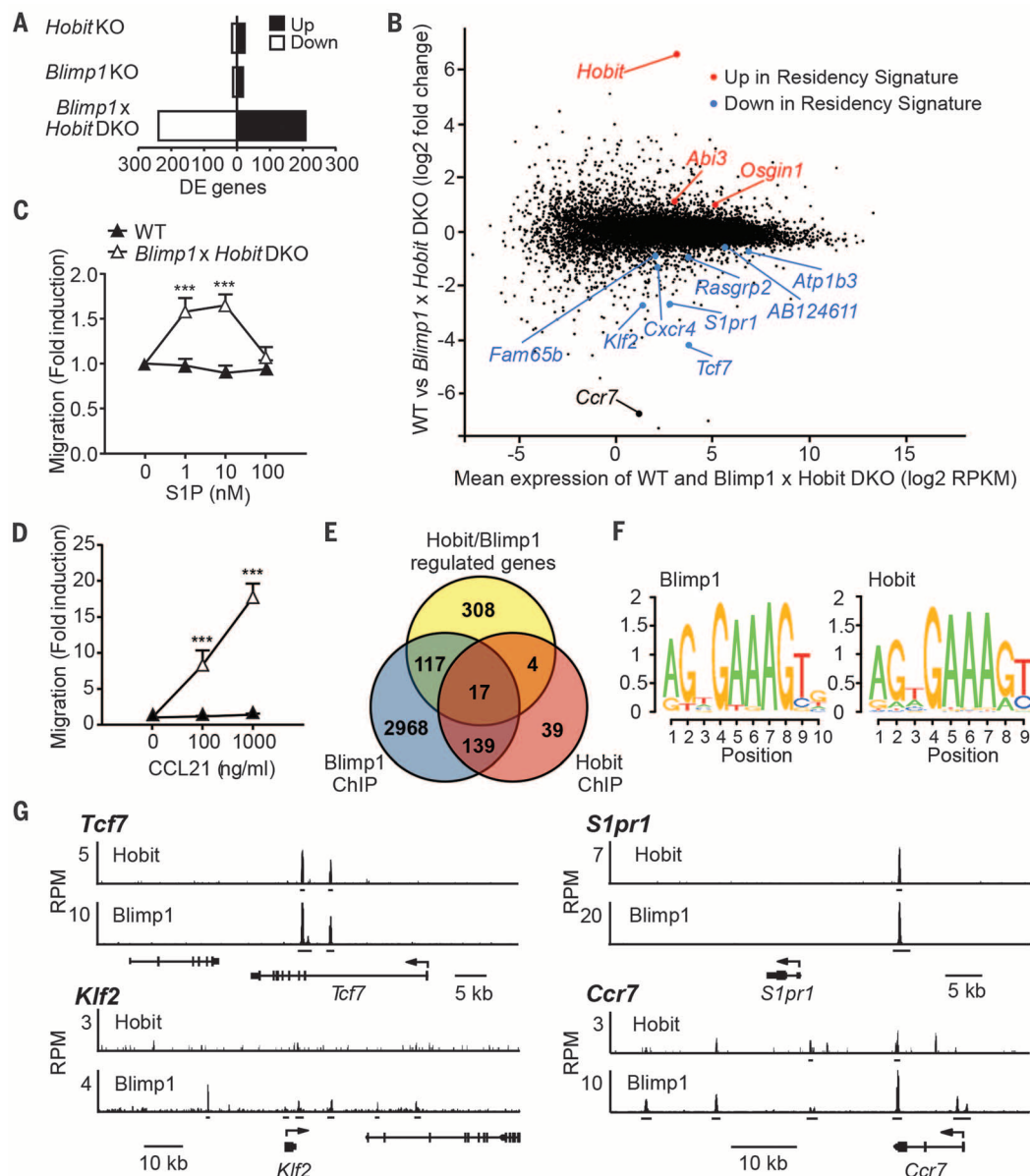


their circulating counterparts (fig. S14, A to C), which suggested that innate and adaptive lymphocytes establish tissue residency in a similar manner. We identified 30 genes, whose expression pattern was specifically associated with tissue residency independent of lineage or tissue of origin (Fig. 3E). This signature included genes required for tissue egress, such as *Klf2* and *S1pr1*, which were tightly down-regulated in resident populations (Fig. 3E). Similarly, down-regulation of *Tcf7*, encoding transcription factor TCF1 and associated with development of circulating memory (20–22), was a common feature of resident lymphocyte populations (Fig. 3E). Note that *Hobit* was the only transcription factor specifically up-regulated in this gene set (Fig. 3E), which underlined its unique position in the transcriptional regulation of tissue-resident lymphocytes.

Hobit and *Blimp1* are highly homologous in their DNA-binding zinc finger domains (2, 23), which suggested overlapping roles in transcriptional regulation. To determine how *Hobit* and *Blimp1* control tissue residency, we used cultured NKT cells that expressed large amounts of *Hobit* and *Blimp1* compared with similarly cultured CD8 T cells (fig. S15A). Consistent with the phenotype of tissue-resident cells, WT NKT cells expressed CD69, whereas NKT cells lacking *Hobit* and *Blimp1* did not (fig. S15B). The combined loss of *Hobit* and *Blimp1* caused the deregulated expression of a large number of genes (Fig. 4A), which suggested that *Hobit* and *Blimp1* coregulate gene expression in a highly synergistic manner. Signature genes of tissue residency were enriched within *Hobit*- and *Blimp1*-regulated genes and included *Klf2*, *S1pr1*, and *Tcf7*, which

were derepressed in the combined absence of *Hobit* and *Blimp1* (Fig. 4B; fig. S15C; and fig. S16, A and B). We also observed derepression of *Ccr7* (Fig. 4B and fig. S16C), which is required for lymphocyte egress from peripheral tissues (24, 25). WT NKT cells did not migrate toward S1P, the ligand for sphingosine-1-phosphate receptor 1 (S1PR1), or CCL21, the ligand for CCR7. In contrast, NKT cells lacking both *Blimp1* and *Hobit* were highly responsive to both chemotactic stimuli (Fig. 4, C and D). In line with this migratory behavior, *Hobit* and *Blimp1* DKO NKT cells localized preferentially to the white pulp and were largely absent from the red pulp of spleen (fig. S16, D to G). To identify directly regulated genes, we performed chromatin immunoprecipitation (ChIP) sequencing using CD8 T cells expressing biotin-tagged *Blimp1* (26) or V5-tagged

Fig. 4. *Hobit* and *Blimp1* cooperate to repress genes required for tissue egress. (A and B) WT, *Hobit* KO, *Blimp1* KO, and *Blimp1* × *Hobit* DKO NKT cells were analyzed by RNA sequencing. DE, differentially expressed. (A) The number of significantly up- (black bars) or down-regulated genes (white bars) in mutant compared with WT NKT cells, as indicated (FDR < 0.05; fold change > 1.5; RPKM > 4). (B) Scatter plot displays log2 fold changes of WT versus *Blimp1* × *Hobit* DKO (y axis) against the mean expression level (x axis) for all expressed genes. Up-regulated tissue residency signature genes are marked in red, down-regulated tissue residency genes in blue, and *Ccr7* in black. (C and D) Migration of WT and *Blimp1* × *Hobit* DKO NKT cells in response to (C) S1PR1 ligand S1P and (D) CCR7 ligand CCL21. (E) Venn diagram displays the overlap between genes bound by either *Hobit* or *Blimp1* in CD8 T cells, as identified by ChIP sequencing, and genes differentially expressed between WT and *Blimp1* × *Hobit* DKO NKT cells. (F) The DNA-binding motif of *Blimp1* (left) and *Hobit* (right) was determined by sequence analysis of binding regions. (G) ChIP-sequencing tracks show binding of *Hobit* or *Blimp1* to *Tcf7*, *Klf2*, *S1pr1*, and *Ccr7* as indicated in CD8 T cells. Significant binding regions are marked by horizontal lines. RPM, reads per million. Data in (A) and (B) are pooled from three independent experiments; data in (C) and (D) display pooled results of three or four independent experiments; data in (E) to (G) are based on one *Hobit* and *Blimp1* ChIP-sequencing experiment each. ****P* < 0.001 as determined by two-tailed Student's *t* test (C) and (D).



Hobit. We identified 4510 genome-wide binding sites for Blimp1, which could be assigned to 3241 genes. Hobit bound 404 sites, >50% of which overlapped with Blimp1 (fig. S17). Note that 78% of the 199 genes bound by Hobit were also bound by Blimp1, whereas 31% of the genes deregulated in the absence of Hobit and Blimp1 were bound by Hobit, Blimp1, or both (Fig. 4E). Hobit and Blimp1 used nearly identical binding motifs (Fig. 4F), which supports the notion of extensive cooperation between both factors. Hobit and Blimp1 bound target sequences within the *Slpr1*, *Ccr7*, and *Tcf7* loci, which suggested direct repression of these genes (Fig. 4G). In addition, Blimp1, but not Hobit, bound within the *Klf2* locus (Fig. 4G). Thus, Hobit and Blimp1 mediate a transcriptional program of tissue residency that is shared among Trm, trNK, and NKT cells and includes the suppression of tissue egress genes.

The recent recognition of Trm cells as essential sentinels at barrier tissues (27–30) highlights the importance of understanding their development. We have characterized a universal transcriptional program of tissue residency that is shared between adaptive and innate lymphocytes at both epithelial and nonepithelial sites. Our findings reveal the central roles of Hobit and Blimp1 in the establishment of tissue residency and indicate that they function by silencing lymphocyte egress from the tissues and by repressing the development of circulating memory cells. The key insights into the transcriptional regulation of Trm cells within this study may assist in the manipulation of tissue-resident memory for the development of vaccine strategies to improve localized immunity.

REFERENCES AND NOTES

- L. K. Mackay et al., *Nat. Immunol.* **14**, 1294–1301 (2013).
- K. P. van Gisbergen et al., *Nat. Immunol.* **13**, 864–871 (2012).
- A. Kallies, A. Xin, G. T. Belz, S. L. Nutt, *Immunity* **31**, 283–295 (2009).
- R. L. Rutishauser et al., *Immunity* **31**, 296–308 (2009).
- S. P. Berzins, F. W. McNab, C. M. Jones, M. J. Smyth, D. I. Godfrey, *J. Immunol.* **176**, 4059–4065 (2006).
- G. Gasteiger, X. Fan, S. Dikiy, S. Y. Lee, A. Y. Rudensky, *Science* **350**, 981–985 (2015).
- D. K. Sojka et al., *eLife* **3**, e01659 (2014).
- S. Y. Thomas et al., *J. Exp. Med.* **208**, 1179–1188 (2011).
- C. Daussy et al., *J. Exp. Med.* **211**, 563–577 (2014).
- S. M. Gordon et al., *Immunity* **36**, 55–67 (2012).
- M. L. Robinette et al., *Nat. Immunol.* **16**, 306–317 (2015).
- A. Kallies et al., *Blood* **117**, 1869–1879 (2011).
- E. M. Steinert et al., *Cell* **161**, 737–749 (2015).
- J. M. Schenkel, K. A. Fraser, D. Masopust, *J. Immunol.* **192**, 2961–2964 (2014).
- L. M. Wakim, A. Woodward-Davis, M. J. Bevan, *Proc. Natl. Acad. Sci. U.S.A.* **107**, 17872–17879 (2010).
- L. M. Wakim et al., *J. Immunol.* **189**, 3462–3471 (2012).
- L. K. Mackay et al., *Immunity* **43**, 1101–1111 (2015).
- A. Xin et al., *Nat. Immunol.* **17**, 422–432 (2016).
- Y. J. Lee, K. L. Holzappel, J. Zhu, S. C. Jameson, K. A. Hogquist, *Nat. Immunol.* **14**, 1146–1154 (2013).
- L. Gattinoni et al., *Nat. Med.* **15**, 808–813 (2009).
- G. Jeannet et al., *Proc. Natl. Acad. Sci. U.S.A.* **107**, 9777–9782 (2010).
- X. Zhou et al., *Immunity* **33**, 229–240 (2010).
- F. A. Vieira Braga et al., *Eur. J. Immunol.* **45**, 2945–2958 (2015).
- S. K. Bromley, S. Y. Thomas, A. D. Luster, *Nat. Immunol.* **6**, 895–901 (2005).
- G. F. Debes et al., *Nat. Immunol.* **6**, 889–894 (2005).
- M. Minnich et al., *Nat. Immunol.* **17**, 331–343 (2016).
- S. Ariotti et al., *Science* **346**, 101–105 (2014).
- T. Gebhardt et al., *Nat. Immunol.* **10**, 524–530 (2009).
- X. Jiang et al., *Nature* **483**, 227–231 (2012).
- J. M. Schenkel et al., *Science* **346**, 98–101 (2014).

ACKNOWLEDGMENTS

We wish to thank L. Mackiewicz and R. Gloury for technical support and M. Jaritz for bioinformatics support. The data presented in this manuscript are tabulated in the main paper and in the supplementary materials. RNA and ChIP sequencing data have been made available under accession numbers GSE70813 and GSE79339 at GEO. *Blimp1*-Bio mice are available from M.B. under a material transfer agreement (MTA) with IMP. *Blimp1* KO, *Blimp1*-GFP and *Blimp1* × *Hobit* DKO mice are available from A.K. under an MTA with The Walter and Eliza Hall Institute and *Hobit* KO and *Blimp1* × *Hobit* DKO mice are available from K.P.J.M.v.G. under an MTA with Sanquin Research. L.K.M. was supported by grant DE140100432 from the ARC and grant 1083685 from the National Health and Medical Research Council of Australia (NHMRC). M.M. and M.B. were supported by the Boehringer Ingelheim and a European Research Council Advanced Grant (291740-LymphoControl) from the European Community's Seventh Framework Programme. A.B. was funded by a Fellowship from the German Research Foundation. R.S. was supported by a Fellowship from the Alexander von Humboldt Foundation. W.S. was supported by grant 1023454 from the NHMRC. N.A.M.K. and

R.A.W.v.L. were supported by grant 1136 of the Landsteiner Foundation of Blood Transfusion Research. D.G.P. was supported by an NHMRC Early Career Fellowship (1054431), and D.I.G. was supported by an NHMRC Senior Principal Research Fellowship (1020770). G.T.B. was supported by a fellowship from the ARC and grant 1042582 from the NHMRC. A.K. was supported by a fellowship from the Sylvia and Charles Viertel Foundation and a project grant (637345) from the NHMRC. F.M.B. and K.P.J.M.v.G. were supported by Vidi grant 917.13.338 from The Netherlands Organization of Scientific Research. This work was supported by the Victorian State Government Operational Infrastructure Support and Australian Government NHMRC Independent Research Institute Infrastructure Support scheme.

SUPPLEMENTARY MATERIALS

www.sciencemag.org/content/352/6284/459/suppl/DC1
Materials and Methods
Figs. S1 to S17
References (31–44)

10 August 2015; accepted 21 March 2016
10.1126/science.aad2035

INNATE IMMUNITY

Mx1 reveals innate pathways to antiviral resistance and lethal influenza disease

Padmini S. Pillai,¹ Ryan D. Molony,¹ Kimberly Martinod,² Huiping Dong,¹ Iris K. Pang,¹ Michal C. Tal,^{1*} Angel G. Solis,¹ Piotr Bielecki,¹ Subhasis Mohanty,³ Mark Trentalange,⁴ Robert J. Homer,⁵ Richard A. Flavell,^{1,8} Denisa D. Wagner,² Ruth R. Montgomery,⁶ Albert C. Shaw,³ Peter Staeheli,⁷ Akiko Iwasaki^{1,8,†}

Influenza A virus (IAV) causes up to half a million deaths worldwide annually, 90% of which occur in older adults. We show that IAV-infected monocytes from older humans have impaired antiviral interferon production but retain intact inflammasome responses. To understand the in vivo consequence, we used mice expressing a functional *Mx* gene encoding a major interferon-induced effector against IAV in humans. In *Mx1*-intact mice with weakened resistance due to deficiencies in *Mavs* and *Tlr7*, we found an elevated respiratory bacterial burden. Notably, mortality in the absence of *Mavs* and *Tlr7* was independent of viral load or MyD88-dependent signaling but dependent on bacterial burden, caspase-1/11, and neutrophil-dependent tissue damage. Therefore, in the context of weakened antiviral resistance, vulnerability to IAV disease is a function of caspase-dependent pathology.

Respiratory infections with influenza A virus (IAV) cause severe morbidity and mortality in humans and animals worldwide. Older humans are highly susceptible to influenza disease. This susceptibility could be due to an inability to mount an effective antiviral response or an incapacity to develop disease tolerance to IAV infection (1–4). We began by comparing the innate immune pathways engaged by IAV infections in peripheral blood monocytes from young-adult (20- to 30-year-old) and older (65- to 89-year-old) human donors (table S1 and fig. S1A). IAV-infected monocytes from older humans showed intact nuclear factor κ B (NF- κ B)-dependent proinflammatory cytokine expression and secretion [interleukin (IL)-6] (fig. S1B and Fig. 1A) and robust inflammasome-dependent cytokine expression and secretion (IL-1 β) (fig. S1C and Fig. 1B). Type

I interferon (IFN) responses to IAV infection, however, were significantly attenuated in older human monocytes (IFN- β) (Fig. 1C). Reduced

¹Department of Immunobiology, Yale School of Medicine, New Haven, CT 06520, USA. ²Program in Cellular and Molecular Medicine, Boston Children's Hospital, Harvard Medical School, Boston, MA, USA. ³Section of Infectious Diseases, Department of Internal Medicine, Yale School of Medicine, New Haven, Connecticut, USA. ⁴Department of Internal Medicine, Yale School of Medicine, New Haven, Connecticut, USA. ⁵Department of Pathology, Yale School of Medicine, New Haven, CT 06520, USA. ⁶Section of Rheumatology, Department of Internal Medicine, Yale School of Medicine, New Haven, CT 06520, USA. ⁷Institut für Medizinische Mikrobiologie und Hygiene, Institute of Virology, University Medical Center Freiburg, Hermann-Herder-Strasse 11, 79104 Freiburg, Germany. ⁸Howard Hughes Medical Institute, Yale School of Medicine, New Haven, CT 06520, USA. *Present address: Institute of Stem Cell Biology and Regenerative Medicine, School of Medicine, Stanford, CA 94305, USA. †Corresponding author. Email: akiko.iwasaki@yale.edu

IFN secretion from older monocytes was not attributable to the expression level of RIG-I, a viral RNA sensor that induces the type I IFN responses that drive antiviral immunity (5, 6) (fig. S1D) or to a particular demographic group (fig. S1, E to G). Similar age-dependent reduction in IFN- β was observed from monocytes transfected with ligands of RIG-I (fig. S2, A to F) and from macrophages

stimulated with polyinosinic-polycytidylic acid (fig. S2, G to I). These data indicate that older human monocytes and macrophages have intact RIG-I signaling to activate proinflammatory cytokines and the inflammasome but have impaired signaling to induce type I IFNs.

Comparison of a broader array of genes revealed that infected monocytes from older donors

showed consistently lower expression of several IFN-stimulated genes (ISGs) (MxA, IFITM2, and ISG15, all of which are known to have antiviral activities for influenza viruses) (Fig. 1D). Furthermore, expression of IRF7, a critical transcription factor for type I IFNs, and STAT1, a type I IFN receptor signaling molecule, was lower in the older cohort. Consequently, older monocytes infected with IAV expressed higher levels of influenza viral genes (NS and M) (Fig. 1D). Selective impairment in IFN responses to other viral infections (7), after vaccination against influenza (8) or downstream of TLR7 (4, 9, 10), suggest that decreased IFN and elevated proinflammatory cytokines are a common characteristic of the aging innate immune system in humans.

To probe the possible in vivo consequences of weak IFN responses in the face of robust inflammation after IAV infection, we sought to employ a relevant mouse model. Older C57BL/6 mice did not show increased susceptibility to IAV infection over young mice; in fact, older mice showed antiviral resistance (fig. S3), failing to phenocopy aging human infections (11). We therefore decided to mimic human innate effector responses using genetic approaches to determine the consequences of the loss of pattern recognition receptors (PRRs) that induce IFNs during IAV infection. Inbred mouse strains, including C57BL/6, carry non-functional alleles of the *Mx1* gene. The myxovirus resistance protein 1 (Mx1) is a dynamin-like guanosine triphosphatase that blocks primary transcription of influenza, presumably by binding to viral nucleoproteins (12–14). We predicted that intact Mx1 would affect the dynamics of viral spread and the host response to IAV infection, and that *Mx1*-sufficient mice would more closely model influenza pathogenesis in humans. As reported previously (15, 16), *Mx1* congenic mice on the C57BL/6 background were highly resistant to IAV (A/PR8) infections as compared with

Fig. 1. Monocytes from old humans have impaired IFN but otherwise intact cytokine responses. Human monocytes from young (age 20 to 30 years; $n = 33$) or old (age 65 to 89 years; $n = 20$) healthy donors were infected with A/PR/8/34 influenza virus at a multiplicity of infection of 10 for 12 hours, after which cell supernatants were collected and analyzed by enzyme-linked immunosorbent assay (ELISA) to measure (A) IL-6, (B) IL-1 β , and (C) IFN- β . Data are pooled from two independent experiments and are presented as means \pm SEM. (D) RNA was isolated from PR8-infected monocytes and was analyzed by quantitative polymerase chain reaction (qPCR) to measure relative gene expression. Gene expression data were arranged in a heat map to identify age-related defects. ** $P < 0.01$; linear mixed-effects models adjusted for covariates, P values from the post hoc t statistics are Hochberg adjusted.

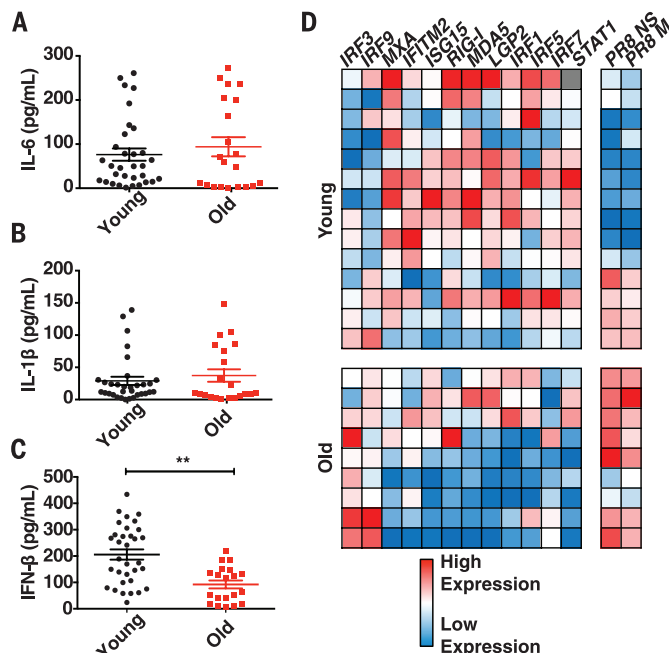
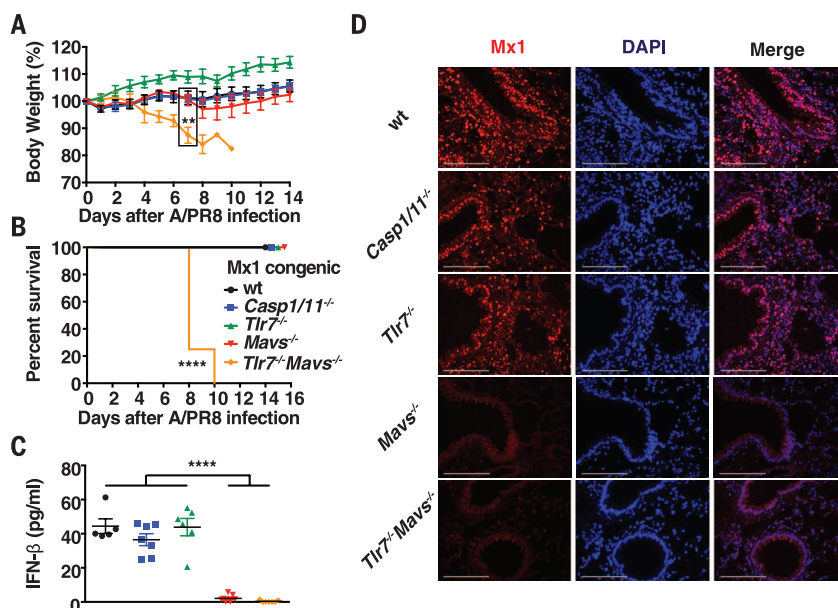


Fig. 2. RLR and TLR7 induce Mx1 expression and protection after influenza A virus infection. Wild-type, *Casp1/11*^{-/-}, *Tlr7*^{-/-}, *Mavs*^{-/-}, and *Tlr7*^{-/-} *Mavs*^{-/-} mice carrying functional *Mx1* alleles were infected intranasally (i.n.) with 100 PFU of influenza virus A/PR/8/34. (A) Weight loss and (B) survival were monitored for 14 days ($n = 5$ to 9 mice per group). (C) Bronchoalveolar lavage (BAL) was collected 48 hours after infection ($n = 5$ to 7 mice per group), and levels of IFN- β were measured by ELISA. Data are means \pm SEM. (D) Mice were sacrificed on day 2 and lungs were fixed in 4% paraformaldehyde. Tissue was embedded in paraffin, sectioned for staining with a rabbit antibody to mouse Mx1, and visualized by fluorescence microscopy [red, Mx1; blue, counter-staining of nuclei with 4',6-diamidino-2-phenylindole (DAPI)]. Samples are representative of 3 to 5 mice per group. **** $P < 0.0001$; ** $P < 0.01$; one-way analysis of variance (ANOVA); log-rank (Mantel-Cox).

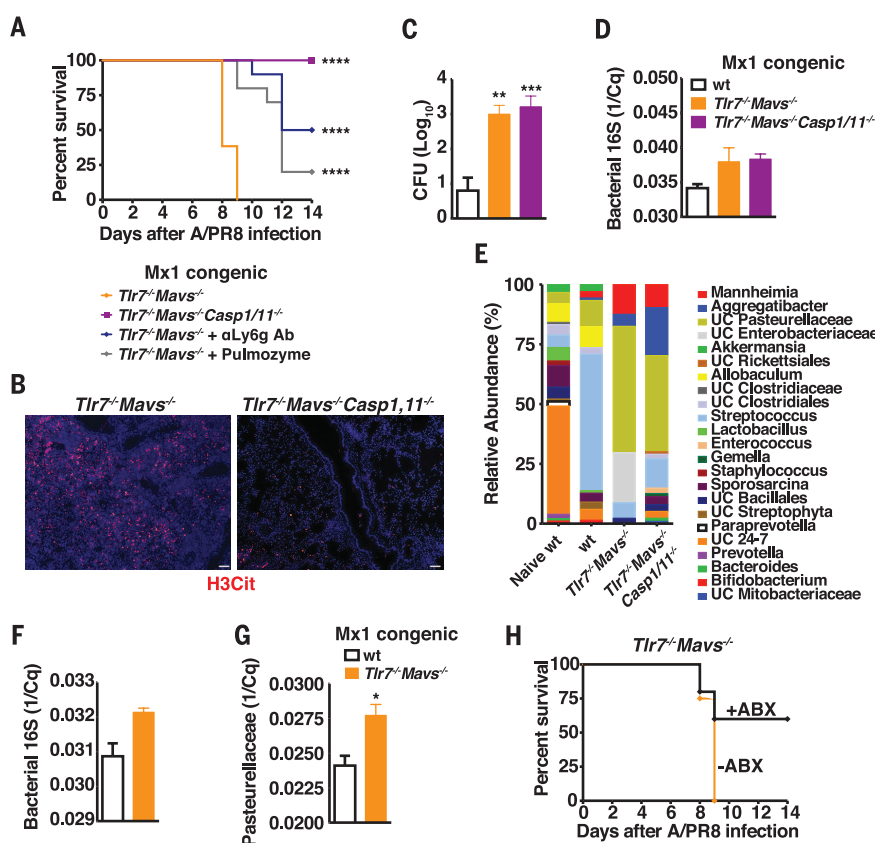
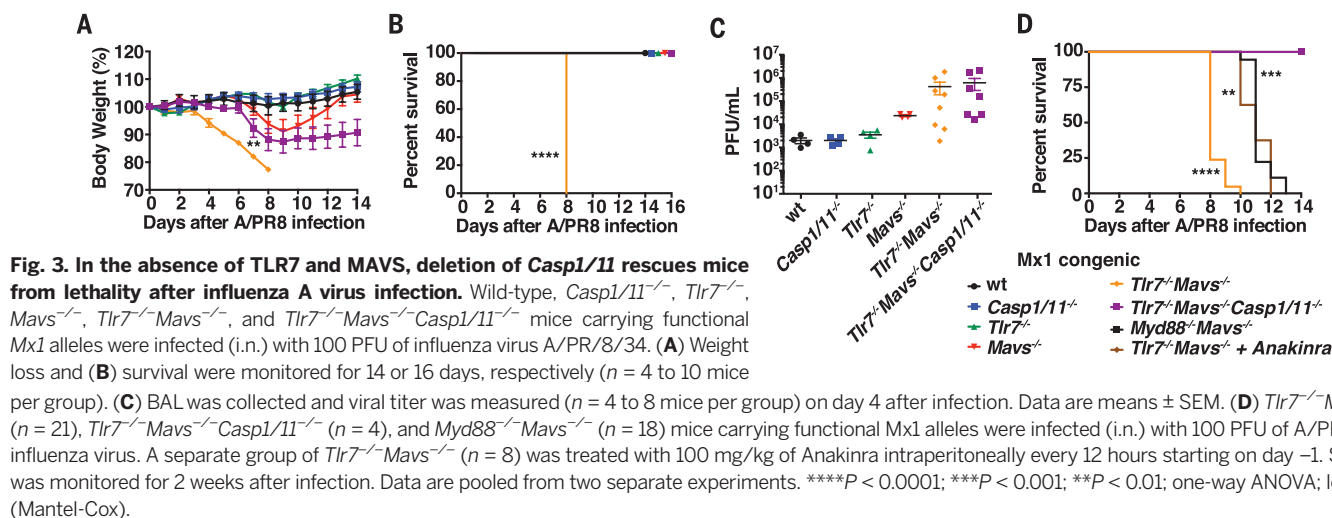


Mx1-deficient C57BL/6 mice (fig. S4). The observed resistance in Mx1 congenic mice was not due to more robust adaptive immunity because these mice showed low levels of T and B cell-mediated responses to IAV, likely because of rapid viral clearance (fig. S4, D and E).

We therefore used Mx1 mice to investigate the relative contributions of the innate immune-sensing pathways during IAV infection: Toll-like receptors (TLRs) and RIG-I, which both induce

type I IFNs (5), and the inflammasome pathway that activates caspase-1, releases IL-1 β and IL-18, and induces pyroptosis (17, 18). At a high dose of viral challenge [10⁶ plaque-forming units (PFU)], *Tlr7*^{-/-} or *Casp1/11*^{-/-} mice survived infection, whereas *Mavs*^{-/-} and *Tlr7*^{-/-} \times *Mavs*^{-/-} mice lost weight and died by day 7 or day 5, respectively, with a high viral burden (fig. S5). After challenge with a lower dose of A/PR8 virus (100 PFU), *Tlr7*^{-/-}, *Mavs*^{-/-}, and *Casp1/11*^{-/-} mice were resist-

ant, but *Tlr7*^{-/-} \times *Mavs*^{-/-} double-deficient mice lost weight and succumbed to infection (Fig. 2, A and B). The mechanism of protection conferred by MAVS and TLR7 in the *Mx1*-sufficient host correlated with the ability of these PRRs to induce IFN- β secretion (Fig. 2C). In contrast, inflammatory cytokine secretion was observed independently of MAVS and TLR7 (fig. S6). Mice deficient in both *Mavs* and *Tlr7* lost Mx1 expression (Fig. 2D and fig. S7) and therefore succumbed



to IAV challenge. Thus, unlike C57BL/6 mice (19–22), Mx1 congenic mice reveal the key innate sensors that confer antiviral resistance, RIG-I and TLR7; these sensors are responsible for the production of type I IFNs that induce Mx1 expression and potently control IAV replication. This is consistent with our results in monocytes from older humans, where impaired RIG-I signaling led to low IFN induction and compromised innate IAV resistance (Fig. 1).

To assess the role of inflammasome activation in the context of an impaired interferon response, we generated Mx1 congenic *Tlr7*^{−/−} × *Mavs*^{−/−} × *Casp1/11*^{−/−} mice. Strikingly, these mice exhibited protection from IAV disease (Fig. 3, A and B) despite having viral loads similar to *Tlr7*^{−/−} × *Mavs*^{−/−} mice (Fig. 3C and fig. S8A). Improved protection was therefore not a function of greater antiviral resistance but a lack of *Casp1/11* activity. *Tlr7*^{−/−} × *Mavs*^{−/−} × *Casp1/11*^{−/−} mice eventually cleared the virus by 30 days after infection (fig. S8B). *Tlr7*^{−/−} × *Mavs*^{−/−} mice also succumbed to infection with a human isolate of the 2009 pandemic strain of H1N1 (pH1N1) faster than other genotypes at two challenge doses (fig. S9). Furthermore, *Tlr7*^{−/−} × *Mavs*^{−/−} × *Casp1/11*^{−/−} mice exhibited longer survival compared with *Tlr7*^{−/−} × *Mavs*^{−/−} mice at a challenge dose of 10⁵ PFU (fig. S9, C and D). These results indicate that after IAV infection, *Casp1/11* deficiency confers a survival advantage in the context of combined *Tlr7* and *Mavs* deficiency.

Next, we investigated the contributions of caspase-1/11-dependent cytokines, IL-1β and IL-18, in driving IAV disease and lethality. MyD88 is an adaptor protein required for signaling downstream of IL-1R and IL-18R (23), as well as TLR7. Unlike *Tlr7*^{−/−} × *Mavs*^{−/−} × *Casp1/11*^{−/−} mice, Mx1 congenic *MyD88*^{−/−} × *Mavs*^{−/−} mice succumbed to A/PR8 infection, albeit with a delayed time course compared with *Tlr7*^{−/−} × *Mavs*^{−/−} mice (Fig. 3D). Infected *MyD88*^{−/−} × *Mavs*^{−/−} mice sustained levels of IAV burden in the lung similar to *Tlr7*^{−/−} × *Mavs*^{−/−} and *Tlr7*^{−/−} × *Mavs*^{−/−} × *Casp1/11*^{−/−} mice (fig. S8B). In addition, treatment with Anakinra (IL-1R antagonist) failed to rescue *Tlr7*^{−/−} × *Mavs*^{−/−} mice from IAV-induced lethality (Fig. 3D). Histological analysis of the lungs (fig. S10) revealed that *Tlr7*^{−/−} × *Mavs*^{−/−} mice sustained severe inflammation around airways and suffered from airway degeneration and epithelial and venular necrosis (fig. S10B, arrow). In contrast, *Tlr7*^{−/−} × *Mavs*^{−/−} × *Casp1/11*^{−/−} mice had less severe inflammation and reduced venular necrosis. Therefore, signaling through IL-1R and IL-18R is insufficient to drive IAV-induced mortality in the absence of RLR and TLR signaling, and a separate function of caspase-1/11, leading to inflammation and tissue damage, is required for lethal disease after IAV infection.

One of the hallmarks of caspase-1/11 activation is the recruitment of neutrophils (24). Neutrophilic infiltration largely accounts for fatal influenza gene signatures (25). Robust and comparable recruitment of many inflammatory leukocytes, including neutrophils, was observed in both *Tlr7*^{−/−} × *Mavs*^{−/−} and *Tlr7*^{−/−} × *Mavs*^{−/−} × *Casp1/11*^{−/−} mice infected with IAV (fig. S11). To determine whether

neutrophils mediate disease and lethality in *Tlr7*^{−/−} × *Mavs*^{−/−} mice carrying functional *Mx1* alleles, we depleted neutrophils in vivo using an antibody to Ly6G. Half of neutrophil-depleted *Tlr7*^{−/−} × *Mavs*^{−/−} mice survived the infection (Fig. 4A), indicating that neutrophils contribute to IAV lethality. Neutrophils mediate clearance of bacteria and fungi but also cause immunopathology, owing to their release of reactive oxygen species and neutrophil extracellular traps (NETs) (26). Notably, the lungs of the IAV-infected *Tlr7*^{−/−} × *Mavs*^{−/−} mice had significantly higher staining for NETs (27) than the *Tlr7*^{−/−} × *Mavs*^{−/−} × *Casp1/11*^{−/−} mice (Fig. 4B and fig. S12). Furthermore, we found that caspase-1/11 was also required for NET formation in the lung after intranasal inoculation of bacterial lipopolysaccharide (LPS) (fig. S13), indicating that the requirement of *Casp1/11* for NET release extends beyond IAV infection. NET digestion by treatment with deoxyribonuclease (DNase) (Pulmozyme) resulted in prolonged survival of *Tlr7*^{−/−} × *Mavs*^{−/−} mice after IAV infection (Fig. 4A). Thus, in the absence of *Tlr7* and *Mavs*, NETosis contributes to mortality after IAV infection, likely in part by inducing collateral tissue damage (28). Despite the lack of innate viral control, depletion of neutrophils or degradation of NETs can induce disease tolerance to influenza.

Older adults (>65 years of age) are most vulnerable to the flu, and many succumb to pneumonia caused by secondary bacterial infections (29, 30). IAV infection and consequent airway epithelial damage are sufficient to enhance bacterial colonization of the lungs (31–35). Therefore, we hypothesized that IAV-induced disease and mortality in the *Tlr7*^{−/−} × *Mavs*^{−/−} mice may be secondary to bacterial infection. Notably, bacterial bloom was observed in the nasal cavity of infected *Tlr7*^{−/−} × *Mavs*^{−/−} and *Tlr7*^{−/−} × *Mavs*^{−/−} × *Casp1/11*^{−/−} mice, as compared with the IAV-resistant wild-type mice (Fig. 4, C and D). In addition, an increase in the abundance of *Pasteurellaceae* was observed in the nasal cavities (Fig. 4E) and lungs (Fig. 4, F and G) of IAV-infected *Tlr7*^{−/−} × *Mavs*^{−/−} and *Tlr7*^{−/−} × *Mavs*^{−/−} × *Casp1/11*^{−/−} mice. Finally, combination antibiotic treatment beginning 3 days after IAV infection partially rescued *Tlr7*^{−/−} × *Mavs*^{−/−} mice from lethality (Fig. 4H). Collectively, these data indicate that a failure to induce type I IFNs promotes viral amplification and tissue damage within the respiratory environment, conducive to bacterial bloom. Neutrophil recruitment and caspase-dependent NETosis contributes to lethality. These results in Mx1 congenic mice are consistent with the notion that age-related defects in innate immunity (reduced IFN responses) could predispose IAV-infected older adults to secondary bacterial infection. A direct implication of our findings is that older adults suffering from IAV infection may benefit from therapeutic strategies that minimize inflammatory responses mediated by neutrophils.

REFERENCES AND NOTES

1. J. S. Ayres, D. S. Schneider, *Annu. Rev. Immunol.* **30**, 271–294 (2012).
2. R. Medzhitov, D. S. Schneider, M. P. Soares, *Science* **335**, 936–941 (2012).

3. L. Råberg, D. Sim, A. F. Read, *Science* **318**, 812–814 (2007).
4. A. C. Shaw, D. R. Goldstein, R. R. Montgomery, *Nat. Rev. Immunol.* **13**, 875–887 (2013).
5. T. Taniguchi, A. Takaoka, *Curr. Opin. Immunol.* **14**, 111–116 (2002).
6. A. Vela, O. Fedorova, S. C. Ding, A. M. Pyle, *J. Biol. Chem.* **287**, 42564–42573 (2012).
7. F. Qian et al., *J. Infect. Dis.* **203**, 1415–1424 (2011).
8. S. Mohanty et al., *J. Infect. Dis.* **211**, 1174–1184 (2015).
9. D. H. Canaday et al., *J. Clin. Immunol.* **30**, 373–383 (2010).
10. A. Sridharan et al., *Age (Dordr.)* **33**, 363–376 (2011).
11. V. Vanhooen, C. Libert, *Ageing Res. Rev.* **12**, 8–21 (2013).
12. P. Staeheli, O. Haller, W. Boll, J. Lindenmann, C. Weissmann, *Cell* **44**, 147–158 (1986).
13. O. Haller, P. Staeheli, M. Schwemmle, G. Kochs, *Trends Microbiol.* **23**, 154–163 (2015).
14. P. Staeheli, R. Grob, E. Meier, J. G. Sutcliffe, O. Haller, *Mol. Cell. Biol.* **8**, 4518–4523 (1988).
15. M. M. Kaminski, A. Ohnemus, M. Cornitescu, P. Staeheli, *J. Gen. Virol.* **93**, 555–559 (2012).
16. K. Moritoh et al., *Jpn. J. Vet. Res.* **57**, 89–99 (2009).
17. J. L. McAuley et al., *PLOS Pathog.* **9**, e1003392 (2013).
18. T. Ichinohe, I. K. Pang, A. Iwasaki, *Nat. Immunol.* **11**, 404–410 (2010).
19. S. Koyama et al., *J. Immunol.* **179**, 4711–4720 (2007).
20. R. Le Goffic et al., *PLOS Pathog.* **2**, e53 (2006).
21. I. K. Pang, P. S. Pillai, A. Iwasaki, *Proc. Natl. Acad. Sci. U.S.A.* **110**, 13910–13915 (2013).
22. S. U. Seo et al., *J. Virol.* **84**, 12713–12722 (2010).
23. O. Adachi et al., *Immunity* **9**, 143–150 (1998).
24. C. A. Dinarello, *Eur. J. Immunol.* **41**, 1203–1217 (2011).
25. M. Brandes, F. Klauschen, S. Kuchen, R. N. Germain, *Cell* **154**, 197–212 (2013).
26. B. G. Yipp, P. Kubes, *Blood* **122**, 2784–2794 (2013).
27. A. Brill et al., *J. Thromb. Haemost.* **10**, 136–144 (2012).
28. M. Saffarzadeh et al., *PLOS ONE* **7**, e32366 (2012).
29. W. W. Thompson et al., *JAMA* **289**, 179–186 (2003).
30. R. A. Medina, A. Garcia-Sastre, *Nat. Rev. Microbiol.* **9**, 590–603 (2011).
31. J. A. McCullers, *Nat. Rev. Microbiol.* **12**, 252–262 (2014).
32. L. A. Pittet, L. Hall-Stoodley, M. R. Rutkowski, A. G. Harmsen, *Am. J. Respir. Cell Mol. Biol.* **42**, 450–460 (2010).
33. S. J. Siegel, A. M. Roche, J. N. Weiser, *Cell Host Microbe* **16**, 55–67 (2014).
34. M. J. Mina, J. A. McCullers, K. P. Klugman, *MBio* **5**, e01040-13 (2014).
35. J. A. McCullers et al., *J. Infect. Dis.* **202**, 1287–1295 (2010).

ACKNOWLEDGMENTS

The data presented in this manuscript are tabulated in the main paper and in the supplementary materials. Sequence data has been publicly released to the general scientific community (NCBI Sequence Read Archive ID SRR3216492). This study was supported by NIH awards AI081884, AI062428, and AI064705 (to A.I.); HHSN272201100019C (to A.C.S. and R. M.); K24 AG02489 (to A.C.S.); T32 AI007019-36 (to P.S.P.); T32 AI007019-38 and T32 AI055403 (to R.D.M.); 5T32HL066987-13 (to K.M.); F31 AG039163 (to M.T.); RO1HL102101 and RO1HL125501 (to D.D.W.); K24 AG042489 (to A.C.S.); P30 AG21342 (Claude D. Pepper Older Americans Independence Center at Yale) (to A.C.S.); and grant SFB1160/P13 from the Deutsche Forschungsgemeinschaft (DFG) (to P.S.). A.I. and R.A.F. are investigators of the Howard Hughes Medical Institute.

SUPPLEMENTARY MATERIALS

www.sciencemag.org/content/352/6284/463/suppl/DC1
Materials and Methods
Table S1

Figs. S1 to S11
References (36–47)

3 February 2016; accepted 15 March 2016
10.1126/science.aaf3926

STRUCTURAL BIOLOGY

The 3.8 Å resolution cryo-EM structure of Zika virus

Devika Sirohi,^{1*} Zhenguo Chen,^{1*} Lei Sun,¹ Thomas Klose,¹ Theodore C. Pierson,² Michael G. Rossmann,^{1†} Richard J. Kuhn^{1†}

The recent rapid spread of Zika virus and its unexpected linkage to birth defects and an autoimmune neurological syndrome have generated worldwide concern. Zika virus is a flavivirus like the dengue, yellow fever, and West Nile viruses. We present the 3.8 angstrom resolution structure of mature Zika virus, determined by cryo-electron microscopy (cryo-EM). The structure of Zika virus is similar to other known flavivirus structures, except for the ~10 amino acids that surround the Asn¹⁵⁴ glycosylation site in each of the 180 envelope glycoproteins that make up the icosahedral shell. The carbohydrate moiety associated with this residue, which is recognizable in the cryo-EM electron density, may function as an attachment site of the virus to host cells. This region varies not only among Zika virus strains but also in other flaviviruses, which suggests that differences in this region may influence virus transmission and disease.

The current Zika virus (ZIKV) epidemic in the Americas is linked to a sudden increase in reported cases of congenital microcephaly and Guillain-Barré syndrome. This led the World Health Organization in February 2016 to declare “a public health emergency of

international concern” (1). ZIKV was first discovered in a sentinel rhesus monkey in the Zika valley of Uganda in 1947 (2). It was subsequently isolated from mosquitoes in 1948 (2) and from humans in 1952 (3). It is a reemerging mosquito-transmitted virus that was relatively unknown

until 2007, when it caused a major epidemic on Yap Island in Micronesia (4), which was followed by outbreaks in Oceania in 2013 and 2014 (5). Since its introduction into Brazil in 2015 (6), the virus has spread rapidly across the Americas (7).

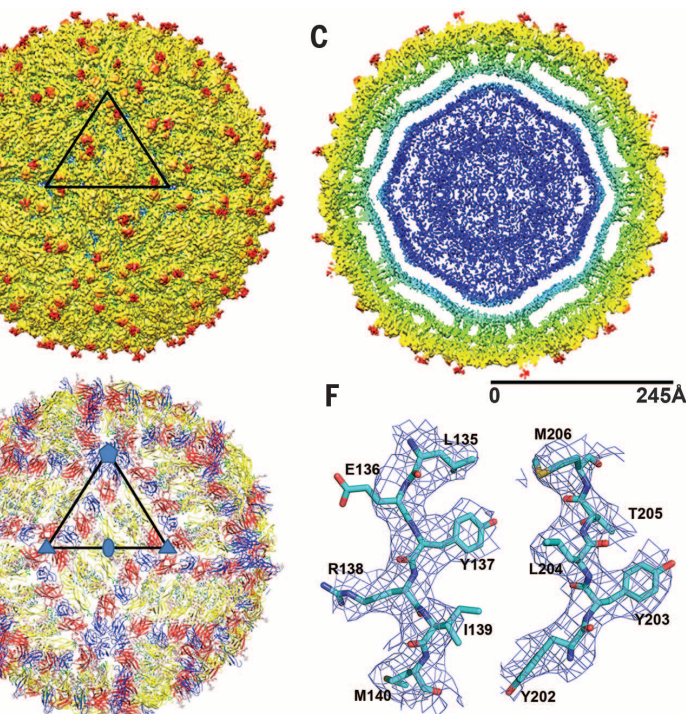
ZIKV belongs to the Flaviviridae family of positive-strand RNA viruses that includes human pathogens such as the mosquito-transmitted dengue virus (DENV), West Nile virus (WNV), Japanese encephalitis virus (JEV), yellow fever virus (YFV), and tick-borne encephalitic virus (8). ZIKV causes a rash and a febrile flulike illness in the majority of symptomatic individuals, but increasing evidence suggests a possibility of neurological abnormalities in developing fetuses (9, 10) and paralysis in infected adults (11). In addition to transmission by mosquitoes, ZIKV may be sexually (12, 13) and vertically transmitted (9, 10). The structure, tropism, and pathogenesis of ZIKV are largely unknown and are the focus of current investigations in an effort to address the need for rapid development of vaccines and therapeutics.

¹Markey Center for Structural Biology and Purdue Institute for Inflammation, Immunology and Infectious Disease, Purdue University, West Lafayette, IN 47907, USA. ²Viral Pathogenesis Section, Laboratory of Viral Diseases, National Institute of Allergy and Infectious Diseases, National Institutes of Health, Bethesda, MD 20892, USA.

*These authors contributed equally to this work. [†]Corresponding authors. Email: mr@purdue.edu (M.G.R.); kuhn@purdue.edu (R.J.K.)

Fig. 1. The cryo-EM structure of ZIKV at 3.8 Å.

(A) A representative cryo-EM image of frozen hydrated ZIKV, showing the distribution of virion phenotypes. Smooth, mature virus particles are shown enclosed in black boxes. A partially mature virus particle is identified by the yellow arrow. (B) A surface-shaded depth-coded representation of ZIKV, viewed down the icosahedral twofold axis. The asymmetric unit is identified by the black triangle. (C) A cross section of ZIKV showing the radial density distribution. Color coding in (B) and (C) is based on radii, as follows: blue, up to 130 Å; cyan, 131 to 150 Å; green, 151 to 190 Å; yellow, 191 to 230 Å; red, 231 Å and above. The region shown in blue fails to follow icosahedral symmetry, and therefore its density is uninterruptable, as is the case with other flaviviruses. (D) A plot of the Fourier shell correlation (FSC). Based on the 0.143 criterion for the comparison of two independent data sets, the resolution of the reconstruction is 3.8 Å. (E) The C α backbone of the E and M proteins in the icosahedral ZIKV particle [same orientation as in (B)], showing the herringbone organization. The



color code follows the standard designation of E protein domains I (red), II (yellow), and III (blue). (F) Representative cryo-EM electron densities of several amino acids of the E protein. Cyan indicates carbon atoms; dark blue, nitrogen atoms; red, oxygen atoms; and yellow, sulfur atoms. Single-letter abbreviations for the amino acid residues are as follows: A, Ala; C, Cys; D, Asp; E, Glu; F, Phe; G, Gly; H, His; I, Ile; K, Lys; L, Leu; M, Met; N, Asn; P, Pro; Q, Gln; R, Arg; S, Ser; T, Thr; V, Val; W, Trp; and Y, Tyr.

Flaviviruses are enveloped viruses containing an RNA genome of about 11,000 bases complexed with multiple copies of the capsid protein, surrounded by an icosahedral shell consisting of 180 copies each of the envelope (E) glycoprotein (~500 amino acids) and the membrane (M) protein (~75 amino acids) or precursor membrane (prM) protein (~165 amino acids), all anchored in a lipid membrane. The genome also codes for seven non-structural proteins that are involved in replication, assembly, and antagonizing the host innate response to infection. During their life cycle, flavivirus virions exist in three major states—immature, mature, and fusogenic—which are non-infectious, infectious, and host membrane-binding states, respectively (8). The virus is initially assembled in the endoplasmic reticulum as a non-infectious “spiky” immature particle, consisting of 60 trimeric E:prM heterodimer spikes (14). Maturation into a “smooth” virus, consisting of 90 dimeric E:M heterodimers (15, 16), occurs in the low-pH environment of the trans-Golgi network through conformational changes of the surface glycoproteins and cleavage of prM into the pr peptide and M protein by the host protease furin. In the immature virus, the pr peptide protects the ~12-amino acid fusion loop on the E protein. Removal of the pr peptide during the maturation process exposes the fusion loop, priming the virus for low pH-mediated endosomal fusion (17). In addition to the aforementioned states, the structure of flavivirus virions can be influenced by temperature (18) and the efficiency of prM cleavage, resulting in a heterogeneous population of particles (19).

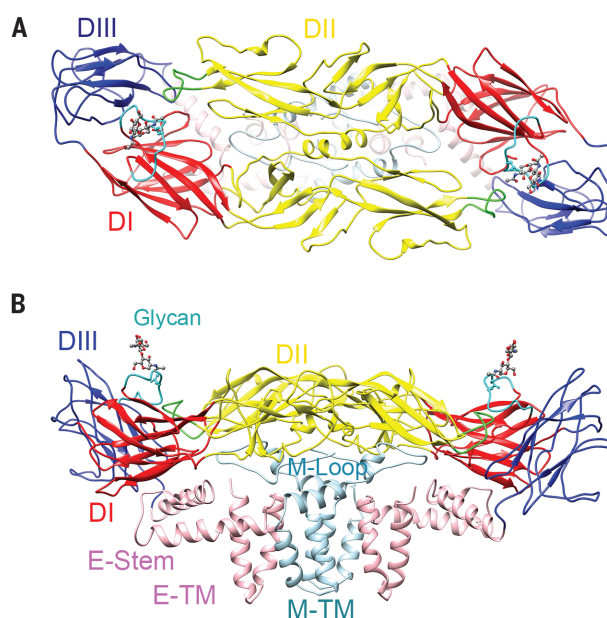
We report here the cryo-electron microscopy (cryo-EM) structure of the mature ZIKV at near-atomic resolution (3.8 Å) and compare it with the structure of other flaviviruses to provide a foundation for detailed analyses of the virology, antigenicity, and pathogenesis of this emerging threat to public health. ZIKV strain H/PF/2013, which was isolated from an infected patient during the 2013–2014 French Polynesia epidemic (20), was grown and purified from mammalian cells at 37°C. It was shown recently that the coding region of this strain has >99.9% amino acid identity to the strain that is currently circulating in Latin America (21). Low-passage Vero cells, derived from African green monkey kidney cells, were chosen for propagating the virus. To ensure a homogeneous population of virions suitable for single-particle reconstruction, virus was purified from Vero cells that overexpressed the host protease furin (Vero-furin). Vero-furin cells (10⁹) were infected with ZIKV at a multiplicity of infection of 0.1. The virus was harvested under conditions of low cytopathic effect and purified using polyethylene glycol 8000, 24% sucrose cushion ultracentrifugation, and a potassium tartrate (10 to 35%)-glycerol (7.5 to 26%) gradient, as previously described (17). The identity of the virus was verified by reverse transcription polymerase chain reaction (RT-PCR) and quantitative RT-PCR (22); the primer sequences are shown in table S1.

The ZIKV preparation was frozen onto lacey carbon EM grids and examined with an FEI

Fig. 2. The structures of the ZIKV E and M proteins.

(A) The E protein dimer is shown in ribbon form, viewed down the twofold axis. The color code follows the standard designation of E protein domains I (red), II (yellow) and III (blue). The underlying stem and transmembrane residues are shown (light pink). The fusion loop (green; fig. S1), the Asn¹⁵⁴ glycan (ball-and-stick representation), and the variable loop surrounding the Asn¹⁵⁴ glycan (cyan; residues 145 to 160) are shown.

(B) Side view of the (E-M)₂, showing the three E ectodomains, as well as the E stem-transmembrane domains (pink) and the M loop and stem-transmembrane domains (light blue; TM, transmembrane). The E and M transmembrane domains are found within the lipid bilayer (Fig. 1C). All residues of M (1 to 75) and all but three residues of E (1 to 501) were identified in the density. The Asn¹⁵⁴ glycan from one monomer is labeled and can be seen projecting from the surface.



Titan Krios electron microscope equipped with a Gatan K2 Summit detector; a magnification of 14,000 in the “super-resolution” mode was used, resulting in a pixel size of 1.04 Å (Fig. 1A). The total exposure time for producing one image composed of 70 frames was 14 s and required a dose rate of 2 electrons Å⁻² s⁻¹. A total of 2974 images were collected, and 64,518 particles were boxed using the automated Appion method (23). Non-reference two-dimensional (2D) classification was performed using the Relion program (24) to select 20,151 particles. The data set was split into two subsets according to the “gold standard” convention (25). The jspr program (26) was used for initial model generation, refinement of the orientation, and centering of the selected particles. After two rounds of 3D classification, 11,842 particles were used to generate a cryo-EM map at an average resolution of 4.2 Å. Application of soft masks improved the overall resolution to 3.8 Å, calculated using the 0.143 Fourier shell correlation criterion (25) (Fig. 1D). The structure of DENV2 serotype (16) was used as a starting point for model building. The atomic model was built manually using the program Coot (27) and refined with Phenix (28) and CNS (29). The final cryo-EM density was Fourier-analyzed. The resultant Fourier coefficients were used as targets for a crystallographic refinement. The final *R*_{work} and *R*_{free} were 34 and 34%, respectively (table S2). The map shows continuous density for the E and M polypeptide chains, and large side-chain densities are also visible in many cases, which was useful for sequence assignment. Except for the last three residues of E at its C terminus, all residues in both the E (residues 1 to 501) and M (residues 1 to 75) proteins were fitted into the density (Fig. 1E). A representative

volume of density is shown in Fig. 1F. Similar to other flaviviruses, the E protein of ZIKV consists of four domains: the stem-transmembrane domain that anchors the protein into the membrane and domains I, II, and III that constitute the predominantly β-strand surface portion of the protein (Fig. 2). The M protein consists of a loop at the N terminus (M loop or soluble M) and stem and transmembrane regions containing one and two helices, respectively, which anchor the M protein to the lipid bilayer (figs. S1 and S2).

The cryo-EM map shows that the mature ZIKV structure is similar to mature DENV (15, 16) and WNV structures (30) (Fig. 1). The radial distances of the core lipid bilayer and envelope ectodomains are similar to those of DENV2 (16) (Fig. 1C). A noticeable feature is the protruding density on the surface of the virus (red in Fig. 1, B and C), which is the glycan on the E protein. The E proteins exhibit the characteristic herringbone structure in the virion, in which there is one (E-M)₂ dimeric heterodimer located on each of 30 two-fold vertices and 60 (E-M)₂ dimeric heterodimers in general positions within the icosahedral protein shell (Fig. 1E). The root mean square deviation between equivalent Cα atoms of the E and M proteins of mature ZIKV and DENV is 1.8 Å. However, by far the biggest difference (up to 6 Å) between equivalent Cα atoms of these viruses is the region around the glycosylation sites (Asn¹⁵⁴ in ZIKV and Asn¹⁵³ in DENV) (Fig. 3). ZIKV has a single glycosylation site in the E protein (Asn¹⁵⁴), whereas DENV is glycosylated at two sites within the E protein (Asn⁶⁷ and Asn¹⁵³) (fig. S2). Dendritic cell-specific intercellular adhesion molecule 3-grabbing nonintegrin (DC-SIGN) and the mannose receptor are putative DENV receptors that

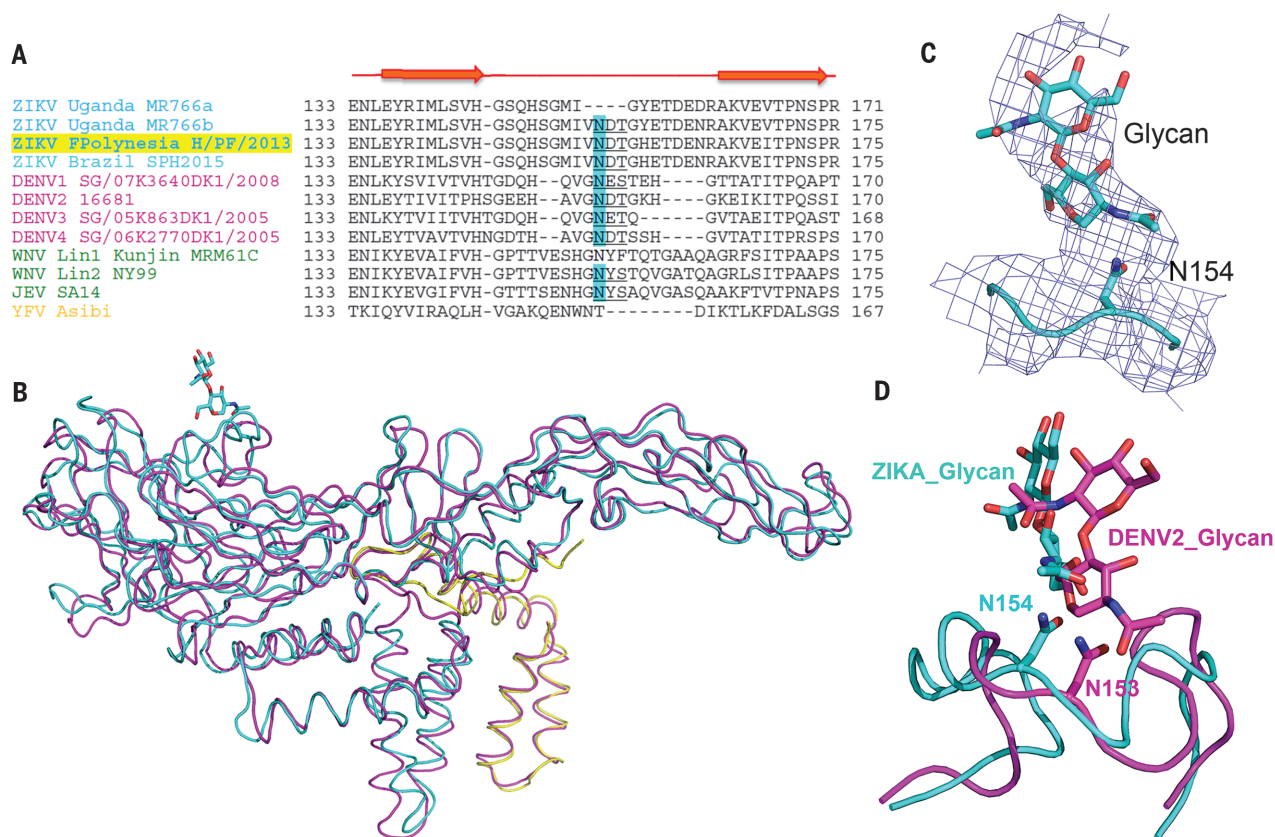


Fig. 3. Comparison of the E protein of ZIKV with that of other flaviviruses. (A) The region of the E protein of ZIKV strain H/PF/2013 (highlighted yellow) and other ZIKV strains is aligned to that of representative mosquito-transmitted flaviviruses. About 40 residues of domain I, centered on the Asn¹⁵⁴ glycosylation site, are compared. The conserved glycosylation site at Asn^{153–154} is highlighted in blue. Red arrows represent secondary structures of ZIKV (sheets). The glycosylation motif N-X-S/T is underlined. The sequences for the flaviviruses were obtained from the Virus Pathogen Database and Analysis Resource. Virus strains for which structural information was available were chosen where possible. GenBank genome accession codes for these viruses are as follows: ZIKV Uganda MR766a, AY632535; ZIKV Uganda MR766b, KU720415; ZIKV FPolynesia H/PF/2013, KJ776791; ZIKV Brazil SPH2015, KU321639; DENV1 SG/07K3640DK1/2008, GQ398255; DENV2 16681, NC001474;

DENV3 SG/05K863DK1/2005, EU081190; DENV4 SG/06K2270DK1/2005, GQ398256; WNV Lin1 Kunjin MRM61C, D00246; WNV Lin2 NY99, DQ211652; JEV SA14, D90194; and YFV Asibi, AY640589. The sequence of the original isolate (ZIKV MR766) varies based on the information source; it remains unclear whether this strain was glycosylated at N¹⁵⁴ at the time of isolation or whether the glycosylation was acquired during passage through mouse brain. The sequences were manually aligned based on the structures of ZIKV and DENV2. (B) Superposition of the C α backbone of the ZIKV and DENV2 E and M proteins. The DENV2 proteins are shown in magenta, the ZIKV E protein is shown in cyan, and the ZIKV M protein is shown in yellow. (C) Electron density representing the glycan at Asn¹⁵⁴ in ZIKV. (D) Superposition of the loop region surrounding the glycosylation site (ZIKV, 144 to 166; DENV2, 144 to 161) that flanks the Asn¹⁵⁴ glycan in ZIKV (cyan) and the Asn¹⁵³ glycan in DENV2 (magenta).

bind to the glycans (31, 32). DC-SIGN was shown by cryo-EM to bind to the glycans at Asn⁶⁷ on two neighboring E proteins of the mature virion (31).

The structures of various flaviviruses alone and in complex with neutralizing antibodies (33) or cellular receptors (31) have been reported previously. These structures have demonstrated multiple mechanisms of antibody neutralization and receptor interactions. Carbohydrate moieties on the virus may be used for cell attachment and probably play a role in disease severity. For DENV, glycosylation at Asn⁶⁷ on the E protein is an attachment site for several cell types that have been shown to be relevant targets of infection in vivo (31, 32). Similarly, glycosylation at Asn¹⁵⁴ in WNV has been linked to neurotropism (34). These observations demonstrate the importance of glycosylation for the attachment of flaviviruses to cells. The carbohydrate densities for ZIKV and DENV2

are not coincident, and the conformation of their surrounding residues is different (Fig. 3). This region varies not only among ZIKV strains (35) but also in other flaviviruses, which suggests that differences in this region influence local virus structure and possibly dynamics (Fig. 3D). In part, this difference is because of an insertion of five residues in ZIKV relative to DENV (Fig. 3A), reflecting a highly variable region of the E protein. The glycan at E residue 154 is located on a loop that is adjacent to the fusion peptide in the neighboring E protein and may control solvent access to the fusion loop. The conserved fusion loop and the neighboring region is an epitope for numerous cross-reactive antibodies that vary considerably in potency and sensitivity to the presence of uncleaved prM on the virion (36). The differences discussed here may modulate the sensitivity of ZIKV to antibodies that bind the fusion

loop epitopes. Furthermore, this region may also be important for attachment to cellular lectin receptors. The differences shown here in E protein structure among ZIKV and other flaviviruses may govern cellular tropism and contribute to disease outcomes.

REFERENCES AND NOTES

- World Health Organization (WHO), *Zika Strategic Response Framework & Joint Operations Plan (January–June 2016)* (WHO, 2016).
- G. W. Dick, S. F. Kitchen, A. J. Haddow, *Trans. R. Soc. Trop. Med. Hyg.* **46**, 509–520 (1952).
- F. N. MacNamara, *Trans. R. Soc. Trop. Med. Hyg.* **48**, 139–145 (1954).
- M. R. Duffy et al., *N. Engl. J. Med.* **360**, 2536–2543 (2009).
- V. M. Cao-Lormeau et al., *Emerg. Infect. Dis.* **20**, 1085–1086 (2014).
- C. Zanluca et al., *Mem. Inst. Oswaldo Cruz* **110**, 569–572 (2015).
- European Center for Disease Prevention and Control (ECDC), *Rapid Risk Assessment. Zika Virus Disease Epidemic: Potential*

- Association with Microcephaly and Guillain-Barré Syndrome. *Third Update*, 23 February 2016 (ECDC, 2016).
8. B. D. Lindenbach, C. L. Murray, H.-J. Thile, C. M. Rice, in *Fields Virology*, D. M. Knipe, P. M. Howley, Eds. (Lippincott Williams & Wilkins, ed. 6, vol. 1, 2013), chap. 25, pp. 712–746.
 9. J. Mlakar et al., *N. Engl. J. Med.* **374**, 951–958 (2016).
 10. R. B. Martinez et al., *MMWR Morb. Mortal. Wkly. Rep.* **65**, 159–160 (2016).
 11. V.-M. Cao-Lormeau et al., *Lancet* **10.1016/S0140-6736(16)00562-6** (2016).
 12. B. D. Foy et al., *Emerg. Infect. Dis.* **17**, 880–882 (2011).
 13. D. Musso et al., *Emerg. Infect. Dis.* **21**, 359–361 (2015).
 14. Y. Zhang et al., *EMBO J.* **22**, 2604–2613 (2003).
 15. R. J. Kuhn et al., *Cell* **108**, 717–725 (2002).
 16. X. Zhang et al., *Nat. Struct. Mol. Biol.* **20**, 105–110 (2013).
 17. I. M. Yu et al., *Science* **319**, 1834–1837 (2008).
 18. X. Zhang et al., *Proc. Natl. Acad. Sci. U.S.A.* **110**, 6795–6799 (2013).
 19. T. C. Pierson, M. S. Diamond, *Curr. Opin. Virol.* **2**, 168–175 (2012).
 20. C. Baronti et al., *Genome Announc.* **2**, e00500-14 (2014).
 21. A. Enfissi, J. Codrington, J. Roosblad, M. Kazanji, D. Rousset, *Lancet* **387**, 227–228 (2016).
 22. R. S. Lanciotti et al., *Emerg. Infect. Dis.* **14**, 1232–1239 (2008).
 23. G. C. Lander et al., *J. Struct. Biol.* **166**, 95–102 (2009).
 24. S. H. Scheres, *J. Struct. Biol.* **180**, 519–530 (2012).
 25. P. B. Rosenthal, R. Henderson, *J. Mol. Biol.* **333**, 721–745 (2003).
 26. F. Guo, W. Jiang, *Methods Mol. Biol.* **1117**, 401–443 (2013).
 27. P. Emsley, B. Lohkamp, W. G. Scott, K. Cowtan, *Acta Crystallogr. D Biol. Crystallogr.* **66**, 486–501 (2010).
 28. P. V. Afonine et al., *Acta Crystallogr. D Biol. Crystallogr.* **68**, 352–367 (2012).
 29. A. T. Brünger et al., *Acta Crystallogr. D Biol. Crystallogr.* **54**, 905–921 (1998).
 30. S. Mukhopadhyay, B. S. Kim, P. R. Chipman, M. G. Rossmann, R. J. Kuhn, *Science* **302**, 248 (2003).
 31. E. Pokidysheva et al., *Cell* **124**, 485–493 (2006).
 32. J. L. Miller et al., *PLOS Pathog.* **4**, e17 (2008).
 33. S. M. Lok, *Trends Microbiol.* **10.1016/j.tim.2015.12.004** (2015).
 34. D. W. Beasley et al., *J. Virol.* **79**, 8339–8347 (2005).
 35. O. Faye et al., *PLOS Negl. Trop. Dis.* **8**, e2636 (2014).
 36. S. Nelson et al., *PLOS Pathog.* **4**, e1000060 (2008).

ACKNOWLEDGMENTS

We thank X. de Lamballerie (Emergence des Pathologies Virales, Aix-Marseille Université, Marseille, France) and the European Virus Archive Goes Global (EVAg) for consenting to the use of the H/PF/2013 ZIKV strain for this study under a material transfer agreement with EVAg's partner, Aix-Marseille Université, and we thank M. S. Diamond (Washington University, St. Louis, MO, USA) for sending the virus. We acknowledge E. Frye for help with sequence alignments. We also acknowledge the use of the Purdue cryo-EM facility. We are grateful to W. Jiang for his jspr program, which was used to perform the anisotropic magnification corrections, and Y. Liu for providing help in submitting the Protein Data Bank (PDB) coordinates. The work presented in this report was funded by the National Institute of Allergy and Infectious Diseases of the NIH through grants R01AI073755 and R01AI076331 to M.G.R. and R.J.K. T.C.P. was supported by the intramural program of the National Institute of Allergy and Infectious Diseases. Supporting information for this research is provided in the supplementary materials. The atomic coordinates and cryo-EM density maps for the mature ZIKV are available at the PDB and Electron Microscopy Data Bank under accession codes 5IRE and EMD-8116, respectively.

SUPPLEMENTARY MATERIALS

www.sciencemag.org/content/352/6284/467/suppl/DC1
Figs. S1 and S2
Tables S1 and S2
References (37, 38)

4 March 2016; accepted 21 March 2016
Published online 31 March 2016
10.1126/science.aaf5316

EVOLUTIONARY GENETICS

A beak size locus in Darwin's finches facilitated character displacement during a drought

Sangeet Lamichhaney,¹ Fan Han,¹ Jonas Berglund,¹ Chao Wang,¹
Markus Sällman Almén,¹ Matthew T. Webster,¹ B. Rosemary Grant,²
Peter R. Grant,² Leif Andersson^{1,3,4,*}

Ecological character displacement is a process of morphological divergence that reduces competition for limited resources. We used genomic analysis to investigate the genetic basis of a documented character displacement event in Darwin's finches on Daphne Major in the Galápagos Islands: The medium ground finch diverged from its competitor, the large ground finch, during a severe drought. We discovered a genomic region containing the *HMG2* gene that varies systematically among Darwin's finch species with different beak sizes. Two haplotypes that diverged early in the radiation were involved in the character displacement event: Genotypes associated with large beak size were at a strong selective disadvantage in medium ground finches (selection coefficient $s = 0.59$). Thus, a major locus has apparently facilitated a rapid ecological diversification in the adaptive radiation of Darwin's finches.

Similar species potentially compete for limited resources when they encounter each other through a change in geographical ranges. As a result of resource competition, they may diverge in traits associated with exploiting these resources (1, 2). Darwin proposed this as the principle of character divergence [now known as ecological character displacement (3, 4)], a process invoked as an important mechanism in the assembly of complex ecological communities (5, 6). It is also an important component of models of speciation (6, 7). However, it has been difficult to obtain unequivocal evidence for ecological character displacement in nature (8, 9). The medium ground finch (*Geospiza fortis*) and large ground finch (*G. magnirostris*) on the small island of Daphne Major provide one example where rigorous criteria have been met (10). Beak sizes diverged as a result of a selective disadvantage to medium ground finches with large beaks when food availability declined through competition with large ground finches during a severe drought in 2004–2005 (11).

Size-related traits can pose problems for the analysis of selection, and Darwin's finch beaks are no exception, as beak size and body size are strongly correlated ($r = 0.7$ to 0.8) (11). We used a combination of multiple regression and selection differential analysis to investigate the 2004–2005 selection event. Statistically, these produced much stronger associations between

survival and beak size ($S = -1.02$, $P < 0.0001$) than between survival and body size ($S = -0.67$, $P < 0.05$). Thus, body size was possibly subject to selection, but beak size was a more important factor affecting the probability of survival independent of body size (11, 12). However, the genetic basis of the selected traits remains unknown. Beak dimensions and overall body size of the medium ground finch are highly heritable (13), but no gene(s) regulating body size have been identified. Furthermore, although some signaling molecules affecting beak dimensions in Darwin's finches have been identified (14), only one regulatory gene, *ALX1*, is known and it regulates variation in beak shape (15), which was not associated with survival in 2004–2005.

We performed a genome-wide screen for loci affecting overall body size in six species of Darwin's finches that primarily differ in size and size-related traits: the small, medium, and large ground finches, and the small, medium, and large tree finches (Fig. 1, A and B, and table S1). Ground finches and tree finches diverged about 400,000 years ago and exhibit ongoing gene flow within and between the two groups (15). By combining species of similar size in different taxa, we minimized phylogenetic effects when contrasting the genomes of species differing in size. We then genotyped individuals of the Daphne population of medium ground finches that succumbed or survived during the drought of 2004–2005. This approach allowed us to identify a locus with major effect on beak size variation that played a key role in the character displacement episode.

We sequenced 10 birds from each of the six species (total 60 birds) to $\sim 10\times$ coverage per individual, using 2×125 -base pair paired-end reads. The sequences were aligned to the reference genome from a female medium ground

¹Department of Medical Biochemistry and Microbiology, Uppsala University, Uppsala, Sweden. ²Department of Ecology and Evolutionary Biology, Princeton University, Princeton, NJ, USA. ³Department of Animal Breeding and Genetics, Swedish University of Agricultural Sciences, Uppsala, Sweden. ⁴Department of Veterinary Integrative Biosciences, Texas A&M University, College Station, TX, USA.
*Corresponding author. Email: leif.andersson@imbim.uu.se

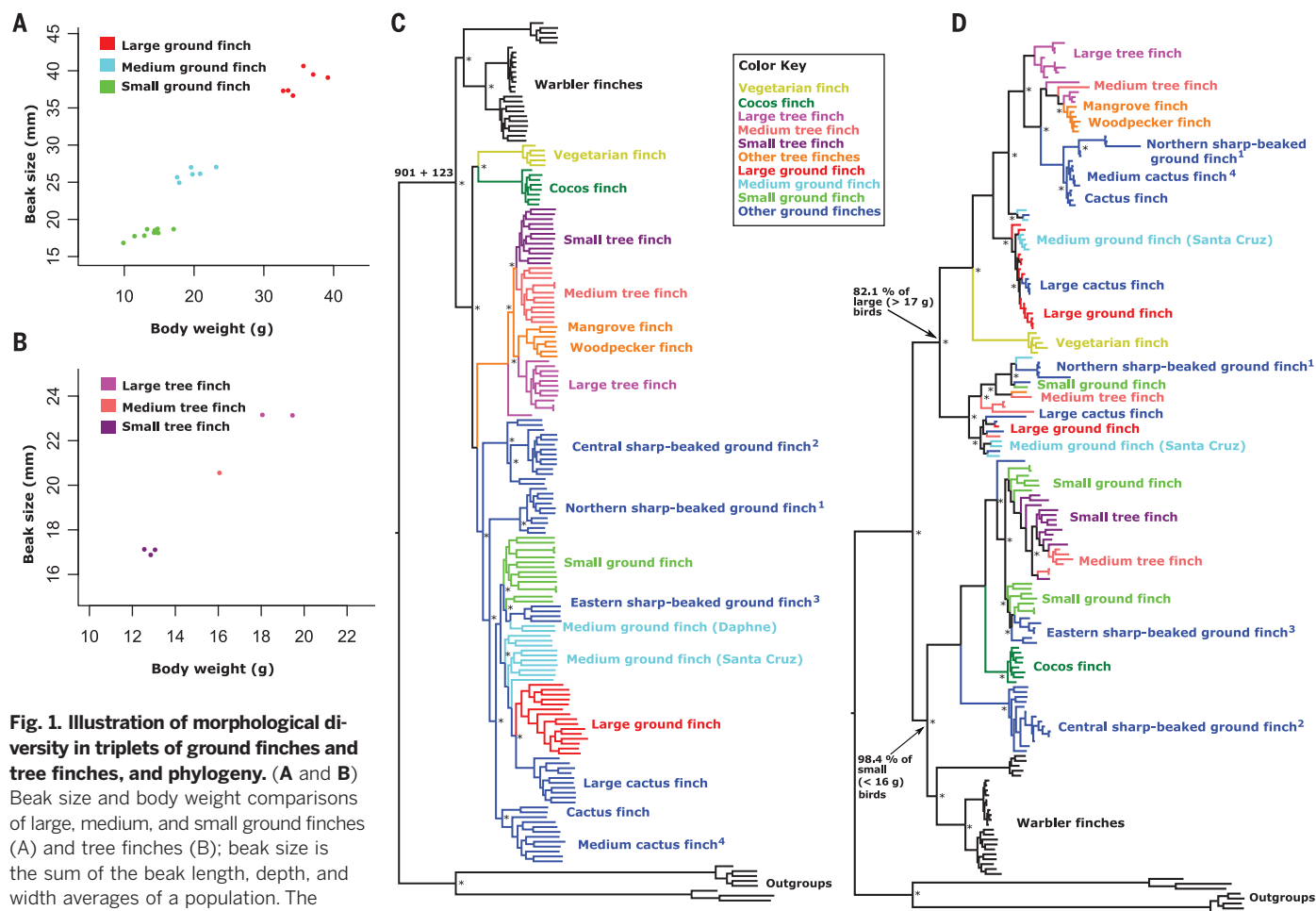


Fig. 1. Illustration of morphological diversity in triplets of ground finches and tree finches, and phylogeny. (A and B) Beak size and body weight comparisons of large, medium, and small ground finches (A) and tree finches (B); beak size is the sum of the beak length, depth, and width averages of a population. The estimates of beak and body size are the population averages; each dot represents a population from a specific island in the Galápagos archipelago. (C) Maximum-likelihood tree using all polymorphic autosomal sites. The estimated divergence time, with its 95% confidence interval based on nuclear sites (15) between warbler and nonwarbler finches, is shown in thousands of years; the corresponding estimate for this split on the basis of mitochondrial DNA cytochrome b sequences is 1.4 ± 0.2 million years (15). (D) Maximum-likelihood tree from the 525-kb region around *HMG2*. All nodes having full local support

on the basis of the Shimodaira-Hasegawa test are marked by asterisks. For sharp-beaked ground finches and medium cactus finch from Genovesa, the revised taxonomy as proposed in (15) is used: ¹northern sharp-beaked ground finch from Wolf and Darwin (*Geospiza septentrionalis*); ²central sharp-beaked ground finch from Santa Cruz, Santiago, and Fernandina (*G. difficilis*); ³eastern sharp-beaked ground finch from Genovesa (*G. acutirostris*); ⁴medium cactus finch from Genovesa (*G. propinqua*).

Table 1. Summary of 60 samples of large, medium, and small ground finches and tree finches used for whole-genome sequencing.

Common name	Species	No. of samples	Island	ID
Large ground finch	<i>Geospiza magnirostris</i>	10	Daphne	LGF
Medium ground finch	<i>Geospiza fortis</i>	10	Santa Cruz	MGF
Small ground finch	<i>Geospiza fuliginosa</i>	10	Santiago	SGF
Large tree finch	<i>Camarhynchus psittacula</i>	8	Pinta	LTF
		1	Marchena	
		1	Isabela	
Medium tree finch	<i>Camarhynchus pauper</i>	10	Floreana	MTF
Small tree finch	<i>Camarhynchus parvulus</i>	10	Santa Cruz	STF

finch (12). We combined these data with sequences from 120 birds, including all species of Darwin's finches and two outgroup species (15),

to call 44,767,199 variable sites within or between populations after stringent variant calling. We constructed a maximum-likelihood phylo-

genetic tree on the basis of all 180 genome sequences (Fig. 1C). This tree was almost identical to our previous tree (15).

A genome-wide fixation index (F_{ST}) scan comparing large, medium, and small ground finches and tree finches (Table 1) identified seven independent genomic regions with consistent genetic differentiation ($ZF_{ST} > 5$) in each contrast (Fig. 2A and table S2). One of these regions (~525 kb in size) showed the strongest differentiation in all three contrasts. The region included four genes: *high mobility AT-hook 2* (*HMG2*), *methionine sulfoxide reductase B3* (*MSRB3*), *LEM domain-containing protein 3* (*LEMD3*), and *WNT inhibitory factor 1* (*WIF1*). This signal was also detected in F_{ST} screens comparing large, medium, and small birds separately within ground and tree finches (fig. S1). *HMG2* is a chromatin-associated protein that appears to lack intrinsic transcriptional activity but potentiates the effect of other transcription factors (16). Because

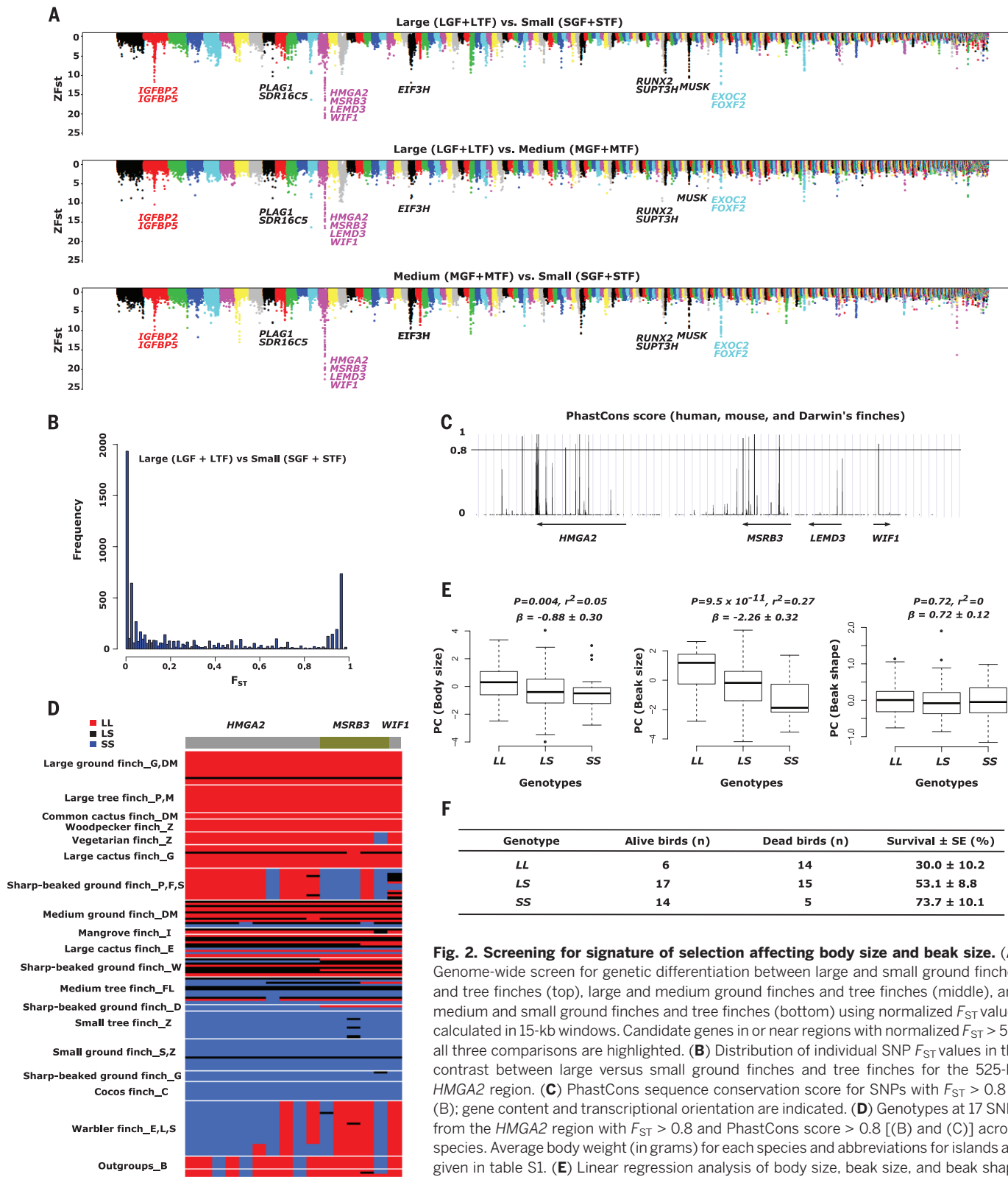


Fig. 2. Screening for signature of selection affecting body size and beak size. (A) Genome-wide screen for genetic differentiation between large and small ground finches and tree finches (top), large and medium ground finches and tree finches (middle), and medium and small ground finches and tree finches (bottom) using normalized F_{ST} values calculated in 15-kb windows. Candidate genes in or near regions with normalized $F_{ST} > 5$ in all three comparisons are highlighted. (B) Distribution of individual SNP F_{ST} values in the contrast between large versus small ground finches and tree finches for the 525-kb *HMGA2* region. (C) PhastCons sequence conservation score for SNPs with $F_{ST} > 0.8$ in (B); gene content and transcriptional orientation are indicated. (D) Genotypes at 17 SNPs from the *HMGA2* region with $F_{ST} > 0.8$ and PhastCons score > 0.8 [(B) and (C)] across species. Average body weight (in grams) for each species and abbreviations for islands are given in table S1. (E) Linear regression analysis of body size, beak size, and beak shape scores among 133 medium ground finches according to *HMGA2* genotype; L and S represent alleles present in birds with large and small beaks, respectively. The distribution of respective morphometric scores in each genotype class is shown as a boxplot together with P values, r^2 scores, and linear regression slopes ($\beta \pm$ SE) from the regression analyses. (F) Survival ($\% \pm$ SE) according to *HMGA2* genotype among 71 medium ground finches experiencing the severe drought in 2004–2005.

a loss-of-function mutation in *Hmga2* causes the pygmy phenotype in mice that exhibits severe growth retardation (17) and because *HMG2* has been associated with variation in height, craniofacial distances, and primary tooth eruption in humans (18, 19), *HMG2* was identified as a candidate gene. We refer to this region as the *HMG2* locus but note that it includes three additional genes that may contribute to phenotypic effects (12).

We constructed a maximum-likelihood phylogenetic tree on the basis of this ~525-kb region, which revealed two major haplotype groups associated with size; 98% of small birds (body weight <16 g) clustered into one group and 82% of the large birds (body weight >17 g) clustered into the other (Fig. 1D). The split between the two haplotypes occurred before the divergence of warbler and nonwarbler finches at the base of the phylogeny (Fig. 1D), about 1 million years ago (Fig. 1C).

We calculated F_{ST} values per SNP (single-nucleotide polymorphism) for all SNPs within the ~525-kb *HMG2* region (Fig. 2B). There were 1327 SNPs with strong genetic differentiation ($F_{ST} > 0.8$) spread across the region, but only one of these was coding (a missense mutation in *MSRB3*), which implies that most or all mutations causing the association with phenotype are regulatory. We identified 17 SNPs showing high genetic divergence between large and small ground finches and tree finches ($F_{ST} > 0.8$) at nucleotide sites in highly conserved regions across birds and mammals (PhastCons score > 0.8) (Fig. 2C). Six of these 17 SNPs cluster at the 3' end of *HMG2*. A comparison with the outgroup species (*Loxia noctis* and *Tiaris bicolor*) shows that the haplotype present in small birds is associated with the derived allele at a majority of these 17 SNPs (13/17; $P = 0.05$, binomial test). Large birds were homozygous for haplotypes belonging to one group, whereas the majority of small birds were homozygous for haplotypes belonging to the other group (Fig. 2D). Segregation is mainly observed in species with intermediate size (medium ground and tree finches).

Large, medium, and small ground finches and tree finches differ markedly both in body and beak size (Fig. 1, A and B, and table S1). Hence, we investigated whether the *HMG2* locus is primarily associated with variation in body size, beak size, or both. As this locus shows segregation (Fig. 2D) in medium ground finches—a species with considerable diversity in both body and beak size (10)—we genotyped an additional 133 individuals of this species for a haplotype diagnostic SNP (A/G) at nucleotide position 7,003,776 base pairs in scaffold JH739900, ~2.3 kb downstream of *HMG2*. This SNP showed a highly significant association with beak size, a significant association with body size, and no association with beak shape among medium ground finches (Fig. 2E). The locus appears to have an additive effect on beak size, where heterozygotes show an intermediate phenotype relative to the two homozygous classes, and linear regression analysis explains as much as 27% of the phenotypic variance in this population.

Six other loci showed consistent associations with overall size, but the genetic differentiation was not as pronounced as for the *HMG2* locus (Fig. 2A). Interestingly, *PLAG1* and *SUPT3H* have previously been associated with height in humans (www.ebi.ac.uk/gwas), and *IGFBP2* encodes a protein that binds insulin-like growth factor I and II in plasma (Fig. 2A). All six loci were segregating in medium ground finches, but none showed a significant association with beak size, body size, or beak shape variation (fig. S2B). The results suggest that the phenotypic effects of these loci are small relative to the effect of the *HMG2* locus.

We genotyped a diagnostic SNP for the *HMG2* locus in medium ground finches on Daphne Major that experienced the severe drought in 2004–2005 ($n = 71$; 37 survived and 34 died) (11). Differential mortality resulted in character displacement through a strong reduction in average beak size. As expected, more *SS* individuals (associated with small beaks) survived, and more *LL* individuals (large beaks) died, with heterozygotes showing intermediate survival, consistent with an additive genetic effect (Fig. 2F). The frequency of the *S* allele was 61% and 37% among those that survived and those that died, respectively ($P = 0.005$, Fisher's exact test, two-sided), with a selection coefficient against *LL* homozygotes as high as $s = 0.59 \pm 0.15$. A linear regression analysis indicated that the shift in allele frequency at this locus explains about 30% of the phenotypic shift in beak size due to natural selection (12). Within genotypic classes, survival was nonrandom. Individuals with small beaks survived better than those with large beaks among the *LL* homozygotes ($F_{1,18} = 4.9$, $P = 0.04$) and among heterozygotes ($F_{1,30} = 10.1$, $P = 0.003$). *SS* homozygotes showed no significant association ($F_{1,17} = 0.55$, $P = 0.47$), probably because so few individuals died ($n = 5$). Thus, we conclude that the relationship between *HMG2* and fitness was mediated entirely by the effect of this locus on beak size or associated craniofacial bones or muscles; developmental research will be necessary to reveal the underlying mechanism for the association. There is no evidence of pleiotropic effects of the gene on other, unmeasured, traits affecting fitness (table S5). Survivors were smaller in body size (11), but our analysis provides no additional insight into the genetic basis of body size variation (Fig. 2E) (12).

Introgressive hybridization can increase genetic variation and facilitate or enhance an evolutionary response to selection and adaptation (20, 21), but the actual genes conferring a selective advantage are rarely known (7, 22). Previous field studies have documented rare but recurring introgressive hybridization on Daphne Major between medium ground finches and small ground finch immigrants (23). Although the sample sizes are small, it appears that the *HMG2***S* allele is fixed in the small ground finch ($n = 14$; fig. S2A). Positive selection for the *S* allele suggests that introgression from the small ground finch contributed to the genetic response to di-

rectional selection and character displacement in the medium ground finch.

Our results provide evidence of two loci with major effects on beak morphology across Darwin's finches. *ALX1*, a transcription factor gene, has been associated with beak shape (15), and here we find that *HMG2* is associated with beak size. *ALX1* and *HMG2* are 7.5 Mb apart on chromosome 1 in chicken and zebra finch, and probably also in Darwin's finches, as expected on the basis of the very high degree of conserved synteny among birds (24). Beak size and beak shape are involved in all the major evolutionary shifts in the adaptive radiation of Darwin's finches (1). They are also subject to strong selection in contemporary time. In the character displacement episode discussed above, beak size was subject to strong directional selection: The standardized selection differential of -0.66 for sexes combined is an exceptionally high value. We have shown that the *HMG2* locus played a critical role in this character shift. The selection coefficient at the *HMG2* locus ($s = 0.59 \pm 0.14$) is comparable in magnitude to the selection differential on the phenotype and is higher than other examples of strong selection, such as loci associated with coat color in mice ($s < 0.42$) (25). The main implication of our findings is that a single locus facilitates rapid diversification. The lack of recombination between the two *HMG2* haplotypes, together with abundant polygenic variation and ecological opportunity (2, 5), may help to explain rapid speciation in this young adaptive radiation (1).

REFERENCES AND NOTES

- P. R. Grant, B. R. Grant, *How and Why Species Multiply: The Radiation of Darwin's Finches* (Princeton Univ. Press, 2008).
- J. B. Losos, *Lizards in an Evolutionary Tree: Ecology and Adaptive Radiation of Anoles* (Univ. of California Press, 2009).
- W. L. Brown Jr., E. O. Wilson, *Syst. Zool.* **5**, 49–64 (1956).
- P. R. Grant, *Biol. J. Linn. Soc. London* **4**, 39–68 (1972).
- D. Schluter, *The Ecology of Adaptive Radiation* (Oxford Univ. Press, 2000).
- D. W. Pfennig, K. S. Pfennig, *Evolution's Edge: Competition and the Origins of Diversity* (Univ. of California Press, 2012).
- M. E. Arnegard et al., *Nature* **511**, 307–311 (2014).
- Y. E. Stuart, J. B. Losos, *Trends Ecol. Evol.* **28**, 402–408 (2013).
- J. A. Tobias et al., *Nature* **506**, 359–363 (2014).
- P. R. Grant, B. R. Grant, *40 Years of Evolution: Darwin's Finches on Daphne Major Island* (Princeton Univ. Press, 2014).
- P. R. Grant, B. R. Grant, *Science* **313**, 224–226 (2006).
- See supplementary materials on Science Online.
- P. R. Grant, B. R. Grant, *Evolution* **48**, 297–316 (1994).
- A. Abzhanov, M. Protas, B. R. Grant, P. R. Grant, C. J. Tabin, *Science* **305**, 1462–1465 (2004).
- S. Lamichaney et al., *Nature* **518**, 371–375 (2015).
- K. Pfannkuche, H. Summer, O. Li, J. Hescheler, P. Dröge, *Stem Cell Rev. Rep.* **5**, 224–230 (2009).
- X. Zhou, K. F. Benson, H. R. Ashar, K. Chada, *Nature* **376**, 771–774 (1995).
- M. N. Weedon et al., *Nat. Genet.* **40**, 575–583 (2008).
- G. Fatemifar et al., *Hum. Mol. Genet.* **22**, 3807–3817 (2013).
- R. C. Lewontin, L. C. Birch, *Evolution* **20**, 315–336 (1966).
- P. W. Hedrick, *Mol. Ecol.* **22**, 4606–4618 (2013).
- K. J. Liu et al., *Proc. Natl. Acad. Sci. U.S.A.* **112**, 196–201 (2015).
- P. R. Grant, B. R. Grant, *Biol. J. Linn. Soc. London* **117**, 812–822 (2016).

24. G. Zhang *et al.*, *Science* **346**, 1311–1320 (2014).
 25. C. R. Linnen *et al.*, *Science* **339**, 1312–1316 (2013).

ACKNOWLEDGMENTS

We thank A. Garcia-Dorado, P. Hedrick, and M. Pettersson for advice concerning statistical analysis, and J. Pettersson and U. Gustafsson for expert technical assistance. NSF (USA) funded the collection of material under permits from the Galápagos and Costa Rica National Parks Services and the Charles Darwin Research Station, and in accordance with protocols of Princeton University's Animal Welfare Committee. The project was supported by the Knut and Alice Wallenberg Foundation. Sequencing was performed by the SNP & SEQ Technology Platform, supported

by Uppsala University and Hospital, SciLifeLab, and Swedish Research Council grants 80576801 and 70374401. Computer resources were supplied by UPPMAX. The Illumina reads have been submitted to the short reads archive (www.ncbi.nlm.nih.gov/sra) with accession numbers PRJNA263122 and PRJNA301892. Raw tree files for constructing Fig. 1, C and D, have been submitted to the TreeBASE database with submission ID S18636 (<http://purl.org/phylo/treebase/phyloids/study/TB2:S18636>). Author contributions: P.R.G. and B.R.G. collected the material; L.A., P.R.G., and B.R.G. conceived the study; L.A. and M.T.W. led the bioinformatic analysis of data; S.L., F.H., J.B., and C.W. performed the bioinformatic analysis with contributions from M.S.A.; and L.A., S.L., B.R.G., and P.R.G. wrote the paper with input

from the other authors. All authors approved the manuscript before submission.

SUPPLEMENTARY MATERIALS

www.sciencemag.org/content/352/6284/470/suppl/DC1
 Materials and Methods
 Supplementary Text
 Tables S1 to S5
 Figs. S1 and S2
 References (26–47)

16 November 2015; accepted 14 March 2016
 10.1126/science.aad8786

HUMAN GENOMICS

Health and population effects of rare gene knockouts in adult humans with related parents

Vagheesh M. Narasimhan,¹ Karen A. Hunt,^{2*} Dan Mason,^{3*} Christopher L. Baker,^{4*} Konrad J. Karczewski,^{5,6*} Michael R. Barnes,⁷ Anthony H. Barnett,⁸ Chris Bates,⁹ Srikanth Bellary,¹⁰ Nicholas A. Bockett,² Kristina Giorda,¹¹ Christopher J. Griffiths,² Harry Hemingway,^{12,13} Zhilong Jia,⁷ M. Ann Kelly,¹⁴ Hajrah A. Khawaja,⁷ Monkol Lek,^{5,6} Shane McCarthy,¹ Rosie McEachan,³ Anne O'Donnell-Luria,^{5,6} Kenneth Paigen,⁴ Constantinos A. Parisinos,² Eamonn Sheridan,³ Laura Southgate,² Louise Tee,¹⁴ Mark Thomas,¹ Yali Xue,¹ Michael Schnall-Levin,¹¹ Petko M. Petkov,⁴ Chris Tyler-Smith,¹ Eamonn R. Maher,^{15,16} Richard C. Trembath,^{2,17} Daniel G. MacArthur,^{5,6} John Wright,³ Richard Durbin,^{1,††} David A. van Heel^{2,††}

Examining complete gene knockouts within a viable organism can inform on gene function. We sequenced the exomes of 3222 British adults of Pakistani heritage with high parental relatedness, discovering 1111 rare-variant homozygous genotypes with predicted loss of function (knockouts) in 781 genes. We observed 13.7% fewer homozygous knockout genotypes than we expected, implying an average load of 1.6 recessive-lethal-equivalent loss-of-function (LOF) variants per adult. When genetic data were linked to the individuals' lifelong health records, we observed no significant relationship between gene knockouts and clinical consultation or prescription rate. In this data set, we identified a healthy *PRDM9*-knockout mother and performed phased genome sequencing on her, her child, and control individuals. Our results show that meiotic recombination sites are localized away from *PRDM9*-dependent hotspots. Thus, natural LOF variants inform on essential genetic loci and demonstrate *PRDM9* redundancy in humans.

Complete gene knockouts, typically caused by homozygous loss-of-function (LOF) genotypes, have helped researchers identify the function of many genes, predominantly through studies in model organisms and of severe Mendelian-inherited diseases in humans. However, information on the consequences of knocking out most human genes is still lacking. Naturally occurring complete gene knockouts offer the opportunity to study the effects of lifelong germline gene inactivation in living humans. A survey of LOF variants in adult humans revealed ~100 predicted LOF genotypes per individual, describing ~20 genes that carry homozygous predicted LOF alleles and hence are likely to be completely inactivated (1). Almost all of these homozygous genotypes were located at common variants with allele frequency >1%, in genes whose loss is likely to have weak or neutral effects on fitness and health (1). In con-

trast, rare predicted LOF genotypes were usually heterozygous and, thus, their overall effect on gene function is not known. A large exome sequencing aggregation study [conducted by the Exome Aggregation Consortium (ExAC)] of predominantly outbred individuals identified 1775 genes with homozygous predicted LOF genotypes in 60,706 individuals (2). Furthermore, 1171 genes with complete predicted LOF were identified in 104,220 Icelandic individuals (3), and modest enrichment for homozygous predicted LOF genotypes was shown in Finnish individuals (4). However, even in these large samples, homozygous predicted LOF genotypes tend to occur at variants of moderate allele frequency (~1%). Hence, these approaches will not readily assess knockouts in most genes, which are lacking such variants.

To identify knockouts created by rare homozygous predicted loss-of-function (rhLOF) variants, we sequenced the exomes of 3222 UK-dwelling

adults of Pakistani heritage who were characterized as healthy, type 2 diabetic, or pregnant (5). These individuals have a high rate of parental relatedness (often through parents who are first cousins); thus, a substantial fraction of their autosomal genome occurs in long homozygous regions inferred to be identical by descent from a recent common ancestor (autozygous). We linked each person's genotype to their health care and epidemiological records, with the aims of (i) describing the properties and assessing the health effects of naturally occurring knockouts in an adult population; (ii) understanding the architecture of gene essentiality in the human genome, through the characterization of the population genetics of LOF variants; and (iii) conducting a detailed study of a *PRDM9* gene knockout, which plays a role in human meiotic recombination (6).

On average, 5.6% of the coding genome was autozygous, much higher than the percentage in outbred populations with European heritage (Fig. 1A and fig. S4). We identified, per individual, an average of 140.3 nonreference predicted

¹Wellcome Trust Sanger Institute, Hinxton, Cambridge CB10 1SA, UK. ²Blizard Institute, Barts and The London School of Medicine and Dentistry, Queen Mary University of London, London E1 2AT, UK. ³Bradford Institute for Health Research, Bradford Teaching Hospitals National Health Service (NHS) Foundation Trust, Bradford BD9 6RJ, UK. ⁴Center for Genome Dynamics, The Jackson Laboratory, Bar Harbor, ME 04609, USA. ⁵Analytic and Translational Genetics Unit, Massachusetts General Hospital, Boston, MA 02114, USA. ⁶Program in Medical and Population Genetics, Broad Institute of MIT and Harvard, Cambridge, MA 02142, USA. ⁷William Harvey Research Institute, Barts and The London School of Medicine and Dentistry, Queen Mary University of London, London E1 2AT, UK. ⁸Diabetes and Endocrine Centre, Heart of England NHS Foundation Trust and University of Birmingham, Birmingham B9 5SS, UK. ⁹TPP, Mill House, Troy Road, Leeds LS18 5TN, UK. ¹⁰Aston Research Centre for Healthy Ageing, Aston University, Birmingham B4 7ET, UK. ¹¹10X Genomics, 7068 Koll Center Parkway, Suite 415, Pleasanton, CA 94566, USA. ¹²Farr Institute of Health Informatics Research, London NW1 2DA, UK. ¹³Institute of Health Informatics, University College London, London NW1 2DA, UK. ¹⁴School of Clinical and Experimental Medicine, University of Birmingham, Birmingham B15 2TT, UK. ¹⁵Department of Medical Genetics, University of Cambridge and National Institute for Health Research (NIHR) Cambridge Biomedical Research Centre, Box 238, Cambridge Biomedical Campus, Cambridge CB2 0QQ, UK. ¹⁶Cambridge University Hospitals NHS Foundation Trust, Cambridge Biomedical Campus, Cambridge CB2 0QQ, UK. ¹⁷Faculty of Life Sciences and Medicine, King's College London, London SE1 1UL, UK.

*These authors contributed equally to this work. †These authors contributed equally to this work. ††Corresponding author. Email: rd@sanger.ac.uk (R.D.); d.vanheel@qmul.ac.uk (D.A.v.H.)

LOF genotypes comprising 16.1 rare heterozygotes (minor allele frequency <1%), 0.34 rare homozygotes, 83.2 common heterozygotes, and 40.6 common homozygotes. Nearly all rhLOF genotypes were found within autozygous segments (94.9%) (5), and the mean number of rhLOF variants per individual was proportional to the rate of autozygosity (Fig. 1B). Overall, we identified 1111 rhLOF genotypes at 847 variants (575 annotated as LOF variants in all GENCODE basic transcripts) in 781 different protein-coding genes (Fig. 1C) (5) in 821 individuals. Autozygous segments were observed across all coding regions, with a density distribution that was not significantly different from random (5) (Shapiro-Wilk test; $P = 0.112$). From these values, we estimate that 41.5% of individuals with 6.25% autozygosity (expected mean for an individual whose parents are first cousins but are otherwise outbred) will have one or more rhLOF genotypes (Fig. 1B).

The majority (422) of the identified genes with rhLOF genotypes had not been previously reported, although 167 had been reported as containing homozygous or compound heterozygous LOF genotypes in Iceland, and 299 appeared in the ExAC data. In total, 107 rhLOF genes were common to all three data sets (5), suggesting a subset of genes that are either tolerant of LOF variants and/or have higher rates of mutation. Eighty-nine rhLOF genotypes were homozygotes without observed heterozygotes, and we identified three individuals who each had five rhLOF genotypes. On the basis of these observations, we predict that in 100,000 individuals with first-cousin-related parents of the same genetic ancestry, at least one knockout would occur in ~9000 of the ~20,000 human protein-coding genes (fig. S3) (5).

We observed a lower density of annotated rare LOF variants within autozygous tracts (where

the genotypes are homozygous) compared with outside autozygous tracts (where they are typically heterozygous), indicating direct negative selection on a fraction of homozygotes (Fig. 2A). We matched each of the 16,708 rare annotated LOF (heterozygous and homozygous) variants to a randomly selected synonymous variant of the same allele frequency and observed 842 rare LOF variants with at least one homozygous genotype versus an average of 975.5 rare synonymous variants with at least one homozygote, which indicates a deficit of 13.7% [95% confidence interval (CI): 8 to 20%] of variants with rhLOF genotypes (Fig. 2B) (5). We attribute this deficit to some rhLOF genotypes resulting in early lethality or severe disease and thus being incompatible with our selection criteria for healthier adults, although our data do not inform whether these cases are due to fewer high-penetrance or more low-penetrance variants. This deficit is higher than in the Icelandic population (6.4%) (3), consistent with that analysis being biased toward more common variants already subject to selection.

We then combined the calculated deficit rate with the observed number of heterozygous annotated LOF variants, integrating across allele frequencies, to obtain a direct estimate of the recessive lethal load per person. This finding suggests that a typical individual from the population we sampled carries 1.6 recessive annotated LOF lethal-equivalent variants in the heterozygous state (5). Our estimate is similar to previous approximations of the lethal load—calculated by correlating the number of miscarriages, stillbirths, and infant mortalities with the level of autozygosity (Fig. 2C) (7, 8)—and is also similar to measurements in other species (9). Using epidemiological data from 13,586 mothers from the same Born in Bradford birth cohort studied in our genetic analysis, we esti-

mated 0.5 lethal equivalents resulting in miscarriage, stillbirth, or infant mortality per individual in our population (5). The difference between our two estimates can be accounted for by the fact that the first includes embryonic deaths, whereas the second involves fatalities occurring only after a registered pregnancy, which suggests that there are twice as many embryonically lethal recessive mutations as those that result in fetal or infant death. Controlling for other effects by comparing to synonymous mutations, we see a significant but moderate decrease ($R_{A/B}$ jackknife test; $P = 0.04$) in the rhLOF mutational load in our Pakistani-heritage population data set compared with outbred populations from the 1000 Genomes Project, although the observed decrease is less than that caused by the historic bottleneck in the Finnish population (FIN in Fig. 2D) (5).

We examined 215 rhLOF genes from our data set that have an exact 1:1 mouse:human gene ortholog. Analysis of mouse gene knockout data revealed 52 genes for which a lethal mouse phenotype had been reported on at least one genetic background (10). Whether or not the mouse ortholog knockout is lethal has no bearing on alteration of protein function, duplication, or changes in gene expression (5). Genes containing rhLOF showed 50% fewer molecular interactions compared with all genes in the STRING interactome data set (Kruskal-Wallis test; $P = 3.4 \times 10^{-9}$); this result was predominantly driven by genes in the binding interaction category (Kruskal-Wallis $P = 9.3 \times 10^{-11}$) (table S4). We saw a similar reduction in the Icelandic data, in contrast to both known pathogenic LOF variants and pathogenic gain-of-function variants reported in the Orphanet reference portal, which showed increased overall molecular interactions (Kruskal-Wallis $P = 1.1 \times 10^{-6}$ and 2×10^{-12} , respectively) (table S4) (5). Furthermore,

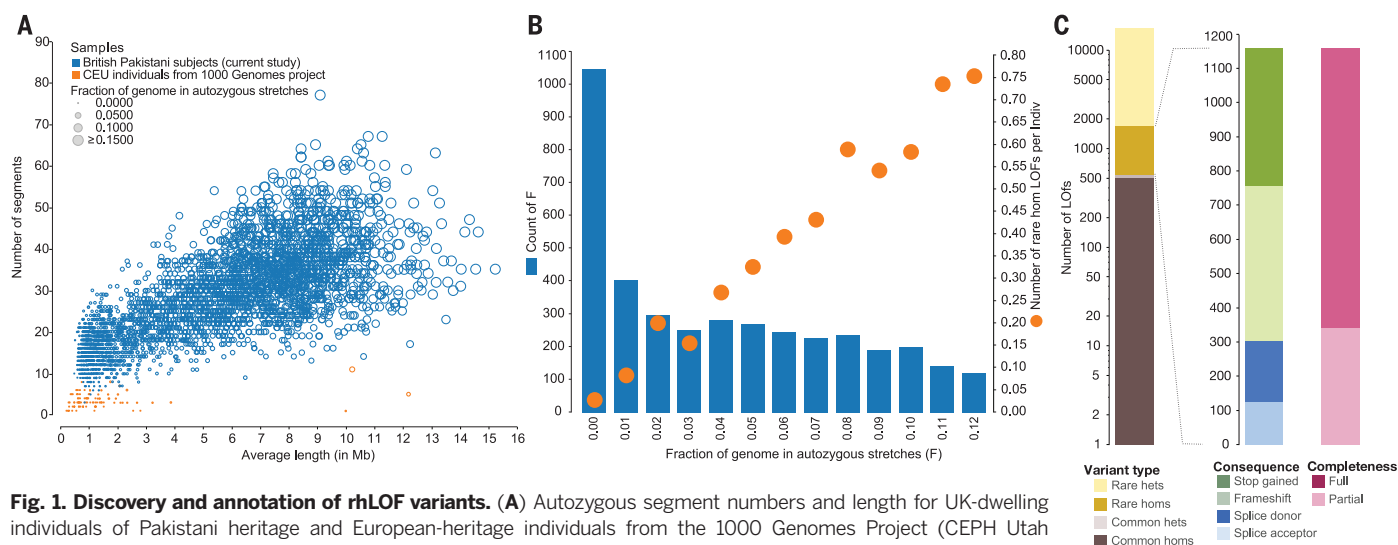


Fig. 1. Discovery and annotation of rhLOF variants. (A) Autozygous segment numbers and length for UK-dwelling individuals of Pakistani heritage and European-heritage individuals from the 1000 Genomes Project (CEPH Utah residents with ancestry from Northern and Western Europe; CEU). (B) Autozygosity and rhLOF in 3222 individuals. The graph shows the number (count) of individuals (left y axis, blue columns) binned by fraction of the autozygous genome (F; x axis) plotted against the mean number of rhLOF genotypes per individual (right y axis, orange circles). (C) Distribution of LOF variants by variant type (allele frequency and heterozygous-only versus those containing a homozygous genotype), predicted protein consequence, and transcript completeness (i.e., whether predicted for a full or partial set of GENCODE basic transcripts for the gene).

rhLOF genes that are drug targets have an 11.4% rate of going from phase 1 clinical trials to approval versus 6.7% for all target-indication pairs (χ^2 test; $P = 0.046$), yet we observed no difference in the proportion of genes known or predicted to be druggable targets (11) when rhLOF genes (15%) were compared to all genes (13%, $P = 0.098$) (5).

In participants from the Born in Bradford study, where full health record data was available, we observed 52 individuals with 54 rhLOF genotypes in recessive disease genes, using the Online Mendelian Inheritance in Man (OMIM) catalog “confirmed” category. We expected that these variants would be enriched for false-positive observations (7). After a quality-control analysis of the sequence-based genotype calls (5), we inspected the annotation of these variants (1). Of the 54 rhLOF genotypes, we considered 16 to be possible genome annotation errors (i.e., incorrectly described as LOF variants) (5) (table S2). Only six of the remaining 38 rhLOF variants were linked to a definite lifetime primary health record diagnosis consistent with the OMIM phenotype, although a further three genotypes were suggestively compatible (table S3). We suggest that the remaining 29 are due to a combination of incomplete penetrance (12–16), late onset of disease (i.e., not yet having occurred), individuals with mild symptoms not seeking medical attention, unrecognized technical issues with sequencing or annotation (e.g., tissue-specific alternative splicing), or dubious

evidence to support the gene-phenotype assignment (in table S3, we assess the available evidence for these possibilities).

We next assessed electronic health records in the Born in Bradford adults, focusing on the time since study recruitment (5). Drug prescription rate and clinical staff consultation rate have previously been shown to correlate strongly with health status (17). We compared individuals with one or more rhLOF genotype ($n = 638$) to individuals without rhLOF ($n = 1524$) and found no association with prescription rate [logistic regression, odds ratio (OR): 1.001, 95% CI: 0.988 to 1.014] or consultation rate (OR: 1.017, 95% CI: 0.996 to 1.038), nor any associations in rhLOF subgroups (5).

One individual in our study was a healthy adult mother with a predicted rare homozygous LOF mutation in *PRDM9*, which we confirmed experimentally (5) (fig. S7, A and B). *PRDM9* is the major known determinant of the genomic locations of meiotic recombination events in humans and mice through its DNA binding site zinc finger domain (6, 18, 19). We excluded the possibility that this rhLOF variant was from a somatic loss-of-heterozygosity event on the basis that this individual’s genotype is heterozygous, not homozygous, on both sides of the 25-Mb autozygous region (fig. S7C). Her lifetime primary- and secondary-care health records were unremarkable. Her genotype predicts protein truncation in the SET methyltransferase domain (thus lacking the DNA-binding zinc finger domain), which

we confirmed by in vitro expression analysis (fig. S8A). We observed no increase in H3K4Me3 global methylation upon transfection (20) of the truncation allele (fig. S8A) and that R345Ter specifically disrupted *PRDM9*-dependent H3K4Me3 methylation at hotspots (fig. S8B).

We performed long-range molecularly phased whole-genome sequencing to determine the locations of meiotic recombination in the maternal gamete transmitted from mother to child and identified 39 candidate crossovers in the process (5). Using maps of double-strand breaks (DSBs) and a maximum likelihood model to account for variability in region size and hotspot density (18), we estimated that only 5.9% (2 log unit CI: 0 to 24%) of the observed *PRDM9*-knockout-duo maternal gamete crossovers matched DSB sites from homozygotes with the wild-type *PRDM9-A* allele (5). In comparison, for a control mother-child Centre d’Etude du Polymorphisme Humain (CEPH) pedigree duo homozygous for *PRDM9-A*, we estimated that 52.1% (CI: 36 to 69%) of the crossovers occurred in known DSB sites. Using similar methods, we saw that 18.5% of the crossovers observed in the *PRDM9*-knockout duo (CI: 1 to 42%) occurred in linkage-disequilibrium-based hotspots versus 75.7% in the control duo [CI: 57 to 89%, consistent with a previously published estimate of an average of 60% of crossovers occurring at hotspots (18)] (5).

Prdm9-knockout mice demonstrate abnormal location of recombination hotspots with enrichment

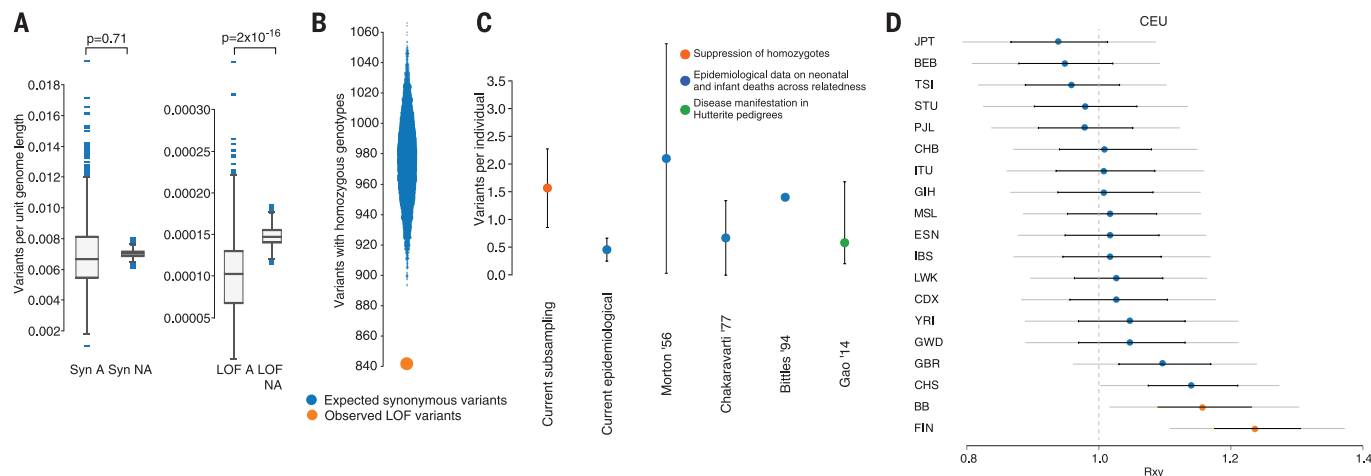


Fig. 2. Population genetic analysis of rhLOF variants. (A) Comparison of the number of LOF variants per unit length in autozygous regions (LOF A) with the expected rate from nonautozygous sections (LOF NA), showing suppression of rhLOFs (t test). A similar analysis of synonymous (Syn) variants revealed no significant differences. (B) Observed number of variants with homozygote genotypes in 16,708 rare LOF variants (orange circle) versus a frequency-matched subsampling of synonymous variants (blue violin plot). (C) Quantification of the recessive lethal load carried, on average, by a single individual. Orange circle, direct subsampling estimate for rhLOF variants from current study; blue circles, epidemiological estimates from correlating infant mortality rates to estimated autozygosity in current and published data; green circle, direct estimate from a large Hutterite pedigree. Black bars denote 95% CIs. (D) Relative number of derived LOF alleles that are frequent in

one population and not another (under neutrality, the expectation is 1.0). Results were calculated for 1000 Genomes Project populations and the current Birmingham/Bradford Pakistani heritage population (BB), as compared with the CEU population. Error bars represent ± 1 (black) or ± 2 (gray) SEs. Significant differences ($R_{A/B}$ jackknife test) from CEU population data are denoted by orange circles. JPT, Japanese (Tokyo, Japan); BEB, Bengali (Bangladesh); TSI, Toscani (Italy); STU, Sri Lankan Tamil (UK); PJL, Punjabi (Lahore, Pakistan); CHB, Han Chinese (Beijing, China); ITU, Indian Telugu (UK); GIH, Gujarati Indian (Houston, TX); MSL, Mende (Sierra Leone); ESN, Esan (Nigeria); IBS, Iberian (Spain); LWK, Luhya (Webuye, Kenya); CDX, Chinese Dai (Xishuangbanna, China); YRI, Yoruba (Ibadan, Nigeria); GWD, Gambian (Western Divisions in the Gambia); GBR, British (England and Scotland); CHS, Southern Han Chinese (China); FIN, Finnish (Finland).

at gene promoters and enhancers, fail to properly repair DSBs, and are infertile (both sexes sterile) (21, 22). Dogs, which lack *PRDM9*, retain recombination hotspots that occur in regions with high GC content (23), unlike in humans or knockout mice. It has been speculated that meiotic recombination in dogs is controlled by an ancestral mammalian mechanism and that *PRDM9* competes and usurps these sites when active in noncanids (23, 24). However, we did not see increased overlap in our *PRDM9*-knockout-*duo* crossover intervals with promoters and their flanking regions or enrichment in GC content, as compared to the control *duo* (5). Thus, the existence of a healthy and fertile *PRDM9*-deficient adult human points to differences in humans versus both mice and dogs and supports the possibility of alternative mechanisms of localizing human meiotic crossovers (25, 26).

Together, these data suggest that apparent *rhLOF* genotypes identified by exome or genome sequencing of adult populations require cautious interpretation. Although this class of variants has the greatest predicted effect on protein function, the loss of most proteins is relatively harmless to the individual. Even in previously annotated disease genes, predicted rare *LOF* homozygotes may not always be as clinically relevant as often considered. This finding is becoming increasingly important now that exome- and genome-sequencing studies of healthier adults are rapidly expanding. We anticipate that further efforts to identify naturally occurring human knockouts—whether in bottlenecked populations or, more efficiently, in individuals with related parents, as described here—will yield both new data relevant to clinical interpretation and new biological insights,

as exemplified by our investigation of a *PRDM9*-deficient healthy and fertile woman.

REFERENCES AND NOTES

1. D. G. MacArthur *et al.*, *Science* **335**, 823–828 (2012).
2. Exome Aggregation Consortium *et al.*, Analysis of protein-coding genetic variation in 60,706 humans. 10.1101/030338 (2015); <http://biorxiv.org/content/early/2015/10/30/030338>.
3. P. Sulem *et al.*, *Nat. Genet.* **47**, 448–452 (2015).
4. E. T. Lim *et al.*, *PLOS Genet.* **10**, e1004494 (2014).
5. See supplementary materials on Science Online.
6. E. D. Parvanov, P. M. Petkov, K. Paigen, *Science* **327**, 835 (2010).
7. R. Chakraborty, A. Chakravarti, *Hum. Genet.* **36**, 47–54 (1977).
8. A. H. Bittles, J. V. Neel, *Nat. Genet.* **8**, 117–121 (1994).
9. A. R. McCune *et al.*, *Science* **296**, 2398–2401 (2002).
10. B.-Y. Liao, J. Zhang, *Proc. Natl. Acad. Sci. U.S.A.* **105**, 6987–6992 (2008).
11. M. R. Nelson *et al.*, *Nat. Genet.* **47**, 856–860 (2015).
12. J. Flannick *et al.*, *Nat. Genet.* **45**, 1380–1385 (2013).
13. H. L. Rehm *et al.*, *N. Engl. J. Med.* **372**, 2235–2242 (2015).
14. K. Walter *et al.*, *Nature* **526**, 82–90 (2015).
15. J. J. Johnston *et al.*, *Am. J. Hum. Genet.* **96**, 913–925 (2015).
16. S. L. Van Driest *et al.*, *JAMA* **315**, 47–57 (2016).
17. S. L. Brilleman *et al.*, *Br. J. Gen. Pract.* **63**, e274–e282 (2013).
18. F. Baudat *et al.*, *Science* **327**, 836–840 (2010).
19. S. Myers *et al.*, *Science* **327**, 876–879 (2010).
20. C. L. Baker *et al.*, *PLOS Genet.* **11**, e1005512 (2015).
21. K. Hayashi, K. Yoshida, Y. Matsui, *Nature* **438**, 374–378 (2005).
22. K. Brick, F. Smagulova, P. Khil, R. D. Camerini-Otero, G. V. Petukhova, *Nature* **485**, 642–645 (2012).
23. E. Axelsson, M. T. Webster, A. Ratnakumar, C. P. Ponting, K. Lindblad-Toh, *Genome Res.* **22**, 51–63 (2012).
24. I. L. Berg *et al.*, *Nat. Genet.* **42**, 859–863 (2010).
25. F. Pratto *et al.*, *Science* **346**, 1256442 (2014).
26. M. Lichten, *Science* **350**, 913 (2015).

ACKNOWLEDGMENTS

The study was funded by the Wellcome Trust (grants WT102627 and WT098051), Barts Charity (grant 845/1796), and the UK Medical Research Council (grant MR/M009017/1). This paper presents independent research funded by the NIHR under its Collaboration for Applied Health Research and Care for Yorkshire and Humber. Core support for Born in Bradford is also provided by the Wellcome Trust (grant WT101597). V.M.N. was supported by

the Wellcome Trust Ph.D. Studentship (grant WT099769). D.G.M. and K.J.K. were supported by the NIH National Institute of General Medical Sciences under award R01GM104371. E.R.M. is funded by the NIHR Cambridge Biomedical Research Centre. H.H. is supported by awards to establish the Farr Institute of Health Informatics Research, London, from the UK Medical Research Council, Arthritis Research UK, the British Heart Foundation, Cancer Research UK, the Chief Scientist Office, the Economic and Social Research Council, the Engineering and Physical Sciences Research Council, NIHR, the National Institute for Social Care and Health Research, and the Wellcome Trust. C.L.B., K.P., and P.M.P. are supported by the NIH (grant GM 099640). Born in Bradford is only possible because of the enthusiasm and commitment of the children and parents who are part of the study. We are grateful to all of the participants, health professionals, and researchers who took part in the Born in Bradford study. We thank B. MacLaughlin (Queen Mary University of London) for assistance and J. Rogers (Health & Social Care Information Centre) for advice. We would like to thank the Exome Aggregation Consortium and the groups that provided exome variant data for comparison. A full list of contributing groups can be found at <http://exac.broadinstitute.org/about>. R.D. declares that he is a founder and nonexecutive director of Congenica, owns stock in Illumina from previous consulting work, and is a scientific advisory board member of Dovetail. M.S.-L. and K.G. are employees of 10X Genomics. H.H. discloses paid consulting for AstraZeneca, and R.C.T. discloses a paid advisory role with Pfizer. Data reported in the paper are presented in the supplementary materials and are available under a data access agreement at the European Genotype-phenome Archive (www.ebi.ac.uk/ega) under accession numbers EGAS00001000462, EGAS00001000511, EGAS00001000567, EGAS00001000717, and EGAS00001001301.

SUPPLEMENTARY MATERIALS

www.sciencemag.org/content/352/6284/474/suppl/DC1
Materials and Methods

Figs. S1 to S8

Tables S1 to S8

References (27–60)

Data S1 to S3

12 November 2015; accepted 18 February 2016

Published online 3 March 2016

10.1126/science.aac8624

Don't miss the debut of ***Science Immunology***.

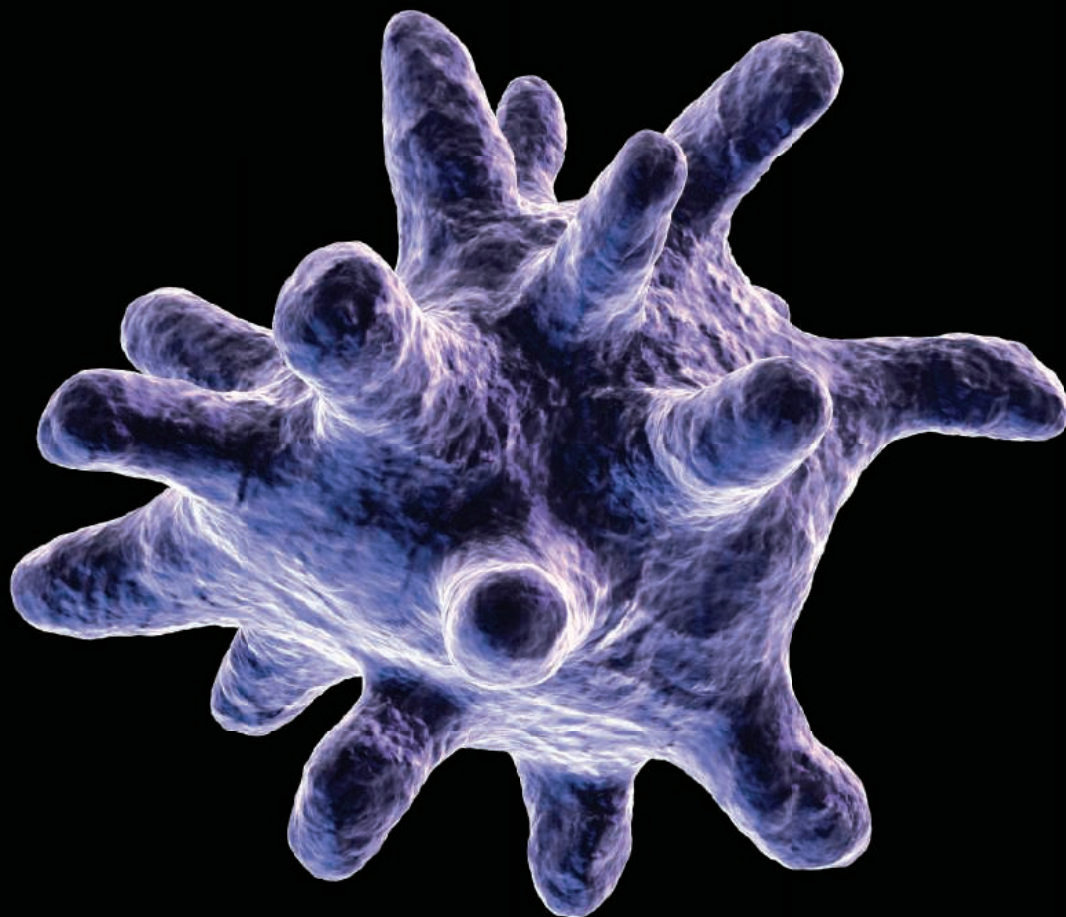


Image: Eraxion / iStockPhoto

————— NOW ACCEPTING PAPERS —————

Science is expanding its reach into immunology—now offering the newest online-only, weekly journal in the *Science* family of publications. *Science Immunology* will provide original, peer-reviewed research articles that report critical advances in all areas of immunological research, including studies that provide insight into the human immune response in health and disease.

Be a part of the *Science Immunology* debut issue publishing Summer 2016!

Submit your manuscript today at
ScienceImmunology.org.

ScienceImmunology

AAAS

The first global award for stem cells and regenerative medicine

BOYALIFE
& Science
Science Translational Medicine
Award in
Stem Cells
and Regenerative
Medicine

Stem cells and regenerative medicine is the new frontier in life sciences. *Boyalife, Science, and Science Translational Medicine* jointly establish a global award to recognize and reward scientists in the fields of stem cells and/or regenerative medicine with a focus on developing cell-based treatments for cancer, degenerative disorders, immunotherapy and stem cells transplantation.

The 2016 award ceremony will be held in San Francisco, on 23rd June, 2016.

The winners will receive:

- ☆ A Grand Prize of \$25,000 and a Runner-Up Prize of \$5,000 will be awarded.
- ☆ The Grand Prize Winning Essay will be published in *Science*; a brief abstract of the Runner-Up Essay will be published in *Science*.

Learn more about the Prize,
visit : www.sciencemag.org/prize/boyalife/rules



AAAS Travels

In Search of

AMELIA EARHART

Explore one of the greatest mysteries of all time!

On the 80th Anniversary of
Amelia's World Flight & Disappearance!

Amelia 2017 Adopt an Expert!

June 21–July 11, 2017

Help in search of Amelia Earhart!

- 1) You can join us yourself.
- 2) You can also *Adopt-an-Expert* and help pay the way of one of the research scientists.

For further information please visit

<http://niku2017.strikingly.com>

You can adopt an expert for just \$8,995 + airfare of \$1,695 from Los Angeles.

For a detailed brochure, call (800) 252-4910

All prices are per person twin share + air



BETCHART EXPEDITIONS Inc.
17050 Montebello Rd, Cupertino, CA 95014
Email: AAASInfo@betchartexpeditions.com
www.betchartexpeditions.com

Advance your
career with expert
advice from
Science Careers.



Download Free Career Advice Booklets!
ScienceCareers.org/booklets

Featured Topics:

- Networking
- Industry or Academia
- Job Searching
- Non-Bench Careers
- And More



Science Careers
FROM THE JOURNAL SCIENCE AAAS

Setting the stage for
the great minds of
diagnostics to
advance medicine
together

Next Generation SUMMIT

EIGHTH ANNUAL



MOVING ASSAYS TO THE CLINIC

AUGUST 23-26, 2016 | GRAND HYATT, WASHINGTON, DC



CONFERENCE PROGRAMS

August 23-24

Enabling Point-of-Care Diagnostics
Circulating Tumor Cells
Companion Diagnostics:
Strategy & Partnerships
Coverage and Reimbursement of
Advanced Diagnostics
DNA Forensics
Clinical NGS Assays
Hospital Laboratory Design and Renovation

August 24-25

Molecular Diagnostics for Infectious Disease
Clinical Application of Cell-Free DNA
Diagnostics to Guide Cancer Immunotherapy
Commercialization of Molecular Diagnostics
Leveraging Pharmacies for Rapid Diagnostics
NGS Diagnostics: Data Considerations,
Annotation and Interpretation

**Register Early
and Save
up to \$350!**

Mention keycode L35

Organized by
Cambridge
HEALTHTECH
Institute

NextGenerationDx.com

Cell Thawing Platform

The ThawSTAR automated cell thawing technology platform now accommodates rapidly developing industries such as cell therapy, which are bringing products to the clinic in a variety of formats. Two thawing systems for 1.5-mL cryogenic vials and 6-mL AT-Closed Vials have been released from Aseptic Technologies, S.A., accelerating the development of an automated platform to thaw cryopreservation bags commonly used to store and deliver larger-volume cell-based therapeutics. The proprietary ThawSTAR thawing system utilizes an adaptive, load-sensing technology that senses the initial starting temperature and phase change initiation, and customizes the thaw for each vial, ensuring consistent and reproducible endpoints. Vials can be inserted directly from liquid nitrogen storage (below -150°C) or from dry ice or ultra-low freezer storage (-80°C).

BioCision

For info: 888-478-2221
www.biocision.com

Automated Incubator

High-capacity cell growth and assay incubation laboratories now have access to a new automated incubation and storage incubator, designed to provide fast plate access and a wide temperature range for application flexibility. The Thermo Scientific Cytomat 10 C450 provides plate access in less than 10 seconds, enabling culturists to access their cells faster, leading to increased productivity. Its flexible design ensures easy integration into existing lab space, while the fully integrated thermal decontamination routine and humidity control decrease the risk of contamination and assay variability. The Cytomat 10 C450 covers a temperature range of 4°C to 50°C to allow application flexibility, and is the next incubator in the series to provide fast plate access through the new plate shuttle technology. The new incubator adopts the ContraCon automated thermal decontamination routine, from the stand-alone HeraCell incubator portfolio. In addition, the integrated HydraSmart technology features an external water tank for easy refill and provides excellent humidity control.

Thermo Fisher Scientific

For info: 800-955-6288
www.thermofisher.com



High-Content Cellular Analysis

The iQue Screener PLUS platform is an integrated instrument, software, and reagent system that enhances the screening workflow from sample preparation to results. It enables rapid, high-content, multiplexed analysis of cells and beads in suspension in 96-, 384-, and 1,536-well plates. The system's patented sample delivery system enables rapid plate processing (less than five minutes for 96 wells), and assays can be miniaturized to conserve precious sample and reduce reagent use. Software-assisted automation, analysis, and experiment-level visualization tools reveal deep insight into complex biology through an easy-to-use, intuitive interface. The iQue Screener PLUS expands choice and flexibility, adding a 405-nm violet laser to the blue (488-nm) and red (640-nm) lasers, along with 15 detection channels, including 13 fluorescence and 2 scatter detectors, which provide richer content through higher-order multiplexing. The expanded range of dyes and fluorochromes for the violet laser adds flexibility and enhanced performance, with lower spectral overlap, increased brightness, better signal-to-noise ratio, and broader applicability.

IntelliCyt

For info: 505-345-9075
www.intellicyt.com

workflows for walkaway automation involving multiple tube types. The LabElite AutoSwap is ideal for any lab dealing with sample storage, retrieval, and processing, such as those found in biobanking, compound management, or forensics settings. Automated decapping saves time and limits the risk of contamination by minimizing the amount of time a tube is open.

Hamilton Storage

For info: 800-648-5950
www.hamilton-storage.com

Automated Cell Culture System

The new SelectT Mk5 automated cell culture system is designed for the routine production of high-quality complex cell lines. The new SelectT system has been extensively redesigned to upgrade its flask-handling and pipetting capabilities, and now comes with an integrated Vi-CELL Cell Viability Analyzer and a new Low Volume Reagent Dispensing module. The SelectT Mk5 system makes an ideal choice for scientists looking for an established method of continuous, unattended large-scale culturing of reproducible assay-ready multiwell plates, and can also support the maintenance and expansion of cell lines requiring more complex handling, such as stem cells. The Vi-CELL was chosen for the new SelectT system because the technology adapts well to the online automated measurement of cell viability and cell number required by SelectT. With the integrated Vi-CELL analyzer, scientists can review numerical and image data in real time while also having access to additional cell culture data provided by the SelectT system.

Sartorius Stedim Biotech

For info: +44-(0)-1763-227200
www.tapbiosystems.com

Automated Tube DeCapper

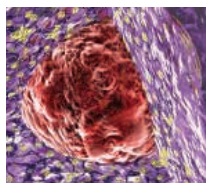
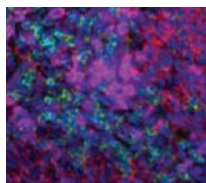
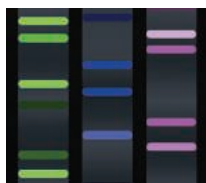
The LabElite AutoSwap adds new functionality to the LabElite automated tube DeCapper. The new AutoSwap enables fast and easy switching of labware-specific DeCapper adapters on the fly without manual intervention, allowing workflows to proceed with different types of tubes. The AutoSwap switches between any two sets of Hamilton adapters, which include options compatible with tubes from all major manufacturers, in 96- or 48-well formats. The new AutoSwap can also be used in integrated robotic

Electronically submit your new product description or product literature information! Go to www.sciencemag.org/about/new-products-section for more information.

Newly offered instrumentation, apparatus, and laboratory materials of interest to researchers in all disciplines in academic, industrial, and governmental organizations are featured in this space. Emphasis is given to purpose, chief characteristics, and availability of products and materials. Endorsement by *Science* or AAAS of any products or materials mentioned is not implied. Additional information may be obtained from the manufacturer or supplier.

want new technologies?

antibodies
apoptosis
biomarkers
cancer
cytometry
data
diseases
DNA
epigenetics
genomics
immunotherapies
medicine
microbiomics
microfluidics
microscopy
neuroscience
proteomics
sequencing
toxicology
transcriptomics



watch our **webinars**

Learn about the latest breakthroughs, new technologies, and ground-breaking research in a variety of fields. Our expert speakers explain their quality research to you and answer questions submitted by live viewers.

VIEW NOW!

webinar.sciencemag.org

Science
AAAS

Brought to you by the *Science*/AAAS
Custom Publishing Office



@SciMagWebinars



Alexander von Humboldt
Stiftung/Foundation



more independence + more opportunities + more scope [search](#)

Sofja Kovalevskaja Award – Become a research group leader in Germany

€ 1.65 million for young researchers from all disciplines

The Alexander von Humboldt Foundation is now calling for applications for the Sofja Kovalevskaja Award, one of the most valuable academic awards in Germany. With funding of up to € 1.65 million, it creates unique opportunities for excellent researchers to conduct their own research in Germany: award winners are invited to spend five years working at the institute of their choice and setting up their own research groups – independently and virtually free of bureaucracy.

Scientists and scholars of all disciplines from abroad who have completed their doctorates within the last six years are eligible to apply. The award targets outstanding talent and a creative approach to research.

The Humboldt Foundation actively promotes equal opportunities and therefore particularly welcomes applications from women researchers.

The closing date for applications is 31 July 2016. More information: www.humboldt-foundation.de/SKP_en

Exzellenz verbindet –
be part of a worldwide network.

Alexander von Humboldt Foundation
Jean-Paul-Str. 12
53173 Bonn
Germany

info@avh.de

www.humboldt-foundation.de



Deciphering Cancer

Antibodies to evaluate key signaling networks involved in cancer metabolism.



Download pathways at www.cellsignal.com/cancerpathways





There's only one **Science**

Science Careers Advertising

For full advertising details, go to ScienceCareers.org and click For Employers, or call one of our representatives.

Tracy Holmes

Worldwide Associate Director
Science Careers
Phone: +44 (0) 1223 326525

THE AMERICAS

E-mail: advertise@sciencecareers.org
Fax: +1 (202) 289 6742

Tina Burks

Phone: +1 (202) 326 6577

Nancy Toema

Phone: +1 (202) 326 6578

Online Job Posting Questions

Phone: +1 (202) 312 6375

EUROPE / INDIA / AUSTRALIA / NEW ZEALAND / REST OF WORLD

E-mail: ads@science-int.co.uk
Fax: +44 (0) 1223 326532

Sarah Lelarge

Phone: +44 (0) 1223 326527

Kelly Grace

Phone: +44 (0) 1223 326528

Online Job Posting Questions

Phone: +44 (0) 1223 326528

JAPAN

Katsuyoshi Fukamizu (Tokyo)

E-mail: kfukamizu@aaas.org
Phone: +81 3 3219 5777

Hiroyuki Mashiki (Kyoto)

E-mail: hmashiki@aaas.org
Phone: +81 75 823 1109

CHINA / KOREA / SINGAPORE / TAIWAN / THAILAND

Ruolei Wu

E-mail: rwu@aaas.org
Phone: +86 186 0082 9345

All ads submitted for publication must comply with applicable U.S. and non-U.S. laws. *Science* reserves the right to refuse any advertisement at its sole discretion for any reason, including without limitation for offensive language or inappropriate content, and all advertising is subject to publisher approval. *Science* encourages our readers to alert us to any ads that they feel may be discriminatory or offensive.

Science Careers

FROM THE JOURNAL SCIENCE AAAS

ScienceCareers.org



Lab Manager Department of Chemistry

This is a full-time, 12-month calendar year professional staff position directly supported by the University at Albany. The successful applicant will manage the operations of the RNA Mass Spectrometry Laboratory. Full description is available at:

<https://albany.interviewexchange.com/jobofferdetails.jsp?JOBID=70284&CNTRNO=0&TSTMP=1460149361232>

The ideal candidate will have: a PhD degree in pertinent disciplines with at least two years post-doctoral experience; extensive hands on experience on mass spectrometry and chromatography instrumentation; preferable background in proteomics and biopolymer analysis; excellent oral and written communication skills; excellent organizational skills; ability to work in a cross-disciplinary environment; demonstrated scientific productivity; ability to work independently but in close cooperation with the PI and the rest of the research group. Salary is competitive and commensurate with experience. Applicants must apply on-line by using the above link. Applicants must provide a resume/CV, statement of research experience and interest, three reference letters.

*The University at Albany is an
EO/AA/IRCA/ADA Employer*

POSITIONS OPEN

BACTERIAL GENE REGULATION AND LYME DISEASE PATHOGENESIS

A POSTDOCTORAL POSITION is available in the laboratory of Dr. Michael Norgard in the Microbiology Department to study virulence gene regulation in *Borrelia burgdorferi*, the Lyme disease spirochete. Studies will focus on the RpoN (Sigma54)-RpoS alternative sigma factor regulatory cascade and, in particular, the role of BosR as a requisite accessory molecule for pathway activation (see Z. Ouyang et al. 2010. BosR [BB0647] controls the RpoN-RpoS regulatory pathway and virulence expression in *Borrelia burgdorferi* by a novel DNA-binding mechanism. PLoS Pathogens 7: e1001272). The position offers the opportunity to conduct research in an attractive, dynamic research environment with outstanding resources. Candidates must have a Ph.D. with a background in bacterial genetics, gene regulation, bacterial pathogenesis, and molecular biology. Experience in spirochetology, animal models, and/or tick biology is a plus. *UT Southwestern Medical Center is an Equal Opportunity/Affirmative Action Employer.* Please send a curriculum vitae and three letters of recommendation to:

Michael V. Norgard, Ph.D.
Chair, Dept. of Microbiology
U.T. Southwestern Medical Center
6000 Harry Hines Blvd.
Dallas, TX 75390-9048
michael.norgard@utsouthwestern.edu

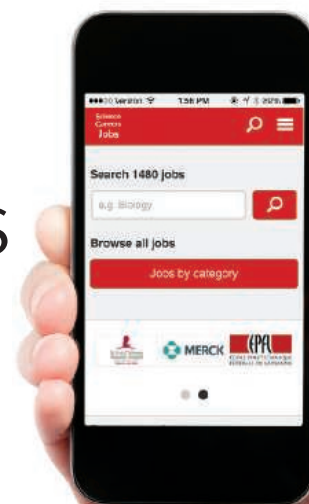
POSTDOCTORAL FELLOWSHIP POSITION

Available at the University of Chicago Institute for Cardiovascular Research. We study molecular mechanisms of arrhythmias and seek a talented candidate (Ph.D. and/or M.D.) with a strong background in electrophysiology, cardiovascular research, metabolism, cell/mitochondrial biology, patch clamp and ion channels. Please submit your application including CV to Cevher Ozcan, M.D., University of Chicago Medicine/Cardiology, 5841 S. Maryland Ave., MC6080, Chicago, IL 60637, E-mail: cozcan@medicine.bsd.uchicago.edu

Download the Science Careers Job App

SEARCH JOBS ON THE GO!

apps.sciencemag.org



Jinan University

An International University Seeking to Grow

In pursuing its goal of becoming a high-level university, Jinan University (JNU) is continuously seeking to attract top-class researchers to greatly enhance the competitiveness of research conducted at the university. It will recruit young researchers from China and overseas through the Thousand Talents Plan. New researchers will be provided with support and training.



暨南大學
JINAN UNIVERSITY

About Jinan University

Jinan University is one of China's "One Hundred Key Universities of 21st Century" (the "211 Project") and is operated under the leadership of the Overseas Chinese Affairs Office of State Council. As the first university established by the state for overseas Chinese students, JNU currently has the largest number of overseas and foreign students and is honored as the "top university for overseas Chinese". Abiding by the motto of "loyalty, sincerity, integrity and respect", the university is committed to cultivating talents with the excellent traditional Chinese moralities and culture. In June 2015, JNU was selected into the "High-level University Construction Program" by Guangdong provincial government. The University has 27 colleges, comprising 62 departments, 188 research institutions, 77 laboratories and offering 89 undergraduate majors, 189 master degree programs in 38 Level-I and 5 Level-II disciplines as well as 74 doctoral degree programs in 15 Level-I and 4 Level-II disciplines. Besides, we have 4 national key disciplines (industrial economics, aquatic biology, finance and literary theory), 8 key disciplines at the level of the Overseas Chinese Affairs Office of the State Council, 20 provincial Level-I key disciplines, and 4 provincial Level-II key disciplines. The University has the following teaching and research bases: a key research base of national humanity & social sciences, a teaching & research base for Chinese language & literature of the Education Ministry, a base for national university cultural quality education, a national base for teaching Chinese as a foreign language, an educational base for overseas Chinese education of the Overseas Chinese Affairs Office of the State Council and a key research base of humanity & social science of Guangdong Province. It also has one national engineering center, 14 ministerial and provincial engineering centers and 13 key ministerial and provincial laboratories.

To achieve the goal of building a high-level university, JNU continues to implement the strategy of "strengthening universities with more talented people" in order to greatly enhance the core competitiveness of talent and sustainable development capacity and to further strengthen the support for the introduction and training of outstanding personnel. For this purpose, the university is now recruiting members or candidates of the "High-level Overseas Young Talents Program" (referred to as the Thousand Young Talents Program) from home and abroad.

Disciplines Open for Recruitment

Optical engineering, information and communication engineering, electronic science and technology, science of Chinese pharmacology, pharmacy, biology, biomedical engineering, ecology, environmental science and engineering, basic medicine, clinical medicine, integration of traditional Chinese and western medicine, traditional Chinese medicine, oral medicine, public health and preventive medicine, nursing, mechanics, cyberspace security, computer science and technology, software engineering, mathematics, chemistry, materials science and engineering, food science and engineering and physics.

Basic Requirements

1. Members of the "Thousand Young Talents Program".
2. Candidates of the "Thousand Young Talents Program" (candidates of the discipline of finance not included). Applicants should meet the following requirements:

- (1) Applicants should consciously adhere to China's laws and regulations, and have good academic ethics;
- (2) Applicants whose research fields are in natural science and engineering technology should be under 40 years old (up to June 1, 2016, the same below);
- (3) Applicants should have acquired a doctoral degree, and have over three years' overseas research and working experience (not including working experience abroad with employment relations remained in China). Applicants who received a doctoral degree in China should not exceed the age limit of 40. Applicants who have received a doctoral degree abroad may be waived from the age limit of 40 if they have outstanding research performance and other great achievements. In such cases, a waiver letter with explanation and proofs is required.
- (4) Applicants should have a permanent teaching or research position in overseas universities, research institutions and enterprises of high prestige.
- (5) Generally, applicants should not have a full-time position in China at the time of application. However, if applicants are already holding a position in China, it should be less than one year that they returned from abroad.
- (6) Applicants should work full time in China once employed.
- (7) Applicants should be the top performers among their peers in the same research field and have potentials to become the leading persons of their field.

Package of Salary & Benefits

JNU will provide recruited members and candidates of "Thousand Young Talents Program" with a competitive package of salary and benefits based on the job position.

1. For members of "Thousand Young Talents Program"

- (1) Salary: no less than ¥500,000 per year (pre-tax).
- (2) Supporting funds for research: ¥1,000,000-3,000,000.
- (3) Housing/settling allowance: no less than ¥2,000,000 (pre-tax).
- (4) Recruited members will be directly employed as a senior professional.
- (5) Recruited members will have the priority to recruit PhD students, post-doctors and research assistants.
- (6) The university will provide applicants assistance in their children's entry into kindergarten, primary school and middle school in Guangzhou.
- (7) Members will enjoy the one-stop service for high-level talents.
- (8) The university will give priority to solve the job transfer of spouse of members.
- (9) Each new recruit is entitled to a central finance subsidy of ¥500,000 and a research fund ranging from ¥1,000,000 to ¥3,000,000, which, once ratified, will be allocated according to schedule. The Guangdong provincial finance will also grant the recruit a supportive fund by a ratio of 1.5:1 in accordance with the one granted by the central finance.

2. Candidates having successfully passed the university review process can sign an employment contract of intent, and apply for the "Thousand Young Talents Program" membership in the name of Jinan University. Candidates who have entered into the defense session are entitled to the following salary and benefits:

- (1) Salary: no less than ¥400,000 per year (pre-tax).
- (2) Supporting funds for research: no less than ¥1,000,000.
- (3) Housing/settling allowance: no less than ¥1,000,000 (pre-tax).
- (4) Recruited members will have the priority to recruit PhD students, post-doctors and research assistants.
- (5) The university will provide applicants assistance in their children's entry into kindergarten, primary school and middle school in Guangzhou.
- (6) Recruited members will enjoy the one-stop service for high-level talents.
- (7) If recruited members are enrolled into the "Thousand Talents Program", they are entitled to all the pay and benefits offered by the university to members of this program.

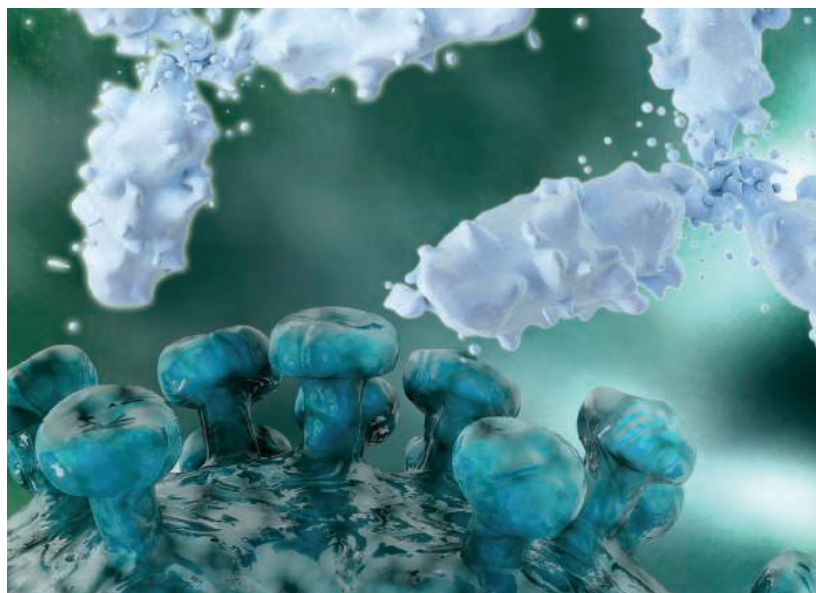
Materials to be Submitted for Application

- (1) One copy of CV;
- (2) A list of research projects, publications (please specify collection by SCI, EI, SSCI, CSSCI as well as journal impact factor and citation frequency) and award-winning achievements during recent 5 years;
- (3) A copy of academic certificate/diploma, certificate of all research projects, awards and patents;
- (4) The full text of five representative papers;
- (5) A Copy of certificate or credential of holding a position abroad or holding an important position in China;
- (6) A work and research plan after joining JNU.

This advertisement is valid permanently. Electronic copies of all the above-mentioned materials are also required at the time of application. Please send them to the official email: otalents@jnu.edu.cn.

Contact Information

Home page of Personnel Department, Jinan University
(<http://personal.jnu.edu.cn/>)
Tel: 0086-20-85227283 (fax available), 0086-20-85223525
Contacts: Mr. Tong, Mr. Liu
Email: otalents@jnu.edu.cn
Address: No. 601, Huangpu Avenue West, Guangzhou, Guangdong, PRC
Post Code: 510632



For recruitment in science, there's only one *Science*.

Special Job Focus:

Immunology

Issue date: May 6

Ads accepted until April 29
if space allows

What makes *Science* the best choice?

- Read and respected by 400,00 readers around the globe
- 75% of readers read *Science* more often than any other journal
- Your ad dollars support AAAS and its programs, which strengthens the global scientific community.

Why choose this Immunology Focus for your advertisement?

- Relevant ads lead off the career section with special immunology banner
- Bonus distribution to Immunology 2016 (AAI), May 13–17, Seattle, WA.

Expand your exposure.

Post your print ad online to benefit from:

- Link on the job board homepage directly to immunology jobs
- Dedicated landing page for jobs in immunology
- Additional marketing driving relevant job seekers to the job board.

Deliver your message to a
global audience of targeted,
qualified scientists.

129,574

subscribers in print
every week

37,942

unique active job seekers
searching for **immunology**
positions in 2015

41,047

applications submitted
for **immunology** positions
in 2015



Produced by the *Science*/AAAS Custom Publishing Office.

SCIENCECAREERS.ORG

Science Careers

FROM THE JOURNAL SCIENCE  AAAS

To book your ad: advertise@sciencecareers.org

The Americas
+202 326 6582
Japan
+81 3 3219 5777

Europe/RoW
+44 (0) 1223 326500
China/Korea/Singapore/Taiwan
+86 186 0082 9345

CALL FOR NOMINATIONS:

Sanofi and the Institut Pasteur are pleased to announce the Sanofi - Institut Pasteur 2016 Awards.

These Awards will honor four scientists, whose outstanding research in the life sciences is contributing to progress in global public health, specifically in the following fields:

**TROPICAL
AND NEGLECTED
DISEASES**

IMMUNOLOGY

**DRUG
RESISTANCE**

NEUROSCIENCE

There will be three categories of awards:

- **One International Senior award**
(€ 150 000)
- **One International Mid-career award¹**
(€ 100 000)
- **Two National Junior awards²**
(€ 75 000 each)

More information and the nomination form are available on the website

www.sanofi-institutpasteur-awards.com

Deadline to submit nominations:
Tuesday, 14th June, 2016

Awards Ceremony:
Tuesday, 13th December, 2016

**SANOFI - INSTITUT PASTEUR
2016 AWARDS**
€ 400 000
FOR BIOMEDICAL RESEARCH

**INSPIRED BY INSTITUT PASTEUR
SUPPORTED BY SANOFI**

A distinguished international Jury will choose the Awardees:

Prof. Peter C Agre, Prof. Elizabeth H. Blackburn, Prof. Pascale Cossart, Prof. Catherine Dulac, Prof. Alain Fischer, Prof. Jörg H. Hacker, Prof. Jules A. Hoffmann, Dr Gary J. Nabel, Prof. Staffan Normark, Prof. Jeffrey V. Ravetch and Prof. Philippe Sansonetti.

Contact: 2016awards@pasteur.fr

¹The candidates should not be more than 52 years old on 1-7-2016 - ²The candidates should not be more than 45 years old on 1-7-2016 and should work in France



www.sanofi-institutpasteur-awards.com



POSITIONS OPEN



**FRED HUTCHINSON
CANCER RESEARCH CENTER**

GASTROENTEROLOGY CLINICIAN-SCHOLAR POSITION AT THE FRED HUTCHINSON CANCER RESEARCH CENTER AND THE UNIVERSITY OF WASHINGTON

The Fred Hutchinson Cancer Research Center (FHCRC) and the University of Washington (UW) Department of Medicine are jointly recruiting a full-time faculty member at the Assistant, Associate, or Full Member level and at the Assistant (0113), Associate (0112) or Full Professor (0111) level without tenure due to funding (WOT), on the Clinician-Scholar/Clinician-Teacher pathway in the Clinical Research Division of the FHCRC and the Division of Gastroenterology of the Department of Medicine at the UW (12-month, multi-year appointments). The faculty member will be an active member of the Gastroenterology/Hepatology Consult Team and GI Cancer Prevention Program at the Seattle Cancer Care Alliance. The applicant is also expected to engage in active clinical research related to gastrointestinal complications of cancer and/or stem cell transplantation, or GI cancers. Candidates must demonstrate a track record of scholarly activities and excellence in clinical care. This role provides the opportunity for 50% patient care.

The primary appointment will be in the Clinical Research Division of the FHCRC, with a joint appointment in the Department of Medicine at the University of Washington. Applicants must have an MD (or foreign equivalent) with board certification in Gastroenterology (or foreign equivalent). In order to be eligible for sponsorship for an H-1B visa, graduates of foreign (non-U.S.) medical schools must show successful completion of all three steps of the U.S. Medical Licensing Exam (USMLE), or equivalent as determined by the Secretary of Health and Human Services. Fred Hutch and University of Washington faculty engage in teaching, research and service. Patient interaction will be

Interested candidates should submit a *curriculum vitae*, three references, and a letter summarizing research goals and career plans to: **David Hockenbery** at www.fredhutch.org/job/7341.

The Fred Hutchinson Cancer Research Center and the University of Washington are Affirmative Action, Equal Opportunity Employers. All qualified applicants will receive consideration for employment without regard to race, color, religion, sex, sexual orientation, gender identity, national origin, age, protected veteran or disabled status, or genetic information.



**FRED HUTCHINSON
CANCER RESEARCH CENTER**

GASTROENTEROLOGY PHYSICIAN/SCIENTIST POSITION AT THE FRED HUTCHINSON CANCER RESEARCH CENTER AND THE UNIVERSITY OF WASHINGTON

The Fred Hutchinson Cancer Research Center (FHCRC) and the University of Washington (UW) Department of Medicine are jointly recruiting a full-time faculty member at the Assistant, Associate, or Full Member level and at the Assistant (0113), Associate (0112) or Full Professor (0111) level without tenure due to funding (WOT), on the Physician/Scientist pathway in the Clinical Research Division of the FHCRC and the Division of Gastroenterology in the Department of Medicine at the UW (12-month, multi-year appointments). The successful candidate is expected to engage in active laboratory research in the fields of gastroenterology/hepatology (GI/liver oncology, mucosal immunology, gut microbiome or biology related to graft-vs.-host disease or sinusoidal obstruction syndrome). The faculty member will also participate in the care of patients with gastrointestinal/hepatic disease at the Seattle Cancer Care Alliance and the UW Medical Center. Candidates must demonstrate a track record of high quality peer-reviewed publications, and evidence of independent research and competitive funding potential.

The primary appointment will be in the Clinical Research Division of the FHCRC, with a joint appointment in the Department of Medicine at the University of Washington. Applicants must have an MD (or foreign equivalent) with board certification in Gastroenterology (or foreign equivalent). In order to be eligible for sponsorship for an H-1B visa, graduates of foreign (non-U.S.) medical schools must show successful completion of all three steps of the U.S. Medical Licensing Exam (USMLE), or equivalent as determined by the Secretary of Health and Human Services. Fred Hutch and University of Washington faculty engage in teaching, research and service.

Interested candidates should submit a *curriculum vitae*, three references, and a letter summarizing research goals and career plans to: **David Hockenbery** at www.fredhutch.org/job/7342.

The Fred Hutchinson Cancer Research Center and the University of Washington are Affirmative Action, Equal Opportunity Employers. All qualified applicants will receive consideration for employment without regard to race, color, religion, sex, sexual orientation, gender identity, national origin, age, protected veteran or disabled status, or genetic information.



For recruitment in science, there's only one *Science*.

Special Job Focus:

Biotechnology

Issue date: May 27

Book ad by May 10 to
guarantee space

Ads accepted until May 20
if space allows

What makes *Science* the best choice?

- Read and respected by 400,00 readers around the globe
- 75% of readers read *Science* more often than any other journal
- Your ad dollars support AAAS and its programs, which strengthens the global scientific community.

Why choose this Biotechnology Focus for your advertisement?

- Relevant ads lead off the career section with special biotechnology banner
- Bonus distributions:
BIO, June 6–9, San Francisco, CA
BIO Career Fair, June 9, San Francisco, CA.

Expand your exposure.

Post your print ad online to benefit from:

- Link on the job board homepage directly to biotechnology jobs
- Dedicated landing page for jobs in biotechnology
- Additional marketing driving relevant job seekers to the job board.

Deliver your message to a
global audience of targeted,
qualified scientists.

129,574

subscribers in print
every week

48,366

unique active job seekers
searching for **biotechnology**
positions in 2015

27,111

applications submitted for
biotechnology positions
in 2015



Produced by the *Science*/AAAS Custom Publishing Office.

SCIENCECAREERS.ORG

ScienceCareers

FROM THE JOURNAL SCIENCE AAAS

To book your ad: advertise@sciencecareers.org

The Americas
+202 326 6582
Japan
+81 3 3219 5777

Europe/RoW
+44 (0) 1223 326500
China/Korea/Singapore/Taiwan
+86 186 0082 9345

2017 VETLESEN PRIZE

ACHIEVEMENT IN THE EARTH SCIENCES

Call for Nominations



Nominations should be sent
prior to 1 August 2016 to:

Sean C. Solomon, Director
Lamont-Doherty Earth Observatory
PO Box 1000
61 Route 9W, Palisades, NY 10964
Tel: 845/365-8729

or via electronic submission to:
vetlesenprize@ldeo.columbia.edu

Lamont-Doherty Earth Observatory
COLUMBIA UNIVERSITY | EARTH INSTITUTE

The Vetlesen Prize, established in 1959 by the G. Unger Vetlesen Foundation, is awarded for scientific achievement that has resulted in a clearer understanding of the Earth, its history, or its relations to the universe. The prize consists of a medal and a cash award of \$250,000. Nominations are now open for the next prize, which will be awarded in 2017.

The prize is awarded to a single individual, who can reside and work anywhere in the world. The prize is administered by Columbia University's Lamont-Doherty Earth Observatory.

Nomination packages should include at least two letters that describe the nominee's contributions to a fuller understanding of the workings of our planet, along with a one-paragraph biographical sketch and the full curriculum vitae of the candidate.

For more information about the Vetlesen Prize:
<http://www.ldeo.columbia.edu/vetlesen-prize>

Past Vetlesen Laureates

- 2015 Stephen Sparks
- 2012 Susan Solomon, Jean Jouzel
- 2008 Walter Alvarez
- 2004 W. Richard Peltier, Sir Nicholas J. Shackleton
- 2000 W. Jason Morgan, Walter C. Pitman III, Lynn R. Sykes
- 1996 Robert E. Dickinson, John Imbrie
- 1993 Walter H. Munk
- 1987 Wallace S. Broecker, Harmon Craig
- 1981 M. King Hubbert
- 1978 J. Tuzo Wilson
- 1974 Chaim L. Pekeris
- 1973 William A. Fowler
- 1970 Allan V. Cox, Richard R. Doell, S. Keith Runcorn
- 1968 Francis Birch, Sir Edward Bullard
- 1966 Jan Hendrik Oort
- 1964 Pentti E. Eskola, Arthur Holmes
- 1962 Sir Harold Jeffreys, Felix Andries Vening Meinesz
- 1960 W. Maurice Ewing

POSITIONS OPEN



AAAS is here – helping scientists achieve career success.

Every month, over 400,000 students and scientists visit ScienceCareers.org in search of the information, advice, and opportunities they need to take the next step in their careers.

A complete career resource, free to the public, *Science Careers* offers hundreds of career development articles, webinars and downloadable booklets filled with practical advice, a community forum providing answers to career questions, and thousands of job listings in academia, government, and industry. As a AAAS member, your dues help AAAS make this service freely available to the scientific community. If you're not a member, join us. Together we can make a difference.

To learn more, visit aaas.org/plusyou/sciencecareers



**European
Environment
Agency**

Call for Expressions of Interest for experts to be appointed members of the Scientific Committee of the European Environment Agency (EEA)

Scope of the call

The EEA organises this call to appoint Scientific Committee members with expertise in one of the following areas as identified by the EEA Management Board:

Socio-technical systems, Socio-ecological systems, Sustainability, and Data.

Interested candidates are invited to look at the full vacancy notice published on the EEA website
<http://www.eea.europa.eu/about-us/governance/scientific-committee/call-for-expressions-of-interest-1>

Candidates must be nationals of one of the 33 EEA member countries.

Deadline for applications: **Friday 10 June 2016, 12.00 CET**

By He Fu

Growth can come in phases

Even though I work with microbes on a daily basis, I never thought I would relate to them in a personal way. Now, though, as I'm finishing up my Ph.D. and reflecting on my graduate school experience, I see an analogy between my own intellectual development as a scientist and the growth cycle of microbes when they are moved to a new environment. In both cases there are lag phases—periods in which there is little visible growth as the organisms adjust to their new surroundings—and growth phases once the organisms “learn” how to flourish. In retrospect I recognize that, for me as well as for the microbes, the seemingly unproductive lag phases, although sometimes discouraging, have been necessary preludes to the following growth phases.

My first lag phase occurred as I was transitioning from my early scientific training in China to my graduate program in the United States. In China, in addition to being taught the basics of lab techniques, I was instilled with the importance of the motto “publish or perish” and a magic number: the impact factor, which is widely accepted there as an objective, accurate measure for evaluating scientists. So I experienced great culture shock when I moved to the University of Illinois, Urbana-Champaign, for graduate school and learned that the impact factor is not as big a deal in the United States. “Then how do you evaluate scientists?” I asked one distinguished professor in my department, who is also involved in professor evaluation and promotion. “We read their papers,” he answered. “From the papers, we understand what problems they are tackling, how difficult they are, and what contributions they made to the field.” This was a revelation to me.

The lag phase continued for my first few semesters of grad school, as I continued to adjust to the transition from China to the United States and from undergraduate training to graduate research. I wasn't making great progress in lab, but the time wasn't wasted. As I conducted my research, read papers, and discussed science with my classmates and professors, I started to appreciate that science is a continuous process of making discoveries through methodical, incremental, and creative problem-solving. Publishing is important, of course, but I began to realize that it is only a piece of the process. I was slowly and steadily transformed, until I was finally ready to emerge from my lag phase.

My first growth phase occurred after I spent the first



“I expect that I will go through more cycles of lag and growth.”

year and a half of grad school on a project that ended up refuting the hypothesis my adviser and I had initially developed. After a brief moment of disappointment and frustration, I decided to persevere by testing a different idea. This new tack led to my first eureka moment and later crystallized into my first conference talk and first publication.

But after that, I found myself in another lag phase. For the last 2 years, I have struggled to generate enough biological material to follow up on my earlier work, and my morale has fallen. Meanwhile, to fulfill another part of the Ph.D. training requirement, I started teaching and therefore could not commit as much time to research as I wanted. Now,

though, after much troubleshooting, I finally have a handle on how to solve the problem that had been holding up my experiments, and I sense that a second growth phase is coming.

As I continue to encounter new situations and tackle new challenges, I expect that I will go through more cycles of lag and growth, and I hope that I will have the perspective and patience to appreciate the lag times as integral parts of my development. As for the many international students living in other countries to pursue your dreams of being scientists, if you are struggling, take heart from the fact that even microbes initially have a hard time when they are transferred into a new culture. ■

He Fu is a Ph.D. candidate in the Department of Microbiology at the University of Illinois, Urbana-Champaign. For more on life and careers, visit science.sciencecareers.org. Send your story to SciCareerEditor@aaas.org.



Growth can come in phases

He Fu (April 21, 2016)

Science Translational Medicine **352** (6284), 486. [doi:
10.1126/science.352.6284.486]

Editor's Summary

This copy is for your personal, non-commercial use only.

- | | |
|----------------------|--|
| Article Tools | Visit the online version of this article to access the personalization and article tools:
http://science.sciencemag.org/content/352/6284/486 |
| Permissions | Obtain information about reproducing this article:
http://www.sciencemag.org/about/permissions.dtl |

Science (print ISSN 0036-8075; online ISSN 1095-9203) is published weekly, except the last week in December, by the American Association for the Advancement of Science, 1200 New York Avenue NW, Washington, DC 20005. Copyright 2016 by the American Association for the Advancement of Science; all rights reserved. The title *Science* is a registered trademark of AAAS.